

ISSN 2189-7093
PRINT ISSN 0919-1038

KURRI

Progress Report

2017

*Institute for Integrated Radiation and Nuclear Science,
Kyoto University*

KURRI Progress Report 2017

APRIL 2017 – MARCH 2018

Published by
Institute for Integrated Radiation and Nuclear Science,
Kyoto University,
Kumatori-cho, Sennan-gun, Osaka 590-0494 Japan

We are pleased that after the extended shutdown since 2014, KUCA restarted on 20th June 2017 and KUR on 29th August 2017. We thank our users for their patience.

Additionally, we began Joint Research 2018 under our new name – Institute for Integrated Radiation and Nuclear Science, Kyoto University (KURNS). Therefore, this is our last report as Research Reactor Institute. Since 1963, our users have comprehensively cultivated their research networks in conjunction with our history; their substantial passion for research has developed the Institute considerably. We will continue to play a distinctive role as a Joint Usage/Research Center, promoting an extensive range of studies from fundamental to applied research with research reactors and accelerators.

It was reassuring to note that the number of applications for Joint Research increased although the reactors had suspended operations for several years. We are proud since this demonstrates that researchers and students support our activity, which endorses our facilities as indispensable tools in their research activities with quantum beam and radioisotope.

Having cultivated a cross-academic community in our institute, we can provide scientists unexpected and unpredictable new fields and applications, thus engendering interdisciplinary research. KURNS' integrated innovation strategy seeks to promote new academic fields through human recourse in our field.

We strive for safe and stable operations for nationwide use, making it our primary mission to provide scientists the opportunity to conduct research. We are happy to dedicate our support to enable users conduct significant interdisciplinary research at KURNS.

June 2018
Yuji Kawabata
Director, KURNS

CONTENTS

I. ANNUAL SUMMARY OF EXPERIMENTAL RESEARCH ACTIVITIES	1
I-1. PROJECT RESEARCHES	2
Project 1 Analyzing Tumor Microenvironment and Exploiting its Characteristics in Search of Optimizing Cancer Therapy Including Neutron Capture Therapy Si. Masunaga (29P1)	3
PR1-1 Estimation of Therapeutic Efficacy of BCNT Based on the Intra- and Intercellular Heterogeneity in ^{10}B Distribution T. Sato and S. Masunga (29P1-1)	4
PR1-2 Design, Synthesis and Biological Evaluation of Pepducin-BSH Conjugates for BNCT A. Isono <i>et al.</i> (29P1-2)	5
PR1-3 HIF-1 Maintains a Functional Relationship between Pancreatic Cancer Cells and Stromal Fibroblasts by Upregulating Expression and Secretion of Sonic Hedgehog M. Kobayashi <i>et al.</i> (29P1-3)	6
PR1-4 Selective Accumulation of Boron-conjugated Liposomes Composed of Dimyristoylphosphatidylcholine to B16F10 Murine Dimyristoylphosphatidylcholine to B16F10 Murine Melanoma Cells in Relation to Fluidity of Cell Membranes S. Kasaoka <i>et al.</i> (29P1-5)	7
PR1-5 The Response of Cancer Cells after BNCR L. Chen <i>et al.</i> (29P1-9)	8
PR1-6 Radiobiological Effect of Extracellular Boron Distribution and Neutron Irradiation K. Nakai <i>et al.</i> (29P1-10)	9
PR1-7 Multilateral Approach toward Realization of Next Generation Boron Neutron Capture Therapy Y. Matsumoto <i>et al.</i> (29P1-11)	10
PR1-8 Attempts to Sensitize Tumor Cells by Exploiting the Tumor Microenvironment Y. Sanada and S. Masunaga (29P1-12)	11
Project 2 Production Mechanism of Radioactive Aerosols Released from Fukushima Daiichi Nuclear Power Plant K. Takamiya (29P2)	12
PR2-1 Effect of Solute on Attachment Behavior of Fission Product to Solution Aerosol Particle K. Takamiya <i>et al.</i> (29P2-1)	13
PR2-2 Particle Size Measurement of Radioactive Aerosol Particles in An Electron LINAC Using a Diffusion Battery System Y. Oki and N. Osada (29P2-2)	14
Project 3 Project Research on Development of Scattering Spectrometers Utilizing Small and Medium Class Neutron Source M. Sugiyama (29P3)	15
PR3-1 Determination of Degree of Deuteration Level of Deuterated Protein Through Small-angle Neutron Scattering R. Inoue <i>et al.</i> (29P3-1)	16
PR3-2 A SAXS Study on the Nanostructure of Gliadin Hydrates with Sodium Chloride N. Sato <i>et al.</i> (29P3-2)	17
PR3-3 Characterization of Nanostructure in Metallic Materials using Small-Angle Scattering Y. Oba <i>et al.</i> (29P3-3)	18
PR3-4 Nanostructure of Hydrated α -, γ -, ω -Gliadins R. Urade <i>et al.</i> (29P3-4)	19
PR3-5 Nano Structure of Metal Hydride by X-ray Small Angle Scattering K. Iwase <i>et al.</i> (29P3-6)	20
PR3-6 Radius of Gyration of Polymer for Viscosity Index Improver at Various Temperatures Evaluated by Small-Angle X-Ray Scattering T. Hirayama <i>et al.</i> (29P3-7)	21

Project 5	Project Research on a Study on Biological Character and Use of the Particle Induced by the Boron Neutron Capture Reaction	
	Y. Kinashi (29P5).....	22
PR5-1	Biological Effects of DNA Alkylating Agents on the Cell Lethal Effects of BNCR	
	Y. Kinashi <i>et al.</i> (29P5-1).....	23
Project 6	Improvement of Characterization Techniques in High-Energy-Particle Irradiation Research	
	A. Kinomura (29P6).....	24
PR6-1	Study on Efficient Use of Positron Moderation Materials	
	A. Kinomura <i>et al.</i> (29P6-1).....	25
PR6-2	Electron-Irradiation Effects on Diffusion Coefficient of Cu in Fe Studied by Three Dimensional Atom Probe	
	T. Toyama <i>et al.</i> (29P6-2).....	26
PR6-3	Change in Positron Annihilation Lifetime of Vacancies by Hydrogen Charging in Tungsten	
	K. Sato <i>et al.</i> (29P6-3).....	27
PR6-4	Gamma-ray Irradiation Effect on ZnO Bulk Single Crystal	
	K. Kuriyama <i>et al.</i> (29P6-4).....	28
PR6-5	Establishment of Technique for Thermal Diffusivity Measurement using TEM Disk Size Miniature Test Specimens for Post-irradiation Experiments	
	M. Akiyoshi <i>et al.</i> (29P6-5).....	29
PR6-6	Positron Annihilation Study of Fe-Cr binary alloy after Electron Irradiation	
	T. Onitsuka <i>et al.</i> (29P6-6).....	30
PR6-7	Study on Free Volume in Diamond-like Carbon Thin Films by Positron Annihilation Spectroscopy	
	K. Kanda <i>et al.</i> (29P6-7).....	31
PR6-8	Thermal Stability of Diamond-like Carbon Films	
	S. Nakao <i>et al.</i> (29P6-8).....	32
Project 7	Development on Neutron Imaging Application	
	Y. Saito (29P7).....	33
PR7-1	Dynamic Observation of Two-Phase Flow using Neutron Radiography	
	Y. Saito and D. Ito (29P7-1).....	34
PR7-2	Visualization and Measurement of Boiling Flow Behaviors in Parallel Mini-channel Heat Exchanger	
	H. Asano <i>et al.</i> (29P7-2, P7-3).....	35
PR7-3	Flow Visualization of Heavy Oil in Packed Bed Reactor by Neutron Radiography	
	T. Tsukada <i>et al.</i> (29P7-4).....	36
PR7-4	Trial Measurement of Void Fraction in Boiling Channel	
	H. Umekawa <i>et al.</i> (29P7-5).....	37
PR7-5	Estimation of the Frost Formation on the Heat Exchanger by Using Neutron Radiography	
	R. Matsumoto <i>et al.</i> (29P7-6).....	38
PR7-6	Study on the Visualization of Organic Matter between Metals in order to Contribute to the Advancement of the Industrial Products	
	K. Hirota <i>et al.</i> (29P7-12).....	39
PR7-7	On the Luminescence of Helium Excimer Clusters Via Neutron-3He Absorption Reaction	
	Y. Tsuji <i>et al.</i> (29P7-13).....	40
PR7-8	Development of Capillary-Plate-Based Fluorescent Plates	
	T. Sakai <i>et al.</i> (29P7-14).....	41
Project 8	Project Research on Nuclear Spectroscopy and Condensed Matter Physics Using Short-Lived Nuclei	
	Y. Ohkubo (29P8).....	42
PR8-1	Isomer Search for Fission Products around A=150 with Energy-sum γ -ray Spectrometry	
	M. Shibata <i>et al.</i> (29P8-2).....	43
PR8-2	Compton Polarimeter for β -delayed γ Rays Using Clover Detector	
	S. Ohno <i>et al.</i> (29P8-3).....	44

PR8-3	Nuclear Spin Relaxation of ^{111}Cd at the A Site in a Spinel Oxide CdIn_2O_4 W. Sato <i>et al.</i> (29P8-5)	45
PR8-4	Observation of Local Fields at the $^{111}\text{Cd}(\leftarrow^{111\text{m}}\text{Cd})$ Sites in Cadmium Titanate S. Komatsuda <i>et al.</i> (29P8-6)	46
Project 9	Project Research of Accelerator-Driven System with Spallation Neutrons at Kyoto University Critical Assembly C. H. Pyeon (29P9)	47
PR9-1	Subcriticality Monitoring for a Reactor System Driven by Spallation Source K. Hashimoto <i>et al.</i> (29P9-1)	48
PR9-2	Basic Study of Beam Transient on Accelerator-Driven System with Spallation Neutron Source N. Aizawa <i>et al.</i> (29P9-2)	49
PR9-3	Measurement of MA Reaction Rates Using Spallation Neutron Source A. Oizumi <i>et al.</i> (29P9-3)	50
PR9-4	Irradiation Experiments of ^{237}Np and ^{241}Am Capture and Fission Reactions in Critical Core W. F. G van Rooijen <i>et al.</i> (29P9-4)	51
PR9-5	Development of Real-time Subcriticality Monitor K. Watanabe (29P9-5)	52
PR9-6	Neutronics of Accelerator-Driven System with Spallation Neutrons C. H. Pyeon and M. Yamanaka (29P9-6)	53
Project 10	Preclinical Study for Development of New Drug for NCT M. Suzuki (29P10)	54
PR10-1	The Synthesis and Biological Evaluation of Fluorescein-Tagged 1-methyl-o-carborane for Boron Neutron Capture Therapy L. Kuzmanic <i>et al.</i> (29P10-1)	55
PR10-2	New Self-assembling Peptide Drug Delivery System with BSH against Human Glioblastoma Cell in BNCT H. Michiue <i>et al.</i> (29P10-2)	56
PR10-3	Functionalization of Hexagonal Boron Nitride Nanosheet with Polyglycerol and its Biomedical Application M. Kyouhei and K. Naoki (29P10-3)	57
PR10-4	Exploring the Use of the Chicken Egg CAM Assay as an Animal Model for BNCT K. Matsumoto <i>et al.</i> (29P10-4)	58
PR10-5	Next Generation A (Aomori) - Research and Development of Novel Boron Drugs in BNCT Therapy S. Ishiyama <i>et al.</i> (29P10-5)	59
PR10-6	Spherical Particle Fabrication of Boron-Iron Complex Material for BNCT Agent with Magnetic Property Y. Ishikawa <i>et al.</i> (29P10-6)	60
PR10-7	Gadolinium-loaded Chitosan Nanoparticles for Neutron Capture Therapy of Cancer: Influence of Particle Size on Tumor-killing Effect <i>in vitro</i> T. Andoh <i>et al.</i> (29P10-7)	61
PR10-8	Evaluation of Boron Neutron Capture Therapy Using Tumor Model Rats or Mice T. Kanematsu <i>et al.</i> (29P10-8)	62
PR10-9	Development of S-Alkylthiododecaborate Containing Amino Acids for BNCT Y. Hattori <i>et al.</i> (29P10-9)	63
PR10-10	<i>In vivo</i> Evaluation of Novel Boron-Containing Compounds for BNCT W. Kurosawa <i>et al.</i> (29P10-10)	64
PR10-11	Development of an Actively-Targeted, Phenylboronic Acid-Installed Nanoparticle Towards Next-Generation Boron Neutron Capture Therapy Y. Nagasaki <i>et al.</i> (29P10-11)	65
PR10-12	Design, Synthesis, and Evaluation of Glucose-type Boron Carriers for BNCT S. Aoki <i>et al.</i> (29P10-12)	66
PR10-13	Enhancing Therapeutic Potential of Boronophenylalanine Using Finely-tuned Poly (vinyl alcohol) T. Nomoto <i>et al.</i> (29P10-13)	67

PR10-14	Development of Boron Cluster Containing Water-Soluble Folate Derivatives As Novel Small Molecular Agents for BNCT H. Nakamura <i>et al.</i> (29P10-14).....	68
PR10-15	Evaluation of Novel Boron Liposome <i>in vivo</i> by Thermal Neutron Irradiation M. Shirakawa <i>et al.</i> (29P10-15).....	69
PR10-16	<i>In vivo</i> Anti-tumour Evaluation of new Boron-containing Compound BN2018 for BNCT R. Ubagai <i>et al.</i> (29P10-16).....	70
Project 11	Clinical Research on Explorations into New Application of BNCT M. Suzuki (29P11).....	71
PR11-1	Clinical Research on Explorations into New Application of BNCT M. Suzuki <i>et al.</i> (29P11-1).....	72
PR11-2	Pilot Study of Single Dose Toxicity Evaluation of ¹⁰ B ₅ H entrapped WOW emulsion on intra-arterial delivery in Pig for Neutron Capture Therapy to Hepatocellular Carcinoma H. Yanagie <i>et al.</i> (29P11-3).....	73
Project 12	Establishment of Integrated System for Dose Estimation in BNCT Y. Sakurai (29P12)	74
PR12-1	Establishment of Characterization Estimation Method in BNCT Irradiation Field using Bonner Sphere and Ionization Chamber Y. Sakurai <i>et al.</i> (29P12-1).....	75
PR12-2	Basic Study on New Type of Neutron Sptrometer for Epi-thermal Energy Region A. Uritani <i>et al.</i> (29P12-2).....	76
PR12-3	Improvement of SOF Detector System for Long-term Stability M. Ishikawa <i>et al.</i> (29P12-3)	77
PR12-4	Resopnse of a Commercial CsI Detector for the Self-activation Method in BNCT Field A. Nohtomi <i>et al.</i> (29P12-4).....	78
PR12-5	Neutron Beam Quality and dose Measurement of the Kyoto University Research Reactor Using Microdosimetric Technique N. Ko <i>et al.</i> (29P12-5).....	79
PR12-6	Study for Microdosimetry using Silicon-on-insulator Microdosimeter in the BNCT Irradiation Field Y. Sakurai <i>et al.</i> (29P12-6).....	80
PR12-7	Estimation of dose Resolution by Gel Detector for BNCT R. Maruta <i>et al.</i> (29P12-7).....	81
PR12-8	Study on the Development of Neutron Fluence Distribution Measurement Device using Thermoluminescence of the Ceramic Plates K. Shinsho <i>et al.</i> (29P12-8).....	82
PR12-9	The Study for Development and Application of Tissue Equivalent Neutron Dosimeter M. Oita <i>et al.</i> (29P12-9).....	83
PR12-10	Development and Evaluation of 3D Polymer Gel Dosimeter for the Measurement of dose Distribution in BNCT S. Hayashi <i>et al.</i> (29P12-10).....	84
PR12-11	Establishment of Beam-quality Estimation Method in BNCT Irradiation Field using Dual Phantom Technique Y. Sakurai <i>et al.</i> (29P12-11)	85
PR12-12	Development of Real-time dose Monitor Using Prompt Rays Imaging Detector for Boron Neutron Capture Therapy H. Tanaka <i>et al.</i> (29P12-12).....	86
PR12-13	Development of Novel Organic Scintillator for Fast Neutron and Its Evaluation in KUR S. Kurosawa <i>et al.</i> (29P10-13)	87
PR12-14	Patient-Position Monitoring System for BNCT Irradiation T. Tanaka <i>et al.</i> (29P12-14).....	88

I-2. COLLABORATION RESEARCHES	89
1. Slow Neutron Physics and Neutron Scattering	
CO1-1 Morphological Control in PS-b-PI-b-PDMS Triblock Copolymer by Mixed-Solvent M. Takenaka <i>et al.</i> (29002)	90
CO1-2 Oligomeric Structures of HSPB5 Variants M. Yohda <i>et al.</i> (29004)	91
CO1-3 Effect of Cancer Associated Histone Mutations in the Nucleosome Structure Y. Arimura <i>et al.</i> (29007)	92
CO1-4 Nanostructure in Ferromagnetic Au Nanoparticles T. Sato <i>et al.</i> (29015)	93
CO1-5 Development of Neutron Imager Based on Hole-type MPGD with Glass Capillary Plate F. Tokanai <i>et al.</i> (29055)	94
CO1-6 Current Status of B-3 Beam Port of KUR, 2017 K. Mori <i>et al.</i> (29063)	95
CO1-7 Study of the Properties of Water and the Physiological Activation Phenomena by using High-Intensity Pulsed Coherent Radiation S. Okuda <i>et al.</i> (29073)	96
CO1-8 First Neutron Focusing Test with a Couple of 900mm Long Ellipsoidal Supermirrors M. Hino <i>et al.</i> (29079)	97
CO1-9 Hydrogen Retention on Plasma Facing Material Irradiated by High Energy Particle Beam K. Tokunaga <i>et al.</i> (29096)	98
2. Nuclear Physics and Nuclear Data	
CO2-1 Study on Neutron Beam Pulse width Dependence in the Nuclear Fuel Measurement by the Neutron Resonance Transmission Analysis F. Kitatani <i>et al.</i> (29041)	99
CO2-2 Measurement of Doppler Effect by Small Accelerator Neutron Source (II) T. Sano <i>et al.</i> (29065)	100
CO2-3 Study on the Non-destructive Nuclide Assay for Nuclear Materials with a Self-indication Method J. Hori <i>et al.</i> (29066)	101
CO2-4 Development of Gamma Imager and Its Application to Identification of Nuclear Materials H. Tomita <i>et al.</i> (29068)	102
CO2-5 Measurements of Epithermal Neutron Detector with a Boron Loaded Plastic Scintillator T. Matsumoto <i>et al.</i> (29072)	103
CO2-6 Study of Isotope Separation via Chemical Exchange Reaction R. Hazama <i>et al.</i> (29099)	104
CO2-7 Reactivity Measurement of Accident Tolerant Control Rod Materials H. Ohta <i>et al.</i> (CA2908)	105
3. Reactor Physics and Reactor Engineering	
CO3-1 Basic Research for Sophistication of High-power Reactor Noise Analysis S. Hohara <i>et al.</i> (29093)	106
CO3-2 Irradiation Experiments of ²³⁷ Np and ²⁴¹ Am Foils for Fission Reactions by 14 MeV Neutrons G. Chiba <i>et al.</i> (CA2901)	107
CO3-3 Neutronics of U-Fueled and Pb-Zoned Core in Accelerator-Driven System C. H. Pyeon <i>et al.</i> (CA2902)	108
CO3-4 Subcriticality Measurement by Advanced Rossi- α Fitting in Accelerator-Driven System C. Kong <i>et al.</i> (CA2903)	109
CO3-5 Measurement of Bismuth Sample Reactivity Worth in A-core of KUCA for ADS M. Fukushima <i>et al.</i> (CA2904)	110

CO3-6	Measurement $^{238}\text{U}(n, \gamma)$ γ ray from Subcritical System Y. Nauchi <i>et al.</i> (CA2906)	111
CO3-7	Development of New Optical Fiber Type Neutron Detector for Reactor Physics Experiments K. Watanabe <i>et al.</i> (CA2907)	112
CO3-8	Measurement of Fundamental Characteristics of Nuclear Reactor at KUCA (II) Y. Kitamura <i>et al.</i> (CA2909)	113
CO3-9	Basic Nuclear Characteristic Measurements at Subcritical Core T. Misawa <i>et al.</i> (CA2910)	114
4. Material Science and Radiation Effects		
CO4-1	Effect on the Switch of the Helicity of Poly (quinoxaline-2,3-diyl)s: A Structural Analysis by Small-Angle X-ray Scattering Y. Nagata <i>et al.</i> (29001).....	115
CO4-2	Nanostructures in Semiconductor Nanocomposite Thin Films Y. Oba <i>et al.</i> (29009)	116
CO4-3	Measurement of Electron Emission Properties of Field Emitter Array under Gamma-ray Irradiation Y. Gotoh <i>et al.</i> (29014)	117
CO4-4	Evaluation of Unintentionally Doped Impurities in Silicon Carbide Substrates using Neutron Activation Analysis Technics T. Makino <i>et al.</i> (29026)	118
CO4-5	Spectrum of Amino Acid in the Millimeter-wave Region using a Diode Detector T. Takahashi (29028)	119
CO4-6	Correlation between Neutron Irradiation Damages and Hydrogen Isotope Retention Y. Oya <i>et al.</i> (29032)	120
CO4-7	Sub-THz Absorption Bands of Ionic Liquids T. Awano and T. Takahashi (29035).....	121
CO4-8	The Correlation between Microstructural Evolution and Mechanical Property Changes in Neutron-irradiated Vanadium Alloys K. Fukumoto <i>et al.</i> (29036)	122
CO4-9	Defects Structure of Electron Irradiated B2 Ordered Alloys F. Hori <i>et al.</i> (29039).....	123
CO4-10	Synthesis of Multi-component Metal Nanoparticles by γ -ray Irradiation Reduction Method F. Hori <i>et al.</i> (29040).....	124
CO4-11	Radioactivation of Accident Tolerant Control Rod Materials H. Ohta <i>et al.</i> (29042).....	125
CO4-12	Neutron Irradiation Effect of High-density MoO_3 Pellets for Mo-99 Production Y. Suzuki <i>et al.</i> (29047).....	126
CO4-13	Research on Resonance Frequency Variation as Function of Exposure Radiation Dose M. Kobayashi <i>et al.</i> (29050)	127
CO4-14	Selection of Borosilicate Glass Composition for Neutron Irradiation Test T. Nagai <i>et al.</i> (29056)	128
CO4-15	Formation of Nano-porous Structures on Whole Surface of Ge Wafer by High-energy Ion Irradiation J. Yanagisawa <i>et al.</i> (29061).....	129
CO4-16	Development of ^{57}Co Mössbauer Source using KURRI-LINAC Y. Kobayashi <i>et al.</i> (29082)	130
CO4-17	Electrolytic Reduction of Calcium Oxide in CaCl_2 -KCl Molten Salt Using Liquid Tin Cathode H. Sekimoto <i>et al.</i> (29088)	131
CO4-18	Development of Mössbauer Spectroscopy for Various Isotopes S. Kitao <i>et al.</i> (29089).....	132
CO4-19	^{197}Au Mössbauer Study of Au Acetylides Y. Kobayashi <i>et al.</i> (29091)	133

CO4-20	Complex Structure of Ions Coordinated with Hydrophilic Polymer 18. Application for Metaric Plating on Resin Surface (2) A. Kawaguchi and Y. Morimoto (29097).....	134
CO4-21	Study on Metal Surface Wettability Enhanced by Radiation Induced Surface Activation T. Hazuku <i>et al.</i> (29098).....	135
CO4-22	Characterization of Heterogeneous Nanostructures Formed in Stainless Steel using Small-Angle Scattering Y. Todaka <i>et al.</i> (29101).....	136
CO4-23	Research on Spin Density Wave in Mixed Anion Layered compounds, Sr ₂ VFeAsO _{3-δ} Y. Tojo <i>et al.</i> (29105).....	137
CO4-24	Vacancy Migration Behavior in a CoCrFeMnNi High Entropy Alloy K. Sugita <i>et al.</i> (29106).....	138
CO4-25	Positron Age-MOmentum Correlation (AMOC) Measurements on Gamma-ray Irradiated Polystyrene H. Tsuchida <i>et al.</i> (29108).....	139
CO4-26	Establishment of Mössbauer Spectroscopy on Rare Earth Er H. Yokota <i>et al.</i> (29138).....	140
CO4-27	Dose Response and Mechanism of Radiophotoluminescence Phenomenon Induced by γ -ray Irradiation in Cu-doped Glass R. Hashikawa <i>et al.</i> (29140).....	141

5. Geochemistry and Environmental Science

CO5-1	INAA and Ar-Ar Dating for Small Extraterrestrial Materials R. Okazaki and S. Sekimoto (29008).....	142
CO5-2	Volcanic and Tectonic History of Intra-oceanic Island Arc Revealed by ⁴⁰ Ar/ ³⁹ Ar Dating Technique O. Ishizuka <i>et al.</i> (29011).....	143
CO5-3	I-Xe Age of a Brecciated Meteorite, NWA2139 H. Sumino <i>et al.</i> (29024).....	144
CO5-4	Clear Descent of Antimony(Sb) Concentration in Atmospheric Aerosol Observed at Sakai, Osaka from 1995 to 2017 N. Ito <i>et al.</i> (29031).....	145
CO5-5	A Study on the Sedimentary Environment of Tokyo-Bay Sediments under Hypoxia Using Instrumental Neutron Activation Analysis M. Matsuo <i>et al.</i> (29034).....	146
CO5-6	Ionic Exchange of Tritium in Water and Hydrogen in Hydroxides H. Hashizume <i>et al.</i> (29044).....	147
CO5-7	Determination of Abundance of Rare Metal Elements in Seafloor Hydrothermal Ore Deposits by INAA Techniques-4: Evaluation of Analytical Accuracy J. Ishibashi <i>et al.</i> (29064).....	148
CO5-8	Ar-Ar Determinations of Petit-spot Submarine Volcanoes N. Hirano <i>et al.</i> (29067).....	149
CO5-9	Basic Study on Radiation-induced Luminescence from Natural Mineral H. Fujita <i>et al.</i> (29070).....	150
CO5-10	Trace Amounts of Halogens (Cl, Br and I) in Andesite and Basalt Reference Materials S. Sekimoto <i>et al.</i> (29076).....	151
CO5-11	Application of Neutron Activation Analysis to Micro Gram Scale of Solid Samples S. Sekimoto <i>et al.</i> (29077).....	152
CO5-12	Comparison of Extractable Organochlorine and Organobromine Speciated by Molecular Weight in Various Environmental Matirices K. Mukai <i>et al.</i> (29085).....	153
CO5-13	Chemical Compositions of Chromitite Reference Materials (CHR-Bkg and CHR-Pt+) N. Shirai <i>et al.</i> (29087).....	154
CO5-14	Fission Track Dating and Thermal History of Hydrothermally Altered Rock Sample H. Ohira and A. Takasu (29095).....	155

CO5-15	Thermal History of Precambrian Metamorphic Rocks H. Hyodo <i>et al.</i> (29112)	156
CO5-16	Applicability Verification of Isotopic Analysis of Cs by TIMS Y. Shibahara <i>et al.</i> (29115)	157
CO5-17	Characteristics of Calcite Thermoluminescence and Its Use for Age Estimate N. Hasebe <i>et al.</i> (29136)	158
CO5-18	Studies on the Binding Mechanism and Stoichiometry of Mercury Atoms in an Organomercury Lyase from Smearred Solution by an <i>in-cell</i> Radioactivation Analysis K. Takamiya and Y. Morimoto (29143)	159

6. Life Science and Medical Science

CO6-1	Structural Study for Higher Ordered Chromatin H. Kurumizawa and M. Sugiyama (29003)	160
CO6-2	Structural Study for the <i>S. pombe</i> Overlapping Dinucleosome M. Koyama <i>et al.</i> (29005)	161
CO6-3	Molecular Mechanism of the Interaction between Transcriptional Factors Sp1 and TAF4 E. Hibino <i>et al.</i> (29006)	162
CO6-4	Study of Localization Estimation of Abasic Sites in DNA Exposed to Radiomimetic Chemicals and ⁶⁰ Co γ -rays K. Akamatsu <i>et al.</i> (29010)	163
CO6-5	SAXS Study on the Structure of Prefibrillar Intermediates for the Formation of Insulin B Chain Amyloid Fibrils N. Yamamoto <i>et al.</i> (29012)	164
CO6-6	Possible Involvement of Aspartyl L-to-D Isomerization of Cell Adhesion Molecule-1 Shedding Products in Neurodegeneration A. Ito and N. Fujii (29019)	165
CO6-7	Structural Characterization of Circadian Clock Potein Complexes H. Yagi <i>et al.</i> (29022)	166
CO6-8	Measurement of Trancemittance Spectra of a Humann Calcificated Aorta Tissue in the Sub-Terahertz Region N. Miyoshi and T. Takahashi. (29029)	167
CO6-9	Study of the Radioresistance Mechanisms of Radioresistant Bacteria T. Saito <i>et al.</i> (29048)	168
CO6-10	Conformational Characterization of Archaeral Homolog of Proteasome-assembly Chaperone PbaA M. Yagi-Utsumi <i>et al.</i> (29054)	169
CO6-11	Dynanic Light Scattering of Ribonuclease A S. Fujiwara <i>et al.</i> (29059)	170
CO6-12	Characterization of Conformational Deformation-coupled Interaction between Immunoglobulin G1 Fc Glycoprotein and a Low-affinity Fcg Receptor S. Yanaka <i>et al.</i> (29062)	171
CO6-13	ATP-dependent Solution Structure of Multi-domain Protein, MurD H. Nakagawa <i>et al.</i> (29074)	172
CO6-14	Production of Medical Radioisotopes Using Electron Linear Accelerator S. Sekimoto and T. Ohtsuki (29078)	173
CO6-15	Chatacterization of Resonance Hybrid of Fe-bound Oxygen in Myoglobin K. Hasegawa <i>et al.</i> (29084)	174
CO6-16	Potential of Boron Neutron Capture Therapy (BNCT) for Metastatic Bone: study with Human Breast Cancer-bearing Animal Model T. Fujimoto <i>et al.</i> (29125)	175
CO6-17	Preparation of F1Fo-ATP Synthase as a Whole Body Complex from Bovine Heart for Structural Analysis by Cryo-electron Microscopy and X-ray Crystallography C. Jiko <i>et al.</i> (29142)	176

7. Neutron Capture Therapy

CO7-1	A Trial Experiment for Establishment of Material Data Base for Low Activation Design Method by Neutron Activation Analysis with KUR K. Kimura <i>et al.</i> (29043)	177
CO7-2	The Feasibility Study of Eu:LiCaF Neutron Detector for an Accelerator-based BNCT D. Nio <i>et al.</i> (29058)	178
CO7-3	Development of <i>closo</i> -Dodecaborate-Conjugated Serum Albumins as Novel Boron Delivery Carriers to Tumor for BNCT N. Nakamura <i>et al.</i> (29121)	179
CO7-4	<i>In vivo</i> Biodistribution Study of new Boron-containing Compound BN2017 for BNCT R. Ubagaki <i>et al.</i> (29122)	180
CO7-5	Severe Adversed Effects after BNCT N. Kamitani <i>et al.</i> (29127)	181
CO7-6	Boron Neutron Capture Therapy Combined with Early Successive Bevacizumab Treatments for Recurrent Malignant S.I. Miyatake <i>et al.</i> (29129)	182
CO7-7	Research on Pretreatment or Concomitant Drug to Augment Therapeutic Effect of BPA-BNCT M. Suzuki and H. Tanaka (29130)	183
CO7-8	The Effect of Boron Neutron Capture Therapy (BNCT) on Normal Tissues or Organs in Mice M. Suzuki <i>et al.</i> (29131)	184

8. Neutron Radiography and Radiation Application

CO8-1	Research and Development of a Neutron Two-dimensional Position Sensitive Detector System S. Satoh <i>et al.</i> (29051)	185
CO8-2	Multi-element Analysis of Cultivated Oysters by Neutron Activation Analysis M. Fukushima <i>et al.</i> (29057)	186
CO8-3	First Result of Neutron Imaging at Reactor with Neutron Flat Panel Detector T. Fujiwara and H. Hino (29081)	187
CO8-4	Development of Neutron Source and Neutron Detector for Non-destructive Assay of Nuclear Materials Y. Takahashi <i>et al.</i> (29109)	188
CO8-5	Integral Test for the Development of Nondestructive Methods Adopted for Integrity Test of Next Generation Nuclear Fuels (N-DeMAIN) K. Nakajima <i>et al.</i> (29120)	189

9. TRU and Nuclear Chemistry

CO9-1	Potentiometric Titration of Gamma-irradiated Natural Organic Matter T. Sasaki <i>et al.</i> (29017)	190
CO9-2	Solubility of Uranium(IV) in the Presence of Isosaccharinic Acid T. Kobayashi <i>et al.</i> (29018)	191
CO9-3	Electronic Absorption Spectra of Tellurium in LiCl-KCl Eutectic Melt Y. Sakamura <i>et al.</i> (29020)	192
CO9-4	Solvent Extraction of Uranium(VI) from Concentrated Calcium Chloride to Organic Solution A. Uehara <i>et al.</i> (29037)	193
CO9-5	Research on The Behavior of Actinides and FPs in Fuel Debris N. Sato <i>et al.</i> (29071)	194

CO9-6	Search for the Vacuum Ultraviolet Photons from ^{229m}Th Reacted with HF Gas Y. Yasuda <i>et al.</i> (29090)	195
CO9-7	Investigation of Coprecipitation with Sm Hydroxide Using KUR Multitracer Y. Kasamatsu <i>et al.</i> (29092)	196
CO9-8	Effect of γ -Ray Irradiation in HNO_3 on Adsorptivity of Long-Chain Cyclic Monoamide Resin M. Nogami <i>et al.</i> (29094)	197
CO9-9	Electrochemical Behavior of Zirconium in Molten Chloride Coexisting Fluoride and Oxide to Develop Processing Nuclear Fuel Debris T. Emori <i>et al.</i> (29102)	198
10. Health Physics and Waste Management		
CO10-1	Estimation Method of Elution Ratio of Radioactive Cs from Incineration Ash with Soil M. Yoneda <i>et al.</i> (29060)	199
CO10-2	Ethnographic Study of Radiation Regulation for Victims Living in a Low Dose Radiation Field post National Decontamination Act in Fukushima M. Takagaki <i>et al.</i> (29104)	200
12. Others		
CO12-1	Profile measurements of Coherent Cherenkov Radiation Matched to the Circular Plane at KURNS-LINAC N. Sei and T. Takahashi (29013)	201
CO12-2	Site Preference of M1/M2 Site of Fe in Pyroxene Structure by Mössbauer Microspectroscopy K. Shinoda and Y. Kobayashi (29023)	202
CO12-3	Instrumental Neutron Activation Analysis of Cl, Br, and I in High Purity Titanium Metal T. Miura <i>et al.</i> (29025)	203
CO12-4	Isotope Dilution-Neutron Activation Analysis on Hafnium Oxide Films T. Takatsuka <i>et al.</i> (29030)	204
CO12-5	The Sturucutre of the DN-polymers under Different Temperature and Humidity T. Tominaga <i>et al.</i> (29033)	205
CO12-6	Electron Induced Noise on Avaranche Photodiode for Ganymede Laser Altimeter of Jovian Icy Satellite Exploerer. M. Kobayashi <i>et al.</i> (29052)	206
CO12-7	Beam Test of a Micro-cell MWPC for a Muon-electron Conversion Search Experiment, DeeMe M. Aoki <i>et al.</i> (29080)	207
CO12-8	Influence of Submerged Condition and Soil on the Cadmium and Arsenic Concentration of Brown Rice T. Inamura <i>et al.</i> (29086)	208
CO12-9	Production and Purification of ^{43}K and ^{136}Cs T. Kubota <i>et al.</i> (29103)	209
CO12-10	Evaluation of SEE tolerance for On-board Computer used in Lean Satellite by using ^{252}Cf H. Masui <i>et al.</i> (29111)	210
CO12-11	Growth of Adsorbed Additive Layer for Further Friction Reduction Confirmed by Multi-Analytical Methods Including Neutron Reflectometry T. Hirayama <i>et al.</i> (29113)	211
CO12-12	Morphorogy Analysis of Precipitates in Cu Alloys with SAXS Measurement T. Miyazawa and Y. Tanaka (29114)	212
CO12-13	Biophysical Studies of <i>Bacillus subtilis natto</i> Y. Yanagisawa <i>et al.</i> (29117)	213
II. PUBLICATION LIST (April 2017 – March 2018)		214

ANNUAL SUMMARY OF EXPERIMENTAL RESEARCH ACTIVITIES

I-1. PROJECT RESEARCHES

PR1 Analyzing Tumor Microenvironment and Exploiting its Characteristics in Search of Optimizing Cancer Therapy Including Neutron Capture Therapy

Si. Masunaga

Particle Radiation Biology, Division of Radiation Life Science, Research Reactor Institute, Kyoto University

BACKGROUNDS AND PURPOSES: Human solid tumors contain moderately large fractions of quiescent (Q) tumor cells that are out of the cell cycle and stop cell division, but are viable compared with established experimental animal tumor cell lines. The presence of Q cells is probably due, in part, to hypoxia and the depletion of nutrition in the tumor core, which is another consequence of poor vascular supply. As a result, Q cells are viable and clonogenic, but stop cell division. In general, radiation and many DNA-damaging chemotherapeutic agents kill proliferating (P) tumor cells more efficiently than Q tumor cells, resulting in many clonogenic Q cells remaining following radiotherapy or chemotherapy. Therefore, it is harder to control Q tumor cells than to control P tumor cells, and many post-radiotherapy recurrent tumors result partly from the regrowth of Q tumor cells that could not be killed by radiotherapy. Similarly, sufficient doses of drugs cannot be distributed into Q tumor cells mainly due to heterogeneous and poor vascularity within solid tumors. Thus, one of the major causes of post-chemotherapy recurrent tumors is an insufficient dose distribution into the Q cell fractions.

With regard to boron neutron capture therapy (BNCT), with ^{10}B -compounds, boronophenylalanine- ^{10}B (BPA) increased the sensitivity of the total cells to a greater extent than mercaptoundecahydrododecaborate- ^{10}B (BSH). However, the sensitivity of Q cells treated with BPA was lower than that in BSH-treated Q cells. The difference in the sensitivity between the total and Q cells was greater with ^{10}B -compounds, especially with BPA. These findings concerning the difference in sensitivity, including other recovery and reoxygenation following neutron irradiation after ^{10}B -compound administration were mainly based on the fact that it is difficult to deliver a therapeutic amount of ^{10}B from ^{10}B -carriers throughout the target tumors, especially into intratumor hypoxic cells with low uptake capacities.

Hypoxia is suggested to enhance metastasis by increasing genetic instability. Acute, but not chronic, hypoxia was reported to increase the number of macroscopic metastases in mouse lungs. We recently reported the significance of the injection of an acute hypoxia-releasing agent, nicotinamide, into tumor-bearing mice as a combined treatment with γ -ray irradiation in terms of repressing lung metastasis. As the delivered total dose increased with irradiation, the number of macroscopic lung metastases decreased reflecting the decrease in the number of clonogenically viable tumor cells in the primary tumor. The metastasis-repressing effect achieved through a reduction in the number of clonogenic tumor cells by irradiation is much greater than that achieved by releasing tumor cells from acute hypoxia. On the other hand, more ^{10}B from BPA than from BSH could be distributed into the acute hypoxia-rich total tumor cell population, resulting in a greater decrease in the number of highly clonogenic P tumor cells with BPA-BNCT than with BSH-BNCT and with neutron beam irradiation only. BPA-BNCT rather than BSH-BNCT has some potential

to decrease the number of lung metastases, and an acute hypoxia-releasing treatment such as the administration of nicotinamide, bevacizumab, wortmannin or thalidomide may be promising for reducing numbers of lung metastases. Consequently, BPA-BNCT in combination with the treatment using these agents may show a little more potential to reduce the number of metastases. Now, it has been elucidated that control of the chronic hypoxia-rich Q cell population in the primary solid tumor has the potential to impact the control of local tumors as a whole, and that control of the acute hypoxia-rich total tumor cell population in the primary solid tumor has the potential to impact the control of lung metastases.

The aim of this research project is focused on clarifying and analyzing the characteristics of intratumor microenvironment including hypoxia within malignant solid tumors and optimizing cancer therapeutic modalities, especially radiotherapy including BNCT in the use of newly-developed ^{10}B -carriers based on the revealed findings on intratumor microenvironmental characteristics.

RESEARCH SUBJECTS:

The collaborators and allotted research subjects (ARS) were organized as follows;

ARS-1 (29P1-1): Optimization of Radiation Therapy Including BNCT in terms of the Effect on a Specific Cell Fraction within a Solid Tumor and the Suppressing Effect of Distant Metastasis. (S. Masunaga, et al.)

ARS-2 (29P1-2): Development of Hypoxic Microenvironment-Oriented ^{10}B -Carriers. (H. Nagasawa, et al.)

ARS-3 (29P1-3)*: Search and Functional Analysis of Novel Genes that Activate HIF-1, and Development into Local Tumor Control. (H. Harada, et al.)

ARS-4 (29P1-4)*: Radiochemical Analysis of Cell Lethality Mechanism in Neutron Capture Reaction. (R. Hirayama, et al.)

ARS-5 (29P1-5): Development of Neutron Capture Therapy Using Cell-Membrane Fluidity Recognition Type Novel Boron Hybrid Liposome. (S. Kasaoka, et al.)

ARS-6 (29P1-6)*: Drug Delivery System Aimed at Adaptation to Neutron Capture Therapy for Melanoma. (T. Nagasaki, et al.)

ARS-7 (29P1-7)*: Molecular Design, Synthesis and Functional Evaluation of Hypoxic Cytotoxin Including Boron. (Y. Uto, et al.)

ARS-8 (29P1-8)*: Bystander Effect on Malignant Trait of Tumor Cells by Irradiation. (H. Yasui, et al.)

ARS-9 (29P1-9)*: Analysis of the Response of Malignant Tumor to BNCT. (M. Masutani, et al.)

ARS-10 (29P1-10): Cell Survival Test by Neutron Capture Reaction Using Boron Compound and Inhibitory Effect on Tumor Growth. (K. Nakai, et al.)

ARS-11 (29P1-11)*: Multilateral Approach Toward Realization of Next Generation Boron Neutron Capture Therapy. (Y. Matsumoto, et al.)

ARS-12 (29P1-12): Analysis of Radiosensitization Effect through Targeting Intratumoral Environmental. (Y. Sanada, et al.)

(*There was not assignment time for experiment using reactor facilities during its operation period of FY 2017.)

Estimation of Therapeutic Efficacy of BNCT Based on the Intra- and Intercellular Heterogeneity in ^{10}B Distribution

T. Sato and S. Masunaga¹

Nuclear Science and Engineering Center, Japan Atomic Energy Agency

¹*Research Reactor Institute, Kyoto University*

INTRODUCTION: In the current treatment planning of boron neutron capture therapy (BNCT), the absorbed doses deposited by $^{10}\text{B}(n,\alpha)^7\text{Li}$, $^{14}\text{N}(n,p)^{14}\text{C}$, and $^1\text{H}(n,n)p$ reactions as well as photons are separately calculated, which are generally referred to as boron, nitrogen, hydrogen, and photon components, respectively. The absorbed doses for each component are weighted by their relative biological effectiveness (RBE) or compound biological effectiveness (CBE) [1] in the treatment planning for estimating the doses equivalent to conventional photon therapy. Note that the concept of CBE, the weighting factor on the boron component, was introduced to express the difference of biological effectiveness between the types of ^{10}B compounds because the therapeutic efficacy depends on the intra- and intercellular heterogeneity in ^{10}B distribution besides RBE. However, the sum of the absorbed dose weighted by fixed RBE or CBE (hereafter, RBE-weighted dose) of each component may not be an adequate index for representing its biological impact, since RBE and CBE vary with the absorbed dose, and the synergistic effect exists in the radiation fields composed by different types of radiation. Thus, the concept of the photon-isoeffective dose that represents the photon dose giving the same biological effect was recently proposed for the treatment planning of BNCT [2]. We therefore developed a model for estimating the RBE-weighted and photon-isoeffective doses of BNCT considering the intra- and intercellular heterogeneity in ^{10}B distribution.

MATERIALS AND METHODS: Our developed model is based on the stochastic microdosimetric kinetic (SMK) model [3], which can estimate the cellular surviving fraction (SF), not from the profiles of radiation imparting energy such as LET, but from the probability densities of the absorbed doses in cell nucleus and its intra-nuclear domains. Thus, the SMK model considers the synergistic effect intrinsically. For extending SMK model to be applicable to BNCT, we calculated the probability densities for each dose component of BNCT using the Particle and Heavy Ion Transport code System, PHITS [4]. Then, the probability densities for actual BNCT radiation fields inside patients are determined by summing up the calculated data for each dose component weighted by its absorbed dose. In this summation, the intra- and intercellular heterogeneity in ^{10}B distribution are also considered. The SF of tumor cells in patients can be evaluated from the calculated probability densities using the SMK model. Four parameters that express cellular characteristics must

be evaluated in the SMK model. In this study, their numerical values were determined by the least-square (LSq) fitting of the SF of tumor cells, which we previously determined *in vivo/in vitro* experiments of mice exposed to reactor neutron beam with concomitant BPA or BSH treatment at various concentrations [5].

RESULTS AND DISCUSSION: Figure 1 shows the experimental and calculated therapeutic efficacy of BNCT in comparison to X-ray therapy as a function of the absorbed dose in tumor. The photon-isoeffective dose can be calculated by the absorbed doses weighted by this relative therapeutic efficacy. The data for three drug conditions, administration of BPA and BSH with 17 ppm, and without ^{10}B compound, are shown in the graph. It is evident from the graph that the relative therapeutic efficacies for the BPA administration are higher than the corresponding data for the BSH case, and they decrease with increase of the absorbed dose in tumor. Our model can satisfactorily reproduce these tendencies, though it slightly overestimates the therapeutic efficacies for the BPA administration. This overestimation is probably due to the ignorance of the inter-cellular heterogeneity in ^{10}B distribution in this calculation. More detailed discussions can be found in our recently published paper [6].

REFERENCES:

- [1] K. Ono, *J Radiat Res* **57** (2016) I83-I89.
- [2] S.J. Gonzalez, *et al.*, *Phys Med Biol* **62** (2017) 7938-7958.
- [3] T. Sato *et al.*, *Radiat Res* **178** (2012) 341-356.
- [4] T. Sato *et al.*, *J Nucl Sci Technol* (2018) DOI: 10.1080/00223131.2017.1419890.
- [5] S. Masunaga *et al.*, *Springerplus* **3** (2014), 128.
- [6] T. Sato *et al.*, *Sci Rep* **8** (2018) 988.

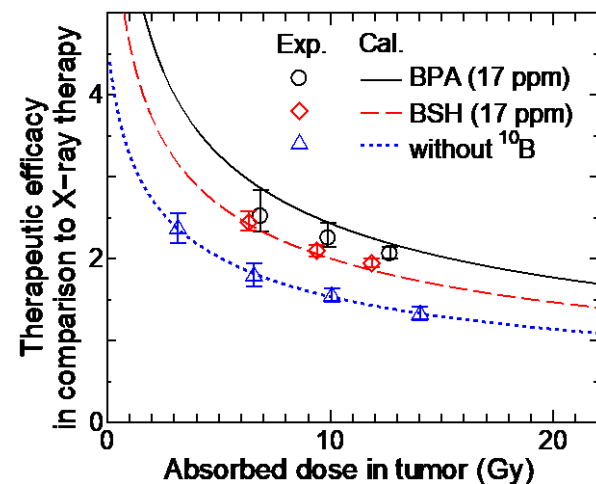


Fig. 1. Experimental and calculated therapeutic efficacy of BNCT in comparison to X-ray therapy.

PR1-2 Design, Synthesis and Biological Evaluation of Pepducin-BSH Conjugates for BNCT

A. Isono, M. Tsuji, T. Hirayama, S. Masunaga¹, and H. Nagasawa¹

Laboratory of Medicinal & Pharmaceutical Chemistry,
Gifu Pharmaceutical University

¹ Research Reactor Institute, Kyoto University

INTRODUCTION: Selective delivery of sufficient quantity of ¹⁰B to tumor cells is essential for the success of boron neutron capture therapy (BNCT). The clinically used boron carrier, sodium mercaptoundecahydro-closo-dodecaborate (BSH: Na₂B₁₂H₁₁SH) is impermeable to plasma membrane due to its highly hydrophilic and anionic property. We found that pepducins, which are artificial lipidated peptides developed as G protein-coupled receptor (GPCR) modulators, enable fluorescein, an anionic molecule, to penetrate membrane directly. From this study, we envisaged that the anionic boron cluster can be delivered into cytosol by using the pepducin as a delivery unit. So, we designed and synthesized pepducin-BSH conjugates and performed structural optimization to improve cellular uptake. (Fig. 1)

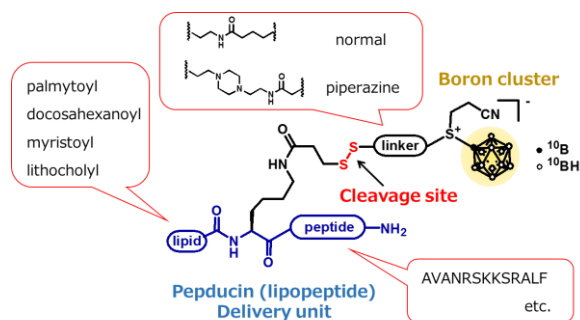
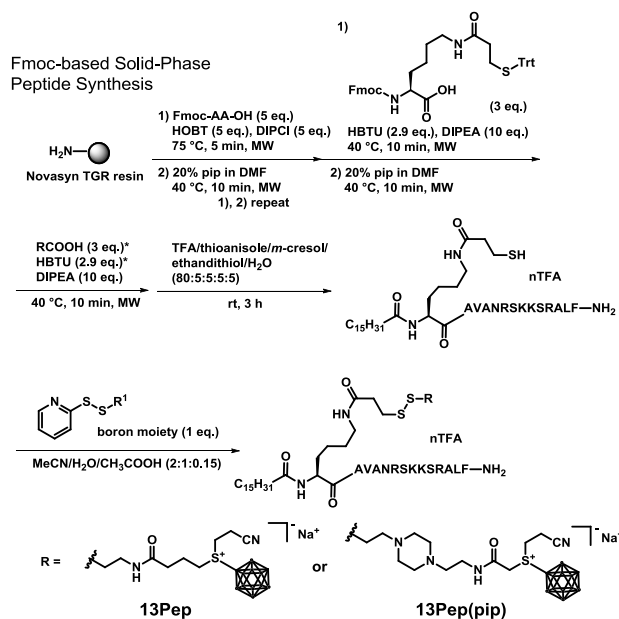


Fig. 1 Structural optimization of pepducin-BSH conjugates.

In the present study, we investigated the biological effects on BNCT of the selected pepducin-BSH conjugates using T98G cells.

EXPERIMENTS: 13Pep and 13Pep(pip) were synthesized based on solid-phase synthesis (Scheme 1). T98G cells were treated with the Peps (10 or 20 μM) at 37 °C for various times, then, washed with PBS three times, and dissolved in 200 μL HNO₃ for 1 h. The boron concentrations of these extracts were measured by inductively coupled plasma-atomic emission spectrometry. To evaluate neutron sensitizing ability of the compounds, T98G cells were treated with 20 μM boron carriers for 24 h. Then the cells were washed with PBS, suspended in serum containing medium and aliquoted into Teflon tubes for irradiation. Cells were irradiated using the neutron beam at the Heavy Water Facility of the Kyoto University Research Reactor (KUR) operated at 1 MW power output. The survival rates of the irradiated cells were determined using conventional colony assays.

RESULTS: Pep13 and Pep13(pip) showed highly cellular uptake into T98G cells. Pepducin carrier was clearly useful for membrane penetration of BSH. (Fig. 2)



Scheme 1 Synthesis of pepducin-BSH conjugates and structures of 13Pep and 13Pep(pip).

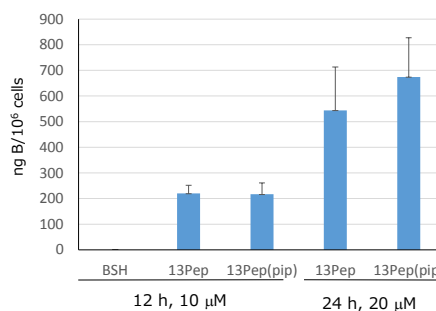


Fig. 2 Intracellular uptake of 13Pep and 13Pep(pip).

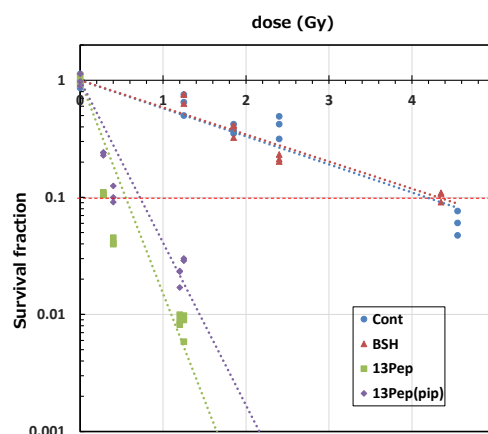


Fig. 3 Survival fraction of T98G cells treated with 13Pep and 13Pep(pip) and irradiated by mixed-neutron beam for BNCT.

The D₁₀ of BNCT was calculated from survival curve shown in Fig. 3. Each D₁₀ was 0.54 Gy for 13Pep, 0.72 Gy for 13Pep(pip) and 4.32 Gy for BSH. From these results, the novel boron carriers, 13Pep and 13Pep(pip) were promising candidates for BNCT. We are now investigating bio distribution and *in vivo* activity.

PR1-3 HIF-1 Maintains a Functional Relationship between Pancreatic Cancer Cells and Stromal Fibroblasts by Upregulating Expression and Secretion of Sonic Hedgehog

M. Kobayashi¹, S. Masunaga², A. Morinibu¹ and H. Harada^{1,3,4}

¹Laboratory of Cancer Cell Biology, Department of Genome Dynamics, Radiation Biology Center, Kyoto University.

²Research Reactor Institute, Kyoto University.

³Hakubi Center, Kyoto University.

⁴PRESTO, Japan Science and Technology Agency (JST).

INTRODUCTION: Pancreatic cancer is a deadly disease because it is highly resistant to conventional therapies. Characteristic features of pancreatic cancer strongly associated with the poor prognoses of patients and therapeutic resistance are the existence of both hypoxic regions and stroma-rich microenvironments.

Accumulating evidence has suggested that a factor associated with the poor prognosis as well as malignant progression of pancreatic cancers is a hypoxia-inducible transcription factor, hypoxia-inducible factor 1 (HIF-1). Once the regulatory subunit of HIF-1, HIF-1 α , becomes stabilized and activated under hypoxic conditions, it, in combination with its binding partner, HIF-1 β , induces the expression of hundreds of genes responsible for malignant cancer progression. Although the positive correlations between HIF-1 α expression levels as well as the volume of hypoxic regions and both the poor prognosis of pancreatic cancer patients and decreased anti-tumor effects of HIF-1 α -targeting drugs in pancreatic tumors have been repeatedly reported, key molecular mechanisms behind them are still unclear.

Another characteristic feature of pancreatic cancers is the stroma-rich microenvironment, which has been reported to result from the activation of the Sonic hedgehog signaling pathway, aberrant proliferation of fibroblasts, and overproduction of extracellular matrix (ECM). Specifically, the mature form of Sonic hedgehog protein (SHH) is secreted from pancreatic cancer cells after removal of the signal peptide and autocatalytic processing. The secreted SHH protein then cancels the negative regulation of smoothened (SMO) by patched (PTCH) through the direct binding of SHH to PTCH on the surface of fibroblasts, leading to the activation of a transcription factor, Gli-1, in fibroblasts. Because Gli-1 has an activity to upregulate cellular proliferation, differentiation, and survival by inducing the expressions of target genes, such as cyclin D1, c-myc, bcl2, and snail, the paracrine signaling is thought to be important in the formation of the stroma-rich microenvironment of pancreatic cancers. Thus, marked efforts have been devoted to clarify the characteristic features of each hypoxic condition and the stroma-rich microenvironment in pancreatic cancers; however, whether and how HIF-1 and the Sonic hedgehog signaling pathway influence each other and

eventually create the pancreatic cancer-distinctive microenvironments have yet to be fully elucidated.

In the present study, we investigated the functional and mechanistic linkage between HIF-1 and Sonic hedgehog signaling to better understand whether and how the stroma-rich microenvironment arises in pancreatic cancers [1]. We revealed that pancreatic cancer cells secrete more SHH under hypoxic conditions by increasing the efficiency of secretion as well as expression of SHH in a HIF-1-dependent manner, and promote the growth of fibroblast cells by stimulating the hedgehog signaling pathway in a paracrine manner.

EXPERIMENTS and RESULTS: Performing Western blotting using antibody against SHH protein, we found that pancreatic cancer cells secreted more Sonic hedgehog protein (SHH) under hypoxia by upregulating its expression and efficiency of secretion in a HIF-1-dependent manner (Fig. 1). Recombinant SHH, which was confirmed to activate the hedgehog signaling pathway, accelerated the growth of fibroblasts in a dose-dependent manner (Fig. 1). The SHH protein secreted from pancreatic cancer cells under hypoxic conditions promoted the growth of fibroblasts by stimulating their Sonic hedgehog signaling pathway. The SHH-mediated growth acceleration was significantly suppressed by a SMO inhibitor, TAK-441. These results suggest that the increased secretion of SHH by HIF-1 is potentially responsible for the formation of detrimental and stroma-rich microenvironments in pancreatic cancers, therefore providing a rational basis to target it in cancer therapy (Fig. 1).

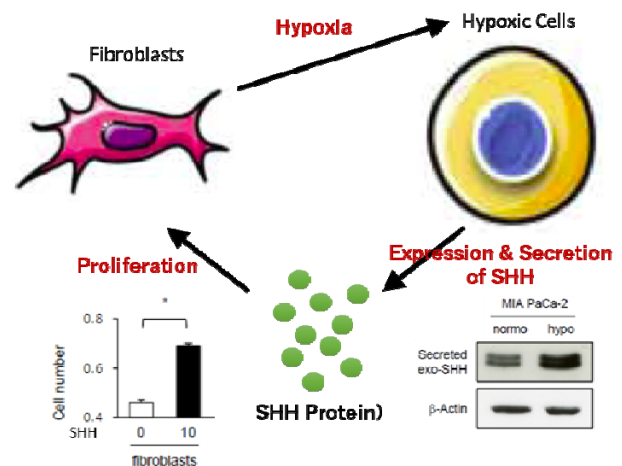


Fig. 1 Positive feedback loop among the upregulation of both expression and secretion of SHH, accelerated proliferation of fibroblasts, and development of hypoxic regions in malignant pancreatic tumor tissues.

REFERENCE:

[1] T. Katagiri *et al.*, *Oncotarget*, **9** (2018) 10525-10535.

Selective Accumulation of Boron-conjugated Liposomes Composed of Dimyristoylphosphatidylcholine to B16F10 Murine Melanoma Cells in Relation to Fluidity of Cell Membranes.

S. Kasaoka, A. Kunisawa, Y. Okishima, Y. Tanaka, H. Yoshikawa, Y. Sanada¹, Y. Sakurai¹, H. Tanaka¹ and S. Masunaga¹

Department of Pharmaceutical Science, Hiroshima International University

¹Research Reactor Institute, Kyoto University

INTRODUCTION: There are many reports that membranes in cancer cells are relatively more fluid compared to healthy cells. Higher membrane fluidity in cancer cells closely relates to their invasive potential, proliferation, and metastatic ability [1]. Liposomes composed of dimyristoylphosphatidylcholine (DMPC) and polyoxyethylenedodecylether were found to inhibit the growth of human promyelocytic leukemia (HL-60) cells without using any drugs [2]. In this study, we have developed a novel boron delivery system using the membrane-fluidity sensitive boron liposomes (MFSBLs) composed of DMPC and borocaptate (BSH)-conjugated chemical compounds for boron neutron capture therapy (Fig. 1).

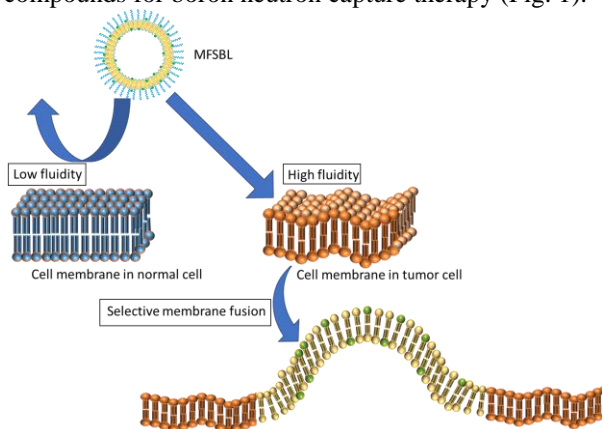


Fig. 1. Selective membrane fusion of boron-conjugated liposomes composed of DMPC to B16F10 murine melanoma cells in relation to fluidity of cell membranes.

EXPERIMENTS: Octadecylamine and 1,2-dimyristoyl-sn-glycero-3-phosphorylethanolamine were conjugated with BSH using the optimal hetero-crosslinking agents for boron compounds. MFSBLs composed of DMPC, polyoxyethylenedodecylether and boron compounds at mole ratios of 8:0.9:1.1 were prepared by sonication method in 5% glucose solution at 45°C with 300 W, followed by filtration with a 0.45 μ m filter. The diameter of MFSBLs

was measured with a light scattering spectrometer. The boron concentration was measured by inductively coupled plasma atomic emission spectrometry. B16F10 murine melanoma cells were pre-incubated with 2.5-10 ppm of ¹⁰B at 37°C for 24 hours before neutron irradiation. The cells were rinsed twice in PBS and suspended in fresh medium. After neutron irradiation the cells were plated into plastic Petri dishes 60 mm in diameter at 200 cells per dish. They were incubated for an additional 7 days to allow colony formation.

RESULTS: MFSBLs had a mean diameter of 59.6 nm and a zeta potential of -11.3 mV. High encapsulation efficiency value from 55% to 89% of ¹⁰B in MFSBLs were obtained. MFSBLs had high stability (95-99%) in the retention of ¹⁰B during storage at 4°C for 4 weeks. All borocaptate-loaded formulations had low cytotoxic effects in human fibroblast cells. MFSBLs were efficiently fused to melanoma cells, but were inefficiently fused to human fibroblast cells. Thus, it is essential to elevate the ¹⁰B concentration in melanoma cells, while maintain low levels of ¹⁰B in normal fibroblast cells. The tumor/normal ratio (T/N ratio) was 3.0. As shown in Fig. 2, MFSBLs showed higher suppression of growth of melanoma cells than BSH solution. This result suggested novel MFSBLs composed of DMPC is useful for ¹⁰B carrier on BNCT for melanoma.

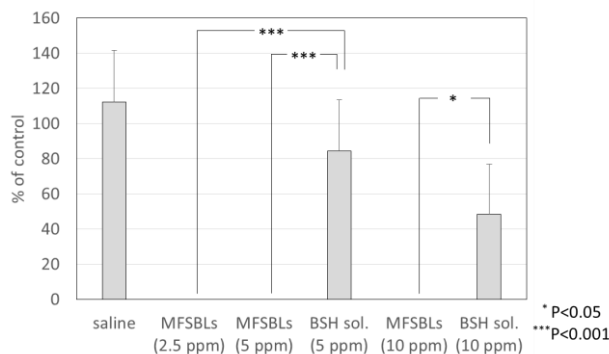


Fig. 2. Suppression of the colony formation of B16F10 cells after in vitro BNCT.

REFERENCES:

- [1] Sherbet GV. Magalit, *Exp Cell Biol.*, **57** (1989) 198-205.
- [2] Y. Matsumoto *et al.* *Int. J. Cancer*, **115** (2005) 377-382.

L. Chen^{1,2}, S. Imamichi¹, T. Itoh¹, Si. Masunaga³, N. Toriya², T. Onodera^{1,2}, Y. Sasaki^{1,2} and M. Masutani^{1,2}

Division of Boron Neutron Capture Therapy, EPOC, National Cancer Center

¹*Lab of Collaborative Research, Division of Cell Signaling, Research Institute, National Cancer Center*

²*Department of Frontier Life Sciences, Nagasaki University Graduate School of Biomedical Sciences*

³*Institute for Integrated Radiation and Nuclear Science, Kyoto University*

INTRODUCTION: Boron neutron capture therapy (BNCT) is based on nuclear reactions between thermal neutron and boron-10 in the cancer cells. The reaction causes alpha particle and lithium nuclei short length with high energy. Boron compounds such as ¹⁰B-boronophenylalanine (BPA) are introduced into cancer cells and neutron beam using nuclear reactor or accelerator-based BNCT system are irradiated. Boron neutron capture reaction (BNCR) efficiently introduces DNA damages¹, however, tumor cell killing is affected by various factors including the uptake of boron compounds and thermal neutron fluence². Therefore, it is difficult in BNCT to calculate the irradiated dose on tumor and normal tissues. We previously observed extensive DNA damage responses including those for DNA double strand breaks after BNCR by the observation of remaining gamma-H2AX and poly(ADP-ribose) in the rat lymphosarcoma model of BNCT³. We also performed comprehensive analysis of mRNA expression and proteome using human squamous carcinoma SAS cells after BNCR⁴. From the comprehensive analysis, expressions of particular mRNAs were increased after BNCR. These gene products may be involved in early response of BNCT. We focused on factors present in culture supernatant including *CSF2* gene product, granulocyte-macrophage colony stimulating factor (GM-CSF), which was increased after BNCR, and metabolites and investigated the functions and dynamics after BNCR or neutron beam irradiation in comparison with the gamma-ray irradiation.

EXPERIMENTS: The experiments with neutron-beam irradiation with KUR Nuclear Reactor was planned but not carried out during FY2017. Neutron-beam irradiations were carried out in the previous experiments at 1

MW in the KUR facility. Human oral squamous cancer SAS cells and melanoma A375 cells were irradiated after 2 hrs incubation with or without ¹⁰B-BPA at 25 ppm. Gamma-ray irradiations were operated at National Cancer Center Research Institute (Tokyo) and Nagasaki University with the ¹³⁷Cs source. The cellular responses including factors and metabolites present in culture supernatants were filtrated and analyzed 6 and 24 hrs after irradiation of therapeutic dose of BNCT and gamma-ray. Cell survival was analyzed by colony formation assay. The siRNA was transfected with LipofectamineTM 3000 Reagent (Thermo Fisher Scientific). The knockdown efficiency of siRNA for *CSF2* was evaluated in the cancer cell lines by measurement of the mRNA levels. The *GUSB* gene was used as a control. GM-CSF levels in culture supernatant were measured using ELISA.

RESULTS: The relative biological effectiveness (RBE) of BNCR for A375 cells was around 2-3 like in the case with SAS and HSG cells. A375 cells show a relatively high basal level of *CSF2* mRNA expression. The siRNA of *CSF2* caused a decrease in *CSF2* mRNA level to around 20% at 10 nM in A375 cells. A decrease of gene product GM-CSF in the culture supernatant was also observed after the siRNA treatment by ELISA analysis. The siRNA treatment of *CSF2* limitedly affected the cell survival after gamma-ray irradiation.

The results suggest that CSF2 may be involved in cancer cell survival after various kinds of radiation as an autocrine factor. This possibility and other biological significances of CSF2 will be investigated after BNCR in the KUR facility.

REFERENCES:

- [1] S.G. Hussein *et al.*, Proc. Montreal Int. Conf. Eds Harvey, Cusson, Geiger, Pearson (U. Mont Press) (1969) 91.
- [2] K. Okano *et al.*, Nucl. Instr. and Meth., **186** (1981) 115-120.
- [3] M. Masutani *et al.*, Appl. Rad. Iso., **104** (2014) 104-108.
- [4] A. Sato *et al.*, Appl. Rad. Iso., **106** (2015) 213-219.

PR1-6 Radiobiological Effect of Extracellular Boron Distribution and Neutron Irradiation

K. Nakai, K. Endo², S. Masunaga¹, Y. Sakurai¹, H. Tanaka¹, F. Yoshida², M. Shirakawa³ and A. Matsumura²

Department of Neuro-rehabilitation, Ibaraki Prefectural University Hospital

¹Research Reactor Institute, Kyoto University

²Department of Neurosurgery, Faculty of Medicine, University of Tsukuba

³Department of Pharmaceutical Sciences, University of Fukuyama

INTRODUCTION: Boron Neutron Capture Therapy (BNCT) is a particle radiation therapy for malignant diseases. The clinical trial of BNCT for malignant brain tumor and head and neck cancers is ongoing. However, Boron distribution of extra-cellular fluid or interstitial tumor tissue during the neutron irradiation and radiobiological effect of neutron irradiation is still unclear. In the previous studies, we have focus on intra-cellular boron concentration and tumor tissue boron concentrations. The goal of this study is, to clarify a role of extra-cellular boron neutron reaction in BNCT.

EXPERIMENTS: U251 human glioma cell lines were cultured in D-MEM supplemented with 10% fetal bovine serum and maintained at 37°C in a humidified atmosphere with 5% CO₂. After trypsinized and counted, cells were suspended in culture medium. To mimicking tumor stroma condition, we made four groups (Fig.1).

First, from 6hr before to end of neutron irradiation, cells were continuously exposed to Boronophenylalanine (BPA 6hr). The second, BPA exposure was from 6hr before irradiation to just before irradiation, neutron irradiation was done after changing culture medium to that of BPA free (BPA 6hr wash). add BPA and Boric Acid (BA) just before neutron irradiation on single cell suspensions (BPA 0hr, Boric Acid). These cells were irradiated at the KUR irradiation system, with boron concentration of 10 and 40 µg/mL ¹⁰B. The cells were assayed for colony formation to determine survival fraction.

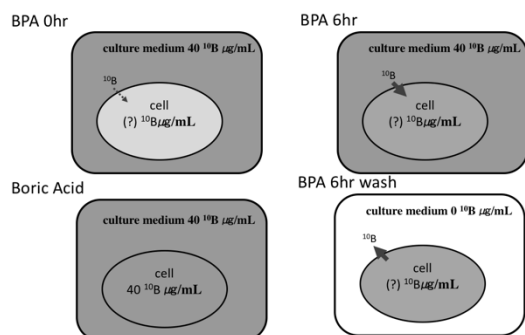


Fig. 1. Schema of the extracellular boron circumstances. Each group has exposed 10 and 40µg/mL ¹⁰B. 0hr BPA, 6hr BPA,6hr BPA wash, Boric Acid.

RESULTS: As shown in Fig. 2, boron effected the survival fraction of U251, but it is not simple concentration-dependent manner. Neutron irradiation time resulted the dose-dependent manner. The reproducibility of these experiments did not assess. 10µg/mL ¹⁰B of Boric Acid effected intensely. It may reflect the intra-cellular 10µg/mL ¹⁰B play the role of cell killing effect. Comparing the “6hr BPA wash” and “6hr BPA”, wash group almost constantly low killing effect, it suggested that extra cellular boron contribute to cell killing.

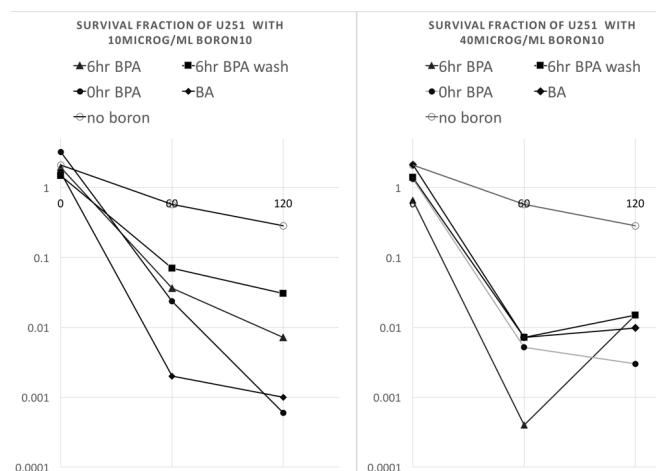


Fig. 2. Survival fraction of U251 cells. Each group has exposed 10 and 40µg/mL ¹⁰B. BPA were added in culture medium, exposure time was 6hr (▲6hr BPA) and just before neutron irradiation (●0hr BPA), 6hr exposure BPA and culture medium was changed before irradiation (■6hr BPA wash), ¹⁰B enriched Boric Acid was added to culture medium, before irradiation(◆BA). White circles indicated survival fraction of cells without boron.

Previous reports [1,2] indicated 6hr or overnight incubation with BPA or sodium borocaptate[3], intracellular concentration of boron was higher than boron concentration in cell culture medium. Chandra *et al.* reported subcellular boron uptake and retention from BPA study[4], from SIMS observations.comparing these previous report, this experiment is insufficiently verified, and it is still in progress, further study is required.

REFERENCES:

- [1] F. Yoshida *et al.*, Cancer Lett, **187** (2002)135-141.
- [2] J. Calpala *et al.*, Radiat Res **146** (1996) 554-560.
- [3] M. Fartmann *et al.*, Appl Surface Sci **231-232** (2004) 428-431.
- [4] S.Chandra *et al.*, J Microscopy **254** (2014) 146-156.

Y. Matsumoto^{1,2}, K. Hattori^{3,4}, H. Arima^{3,4}, K. Motoyama^{3,4}, T. Higashi^{3,4}, N. Fukumitsu^{1,2}, T. Aihara^{1,2}, H. Kumada^{1,2}, K Tsuboi^{1,2}, M Sanada⁵, S. Masunaga⁵ and H. Sakurai^{1,2}

¹Faculty of Medicine, University of Tsukuba

²Proton Medical Research Center, University of Tsukuba Hospital

³CyDing Co., Ltd

⁴Faculty of Life Sciences, Kumamoto University

⁵Research Reactor Institute, Kyoto University

INTRODUCTION: Currently, the development of next-generation boron neutron capture therapy using accelerator that can be installed together with hospitals at multiple facilities is underway. Despite its clinical usefulness, BNCT utilizes neutrons from conventional nuclear reactors, and it is difficult to disseminate it due to complications of handling and regulatory matters when handling it as a medical device, and adaptive diseases are also caused by brain tumors and other diseases Head and neck cancer etc. are limited. Since accelerator BNCT can be safely operated compared to nuclear reactor BNCT and the high neutron flux can treat cancer of the trunk which was not targeted by BNCT in the past. However, there are very few environments in which basic biological experiments can be conducted by BNCT, and it is difficult to say that accumulation of experimental data is sufficient. We will develop an accelerator neutron source for clinical medicine as a priority issue of the Tsukuba International Strategy Comprehensive Special Zone and some biological experiments were started using accelerator BNCT at May of 2017, and we confirm the biological effect of reactor BNCT in parallel. The purpose of this research project is to accumulate knowledge as the foundation of the development of BNCT from the viewpoint of the possibility of expansion of adaptive disease, the treatment effect by new boron compound, and the change of treatment effect accompanying the change of irradiation condition.

EXPERIMENTS: In FY2007, we refuse that the accelerator BNCT device in Tokai village is not a state where biological experiments can be steadily performed, but it is only one experimental result on January 30, 2018 in KUR. The cytotoxic effects were examined using two novel boron drugs that are going to collaborate with external companies (ND201-BSH). ND201-BSH is a novel boron drug in which BSH is encapsulated in folate - modified cyclodextrin (ND201) and active accumulation on cancer cells with highly expressed folate is added to BSH. BPA and BSH were also used as reference boron compounds.

Cells were seeded in T75 cell culture flasks and treated with each compound. The concentration of ¹⁰B in medium were fixed to 20 ppm for BPA and BSH and 2 ppm

for ND201-BSH, respectively. After 1h, medium including ¹⁰B were washed out and cells were washed with PBS (-), soaked with trypsin-EDTA solution and harvested with new fresh medium. Adequate number of cells were put into the irradiation cryotube (Japan Genetics Co, Ltd.) and irradiated with thermal neutron produced by KUR. After irradiation, cells were analyzed with classical colony formation assay technique. Cells were harvested from cryotube and the cell number was counted with blood cell counting board. Then, cells were diluted to adequate concentration and reseeded into 6 cm cell culture dishes. After 14 days, colonies were fixed with 100% ethanol and transported from KUR to University of Tsukuba. Then, colonies were stained with 1% methylene blue solution and counted. Kaleida graph software was used for the drawing and analysis of the survival curves, and cells showed a linear survival curve without shoulder after BNCT, therefore LQ model with β value set to 0 was used to fit the experimental data.

RESULTS: As shown in Fig. 1, colon-26 showed linear survival curves after each BNCT. The survival curves after thermal neutron alone and BSH treatment group showed straight with a gradual slope. On the other hand, the BPA and ND201-BSH groups showed steep survival curves. Surprisingly, ND201-BSH shows a significant cell killing effect at only 1 ppm, which is ¹⁰B concentration of 1/10 of BPA. From these results, it was suggested that the use of ND201-BSH in the case of cancers in which the folate receptor was highly expressed also proved to be more useful with BNCT with a smaller amount of ¹⁰B.

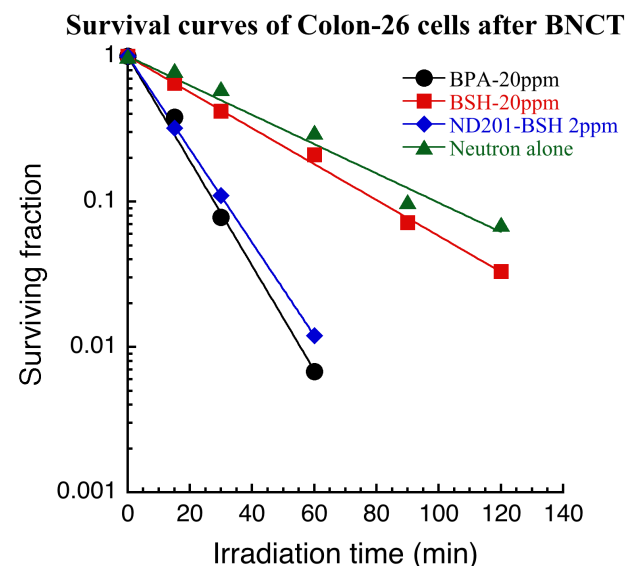


Fig. 1. Survival curves of Colon-26 cells after BNCT with BPA, BSH and ND201-BSH.

PR1-8 Attempts to Sensitize Tumor Cells by Exploiting the Tumor Microenvironment

Y. Sanada and S. Masunaga

Radiation Biology, Research Reactor Institute, Kyoto University

INTRODUCTION: Hypoxia and glucose deprivation have been suggested to play important roles in resistance to radiation [1]. Attempts to sensitize tumor cells by exploiting the tumor microenvironment have been studied. A major mediator of the cellular hypoxic response, hypoxia inducible factor 1 (HIF-1), is a potential target for cancer therapy, because it transcriptionally regulates a number of genes, including those involved in glucose metabolism, angiogenesis and resistance to chemotherapy and radiation therapy [2]. Moreover, many cytotoxic agents that selectively kill tumor cells under low glucose conditions, including metformin, were reported [3]. In the present study, we investigated whether the disruption of Hif-1 α affects the sensitivity of murine squamous cell carcinoma (SCC VII) cells to metformin and if metformin functions as a radiosensitizer using SCC VII cells [4].

EXPERIMENTS: Hif-1 α -deficient SCCVII cells were established through the CRISPR/Cas9 system. In vitro, cell death was evaluated using image-based cytometer; propidium iodide (PI)-positive cells were identified as dead cells. In vivo, tumor-bearing mice were intraperitoneally administered metformin and then subjected 2 h later to acute whole-body γ -ray irradiation. A clonogenic cell survival assay and micronucleus (MN) assay were performed after tumors were disaggregated by stirring in PBS containing 0.05% trypsin.

RESULTS: The disruption of Hif-1 α enhanced the cytotoxicity of metformin against SCC VII cells under glucose-free and/or hypoxia-mimetic conditions in vitro. SCC VII Hif-1 α -deficient cells from tumor-bearing mice exhibited lower cell survival than SCC VII cells, suggesting that the disruption of Hif-1 α strongly influenced viability in the tumor microenvironment; however, additional decreases were not observed in the survival of SCC VII Hif-1 α -deficient cells after the in vivo administration of metformin. While no radiosensitivity was found in SCC VII tumors after the in vivo treatment with metformin, a significant enhancement in radiosensitivity was noted in Hif-1 α -deficient SCC VII tumors (Fig. 1). Metformin increased the micronucleus frequency in SCC VII

Hif-1 α -deficient SCC VII cells, which may reflect a reduced DSB repair capacity because micronucleus are a consequence of unrepaired DSBs. Although metformin itself was shown to reduce the stabilization of HIF-1 α , our results suggest that the additional downregulation of HIF-1 α is effective for sensitizing tumor cells.

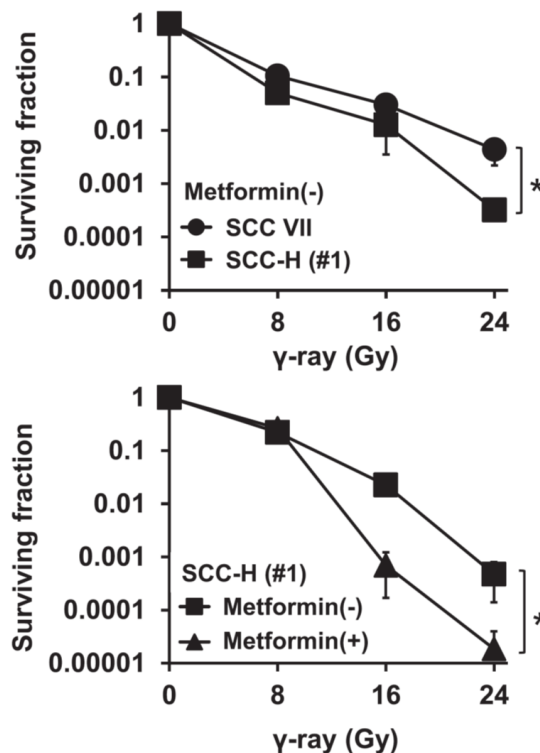


Fig. 1. Cell survival curves for the total cell population from SCC VII and SCC VII Hif-1 α -deficient (SCC-H) tumors irradiated with γ -rays on day 14 after the tumor cell inoculation

REFERENCES:

- [1] J. Li *et al.*, *Cell Biochem Funct*, **27** (2009) 93–101.
- [2] Z. Luo *et al.*, *Neuropharmacology*, **89** (2015) 168–174.
- [3] Y. Zhuang *et al.*, *PLoS One*, **9** (2014):e108444.
- [4] Y. Sanada *et al.*, *Int. J. Rad. Biol.* **94** (2017) 88-96.

K. Takamiya

Research Reactor Institute, Kyoto University

OBJECTIVE: Radioactive aerosols is one of the most important materials released in the severe accident of Fukushima Daiichi Nuclear Power Plant. The chemical and physical properties has been investigated for radioactive aerosols in the air and soil samples by various methods, and their properties have become cleared. On the other hand, their production mechanism in the reactor building has not been elucidated because the environment in the reactor buildings was anomalous: for example, high temperature, high dose rate, etc. In this project research, the production mechanism and measurement technique of radioactive aerosols have been studied experimentally to elucidate the generation mechanism in such particular environment. In addition, the behavior of radioactive aerosols after their deposition in the environment has been studied using simulated aerosols produced by radioactive aerosol generator developed in the present project.

RESEARCH SUBJECTS: The project research is composed by five individual subjects in this year period. One is developments of production method of radioactive aerosols for simulation experiments, one is development of measurement method of radioactive aerosols, and two are elucidation of the production mechanism of aerosol under the specific situation. And one subject about interaction of radioactive cesium in the environment was added in the previous year period. The respective subjects of the research groups of this project are described as follows;

- P2-1: Development of production method of radioactive aerosols by attaching radioisotopes to aerosol particles
- P2-2: Development of measurement method of radioactive aerosols under severity conditions
- P2-3: Investigation for production process of insoluble radioactive particles released from FDNPP
- P2-4: Study for production mechanism of radioactive aerosols in the presence of sea water
- P2-5: Interaction of radioactive cesium and suspended particles in river water

In this year period, experiments of subjects P2-3, -4 and -5 were not carried out because of limited operation of KUR.

RESULTS: In the subject P2-1, experiments using solution aerosol which was generated from three different sodium halide (sodium chloride, sodium bromide and sodium iodide) solution with various concentrations (0.005,

0.01 and 0.02 M) have been performed to elucidate the effect of solute on the attachment process of fission products to solution aerosol particles by the electrostatic interaction. The relationship between the attachment ratio of ^{104}Tc and total surface area of aerosol particles were obtained for each sodium halide solution aerosols of different concentrations. The equilibrium constant K was estimated by fitting to the relationship using adsorption equilibrium equation. In comparison of estimated K values among different solutes in the same concentration, it was found that the order of magnitude of K values is $\text{NaCl} \lesssim \text{NaBr} < \text{NaI}$. This order can be understood by the high anion concentration as compared with cation near the surface of aerosol particles as described in our previous report. On the other hand, in comparison of K values among the same solute in different concentrations, it seems that K values have no relation with the solute concentration. If the anion concentration near the surface of aerosol particles affect equilibrium constants, equilibrium constant could depend on the concentration. The reason of the independence might be caused by crystallization of solution aerosol particles. The anion concentration near the surface decreases if the crystallization occurred, which could induce decrease of K values. The concentration dependence has not been clear in the present research but will be elucidated by measurements using solutions of lower concentration in the future.

For the development of measurement method of radioactive aerosols under severity conditions (P2-2), an air irradiation experiment was performed in the 46-MeV electron linear accelerator facility of Institute for Integrated Radiation and Nuclear Science, Kyoto University. In the irradiation experiment, the performance of a newly assembled screen-type diffusion battery system consisting of three air-tight wire screen cylinders was examined. In the target room of the accelerator, a stainless steel irradiation tube was placed at a rear position of the tantalum target. During the irradiation, aerosol-free air was introduced to the tube from the experiment room next to the target room. The target was bombarded with a 30-MeV electron beam to produce bremsstrahlung and neutrons. The bremsstrahlung ionizes air and produces the radiation-induced aerosol. The particle size of ^{13}N -bearing aerosols formed in the accelerator was estimated using a combination technique of wire screens and imaging plate. Additionally the size distributions were measured by a scanning mobility particle sizer (SMPS) to compare the result with the developed system. Preliminary results showed that size of nano aerosol particles was in good agreement with that obtained with SMPS in the geometric mean diameter range of 10 to 15 nm. However, the size analysis for the ^{13}N -bearing particles was unsuccessful at the present stage because of low intensity of photostimulated luminescence of the imaging plate. It was mainly caused by subtraction of the gas condensation effect.

PR2-1 Effect of Solute on Attachment Behavior of Fission Product to Solution Aerosol Particle

K. Takamiya, Y. Nishizawa, S. Sekimoto, Y. Oki and T. Ohtsuki

Institute for Integrated Radiation and Nuclear Science, Kyoto University

INTRODUCTION: Radioactive aerosol is one of transporting medium of radioactive materials, and transferred radioactive cesium and other radioactive materials from inside of the reactor building to the environment in the accident of Fukushima Daiichi Nuclear Power Plant. It was reported that the potential transport medium for radioactive cesium were sulfate aerosols[1]. But chemical form of radioactive cesium in the reactor building and attachment process to sulfate aerosol particles didn't become clear. The generation process of radioactive aerosols by attaching fission products to solution aerosol particles has been investigated experimentally by our research group. And it was found that there are two types of attachment processes; one is caused by geometric collision and another is induced by electrostatic interaction between a fission product and an aerosol particle. In the present work, experiments using solution aerosol which was generated from three different sodium halide solution with various concentrations have been performed to elucidate effect of solutes on the attachment process of fission products to solution aerosol particles by the electrostatic interaction.

EXPERIMENTS: The detail of the generation method of radioactive aerosols by attaching fission products to solution aerosol particles was shown in the previous reports [2, 3]. The fission products were released from a ^{252}Cf source in a chamber. The ^{252}Cf source was covered by a Havar foil of 50 μm thick to reduce the kinetic energy of fission products in the present experiments. Primary aerosols were generated from sodium halide solution (sodium chloride, sodium bromide and sodium iodide) of various concentration (0.005, 0.01 and 0.02 M) and injected into the chamber. The radioactive aerosol produced by attaching fission products to aerosol particles in the chamber were collected by a polycarbonate filter. On the other hand, all fission products released from the ^{252}Cf source into the chamber were collected by a grease-applied cellulose filter placed directly on the source. Gamma-ray spectrometry using a Ge-detector was performed for both filters to detect the gamma-ray emitted from the fission products, and the attachment ratio of fission products to aerosol particles was estimated from the ratio between fission product photo peak areas collected by both filters. In the present work, the attachment ratio for only ^{104}Tc could be estimated with enough statistics.

RESULTS: The relationship between the attachment ratio of ^{104}Tc and total surface area of aerosol particles were obtained for solution aerosols of three different sodium halide (NaCl, NaBr and NaI) of three different concentrations (0.005, 0.01 and 0.02 M). The equilibrium constant

K was estimated from the relationship as described in the previous report [4] and shown in Fig. 1. The upper, middle and lower panels indicate the relationship between equilibrium constants and concentration of solute for NaCl, NaBr and NaI, respectively. In comparison of K values among different solutes in the same concentration, it was found that the order of magnitude of K values is $\text{NaCl} \approx \text{NaBr} < \text{NaI}$. This order can be explained by the high anion concentration as compared with cation near the surface of aerosol particles [5] as described in the previous report [4]. And in comparison of K values among the same solute in different concentrations, K values increase from the concentration of 0.005 M to 0.01 M but decrease from that of 0.01 M to 0.02M. If the anion concentration near the surface of aerosol particles affect equilibrium constants, equilibrium constant could increase as concentration increase. The decrease of K values might be caused by crystallization of solution aerosol particles [6]. The anion concentration near the surface decreases if the crystallization occurred, which induces a decrease of K value. Even after taking into consideration the effect of the crystallization, the increase of K values from concentration of 0.05 M to 0.01 M could suggest that there is concentration effect on the attachment behavior of ^{104}Tc to solution aerosol particles.

This work was supported by JSPS KAKENHI Grant Numbers JP24110005 and JP26286076.

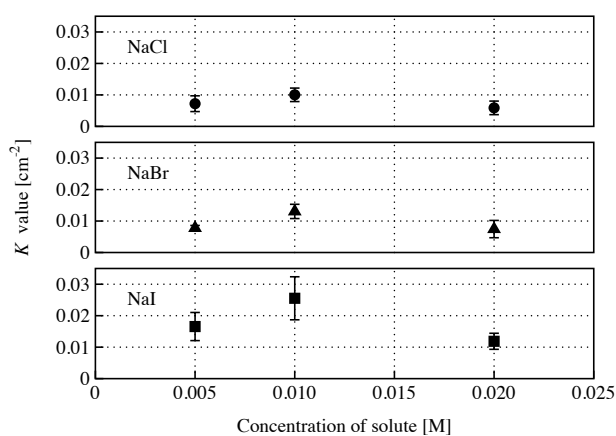


Fig. 1 Relationship between the equilibrium constant and concentration of solute.

REFERENCES:

- [1] N. Kaneyasu *et al.*, *Environmental Science & Technology*, **46** (2012) 5720-5726.
- [2] K. Takamiya *et al.*, *J. Radioanal. Nucl. Chem.*, **307** (2016) 2227-2230.
- [3] K. Takamiya *et al.*, *J Radiat. Prot. Res.*, **41** (2016) 350-353.
- [4] K. Takamiya *et al.*, *KURRI Progress Report 2016* (2017) 45-45.
- [5] P. Jungwirth *et al.*, *Chem. Rev.*, **106** (2006) 1259-1281.
- [6] A. A. Pawar *et al.*, *Aerosol Sci. Technol.*, **47** (2013) 383-394.

PR2-2 Particle Size Measurement of Radioactive Aerosol Particles in an Electron LINAC Using a Diffusion Battery System

Y. Oki and N. Osada¹

Research Reactor Institute, Kyoto University

¹Advanced Science Research Center, Okayama University

INTRODUCTION: Radiation-induced aerosol particles in the size range of several nm to ca. 100 nm are often observed in air of accelerator rooms during machine operation. The particles are produced by an air ionization process by primary beams or by secondary radiation emitted from beam loss points. The particles incorporate radioactive atoms to form radioactive particles. The size for radioactive particles was often measured using a wire screen technique in accelerator facilities. Convenient size measurement techniques are needed from the viewpoint of radiation protection in accelerator facilities.

In this work, an air irradiation experiment was performed in the 46-MeV electron linear accelerator (LINAC) facility of the Research Reactor Institute (KURRI) to examine performance of a newly assembled screen-type diffusion battery system. We tried to analyze particle size distributions for both the whole radiation-induced aerosols particles and the particles bearing a radioactive atom.

EXPERIMENTS: The new diffusion battery (DB) system consisting of three air-tight wire screen cylinders was assembled. Each cylinder contained a stack of 500-mesh stainless steel wire screens, and it was connected to a ball valve and a mass flow controller to change a flow rate independently. The valve and mass flow controller were controlled by a PC for unmanned measurement of aerosol size distribution.

When very fine aerosol particles pass through a stack of wire screens, a part of the particles are trapped on the screens by their diffusion according to their particle size. The loss by the screens is expressed as a function of particle size, coarseness and number of screens, and flow rate of particles. The particle diameter can be calculated by measuring the penetration ratio (N/N_0), where N_0 and N are number concentrations of the aerosol particles before and after penetrating screens, respectively.

Irradiation: In the target room a stainless steel irradiation tube was placed at a rear position of the tantalum target. During the irradiation, aerosol-free air was introduced to the tube from the experiment room next to the target room. The target was bombarded with a 30-MeV electron beam to produce bremsstrahlung and neutrons. The bremsstrahlung ionizes air and produces the radiation-induced aerosol. The beam current was ca. 10-100 μ A.

Size measurement for the whole radiation-induced aerosol particles: The irradiated air was simultaneously in-

troduced to the two wire screen cylinders A and B. The air flow rate for Cylinder A was gradually changed from 0 to 15 L/min, while that for Cylinder B was decreased from 15 to 0 L/min so that the total flow rate was maintained constant not to change irradiation rate of air in the irradiation tube. The irradiated air was sampled from both the upstream and downstream positions of the cylinders. The sampled air was introduced a condensation particle counter (CPC) to measure number concentration of the aerosol particles.

Size measurement for ¹³N-bearing aerosol particles: In the previous work, particle size of ¹¹C-bearing aerosols formed in the FFAG proton accelerator of KURRI was estimated using a combination technique of wire screens and imaging plate (IP) [1]. The same technique was applied to the electron LINAC facility in this work. The irradiated air was introduced to Cylinders A and B at the same air flow rate. Each cylinder had 40 pieces of the 500-mesh screen and a PTFE backup filter. An additional PTFE filter was placed at the upstream of Cylinder B. In the electron LINAC, ¹³N (half life: 9.965 min) is dominant radionuclide in air, and more than 90 % of ¹³N exist as gas form. In such a circumstance, the ¹³N gas often interfere the aerosol size measurement [2] due to condensation of the gas on the surface of the screens. Cylinder B was used estimation of the condensation by removing aerosol particles by the front PTFE filter. Activities of the screens and filters were simultaneously measured with a large IP (43 x 35 cm).

RESULTS: A scanning mobility particle sizer (SMPS) with nano-DMA was used for comparison with the DB system. The size distribution was confirmed to have a lognormal shape using SMPS in advance. The penetration ratios (N/N_0) obtained by changing air flow rate were fitted to a theoretical function [3] for lognormal distributions to obtain the geometric mean and geometric standard deviation of particle diameter.

Preliminary results showed that size of nano aerosol particles was in good agreement with that obtained with SMPS in the geometric mean diameter range of 10 to 15 nm. However, the size analysis for the ¹³N-bearing particles was unsuccessful at the present stage because of low intensity of photostimulated luminescence (PSL) of the IP. It was mainly caused by subtraction of the gas condensation effect.

REFERENCES:

- [1] Y. Oki, *et al.*, J. Radiat. Prot. Res., **41** (2016) 216-221.
- [2] N. Osada, Y. Oki, *et al.*, Prog. Nucl. Sci. Tech., **1** (2011) 483-486.
- [3] Y.S. Cheng and H.C. Yeh, J. Aerosol Sci., **11** (1980) 313-320.

PR3 Project Research on Development of Scattering Spectrometers Utilizing Small and Medium Class Neutron Source

M. Sugiyama

Research Reactor Institute, Kyoto University

Objectives and Allotted Research Subjects: The aim of this project is to evaluate and improve the possibility of small-angle neutron scattering (SANS) utilizing small and medium class neutron source since KUR-SANS, KUMASANS, is one of typical examples of SANS spectrometers installed at medium class neutron source. However, in this year, there was no enough machine times because of no operation in the first half year and the commissioning in the later half year. Under this circumstance, some works were performed with small-angle x-ray scattering spectrometers in our laboratory, or the others were carried out with SANS spectrometer in other facilities.

ARS-1: Determination of degree of deuteration level of deuterated protein through small-angle neutron scattering. (R. Inoue, K. Morishima, N. Sato, M. Sugiyama)

ARS-2: A saxs study on the nanostructure of gliadin hydrates with sodium chloride. (N. Sato, R. Urade, Y. Higashino, R. Inoue, K. Morishima, M. Sugiyama)

ARS-3: Characterization of Nanostructure in Metallic Materials using Small-Angle Scattering. (Y. Oba, N. Sato, R. Inoue and M. Sugiyama)

ARS-4: Nanostructure of Hydrated α -, γ -, ω -Gliadins. (R. Urade, Y. Higashino, Y. Kitao, N. Sato, M. Sugiyama, R. Inoue and Y. Sakamaki)

ARS-6: Nano structure of metal hydride by X-ray small angle scattering. (K. Iwase, K. Mori, Y. Oba, R. Inoue, M. Sugiyama)

ARS-7: Radius of Gyration of Polymer for Viscosity Index Improver at Various Temperatures Evaluated by Small-Angle X-Ray Scattering. (T. Hirayama, R. Takahashi, K. Tamura, N. Sato, M. Sugiyama, M. Hino, Y. Oba)

Main Results and Contents of This Project:

ARS-1: Inoue et.al. have determined the degree of deuteration level of deuterated protein through SANS method with Quakka in ANSTO. The control of deuteration level of deuterated protein is a key technology in the next generation of neutron biology.

ARS-2: Sato et.al. investigated the nanostructure of gliadin hydrates with sodium chloride using an in-house SAXS instrument (NANO-PIX, Rigaku) installed at Institute for Integrated Radiation and Nuclear Science, Kyoto University, instead of SANS. He shows the addition of NaCl makes the contraction effect of NaCl to the gliadin hydrates.

ARS-3: Oba et.al. are challenging that the characterization of nanostructure in metallic materials using both small-angle x-ray scattering and small-angle neutron scattering. In this year, his group mainly used an in-house SAXS instrument with Mo source (NANO-viewer, Rigaku) installed at Institute for Integrated Radiation and Nuclear Science, Kyoto University, and proved that Mo radiation is useful for the metallic materials even with in-house source.

ARS-4: Urade et.al. are investigating wheat flour dough of which physical properties mainly depend upon the wheat protein Gliadin. In this study, her group studied the structural difference of types of Gliadins, α -, γ -, ω -gliadins, in nano scale. SAXS analyses suggested that the C-terminal helix-rich structures of α - and γ -gliadins may cause the density fluctuation inside aggregates.

ARS-6: Iwase et.al. studied nano structure of metal hydride by Mo-source-X-ray small angle scattering (NANO-viewer, Rigaku), which is installed at Institute for Integrated Radiation and Nuclear Science, Kyoto University. The fractal dimension of the particle surface was estimated from the slope of a SAXS profile. As a result, the particle surface of Pr₂Co₇ was smooth.

ARS-7: Hirayama et.al. evaluated polymer viscosity index improver at various temperatures with small-angle x-ray scattering by an in-house SAXS instrument (NANO-PIX, Rigaku) installed at Institute for Integrated Radiation and Nuclear Science, Kyoto University. The result indicates that Olefin copolymers form largesized aggregate with a fractal-like structure in squalane even when the concentration was low, but the result conflicts from the past perception.

PR3-1 Determination of Degree of Deuteration Level of Deuterated Protein Through Small-angle Neutron Scattering

R. Inoue, K. Morishima, N. Sato and M. Sugiyama

Research Reactor Institute, Kyoto University

INTRODUCTION: Small-angle Neutron (SANS) technique gives the overwhelming opportunity for structural analyzes on various target samples. Especially, contrast-variation SANS (CV-SANS) technique [1], which utilizes the modulation of scattering contrast between solute and solvent, offers the better opportunity for studying the partial structure of complex biomacromolecules. However, the procedure for determining the degree of deuteration level of prepared deuterated biomacromolecules has not been well established up to now. We then try to utilize SANS technique for the determination of degree of deuteration level of deuterated protein. As a first trial, we prepared partially deuterated protein, which was expected to be contrast matched with D₂O. We try to verify whether or not such prepared partially deuterated protein is experimentally invisible in D₂O by SANS.

EXPERIMENTS: We firstly prepared 75% deuterated α B-crystallin by tuning the mixing ratio of hydrogenated and deuterated glucose in 75% D₂O. Prior to the SANS measurement, we also performed small angle X-ray scattering (SAXS) measurement with 75% deuterated α B-crystallin to check the absence of aggregation. SAXS measurements were performed with NANOPIX (Rigaku Corporation, Japan) equipped with HyPix-6000. A Cu K- α line (MicroMAX-007HF) was used as a beam source, which was further focused and collimated with a confocal multilayer mirror. Since KUMASANS, which is installed at our institute is still on the way to restart. Hence, SANS measurements on prepared 75% deuterated α B-crystallin was performed with QUOKKA installed at Australian Nuclear Science and Technology Organization (ANSTO). The wavelength of neutron and sample to detector distance was 6 Å and 8 m, respectively. To modulate the scattering contrast, we prepared 75% deuterated α B-crystallin in 0%, 60% and 100% D₂O. All the SAXS and SANS measurements were performed at 37 °C.

RESULTS: Fig.1 shows SAXS profile from 75% deuterated α B-crystallin at the concentration of 0.45 mg/mL. It can be clearly seen the absence of upturn at low Q region. From the Guinier analysis, the radius of gyration (R_g) was estimated to 52.8±1.0 Å and this size is consistent with that reported in our previous results [2]. Fig. 2 (a) shows the concentration scaled SANS profiles from 75% deuterated α B-crystallin in 0%, 60% and 100% D₂O, respectively. With increasing the volume fraction of D₂O, the scattering intensity tends to decrease, implying the decrease of scattering contrast. Fig. 2 (b) indicates the volume fraction of D₂O dependence of $(I(0)/c)^{0.5}$, which is nearly comparable to scattering contrast. In accordance

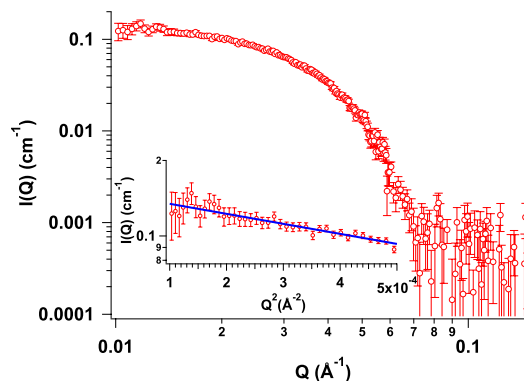


Fig. 1 SAXS profile from 5% deuterated α B-crystallin at the concentration of 0.45 mg/mL. Inset indicates the result of Guinier analysis.

with the tendency shown in Fig. 2 (a), $(I(0)/c)^{0.5}$ decreased with increasing the volume fraction of D₂O. $(I(0)/c)^{0.5}$ intersected with $(I(0)/c)^{0.5}=0.0$ at 97.5 % D₂O, certifying the nearly contrasted with 100% D₂O. As a

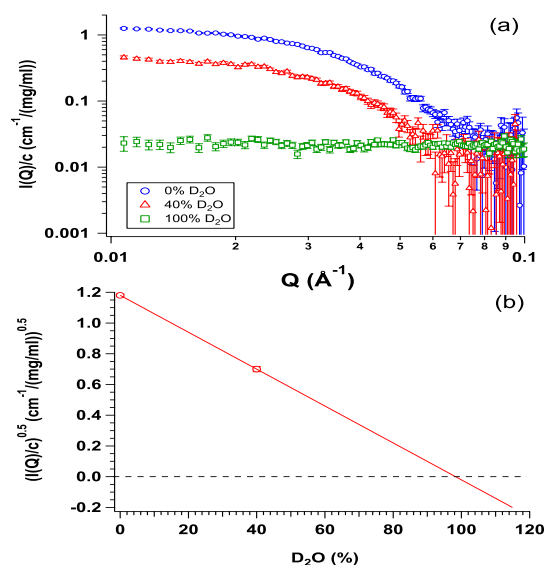


Fig. 2 (a) SANS profile from 75% deuterated α B-crystallin in 0%, 40% and 100% D₂O. (b) The volume fraction of D₂O dependence of $(I(0)/c)^{0.5}$.

next step, we will prepare different deuteration level of deuterated protein and further check the reliability of determination of degree of deuteration of protein with SANS.

REFERENCES:

- [1] M. Sugiyama *et al.*, BBA, **1862** (2018) 253-274.
- [2] R. Inoue *et al.*, Sci. Rep. **6** (2016) 29208.

PR3-2 A SAXS Study on the Nanostructure of Gliadin Hydrates with Sodium Chloride

N. Sato, R. Urade, Y. Higashino¹, R. Inoue, K. Morishima, and M. Sugiyama

Institute for Integrated Radiation and Nuclear Science, Kyoto University

¹*Graduate School of Agriculture, Kyoto University*

INTRODUCTION: Since ancient times a wide variety of wheat flour foods have been produced and consumed worldwide. Wheat flour foods with high quality and processability can be made from wheat dough having proper physical properties. As is well-known, physical properties of wheat dough is mainly ascribable to those of gluten formed in the dough. More in detail, gluten is composed of two major wheat proteins: gliadin and glutenin. Gliadin is responsible for viscous behavior of gluten, while glutenin is for elastic behavior of it. Therefore it is essential to clarify the nature of these proteins for thorough understanding of physical properties of wheat dough. It had been known that gliadins were only soluble in 60–70% ethanol-water solutions or dilute acids. However recent study revealed that gliadins can be extracted into pure water from NaCl-containing dough [1], which enables the investigation of wheat proteins in the environment more similar to real dough. From this point of view, we have been studying the nanostructure of gliadins in aqueous solutions or hydrates by small-angle X-ray scattering (SAXS) [2]. SAXS is useful for the nanostructural analysis on opaque, disordered and condensed materials, and has been widely employed for the study on soft matters such as polymer gel, colloid and rubber. Our previous study elucidated that gliadin hydrates with a concentration of 40wt% shows a broad peak around scattering vector of 0.4 nm^{-1} in its SAXS profile. This peak indicates the presence of density fluctuation within gliadin aggregates of which the correlation length is ca. 15nm. Furthermore, the addition of NaCl greatly affects the density fluctuation of gliadin hydrates. The peak due to fluctuation gradually diminishes and the correlation length becomes smaller with increasing NaCl concentration. Since the physical properties of gliadins, such as water retention and viscoelasticity, is highly dependent on NaCl concentration, there exists close relationship between nanostructures and physical properties of gliadin hydrates in the presence of NaCl. However, it is still unknown what kind of effect acts on the interaction between gliadin molecules and induces the change of nanostructure of the aggregates. In this study, we carried out SAXS measurements for various gliadin hydrates as different concentrations of urea was added to clarify the mechanism of NaCl effect acting on the association of gliadin molecules.

EXPERIMENTS: Gliadins were prepared by the same method as reported before [1]. Samples were put into 1-nm-thick aluminum cells with optical windows made of 7- μm -thick Kapton film. SAXS measurements were

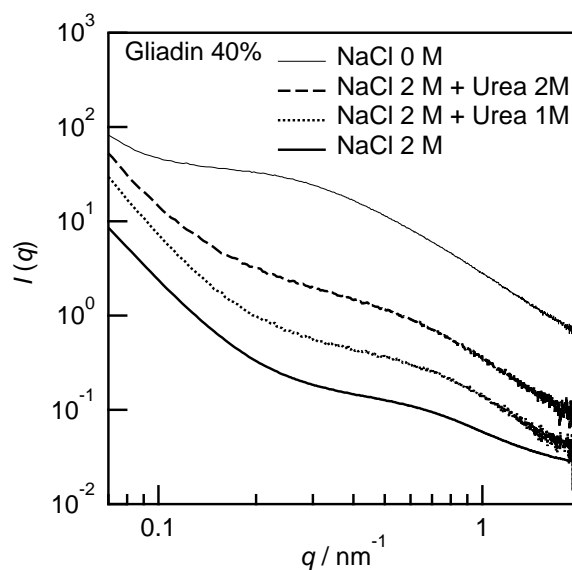


Fig 1. SAXS profiles of 40% gliadin hydrates containing 2 M NaCl together with various concentrations of urea. Each profile is vertically shifted for clarity.

performed with an in-house SAXS instrument (NANOPIX, Rigaku) installed at Institute for Integrated Radiation and Nuclear Science, Kyoto University. The wavelength of X-ray was 1.54 \AA and the camera length was 1300 mm. Typical exposure time was 300 sec. All measurements were carried out at $25 \text{ }^\circ\text{C}$.

RESULTS: Hydrogen bonding between amino acids of proteins is known to be suppressed in the presence of urea. Therefore, it is expected that influence of hydrogen bonding on the effect of NaCl can be clarified by SAXS measurements for gliadin aggregates with different concentrations of urea. Fig. 1 shows the results. As was same as the previous results, broad peak at $q = 0.4 \text{ nm}^{-1}$ without NaCl became small and shifted higher to 0.8 nm^{-1} at a NaCl concentration of 2 M. This demonstrates the contraction effect of NaCl to the gliadin hydrates. By adding urea, however, the peak at 0.8 nm^{-1} slightly shifted back to lower q , and the profiles became similar to that of gliadins without NaCl. This suggests that hydrogen bonding between gliadin molecules is partly responsible for the contraction of gliadin hydrates with NaCl. Nevertheless, the change induced by urea was so small that other interaction such as hydrophobic interaction is assumed to be far more dominant to the effect of NaCl on the contraction of gliadin hydrates. Further SAXS experiments to examine intermolecular interaction, for example, measurements of gliadins with deamidation of glutamine residues is now underway.

REFERENCES:

- [1] T. Ukai, Y. Matsumura, R. Urade, *J. Agric. Food Chem.*, **56** (2008) 1122-1130.
- [2] N. Sato, *et al.*, *J. Agric. Food Chem.*, **63** (2015) 8715-8721.

PR3-3 Characterization of Nanostructure in Metallic Materials using Small-Angle Scattering

Y. Oba, N. Sato¹, R. Inoue¹ and M. Sugiyama¹

Materials sciences Research Center, Japan Atomic Energy Agency

¹Institute for Integrated Radiation and Nuclear Science, Kyoto University

INTRODUCTION: Small-angle scattering (SAS) is a powerful technique to characterize nanostructures in a wide variety of materials. In particular, SAS is suitable for metallic materials because of the large gauge volume compared to electron microscopy. Another advantage is high penetration power of probe beams (X-ray and neutron). The application of SAS is now spreading into the metallic materials.

However, little opportunity to perform SAS measurements has restricted the further expansion of the SAS application. This is particularly remarkable for small-angle neutron scattering (SANS), which requires large facilities such as research reactors or accelerators.

To overcome this situation, it is necessary to use existing SANS instruments more effectively. The SANS instrument CN-2 KUMASANS installed at the Kyoto University research reactor (KUR) plays an important role because it is available for the metallic materials [1]. Further improvement of the CN-2 KUMASANS is effective for the metallic materials.

Another solution is the support by small-angle X-ray scattering (SAXS). It is relatively easy to access to laboratory-scaled SAXS instruments, which can provide plenty of machine time. Structural information obtained by SAXS is basically same as that by SANS. In this study, the improvement of the CN-2 KUMASANS was first carried out for more effective use targeting the metallic materials. In addition, the new SAXS instrument installed at the Integrated Radiation and Nuclear Science was examined.

EXPERIMENTS: The SANS experiment was conducted at the CN-2 KUMASANS [1]. The SAXS experiments were performed using a SAXS instrument equipped with Mo K α radiation (Nano-viewer, RIGAKU).

RESULTS: For the CN-2 KUMASANS, a vacuum sample chamber was installed at the sample area, which was previously in air separated from upstream and downstream vacuum chambers by vacuum windows (Fig. 1). As the result, background scattering contributions from air and from the vacuum windows are eliminated. This is effective for vacuum resisting samples such as most metallic materials.

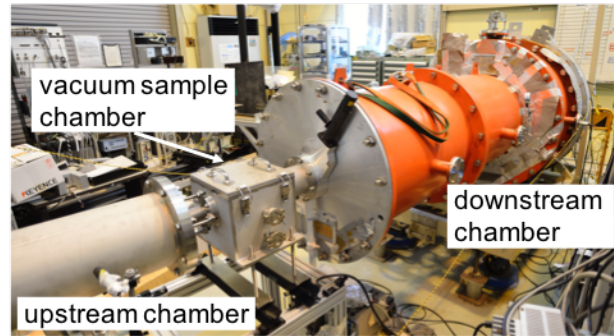


Fig. 1. Vacuum sample chamber installed at the CN-2 KUMASANS.

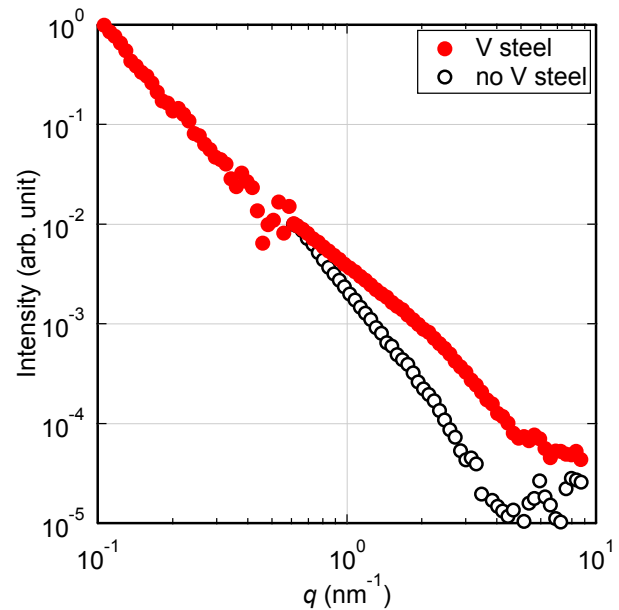


Fig. 2. Typical SAXS profiles of the steels with/without precipitates. Vanadium (V) steel contains the precipitates of vanadium carbide.

Fig. 2 shows the SAXS profiles of the steels containing nanosized precipitates of vanadium carbide. A shoulder around $q=2 \text{ nm}^{-1}$ is observed. This indicates that the SAXS with the Mo radiation is useful for the metallic materials. Furthermore, a new sample changer was installed in the SAXS instrument. This allows sequential measurements of up to 49 samples. This is important for effective use of the machine time.

REFERENCE:

[1] M. Sugiyama and Y. Maeda, Jpn. J. Appl. Phys., **33** (1994) 6396-6402.

R. Urade, Y. Higashino, Y. Kitao, N. Sato¹ M. Sugiyama¹,
R. Inoue¹ and Y. Sakamaki¹

Graduate School of Agriculture, Kyoto University
¹ Research Reactor Institute, Kyoto University

INTRODUCTION: Rheological properties of wheat flour dough are dependent on the physical properties of gluten. Gluten consists mainly of two types of proteins: glutenins and gliadins [1]. Among them, gliadins are composed of α -, γ - and ω -gliadins and responsible for the viscosity of dough [2]. Since gliadins are monomeric proteins, gliadin nanostructure formed by noncovalent intermolecular associations are thought to be responsible for its viscoelastic properties. Hence, detailed analysis on nanostructure of gliadins are essential to understand the rheological properties of hydrated gliadins at the molecular level. In this study, we fractionated α -, γ - and ω -gliadins and performed SAXS analysis of the each hydrated α -, γ - and ω -gliadins.

EXPERIMENTS: Gliadins were isolated from wheat flour by the method established previously [3, 4]. Each gliadins was separated by using a column embedded with SP Sephadex C-50 resin (GL Sciences) and eluting with elution solution (2M urea, 0.04M ethlendiamine, 0.08M HCl pH 3.1). Gliadins in the eluted fractions were determined by western blot analysis after SDS-PAGE. Anti- α -gliadin or γ -gliadin serum for western blot analysis were prepared using recombinant C-terminal domains of α -gliadin or γ -gliadin expressed in *E. coli*. The separated gliadins were subjected on the gel filtration column chromatography on a SPS C-50 column (GL Sciences) equilibrated with 2M Urea, 0.05M NaCl, CH₃COOH pH3.1. once or twice to remove contaminated glutenins. The purified gliadins were dialyzed against distilled water and lyophilized. SR-VUV CD spectra of gliadins were measured at BL12 of the Hiroshima Synchrotron Radiation Center (HiSOR). A nanostructure of gliadins in distilled water was investigated by SAXS analysis. SAXS experiments were carried out with NANOPIX (Rigaku) in Kyoto University Research Institute (KURRI) or at the beam line BL-10C of Photon Factory, a synchrotron radiation facility of Institute of Materials Structure Science, High Energy Accelerator Research Organization (KEK). The dilute solution samples were measured in an aluminum cell with 20- μ m thick quartz windows, while viscous hydrated solids concentrated solutions (40 wt%) in a PTFE sandwich cell with windows of 7.5- μ m thick Kapton® films (TORAY-DuPont).

RESULTS: Gliadins were separated to three α -gliadin fractions, one γ -gliadin fraction and one ω -gliadin fraction by the first ion-exchange column chromatography. From the SR-VUV CD spectra, contents of α -helix and

β -strand of α -, γ - and ω -gliadins were calculated to be 27-31% and 16-19%, 25% and 20%, and 6.2% and 45%.

Guinier and cross-section Guinier analyses of SAXS data from 0.1% gliadins proved that α -, γ - and ω -gliadins in water had a size larger than those in 70% ethanol [5]. At 40 wt%, all gliadins formed gel-like pastes. α -fa-gliadins and γ -gliadins showed SAXS profiles with a shoulder peak at 0.4 nm⁻¹ and a steep rise in the low-q region owing to large aggregation. Omega-gliadins showed a SAXS profile with only steep rise in the low-q region. These results suggested that the C-terminal helix-rich structures of α - and γ -gliadins may cause the density fluctuation inside aggregates (Figure 1).

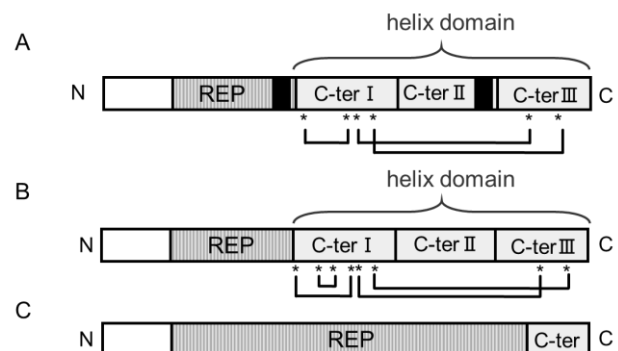


Figure 1 Diagrams representing the structure of gliadins.

A, α -gliadins; B, γ -gliadins; and C, ω -gliadins. The repetitive domains (REP) of α -gliadins, γ -gliadins or ω -gliadins are composed of a single repeat motif of five to eight residues with the following consensus sequence: P(F/Y)PQ₃₋₅, seven to 10 residues with the following consensus sequence: PFPQQ₀₋₁(PQQ)_{1,2} or a single repeat motif of six to 11 residues with the following consensus sequence: PFPQ_{1,2}PQ_{1,2}, respectively. N = N-terminal region, REP = repetitive domain. C-ter I, II, III represent a C-terminal cysteine-rich region, a glutamine-rich region and a terminal conserved sequences. Asterisks represent cysteine residues. All cysteines form in intramolecular disulfide bonds (association lines). α -Gliadins contain two polyglutamine stretches (black bars) in the C-terminal part of the REP domain and C-ter II region.

REFERENCES:

- [1] F. MacRitchie and P. L. Weegels. Structure and functional properties of gluten. "Wheat, 4th ed." AACC International Press, 2009.
- [2] M. Cornec *et al.*, *J. Cereal Sci.*, **19** (1994) 131-139.
- [3] T. Ukai *et al.*, *J. Agric. Food Chem.*, **56** (2008) 1122-1130.
- [4] N. Sato *et al.*, *J. Agric. Food Chem.* **63**, 8715-8721, 2015.
- [5] N. Thomson *et al.*, *Biochim. Biophys. Acta.*, **1430** (1999) 359-366.

K. Iwase¹, K. Mori, Y. Oba², R. Inoue and M. Sugiyama

Research Reactor Institute, Kyoto University

¹Department of Materials Science and Engineering, Ibaraki University

²Japan Atomic Energy Agency

INTRODUCTION: The phase diagram for a Pr–Co system was previously reported [1,2]. This phase diagram shows nine phases in the equilibrium state: Pr₃Co, Pr₇Co₃, Pr₂Co_{1.7}, PrCo₂, PrCo₃, Pr₂Co₇, Pr₅Co₁₉, PrCo₅, and Pr₂Co₁₇. It is known that Pr–Co binary alloys absorb hydrogen. Kuijpers investigated the hydrogen absorption–desorption property of PrCo₅. The maximum hydrogen capacity was approximately 0.6 H/M at 294 K. A plateau region was observed in the P–C isotherm. The pressure corresponding to this plateau was 0.05 MPa. The enthalpy of the hydride formation was determined to be -38.5 kJ/mol H₂ from the Van't Hoff plot. The PrCo₅–H system was reported by Ichinose et al. and Yamamoto et al. Hydride phases, PrCo₅H_{2.7} and PrCo₅H_{4.69}, were prepared by exposing the alloy to hydrogen gas at 1–5 MPa at room temperature. Burnasheva et al. reported on the structure of the hydride phase based on RCo₃ compounds (R = Ce, Pr, Nd, Y, etc.). The maximum hydrogen capacity of PrCo₃ reached 1.2 H/M. PrCo₃, Pr₂Co₇, and Pr₅Co₁₉ all have superlattice structures. The crystal structure of the PrCo₃ was previously reported. The alloy was prepared by arc-melting and high-energy milling. After heat treatment, a PuNi₃-type structure was obtained. Khan investigated the crystal structure of Pr₅Co₁₉ with a Ce₅Co₁₉-type structure. However, the structural information parameter of Sm₅Co₁₉-type Pr₅Co₁₉ was not reported.

The present study focused on the nano structural changes that occur during the hydrogen absorption–desorption process of the Pr₂Co₇ with a Ce₂Ni₇-type structure. We paid close attention to the different hydrogenation behaviors of Pr₂Co₇, Pr₂Ni₇, and La₂Ni₇. Detailed nano structural information for Pr₂Co₇H_x was not reported.

EXPERIMENTS: SAXS data were collected using a Rigaku NANO-Viewer with Mo-K α radiation monochromatized using a confocal mirror and a two-dimensional detector (PILATUS-100k). The voltage and current of the X-ray generator in this measurement were 50kV and 24 mA. The sample was set under vacuum. The incident x-ray was focused using a two-dimensional confocal mirror and collimated using the pinhole technique. The distance between the samples and the detector was 1.06 m, which covers q range from 0.06 to 10 nm⁻¹. The fractal dimension of the particle surface, DS, can be extracted from the slope of a SAXS profile, $I(q)$, in the Porod region, that is,

$$I(q) \propto q^{-\alpha} \quad (1)$$

$$Ds = 6 + \alpha \quad (2)$$

where q is the magnitude of a scattering vector ($= 4\pi\sin\theta / \lambda$, where 2θ is the scattering angle and λ is the X-ray wavelength). It is a smooth surface as DS is close to 2, but a rough surface as DS is close to 3.

RESULTS: The SAXS profiles of Pr₂Co₇ and Pr₂Co₇H_{7.2} are shown in Fig. 1. Super-reflection peak of Pr₂Co₇ with Ce₂Ni₇-type, 002, and that of the Pr₂Co₇H_{7.2} with orthorhombic, 002, were clearly observed in the q region between 4.10 nm⁻¹ and 6.0 nm⁻¹. The shoulder existed in the q region between 1.30 nm⁻¹ and 3.90 nm⁻¹, which was caused by CaCu₅-type phase. The original alloy consisted of 91% Ce₂Ni₇-type and 9% CaCu₅-type. The DS value was obtained from the least-squares fit in the q range between 0.10 nm⁻¹ and 0.68 nm⁻¹. As a result, DS was estimated at 1.5 and 2.0, meaning that the particle surface of undeuterated Pr₂Co₇ was smooth.

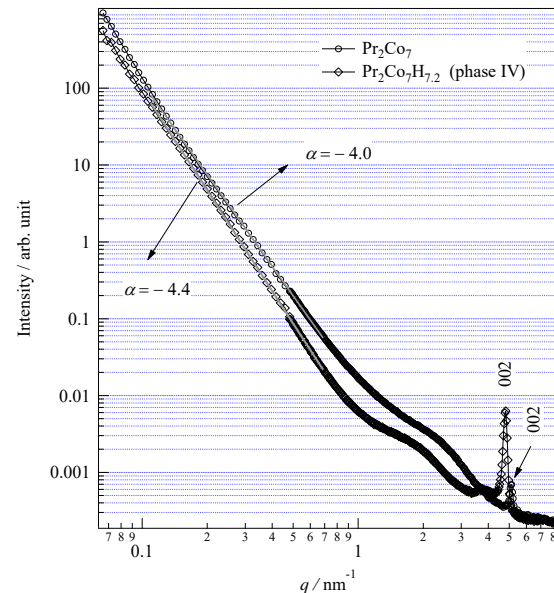


Fig. 1 SANS profiles, $I(q)$, for Pr₂Co₇ and Pr₂Co₇H_{7.2} (H/M = 0.8)

REFERENCES:

- [1] Ray AE., A review of the binary rare earth-cobalt alloy systems. Cobalt 1974;1:13-8.
- [2] Okamoto H. editor. Binary alloy phase diagrams. 2nd ed. Ohio: ASM International, Materials Park; 1996. plus updates.

PR3-6 Radius of Gyration of Polymer for Viscosity Index Improver at Various Temperatures Evaluated by Small-Angle X-Ray Scattering

T. Hirayama, R. Takahashi¹, K. Tamura², N. Sato³, M. Sugiyama³, M. Hino³ and Y. Oba⁴

Dept. of Mechanical Eng., Doshisha University
¹Dept. of Mechanical Eng., Graduate School of Doshisha University

² Idemitsu Kosan Co., Ltd.

³Institute for Integrated Radiation and Nuclear Science, Kyoto University

⁴Japan Atomic Energy Agency

INTRODUCTION: Lubricating oils are necessary for friction reduction and high wear durability of sliding surfaces in machine components, and the development of the best oils is strongly required from industry. Viscosity index improver (VII) is a kind of additives for relieving the reduction of viscosity of lubricating oil due to temperature rise. Classical textbooks say that the VII molecules work with changing their equivalent radius in base oil in accordance with oil temperature. However, there are only few papers investigating the equivalent radius of VII molecules by small-angle X-ray scattering (SAXS) and/or small-angle neutron scattering (SANS), and there is still room for discussion of the behavior and working mechanism of VII molecules in oil. This study tried to investigate the radius of gyration of several kinds of VII polymers in base oil at various temperatures by SAXS, and the behavior of polymers was checked and discussed.

EXPERIMENT: To investigate the radius of gyration of VII polymer, we used a SAXS instrument (NANOPIX, Rigaku) with a Cu-target X-ray source emitting X-ray with a wavelength of 1.54 Å, a characteristic line of Cu-K α . The 1.2 mm-thick aluminum cells having a optical windows made of 20- μ m thermally-resistant engineering plastic film (Superio-UT, Mitsubishi chemical) was used for the measurement. The cell temperature increased to be 25, 40, 60, 80 and 100°C in turn, and the last measurement was carried out at 25°C again after cooling for checking if the VII molecule degenerated or not by heat. Olefin copolymers (OCP) type VII was prepared as a typical one used in engine oil as a first trial. Squalane was used as a model base oil, and the concentrations of OCP into squalane were 0.17, 0.5 and 1.0 mass%.

RESULTS AND DISCUSSION: The SAXS intensity profiles versus scattering vector q from squalane with 0.5 mass%-OCP VII at various temperatures were shown in Fig. 1. The profiles were obtained by subtracting the intensity profiles from pure squalane at each temperature previously measured with the same liquid cell. We can see that the intensity profiles had little change even if the temperature changed. It means that the size and shape of

OCP molecules was hardly changed in the observed range regardless of temperature rise, and this result contradicts the fact that the OCP effectively work as VII. The profiles from the squalane with OCP with various concentrations are shown in Fig. 2. Though scattering intensity increased in accordance with the increase in concentration as expected, the slopes of each profile around $q=0.1 \text{ nm}^{-1}$ were almost same, about $\propto -q^{2.8}$. It indicates that OCP molecules form large-sized aggregate with a fractal-like structure in squalane even when the concentration was low, but the result conflicts with the past perception. We will continue to measure the other types of VII polymers by SAXS to clarify how we should explain the SAXS profiles from oil-soluble polymers in oil.

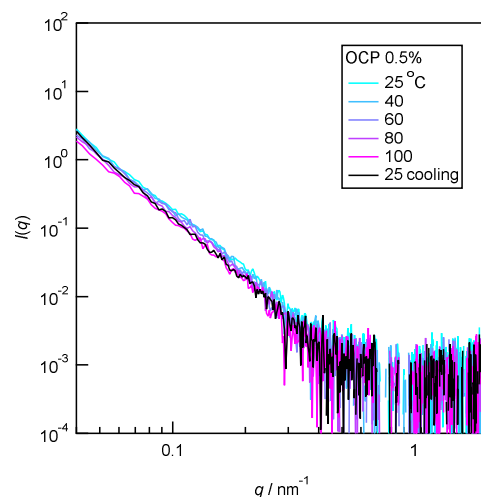


Fig. 1. SAXS intensity profiles from squalane with 0.5 mass%-OCP VII at various temperature.

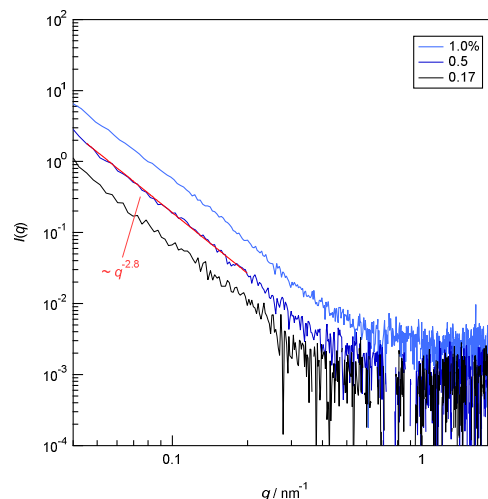


Fig. 2. SAXS intensity profiles from squalane with OCP VII with various concentration at 25°C.

PR5 Project Research on a Study on Biological Character and Use of the Particle Induced by the Boron Neutron Capture Reaction

Y. Kinashi

Research Reactor Institute, Kyoto University

Objectives and Participating Research Subjects

In this project, we are intending to develop the new application using the characteristics of the particles from the neutron capture reaction. Our project researchers were not able to carry out own experiments enough because KUR has been almost stopping during this year.

PRS-2 was not able to carry out its experiments because KUR has been almost stopping during this year.

PRS-3 was not able to carry out its experiments because KUR has been almost stopping during this year. The nuclear reactor operated again, but I did not get experiment days at my convenience.

PRS-4 was not able to carry out its experiments because KUR has been almost stopping during this year.

PRS-1 Analysis of mutation in the mammalian cells induced by BNCR (boron neutron capture reaction)
(Y. Kinashi *et al.*)

PRS-2 Analysis of double strand breaks in the mammalian cells induced by BNCR
(S.Takahashi *et al.*)

PRS-3 Development of the PARP repressor reinforced in its function by BNCR
(Y.Uto *et al.*)

PRS-4 Development of the model animal showing the blood vessel damage by BNCR
(R. Wate *et al.*)

Main Results and Contents

PRS-1 investigated that the biological effects of the combination of the BNCR (Boron Neutron Capture Reaction) and Temozolomide (TMZ) that is DNA alkylating agent on the T98G and A172 human glioblastoma cells were investigated. Our results suggested that TMZ treatment has no sensitization effect of radiation in A172 cells with low MGMT (methyl guanine methyl transferase) gene expression that is the DNA repair enzyme. T98G cells with high MGMT gene expression were resistance to TMZ. The enhancement effect of the combination of neutron irradiation and TMZ treatment was not found in T98G cells.

We were not able to carry out experiments sufficiently because KUR has been almost stopping during this year.

PR5-1 Biological Effects of DNA Alkylating Agents on the Cell Lethal Effects of BNCR

Y. Kinashi, R. Akayama and S. Takahashi

Research Reactor Institute, Kyoto University

INTRODUCTION: Most BNCT (Boron Neutron Capture Therapy) patients have already received chemotherapy. Especially many brain tumor patients are taking temozolomide (TMZ) treatment. TMZ is a DNA-alkylating agents and particularly effective cancer drug for glioblastoma. In this study, we investigated the sensitivity of the glioblastoma cell lines of T98G (p53 mutated) and A172 (p53 wild) after exposure to neutron irradiation and TMZ.

MATERIALS & METHODS: The glioblastoma cell lines of T98G (p53 mutated) and A172 (p53 wild) are purchased from Riken BRC Cell Bank. TMZ solution prepared by the medium, and removal washing with phosphate buffered saline after 23 hours incubation. In the experiment exposed with TMZ, T98G cells showed TMZ resistance about 10 times higher than A172 cells. The confluent cells in a culture dish were transferred into a Teflon tube and irradiated with a thermal neutron beam in the Research Reactor of Institute for Integrated Radiation and Nuclear Science, Kyoto University. A portion of the irradiated cells was checked to determine the cell survival rate using the conventional colony formation assay immediately after irradiation. The gamma-rays irradiation for cells was carried out using Co-60 gamma-ray facility. After irradiation, cells were seeded on a Petri dish and incubated for 14 days. The survival curve creates a Plating Efficiency of each treatment and control groups compared survival rate.

RESULTS and DISCUSSION: T98G cells are resistance to TMZ because they have MGMT (methylguanine methyltransferase) gene expression that is the DNA repair enzyme. The IC50 value of TMZ for each cell line was 443 μ M for the T98G and 43 μ M for A172, respectively. Table 1 shows the survival data observed differences in sensitivity of the between two cells. The cell killing effect of neutron for each brain tumor cell was higher than gamma rays.

Table1. RBE (Relative Biological Effectiveness) calculated from D₁₀ dose*

	A172	A172 +B10 (20ppm)	T98G	T98G +B10 (20ppm)
D ₁₀ (Gy) of neutron	1.7	0.82	5.2	1.1
D ₁₀ (Gy) of γ -ray**	4.8		7.0	
RBE	2.8	5.9	1.3	6.4

* Each D₁₀ value was obtained from a survival curve

** Co⁶⁰ gamma-ray system

Furthermore, the RBE of T98G was higher than A172 under the BNCR. These results indicate that BNCT is suitable for treatment of radio-resistant brain tumors.

In the combination study of neutron and TMZ, there was no apparent change in the D₁₀ value of T98G cells. D₁₀ value decreased slightly after the gamma-ray and TMZ in A172 cells. These results show that TMZ treatment has the sensitization effect of radiation in A172 cells. The A172 cells that alkylation repair activity is low and cells have high susceptibility to TMZ. TMZ concluded that further enhance the cell-killing effect of radiation. It is generally known that patients with glioblastoma with MGMT gene silencing have the benefit from TMZ and survival benefit for the chemoradiotherapy^[1]. Further studies will be needed to analyze whether synergy effect of the combination of BNCT and TMZ in various brain tumors showing low TMZ expression.

[1] M.E.Hegi *et al.*, N. Engl. J. Med., **352** (2005) 997-1003.

A. Kinomura

*Institute for Integrated Radiation and Nuclear Science,
Kyoto University*

OBJECTIVES: Irradiation facilities of high-energy particles for neutrons (Material Controlled irradiation Facility), ions (e.g., Heavy ion irradiation facility) and electrons (Temperature-controlled irradiation facilities, KUR-LINAC) have been extensively developed at the Institute for Integrated Radiation and Nuclear Science. The developed facilities have been in operation and opened for joint research projects. One of the objectives of this project is to further improve or optimize irradiation facilities for advanced irradiation experiments.

As characterization techniques for irradiated materials, a slow positron-beam system and a focused ion beam system have been developed and introduced, respectively, in addition to previous characterization facilities such as an electron microscope, an electron-spin-resonance spectrometer, a bulk positron annihilation spectrometer and a thermal desorption spectrometer. Another objective is to introduce new techniques or reconsider analytical methods of previously used characterization techniques.

Based on these two objectives, we expect the enhancement of previous studies and the attraction of new users for the joint research program.

The allotted research subject (ARS) and individual co-researchers are listed below.

ARS-1:

Study on Efficient Use of Positron Moderation Materials (A. Kinomura *et al.*)

ARS-2:

Electron-irradiation effects on diffusion coefficient of Cu in Fe studied by three dimensional atom probe (K. Inoue *et al.*)

ARS-3:

Change in Positron Annihilation Lifetime of Vacancies by Hydrogen Charging in Tungsten (K. Sato *et al.*)

ARS-4:

Gamma-ray irradiation effect on ZnO bulk single crystal (K. Kuriyama *et al.*)

ARS-5:

Establishment of technique for thermal diffusivity measurement using TEM disk size miniature test specimens for post-irradiation experiments (M. Akiyoshi *et al.*)

ARS-6:

Positron Annihilation Study of Fe-Cr binary alloy after Electron Irradiation (T. Onitsuka *et al.*)

ARS-7:

Study on Free Volume in Diamond-like Carbon Thin Films by Positron Annihilation Spectroscopy (K. Kanda *et al.*)

ARS-8

Thermal stability of diamond-like carbon films (S. Nakao

et al.)

RESULTS: In ARS-1, the performance of the brightness enhancement system of the slow positron-beam system of Kyoto University research Reactor (KUR) was evaluated by using a positron beam as the KUR operation was approved and restarted.

In ARS-2, electron-irradiation for Fe-1.0wt.%Cu alloy was performed with energy of 8 MeV at KUR LINAC. The irradiation temperature was about 750 K.

In ARS-3, high purity tungsten irradiated by 8 MeV electrons were characterized by positron lifetime spectroscopy. After hydrogen charging, the second lifetime decreased because the single vacancies are decorated with hydrogen.

In ARS-4, green luminescence of ZnO after Co-60 gamma-ray irradiation increased by about 14% compared with that of unirradiated ZnO, suggesting that oxygen vacancy and zinc vacancies were introduced by Compton scattering during gamma-ray irradiation.

In ARS-5, the miniature specimen for measurement of thermal diffusivity was validated and this result will be widely used in future materials irradiation studies.

In ARS-6, Fe-40Cr alloy samples after electron irradiation by KURRI-LINAC were characterized by positron annihilation spectroscopy. The result indicated that the rapid increase in the W-parameter due to irradiation.

In ARS-7, positron annihilation measurement was performed at the slow positron beam system (B-1) for three types of DLC (diamond-like carbon) films. The result of S parameters can be considered that hydrogen atoms narrow the free volume in the DLC film.

In ARS-8, the TDS (thermal desorption spectroscopy) measurement at high temperature up to 800 °C was carried out for various DLC and carbon films. There is a possibility that the structural changes may be driven by the creation and annihilation of vacancy and defects caused by hydrogen desorption.

SUMMARY: In addition to developments on the slow positron beamline and a sample holder for electron irradiation, combinations of new materials and different irradiation/characterization techniques were continued. These studies were performed in the line of the objectives of this project. Further studies are in progress for the following year.

A. Kinomura, N. Oshima¹, Y. Kuzuya and A. Yabuuchi

*Institute for Integrated Radiation and Nuclear Science,
Kyoto University*

¹*National Institute of Advanced Industrial Science and
Technology (AIST)*

INTRODUCTION: Positron annihilation spectroscopy is a unique analytical method to detect vacancies, voids and free volume of materials. Energy-variable mono-energetic positron beams (slow positron beams) are important to perform depth-dependent positron annihilation spectroscopy of thin films or surface layers. Intense positron sources are required to efficiently obtain slow positron beams. Positron sources based on pair creation have higher intensity than radioisotope-based positron sources. Therefore, positron sources using pair-creation by gamma-rays from a nuclear reactor have been developed by using Kyoto University research Reactor (KUR). In the case of the KUR, the source size of the KUR slow positron beam is approximately 30 mm in diameter. For typical sample sizes of materials analysis (≤ 10 mm), it is necessary to reduce beam sizes efficiently while keeping beam intensity as high as possible. For this purpose, brightness enhancement techniques are used. In this study, we have evaluated the brightness enhancement system in the KUR slow positron beam system.

EXPERIMENTS: The brightness enhancement system of the KUR slow positron beam system has been examined using electron beams after the system was installed [1], since the KUR was not in operation for about 3 years to comply with a new safety criteria. As the KUR operation was restarted on August 2017, the brightness enhancement system was accordingly evaluated by a reactor-based positron beam.

Three types of experiments were performed for the brightness enhancement system: (1) Optimization of bias-voltages and solenoid/Helmholtz coil currents to maximize positron-beam intensities. (2) Examination of focusing performance of the brightness enhancement system. (3) Efficiency evaluation of remoderator thin films.

RESULTS: The positron source of the KUR slow positron beamline consists of a W converter, two W moderator and extraction electrode, where bias voltages can be applied to each part. Slow positrons generated at the source was transported by magnetic fields formed by solenoid or Helmholtz coils along the beamline to the brightness enhancement system and a sample chamber. Several steering coils were attached to the beamline to optimize beam trajectories. The best combination of voltages for the source components and currents for solenoid, Helmholtz and steering coils was determined by observing the phosphor-screen images and intensities of annihilation gamma-rays on the microchannel plates (MCP's) as shown in Fig. 1. Note that the MCP2 is positioned at the focal point of the lens in the brightness

enhancement system. After the optimization, the positron intensity at the sample chamber was measured to be 2.4×10^6 e⁺/s for the 5 MW operation.

Spot sizes of the positron beam were measured from pictures of the MCP phosphor screens before and after the brightness enhancement. Spot sizes for horizontal and vertical directions were slightly different. A spot area was reduced by a factor of ~ 20 after focusing at the brightness enhancement system.

Remoderation efficiencies were evaluated from annihilation gamma-ray intensities by comparing MCP1 and MCP3 in Fig. 1. Fig. 2 shows the typical gamma-ray spectra measured by a Ge detector. Gamma-ray intensities were calculated after the subtraction of background gamma-rays without introducing the positron beam. The efficiency was measured to be $\sim 2\%$.

In summary, the brightness enhancement system of the KUR slow positron system was evaluated with a positron beam during the KUR operation. Demagnification factors and remoderation efficiencies were successfully measured. We plan further optimization of the system in the near future.

REFERENCE:

[1] Y. Kuzuya et al. J. Phys. Conf. Series 791 (2017) 012012.

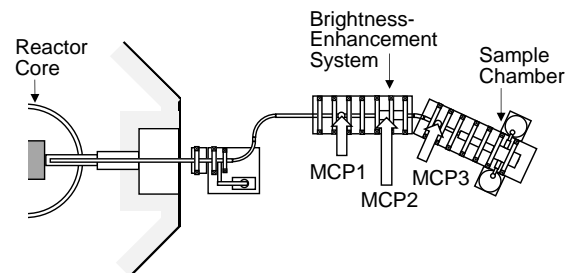


Fig. 1. Schematic view of the beamline and the positions of the brightness enhancement system and microchannel plates (MCP1, MCP2 and MCP3).

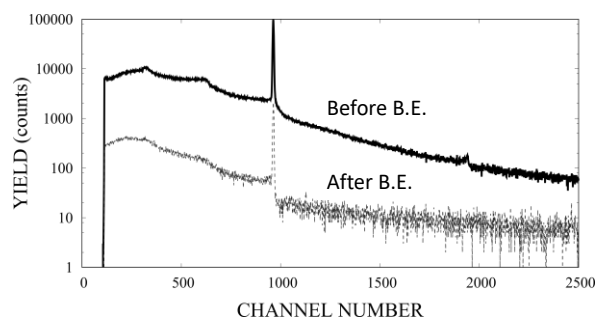


Fig. 2. Gamma-ray spectra before and after brightness enhancement (B.E.).

PR6-2 Electron-Irradiation Effects on Diffusion Coefficient of Cu in Fe Studied by Three Dimensional Atom Probe

T. Toyama, K. Inoue, Y. Nagai, Y. Shimizu, M. Shimodaira, Y. Tu, C. Zhao, T. Onitsuka¹, A. Kimomura², T. Yoshiie², Q. Xu² and A. Yabuuchi²

Institute for Materials Research, Tohoku University
¹Research Institute of Nuclear Engineering, Fukui University
²Research Reactor Institute, Kyoto University

INTRODUCTION: Reactor pressure vessel (RPV) is one of the most important parts in nuclear power plant since RPV holds nuclear fuels, control rods and primary cooling water. Therefore, irradiation-induced embrittlement of RPV steels is vital issue for the safe operation of nuclear power plants. Substantial studies have revealed that nano-sized Cu precipitates are formed by neutron-irradiation and cause the embrittlement. In order to understand the kinetics of Cu precipitation, the diffusion coefficient, D , of Cu in Fe is the important basic quantities [1, 2].

It is predicted that diffusivity of Cu may be strongly affected by irradiation [3]; for example, diffusivity is greatly enhanced by irradiation because vacancies and interstitials, which are necessary for diffusion of solute atoms, are remarkably induced during irradiation. Such enhancement of diffusion has been modeled and simulated, however, experimental studies are very limited at present. We employ KUR LINAC to induce simple Frenkel pairs, and investigate the electron-irradiation effects on Cu diffusivity in Fe. In the previous report, we studied Cu diffusivity by using conventional Cu-Fe diffusion couples but the irradiation-effects was not very clear probably due to the detection limitation of three-dimensional atom probe (3D-AP). In this study, Fe-1.0wt.%Cu alloy is electron-irradiated at KUR LINAC to investigate the D of Cu in Fe via the kinetics of Cu precipitation.

EXPERIMENTS: Fe-1.0wt.%Cu alloy was made from high-purity (5N) Fe and Cu. A plate of 5 mm × 5 mm × 1 mm was fabricated and the surface of the sample was mechanically polished with abrasive papers of #2000. After removal of the machined layer by chemical polishing, the sample was annealed at 1100K for 4 hours followed by quenching into ice-water.

Electron-irradiation was performed with electron beam with energy of 8 MeV at KUR LINAC. The irradiation temperature and the irradiation time were about 750 K and 30000 seconds, respectively.

After electron-irradiation, needle-like samples for 3D-AP were fabricated with focused-ion beam apparatus. In 3D-AP measurement, a voltage pulse mode was employed at temperature of 50 K, pulse fraction of 20%, and a repetition frequency of 200 kHz.

RESULTS: Figure 1 shows atom map of Cu in the electron-irradiated Fe-Cu alloy. 3D-AP measurements were performed for several needle-like samples, and the similar results to fig. 1 were obtained. Cu precipitates were clearly observed and the number density and the average size of Cu precipitates were analyzed with the standard analysis method. The Cu concentration in Fe matrix was also analyzed. With these parameters, the diffusion coefficient of Cu was estimated by using a formula concerning the diffusion coefficient and precipitation kinetics [4]. Figure 2 shows the Arrhenius plot of the D of Cu in Fe in the studied sample together with the D under thermal-aged samples [1]. The D obtained in this study was 9~23 times higher than that in thermal-aged condition, clearly indicating that the Cu diffusivity is enhanced by electron-irradiation. In future work, the Fe-Cu alloys will be irradiated at the temperature other than 750K to reveal the temperature dependency of D for further understanding of the electron-irradiation effects on D .

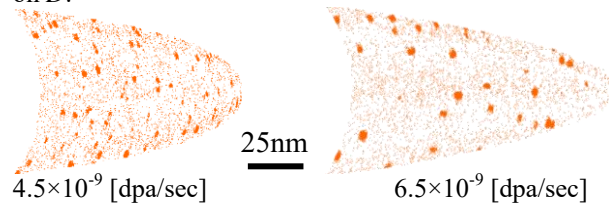


Figure 1: Atom maps of Cu in the electron-irradiated Fe-1.0wt.%Cu alloy.

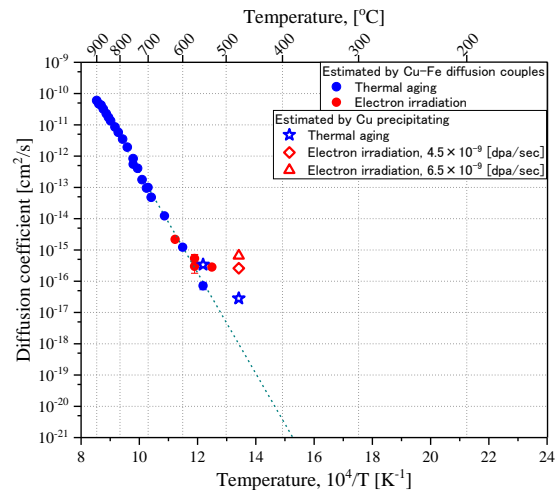


Figure 2: Arrhenius plot of the diffusion coefficient of Cu in Fe.

REFERENCES:

- [1] T. Toyama *et al.*, *Scrip. Mater.*, **83** (2014) 5-8.
- [2] M. Shimodaira *et al.*, *Mater. Trans.*, **9** (2015) 1513-1516.
- [3] R. Sitmann, *J. Nucl. Mater.*, **69&70** (1968) 386-412.
- [4] For example, M. Koiwa and H. Nakajima, *Diffusion in materials* (Uchidarokakuho, 2009).

K. Sato, A. Hirotsako, K. Ishibashi¹, Y. Miura, Q. Xu¹, A. Kinomura¹, T. Yoshiie¹

Graduate School of Science and Engineering, Kagoshima University

¹*Research Reactor Institute, Kyoto University*

INTRODUCTION: The study of defect-hydrogen isotope complexes is an important issue for the structural materials of fusion reactor. In fusion reactor, neutrons introduce not only a variety of defects but also hydrogen and helium atoms formed by nuclear reaction of (n,p) and (n, α), respectively. In plasma-facing materials (PFMs), hydrogen isotopes penetrate by exposure to fusion plasma. The hydrogen isotopes interact with the irradiation-induced defects, and remain in the materials [1–3]. Retention of hydrogen isotopes leads to a decrease in mechanical properties of materials, e.g. hydrogen embrittlement etc. Tungsten is one of strong candidates for PFMs, which have high melting point, high thermal conductivity, and low sputtering erosion. However, hydrogen solubility is quite low, and interaction between hydrogen atoms and defects is strong [4]. Therefore, to study the interaction between hydrogen and defects is especially important in tungsten. In this study, we estimate the number of hydrogen trapped at single vacancies by the following procedures. (1) Vacancies are introduced to re-crystallized tungsten by electron irradiation. (2) Hydrogens are charged to the electron-irradiated samples. (3) The change in positron annihilation lifetime (PAL) by hydrogen charging is detected. (4) PAL is simulated using the exact structure obtained by the first principle calculation. (Hydrogens are put on the inner surface of vacancies.) (5) Results between experiments and simulations are compared.

EXPERIMENTS: High purity tungsten (99.95%, A.L.M.T. Corp.) samples were used in this study. Samples with diameters of 5 mm were cut by wire electric discharge machine from 0.2 mm thick sheets and annealed at 1773 K for 1 h in a vacuum ($< 10^{-4}$ Pa) for re-crystallization. Defects were introduced by irradiation with electrons at 8 MeV using the Electron Linear Accelerator of the Research Reactor Institute, Kyoto University. The irradiation doses were 1.4×10^{22} , 3.0×10^{22} , and 6.6×10^{22} /m² (1.4×10^{-4} , 2.9×10^{-4} , 6.4×10^{-4} dpa). For dose calculations, we used the atomic displacement cross section of 70.4 barns and the displacement threshold energy of 84 eV [5]. The irradiation temperature was kept at 363 ± 10 K by water cooling. All samples were electropolished after electron irradiation to remove oxidation layers formed by water cooling. High pressure hydrogen charging (H.C.) was employed in this study. Pressure, temperature, and time for H.C. was 5.8 MPa, 573 K, and 240 h, respectively. Before H.C., electron-irradiated samples were annealed at 573 K for 240 h (same condition as

the H.C.) in a vacuum to avoid the formation of vacancy clusters during H.C. The PAL measurements were performed at room temperature. The system used in this study was a fast-fast coincidence system with a time resolution of 190 ps (full width at half maximum; FWHM). The PAL spectra were accumulated with a total count of approximately 3×10^6 and were analyzed using the PALSfit package [6].

RESULTS: In tungsten irradiated with electrons at doses of 6.4×10^{-4} dpa, before annealing at 573 K for 240 h, small interstitial clusters are formed by electron irradiation, and positrons are annihilated at not only vacancies but also small interstitial clusters, however, during annealing, interstitial clusters are annihilated at sinks or grow. Therefore, although the PAL spectrum could not be decomposed into two components after electron irradiation, we could accomplish it after annealing. From the PAL of approximately 175 ps after annealing, vacancy clusters are not formed by annealing. After H.C., τ_2 decreases because the single vacancies are decorated with hydrogen. Until the isochronal annealing at 523 K, τ_1 , τ_2 , τ_m , and I_2 are almost constant. After annealing at 573 K for 1 h, τ_1 , τ_2 , and τ_m increase and I_2 decreases, which denotes the formation of vacancy clusters. When the annealing time at 573 K increases, τ_2 increases further. This means the growth of vacancy clusters.

The change in the PAL at doses of 2.9×10^{-4} dpa before and after annealing at 573 K for 240 h is also caused by the annihilation or growth of interstitial clusters. Trend of the change in the PAL is almost the same as that of the sample at doses of 6.4×10^{-4} dpa. In the annealing at 573 K for 10 h, the PAL starts to increase. I_2 is almost constant until the annealing at 573 K for 20 h. These are different from that of the sample at doses of 6.4×10^{-4} dpa. Therefore, this increase of the PAL in the annealing at 573 K for 10 h is due to the dissociation of hydrogen atoms from vacancies. After annealing at 573 K for 44 h, I_2 decreases and τ_2 gradually increases with increasing the annealing time. This indicates the formation of vacancy clusters. Kato *et al.* reported that hydrogen assisted the formation of di-vacancies (hydrogen-di-vacancy complexes were very stable) [7]. This mechanism may make the formation of vacancy clusters easy in this study. When samples did not contain hydrogen, Sato *et al.* did not detect the formation of vacancy clusters in tungsten irradiated with electrons at doses of 3.2×10^{-5} dpa by the isochronal annealing [5].

REFERENCES:

- [1] N. Yoshida, *J. Nucl. Mater.*, **266-269** (1999) 197.
- [2] M. Tokitani *et al.*, *J. Nucl. Mater.*, **363** (2007) 443.
- [3] V.Kh. Alimov *et al.*, *J. Nucl. Mater.*, **375** (2008) 192.
- [4] K. Ohsawa *et al.*, *Phys. Rev.*, B **82** (2010) 184117.
- [5] K. Sato *et al.*, *Nucl. Mater. Ene.*, **9** (2016) 554.
- [6] J.V. Olsen *et al.*, *Phys. Stat. Sol.*, C **4** (2007) 4004.
- [7] D. Kato *et al.*, *J. Nucl. Mater.*, **417** (2011) 1115.

K. Kuriyama, Y. Torita, K. Sato, J. Tashiro, K. Kushida¹, A. Yabuuchi², Q. Xu² and A. Kinomura²

College of Engineering and Research Center of Ion Beam Technology, Hosei University

¹Osaka Kyoiku University

²Research Reactor Institute, Kyoto University

INTRODUCTION: Examining the defects caused by various radiations to ZnO and GaN by assuming the space environment is important. In our previous study, we reported the modification of the yellow luminescence in GaN bulk single crystal by gamma-ray irradiation [1]. The resistivity varies from 30 Ωcm for an un-irradiated sample to $10^4 \Omega\text{cm}$ for gamma-ray irradiated one. The high resistivity was attributed to the carrier compensation due to the deep acceptor level relating to interstitial nitrogen atoms. We also reported that the persistent photoconductivity by electron-irradiated ZnO [2] and a shallow donor level relating to hydrogen interstitial by H-ion implanted ZnO [3]. In the present study, we report the green luminescence (GL) in ZnO bulk single crystals caused by gamma-ray irradiation.

EXPERIMENTS: ZnO bulk single crystals with a thickness of 500 μm were used. The crystals were irradiated at room temperature with gamma-rays of 1.17 and 1.33 MeV from a cobalt-60 source of Kyoto University Research Reactor Institute. Samples were irradiated with an absorption dose rate of 1.771 KGy/h. Total gamma-ray dose was 170 kGy. The resistivity varied from $4.1 \times 10^4 \Omega\text{cm}$ for an un-irradiated sample to $3.1 \times 10^2 \Omega\text{cm}$ for gamma-ray irradiated one. Photoluminescence (PL) spectra were measured at 16 K using a He-Cd laser.

RESULTS: The band edge emission was observed at 275 nm in both un-irradiated and gamma-ray irradiated samples. The GL from the un-irradiated ZnO with a peak at 535 nm (2.31 eV) was observed at around 430 nm to 670 nm, whereas the GL intensity of the gamma-ray irradiated ZnO increased to about 14 % in comparison with that of un-irradiated ones, suggesting that oxygen vacancy (V_{O}) and zinc vacancy (V_{Zn}) were induced by Compton electrons emitted by the gamma-ray irradiation. This PL peak is a superposition

consisting of the $\sim 490 \text{ nm}$ -emission relating to the V_{Zn} and $\sim 530 \text{ nm}$ -emission relating to V_{O} . The PL intensity of V_{O} is eight times larger than that of V_{Zn} . The existence of V_{Zn} would suggest the formation of zinc interstitial (Zn_i). In analogy with the low resistivity after Al-implanted ZnO [4], the origin of the low resistivity in gamma-ray irradiated ZnO would be attributed to the Zn_i located at $\sim 30 \text{ meV}$ below the conduction band [5].

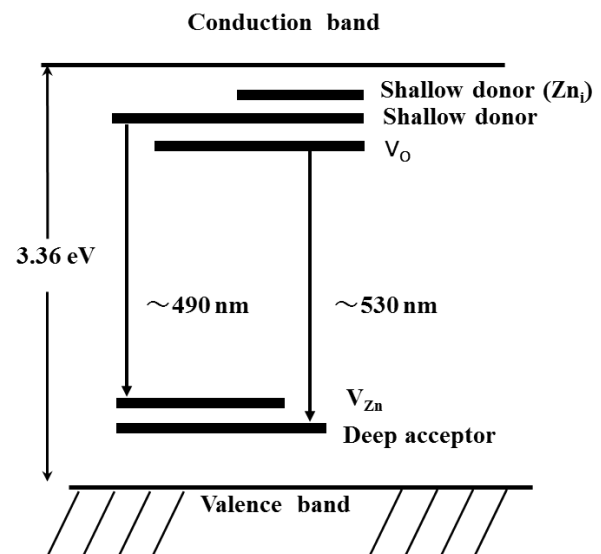


Fig.1 Schematic energy level of the green luminescence in gamma-ray irradiated ZnO. The gamma-ray induced shallow donor relating to zinc interstitial (Zn_i) is located at about 30 meV below the conduction band.

REFERENCES:

- [1] Y. Torita, N. Nishikata, K. Kuriyama, K. Kushida, A. Kinomura, and Q. Xu, Proceedings of ICPS2016 (Journal of Physics, IOP(UK)) **864**, 012016 (2017).
- [2] T. Oga, Y. Izawa, K. Kuriyama, K. Kushida, and Q. Xu, Solid State Commun., **151** (2011) 1700.
- [3] T. Kaida, K. Kamioka, T. Ida, K. Kuriyama, K. Kushida, and A. Kinomura, Nucl. Instrum, Method Phys. Res. B, **332** (2014) 15.
- [4] T. Oga, Y. Izawa, K. Kuriyama, K. Kushida, and A. Kinomura, J. Appl. Phys., **109** (2011)123702.
- [5] D. C. Look, J. W. Hemsky, and J. R. Sizelove, Phys. Rev. Lett., **82** (1999) 2552.

PR6-5 Establishment of Technique for Thermal Diffusivity Measurement using TEM Disk Size Miniature Test Specimens for Post-irradiation Experiments

M. Akiyoshi, M. Yashiki¹ and A. Kinomura²

Radiation Research Center, Osaka Prefecture University

¹Grad. School of Eng., Osaka Prefecture University

²Research Reactor Institute, Kyoto University

INTRODUCTION:

Radioactivity levels for conventional thermal diffusivity test specimens are often prohibitively high for examination with candidate metallic materials, such as tungsten and reduced activation steels for fusion energy. Therefore, in the ongoing Japan-US PHENIX project, irradiation in the High Flux Isotope Reactor (HFIR) was performed with the miniature specimen form of diameter (D) 3mm×thickness (T) 1/2 mm small disk for thermal diffusivity measurement. In this study, the thermal diffusivity measurement of this D3TH miniature specimen is validated using a Netzsch LFA-467 'Hyper Flash' thermal analyzer and 'Graphene Nanoplatelets containing agent'. With careful surface treatment and data analysis, the D3TH specimens showed almost the same value as the diameter 10mm×thickness 2mm (D10T2) standard specimens.

EXPERIMENTS and RESULTS:

Using the conventional Netzsch LFA-457 thermal analyzer, a D3TH specimen was measured to verify the influence of thickness. With this system, the pulse-width of the laser flash is not fast enough to measure a tungsten specimen of 0.5mm thickness correctly, and consequently, the result showed large difference between D10T2 standard specimen and D3TH miniature specimens. Then, using a new Netzsch LFA-467 'Hyper Flash' thermal analyzer, a D10TH specimen was measured to verify the influence of thickness. In this system, the pulse-width of laser flash is enough fast to measure β -SiC specimens of 0.5mm thickness correctly.

However, the first measurement showed a large disagreement from the standard specimen, which was considered to be caused by the surface treatment. Netzsch resolved this problem with the surface treatment 'Graphene Nanoplatelets containing agent'[1] that can be applied as a very thin coating. Fig. 1 shows a very thin, sparse coated surface. Even such a thin coating on a polished tungsten specimen enabled the thermal diffusivity to be measured correctly. Finally, using the Netzsch LFA-467 with the Graphene agent, D3TH specimens were evaluated successfully at a room temperature and a tungsten specimen was measured at elevated temperature. Fig. 2 shows the thermal diffusivity of the tungsten specimens at elevated temperature. In this figure, the D3TH specimen shows almost same thermal diffusivity especially at higher temperatures. The obtained $\alpha(300)$

from the fitting curve for D10T1 standard specimen was $66.6\text{mm}^2/\text{s}$, and for D3TH $68.2\text{mm}^2/\text{s}$ that is only 2.3% higher than the standard specimen. This difference is small enough for the continued use of the D3TH specimen size for the actual application.

CONCLUSION:

It is concluded that the miniature specimen for measurement of thermal diffusivity is validated and this result will be widely used in future materials irradiation studies. This result is already reported at ISFNT-13 and published in Fusion Engineering and Design[2].

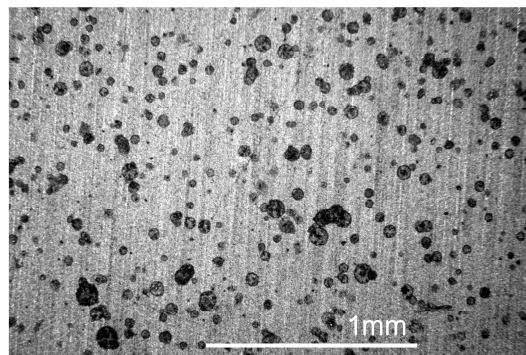


Fig.1 Sparsely coated surface of a specimen using a 'graphene nanoplatelets containing agent'.

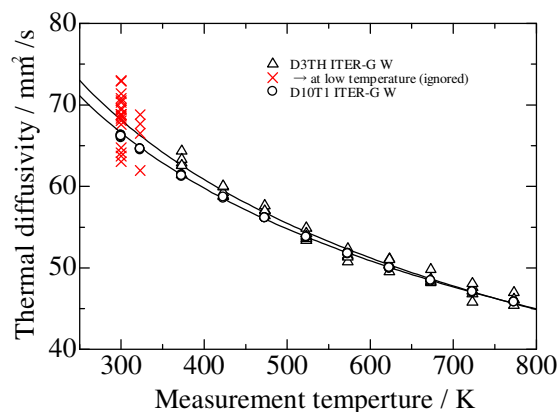


Fig. 2 Validation of thermal diffusivity measurement using D3TH (diameter 3mm × thickness 0.5 mm) tungsten specimen using Netzsch LFA-467 and graphene agent

REFERENCES:

- [1] Y. Ishibashi *et al.*, The 37th Japan Symposium on Thermophysical Properties, Nov.28-30, 2016, Okayama.
- [2] M. Akiyoshi, R. Kasada, Y. Ishibashi, L.M. Garrison, J.W. Geringer, W.D. Porter and Y. Katoh, Validation of miniature test specimens for post-irradiation thermal diffusivity measurement, Fusion Engineering and Design (in press, <https://doi.org/10.1016/j.fusengdes.2018.03.008>)

PR6-6 Positron Annihilation Study of Fe-Cr binary alloy after Electron Irradiation

T. Onitsuka, K. Sato¹ and Q. Xu², A. Kinomura²,
A. Yabuuchi² and K. Fukumoto

Research Institute of Nuclear Engineering, Fukui University

¹*Graduate School of Science and Engineering, Kagoshima University*

²*Institute for Integrated Radiation and Nuclear Science, Kyoto University*

INTRODUCTION: High-chromium (9-12%Cr) Ferritic/martensitic steels are attractive candidate material for various nuclear energy systems. The phase decomposition into the Fe-rich and the Cr-rich phases are the main reason for the so-called 475 °C embrittlement that may occur in technologically important structural materials made on the base of Fe-Cr alloys such as High-chromium steels, if subjected to temperatures between 300 and 600 °C [1]. This phase decomposition and irradiation induced degradation are expected to be the critical issues for reactor operation. The purpose of this study is to examine the effect of thermal aging and the irradiation on the phase decomposition of the high-chromium Ferritic/martensitic steels. In the previous study, we authors have reported on the result of electron irradiation experiment at 100 °C. In this paper, we report on the result of the electron irradiation experiment at 475 °C.

EXPERIMENTS: Simple binary Fe-40Cr model alloy was made by arc melting under argon atmosphere in a water-cooled copper hearth. All the ingots were melted and inverted three times in order to promote chemical homogeneities. The obtained ingot was conducted by solution heat treatment at 850 °C for 2 h followed by water quenching, and then, machined to the dimensions of 10 mm × 10 mm × 0.5mm. The electron irradiation at 475 °C in the helium atmosphere, was performed up to 0.33×10^{-3} dpa via the 8 MeV KURRI-LINAC. After the irradiation, all specimens were mechanically polished and then electrolytically polished to clean the surface. Finally microstructural characterization was performed by positron annihilation lifetime measurement and Coincidence Doppler Broadening (CDB) of positron annihilation radiation measurement to examine the microstructural change in atomic level during irradiation and thermal aging process.

RESULTS: Table. 1 shows the result of positron lifetime measurement in irradiated and unirradiated Fe-40Cr, and pure bulk materials (Fe and Cr). Only one lifetime component was found in the irradiated specimens as well as the unirradiated specimens. The lifetime for the irradiated specimens around 107 psec are very close to the lifetime in the unirradiated specimens. This shows that there is no vacancy-type defects could be found after irradiation. Based on previous studies, it is believed that small vacancy clusters become thermally unstable at

higher temperature such like 475 °C and more likely to dissociate into single vacancies which can move immediately and then disappear on various sinks such as free surfaces, grain boundaries. Fig.1 shows the S-W plots obtained from the CDB measurements in the Fe-40Cr alloy before (as W.Q.) and after the irradiation. In general, when the positron is trapped in vacancy-type defect, the S-parameter increases but the W-parameter decreases. On the other hand, when the Fe/Cr phase decomposition occurred, the W-parameter increases but the S-parameter decreases. The result indicated that the rapid increase in the W-parameter due to irradiation. Thus, it might be inferred from these results that the early stage of phase decomposition was detected in the irradiated specimens. Further studies and experiments are necessary in order to make it clear the difference between the aging effect and the irradiation effect.

REFERENCE:

[1] K. Okano *et al.*, Nucl. Instr. and Meth., **186** (1981) 115-120.

Table. 1. Measured positron lifetimes in the irradiated and unirradiated specimens.

Specimen	dpa (10^{-3})	Irradiation Temp. (°C)	Irradiation Time (h)	Positron lifetime (psec)
Fe (bulk)	-	-	-	105.4
Cr (bulk)	-	-	-	105.6
Fe-40Cr	-	-	-	107.5
Fe-40Cr	0.03	475	2	107.3
Fe-40Cr	0.33	475	20	107.1

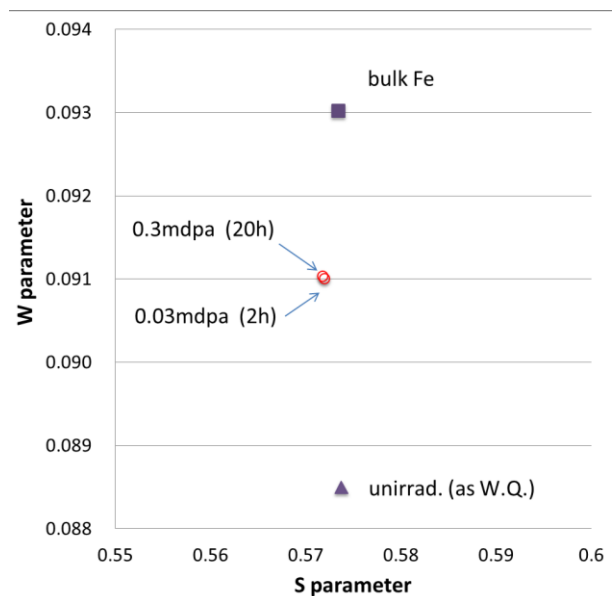


Fig. 1. Plot of the S-W values of the irradiated specimens. Unirradiated Fe-40Cr (W.Q.) and pure bulk Fe are also plotted.

K. Kanda, F. Hori¹, A. Yabuuchi² and A. Kinomura²*Laboratory of Advanced Science and Technology for Industry, University of Hyogo*¹*Department of Materials Science, Osaka Prefecture University*²*Institute for Integrated Radiation and Nuclear Science, Kyoto University*

INTRODUCTION: Amorphous carbon films, which are usually called diamond-like carbon (DLC) films, have attracted considerable attention in recent years for many reasons, such as excellent corrosion resistance, high hardness, and high wear resistance [1]. The structure of DLC films is complex, being comprised of an amorphous mixture of sp^2 and sp^3 hybridized carbon atoms combined with hydrogen atoms in the local structure [2]. The chemical structure in terms of the coordination of carbon (sp^2 and sp^3 hybridization) and hydrogen atoms are the most important factors governing the quality of DLC films and they are used as classification criteria in ISO20523 published in 2017 [3]. However, DLC films have another structural factor, free volume. Free volume was considerable to connect strongly with several important properties of DLC film, such as hardness, Young modulus, and friction coefficient, but it has not been investigated. Positron annihilation spectroscopy (PAS) is a powerful tool for measuring free volume in material. In the present study, several DLC films were analyzed by PAS to evaluate the free volume in DLC films.

EXPERIMENTS: We prepared four kinds of DLC films using different three deposition methods, 1) filtered cathodic vacuum arc (FCVA) method, 2) ion plating (IP) method, and 3) plasma enhanced chemical vapor deposition (PECVD) method. FCVA DLC film and IP-DLC film were typical DLC film used as hard film, which densities were expected about 2 g/cm^3 and hydrogen contents in these film were expected to lower 20 %. PE-CVD DLC film was highly hydrogenated DLC film, whose hydrogen content was estimated $\approx 40 \%$ and its density was obtained to 1.25 g/cm^3 . Last sample was prepared by the PE-CVD DLC film exposed to synchrotron radiation (SR) at BL06 in the NewsUBARU synchrotron facility of the University of Hyogo [4]. The SR at the BL06 sample stage had a continuous spectrum from the infrared to soft X-ray region and an energy below 1 keV. Every DLC films were deposited onto Si substrate and their film thickness were 100~200 nm.

PAS measurement was performed at the slow positron beam system (B-1). Energy of incident positron, E , ranging 0.5 - 15 keV. Doppler broadening profiles of annihilation γ -rays were obtained using a Ge detector for each positron energy. The low momentum part of spectra was characterized by the S parameter, which is defined as the number of annihilation events over the range of $511 \pm$

0.76 keV.

RESULTS: Figure 1 shows the S parameter as a function of incident positron energy E for the FCVA DLC film, IP DLC film, and PECVD DLC film. The S values in the E region lower than 2 keV can be considered to attribute to the annihilation of positrons trapped in free volume in the DLC films. The S values of PECVD DLC film were smaller than those of FCVA DLC film and IP DLC film, in spite of the fact that the density of PECVD DLC film was low. These results can be considered that hydrogen atoms narrow the free volume in the DLC film.

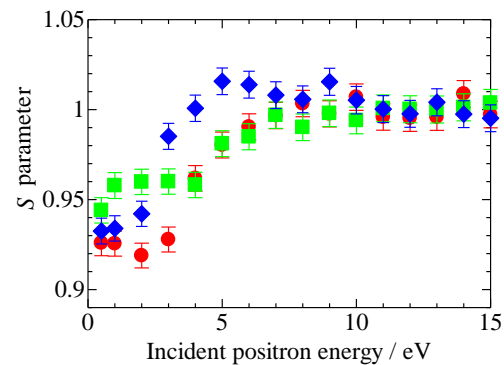


Fig. 1. S parameter as a function of positron energy E for FCVA DLC film \blacklozenge , IP DLC film \blacksquare , and PECVD DLC film \bullet .

Figure 2 shows the S parameter for the PECVD DLC film and the PECVD DLC film exposed to SR. The S value of PECVD DLC film was raised by the exposure to SR. This increase was ascribable to the enhancement of free volume in the PECVD DLC film by desorption of hydrogen from film due to excitation of soft X-rays [5].

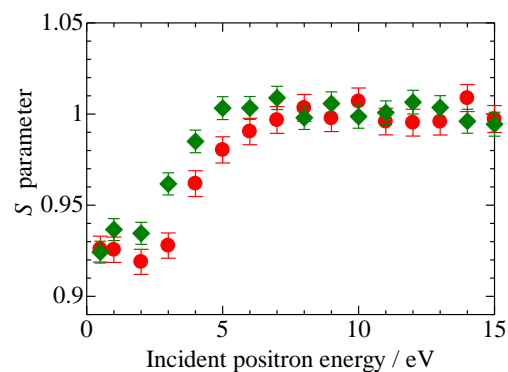


Fig. 2. S parameter as a function of positron energy E for PECVD DLC film \bullet and that exposed to SR \blacklozenge .

REFERENCES:

- [1] S. Aisenberg *et al.*, *J. Appl. Phys.*, **42** (1971) 3963.
- [2] J. Robertson, *Surf. Coat. Technol.*, **50** (1992) 185.
- [3] ISO20523, "Carbon based films – Classification and designations".
- [4] K. Kanda *et al.*, *Jpn. J. Appl. Phys.*, **42** (2003) 3983.
- [5] K. Kanda *et al.*, *Jpn. J. Appl. Phys.*, **50** (2011) 055801.

S. Nakao, X. Qu¹, A. Yabuuchi¹ and A. Kinomura¹

Structure Materials Research Institute, National Institute of Advanced Industrial Science and Technology
¹Institute for Integrated Radiation and Nuclear Science, Kyoto University

INTRODUCTION: Diamond-like carbon (DLC) films have attracted much attention because of their excellent mechanical properties, such as high hardness, high wear resistance and low friction coefficients. However, the properties strongly depend on the microstructure of the films which is varied by the deposition conditions and methods. Recently, DLC or carbon films are categorized from type I to VI, which includes graphite-like carbon (GLC) and polymer-like carbon (PLC).

The thermal stability of the films is of importance for practical applications. However, the thermal stability is not always enough to use it at high temperature. It is considered that the changes of the microstructure at high temperature should be responsible for the degradation of the properties. The structural changes are related to H desorption and behavior of defects at high temperature. Many studies have been carried out on the thermal stability of DLC films. However, the principal phenomena, such as defect behavior, are not always clear. Therefore, to make clear the thermal stability of DLC or carbon films, the examination of every type of DLC films (type I to VI) are necessary. The aim of this study is to clarify the relationship between the thermal stability and the behavior of defects and bonded hydrogen in several types of DLC films by positron annihilation and thermal desorption (TDS) method.

In a previous report [1], the films of type I and IV were examined by TDS measurement in the range of room temperature (RT) to 600°C and it was found that hydrogen desorption was clearly observed around 400°C in the case of type IV films. On the other hand, type I films did not change significantly until 600°C. The result suggested that further high temperature was required to characterize all films. In this study, the TDS measurement at further high temperature up to 800°C is carried out together with other types of DLC and carbon films.

EXPERIMENTS: Samples of A – E for TDS measurement are listed in Table 1. Type I (ta-C) and III (a-C) films were prepared by arc ion plating (AIP) at Nippon ITF Inc. and high-power impulse magnetron sputtering (HiPIMS), respectively. Type IV (a-C:H), V (GLC) and VI (PLC) films were deposited by plasma-based ion implantation (PBII) under the different conditions. The details on the PBII system were reported elsewhere [2]. Si wafer was used as substrate. The TDS spectra of Si substrate were also measured for comparison (not shown). The samples were thermally heated from RT to approximately 800°C. The desorption H, H₂, D and DH were detected.

Sample	Type	Description	Preparation
A	I	ta-C	AIP
B	III	a-C	HiPIMS
C	IV	a-C:H	PBII
D	V	GLC	PBII
E	VI	PLC	PBII

RESULTS: Figure 1 shows the H₂ desorption spectra of the samples at elevated temperature. The desorption increases with increasing temperature. For the sample A, however, no significant desorption peak of H₂ is observed in this range. The tendency is almost the same as Si substrate. This shows that the sample A is thermally stable up to 800°C. On the other hand, the desorption is gradually increased around 600°C for the samples of B – D. In the case of sample E, the desorption begins to increase around 400°C. These results show that hydrogen is released from the films over 600°C and 400°C for the samples B – D and the sample E, respectively. From the results, it is suggested that thermal stability of sample A is the best among the samples. In addition, the structural changes should begin around 600°C and 400°C due to hydrogen release for the sample B – D and the sample E, respectively. There is a possibility that the structural changes may be driven by the creation and annihilation of vacancy and defects caused by hydrogen desorption. Positron annihilation measurement will be planned next time.

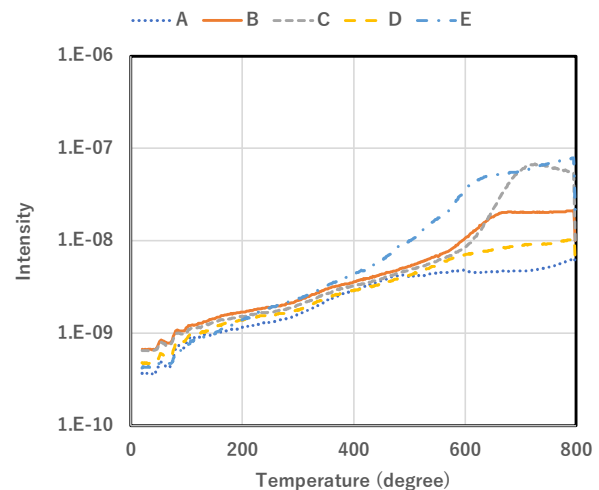


Fig.1 Thermal desorption spectra of H₂ for the samples A – E as a function of elevated temperature. The samples A – E correspond to the films of type I, III, IV, V and VI, respectively.

REFERENCES:

- [1] S. Nakao *et al.*, KURRI Progress Report 2016, 28P12-8 (2016) 57.
- [2] S. Miyagawa *et al.*, Surf. Coat. Technol., **156** (2002) 322-327.

Y. Saito

Research Reactor Institute, Kyoto University

1. Objectives and Allotted Research Subjects

Neutron imaging provides valuable information which cannot be obtained from an optical or X-ray imaging. The purpose of this project is to develop the imaging method itself and also the experimental environment for expanding the application area of the neutron imaging. The allotted research subjects are as follows:

- ARS-1 Measurements of Multiphase Dynamics by Neutron Radiography (Y. Saito *et al.*)
- ARS-2 Visualization and Measurement of Flow Behavior in Industrial Equipment (H. Asano *et al.*)
- ARS-3 Visualization and Measurement of Adsorption/Desorption Process of Ethanol in Activated Carbon Adsorber for Adsorption Heat Pump (N. Asano *et al.*)
- ARS-4 Visualization of heavy oil in packed bed reactor by neutron radiography (T. Tsukada *et al.*)
- ARS-5 Characteristics of the Void Fraction under Transient Condition (H. Umekawa *et al.*)
- ARS-6 Estimation of the Frosting and Defrosting Phenomena by Using Neutron Radiography (R. Matsumoto *et al.*)
- ARS-7 Neutron imaging and optics development using simulation of VCAD Systems (Y. Yamagata *et al.*)
- ARS-8 Water and Salt Distribution in a Rice Hull Medium under Sodium Chloride Solution Culture (U. Matsushima *et al.*)
- ARS-9 Measurement of Water Content in Hardened Cement Paste by Neutron Imaging (T. Numao *et al.*)
- ARS-10 In-situ Neutron Radiography Investigation on the Hydraulic Behavior of High Strength Cement Paste under High Temperature (M. Kanematsu *et al.*)
- ARS-11 Evaluation of coolant distribution in a flat heat-pipe type heat spreader (K. Mizuta *et al.*)
- ARS-12 Visualization of Organic Materials for Development of Industrial Applications (A. Uritani *et al.*)
- ARS-13 Visualization of Coolant Flow in a Micro-Structured Wick (Y. Tsuji *et al.*)

2. Main results and the contents of this report

Due to the limitation of beam time at the KUR, all of the scheduled experiments could not be performed for fiscal 2017. However, some new results have been obtained and also the new imaging system was developed

by X-ray imaging as follows:

ARS-1 applied X-ray and neutron imaging to two-phase flow behavior. Simultaneous measurement system with high frame-rate neutron and X-ray imaging was developed and the system was tested for the air-water two-phase flow.

ARS-2 and 3 applied neutron imaging to boiling two-phase flow in parallel mini-channel heat exchanger. HFC-134a and FC3283 were used as the refrigerant and the heat medium, respectively. The heat exchanger was manufactured by diffusion bonding of thin stainless steel plates, and consists of single-layer refrigerant and heating medium parallel channels. The neutron imaging system at the B4 port was utilized for the measurements, and that at E2 port was also utilized for preliminary experiments. From the experimental results, the effect of the inlet orifices have been investigated.

ARS-4 applied neutron imaging to the flow visualization of heavy oil in packed bed reactor. Heavy oil and N₂ gas were supplied to the experimental apparatus, and they flowed co-currently through the packed bed, which consists of Al₂O₃ particles having the diameter of 1 or 3mm. From the experimental results, a flow channeling was observed depending on the experimental conditions.

ARS-5 applied the neutron imaging to microchannel heat exchanger and subcooled boiling. Quenching phenomena in the microchannel heat exchanger was visualized and the effect of flow direction was investigated for the subcooled boiling.

ARS-6 applied neutron imaging to frosting behavior in cooling heat exchange system. 3-D frost density was clearly visualized by the neutron CT imaging system at the B4 port.

ARS-12 performed quantification of neutron imaging by using two-different neutron source (KUR-E2 and NUANS). A detector indicated manufactured by J-PARC was used for the imaging and the spatial resolution of neutron imaging at the two neutron imaging facilities was compared each other.

ARS-13 developed new measurement technique of the superfluid. Helium excimer was used as the tracer in the superfluid helium. In the experiments at the B4 port, the emission of by helium excimer clusters via neutron-³He absorption reaction was clearly observed.

ARS-14 developed capillary-plate-based fluorescent plates and the detail characteristics were examined at the E2 port.

PR7-1 Dynamic Observation of Two-Phase Flow using Neutron Radiography

Y. Saito and D. Ito

*Institute for Integrated Radiation and Nuclear Science,
Kyoto University*

INTRODUCTION: Neutron radiography (NRG) is a powerful tool for fluid flow visualization as well as two-phase flow research. Gas-liquid two-phase flows in a metallic pipe have been visualized clearly by using NRG. However, it would be still difficult to obtain dynamic information on such flows by NRG, because of insufficient neutron flux from neutron sources and poor efficiency of imaging devices. In this work, our imaging system was improved for high frame rate NRG. Then, the system was applied to air-water two-phase flow measurements in a circular pipe. In addition, a simultaneous measurement with X-ray radiography (XRG) was performed to compare the acquired transmission images of the two-phase flow.

EXPERIMENTS: Experiments were performed at the B-4 supermirror neutron guide facility [1] of the Institute of Integrated Radiation and Nuclear Science, Kyoto University. The neutron flux of the B-4 port is 7.5×10^7 n/cm²s and the beam width and height at the beam exit are 10 mm and 75 mm, respectively. An imaging system for high frame rate NRG consists of a neutron converter, a dark box with a single mirror, an ultrasensitive lens, an optical image intensifier and a high-speed camera, as shown in Fig.1. In the present system, high sensitivity high-speed camera (AX-50, Photron) was applied to enhance the temporal resolution. In addition, XRG system was installed in the B-4 facility to compare the imaging results. The XRG system consists of an X-ray generator, an X-ray image intensifier and a high-speed camera. The applied voltage and current of the X-ray generator were 150 kV and 2.3 mA, respectively. These systems were arranged as the X-ray beam direction is perpendicular to the direction of the neutron beam, as shown in Fig.1. Two high-speed cameras and the optical image intensifier were synchronized for simultaneous observation.

The test section is a vertical circular pipe which is made from polycarbonate. The inner diameter is 20 mm and the wall thickness of the test pipe is 1 mm. The water was circulated by a pump and the compressed air was injected from the upstream of the test section. The flow rates of water and air were monitored by flow meters.

RESULTS: The typical neutron and X-ray transmission images of air bubble in water are shown in Fig.2. In the present experiments, the frame rate of 10,000 Hz could be achieved by using the improved NRG system. By comparing two images, they represent different characteristics. In the air-water two-phase flow, water has

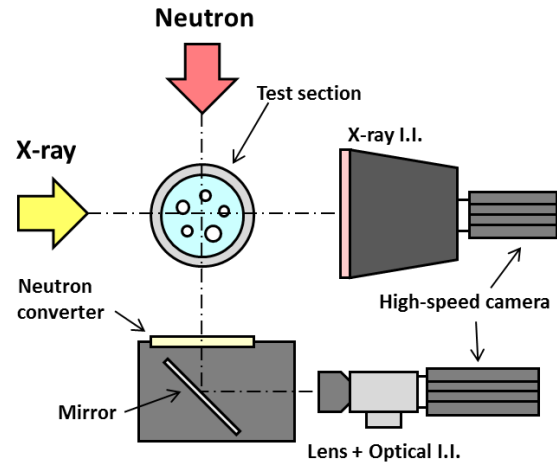


Fig. 1 Schematic diagram of simultaneous measurement with high frame-rate neutron and X-ray radiography systems.

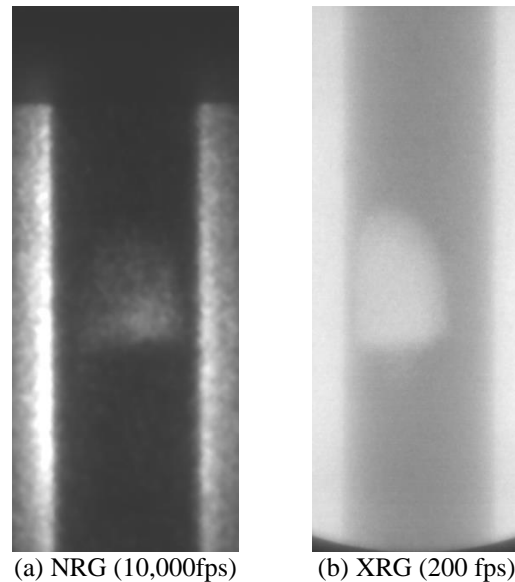


Fig. 2 Neutron and X-ray transmission images of air-water two-phase flow.

high neutron attenuation coefficient, therefore it is difficult to detect the small bubble in water. However, visualization of detailed flow structure will be possible by combining with X-ray imaging results. This simultaneous imaging technique would be useful for the clarification of multiphase flow dynamics such as steam explosion.

REFERENCE:

- [1] Y. Saito, *et al.*, Nucl. Instr. Meth. Phys. Res., A, **651** (2011) 36-41.

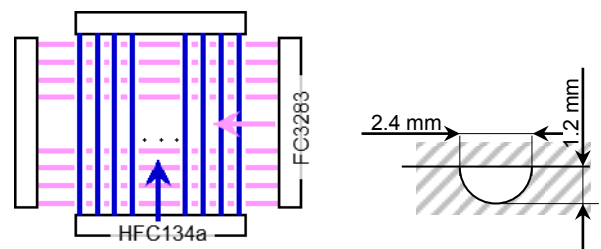
H. Asano, H. Murakawa, K. Sugimoto, R. Moriyasu,
D. Ito¹ and Y. Saito¹

Department of Mechanical Engineering, Kobe University
¹Research Reactor Institute, Kyoto University

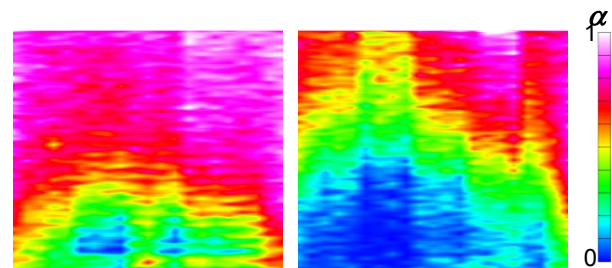
INTRODUCTION: Compactness and reduction in temperature difference between fluids are still strongly required for heat exchanger used in binary power cycles for waste heat utilization and refrigeration/heat pump systems. One of the way is to increase heat transfer area density. Microchannel compact heat exchanger manufactured by diffusion bonding process is developed. Since smaller diameter leads to larger pressure loss, micro channel heat exchanger has many parallel channels. Therefore, in the case that the heat exchanger is used for evaporator, refrigerant flow distribution often causes a deterioration in the heat transfer performance. On the aspect of heat exchanger, the temperature of heating medium will decrease by heat exchange in an evaporator. The temperature change means the decrease in temperature difference between fluids, and lead to the change in heat flux. It is important to understand the boiling flow distribution in parallel refrigerant channel. In this study, boiling flow behaviors in a single layer microchannel heat exchanger had been visualized by neutron radiography.

EXPERIMENTS: HFC-134a and FC3283 were used as the refrigerant and the heating medium, respectively. The configuration of the tested mini-channel heat exchanger is shown in Figure 1. The heat exchanger was manufactured by diffusion bonding of thin stainless steel plates, and consists of single-layer refrigerant and heating medium parallel channels. The number of channels are 21 for the refrigerant and 20 for the heating medium. Each channel has semicircular cross-section as shown in Fig. 1(b). The refrigerant channels were placed in crossed arrangement with the channels of the heating medium. The refrigerant was supplied to the vertically placed test section as a liquid single-phase flow close to saturated liquid, and evaporated by heating from FC3283. Since the temperature of FC3283 decreases in the flow direction, heat transfer rate will be higher on the left side due to the larger temperature difference. The neutron radiography system at B4 beam line was utilized for the measurements, and the system at E2 beam line was also utilized in the preliminary experiments. Radiographs on a scintillation converter were recorded by a cooled CCD camera with the exposure time of 30 seconds and the pixel size of 87.9 $\mu\text{m}/\text{pixel}$. Since the visualized area cannot cover the width of the test section, radiographs were taken by dividing 5 areas. Mass flux of the refrigerant and heating medium was set to 50, 100 $\text{kg}/(\text{m}^2 \cdot \text{s})$ and 460, 920 $\text{kg}/(\text{m}^2 \cdot \text{s})$, respectively.

RESULTS: Void fraction distributions can be obtained from some image processing using images with and without refrigerant. The obtained results of void fraction, α , distribution are shown in Fig. 2. At first, one dimensional distribution was measured for each channel. Then, the results for 21 channels are shown as an image with 21 pixels in horizontal. Void fractions are shown in color scale. Heat transfer rates are shown in Table 1 with the flow conditions. Fig. 2(b) shows the results for the test section with orifices at the inlet of each refrigerant channel for flow stabilization into parallel channels. Void fraction in the center region became higher. The reason might be maldistribution of refrigerant where mass flow rate was larger at the center. Void fraction through the right path was higher than the left path. The effect of the inlet orifices to improve the flow distribution was not observed in the experiments.



(a) Channel arrangement (b) Cross-section
Fig. 1 Channel configuration of cross-flow type evaporator.



(a) Without inlet orifices (b) With inlet orifices
Fig. 2 Void fraction distribution.

$(G_r=100 \text{ kg}/(\text{m}^2 \cdot \text{s}), G_{FC}=460 \text{ kg}/(\text{m}^2 \cdot \text{s}),$
 $T_{FCin}=47.2 \sim 47.3 \text{ }^\circ\text{C})$

Table 1 Heat transfer performance.

	Fig. 3 (a)	Fig. 3 (b)
Refrigerant (HFC134a)		
Evaporating pressure [MPa]	0.585	0.632
Inlet temperature [$^\circ\text{C}$]	19.5	19.8
Inlet subcooling degree [K]	1.3	3.5
Heating medium (FC3283)		
Inlet temperature [$^\circ\text{C}$]	47.2	47.3
Outlet temperature [$^\circ\text{C}$]	41.8	42.8
Heat transfer rate [W]	115.8	98.1

PR7-3 Flow Visualization of Heavy Oil in Packed Bed Reactor by Neutron Radiography

T. Tsukada, M. Kubo, E. Shoji, K. Yamagiwa, S. Takami¹, K. Sugimoto², D. Ito³ and Y. Saito³

Dept. of Chemical Engineering, Tohoku University

¹ Dept. of Materials Science and Engineering, Nagoya University

² Dept. of Mechanical Engineering, Kobe University

³ Institute for Integrated Radiation and Nuclear Science, Kyoto University

INTRODUCTION: With an increase in the demand for petrochemical feedstock and middle distillate, utilization of heavy oil such as atmospheric or vacuum residue is also necessary. Since the heavy oil has high viscosity and its quality is low, however, desulfurization and upgrading processes are required to use the heavy oil effectively. A trickle bed reactor, in which heavy oil and hydrogen gas are flowed concurrently through a packed bed of catalytic particles, is generally used in the upgrading process. Since channeling and consequent hot spots decrease the performance in the reactor, the understanding of flow behavior in the reactor is significant.

Recently, the development of CFD simulator of hydrodynamics and reactions in the reactor has been advanced to clarify the flow behavior. On the other hand, the experimental works on flow visualization of the heavy oil have not been conducted. This is because the reactor was made of metal for operation at high pressure and high temperature, and consequently the visualization using visible light was not available. Therefore, in this work, the flow visualization of heavy oil in the packed bed reactor was performed by neutron radiography.

EXPERIMENTS: In the neutron radiography for the flow visualization of heavy oil, the Kyoto university research reactor (KUR) was utilized as neutron source. Fig. 1 shows the schematic diagram of the apparatus used here. The heavy oil and N₂ gas were supplied concurrently to a packed bed reactor, i.e., a 1/2-inch stainless steel tube

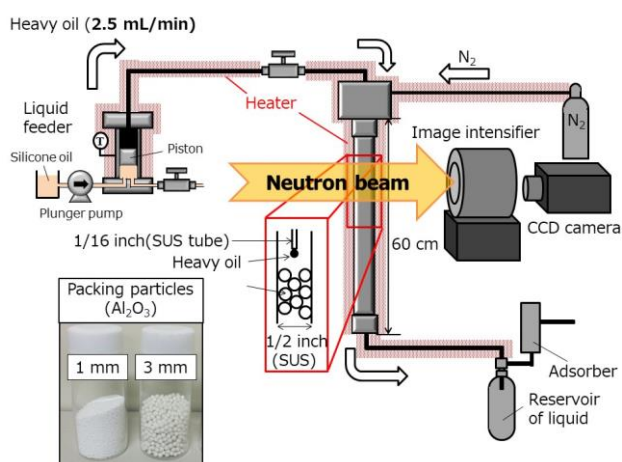


Fig. 1 Schematic diagram of experimental apparatus

filled with Al₂O₃ particles having the diameter of 1 or 3 mm. Atmospheric residue (AR) was used as the heavy oil sample. The reactor was heated to temperatures of 100°C and 250°C to change the viscosity of heavy oil. The flow rate of heavy oil was set to 2.5 mL/min, while that of N₂ gas was changed. The reactor was operated at atmospheric pressure. An image intensifier and a CCD camera at the framerate of 30 fps were used to obtain visualization images of the unsteady flow behavior. An image processing to reduce noises was performed for the obtained images.

RESULTS: The flow behavior of heavy oil in the reactor varied depending on the experimental conditions. Fig. 2 shows the effect of the temperature on the flow behavior of heavy oil in the reactor. Since the viscosity of heavy oil markedly varies with temperature, that is, the viscosity of heavy oil at 100°C is 10 times larger than that at 250°C, the head velocity of heavy oil flowing down at 100°C became approximately half that at 250°C for the particle diameter of 1 mm. In addition, the heavy oil at 100°C spread radially to the wall of the tube, whereas the heavy oil at 250°C did not spread. In the case of 3 mm particle diameter, the heavy oil did not spread at both 100°C and 250°C compared with the case of 1 mm particles, and the flow channeling occurred in the packed bed.

CONCLUSION: Neutron radiography is a useful technique to visualize the flow behavior of heavy oil in a packed bed reactor, whose wall was made of metal, at high temperature.

ACKNOWLEDGEMENT: This research was supported by Ministry of Economy, Trade and Industry (METI) and Japan Petroleum Energy Center (JPEC).

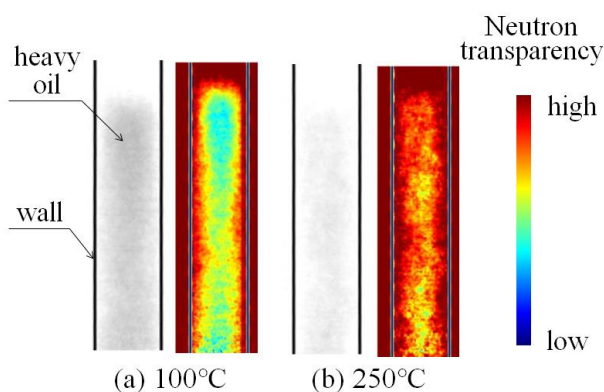


Fig. 2 Effect of reactor temperature on flow behavior in the reactor when the packing particle diameter is 1 mm and the flow rate of N₂ gas is 1 L/min. Here, the left side in (a) or (b) is the image after background subtraction, and the right side is the image converted by color mapping.

H. Umekawa, T. Ami, M. Kitagawa, T. Kitanaka,
Y. Kawazoe, K. Saito, Y. Saito¹ and D. Ito¹
Dept. Mechanical Engineering, Kansai University

¹Institute for Integrated Radiation and Nuclear Science,
Kyoto University

INTRODUCTION: Void fraction is a fundamental and important information of two-phase flow. As the measuring procedure of void fraction, neutron radiography has suitable performance, but several limitation exists. In this term, three trials have been done to evaluate the adaptability of neutron radiography to new object. In this report, these results are briefly introduced.

EXPERIMENTS:

1. Microchannel heat exchanger:

Recently microchannel heat-exchanger has been used by actual equipment, such as air conditioning unit. In these systems, the mal-distribution of the flow has not been fully understood under non-uniform heating condition. These heat exchanger has small parallel tubes with less than 1mm tube diameter, and gap between each channel is less than 0.1mm. Figure 1 is the example of the visualization results and photograph of microchannel heat exchanger. In this trial, working fluid, exposure period, beam slit to enhance the spatial resolution and construction of heat exchanger have been estimated.

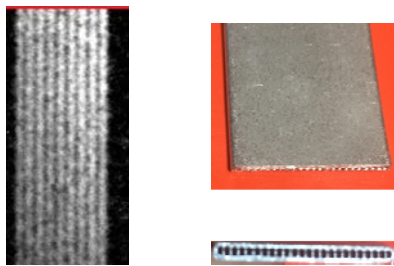


Fig. 1 Micro Channel Heat-exchanger.

2. Quenching Phenomena

During the quenching process of high temperature tubes, Inverted annular flow (IAF) will be generated. In this

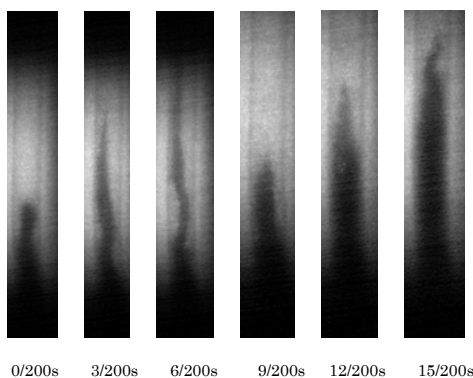
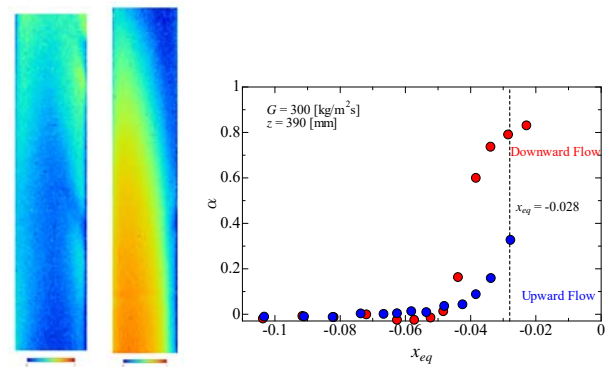


Fig.2 Quenching phenomena

region, estimation of the void fraction is quite important, but enough data has not existed. To estimate the IAF, the quantitative measurement in dynamic process is required. In this trial, to decide the detail experimental condition and suitable frame rate to keep the spatial resolution, dynamic image was taken under several conditions. Figure 2 is example of successive image by using Neutron Image Intensifier and a high speed camera. As shown in these results, the liquid core movement is relatively slow owing to the large slip between liquid and vapor. It means the possibility of the measurement of void fraction of IAF by this procedure, but more enhancement of the spatial resolution is required.

3. Subcooled Boiling

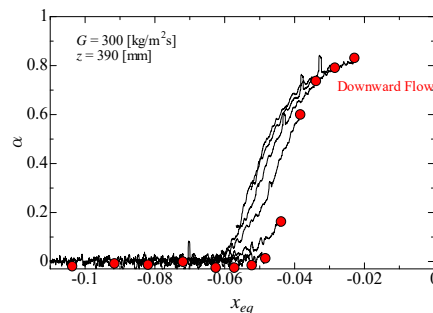
In this investigation, void fraction under upward and downward flow condition were measured. Figure 3(a) is the void fraction distribution, and void fraction at 390mm obtained by changing the heat flux is plotted against thermal equilibrium quality in Fig.3(b). In this condition, upward flow and downward flow take a quite different tendency. Figure 3(c) is the same data with Fig.3(b), but solid line corresponds to the void fraction under same heat flux of different location. As shown in Figure, downward flow condition takes quite different tendency influenced by magnitude of heat flux. This tendency may be explained by the effect of buoyancy.



Upward Downward

(a)

(b)



(c)

Fig.3 Void fraction of subcooled boiling

R. Matsumoto, T. Uechi¹, Y. Nagasawa¹, T. Shiokawa¹,
D. Ito² and Y. Saito²

Faculty of Engineering Science, Kansai University
¹*Graduate School of Science and Engineering, Kansai University*
²*Institute for Integrated Radiation and Nuclear Science, Kyoto University*

INTRODUCTION: Heat exchangers which are operated at 0 °C below are subjected to occurring the frost deposition and its growth. The structure of frost is porous consisted of ice crystal and air. Therefore the thermal conductivity is low, and the frost layer becomes the thermal resistance between the cooling surface and ambient air. Matsumoto et al. [1] reported the two dimensional distribution of the frost deposition rate on the plate fin-tube heat exchanger by using neutron radiography (NRG). Neutrons are strongly attenuated by the water molecules in the frost layer, but not by the aluminum heat exchanger. The frost formation can be quantitatively estimated based on the neutron beam attenuation. By applying the computed tomography, the three dimensional frost formation can be visualized. In this study, the three dimensional distribution of the frost deposition and the frost density profiles on the plate fin-tube heat exchanger are quantitatively estimated by using the neutron computed tomography imaging at KUR B-4 radiation port.

EXPERIMENTS: Fig.1 shows the schematic view of the experimental apparatus. Cooled humid air adjusted to the flow rate 70 L/min was supplied to the test section. The test section consisted of Styrofoam block duct with a cross section of 68 mm x 150 mm and the aluminum plate fin-tube heat exchanger. The heat exchanger consisted by 6 fins with 60 mm in height, 28 mm in width, 0.25 mm in thickness, and together with two tubes of an outer 8.5 mm. Fin pitch was 5 mm. The heat exchanger was cooled by -22 °C fluorinert. The frosting duration was 60 min. CCD camera (Princeton Inst., 16-bit, 1024 × 1024 pixels) set in the inside a light-tight camera box. Two mirrors reflect the visible ray image from the converter with the 6LiFZnS scintillator screen mounted onto the front end of the camera box. 600 neutron radiography (NRG) images were taken by the CCD camera with an exposure time of 5 sec by rotating the heat exchanger through 180 degrees.

RESULTS: Fig.2(a) shows the digital camera image of the heat exchanger taken from the downstream-side. Frost covered the fins. Fig.2 (b) shows the NRG images after 60 min frosting duration. Frost formation on the plate fin and tube surfaces could be clearly visualized by neutron radiography. The tomographic image of x-y plate at a z position was reconstructed from the lateral line-date of 600 projection images. The tomographic image was expressed by the linear attenuation coefficient μ . The frost density ρ can be calculated from $\rho = \mu / \mu_{m,ice}$, in which $\mu_{m,ice}$ is the mass attenuation coefficient of ice. Fig.3 shows the three dimensional frost density distributions. At the fin edge, high frost deposition are observed, however, the frost layer is thin in the wide area of the wake region. The three dimensional frost density profile can be estimated by using 3D neutron computed tomography.

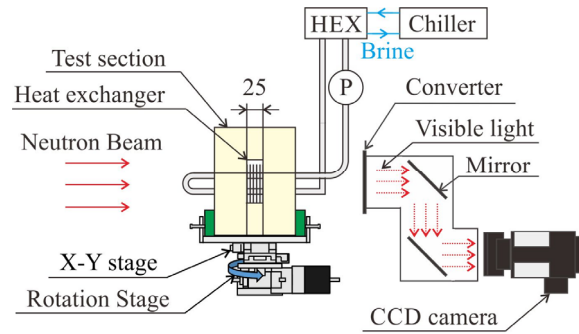
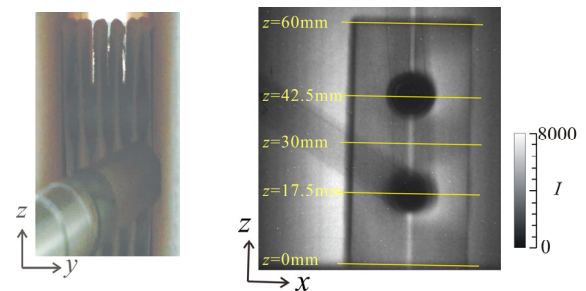


Fig.1 Schematic view of the experimental apparatus



(a) Digital camera image

(b) NRG image

Fig. 2 Digital camera image and NRG image

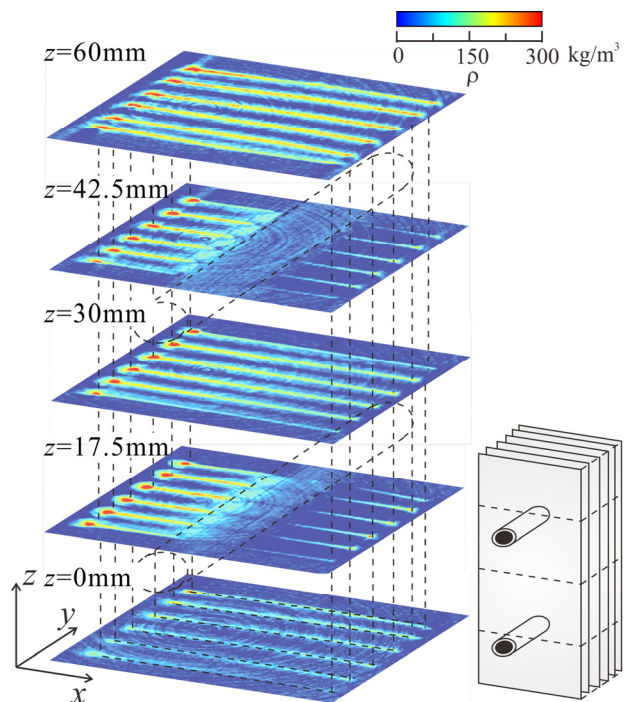


Fig.3 Three dimensional frost density distributions

REFERENCE:

[1] R. Matsumoto, et al., Proceedings of the International Heat Transfer Conference IHTC-15, IHTC15-9144, Kyoto, pp. 3603-3615

PR7-6 Study on the Visualization of Organic Matter between Metals in order to Contribute to the Advancement of the Industrial Products

K. Hirota, H. M. Shimizu, M. Kitaguchi, Y. Tsuchikawa, S. Imajo, S. Awano, A. Uritani¹, K. Watanabe¹, S. Yoshihashi¹, A. Yamazaki¹ and Y. Saitoh²

Graduate School of Science, Nagoya University
¹*Graduate School of Engineering, Nagoya University*
²*Institute for Integrated Radiation and Nuclear Science, Kyoto University*

INTRODUCTION: Mechanical and industrial products such as automobiles and aircraft are progressing with higher performance and higher accuracy in Japan. One of the demands at the development site of these state-of-the-art products is visualization of the state of organic films (oil film, grease, electrolyte, etc.) existing between metals, which can not be seen directly by our eyes. In this research, we will explore the possibility of observing the dynamic state of the organic film (shape, properties, thickness distribution) and its dynamic change mainly between automobile parts as an example.

At present Nagoya University is constructing an accelerator driven small neutron source (NUANS) and neutron radiography ports [1,2]. We are also proceeding with the quantitative evaluation of the difference in performance among the radiography ports by measuring and comparing the same sample with two devices. This year, we produced a camera for radiography to be used at NUANS, so we evaluated its performance in KUR E2 port.

EXPERIMENTS: The detector indicator was set at the front of the radiography camera box and evaluates the spatial resolution. Two camera boxes of used E2 and NUANS were measured for comparison. These two camera boxes were used same CCD and optics systems, almost same performance can be expected. The scintillator thickness dependence was also checked.

RESULTS: As shown in Fig. 1, clear radiography images are available to get by both camera boxes. The X-axis projections of the comb shape indicators are shown in fig.2, which left and right are reversed. We can see the almost 0.1mm resolution at all scintillator conditions. It is confirmed that the both camera boxes have almost same performance despite the increase of the white spots due to the radiation damage of long-term use at E2 port.

The ⁶LiF/ZnS(Ag) scintillator thickness is also checked. The spatial resolution slightly drops at 200 microns thickness. This is because of the scintillating light spreading in the scintillator. The S/N ratio of the image for 200 microns thickness is better than for 100 microns.

These imaging camera box are useful for visualization of organic matter.

New imaging detector was also evaluated, which was LiF coated Si-pixel detector. Since this detector counts

events where the output voltage above the threshold energy, gamma rays can be separated to some extent. Although CCD can not eliminate the contribution of gamma rays because it integrates charge, this detector can be excluded, so it is promising as a future neutron detector.

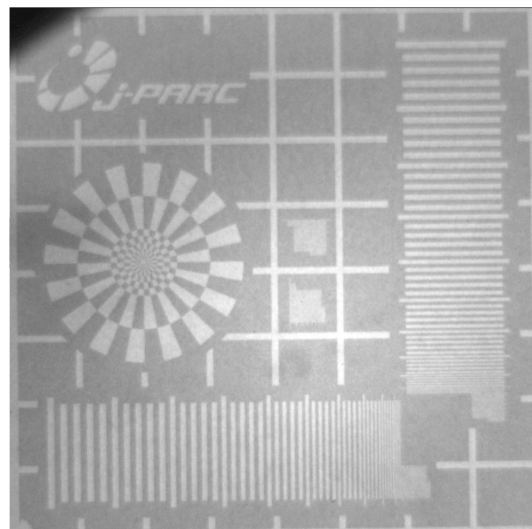


Fig. 1. The X axis projection image of the detector indicator.

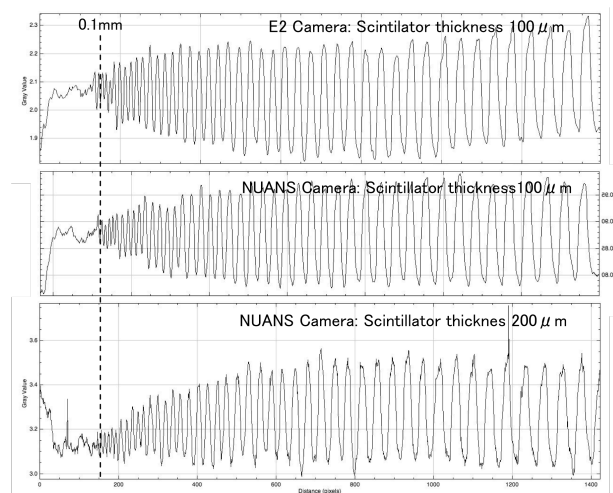


Fig. 2. The X axis projection image of the detector indicator.

REFERENCES:

- [1] K.Hirota, PoS(KMI2017) 025.
- [2] I.Ito, PoS(KMI2017) 068.
- [3] X.Llopart, et.al., Nucl. Instrm. Meth. A**581** (2007) 485.

Y. Tsuji¹, T. Matsushita², V. Sonnenschein¹, K. Hirota²,
S. Suzuki¹, S. Kokuryu¹, D. Ito³ and K. Saito³

¹Graduate School of Engineering, Nagoya University
Department of Energy Engineering and Science

²Graduate School of Science, Nagoya University
Department of Physics

³Graduate School of Science, Kyoto University
Research Reactor Institute, Kyoto University

INTRODUCTION: Below about 2.17 K, liquid ^4He transits to the superfluid phase in which an inviscid irrotational superfluid component coexists with a viscous normal-fluid component. As a quantum fluid, superfluid helium exhibits many interesting properties. In recent ten years, new techniques have been applied to visualize the flow of superfluid helium and measure the local velocity fluctuation. Among these the most powerful one is the particle image velocimetry (PIV) which is a potential tool to measure the local velocity and promises to provide us a deep understanding of complex superfluid motions.

Helium excimers have advantages as a tracer particle of PIV such as, (i) the molecule size is several angstroms, (ii) a neutral particle in superfluid, and (iii) do not aggregate. The neutron- ^3He absorption reactions proposed here is a possible method to generate small clusters of the helium excimers, which can be detected as individual tracer particles that follow faithfully the motion of the normal-fluid component in superfluid helium. This technique will allow unambiguous determination of the complete normal-fluid velocity field.

EXPERIMENTS: To observe the triplet He_2^* excimers, the laser-induced fluorescence can be used. Figure 1 shows energy levels of a triplet excimer in liquid He. When 905 nm laser is applied, a 905 nm photon excites an excimer from the ground state a to the metastable state c , and then, it is further raised to the excited state d by absorption of another 905 nm photon. The d state decays to the b state, emitting a detectable 640 nm photon. Therefore, to excite the fluorescence, an excimer in the intermediate state c excited by one 905 nm photon has to meet another 905 nm photon within the c state lifetime approximately 4 nsec. When the b state relaxes back to the ground state a , the transition becomes cyclic and can be repeated during the lifetime ~ 13 sec of the triplet excimer. The sample liquid ^4He is stored in a stainless Dewar with 4 quartz optical windows. Space for liquid ^4He is 16 cm in diameter and about 1 m height. Neutron beam (B-4 line) with the cross section about 1 cm^2 is injected to the sample space through 2 quartz windows of Dewar.

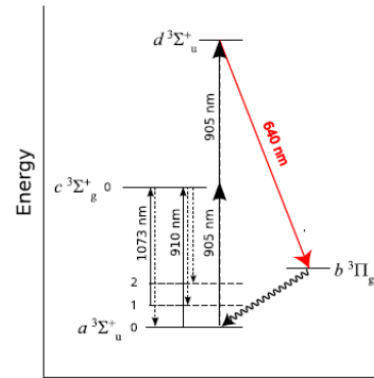


Fig. 1: Energy levels of a triplet He_2^* excimer in liquid helium. *W.G. Rellergert et al., PRL 100, 025301 (2008)*

RESULTS: Fluorescence from 640 nm photons are collected by detectors with 640 nm bandpass filters through the other 2 windows in directions perpendicular to the neutron beam, to avoid direct detection of laser photons. First, 2 photomultipliers are employed for the detector, and resulted signals are recorded for each 905 nm pulse. At this condition, the configuration of the excitation laser system is optimized, while the possibility of dark current is excluded. Figure 2 shows the results of signal recorded by photomultipliers. The sharp spike at 100 ns is the pump laser at 905nm pulse. Figure 2(a) and (b) are with neutron and without neutron, respectively. It is difficult to remove the background light completely, then they are recorded in Fig.2(a). It is clearly observed that the emission by helium excimer clusters via neutronon- ^3He absorption reaction in Fig.2(b).

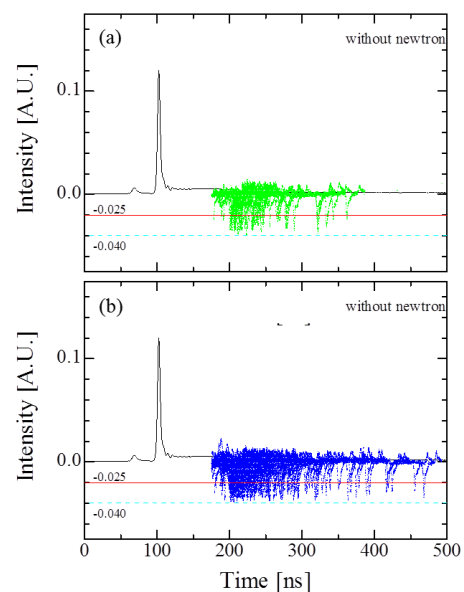


Fig.2: Recorded signal of photomultipliers. (a)without neutron, (b)with neutron

T. Sakai, H. Iikura, M. Matsubayashi, D. Ito¹ and
Y. Saito¹

Materials Sciences Research Center, Japan Atomic Energy Agency

¹*Research Reactor Institute, Kyoto University*

INTRODUCTION: Fluorescent plates are widely used for neutron radiography. In the case of the imaging devices, the spatial resolution of fluorescent plates conflicts with their detection efficiency. In general, a thicker phosphor layer increases the efficiency, but adversely affects the resolution because of blurring [1]. In this work, we developed a new approach to fabricate micro-structured fluorescent plates. The devices consist of capillary plates and fine phosphor grains [2]. Capillary plates are glass plates on which tiny capillaries are arrayed in two-dimensions periodically [3]. Herein, we introduce the development of fine fluorescent plates for neutron radiography imaging device.

EXPERIMENTS: The original capillary and phosphor-packed plates were observed using an optical microscope. The micrographs of the plates are shown in Fig. 1. All holes are clearly observed to be filled with the phosphor grains. The plate material was borosilicate glass. The specifications of the plates are as follows: plate thickness, 0.4 mm; diameter of each capillary, 25 μm ; pitch of each hole, 31 μm ; open area ratio, 59 %; diameter of effective area, 20 mm. The phosphor grains were sifted silver-activated zinc sulfide (ZnS:Ag) with a mean particle size of approximately 7 μm [1]. ZnS:Ag is one of the most popular phosphors because it exhibits excellent efficiency with a maximum emission wavelength of 450 nm [4]. The plates are impregnated with ¹⁰B-enriched orthoboric acid to add neutron detection sensitivity.

The neutron imaging experiments were performed at KUR E-2. The images were collected using a CCD camera as shown in Fig. 2.

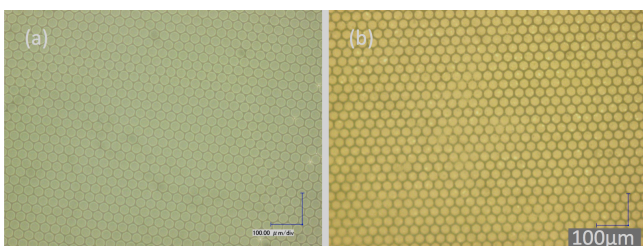


Fig. 1 Micrographs of the original (a) and phosphor-packed (b) capillary plates.

RESULTS: Neutron induced fluorescence is clearly observed and the fluorescence is relatively uniform. The spatial resolution is not evaluated yet, but the line-pairs are evident as shown in Fig. 2 (b).

We have developed the micro-structured fluorescent plates successfully. Microscopic images revealed that each capillary was well filled with phosphor grains and functioned as a microcolumnar fluorescent material.

Impregnation with ¹⁰B-enriched orthoboric acid is effective to add neutron sensitivity to the fluorescent plates. The fabricated fluorescent plates are expected to be useful in high-spatial-resolution imaging devices with good detection efficiency. The next step of the work is to increase the neutron detection efficiency. The metal coating inside the capillary walls is considered to be a promising method.

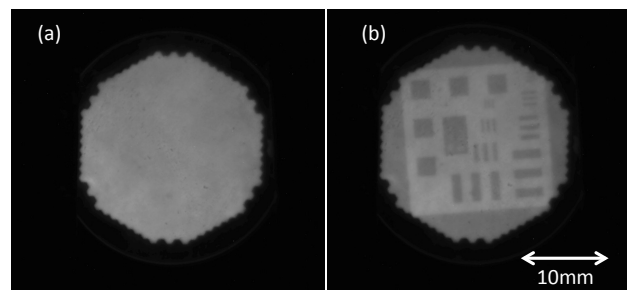


Fig. 2 Results of fluorescent plates neutron imaging. The plate was exposed to neutrons for 10 minutes. Images (a) and (b) are no object and a line-pair indicator [5] images, respectively.

REFERENCES:

- [1] T. Sakai *et al.*, Nucl. Instr. and Meth. Phys. Res. B 332 (2014) 1238.
- [2] T. Sakai *et al.*, JPS Conf. Proc. 11, 020005 (2016).
- [3] HAMAMATSU PHOTONICS K. K. website: <<http://www.hamamatsu.com/jp/en/product/category/3200/3032/index.html>>.
- [4] Seung Kyu Lee *et al.*, Prog. in Nucl. Sci and Tech., Vol.1, (2011) pp.194-197.
- [5] R. Yasuda *et al.*, Physics Procedia 43 (2013) pp.196-20.

Y. Ohkubo

Research Reactor Institute, Kyoto University

Objective and Participating Research Subjects

Because of the suspension of the reactor (KUR) operation for the last three periods, we could not execute any irradiation experiments in a three-year project research named the same title of the present project research. In the late August of this period, the operation of KUR restarted and we also restarted the project research, the main objectives of which are the investigation of the nuclear structure of unstable neutron-rich nuclei and also the local properties of matters using short-lived nuclei.

Unfortunately, several troubles interrupted the operation of KUR and moreover a different trouble made the on-line isotope separator (KUR-ISOL) unavailable for several weeks so that two research subjects (29P8-1 and 29P8-4) were not executed at all and the other research subjects of the project (29P8) were carried out incompletely.

The research subjects reported here are as follows:

- 29P8-2 Isomer search for fission products around $A = 150$ with energy-sum γ -ray spectrometry
- 29P8-3 Compton polarimeter for β -delayed γ rays using clover detector
- 29P8-5 Nuclear spin relaxation of ^{111}Cd at the A site in a spinel oxide CdIn_2O_4
- 29P8-6 Observation of local fields at the $^{111}\text{Cd}(\leftarrow ^{111\text{m}}\text{Cd})$ sites in cadmium titanate

Main Points Described in the Reports in the Following Four Pages

M. Shibata *et al.* (29P8-2) took γ -ray spectra associated with the β^- decay of ^{144}Ba , ^{150}Ce , and ^{152}Ce in the singles and add-back modes of their γ -ray detection system with a clover detector in order to search for an unknown isomer state in an odd-odd nucleus ^{144}La in particular, which is in turn expected to be able to solve the so-called Q_β puzzle in ^{144}La . The trick of searching for an unknown isomer state with the clover detector is as follows: For an isomeric γ -ray transition, the intensity is higher in the add-back mode than in the singles mode, whereas the intensity of a γ -ray in a cascade is lower in the add-back mode than in the singles mode. They obtained ^{144}Ba , ^{150}Ce , and ^{152}Ce as thermal neutron-induced fission products of ^{235}U at the KUR-ISOL. The detailed data analyses are in progress.

Y. Kojima *et al.* (29P8-3) are trying to measure the linear polarization of γ -rays from short-lived β decaying nuclei using the above mentioned clover detector and additional coaxial Ge detectors in order to obtain the multipolarities of those γ -rays. The clover detector is

used as a Compton polarimeter. They first measured the γ -ray energy dependence of the polarization sensitivity of the polarimeter using standard γ -ray sources ^{60}Co , ^{134}Cs , and ^{152}Eu , and then measured the Compton scattering asymmetry for ^{140}Cs and ^{146}La which were produced and separated at KUR-ISOL. They obtained preliminary asymmetry values for the 258-keV and 410-keV γ -rays from ^{146}La .

W. Sato *et al.* (29P8-5) studied the local fields at the two metal sites of CdIn_2O_4 , which is expected to be optoelectronic, using the time-differential perturbed-angular-correlation (TDPAC) technique. They used two TDPAC nuclear systems with a common probe nuclear state, the 245-keV ^{111}Cd state having a nuclear spin of 5/2: one arising from ^{111}In (commercially available) and the other from $^{111\text{m}}\text{Cd}$ (produced using a pneumatic system at KUR). It is natural to consider that ^{111}In and $^{111\text{m}}\text{Cd}$ occupy the In site and the Cd site in CdIn_2O_4 , respectively and that the 245-keV ^{111}Cd state arising from ^{111}In and that from $^{111\text{m}}\text{Cd}$ feel the corresponding static electric field gradients. This is the case for the former. However, unexpectedly, the 245-keV ^{111}Cd state arising from $^{111\text{m}}\text{Cd}$ feels a dynamic perturbation. The cause of the dynamic perturbation is under consideration.

S. Komatsuda *et al.* aim at obtaining with the $^{111}\text{Cd}(\leftarrow ^{111\text{m}}\text{Cd})$ -TDPAC technique microscopic information on the ferroelectric to paraelectric phase transition in perovskite oxides CdTiO_3 and Ca-doped CdTiO_3 . They first of all examined the preparation condition for CdTiO_3 by taking a room-temperature TDPAC spectrum of $^{111}\text{Cd}(\leftarrow ^{111\text{m}}\text{Cd})$ in CdTiO_3 (29P8-6). Because $^{111\text{m}}\text{Cd}$ is short lived (its half-life is 49 min), it is necessary to shorten the preparation process as much as possible. They confirmed together with the powder X-ray diffraction method that for the preparation condition they used, $^{111\text{m}}\text{Cd}$ occupies the Cd site of CdTiO_3 prepared with no secondary phase.

PR8-1 Isomer Search for Fission Products around $A=150$ with Energy-sum γ -ray Spectrometry

M. Shibata, S. Ohno¹, H. Kamada¹, T. Yamashita¹,
Y. Kojima and A. Taniguchi²

Radioisotope Research Center, Nagoya University

¹School of Engineering, Nagoya University

²Research Reactor Institute, Kyoto University

INTRODUCTION: Decay scheme information of fission products of ^{235}U are important for both nuclear engineering and nuclear physics. Concerning fission products around mass number 150, doubly-odd nuclei have not been studied well and the decay information are scarce compared to odd mass nuclei. Especially, isomeric states are expected in the doubly-odd nuclei. For example, a long-lived isomeric state at 150.3 keV whose half-life is longer than 5s in ^{156}Pm has been proposed [1] and $^{152,154}\text{Pm}$ and ^{152}Pr also have isomeric states. These isomeric states are interpreted as the spin flip-flop transition. Therefore the other isotopes are expected to have isomeric states.

As described in ref. [2], in ^{144}La , three different Q_{β} -values were proposed by the β -ray spectra gated by γ -rays. One of the reason of the differences are considered to be discrepancies of decay schemes because the gated γ -rays are placed at different position between the decay schemes. Another Q_{β} -value was proposed by the total absorption detector [2], nevertheless, the problem still remains. There is a possibility that an unidentified isomer exists. To solve the “ Q_{β} -puzzle”, reconstruction of the decay scheme and search for the isomer are desired.

As described in ref. [3, 4], our clover detector has four identical Ge crystals and each Ge works independently. The detector can measure in not only singles mode but also add-back mode by using a VME-based data acquisition system. In the energy-sum γ -ray spectrometry, sum peaks of cascade γ -rays are observed more intensively in the add-back mode, and each cascade γ -ray is observed weakly compared to that of singles mode. Therefore the long-lived isomeric transitions are expected to be observed intensively in the add-back mode.

In this experiments, the β -decay study of ^{144}Ba , ^{150}Ce and ^{152}Ce were carried out by means of the energy-sum γ -ray spectrometry using the clover detector.

EXPERIMENTS: The experiments were performed at the on-line mass separator KUR-ISOL at the Kyoto University Reactor, a 72 mg of 93%-enriched $^{235}\text{UF}_4$ target being inserted in a through-hole. The isotopes of interests were produced with the thermal neutron-induced fission of ^{235}U . The produced radioactive isotopes were transported by a gas jet of He- N_2 and were ionized by a thermal-ionization type ion source. The mass-separated radioactive beam was incident on an aluminized Mylar tape set in the computer controlled tape transport system. The tape was moved a predetermined period to reduce the background from their daughter nuclei. The γ -rays associated with the decay of each isotope were measured by means of energy-sum γ -ray spectrometry. For ^{144}Ba ($T_{1/2}=11.5$ s), the

collection-measurement cycle was set at 22 s–22 s and was repeated for 10 hours. The detector was shielded with 10 cm-thick lead blocks and 10 cm-thick borated polyethylene blocks outside them in order to reduce the background neutrons and γ -radiation.

RESULTS: The measured γ -ray spectra associated with the β decay of ^{144}Ba in the singles and add-back modes are shown in Fig. 1. The closed circles indicate the coincidence γ -rays with the La x-rays. At present, the excited states and γ -rays of daughter nucleus ^{144}La are proposed up to 1240 keV and 922.4 keV, respectively. The evaluated Q_{β} -values of ^{144}Ba is 3083 keV [5], then, higher-lying levels and γ -rays are expected be observed by the experiment using the clover detector. The detailed analysis is in progress also for ^{150}Ce and ^{152}Ce .

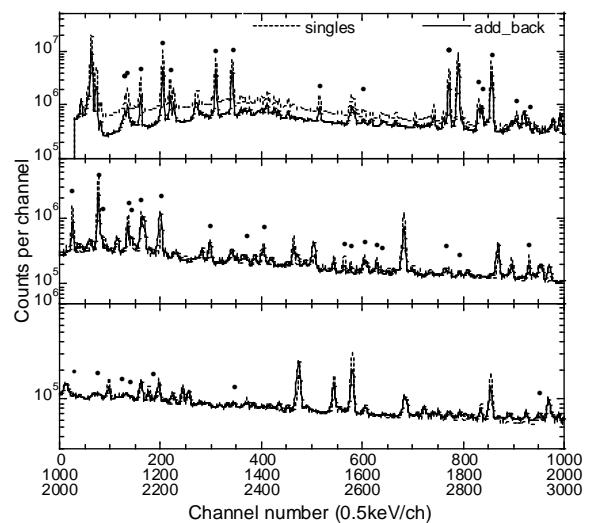


Fig. 1 Singles and add-back spectra for γ -rays associated with the β decay of ^{144}Ba . The closed circle indicates the coincidence γ -ray with the La x-rays in the preliminary analysis.

CONCLUSIONS: The β -decay study for the doubly-add nuclei of fission products were carried out by means of the energy-sum γ -ray spectrometry. The measurement by clover detector coupled with ISOL is effective to the decay study. Especially, there are some newly observed γ -ray in the decay of ^{144}Ba . To solve the Q_{β} -puzzle in ^{144}La , further analyses are desired.

REFERENCES:

- [1] M. Shibata *et al.*, Eur. Phys. J., A 31 (2007) 171-176.
- [2] M. Shibata *et al.*, J. Phys. Soc. Jpn., 71 (2002) 1401-1402.
- [3] Y. Shima *et al.*, Appl. Rad. Isot., 91(2014)97-103.
- [4] T. Yamashita *et al.*, Appl. Rad. Isot., 135 (2018)131-134.
- [5] M. Wang *et al.*, Chin. Phys. C 36 (2012) 1603-2014.

S. Ohno, Y. Kojima¹, H. Kamada, T. Yamashita,
A. Taniguchi² and M. Shibata¹

Graduate School of Engineering, Nagoya University

¹Radioisotope Research Center, Nagoya University

²Research Reactor Institute, Kyoto University

INTRODUCTION: Gamma-ray multipolarities are one of the most important properties for nuclei. For example, experimental data on them and also those on spins and parities of nuclear levels are necessary for discussion on nuclear deformation.

The linear polarization of γ rays is useful in determining the multipolarities. The linear polarization is usually measured using a Compton polarimeter consisting of two or more γ -ray detectors because the Compton scattering is a polarization-sensitive process. In this technique, a Compton scattering asymmetry A in orthogonal directions is determined by means of coincidence measurements. After correcting the A -value using the polarimeter sensitivity Q , the value of A/Q is compared with the degree of polarization P which has been calculated for various multipolarities. This method is often used for in-beam γ -ray spectroscopies. However, it rarely applies for γ rays following decays of short-lived nuclei. This is because the latter case needs an additional detector (directional detector) in order to define the *reference plane* and the triple coincidence measurement makes the overall detection efficiency low.

Our group is trying to apply a clover Ge detector [1] to the linear polarization measurements for short-lived β -decaying nuclei. The clover detector contains four large Ge crystals (80mm ϕ , 90mm in length) packed closely. Thus, we expect that the clover detector enables the polarization measurement for β -delayed γ rays to be made. In this report, we present the status of this research and preliminary results of the first on-line experiment at KUR-ISOL [2].

EXPERIMENTS: The detection system consisted of the clover detector as a polarimeter, a coaxial Ge detector as a directional detector, and another coaxial detector to deduce correction factors of detection efficiencies. The pre-amplifier signals from the detectors were processed by a VME-based data acquisition system and recorded in a list mode.

First, ⁶⁰Co (40 kBq), ¹³⁴Cs(9.5 kBq) and ¹⁵²Eu(27 kBq) standard sources were measured to reveal properties of the system such as energy dependence of the polarization sensitivity. In order to find the optimum measuring condition, we repeated measurements, placing the clover and coaxial Ge detectors (relative efficiencies of 38% and 60%) in different geometry arrangements.

Then, we measured short-lived ¹⁴⁰Cs and ¹⁴⁶La nuclei. They were prepared at KUR-ISOL, following the thermal neutron induced fission of ²³⁵U. The fission products were thermalized in the target chamber, and transported to an ion source by gas jet stream. After ionization, the

nuclei were mass-separated and implanted into an aluminized Mylar tape. Each detector was placed at 10 cm from the source (see below). The measuring time was 3 h for ¹⁴⁰Cs and 17 h for ¹⁴⁶La.

RESULTS: The list data were analyzed using an off-line sorting program. Signals recorded within 490 ns were taken as coincident events.

Asymmetry of the Compton scattering was observed for E2-E2 γ cascades in the decay of ⁶⁰Co, ¹³⁴Cs and ¹⁵²Eu. The polarimeter sensitivity Q was deduced using the experimental and theoretical asymmetry value [3]. The best performance was obtained when the source-to-detector distance is 10 cm and the directional detector is the 60% coaxial detector. The energy dependence of the sensitivity Q in this condition was shown in Fig. 1. The 344- and 411-keV γ rays from ¹⁵²Eu show large uncertainties because of poor statistics. We need a further measurement for ¹⁵²Eu.

From the measurements at KUR-ISOL, preliminary asymmetry values were obtained for ¹⁴⁶La to be about -0.05 for 258-keV and 0.03 for 410-keV E2 γ ray. Further measurements are needed to improve the precision.

Another problem found in the experiments at KUR-ISOL is intense background radiations. They cause random coincidence and reduce counts associated with the Compton scattering. To solve this problem, a heavier shield should be placed around the clover detector. Also, data analysis to remove (or reduce) random summing effects is planned.

SUMMARY: It has been found that a clover Ge detector works as a Compton polarimeter for β -delayed γ rays. However, further improvement is required to use the polarimeter at KUR-ISOL.

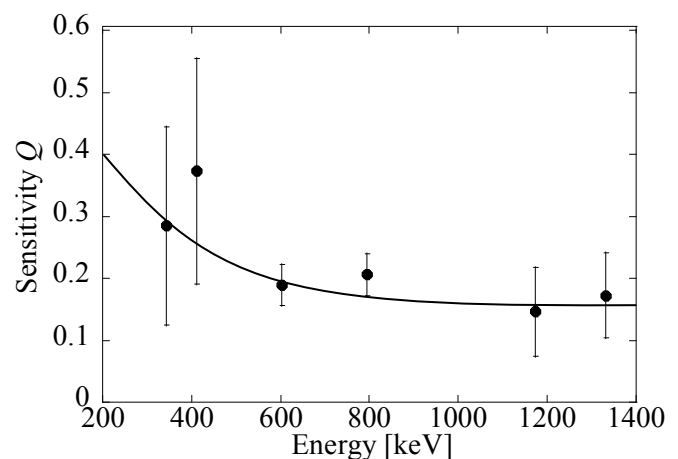


Fig. 1. The polarization sensitivity as a function of incident γ -ray energy. The curve is only a guide to the eye.

REFERENCES:

- [1] Y. Shima *et al.*, Appl. Radiat. Isot. **91** (2014)97-103.
- [2] A. Taniguchi *et al.*, Nucl. Instr. and Meth. A, **351** (1994)378-382.
- [3] D.R. Hamilton, Phys. Rev. **74** (1948) 782-788.

PR8-3 Nuclear Spin Relaxation of ^{111}Cd at the A Site in a Spinel Oxide CdIn_2O_4

W. Sato, S. Komatsuda¹, and Y. Ohkubo²

Institute of Science and Engineering, Kanazawa University

¹*National Institute of Technology, Ichinoseki College*

²*Research Reactor Institute, Kyoto University*

INTRODUCTION: Spinel oxides exhibit various physical properties depending on the constituent metal elements and on their residence positions. Optoelectronic response is one of the most interesting phenomena observed for the oxide group [1]. From the view point of fundamental physics as well as technology applications, therefore, an atomic level investigation of the physical properties of these oxides is very important. In the present work, we measured local fields at the metal sites in CdIn_2O_4 , an expected optoelectronic material, to obtain microscopic information by means of time-differential perturbed angular correlation (TDPAC) spectroscopy with two different probes $^{111}\text{In}(\rightarrow^{111}\text{Cd})$ and $^{111\text{m}}\text{Cd}(\rightarrow^{111}\text{Cd})$. In this report, unexpected nuclear spin relaxation of the $^{111\text{m}}\text{Cd}(\rightarrow^{111}\text{Cd})$ probe is presented [2].

EXPERIMENTS: Well-mixed stoichiometric amounts of CdO and In_2O_3 were pressed into a disk, and sintered in air at 1373 K for 45 min. After the confirmation of successful synthesis of CdIn_2O_4 by a powder X-ray diffraction pattern, the sample was doped with $^{111}\text{In}(\rightarrow^{111}\text{Cd})$ in HCl solution and underwent heat treatment in air at 1373 K for 3 h for the thermal diffusion of the radioisotope. A TDPAC measurement was then performed for the $^{111}\text{In}(\rightarrow^{111}\text{Cd})$ probe on the 171-245 keV cascade γ -rays with the intermediate state of $I = 5/2$ having a half-life of 85.0 ns.

Neutron irradiation was performed for cadmium oxide (CdO) enriched with ^{110}Cd in Kyoto University Reactor to produce radioactive $^{111\text{m}}\text{Cd}$ by a neutron capture reaction. The radioactive $\text{Cd}(^{111\text{m}}\text{Cd})\text{O}$ powder was well mixed in a mortar with CdIn_2O_4 prepared in advance, and sintered in air at 1373 K for 45 min. A TDPAC measurement was carried out for the $^{111\text{m}}\text{Cd}(\rightarrow^{111}\text{Cd})$ probe on the 151-245 keV cascade γ -rays with the same intermediate state as the $^{111}\text{In}(\rightarrow^{111}\text{Cd})$ probe. In the present work, we obtained the perturbed angular correlation as a function of the time interval of the cascade γ -ray emissions by the following expression:

$$A_{22}G_{22}(t) = \frac{2[N(\pi, t) - N(\pi/2, t)]}{N(\pi, t) + 2N(\pi/2, t)}, \quad (1)$$

where A_{22} denotes the angular correlation coefficient, $G_{22}(t)$ the time-differential perturbation factor as a function of the time interval t between the cascade γ -ray emissions, and $N(\theta, t)$ the number of the coincidence events observed at an angle θ .

RESULTS: The room-temperature TDPAC spectrum of $^{111}\text{In}(\rightarrow^{111}\text{Cd})$ embedded in CdIn_2O_4 is shown in Fig. 1(a).

The spectrum shows oscillatory structure characteristic of the electric quadrupole interaction of the probe nucleus on the intermediate state ($I = 5/2$) with the extranuclear charge distribution. Thus, we analyzed the spectrum with the following time-differential perturbation factor $G_{22}(t)$ assuming a relative width δ to the centroid of the frequencies ω_n :

$$G_{22}(t) = \sigma_{2,0} + \sum_{n=1}^3 \sigma_{2,n} \cos(\omega_n t). \quad (2)$$

Because In ions are known to reside in the distorted octahedral B site in CdIn_2O_4 , it is plausible that the present $^{111}\text{In}(\rightarrow^{111}\text{Cd})$ probe also occupies the B site; the quite large quadrupole frequency $\omega_Q = 14.04 \text{ Mrad s}^{-1}$ is consistent with this interpretation.

Figure 1(b) shows the room-temperature TDPAC spectrum of the $^{111\text{m}}\text{Cd}(\rightarrow^{111}\text{Cd})$ probe incorporated in CdIn_2O_4 . An unexpected pattern was observed in the spectrum; the directional anisotropy of the γ - γ cascade shows a fast attenuation, implying nuclear spin relaxation caused by the extranuclear perturbation. A possible cause of the spin relaxation is dynamic fluctuation of the probe nucleus relative to the extranuclear charge distribution. Taking this assumption into account, the spectra were tentatively fitted with the following time-differential perturbation factor:

$$G_{22}(t) = \exp(-t/\tau_c) G_{22}^{\text{static}}(t). \quad (3)$$

Here, we assumed slow fluctuation in the relative motion of the extranuclear field. In Eq. (3), τ_c ($= 39(4) \text{ ns}$ at room temperature) stands for the reorientational correlation time of the probe nucleus and $G_{22}^{\text{static}}(t)$ is the static perturbation factor. Because it is considered that $^{111\text{m}}\text{Cd}$ probes mainly occupy the tetrahedral A site in CdIn_2O_4 , however, it is difficult to ascribe the relaxation to the thermal motion of the probe ions confined in the small tetrahedral space. Further detailed investigation in a wide temperature range would be needed for the determination of the origin of the spectral damping.

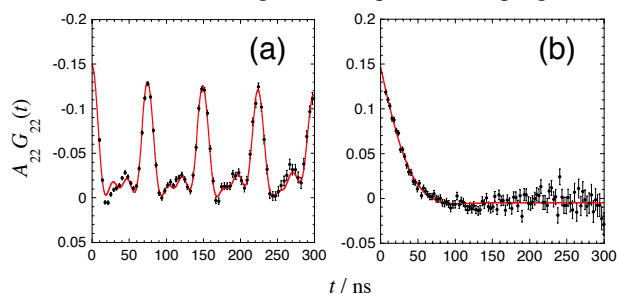


Fig. 1. TDPAC spectra (a) of $^{111}\text{In}(\rightarrow^{111}\text{Cd})$ and (b) of $^{111\text{m}}\text{Cd}(\rightarrow^{111}\text{Cd})$ in CdIn_2O_4 measured at room temperature.

REFERENCES:

- [1] B. Boujnah *et al.*, J. Appl. Phys. **116** (2014) 123703 (1-7).
- [2] W. Sato *et al.*, J. Radioanal. Nucl. Chem. <https://doi.org/10.1007/s10967-018-5855-8>.

PR8-4 Observation of Local Fields at the $^{111}\text{Cd}(\leftarrow^{111\text{m}}\text{Cd})$ Sites in Cadmium Titanate

S. Komatsuda, W. Sato¹ and Y. Ohkubo²

Liberal Arts and Sciences, Natural Sciences, National Institute of Technology, Ichinoseki College

¹*Institute of Science and Engineering, Kanazawa University*

²*Research Reactor Institute, Kyoto University*

INTRODUCTION: The perovskite oxides ABO_3 exhibit various electronic properties, depending on their combination of A and B ions. The cadmium titanate (CdTiO_3) has been attracting much attention as a ferroelectric oxide, and its technological applications are strongly expected. It is reported that CdTiO_3 exhibits a phase transition from the ferroelectric to paraelectric at about 85 K, and this transition temperature is affected by calcium (Ca) doping on the Cd site in CdTiO_3 [1]. Because it is necessary for a practical use of CdTiO_3 to obtain more microscopic information on this transition mechanism, we investigated the local structures in CdTiO_3 and Ca-doped CdTiO_3 by means of the time-differential perturbed angular correlation (TDPAC) method using the $^{111}\text{Cd}(\leftarrow^{111\text{m}}\text{Cd})$ probe. In the present work, in order to ascertain the doping condition of the $^{111}\text{Cd}(\leftarrow^{111\text{m}}\text{Cd})$ probe, we initially examined the site occupied by the $^{111}\text{Cd}(\leftarrow^{111\text{m}}\text{Cd})$ in undoped CdTiO_3 .

EXPERIMENTS: About 3 mg of CdO enriched with ^{110}Cd was irradiated with thermal neutrons in a pneumatic tube at Kyoto University Reactor, and radioactive $^{111\text{m}}\text{Cd}$ was generated by $^{110}\text{Cd}(n, \gamma)^{111\text{m}}\text{Cd}$ reaction. The neutron-irradiated CdO powder was then added into stoichiometric amount of TiO_2 powder and nonradioactive CdO powder to synthesize the polycrystalline CdTiO_3 powder. The powders were mixed in the mortar. The powders were pressed into disks and sintered in air at 1373 K for 45 min. It was confirmed from the powder XRD pattern for the nonradioactive sample that calcining at 1373 K for 45 min is sufficient to synthesize a single phase CdTiO_3 . The TDPAC measurement was carried out for the 151-245 keV cascade γ rays of the $^{111}\text{Cd}(\leftarrow^{111\text{m}}\text{Cd})$ probe with the intermediate state of $I = 5/2$ having a half-life of 85.0 ns.

RESULTS: Figure 1 shows the TDPAC spectrum of $^{111}\text{Cd}(\leftarrow^{111\text{m}}\text{Cd})$ probe in CdTiO_3 . The measurement was performed at room temperature. The directional anisotropy on the ordinate, $A_{22}G_{22}(t)$, was deduced with the following simple operation for delayed coincidence events of the cascade:

$$A_{22}G_{22}(t) = \frac{2[N(\pi, t) - N(\pi/2, t)]}{N(\pi, t) + 2N(\pi/2, t)}. \quad (1)$$

Here, A_{22} denotes the angular correlation coefficient, $G_{22}(t)$ the time-differential perturbation factor as a function of the time interval, t , between the relevant cascade γ -

ray emissions, and $N(\theta, t)$ the number of the coincidence events observed at angle, θ . The oscillatory structure observed in Fig.1 reflects electrostatic interactions between the probe nucleus and the extranuclear field because the sample consists of no magnetic materials. We thus performed least squares fits to the spectrum in Fig. 1 with $G_{22}(t)$ expressed as

$$G_{22}(t) = \sigma_{2,0} + \sum_{n=1}^3 \sigma_{2,n} \cos(\omega_n t) \quad (2)$$

For all symbols in eq.(2), refer to our previous paper[2]. The electric field gradient (EFG) and asymmetry parameter value were estimated to be $V_{zz} = 5.5(9) \times 10^{21} \text{ Vm}^{-2}$ ($\eta = 0.60$). This EFG value shows a good agreement with that obtained for $^{111\text{m}}\text{Cd}$ probe in CdTiO_3 sample[3]. Since the present spectrum can be reproduced by the fit assuming a single component, $^{111\text{m}}\text{Cd}$ probes occupy the Cd site in CdTiO_3 . Relating to the η value, the large η value is probably due to the distortion of their orthorhombic structure. For more information on the microstructure of CdTiO_3 , TDPAC measurements over a wide range of temperature and sample preparation of Ca-doped CdTiO_3 are now in progress.

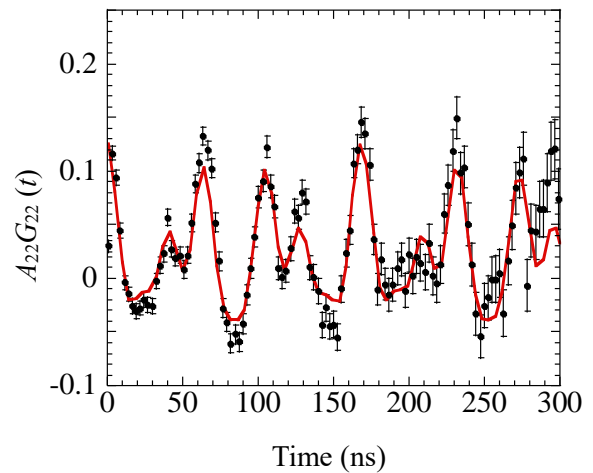


Fig. 1. TDPAC spectrum of $^{111}\text{Cd}(\leftarrow^{111\text{m}}\text{Cd})$ probe in CdTiO_3 at room temperature. The line is the result of a least-squares fit with eq.(2).

REFERENCES:

- [1] H. Taniguchi *et al.*, *Phys. Rev. B* **84** (2011) 174106 (1-5).
- [2] S. Komatsuda *et al.*, *J. Appl. Phys.* **116** (2014) 183502 (1-5).
- [3] I. J. R. Baumvol *et al.*, *J. Phys. Chem. Solids* **39** (1978) (175-178).

C. H. Pyeon, M. Yamanaka, K. Hashimoto¹, N. Aizawa², A. Ohizumi³, W. F. G van Rooijen⁴ and K. Watanabe⁵

Institute for Integrated Radiation and Nuclear Science, Kyoto University

¹*Atomic Energy Research Institute, Kindai University*

²*Graduate School of Engineering, Tohoku University*

³*Nuclear Science and Engineering Center, Japan Atomic Energy Agency*

⁴*Research Institute of Nuclear Engineering, University of Fukui*

⁵*Graduate School of Engineering, Nagoya University*

INTRODUCTION: At the Kyoto University Critical Assembly (KUCA), a series of the accelerator-driven system (ADS) experiments [1]-[5] had been carried out with the combined use of A core (solid-moderated and -reflected core) and the fixed-field alternating gradient (FFAG) accelerator. The Project research was composed of six research teams in domestic: Kindai University; Tohoku University; Japan Atomic Energy Agency (JAEA); University of Fukui, Nagoya University; Institute for Integrated Radiation and Nuclear Science, Kyoto University (former the Kyoto University Research Reactor Institute). In the Project research organized by the Institute for Integrated Radiation and Nuclear Science, Kyoto University, the ADS core was comprised of Uranium (U)-fueled and lead (Pb)-zoned core shown in Fig. 1, and 100 MeV protons generated by the FFAG accelerator was injected onto the lead-bismuth (Pb-Bi) target. For an injection of 100 MeV protons onto the Pb-Bi target, spallation neutrons were observed with a wide spectrum of high-energy neutrons, and were contributed to neutron multiplication of the U-Pb core. The objectives of the Project research were to examine experimentally neutron characteristics of the U-Pb core modeling actual ADS experimental facilities, and to investigate applicability of current measurement technologies and numerical methodologies to the ADS experiments with spallation neutrons at KUCA.

EXPERIMENTS: In the ADS experiments with spallation neutrons, main characteristic of proton beams by the FFAG accelerator were shown as follows: 100 MeV energy; 20 Hz frequency; 100 ns repetition rate; 30 to 70 pA intensity; 15 mm diameter beam spot. The research topics were revealed in each research team as follows:

- Subcriticality measurement by the Noise method (Kindai University)
- Measurement of reaction rate distribution (Tohoku University)
- Minor Actinide irradiation (JAEA)
- Measurement of neutron yield and neutron spectrum (University of Fukui)
- On-line monitoring of kinetic parameters (Nagoya University)

- Neutronics of U-Pb core in ADS (Kyoto University)

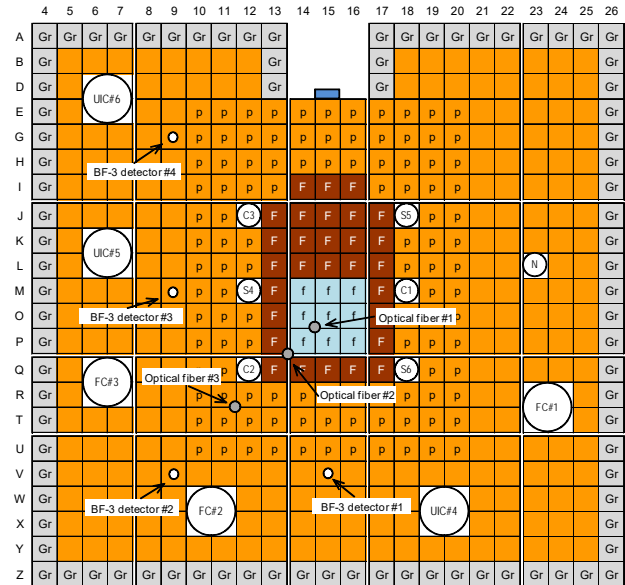


Fig. 1. Top view of U-Pb core configuration at KUCA

RESULTS: From the results of a series of ADS experiments, special attention was made to the following items: applicability of the Noise method to subcriticality measurement in ADS with spallation neutrons (Kindai); subcriticality dependency on reaction rate distributions (Tohoku); feasibility study on MA irradiation by spallation neutrons (JAEA); observation of high-energy neutron spectrum by spallation neutrons (Fukui); feasibility study on on-line monitoring of kinetic parameters by spallation neutrons (Nagoya); benchmarks on kinetic parameters in U-Pb core of ADS with spallation neutrons (Kyoto).

CONCLUSION: The Project research of ADS with spallation neutrons was successfully conducted with the combined use of U-Pb core and FFAG accelerator at KUCA. A series of static and kinetic ADS experiments revealed importantly applicability of current measurement methodologies to upcoming actual ADS facilities in the future.

REFERENCES:

- [1] C. H. Pyeon, *et al.*, J. Nucl. Sci. Technol., **46**, (2009) 1091-1093.
- [2] C. H. Pyeon, *et al.*, Nucl. Eng. Technol., **45**, (2013) 81-88.
- [3] C. H. Pyeon, *et al.*, Nucl. Technol., **192**, (2013) 181-190.
- [4] C. H. Pyeon, *et al.*, Ann. Nucl. Energy, **105**, (2017) 346-354.
- [5] C. H. Pyeon, *et al.*, J. Nucl. Sci. Technol., **55**, (2018) 190-198.

PR9-1 Subcriticality Monitoring for a Reactor System Driven by Spallation Source

K. Hashimoto, W. Sugiyama, S. Hohara, A. Sakon,
K. Nakajima¹, C. H. Pyeon² and T. Sano²

Atomic Energy Research Institute, Kindai University
¹Graduate School of Science and Engineering, Kindai
University

²Research Reactor Institute, Kyoto University

INTRODUCTION: Feynman- α Method has been frequently employed to determine subcritical reactivity of nuclear reactor systems driven by Poisson source such as Am-Be neutron source. Recent theoretical studies indicated that a drive by Non-Poisson source such as spallation source enhanced the correlation amplitude Y_∞ . The objectives of this study are to confirm experimentally the enhancement and to derive some characteristics of the spallation in a lead target from the enhancement.

EXPERIMENTS: A subcritical system was constructed on the A loading of the Kyoto University Critical Assembly. The system had a lead target, to which 100MeV proton beam was drawn to cause spallation reactions. The repetition period of the proton pulse beam was 50msec. Time-sequence counts data from five BF₃ proportional counters were acquired at several control rod patterns. For comparison, we also acquired time-sequence data under drives by Am-Be neutron source.

RESULTS: Figure 1 shows a gate-time dependence of Y obtained under a drive by Am-Be neutron source. The Y is a statistical indication of neutron-correlation amplitude and is defined as variance-to-mean ratio minus one of neutron counts registered within the gate. The correlation amplitude Y is small but the gate-time dependence can be observed just as expected.

Figure 2 shows a gate-time dependence of Y obtained under a drive by spallation source. Contrary to our expectation, the Y is unusually high and has an increasing tendency with longer gate time. This is because the proton beam intensity was much unstable throughout our experiments and consequently reactor power was largely fluctuated. In order to overcome this difficulty, the following formula was applied to the Feynman- α analysis under an unstable drive by spallation source.

$$Y(T) = Y_\infty \left[1 - \left(1 - e^{-\alpha T} \right) / \alpha T \right] + cT. \quad (1)$$

The last term of the above equation was additionally introduced to consider a power drift with time scales of delayed neutrons [1]. The least-squares fit of the above equation was done to only the Y data at gate times of the integral multiple of pulse repetition period (50msec) [2]. Figure 3 shows a ratio of correlation amplitudes between spallation and Am-Be neutron source. We can observe a tendency of correlation amplitude enhanced by spallation source, however, the statistical error of the ratio is unac-

ceptably large. The further advancement of data analysis is in progress.

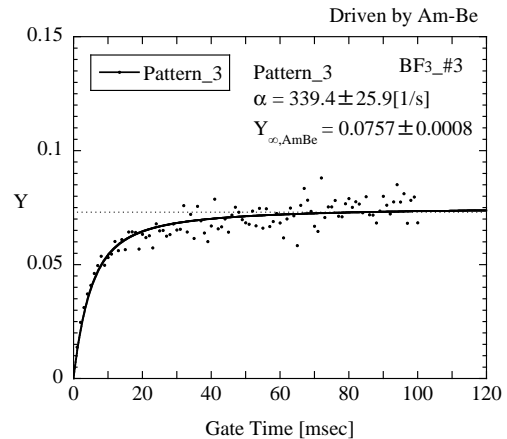


Fig.1. Y obtained in a subcritical system driven by Am-Be neutron source.

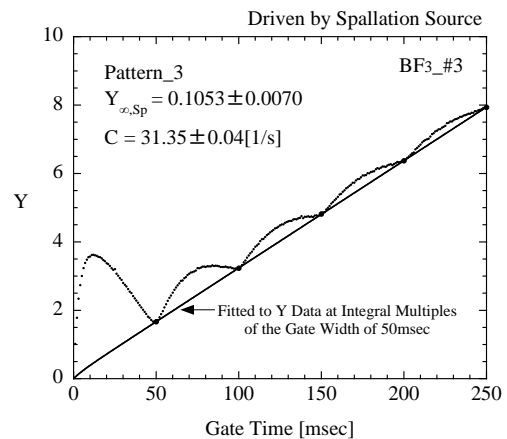


Fig.2. Y obtained in a subcritical system driven by unstable spallation neutron source.

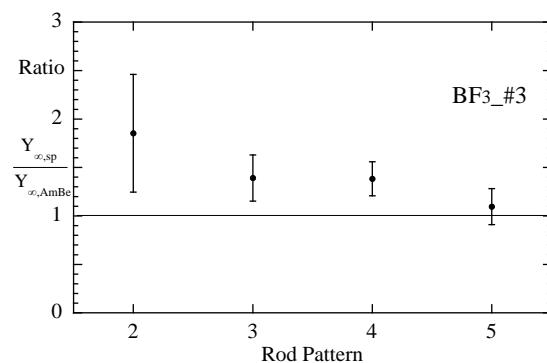


Fig.3. Ratio of correlation amplitudes between spallation and Am-Be neutron source.

REFERENCES:

- [1] K. Hashimoto *et al.*, J. Nucl. Sci. Technol., **36** (1999) 555-559.
- [2] H. Taninaka *et al.*, J. Nucl. Sci. Technol., **48** (2011) 1272-1280.

Basic Study of Beam Transient on Accelerator-Driven System with Spallation Neutron Source

N. Aizawa, D. Maeda, H. Saito, R. Takasugi, M. Yamana¹ and C. H. Pyeon¹

Graduate School of Engineering, Tohoku University
¹ Institute for Integrated Radiation and Nuclear Science, Kyoto University

INTRODUCTION: An accelerator-driven system (ADS) is operated with the use of spallation neutrons generated by an accelerator beam. The core behavior is dependent on the beam condition, and some studies reported that the beam transient (transient by beam variation) has a possibility to cause core damage [1]. The experimental study of the beam transient on ADS has been planned to examine the change of core characteristics such as reaction rate distributions and neutron multiplication. FY 2017 was the first year of the ADS experiment with spallation neutron source, and the experiment was performed under the standard beam condition to understand the basic core characteristics.

EXPERIMENTS: The ADS experiment was carried out in the KUCA A core with spallation neutron source generated by the reaction of 100 MeV proton beam and Pb-Bi target. Fig. 1 shows the core configuration. The core is composed of PE (Polyethylene) moderated normal fuel assemblies “F” (1/8”p60EUEU), Pb-zoned fuel assemblies “f” which the PE plate was replaced with Pb plate in the central 40 fuel cells and PE moderators “p.” All control and safety rods were withdrawn in the experiment, and four core patterns were configured by changing the number of normal fuel assembly in the row I and J. The subcriticality was ranged between 2487 and 5400 pcm. The 1 mm-diameter In wire was set along (B-P, 13-14) at the axial position of 700 mm from the bottom of core and the In foil was also attached near target to measure the reaction rate distribution by neutron activation analysis of ¹¹⁵In(n, γ)^{116m}In and ¹¹⁵In(n, n’)^{115m}In.

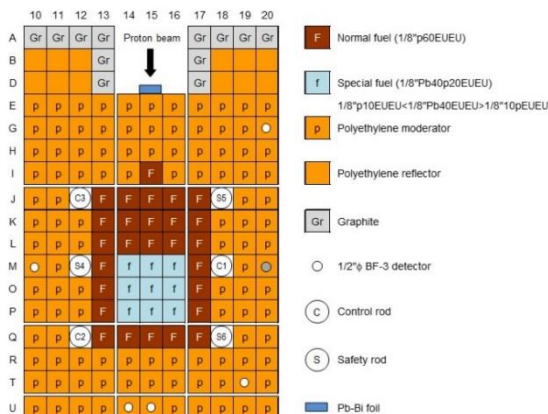


Fig. 1. Top view of the ²³⁵U-fueled and Pb-zoned core

The measurement results were evaluated with the combined use of the PHITS, MVP and JENDL-4.0 library, 29P9-2

and the subcritical multiplication factor k_s were calculated on the basis of a reaction rate distribution as follows:

$$k_s = \frac{F}{F + S} \tag{1}$$

where F is the total number of fission neutrons and S is that of source neutrons. The calculation method of F and S was referred to Refs. [2]-[4].

RESULTS: Fig. 2 shows the ¹¹⁵In(n, γ)^{116m}In reaction rate distribution at the subcriticality of 2487 pcm as one example of the evaluation by the numerical calculations. Small differences were seen around the PE region but the calculated distribution was agreed well with the experimental one. The similar evaluation results were obtained in the other three core patterns, and a series of calculations were confirmed to reproduce the experiment results. The subcritical multiplication factor k_s was also calculated as presented in Table 1. The experiment results were larger than calculation ones in all cases but the differences were small as seen from the C/E values.

The basic core characteristics were successfully obtained on the standard beam condition in FY 2017, and on the basis of the obtained data, the experiment with different conditions such as beam and core configuration is planned.

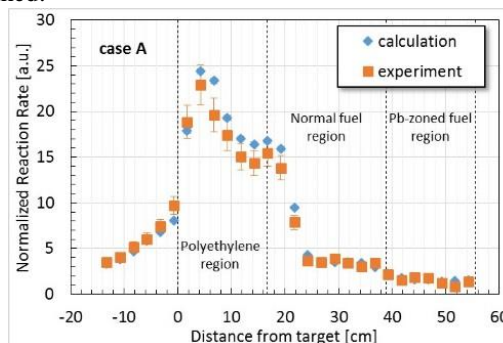


Fig. 2. Comparison of ¹¹⁵In(n, γ)^{116m}In reaction rate distribution between measurement and calculation results at the subcriticality of 2487 pcm.

Table 1 Comparison of k_s between calculation and measurement values with different subcriticalities

subcriticality [pcm]	calculation	experiment	C/E
2487	0.660 ± 0.004	0.683 ± 0.050	0.97 ± 0.07
4016	0.486 ± 0.003	0.527 ± 0.036	0.92 ± 0.06
4924	0.422 ± 0.002	0.438 ± 0.029	0.96 ± 0.06
5400	0.385 ± 0.002	0.386 ± 0.025	1.00 ± 0.06

REFERENCES:

[1] N. Aizawa *et al.*, J. Nucl. Sci. Technol., **49** (2012) 888 .
 [2] C. H. Pyeon *et al.*, Nucl. Technol., **192** (2015) 181.
 [3] H. Shahbunder *et al.*, Ann. Nucl. Energy, **37** (2010) 1214.
 [4] H. Shahbunder *et al.*, Ann. Nucl. Energy, **37** (2010) 592.

PR9-3 Measurement of MA Reaction Rates Using Spallation Neutron Source

A. Oizumi¹, M. Fukushima¹, K. Tsujimoto¹,
M. Yamanaka², T. Sano², and C. H. Pyeon²

¹Nuclear Science and Engineering Center, Japan Atomic Energy Agency

²Institute for Integrated Radiation and Nuclear Science, Kyoto University

INTRODUCTION: To transmute minor actinides (MAs) partitioned from the high level waste, the Japan Atomic Energy Agency (JAEA) has investigated neutronics of an accelerator-driven system (ADS): a lead-bismuth (Pb-Bi) eutectic cooled subcritical reactor with 800 MW thermal power. In the nuclear transmutation system such as ADS, the nuclear data validation of MA is required to reduce the uncertainty caused by the nuclear data of MA. To validate the nuclear data, many independent experimental data need to be mutually compared. An expansion of integral experimental data is the important issue since there is limited number of experimental data of MA. The Kyoto University Critical Assembly (KUCA) has a potential capability to perform the simulated experiment of ADS using a hybrid system of spallation neutron source and a subcritical core. This study aims to measure the reaction rates of neptunium-237 (²³⁷Np) and americium-241 (²⁴¹Am) using the spallation neutron source in KUCA.

EXPERIMENTS: The MA irradiation experiments were conducted at A-core in KUCA with the fixed-field alternating gradient (FFAG) proton accelerator. Fission reaction rates were measured by using a back-to-back (BTB) fission chamber (diameter: 40mm, height: 42mm). The BTB fission chamber having two foils (mass: 10μg/nuclide) such as uranium-235 (²³⁵U) and MA (²³⁷Np or ²⁴¹Am), was installed just behind the Pb-Bi target as shown in Figure 1.

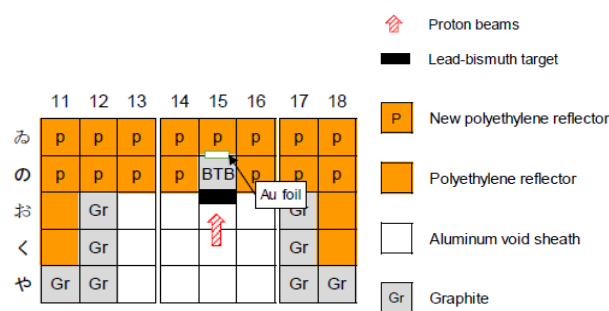


Figure 1. Loaded position of the BTB fission chamber and the Au foil in the A-core of the KUCA.

The pulsed-height distribution from the BTB fission chamber was acquired under the proton beam condition, such as 100 MeV energy, 20 Hz period, 100 ns beam width, and 47 pA current for 3 hours. Moreover, two gold

(Au) foils (diameter: 3mm, thickness: 0.05mm) were attached at the rear of the BTB fission chamber as a reference of capture reaction rates of MA.

RESULTS: The distributions of pulsed height of ²³⁷Np and ²⁴¹Am fission reactions were observed as shown in Figure 2. These distributions were significantly different from the ones generally observed in critical and pulsed neutron source (PNS) experiments. Therefore, they would contain not only signals of fission reactions but also noise due to detection of the ionizing signal of gas in the BTB fission chamber generated by the γ ray coming from the collision between 100MeV proton beams and the Pb-Bi target. On the other hand, the γ ray from ²³⁷Np foil was measured for the capture reactions. After the irradiation, 213 counts were detected for 68 hours using the high-purity germanium detector. The capture reaction rate of ²³⁷Np converted from the γ ray count was $(1.21 \pm 0.97) \times 10^7$ #/cm³/s. Moreover, the capture reaction rate of ¹⁹⁷Au was $(1.34 \pm 0.11) \times 10^8$ #/cm³/s. Here, the result of this experiment was compared with that of the critical experiment which was available to be measured the fission reaction rates of ²³⁷Np and ²⁴¹Am using the same BTB fission chamber. The capture reaction rates of ²³⁷Np and ¹⁹⁷Au were $(1.01 \pm 0.13) \times 10^8$ #/cm³/s and $(9.86 \pm 0.88) \times 10^7$ #/cm³/s in the critical experiment, respectively. Consequently, reducing the influence of the γ generated by the nuclear spallation reaction and extending the duration of the irradiation to 24 or more hours would be necessary for detecting signals of fission reactions under the spallation neutron source.

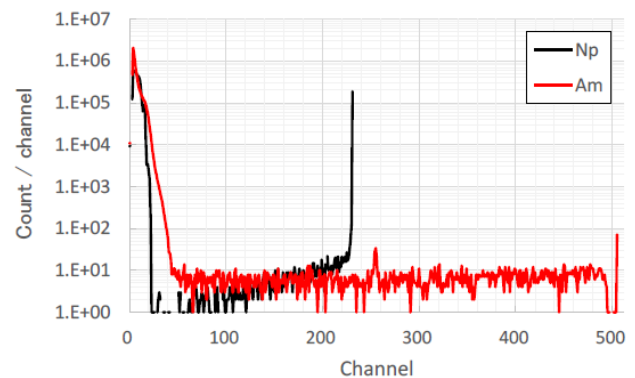


Figure 2. Signals from BTB fission chamber in the irradiation experiment using the nuclear spallation neutron source.

ACKNOWLEDGEMENT: A part of this study is the result of “Research and development to solve the engineering issues for transmutation system using accelerator-driven system” carried out under the Innovative Nuclear Research and Development Program by the Ministry of Education, Culture, Sports, Science and Technology of Japan.

PR9-4 Irradiation Experiments of ^{237}Np and ^{241}Am Capture and Fission Reactions in Critical Core

W. F. G. van Rooijen, M. Yamanaka¹ and C. H. Pyeon¹

Research Institute of Nuclear Engineering, University of Fukui

¹ Institute for Integrated Radiation and Nuclear Science, Kyoto University

INTRODUCTION: The underlying issue of the nuclear power generation is remained in the treatment of the high-level radioactive waste (HLW) contained in spent fuel. For treatment of HLW, the simple strategy had been proposed to manage spent fuels underground named as “once-through fuel cycle.” Once-through cycle has an advantage over the easiness of the treatment from unnecessary of chemical processing, however, poses the difficulty to maintain the structural soundness of management facility for over one million year to decay out the HLW, burdening the geological site. As an advanced proposal, the burden reduction to the geological site has attempted by loading minor actinides (^{237}Np and ^{241}Am), which are main cause of radiotoxicity in HLW, to nuclear power reactor (hard neutron spectrum) for transmutation after the chemical extraction from spent fuels.

In the reactor design analysis for the transmutation system such as the accelerator-driven system (ADS), the uncertainty induced by the nuclear data of ^{237}Np and ^{241}Am capture and fission reactions are estimated very large and as the dominant nuclide to the safety parameter [1]. To reduce the uncertainty by ^{237}Np and ^{241}Am fission (which is difficult reaction to measure the cross section in general) and capture reactions, an irradiation experiment is requisite as accumulation of integral experiments by loading their foils to the fast reactor with previous study [2-3] for acquiring important reaction rates.

In this study, special attention was paid for the fabrication of ^{237}Np and ^{241}Am foils from their solute and testing the validity by irradiation experiment with hard spectrum core at the Kyoto University Critical Assembly (KUCA).

EXPERIMENTAL SETTINGS: For the irradiation experiment, critical core was prepared and composed of lead-loaded fuel rod “f,” and polyethylene-moderated fuel rod “F” as shown in Fig.1. H/U value at irradiation spot was about 50, which is comparative hard spectrum in the KUCA-A core. Fabricated ^{237}Np and ^{241}Am foils were inserted into the back-to back (BTB) type double fission chamber separately. The advantage of BTB fission chamber is to enable the measurement of fission reaction by the objective foil (^{237}Np and ^{241}Am) and reference foil (^{235}U) in almost same position at the same time. Thus, measured result could be fission reaction rate ratio of the objective foil to the reference one. The foils were irradiated for about 1 hour under a thermal power of 3.5 W. After irradiation, ^{237}Np foil was extracted from the BTB fission chamber, and γ -ray was measured for ^{237}Np capture reaction rates.

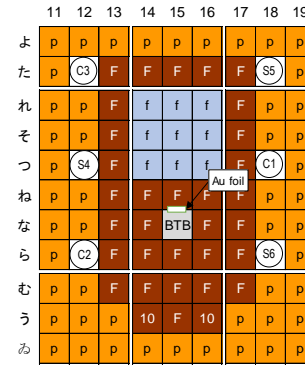


Fig. 1. Critical core for MA irradiation experiments.

RESULTS: The pulsed height of ^{235}U and ^{237}Np during the irradiation indicated double peak as shown in Fig. 2, implying that two fission fragment could be detected having different energy. Thus, the MA foils were considered successfully fabricated from their solvent. In case of ^{241}Am , the pulse height did not show distributed in 1 hour irradiation because the small number of ^{241}Am is permitted to insert into the KUCA-A core. However, both fission reaction rate ratios were obtained in both foils, and, ^{237}Np capture reaction rates were measured by γ -ray detection after the irradiation, as shown in Table 1.

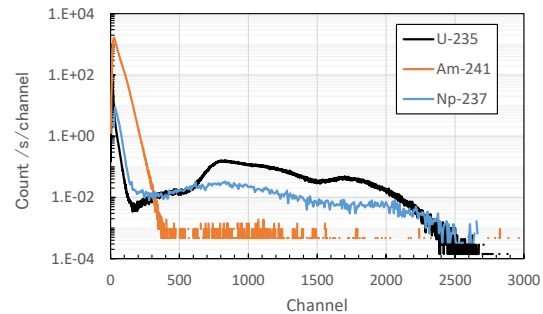


Fig. 2. Pulsed height from BTB fission chamber.

Table 1. Fission reaction rate ratio by $^{237}\text{Np}/^{235}\text{U}$ and $^{241}\text{Am}/^{235}\text{U}$ and ^{237}Np capture reaction rate.

Nuclide	Fission reaction rate ratio to ^{235}U	Capture reaction rate [1/cm ³ /s]
^{237}Np	0.01381	$(4.26 \pm 0.11) \times 10^8$
^{241}Am	0.03149	-

REFERENCES:

- [1] G. Chiba *et al.*, J. Nucl. Sci. Technol., **53** (2016) 1653-1661.
- [2] H. Unesaki *et al.*, J. Nucl. Sci. Technol., **38** (2001) 600-606.
- [3] T. Iwasaki *et al.*, J. Nucl. Sci. Technol., **39** (2002) 920-923.

K. Watanabe, T. Endo, A. Uritani, A. Yamazaki, M. Yamana¹ and C. H. Pyeon¹

Graduate School of Engineering, Nagoya University
²Research Reactor Institute, Kyoto University

INTRODUCTION: The accelerator-driven subcritical (ADS) system has been developed for producing energy and for transmuting minor actinides and long-lived fission products [1-2]. The ADS system should be designed to be subcritical condition in any case and desirably monitored in real time. Real-time monitoring of subcriticality is important task for ensuring safety in ADS reactor operation. Iwamoto et al. already demonstrated real-time subcriticality monitoring for ADS system, in which they used only a pulsed neutron source (PNS) method [3]. However, to assure validity of the measured subcriticality, the subcriticality is desired to be determined by more than two methods. In this study, we attempt to measure the subcriticality in real time with the PNS method and a method based on reactor noise analysis simultaneously. As the subcriticality measurement algorithm based on reactor noise analysis, we applied the Rossi- α method.

EXPERIMENTS: Measurements of subcriticality were conducted in A-core of Kyoto University Critical Assembly (KUCA). As a pulsed neutron source, a Pb-Bi target bombarded with 100 MeV protons. The repetition rate of the pulsed proton beam was 20Hz. We applied a Transparent Rubber SheeT type Eu: LiCaAlF₆ (TRUST Eu:LiCAF) scintillator as a neutron detector. The size of the TRUST Eu:LiCAF was 5x5x180 mm³. The scintillation photons were detected with a photomul-

tiplier tube (PMT) through a wavelength-shifting fiber (WLSF). The PMT signal was fed into a digital signal processor. In this processor, signal waveform was digitized and processed with a Field-Programmable Gate Array (FPGA). The information of pulse height, rise time and detection timing were extracted and transferred to an analysis computer. The analysis computer processed these data and calculated the subcriticality. The detector was placed at the polyethylene moderator region. The subcriticality was changed by inserting control and safety rods.

RESULTS: Figure 1 shows the time profile of neutron counts triggered by incident neutron pulses. In this time profile, the area ratio of prompt and delayed neutrons indicates the subcriticality. The subcriticality can also be estimated from the decay time of prompt neutrons. Figure 2 shows the signal pulse interval spectrum. Prompt neutrons produce an exponential decay component. This decay constant is also proportional to the subcriticality. Figure 3 shows the time trends of the measured neutron counts and measured subcriticality. Our system was confirmed to be able to determine the subcriticality with, at least, ten seconds time resolution.

REFERENCES:

- [1] Pyeon CH, Lim JY, Takemoto Y et al, *Ann. Nucl. Energy*, **38** (2011) 2298–2302
- [2] Pyeon CH, Yagi T, Sukawa K et al., *Nucl. Sci. Eng.*, **177** (2014) 156-168
- [3] Iwamoto H, Nishihara K, Yagi T, Pyeon CH, *J. Nucl. Sci. Technol.*, **54** (2017) 432-443

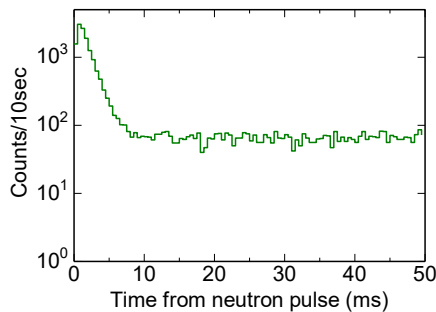


Fig. 1 Time profile of neutron counts triggered by incident neutron pulses.

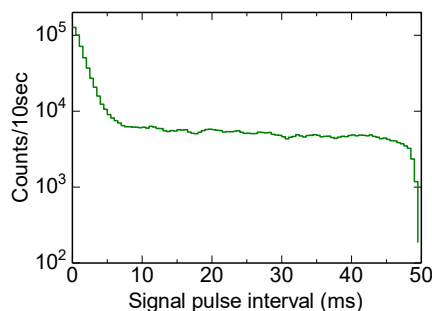


Fig. 2 Signal pulse interval spectrum of each detected signals.

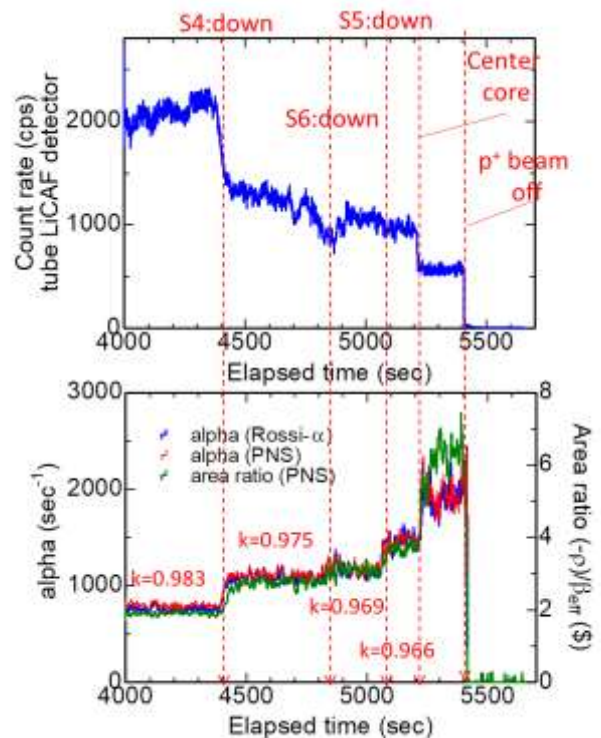


Fig. 3. Time trend of the measured neutron counts (top) and the measured subcriticality (bottom).

C. H. Pyeon and M. Yamanaka

Institute for Integrated Radiation and Nuclear Science,
Kyoto University

INTRODUCTION: The accelerator-driven system (ADS) has been proposed to reduce the amount of the minor actinides, generated from the daily operation of the commercial power plants, by the transmutation in the hard spectrum core at the subcritical states with the spallation neutrons by 1.5 GeV proton injection onto lead-bismuth (Pb-Bi) target [1]. To operate the ADS cores, the reactor design needs to make the analyses by the combination of the subcritical reactor and the external neutron source. Further, for the ADS as a new concept reactor, the subcriticality monitoring is also requisite to ensure the design accuracy and the safety of actual operation because the operation result is not existed.

In the subcriticality monitoring, measured subcriticality is converted from dollar units into pcm ones with the use of the kinetics parameter. However, the kinetics parameters are widely used by the estimation in eigenvalue calculations without the external neutron source, being questionable to apply the parameters to subcriticality measurements.

At the Kyoto University Critical Assembly (KUCA), to examine the validity of kinetics parameters obtained by the eigenvalue calculations for the subcriticality measurements, the ADS experiments were carried out with the use of two-zoned core, having very hard spectrum by Pb-loaded fuel inside, and spallation neutrons by 100 MeV proton injection onto the Pb-Bi target. In this study, the objective is placed on the examination of the validity of kinetics parameters through subcriticality measurements by the prompt decay neutron constant α in the ADS experiments in a wide range of subcriticality.

EXPERIMENTAL SETTINGS: The two-zoned core was constituted at KUCA-A core with the use of two different fuel rods (f: Pb-loaded fuel, F: polyethylene-moderated fuel in Fig.1), to attain hard spectrum modeling actual ADS core, and polyethylene reflector termed “p,” as shown in Fig.1. For the subcritical measurements, four BF₃ and one LiCaF fiber detectors were placed around the core, and also three LiF fiber detectors between the gaps inside the core. 100 MeV protons were prepared by the fixed-field alternating gradient accelerator under the condition of pulsed frequency of 20 Hz, beam current of about 50 pA, and pulsed width of about 100 ns, and was injected onto the Pb-Bi target to supply pulsed spallation neutrons to the subcritical core. The α value was obtained by the fitting of pulsed neutron source (PNS) histogram in the PNS method. The subcriticality was varied by the fuel replacement for polyethylene reflector in 7 cases, ranging between subcriticality 500 and 7400 pcm.

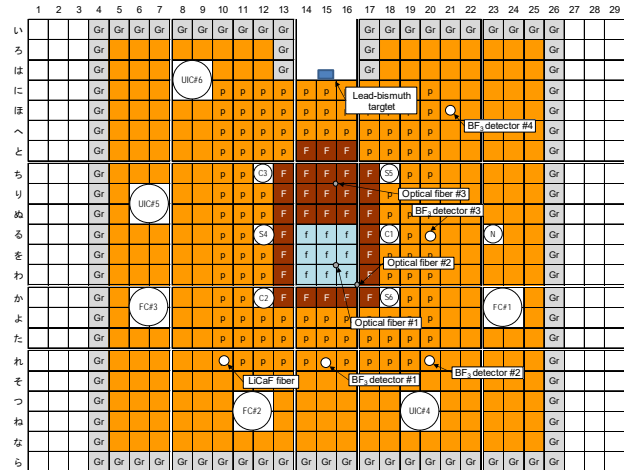


Fig. 1. Critical two-zoned core in KUCA (Case I).

RESULTS: The α values were quantified with the use of subcriticality, effective delayed neutron fraction and generation time by the eigenvalue calculations with MCNP6.1 for each subcriticality case. The results of measured α values by the detector placed on the different position around and inside the core indicated spatial effect especially in deep subcriticality at Cases V through VII. Further, in the comparison between the calculated and measured α values, the calculated α agreed with measured one in Cases I and II. However, calculated α value by the eigenvalue calculations showed a discrepancy with measured one, as the subcriticality became deeper in Cases III through VII, suggesting that the kinetics parameters were also differed by existing the external neutron source at a deep subcriticality, and kinetics parameters should be estimated in the fixed-source calculations.

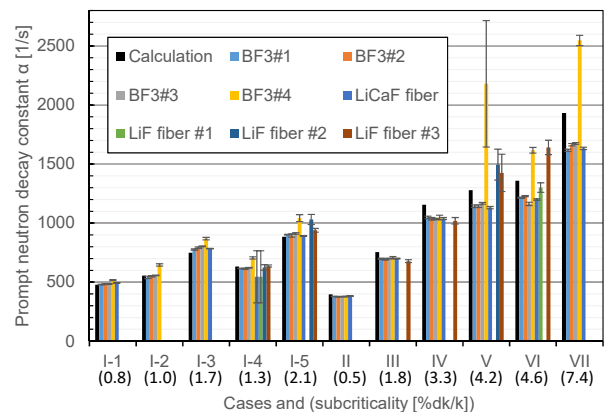


Fig. 2. Results of subcriticality with the use of prompt neutron decay constant α .

REFERENCE:

[1] H. Iwamoto *et al.*, J. Nucl. Sci. Technol., **53** (2016) 1585-1594.

M. Suzuki

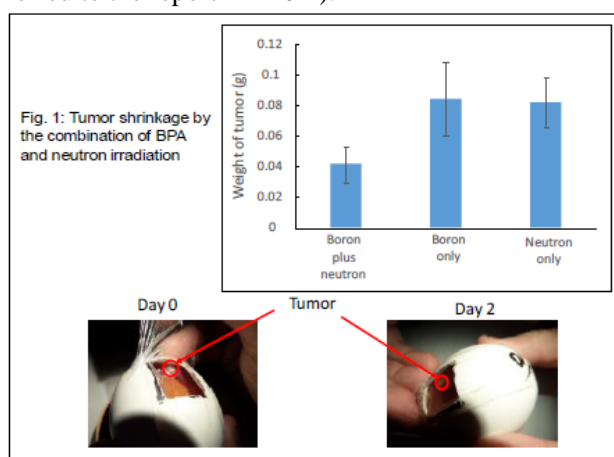
Research Reactor Institute, Kyoto University

Summary

In this research project, fifteen research project were included. Gadolinium-containing compounds were studied in two studies (P10-7 and P10-12). In other thirteen studies, boron-containing compounds were studied. New boron drugs studied in this project consist of eight small boron molecular agents and five nanoparticles.

In the fifteen projects, new compounds in ten projects were tested on efficacy of tumor control or cell killing using neutron irradiations.

In five research project (P10-8, P10-10, P10-13, P10-15 and P10-16), in-vivo study using tumor-implanted mice or rats were carried out. In one project (P10-4), tumor-implanted egg was interestingly used as shown in the below figure (the detail is referred to the report in P10-4).



In one research projects (P10-14), in-vitro study with neutron irradiation was carried out. In two projects (P10-5, P10-9), a pharmacokinetic studies of new boron compounds were done.

In vivo study

The results in five in-vivo studies using tumor-bearing mice or rat studies are summarized as bellow.

P10-8: Two studies using two new boron compounds were done. Study 1: A significant prolongation of median survival time (MST) in survival time in borophenylalanine (BPA) and novel pteroyl clo-

so-dodecaborate conjugate (PBC)-BNCT group was obtained compared with the other single agent (BPA or PBC)-BNCT group.

Study 2: Sensitization of the 5-aminolevulinic acid (ALA) in BPA-BNCT was examined. The mice in the BPA-BNCT with ALA group obtained a significant prolongation in survival time compared with BPA-BNCT group.

P10-10: New boron compounds, BN1229 and BN1242 were tested in this research. A significant tumor growth inhibitory effect was observed in BN1242 group compared with the untreated control.

P10-13: Complex of BPA and poly vinyl alcohol (PVA) which has many BPA molecules was tested. PVA-BPA-BNCT exhibited drastic antitumor activity and tumor regrowth was not observed even at day 18.

P10-15: Novel liposome modified with novel lipid (name PBL) as boron delivery system (BDS) was tested. The PBL-liposome and borocaptate sodium (BSH)-encapsulated PBL-liposome significantly inhibited the tumor growth as compared to other control groups.

P10-16: Novel boron compound, BNC2018 was tested. The tumor growth suppression effects derived the highly tumor retnivity of BN2018 by BNCT.

In vitro study

The results in one in-vitro studies using neutron irradiation are summarized as bellow.

P10-14: A novel boron compound, PBC, was tested. PBC demonstrated their cytotoxicity with neutron irradiation.

Other new boron or gadolinium compounds which were not tested with neutron irradiation will be expected to be examined in 2018-2019.

L. Kuzmanic, M. Takagaki¹, K. Uno¹, M. Suzuki²
and NS. Hosmane

¹Dept Chem & Biochem, Northern Illinois Univ

²Louis Pasteur Center for Medical Research

³Institute for Integrated Radiation and Nuclear
Science, Kyoto Univ

Despite extensive efforts, it is difficult to ensure that the selective targeting of ¹⁰B will be successful. One can argue whether Locher's BNCT theory feasible? Scientists have made extensive effort to answer this question and to discuss the potential future problems of BNCT. From the viewpoint of boron chemistry, the conditions required for boron/gadolinium targeting are: (1) a low toxicity, (2) the ability to be held in a tumor and/or tumor cells selectively for a certain period of time, (3) to be rapidly excreted from the body system. These points are essential, but to achieve each of these at the same time is a very difficult task.

We have investigated the theranostic (therapeutic+diagnostic) agent exhibiting cellular quantitative distribution in *in-vitro* using a fluorescent density microscope without any neutron irradiation. Also, fluorescent chemical substances have the potential to be utilized for intraoperative probing of the tumor by using fluorescent surgical microscopy. Two carboranes conjugating-ligands have been synthesized and the properties of fluorescent sensors for boron derivatives are reported. This appears to be a useful method for the screening of boron compounds without neutrons.

Fluorescein was conjugated with 1-methyl-*o*-carborane (**Figure 1**) via a Williamson ether synthesis and biologically evaluated through studies in pancreatic cancer (MIA PaCa-2) and squamous cell carcinoma (SCC-VII) cell lines. Cellular uptake was confirmed through phase contrast, fluorescent, and confocal microscopy, as well as flow cytometric data. Uniform distribution of the carboranyl-fluorescein derivative was observed in both SCC-VII (**Figure 2**) and MIA PaCa-2 (**Figure 3**). The cytotoxicity of fluorescein-tagged 1-methyl-*o*-carborane in SCC-VII was determined using a WST-8 assay. An IC₅₀ of 1 mM or 21 ppm ¹⁰B was observed, reflecting moderate toxicity relative to that of BSH

(28 mM) and BPA (7.9 mM). This moderate cytotoxicity and uniform distribution of the carboranyl-fluorescein derivative following cellular uptake in both SCC-VII and MIA PaCa-2, as well as its higher boron content relative to boronated agents currently employed in clinical trials, provide justification for further evaluation as a potential delivery agent for BNCT. Biodistribution studies and survival assays are scheduled at IIRNS of Kyoto University on this FY2018.

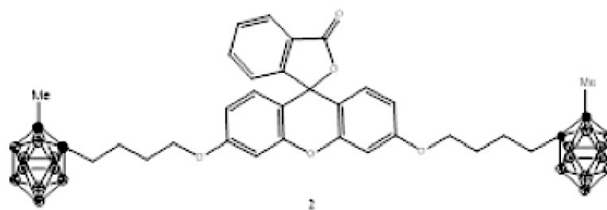


Figure 1: The molecular structure of fluorescein-tagged 1-methyl-*o*-carborane.

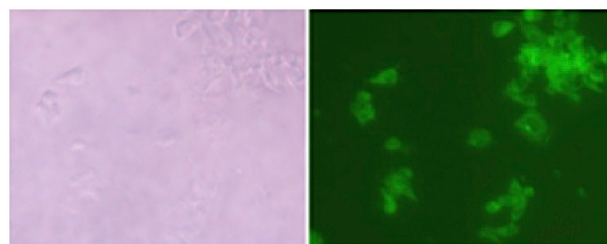


Figure 2. The microdistribution of carboranyl-fluorescein conjugate 1 in SCC-VII cells. (A) Light microscopic image of SCC-VII cells treated with compound 1. (B) Fluorescent microscopic image of SCC-VII treated with compound 1.

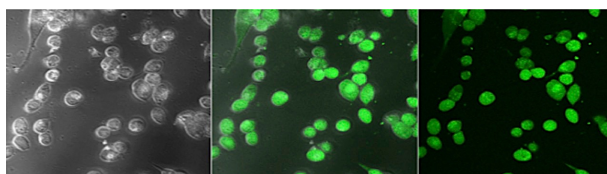


Figure 3. Fluorescent microscopic images of MIA PaCa-2 cells containing a 40 µg/mL sample of carboranyl-fluorescein conjugate 1 in DMSO: (A) black and white filter, (B) merged black/white and green filter, and (C) green filter.

PR10-2 New Self-assembling Peptide Drug Delivery System with BSH against Human Glioblastoma Cell in BNCT

H. Michiue, A. Fukunaga¹, N. Kondo², Y. Sakurai² and H. Matsui¹

Neutron Therapy Research Center, Okayama University

¹Department of Physiology, Okayama University Graduate School of Medicine, Dentistry and Pharmaceutical Sciences

²Research Reactor Institute, Kyoto University

INTRODUCTION: Glioblastoma multiforme (GBM) is the most common malignant central nervous system primary tumor, and not curable. BNCT (boron neutron capture therapy) is the effective treatment against GBM in present multimodal therapy. In BNCT in GBM, one of the keys to success can depend on the boron compounds. The adequate boron delivery into all of every tumor cells is essential for BNCT to GBM. The combination of BSH and BPA in clinical GBM BNCT showed very good results and that meant the multi boron use in BNCT was one answer to next step of BNCT. In this time, we showed results of the new self-assembling peptide DDS with BSH toward clinical application.

EXPERIMENTS: We established the simple A6K/BSH complex making method, as just mixture the BSH and A6K water solution by itself. The BSH/A6K complex with different mixture ratio showed different shape and different diameter of complex in SEM image. We decided the particular mixture ratio of A6K/BSH, 1:10 mol ratio, complex as the most fitted for drug delivery system to brain tumor. The ideal range of particle size of DDS is 20nm to 200 nm, and ours' complex diameter was about 40nm. Next, we administrated BSH/A6K complex to human glioma cell lines and measured intracellular boron uptake. The intracellular boron concentration with BSH/A6K complex in U87 delta EGFR was 10 times higher than that with BSH. We reconfirmed the particular mixture ratio of BSH/A6K, 1:10 complex as the most fitted for drug delivery system to brain tumor. Finally, we administrated BSH or A6K/BSH complex to glioma cells and irradiated neutron *in vitro*.

RESULTS: As shown in Fig. 1, WST-1 assays showed that the group of A6K/BSH complex and, 15min or 30min inhibited U87 DELTA EGFR proliferation. On the

other hand, only BSH administration group with 15min and 30min.

CONCLUSION: The new boron DDS with A6K/BSH complex is prospective drug for next generation of BNCT.

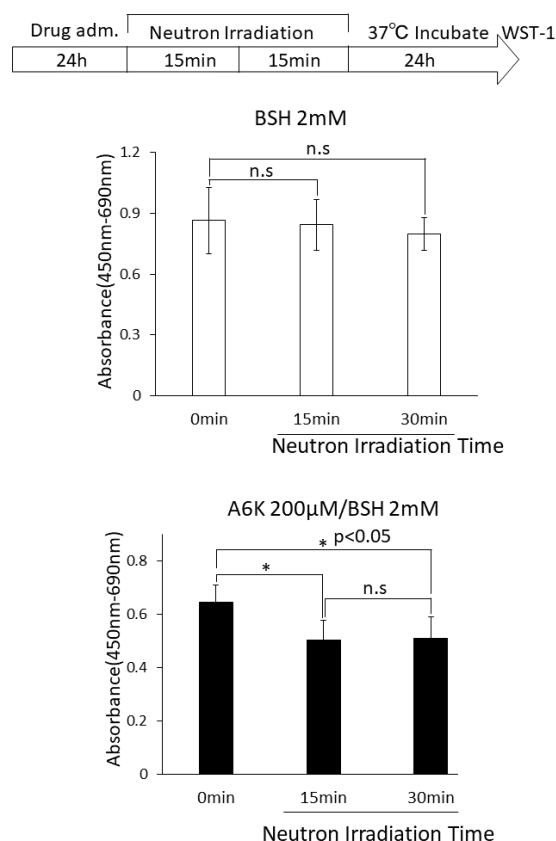


Fig.1 WST-1 assay results after administration of BSH or A6K/BSH complex and irradiation of neutron 0, 15min or 30min.

Functionalization of Hexagonal Boron Nitride Nanosheet with Polyglycerol and its Biomedical Application

M. Kyouhei and K. Naoki

Graduate School of Human and Environmental Studies, Kyoto University

We have reported that polyglycerol (PG) functionalization gives better hydrophilicity than polyethylene glycol (PEG) and is applicable to a wide variety of nanoparticles such as nanodiamond [1] and iron oxide nanoparticle [2]. In addition, a number of hydroxy groups in PG can be used for further derivatization to add more functions to the nanomaterials as a drug carrier and an imaging probe [3]. In this paper, hexagonal boron nitride (h-BN) is functionalized with PG followed by indocyanine green (ICG) derivative to give the imaging probe with near infrared (NIR) fluorescence and good aqueous dispersibility.

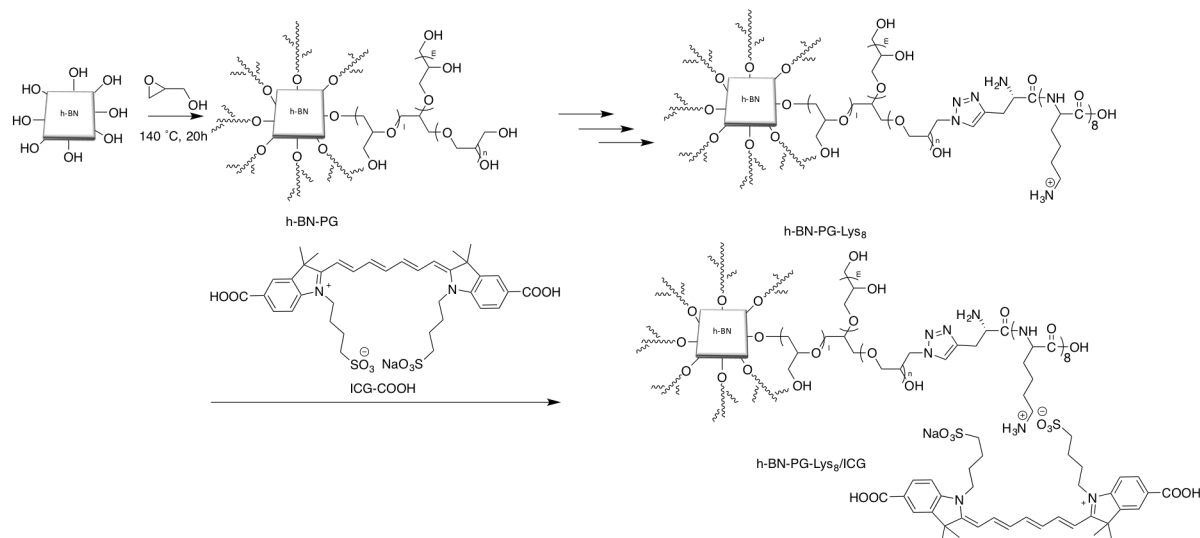
h-BN was functionalized with PG through ring opening polymerization of glycidol as shown in Scheme 1. We confirmed PG functionalization with FT-IR, and solution phase ^1H and ^{13}C NMR. The resulting h-BN-PG exhibited good aqueous dispersibility (2 mg/mL) due to the relatively high PG weight ratio of 25%. Further derivatization of h-BN-PG was carried out to immobilize the ICG derivative as

shown in Scheme 1. The hydroxy groups were converted to azido ($-\text{N}_3$) through tosylate ($-\text{OTs}$), and the resulting h-BN-PG- N_3 was conjugated with octalysine (Lys_8) by click chemistry. Indocyanine green (ICG) derivative was immobilized through electrostatic interaction between Lys_8 and ICG derivative [4]. The obtained h-BN-PG- Lys_8/ICG will be applied to in vitro and in vivo cancer imaging.

REFERENCES:

- [1] L. Zhao, T. Takimoto, M. Ito, N. Kitagawa, T. Kimura, and N. Komatsu,* *Angew. Chem. Int. Ed.*, **50** (6) (2011) 1388-1392.
- [2] L. Zhao, T. Chano, S. Morikawa, Y. Saito, A. Shiino, S. Shimizu, T. Maeda, T. Irie, S. Aonuma, H. Okabe, T. Kimura, T. Inubushi, and N. Komatsu,* *Adv. Funct. Mater.*, **22** (24) (2012) 5107-5117.
- [3] L. Zhao, Y.-H. Xu, H. Qin, S. Abe, T. Akasaka, T. Chano, F. Watari, T. Kimura, N. Komatsu,* and X. Chen* *Adv. Funct. Mater.*, **24** (34) (2014) 5348-5357.
- [4] L. Zhao, H. Yang, T. Amano, H. Qin, L. Zheng, A. Takahashi, S. Zhao, I. Tooyama, T. Murakami, N. Komatsu,* *J. Mater. Chem. B*, **4**(47) (2016) 7741-7748.

Scheme 1. Synthesis of h-BN-PG- Lys_8/ICG from h-BN through h-BN-PG and h-BN-PG- Lys_8 .



PR10-4 Exploring the Use of the Chicken Egg CAM Assay as an Animal Model for BNCT

K. Matsumoto, T. Doan, M. Suzuki¹ and F. Tamanoi

Institute for Integrated Cell-Material Sciences, Institute for Advanced Study, Kyoto University

¹*Particle Radiation Oncology Research Center, Institute for Integrated Radiation and Nuclear Science, Kyoto University*

INTRODUCTION: Tamanoi lab has recently established the chicken egg CAM model as an attractive model for studying therapy options for ovarian cancer [1]. In this model, ovarian cancer cells are transplanted onto the CAM (chorioallantoic membrane) of fertilized eggs. Tumor is formed within three to four days. The aim of our experiment is to investigate whether this model can be used as an animal model to examine efficacy of BNCT therapy.

EXPERIMENTS: Fertilized chicken eggs were incubated for ten days and then a window was made on the egg shell and OVCAR8 ovarian cancer cells were transplanted onto the CAM membrane. Three days later, tumor was formed. After injecting ¹⁰BPA into the blood vein that runs through the CAM membrane and is connected to the chick embryo (2.35 mg BPA per egg), the eggs were exposed to neutron at the nuclear reactor for 1 hour. Effect of the tumor was examined by observing tumor size as well as by examining tumor weight two days after the exposure.

RESULTS: As shown in Fig. 1, relatively large tumor was formed three days after ovarian cancer cell transplantation. The tumor was observed easily before the neutron exposure (Day 0). However, two days after the exposure, the size of the tumor observed was much smaller (bottom panel).

The upper figure shows the measurement of tumor weight. The weight of tumor was significantly smaller when the eggs were injected with BPA and then exposed to the neutron beam. Compared with this combined treatment, tumor weight was higher with a single treatment either with BPA (BPA only) or with neutron exposure (neutron only).

Five eggs were used per group in these experiments. One egg was used to measure the amount of boron in the tumor. This was measured to be 12.1 ppm.

In this experiment, we had to examine tumor two days after the neutron exposure due to scheduling constraint. Ideally, the tumor weight should be measured at three or four days after the neutron exposure.

CONCLUSION AND FUTURE PROSPECTS:

Our results suggest that the chicken egg CAM model can be used to examine the effect of BNCT therapy. Instead of BPA compound, other types of compounds carrying boron-10 can be used. In the next experiment, we plan to use tumor targeting nanoparticles containing BPA.

The chicken egg CAM model has a number of attractive features as an animal model. First, tumor can form rapidly in this model. Second, large number of eggs could be used for experiments. Finally, eggs are inexpensive, as the cost of an egg is less than 100 yen.

REFERENCE:

[1] B. Vu *et al.*, Scientific Reports, in press (2018).

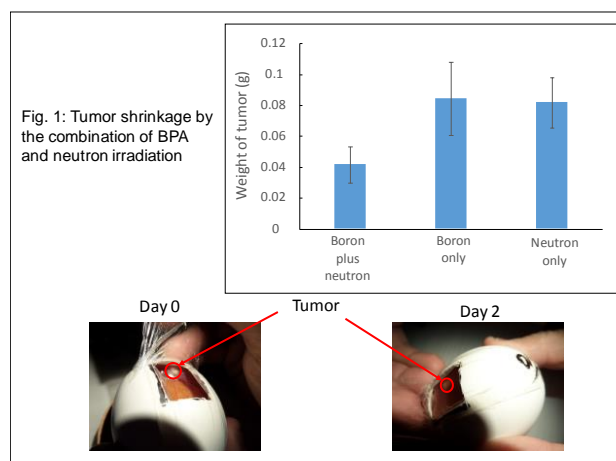


Fig.1. Tumor size and weight after BPA injection and neutron exposure.

PR10-5 Next Generation A (Aomori) - Research and Development of Novel Boron Drugs in BNCT Therapy

S. Ishiyama, C. Ohyama¹, Y. Hashimoto¹, K. Mori¹, S. Hatakeyama¹, T. Yoneyama¹, T. Tanaka¹ and M. Suzuki²

Graduate School of Science, Hirosaki University

¹Graduate school of Medicine, Hirosaki University

²Institute for integrated radiation and nuclear science, Kyoto University

INTRODUCTION: In Aomori Prefecture, "Prefectural Government Refuge against the shortest life time with high death rate" is taken as the prefectural government, Hirosaki University (Faculty of Medicine / Graduate School of Science and Engineering) received this, "Next generation A (Aomori) - Research and development on BNCT treatment "started. The main core technologies related to next-generation A-BNCT therapy are (1) development of new boron medicines, (2) A-BNCT treatment technology and (3) POST / BNCT regeneration technology, and this joint research aims at technological development for practical application concerning (1). New boron drug development In Hirosaki University, IF7-B series (10B-IF7) in which boron nuclide 10B is bound to 7-mer peptide (IFLLWQR; IF7 peptide) 1) -2) which selectively binds to tumor vascular endothelial cells , 10 BSH-IF 7, 10 BPA-IF 7). In this core research, demonstration experiments on the pharmacokinetics, toxicity test and BNCT treatment effect for practical application of the relevant IF7-B series are conducted by nuclear reactor irradiated animal experiments

EXPERIMENTS: In the fiscal year ending March 31, 2010, we will mainly focus on pharmacokinetic examinations by small animal experiments of IF7-B series drugs (3 species). An animal tumor model in which mouse bladder cancer cells (MBT 2) were seeded at the mouse thigh in Hirosaki University was prepared and injected with a boronic agent (IF 7 - BPA, IF 7 - BSH, BPA, BSH) from the mouse tail vein. Mice were sacrificed after drug administration (after 20 minutes, 40 minutes, 60 minutes, 90 minutes, 120 minutes, 240 minutes), and the tumor area and normal organs (liver, kidney, heart, bladder, lung , Brain, spleen, skin, blood) to Teflon containers (10 in total) and then transported to the Kyoto University Reactor. After transportation, measured boron concentration in prompt gamma ray assay(PGA) in E3 duct compartment.

RESULTS: As shown in Fig. 1, sodium borocaptate (BSH). Fig. 1 shows the ¹⁰B concentration in the organ of 13 sites taken out from the mouse specimen after 20 minutes of BSH (Fig.1 (a)) and the new boron drug IF 7-BSH (Fig.1 (b)) by tail injection, respectively. However, in experiments with IF7-BSH, experiments were conducted using multiple specimens.

Immediately after injection of both boron drugs (after 5 minutes), the concentration of 10B in various organs including the tumor tissue once increased, but showed a tendency to decrease with the lapse of time. In contrast, in the tumor tissue 10B concentration accumulation ad-

vanced with time and increased to about 35 ppm at the lapse of 20 minutes after injection. As a result, when comparing the accumulation of both boron drugs, the accumulation of IF7-BSH was higher than that of BSH.

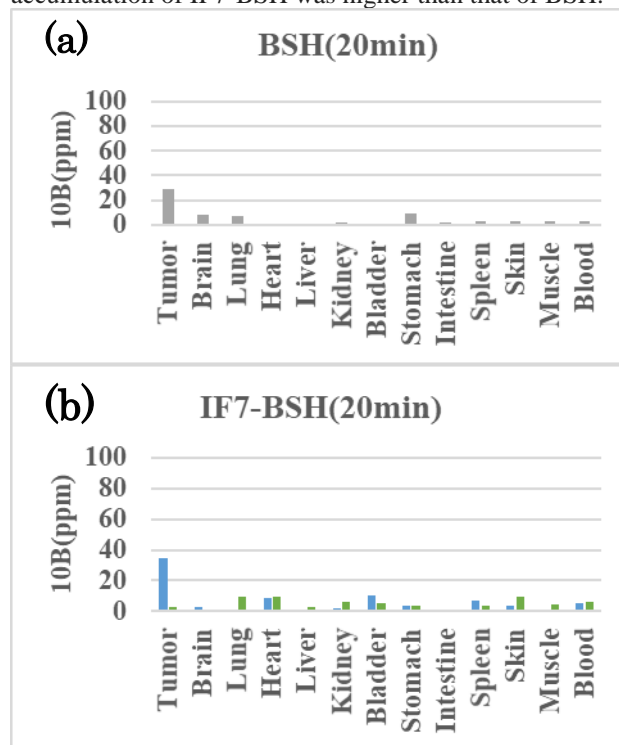


Fig. 1. ¹⁰B condensation in various internal organs including tumor site. In the case of BSH(a) and IF7-BSH. In comparison with BSH, a low level of accumulation was achieved in tumor tissue at 20 minutes after administration of IF7-BSH.

In conventional BSH, since it is not incorporated into the tumor cell, too high accumulation degree can not be obtained at the tumor site. On the other hand, IF7 constituting IF7 - BSH was designed to target ANNEXIN1 which precipitates outside the vascular endothelial cells when tumor tissue forms new blood vessels. Therefore, in this animal experiment it was thought that high ¹⁰B enrichment in tumor tissue could be achieved mainly because IF7 of this compound played the role of boron carrier.

In comparison with BSH, a low level of accumulation was achieved in tumor tissue at IF 7 20 minutes after administration.

REFERENCES:

- [1] Mirzaei HR, *et al.* J Cancer Res Ther. 2016.
- [2] Takahara K, *et al.* Plos One 20.

PR10-6 Spherical Particle Fabrication of Boron-Iron Complex Material for BNCT Agent with Magnetic Property

Y. Ishikawa, N. Koshizaki¹ and M. Suzuki²

Nanomaterial Research Institute, National Institute of Advanced Industrial Science and Technology (AIST)

¹Graduate School of Engineering, Hokkaido University

²Research Reactor Institute, Kyoto University

INTRODUCTION: Submicrometer-sized spherical particles of boron compounds are expected to show high therapeutic efficiency in BNCT due to the high B content of the particle. For example, boron carbide (B_4C) particle with 200 nm in diameter contains 4.6×10^8 of B atoms. Our group attempted submicrometer-sized spherical particle fabrication of boron-iron complex for BNCT agent with an enhanced MRI contrast. In this study, a crystalline structure and chemical composition of fabricated particles composed of boron and iron were analyzed.

EXPERIMENT: Mixture of amorphous boron particles and $\alpha\text{-Fe}_2\text{O}_3$ particles suspended in ethanol was stirred with a propeller driven by a rotational device. The suspension mixture was irradiated with a Nd:YAG laser (pulse width: 7 ns, wavelength: 532 nm, pulse frequency: 30 Hz) for 24 h. Submicrometer-sized spherical particles were obtained by this laser irradiation [1]. The suspended particles after laser irradiation were collected with a centrifugation. The collected particles were treated with 1 M HCl aqueous solution to selectively remove unreacted $\alpha\text{-Fe}_2\text{O}_3$ particles for 6 h, followed by a magnetic separation using a neodymium magnet to eliminate boron and/or boron carbide particles without iron inclusion. Obtained particles were analyzed using an X-ray diffraction (XRD), a high-angle annular dark field scanning transmission electron microscope (HAADF-STEM), and an X-ray photoelectron spectroscopy (XPS).

RESULTS: XRD pattern of obtained particles is shown in Figure 1. The particles contained FeB and B_4C crystalline phases. Figure 2 depicts HAADF-STEM image and elemental distribution images of B, Fe, C, and O. By comparing these images, most particles contained both B and Fe. This result indicates that most particles formed complex of FeB and B_4C and/or B, and is consistent with the XRD result. However, these particles also included O. Therefore, these magnetically collected particles consisted of crystalline FeB, and B_4C , and amorphous compound of Fe and O and/or Fe, B, and O. According to XPS analysis, the atomic ratio of B, Fe, and O in the obtained particles was 5, 50, and 45 %.

A fabrication of Fe-B complex particles with high B content is still a future challenge.

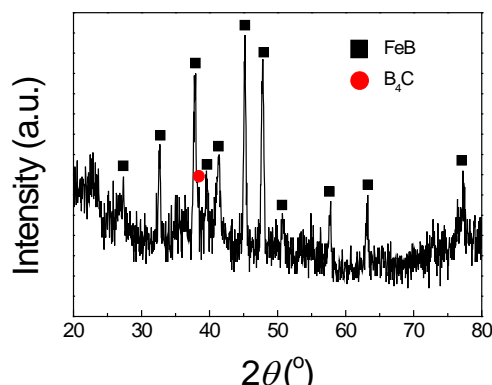


Fig. 1 XRD pattern of magnetically collected particles.

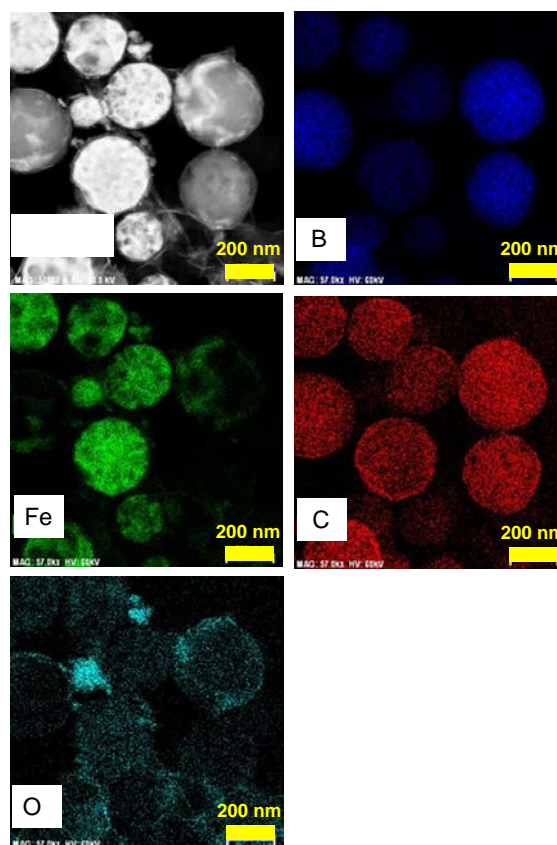


Fig. 2 HAADF and elemental distribution images of magnetically collected particles.

REFERENCE:

[1] Y. Ishikawa *et al.*, Appl. Phys. Lett., **91**, 16, (2007) 161110.

PR10-7 Gadolinium-loaded Chitosan Nanoparticles for Neutron Capture Therapy of Cancer: Influence of Particle Size on Tumor-killing Effect *in vitro*

T. Andoh, Y. Nakatani, M. Suzuki¹, T. Takada², Y. Sakurai², T. Fujimoto³, and H. Ichikawa

Faculty of Pharmaceutical Sciences and Cooperative Research Center of Life Sciences, Kobe Gakuin University

¹*Particle Radiation Oncology Research Center, Institute for Integrated Radiation and Nuclear Science, Kyoto University*

²*Division of Radiation Life Science, Institute for Integrated Radiation and Nuclear Science, Kyoto University*

³*Department of Orthopaedic Surgery, Hyogo Cancer Center*

INTRODUCTION: Gadolinium neutron capture therapy (Gd-NCT) is cancer therapy that utilizes γ -rays and electrons emitted as a result of $^{157}\text{Gd} (n, \gamma) ^{158}\text{Gd}$ reactions. We have been developing gadolinium-loaded chitosan nanoparticles (Gd-nanoCPs) as a means of controlling Gd delivery in Gd-NCT. Accumulation of Gd in Gd-nanoCP-treated tumors is based primarily on the bioadhesive (cationic), biocompatible (nontoxic), and biodegradable (bioerodible) properties of chitosan nanoparticles. Our previous studies demonstrated that neutron-capture reactions after intratumoral (i.t.) injection of Gd-nanoCPs in tumor-bearing mice can significantly suppress tumor growth; however, the inhomogeneous distribution of Gd-nanoCPs in tumor masses prevents complete cure [1]. In addition, it is not clear how γ -rays and electrons relate to the tumor-killing effect. One can expect that reducing chitosan particle size in Gd-nanoCPs will improve the heterogeneous distribution of Gd in tumor tissues and increase the tumor-killing effect of electrons by shortening the adhesion length between Gd-nanoCPs and tumor cells. Thus, we aimed to investigate the effect of nanoparticle size on the tumor-killing effect of Gd-nanoCPs in Gd-NCT.

EXPERIMENTS: Gd-nanoCPs were prepared with chitosan and Gd diethylenetriamine pentaacetic acid (Gd-DTPA) using a water-in-oil (w/o) emulsion-droplet coalescence technique [2]. Two grades of chitosan with different molecular weights (MWs; 10 and 950 kDa) were used to manipulate Gd-nanoCP particle size. B16F10 mouse melanoma cells were employed to evaluate the cellular association properties of Gd-nanoCPs and the tumor-killing effect of thermal neutron irradiation. Tumor-killing effect was evaluated by a cellular viability assay after thermal neutron irradiation.

RESULTS: The use of two grades of chitosan made it possible to obtain Gd-nanoCPs of different sizes and Gd content: Gd-nanoCPs prepared using chitosan with a higher MW (950 kDa) had a mean particle size and Gd content of 468 nm and 7.5 wt%, respectively

(Gd-nanoCP-400); Gd-nanoCPs prepared using chitosan with a lower MW (10 kDa) had a mean particle size and Gd content of 185 nm and 24 wt%, respectively (Gd-nanoCP-200). The tumor-killing effect of Gd-nanoCPs in the Gd-NCT groups was significant, but efficacy was dependent on the micrometric properties of Gd-nanoCPs. Most notably, Gd-nanoCP-200 exhibited a stronger tumor-killing effect than did Gd-nanoCP-400 at the same Gd dose, and the tumor-killing effect of Gd-nanoCP-200 was the same as that of Gd-nanoCP-400 at less than half the Gd-nanoCP-400 Gd dose. This tumor-killing effect could be ascribed to the higher association between Gd-nanoCPs and tumor cells; improved distribution of Gd in cells exposed to Gd-nanoCP-200; and increased influences due to Auger and Coster-Kronig electrons, which have shorter path lengths and stronger tumor-killing ability than do γ -rays. Indeed, cells associated with uptake and adhesion that were exposed to Gd-nanoCP-200 had significantly higher Gd concentrations than those exposed to Gd-nanoCP-400 at less than half the Gd-nanoCP-400 Gd dose. Then the Gd concentration reached $38 \mu\text{g} / 10^6$ cells for Gd-nanoCP-200 at $15 \mu\text{g} \text{ Gd/mL}$ culture medium and $17 \mu\text{g} / 10^6$ cells for Gd-nanoCP-400 at $40 \mu\text{g} \text{ Gd/mL}$ culture medium, respectively. Our results demonstrated that reducing Gd-nanoCP particle size is an effective way to improve cellular affinity for Gd-nanoCPs and enhance the tumor-killing effect of Gd-NCT.

REFERENCES:

- [1] H. Ichikawa *et al.*, *Appl Radiat Isot.*, **88** (2014) 109–113.
- [2] H. Tokumitsu *et al.*, *Pharm. Res.* **16** (1999) 1830–1835.

T. Kanemitsu, S. Kawabata, M. Fukumura,
R. Hiramatsu, N. Nonoguchi, M. Suzuki¹, S.
Masunaga¹, K. Ono², T. Kuroiwa, S. Miyatake³ and
H. Nakamura⁴

*Department of Neurosurgery, Osaka Medical College 1
Kyoto university research reactor institute*

*²Osaka Medical College, Kansai BNCT Medical
Center*

*³Section for Advanced Medical Development, Cancer
Center, Osaka Medical College*

*⁴Laboratory for Chemistry and Life Science, Institute
of Innovative Research, Tokyo Institute of Technology*

1st study

Introduction

Folic acid (FA) has high affinity for the folate receptor (FR), which is limited-expressed in normal human tissues and over-expressed in many tumor cells, including glioblastoma [1,2]. We developed a novel pteroyl closo-dodecaborate conjugate (PBC) in which the pteroyl group is known to interact with FR. The purpose of this study was to evaluate the therapeutic efficiency of PBC using F98 glioma-bearing rats *in vivo* boron neutron capture therapy (BNCT).

Materials and Methods

We used two boron compounds; Boronophenylalanine (BPA) and PBC. For *in vivo* study, F98 glioma bearing rats were divided to five groups: untreated controls, neutron irradiation controls, BNCT with BPA (i.v.) , BNCT with PBC (CED), and BNCT with combination of BPA (i.v.) and PBC (CED).

Results

Median survival times (MST) of untreated and irradiated controls were 23 and 26 days, respectively, while rats that received PBC(CED), followed by BNCT, had a MST of 31 days, which were similar to those obtained following i.v. administration of BPA (30 days). And the combination group had a MST of 38 days. In combination of PBC (CED) and BPA (i.v.), a significant prolongation in survival time was obtained compared with the single agent groups.

2nd study

Introduction

BPA used in BNCT is a ¹⁰B-derivative of phenylalanine transported into tumor cells by neutral amino acid transporters. 5-aminolevulinic acid (ALA) is also a natural amino acid selectively accumulating in neoplastic cells and inducing photoactivatable porphyrins, mainly protoporphyrin-IX (PpIX) [3,4].

Materials and Methods

In the present study, we examined whether ALA can sensitize glioma to BPA-based BNCT. We used two cell line; a human glioma stem cell (GSC) line; GB13 and a mouse GSC line; TS. For *in vivo* BNCT, GB13-intracerebrally implanted animals were divided into 6 groups; control, ALA-only, neutron-irradiation only, ALA-neutron irradiation, BNCT only, ALA-BNCT. 80 mg/kg of ALA was orally given to animals 24 hours prior to BPA administration.

Results

The ALA-BNCT group (28 days) obtained a significant prolongation in survival time compared with BNCT only group (25 days) .

REFERENCES:

- [1] Sudimack JJ, Adams D, Sekido M, Barth RF: *Pharmaceutical research*, **19** (2002) 1502-1508.
- [2] Stevens PJ, Sekido M, Lee RJ: *Anticancer research*, **24** (2004) 161-165.
- [3] Printip Wongthai, Kohei Hagiwara, Yurika Miyoshi: *Cancer Sci*, **106** (2015) 279-86.
- [4] Yang, X., Palasuberniam, P., Kraus, D.: *Int J Mol Sci.*, **16** (2015) 25865-80.

PR10-9 Development of S-Alkylthiododecaborate Containing Amino Acids for BNCT

Y. Hattori, I. Nakase¹, M. Suzuki², S. Tanimori³ and M. Kirihaata

Research Center of BNCT, Osaka Prefecture University

¹Organization for Research Promotion, Osaka Prefecture University

²Research Reactor Institute, Kyoto University

³Graduate School of Life and Environmental Sciences, Osaka Prefecture University

INTRODUCTION: Boron-neutron capture therapy (BNCT) is based on the nuclear fission reaction of a ¹⁰B-atom with thermal and/or epithermal neutrons to yield high linear energy transfer α particles (⁴He) and recoiling ⁷Li nuclei in tumor cells, and has attracted attention in terms of its potential therapeutic effects on malignant brain tumors, head and neck cancer, and melanoma [1]. A boron delivery agent (boron carrier) with high therapeutic efficiency and low adverse effects is crucial for successful BNCT. For a boron compound to be successful in BNCT, the following criteria must be met: high tumor-targeting selectivity (T/N > 3–4:1), low systemic toxicity, and boron concentration of 20 μ g ¹⁰B/g in tumor tissues. Although many kinds of boron compounds such as amino acids, nucleic acids, and sugars have been reported as boron carriers for BNCT, only two compounds are used clinically for the treatment of cancer using BNCT: *p*-borono-L-phenylalanine (BPA) and mercapto-*closo*-undeca-hydrododecaborate (BSH) (Fig. 1).

While developing a new boron carrier for BNCT, we have designed and synthesized a thiododecaborate ([B₁₂H₁₁S]²⁻) unit containing L-amino acids. In vitro evaluation of a BSH-amino acid (DBA, **1**) suggested that DBA might be a potential delivery agent for BNCT [2]. To develop a new boron carrier for BNCT, we designed and synthesized a novel thiododecaborate unit containing amino acids (AS-DBA, **2**), in which the B₁₂H₁₂ cluster is linked to the organic moiety through alkylated S⁺ λ^3 sulfonyl groups. These novel boron compounds have enhanced hydrophobicity and cell membrane permeability owing to a reduced negative charge (-1) and the introduced alkyl chain. Here, we present the biological evaluation of novel boron compounds **2a-g** as boron carriers for BNCT.

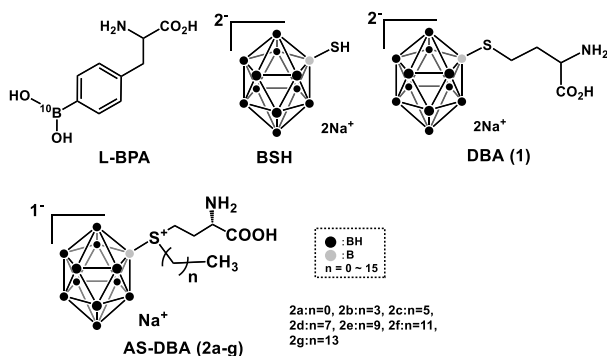


Fig. 1. Boron compounds for BNCT.

RESULTS and Discussion: To evaluate the AS-DBAs, we examined the cytotoxicity, water solubility, and cellular uptake of AS-DBAs and compared them with that of BPA, BSH, and DBA.

The water solubility of **2a-g** was higher than that of BPA (BSH, **1**, **2a-g**: >40 g/L, BPA: 1.6 g/L). The cytotoxicity of AS-DBA **2a-g** was marginally low (IC₅₀ >0.1 mM in C6 glioma cells). However, the cytotoxicity of AS-DBAs was higher than that of L-BPA (IC₅₀ >10 mM).

In the next step, we measured the boron concentrations in C6 glioma cells by ICP-OES (Fig. 2). The AS-DBAs with a short alkyl chain (**2a-c**, n = 0–5) delivered a small amount of ¹⁰B atoms to C6 cells, whereas AS-DBAs with medium alkyl chains delivered a large amount of ¹⁰B atoms (**2d-g**, n = 0–5). In particular, the intracellular boron concentration of dodecylated AS-DBA **2f** in C6 cells was five times greater than that of L-BPA, with fewer doses of the drug (**2f**: 0.1 mM, BPA: 1.2 mM).

Our results show that AS-DBAs with medium alkyl chains **2d-2g** are useful as ¹⁰B carriers. In vivo evaluation of AS-DBAs are ongoing and the results will be reported soon.

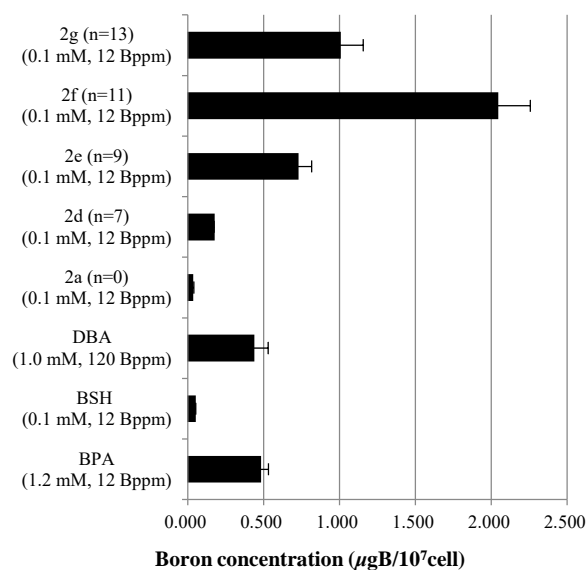


Fig. 2. Amount of boron compounds incorporated into C6 glioma cells.

REFERENCES:

- [1] H. A. Soloway *et al.*, Chem. Rev., **98** (1998), 1515-1562.
- [2] Y. Hattori *et al.*, J. Med. Chem., **55** (2012), 6980-6984.

W. Kurosawa, Y. Suga, K. Matsumoto, R. Ubagai, Y. Iwai, Y. Okamatsu, Y. Kitahara, T. Tsurubuchi¹, F. Yo-shida¹, A. Zaboronok¹, M. Shirakawa², M. Suzuki³, Y. Sa-kurai³, H. Tanaka³, K. Nakai⁴ and A. Matsumura¹

Institute for Innovation, Ajinomoto Co., Inc.

¹Department of Neurosurgery, Faculty of Medicine, University of Tsukuba

²Department of Pharmaceutical Sciences, University of Fukuyama

³Research Reactor Institute, Kyoto University

⁴Department of Neuro-rehabilitation, Ibaraki Prefectural University Hospital

INTRODUCTION

Boron neutron capture therapy (BNCT) is gaining attention as a state-of-the-art minimally invasive cancer treatment [1]. Up to now, clinical studies using boronophenylalanine (BPA) and sodium borocaptate (BSH) as ¹⁰B delivery agents for neutron capture reaction have been conducted [2,3]. However, continuous administration of their high concentrations is needed to keep sufficient ¹⁰B tumor concentration. Therefore, we have developed novel boron-containing low molecular compounds efficient in accumulation and retention in tumor.

MATERIALS AND METHODS

3×10^6 of mouse colon carcinoma (CT26) cells were injected in the right thigh of 5-week-old female Balb/c mice. Two weeks after injection tumor-bearing (avg. 324 mm³) mice were grouped as follows: BN1229, BN1242, BSH, radiation only, and without treatment. BN1229 (57 mg [¹⁰B]/kg, n=8) and BN1242 (57 mg [¹⁰B]/kg, n=8) were injected 24 hours before irradiation. BSH (100 mg/kg with 57 mg [¹⁰B]/kg, n=5) was injected 2 hours before irradiation for comparison. Groups with radiation only (n=7) and without treatment (n=6) were used as controls.

The irradiation was performed with thermal neutrons with a flux of $1.6\text{-}3.5 \times 10^{12}$ neutrons/cm² over 1 hour.

The tumor size (mm³) was calculated as the long diameter multiplied by the short diameter squared and further divided by 2, in the period starting prior the treatment till 26 days after irradiation.

RESULTS

BN1229, BN1242, and BSH groups showed decrease in tumor size compared to controls (Fig.1 a). The tumor size was independent of the body weight in all mice (Fig.1 b). Because of the large variation in tumor size at the time of grouping, comparison between groups on the 26th day after irradiation was done in mice with a tumor size of 200 mm³ or less before irradiation. A significant tumor growth inhibitory effect was observed in BN1242 group compared

to the untreated control 26 days after irradiation (Fig.1 c-1). The BN1242 compound also showed tendency of efficiency in tumor size decrease over BSH and irradiation only. We assume that BN1242 is a candidate boron compound for further investigation that showed high accumulation in tumor even 24 hours after injection.

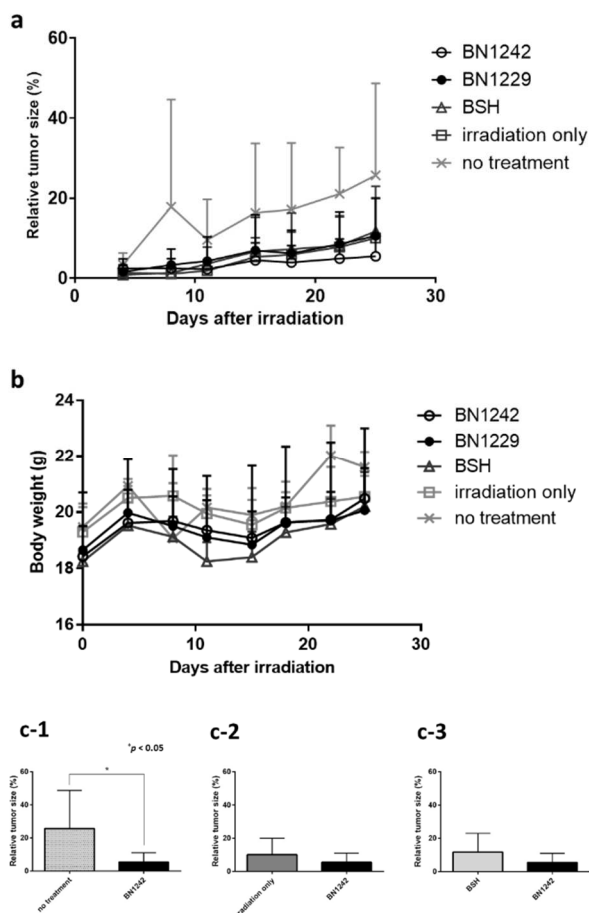


Fig. 1. BNCT of tumor-bearing mice with ¹⁰B-enriched compounds. (a) Tumor growth ratio after 1 hour - thermal neutron irradiation ($1.6\text{-}3.5 \times 10^{12}$ neutrons/cm²) with the injection of BN1242 or BN1229 24 hours, and BSH 2 hours before irradiation, and irradiation only and untreated groups as controls. (b) Mice body weight after thermal neutron irradiation. (c) Tumor growth comparison in mice with initial tumor size of 200 mm³ or less between BN1242 (n = 7) and (c-1) untreated control (n = 3), (c-2) irradiation only (n = 4), and (c-3) BSH (n=4) 26 days after irradiation.

REFERENCES

1. Sato E, Zaboronok A, Yamamoto T, *et al.* *J Radiat Res.* 2018 Mar 1;59(2):101-107.
2. Yamamoto T, Nakai K, Tsurubuchi T, *et al.* *Appl Radiat Isot.* 2009 Jul;67(7-8 Suppl):S25-6.
3. Wang LW, Chen YW, Ho CY, *et al.* *Int J Radiat Oncol Biol Phys.* 2016 May 1;95(1):396-403.

PR10-11 Development of an Actively-Targeted, Phenylboronic Acid-Installed Nanoparticle Towards Next-Generation Boron Neutron Capture Therapy

Y. Nagasaki^{1,3}, A. Kim¹ and M. Suzuki⁴

¹Department of Materials Sciences, Graduate School of Pure and Applied Sciences, University of Tsukuba,

²Masters Program in Medical Sciences, Graduate School of Comprehensive Human Sciences, University of Tsukuba,

³Center for Research in Isotopes and Environmental Dynamics (CRIED), University of Tsukuba,

⁴Radiation Oncology Research Laboratory, Institute for Integrated Radiation and Nuclear Science, Kyoto University

INTRODUCTION

The boron neutron capture therapy (BNCT) is based on binary approach that combination of non-invasive thermal neutron irradiation and administration of boron-10 compounds can result in small-range nuclear fission, followed by tumoricidal effects. During the last decade, much efforts have been made for the establishment of safe and stable neutron sources such as linear accelerators, so that in the near future the BNCT may be propagate much rapidly, through the local hospitals.

Nevertheless, most of the BNCT agents, whether in pre-clinical development or clinical trials, have shown significant obstacles, limiting further clinical translations. For instance, one of only clinically approved BNCT agent, boronophenylalanine (BPA), is a low-molecular weight compound with extremely rapid renal clearance, thus requires continuous injection through the vein for few hours, even during the irradiation. The boron concentration in the blood circulation at the moment of neutron irradiation should be high, not only narrowing down the therapeutic window of the BNCT agent, but also inducing critical damage to the healthy tissues.

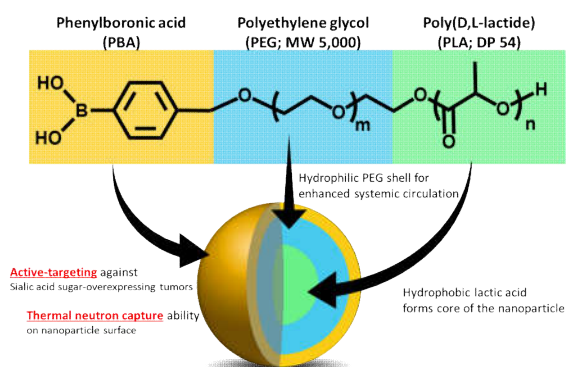


Figure 1. Schematic design of the PBA-installed nanoparticle (PBA-NP)

Herein, to address aforementioned issues by enhancing systemic circulation as well as tumor-specific accumulation of the BNCT agent, our group designed and synthesized a polymeric nanoparticle, as shown in Fig. 1. This nanoparticle is decorated with phenylboronic acid (PBA) groups on the surface, granting thermal neutron capture ability as well as sialic-acid targeting ability. The cellular expression level of sialic acid is known to be linked to the metastatic ability of malignant tumor cells, thus our developed PBA-decorated nanoparticle (PBA-NP) is supposed to be selectively bind on and accumulated in highly metastatic tumor cells. Moreover, being protected by PEG chains, the core-shell supramolecular structure of the PBA-NP is likely to prevent aggregation and degradation in the systemic circulation, may result in extremely high tumor/blood (T/B) ratio after one-shot intravenous injection, by when the PBA-NP is highly accumulated in the tumor tissue, while it is already excreted from the systemic circulation.

EXPERIMENTS

The block copolymer consists of PBA-PEG and PLA (PBA-PEG-*b*-PLA) was synthesized by anionic ring-opening polymerization of ethylene oxide (EO) and D, L-lactic acid on alkoxyated 4-carboxyphenylboronic acid. Then, the PBA-PEG-*b*-PLA was dissolved in dimethylformamide (DMF), followed by dialysis against pure water, to remove organic solvent and to generate the nanoparticles by oil-in-water (o/w) emulsion method. *In vitro* tumor cell recognition ability of the prepare nanoparticles (PBA-NP) was evaluated by confocal laser scanning microscope (CLSM) observation of highly metastatic human breast cancer cells (MDA-MB-231) as well as bovine aortic endothelial cells (BAOEC), pre-treated with PBA-NP or control nanoparticles that having no active PBA groups on the surface. For the evaluation of *in vivo* tumor-targeting ability, orthotopic skin cancer model was prepared by intradermal injection of mouse melanoma cell line (B16-F10) to the C57BL/6/j mice, followed by intravenous injection of PBA-NP, sacrificed 48 hr post-injection, harvested the tumor, prepared cryo-sections, then observed with CLSM.

RESULTS

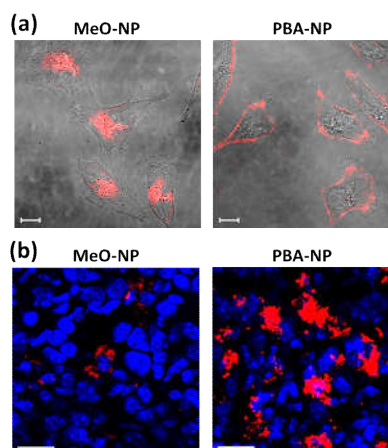


Figure 2. Selective accumulation property of the PBA-NP, compared with methoxy group-installed control nanoparticle (MeO-NP). (a) *in vitro* cancer cell membrane recognition ability of the PBA-NP, MDA-MB-231 cells co-incubated with the nanoparticles for 5 mins. (b) *in vivo* tumor targeting effect of the PBA-NP, observed on cryo-sections prepared from the tumors harvested 48 hr-post intravenous injection. (Blue: Nuclei, Red: Rhodamine-labeled nanoparticles, Scale bars = 20 μ m)

Prepared nanoparticles were stable in physiological salt concentration and 10% serum containing cell culture media (data now shown). As shown in Fig. 2a, PBA-NP could recognize and bind on cellular membrane of sialic-acid overexpressing MDA-MB-231 cells within 5 mins of co-incubation, while the control nanoparticles (MeO-NP) were instantly internalized into the cytosol, presumably by endocytosis. This result strongly suggests that the PBA-NP would be selectively bound on cancer cell membrane, likely to facilitate tumor-specific accumulation, while the MeO-NP would be non-specifically internalized into the normal cells. In accordance with *in vitro* evaluations, *in vivo* intratumoral distribution of the PBA-NP after the intravenous injection, shown in Fig. 2b also supports its selective accumulation ability on *in vivo* administration.

PR10-12 Design, Synthesis, and Evaluation of Glucose-type Boron Carriers for BNCT

S. Aoki, Y. Hisamatsu, K. Tamura, H. Ueda, B. Shahni, M. Suzuki¹, S. Masunaga¹, N. Kondo¹, Y. Sa-kurai¹ and K. Ono¹

Faculty of Pharmaceutical Sciences, Tokyo University of Science

¹*Research Reactor Institute, Kyoto University*

INTRODUCTION: Boron neutron capture therapy (BNCT) is one of powerful therapies for local tumor control in the treatment of brain tumor, melanoma, and so on [1]. To date, only two boron-containing drugs, L-4-boronophenylalanine (BPA) and BSH (sodium mercaptoundecahydrododecaborate, Na₂B₁₂H₁₁SH), have been approved as clinically test compounds, and discovery of better BNCT agents is highly required. Our object in this work is to develop new methods for the tumor-specific accumulation of boron-containing compounds and the real-time detection of B concentrations in local tumor tissues.

Recently, we reported on a new concise and versatile synthesis of the derivatives of sulfoquinovosyl acylpropanediol (SQAP), which has been reported to show a variety of biological activities, including accumulation in tumor cells and the inhibition of tumor cell grow. For instance, a SQAP derivative having *o*-carborane unit (**4**) was synthesized via substitution reaction of the intermediate **2** and **3** [2]. However, intracellular uptake of **4** in cancer cells was not so high as those of BPA (+ fructose) and BSH.

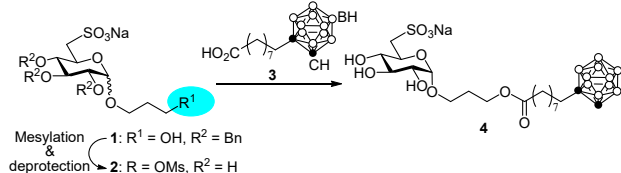


Fig 1. Synthesis of SQAP derivatives bearing *o*-carborane moiety.

These results prompted us to design and synthesize new B-carriers based on the glucose and glucosamine scaffolds, because it is known that facilitative glucose transporters (GLUTs) and sodium dependent glucose transporter (SLGTs) are highly expressed on cancer cells. For instance, GLUT1 is broadly overexpressed in various cancers, including hepatic, pancreatic, breast, esophageal, brain, renal, lung, cutaneous, colorectal, endometrial, ovarian, and cervical. Therefore, glucose and glucosamine analogs that have Michael

acceptor units to accommodate thiols were designed and synthesized in this work.

EXPERIMENTS and RESULTS:

Design and synthesis of new carriers of boron-containing compounds.

In this work, we designed and synthesized a D-glucosamine derivative having a maleimide moiety, which functions as a conjugate acceptor of various thiols such as BSH, at the 2-position (**5** in Fig. 2), of D-glucosamine, which was easily available from D-glucosamine, as shown in Fig. 2. The synthesized **5** was reacted with BSH and other thiol derivatives having boron to obtain **6**. Cytotoxicity of the analogs of **6** to cancer cells such as HeLa and A549 cells was evaluated by MTT assay and their intracellular uptake to these cancer cells was examined by ICP-MS (inductivity coupled plasma-mass spectrometer). It was found that intracellular uptake of these compounds are lower than our reference compound [3], boronobenzyl-cyclen (cyclen = 1,4,7,10-tetraazacyclododecane) [4], albeit these toxicity were relatively low. The improvement of the design of these B-carriers are now in progress.

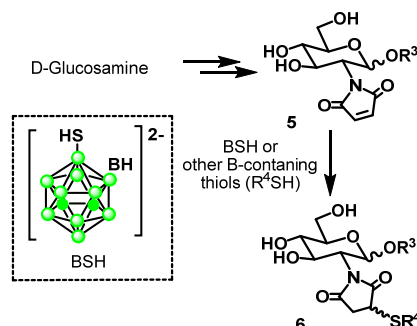


Fig 2. Synthesis of boron carriers based on glucosamine analogs.

REFERENCES:

- [1] a) R. F. Barth *et al.*, *Clin. Cancer Res.*, **11** (2005) 3987-4002. b) R. F. Barth *et al.* *Rad. Oncol.* **7** (2012) 146-166.
- [2] T. Tanaka *et al.*, *Chem. Pharm. Bull.* **65** (2017) 566-572.
- [3] H. Ueno *et al.* Manuscript in preparation.
- [4] M. Kitamura *et al.* *Inorg. Chem.* **50** (2011) 11568-1158

T. Nomoto, Y. Inoue, Y. Yao, M. Suzuki¹ and N. Nishiyama

Laboratory for Chemistry and Life Science, Institute of Innovative Research, Tokyo Institute of Technology

¹Research Reactor Institute, Kyoto University

INTRODUCTION: Boronophenylalanine (BPA) is one of the most promising boron drugs for boron neutron capture therapy (BNCT), because it can be taken up selectively by cancer cells through the large neutral amino acid transporter 1 (LAT1), which is reported to be overexpressed on many malignant tumor cells [1]. Although BPA has exhibited efficient accumulation within numerous types of tumors, its therapeutic efficacy has been some-times compromised by untoward quick clearance from the target tumor. The clearance from the tumor cells may be due to antiport mechanism of LAT1; intracellular BPA should be excreted when extracellular BPA concentration is lowered [2].

To facilitate the intracellular retention of BPA, we have recently synthesized finely-tuned poly(vinyl alcohol) (PVA), and prepared the complex of BPA and PVA (PVA-BPA) via the formation of boronic acid-diol bonds. Since PVA-BPA has many BPA molecules in its structure and ex-poses the structure of phenylalanine of BPA, which is re-ported to be the critical structure for interaction with LAT1 [3], PVA-BPA can induce multivalent interaction with LAT1 on tumor cells, resulting in its efficient intracellular internalization through LAT1-mediated endocytosis. Prob-ably because PVA-BPA can be localized in endo-/lyso-somes and avoid untoward efflux from the target cells, PVA-BPA importantly revealed prolonged intracellular re-tention in *in vitro* condition. In addition, in *in vivo* study, PVA-BPA showed efficient tumor accumulation and dras-tically improved tumor retention compared to conven-tional BPA. Thus, in this study, we have examined the therapeutic potential of PVA-BPA in BNCT using Kyoto Uni-versity Research Reactor (KUR).

EXPERIMENTS: BALB/c mice bearing subcutaneous CT26 tumors were used in this study. PVA-BPA or the fructose-BPA complex was intravenously injected to the mouse (10 mg BPA/mouse), and the thermal and epither-mal neutrons were irradiated to the tumor using KUR 3 or 6 h after the injection. Size of tumor was measured using a caliper, and tumor volume (V) was calculated using the following equation:

$$V = 1/2 \times a \times b^2,$$

where a and b denote major and minor axes of a tumor, respectively.

RESULTS: As shown in Fig. 1, fructose-BPA significantly suppressed the tumor growth, indicating its excel-lent clinical therapeutic potential. However, apparent tu-

mor regrowth was observed at day 15, which may be explained by the untoward efflux of BPA from the tumor and the eventually compromised therapeutic efficacy.

In contrast, PVA-BPA exhibited drastic antitumor activity, and tumor regrowth was not observed even at day 18. Since PVA-BPA can efficiently accumulate within the tumor and retain for a prolonged period, PVA-BPA might maintain high intratumoral boron concentration that is sufficient to obtain strong antitumor activity during neutron irradiation (50 min). This explanation is supported by the strong antitumor activity obtained by PVA-BPA and neutron irradiation 6 h after the injection; PVA-BPA could exhibit high intratumoral boron concentration even 6 h after the injection. It should be also noted that histological analysis of the tumor treated with PVA-BPA with 3 h interval between injection and irradiation revealed the cell death of almost all the tumor cells. These results indicate that PVA-BPA may be a promising boron delivery system to accomplish efficient BNCT.

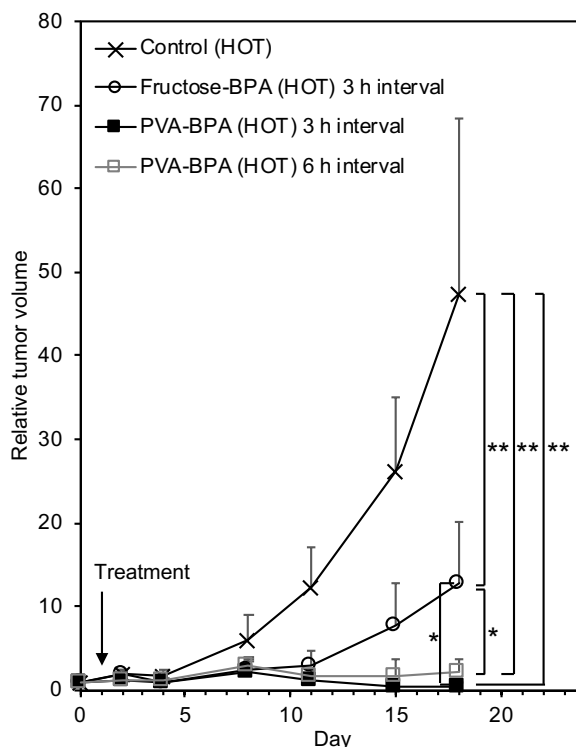


Fig. 1. Antitumor effect of fructose-BPA and PVA-BPA. At day 1, the samples were injected and neutrons were irradiated to the tumor.

REFERENCES:

- [1] M. J. Luderer *et al.*, *Pharm. Res.*, **32** (2015) 2824-2836.
- [2] A. Wittig *et al.*, *Radiat. Res.*, **153** (2000) 173-180.
- [3] E.G. Geier *et al.*, *Proc. Natl. Acad. Sci. U. S. A.*, **110** (2013) 5480-5485.

PR10-14 Development of Boron Cluster Containing Water-Soluble Folate Derivatives As Novel Small Molecular Agents for BNCT

H. Nakamura¹, F. Nakagawa^{1,2}, and M. Suzuki³

¹ Laboratory for Chemistry and Life Science, Institute of Innovative Research, Tokyo Institute of Technology

² School of Life Science and Technology, Tokyo Institute of Technology

³ Research Reactor Institute, Kyoto University

INTRODUCTION: Development of new boron compounds is still indispensable for expanding the application of boron neutron capture therapy (BNCT) for the treatment of various cancers. For successful treatment of cancer by BNCT, a boron compound requires high tumor accumulation, low toxicity and water solubility. In order to achieve these criteria, we focused on folate receptor (FR). FR is a cell surface protein that takes folic acid into the cell by receptor-mediated endocytosis. It is well known that one of the FR, FR α , is overexpressed on the surface of many cancer cells, for example ovary, lung, breast and kidney cancers. Kettenbach et al. developed a carborane-containing folate derivatives that was found to accumulate to KB cells [1], although the water solubility was relatively low. Herein, we designed and synthesized pteroyl *closo*-dodecaborate conjugates (PBCs).

EXPERIMENTS:

U-87MG human brain tumor cells were transferred to the atomic reactor (KUR; Kyoto University Research Reactor) and incubated with the culture medium (RPMI1640) in 96 well plate at a density of 3.0×10^4 cells/well for 12 h. The cells were exposed by L-BPA, PBC1 and PBC4 dissolved in medium at 5, 10, 25 ppmB for 3 h then the cells were irradiated at KUR with reactor thermal neutron beams for 0, 10, 25, 60 min. After neutron irradiation, medium was removed and 100 μ L medium was added. The cells were cultured at 37°C for 22 h, then added 10 μ L MTT (5 mg/mL dissolved in water) and incubated at 37°C for 2 h. After incubation, the medium was removed and 100 μ L DMSO was added. The measurement was performed by reading absorbance 595 nm.

RESULTS: U-87MG cells were incubated with PBC1, PBC4, and L-BPA for 3 h at various concentrations (5-25 ppmB), and neutron irradiation was carried out for 0-60 min. Irradiation time-dependent cell viability was shown in Figure 1. It was expected that BNCT effect higher than that of L-BPA because both PBC1 and PBC4 were highly taken up by U-87MG cells due to highly expression of FR α . Indeed, our preliminary study revealed that both PBC1 and PBC4 were accumulated into U-87MG cells higher than L-BPA. However, the results were not as expected. For example, in the case of PBC1, higher cytotoxicity was observed at doses of 5 and 10 ppmB. The cell viability at 25 ppmB was similar level to that of the

control (no treatment), revealing that neutron flux was not sufficient. In the case of PBC4, highest cytotoxicity was observed at 25 ppmB. L-BPA showed the similar phenomena to PBC1: the highest cytotoxicity was observed at 5 ppmB. Furthermore, the significant cytotoxicity was not observed in all cases: cell viabilities were around 80%. These results indicate that the neutron flux was not sufficient in the current irradiation experiments.

In conclusion, we developed boron cluster containing water-soluble folate derivatives (PBCs) and demonstrated their cytotoxicity with neutron irradiation at KUR. However, significant cytotoxicity was not observed in all cases due to insufficient neutron flux. We will conduct the neutron irradiation again under the modified conditions in the next year.

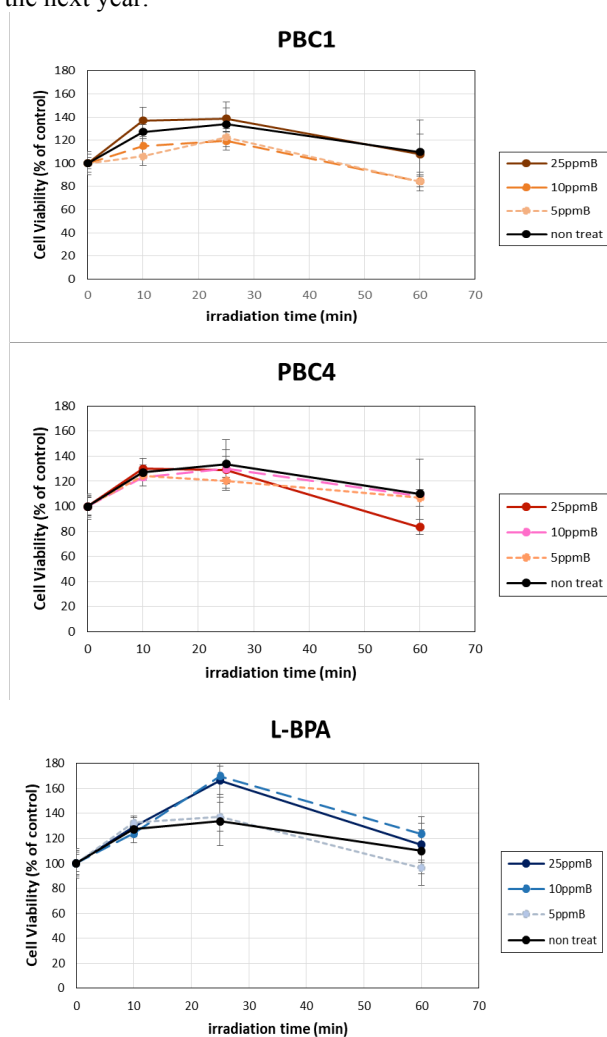


Fig. 1. Survivals of U-87MG cells incubated with various boron compounds after neutron irradiation.

REFERENCE:

[1] K. Kettenbach, *et al.*, *Radiochimica Acta.*, **103** (2015) 799-809.

PR10-15 Evaluation of Novel Boron Liposome *in vivo* by Thermal Neutron Irradiation

M. Shirakawa^{1,2}, K. Nakai³, F. Yoshida², T. Tsurubuchi², M. Suzuki⁴, T. Takata⁴, A. Matsumura² and H. Tomida¹

¹ Department of Pharmaceutical Sciences, University of Fukuyama

² Department of Neurosurgery, Faculty of Medicine, University of Tsukuba

³ Department of Neuro-rehabilitation, Ibaraki Prefectural University Hospital

⁴ Research Reactor Institute, Kyoto University

INTRODUCTION: For the tumor treatment, Boron Neutron Capture Therapy (here in after, also referred to as “BNCT”) is attracting attention as one of the radiation therapy. BNCT could be treated only a malignant tumor cells selectively without damage to normal cell compared with conventional radiation therapy.

Recently, as method of boron accumulation, BDS (Boron Delivery System) using DDS (Drug Delivery System) is remarkable in BNCT. A liposome which is widely used as DDS material is prior for BDS.

Therefore, we developed novel lipid (name PBL^[1]) and prepared liposome using this lipid. In this report, we have irradiated the liposome *in vivo*.

EXPERIMENTS: The liposome modified with PBL prepared using the lipids by conventional lipid-film method^[2] and the constant ratio(Table.1). BSH was encapsulated to liposome by freeze-thaw method^[3]. The resulting liposomes were extruded with an extruder through a polycarbonate membrane with a 100-nm pour size, yielding the boron liposome.

Table.1) Lipid construction (molar ratio)

Lipid	DSPC	Cholesterol	PBL
PBL-liposome	48	48	4

The cancer-bearing models were prepared by grafting mouse colon cancer cells (CT26, 3×10^6 cells) to the right thighs of BALB/cA mice (female, 5 weeks old, weighing 16-20 g) to have a tumor diameter of 6-8 mm.

After 2 weeks, each samples (Table.2) were injected to the tail vein of the prepared tumor-bearing mice and, after 48 hours, neutron irradiation was conducted with KUR. BSH was injected 2 hours before irradiation as positive control group. The thermal neutron dose was 5.2×10^{12} neutrons/cm² for 2 hours.

Table.2) Samples and the concentration of ¹⁰B.

Sample	PBL-liposome	BSH-encapsulated PBL-liposome	free BSH
¹⁰ B conc. [mgB/kg]	10	15	57
Lipid conc. [mg/mL]	108	108	—

The tumor size was determined over time after the irradiation until Day 26 so as to compare the effect of inhibiting tumor growth with the control group. The tumor sizes were determined according to the following formula.

$$\text{tumor size (mm}^3\text{)} = (\text{Long diameter (mm)} \times (\text{Short diameter (mm)})^2) / 2$$

RESULTS: As shown in Figure 1, the PBL-liposome and BSH-encapsulated PBL-liposome significantly inhibited the tumor growth as compared to other control groups onward Days 11. In particular, the tumor did not grow until Day 11.

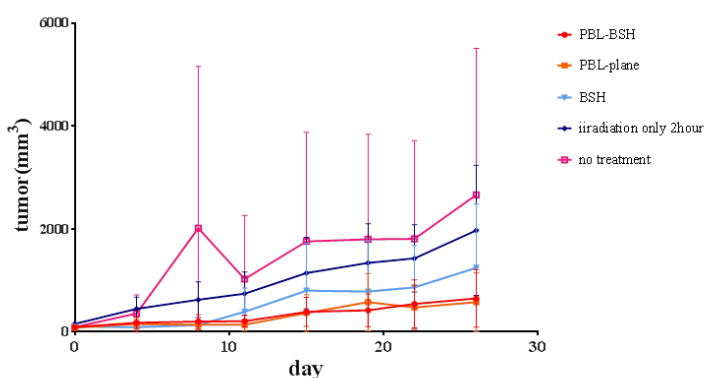


Fig.1) Anti-tumor effect of BNCT by boron liposome.

Tumor growth size after thermal neutron irradiation with the injection of PBL-liposome (PBL-plane, n=3), BSH-encapsulated PBL-liposome (PBL-BSH, n=6) and free BSH (BSH, n=4). As controls, tumor growth size with irradiation only (n=6) and untreated (no treatment, n=3).

REFERENCES:

- [1] M. Shirakawa, K. Nakai, A. Matsumura., Boron cluster-modified PEG lipid derivative, and molecular assembly using the same., Japanese Patent No. 6206925 and European Patent No.2889302.
- [2] A.D. Bangham *et al.*, J. Mol. Biol., 13, 238-252 (1965).
- [3] N. Oku., LIPOSOME NO SAKUSEI TO ZIK-KENNHOU (Preparation of liposome and the experiment), pp43-63, HIROKAWA publishing co. (1994).

R. Ubagai, W. Kurosawa, K. Matsumoto, Y. Suga, Y. Kitahara, Y. Sakurai¹, K. Mouri¹, D. Novriana¹, M. Yanagawa², T. Nomoto³, N. Nishiyama³, T. Fujino⁴, T. Nagasaki⁵, H. Takahashi⁶, H. Yanagie¹, H. Tanaka⁷, Y. Sakurai⁷, K. Ono⁷ and M. Suzuki⁷

Institute for Innovation, Ajinomoto Co., Inc., ¹Niigata University of Pharmacy and Applied Life Sciences, ²Obihiro University of Agriculture and Veterinary Medicine, ³Tokyo Institute of Technology, ⁴Saitama Medical University, ⁵Graduate School of Engineering, Osaka City University, ⁶Graduate School of Engineering, The University of Tokyo, ⁷Research Reactor Institute, Kyoto University

INTRODUCTION: *p*-Boronophenylalanine (¹⁰BPA) and sodium borocaptate (¹⁰BSH) as neutron capture agents show superior selective tumour accumulation property, but low tumour retentivity, so administration several hours before the radiation and persistent administration are necessary for effective BNCT in clinically.

In this study, we synthesized the novel boron compound which had superior tumour retentivity, and evaluated the anti-tumour effect by neutron capture reaction.

EXPERIMENTS: We prepared the tumour bearing mice model after injection of CT26 mouse colorectal cancer cells (3×10^6 cells) into the right femoral region subcutis of the female Balb/c mice.

Two dosage of BN2018 (7.2 mg [¹⁰B]/kg, 14.4 mg [¹⁰B]/kg) as tested compound, and fructose chelate of ¹⁰BPA 300 mg/kg (14.4 mg [¹⁰B]/kg) as a positive control was administrated by tail vein injection under awakening 24 hours (BN2018), 2 hours (¹⁰BPA) before radiation, respectively (each group n=7). As the control group, group of irradiation only (n=9), group of BN2018 (14.4 mg [¹⁰B]/kg) administration (n=4), and untreated group (n=7) were used.

The tumour-bearing mice were irradiated with epi-thermal neutrons of 3×10^{12} n/cm² average fluence at the KUR. The reactor power was 1MW, and irradiation was carried out for 60min. After irradiation, the effect of BNCT was evaluated on the basis of tumour volume (calculated as $1/2 \times \text{length} \times \text{width}^2$) until 26th days postirradiation.

RESULTS: The results of epi-thermal neutron irradiation is shown in Fig. 1. The effect on weight in all individuals was not found (a). Tumour growth suppression effect was found in the comparison of the tumor volume increase rate for untreated group in the BN2018 administrated group and the ¹⁰BPA administrated group (b). In comparison between groups of the 26th day post-irradiation in the individual which is with 210mm³ or less of tumour size before the irradiation, the tumor growth suppression effect in the BN2018 (7.2 mg of [¹⁰B]/kg) administrated group is significantly found compared with untreated group (c-1). Only a tendency to suppression was confirmed compared with the group of

irradiation only (c-2). It was also found that the BN2018 had slightly weak depression effect compared to the ¹⁰BPA administrated group (c-3).

We could be confirmed that the tumour growth suppression effects by BNCT in the group of BN2018 (7.2 mg of [¹⁰B]/kg) administrated 24 hours before irradiation is equal to the effects in the group of ¹⁰BPA (14.4 mg of [¹⁰B]/kg) administrated 2 hours before irradiation.

In this study, we showed the tumour growth suppression effects derived the highly tumour retentivity of BN2018 by BNCT. This novel compound has possibility to be applied to BNCT as tumour selective ¹⁰B compound in future.

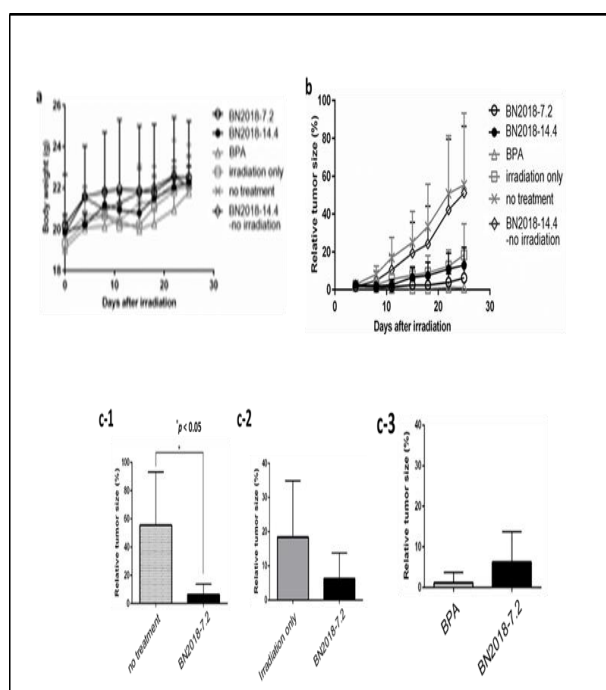


Fig. 1. BNCT for tumor-bearing mice after thermal neutron irradiation for 1 hr (3×10^{12} neutrons/cm²). (a) Average bodyweight of mice. (b) Tumor growth ratio of tumor-bearing mice with injection of ¹⁰B-enriched BN2018 (7.2 mg [¹⁰B]/kg and 14.4 mg [¹⁰B]/kg) 24 hr before irradiation, ¹⁰BPA (14.4 mg [¹⁰B]/kg) 2 hr before irradiation, or irradiation only. The mice without treatment served as controls. (c) Tumor growth ratio of tumor-bearing mice with a tumor size of 210 mm³ or less before irradiation with injection of ¹⁰B-enriched BN2018 (n = 5, 7.2 mg [¹⁰B]/kg) vs. (c-1) no treatment (n = 5), (c-2) irradiation only (n = 9) and (c-3) ¹⁰B-enriched BPA (n = 7, 7.2 mg [¹⁰B]/kg) 26 days after thermal neutron irradiation.

M. Suzuki

Research Reactor Institute, Kyoto University

Summary

This research projects consists of three clinical research programs on BNCT for malignancies other than malignant brain tumors or head and neck cancers. In P11-1, three patients were treated with BNCT. In P11-2, no patient was recruited in their study. In P11-3, no patient was recruited in their study. Yanagie (Principal investigator of P11.3) et al. reported basic study on BNCT for hepatocellular carcinoma (HCC) using a pig.

P11-1

In P11-1 clinical research study, three patients including two malignant soft tissue tumors and one malignant plural mesothelioma (MPM) were treated with BNCT. BNCTs for two malignant soft tissue tumors, clear cell sarcoma and synovial sarcoma, were the first attempts in the world. BNCT for MPM was carried out to alleviate the symptom such as stiffness of neck or back from huge tumors of MPM.

Summary of the BNCT procedure and dose-distribution in the BNCT for MPM was reported in the report of P11-1.

Details of the case reports of three cases will be reported after proving the consequence of BNCTs.

P11-3

Yanagie et al. reported a preclinical study on feasibility of intra-arterial injection of ^{10}B SH entrapped water-in-oil-in-water (WOW) emulsion using pig. They performed intra-arterial injection according to the injection data that maximum dose 0.8mL/kg was injected for rabbit experiments, equivalent maximum dose for pig is possible to be injected 8mL/body. Transient hypotension at a 2mL infusion of WOW emulsion was happened in this experiment, but it was improved. The constitution drugs of this emulsion are safety, because ^{10}B SH is used in a clinic of BNCT, and the lipiodol and the surfactant HCO40 are authorized from the Ministry of Health.

The abnormal changes in the liver, the kidney, the heart, the pancreas were not found in the histopathologic examination one week after intra-arterial injection of ^{10}B SH entrapped WOW emulsion.

M. Suzuki, S. Masunaga, Y. Kinashi, H. Tanaka, Y. Sakurai, N. Kondo, Y. Tamari, T. Fujimoto¹, E. Shibata² and T. Kijima²

Research Reactor Institute, Kyoto University

¹*Department of Orthopedic Surgery, Hyogo Cancer Center*

²*Division of Respiratory Medicine, Department of Internal Medicine, Hyogo College of Medicine*

Introduction

Boron neutron capture therapy (BNCT) has been applied mainly for the treatment of locally recurrent malignant brain tumors or head and neck cancers in the irradiated region using neutron beams from the research reactor. In some BNCT clinical trials, the survival data or tumor response were suggested to be better compared those by other clinical studies. Collaborative project to develop an accelerator-based (AB)-BNCT system between Sumitomo Heavy Industrial and Kyoto University succeeded to construct available cyclotron-based AB-BNCT system.

Clinical trials using the AB-BNCT system are currently in progress. The targets of the ongoing clinical trials are two malignancies as follows: recurrent malignant gliomas and head and neck cancers. In a few years, the system and boron-containing drug is expected to get medical device approval and pharmaceutical approval from national agency. Since the AB-BNCT system installed in the hospital is available to more patients suffering from malignant tumors compared with those by the BNCT using research reactor. However, in a few years before getting medical device approval and pharmaceutical approval, patients with malignant tumors other than malignant gliomas and head and neck cancers will be treated with research reactor-based BNCT. When the AB-BNCT system will be applicable to many clinical trials to search for new application of BNCT in the hospitals, experience of BNCT for new malignancies will be helpful for the new clinical AB-BNCT trials.

We treated two patients with malignant tissue soft tissue sarcoma and one patient with malignant pleural mesothelioma (MPM) in this research program. In this report, we present summary of the BNCT for malignant pleural mesothelioma.

BNCT for malignant pleural mesothelioma

A 64 year-old man with MPM had received a number of chemotherapy cycles. His main symptom was stiffness of the neck and back. The large MPM tumors refractory to the chemotherapy located mainly

between the dorsal and lateral skin of the thorax and the pleura rather than between the pleura and the lung parenchyma. He referred to our center for further treatment of MPM with BNCT. Since the tumor was so large that the epithermal neutron beam using the maximum-sized collimator could not encompass all the volume of the tumor, the BNCT was carried out in order to alleviate the symptom.

The BNCT for the large MPM tumors mainly located between the dorsal and lateral skin of the thorax and the pleura was performed with an epithermal neutron beam using a 24 x 24 cm square collimator. The irradiation time, 20 minutes, was determined according to the dose constraint for the skin. Dose constraint was set to 9.0 Gy-Eq as a maximum dose for the skin. The dose delivered to the tumors ranged from 0.1 to 58 Gy-eq. Since approximately one third of the whole tumor volume existed out of the collimator, the tumor volume greater than 50 % of the tumor received less than 20 Gy-eq. However, the tumor volume greater than 1,500 cm³ was irradiated with the dose greater than 20 Gy-eq. The maximum dose delivered to the liver, left lung and spinal cord was 4.6 Gy-eq, 7.5 Gy-eq and 1.9 Gy-eq, respectively. The mean left lung dose was 2.8 Gy-eq. For two month after BNCT, no acute adverse event greater than grade 3 was experienced. At two months after BNCT, a grade 2 lymphopenia developed. The computed tomography (CT) examined at one month after BNCT, the tumor size remained stable in size.

No severe acute adverse event was observed in the treatment of large MPM tumor with BNCT.

PR11-2 Pilot Study of Single Dose Toxicity Evaluation of ¹⁰BSH Entrapped WOW Emulsion on Intraarterial Delivery in Pig for Neutron Capture Therapy to Hepatocellular Carcinoma

H. Yanagie^{1,2,3}, M. Fujihara⁴, Y. Sakurai^{1,3}, K. Mouri^{1,3}, Y. Morishita⁵, M. Yanagawa⁶, Y. Nonaka⁷, Y. Ohno⁸, S. Maruyama⁸, K. Oyama⁸, K. Seguchi⁹, Y. Sakurai¹⁰, H. Tanaka¹⁰, M. Suzuki¹⁰, S. Masunaga¹⁰, K. Ono¹⁰, S. Higashi⁹, M. Ono^{3,11}, J. Nakajima^{3,12}, M. Eriguchi⁸ and H. Takahashi^{2,3}

¹Niigata University of Pharmacy and Applied Life Sciences, ²Dept of Nuclear Engineering & Management, Graduate School of Engineering, The University of Tokyo, ³Cooperative Unit of Medicine & Engineering, The University of Tokyo Hospital, ⁴SPG Techno Ltd. Co., ⁵Dept of Human & Molecular Pathology, Graduate School of Medicine, The University of Tokyo, ⁶Obihiro University of Agriculture & Veterinary Medicine, ⁷Keiai-kai Hoyo Hospital, ⁸Dept of Surgery, Shin-Yamanote Hospital, ⁹Kojin-kai Medical City East Hospital, ¹⁰Research Reactor Institute, Kyoto University, ¹¹Dept of Cardiac Surgery, The University of Tokyo Hospital, ¹²Dept of Thoracic Surgery, The University of Tokyo Hospital, JAPAN

INTRODUCTION: The principle of cancer cell destruction in boron neutron capture therapy (BNCT) is due to the nuclear reaction between ¹⁰B and thermal neutrons to release alpha-particles (⁴He) and lithium-7 ions (⁷Li) after delivery of ¹⁰B atoms to cancer cells selectively. The ⁴He kills cells in the range of 10 µm from the site of ⁴He generation.

Higashi et al prepared a long term inseparable Water-in-oil-in-water (WOW) emulsion by the double emulsification technique to be used in arterial injection therapy to treat patients with hepatocellular carcinoma (HCC) [1, 2].

WOW emulsion could deliver high concentration of 10Boron compounds to cancer tissues, so we applied this delivery system to BNCT. We performed preclinical BNCT study for VX-2 rabbit tumour model using 10BSH-entrapped WOW [3], and also proceeded clinical BNCT study for HCC using this WOW system [4].

In this study, we prepared ¹⁰BSH-entrapped WOW, and evaluated the toxicity by checking histopathological findings after intra-hepatic injection of ¹⁰BSH entrapped WOW emulsion in healthy rabbits.

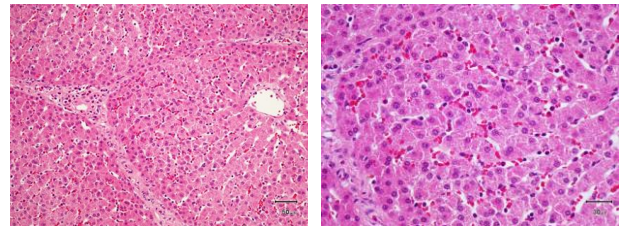
EXPERIMENTS: As a part of the pilot safety evaluation of ¹⁰BSH-entrapped WOW emulsion(175mg ¹⁰BSH/mL), the test article was dosed once by hepatic arterial administration to one female healthy pig at 0.05mL/kg to investigate its toxicity. The investigated items included clinical observation, measurement of body weights and food consumption, blood chemistry, and histopathological findings.

RESULTS: We performed intra-arterial injected ¹⁰BSH entrapped WOW emulsion. According to the injection data that maximum dose 0.8mL/kg was injected for rabbit experiments, equivalent maximum dose for pig is possible to be injected 8mL/body. Transient hypotension at a 2mL infusion of WOW emulsion was happened in this experiment, but it was improved. The constitution drugs of this emulsion are safety, because ¹⁰BSH is used in a clinic of BNCT, and the lipiodol and the surfactant

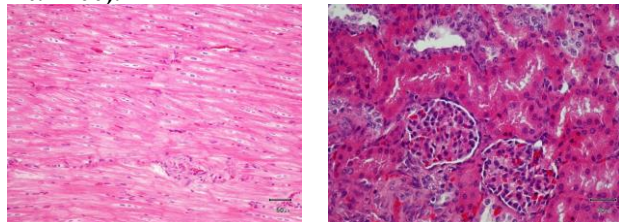
HCO40 are authorized from the Ministry of Health.

The abnormal change in the liver, the kidney, the heart, the pancreas were not found in the histologic examination one week after intra-arterial injection of ¹⁰BSH entrapped WOW emulsion.

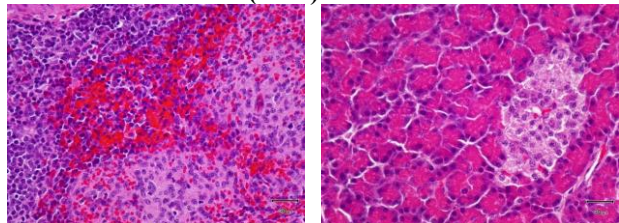
In the next experiments, we hope to increase a dose in quantity of WOW emulsion with an anti-histamine drug or steroid administration to prevent shock or hypotension before hepatic arterial infusion. We hope to refer these results of toxicity examinations to the clinical studies of BNCT to hepatocellular carcinoma with intra-arterial boron delivery using WOW emulsion.



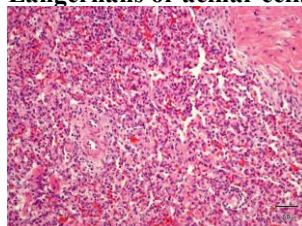
Liver: Hepatocellular denaturation and the destruction are absent (Lt: x200, Rt: x400).



Heart: There is no denaturation of cardiac muscle cells (x400). Kidney: There is no glomerulus or tubular denaturation(x400).



Spleen: There is no lymphatic nodule-centered denaturation(x400). Pancreas: There is no islet of Langerhans or acinar cells denaturation(x400).



Lung: The denaturation of pulmonary epithelial cells is absent(x200).

REFERENCES:

- [1] S Higashi *et al.*, *Cancer*, **75** (1995)1245–1254.
- [2] I. Kushima *et al.*, *Eur J Radiol.*, **69** (2009)114-9.
- [3] H Yanagie *et al.*, *Br J Radiol.* (2017) [Epub ahead of print] doi:10.1259/bjr.20170004.
- [4] H Yanagie *et al.*, *Appl Radiat Isot.*, **88** (2014)32-7.

Y. Sakurai

*Institute for Integrated Radiation and Nuclear Science,
Kyoto University*

BACKGROUNDS AND PURPOSES:

Several types of accelerator-based irradiation system for boron neutron capture therapy (BNCT) are under development at present. But, there are a number of subjects, which should be improved for the further advance and generalization of BNCT.

In the viewpoints of medical physics and engineering, the advance for dose estimation is one of the important subjects. For the characterization of irradiation field, quality assurance and quality control (QA/QC), clinical irradiation to actual patient, and so on, an ultimate goal is to perform the three-dimensional and real-time dose estimation in discriminating for thermal, epi-thermal and fast neutron doses, gamma-ray dose, and boron dose, with simplicity and low effort. Considering about this ultimate dose estimation, several kinds of dose estimation method are studied. It is so difficult to realize the ultimate dose estimation using only one method, but it is necessary to combine more than two methods.

The purposes of this project research are the advance for the respective dose estimation methods, and the establishment of an integrated system for dose estimation in BNCT.

In the first year of this research project, 2017, the fundamental characterization for the respective methods was performed mainly using Heavy Water Neutron Irradiation Facility of KUR, and the direction for the advance was decided.

RESEARCH SUBJECTS:

The collaboration and allotted research subjects (ARS) were organized as follows;

ARS-1 (29P12-1): Establishment of characterization estimation method in BNCT irradiation field using Bonner sphere and ionization chamber. (Y. Sakurai, R. Uchida, T. Takata, H. Tanaka, S. Shiraishi, N. Ko, K. Okazaki, T. Kawamura, M. Sato, K. Akita, and M. Suzuki)

ARS-2 (29P12-2): Basic study on new type of neutron spectrometer for epi-thermal energy region. (A. Uritani, N. Suda, K. Watanabe, S. Yoshihashi, A. Yamazaki, H. Shimizu, and Y. Sakurai)

ARS-3 (29P12-3): Improvement of SOF detector system for long-term stability. (M. Ishikawa, Y. Murayama, K. Baba, Y. Sakurai, and M. Suzuki)

ARS-4 (29P12-4): Response of a commercial CsI detector for the self-activation method in BNCT field. (A. Nohtomi, R. Kurihara, G. Wakabayashi, Y. Sakurai, and T. Takata)

ARS-5 (29P12-5): Neutron beam quality and dose measurement of the Kyoto University Research Reactor using microdosimetric technique. (N. Ko, S. Endo, K. Tanaka, T. Kajimoto, M. Takada, T. Takata, Y. Sakurai, and H. Tanaka)

ARS-6 (29P12-6): Study for microdosimetry using silicon-on-insulator microdosimeter in the BNCT irradiation field. (Y. Sakurai, N. Ko, R. Uchida, T. Takata, H. Tanaka, T. L. Tran, J. Davis, S. Guatelli, A. Rozenfeld, N. Kondo, and M. Suzuki)

ARS-7 (29P12-7): Estimation of dose resolution by gel detector for BNCT. (R. Maruta, K. Tanaka, Y. Murakami, Y. Sakurai, T. Kajimoto, H. Tanaka, T. Takata, and S. Endo)

ARS-8 (29P12-8): Study on the development of neutron fluence distribution measurement device using thermoluminescence of the ceramic plates. (K. Shinsho, S. Yanagisawa, Y. Koba, G. Wakabayashi, and H. Tanaka)

ARS-9 (29P12-9): The study for development and application of tissue equivalent neutron dosimeter. (M. Oita, T. Kamomae, T. Takada, and Y. Sakurai)

ARS-10 (29P12-10): Development and evaluation of 3D polymer gel dosimeter for the measurement of dose distribution in BNCT. (S. Hayashi, Y. Sakurai, M. Suzuki, T. Takata, and R. Uchida)

ARS-11 (29P12-11): Establishment of beam-quality estimation method in BNCT irradiation field using dual phantom technique. (Y. Sakurai, T. Takata, H. Tanaka, N. Kondo, and M. Suzuki)

ARS-12 (29P12-12): Development of real-time dose monitor using prompt rays imaging detector for boron neutron capture therapy. (H. Tanaka, K. Okazaki, T. Takata, Y. Sakurai, and M. Suzuki)

ARS-13 (29P12-13): Radiation damage experiment on novel scintillator material and study on material for development of irradiation monitor in BNCT. (S. Kurosawa, A. Yamaji, T. Horiai, S. Kodama, and H. Tanaka)

ARS-14 (29P12-14): Basic study for QA/QC in BNCT irradiation field. (S. Nakamura, T. Nishio, H. Okamoto, A. Wakita, S. Ito, J. Itami, H. Igaki, M. Munechika, S. Tanaka, Y. Sakurai, H. Tanaka, T. Takata, and M. Suzuki)

ARS-15 (29P12-15): Patient-position monitoring system for BNCT irradiation. (T. Takata, H. Tanaka, Y. Sakurai, and M. Suzuki)

For ARS-14, no results were obtained because no machine time were used due to the short of operation time of KUR and the schedule of the collaborators. So, the report of this research subject is not appeared.

PR12-1 Establishment of Characterization Estimation Method in BNCT Irradiation Field using Bonner Sphere and Ionization Chamber

Y. Sakurai, R. Uchida¹, T. Takata, H. Tanaka, S. Shiraishi¹, N. Ko¹, K. Okazaki¹, T. Kawamura¹, M. Sato¹, K. Akita^{1,2} and M. Suzuki

Institute for Integrated Radiation and Nuclear Science, Kyoto University

¹*Graduate School of Engineering, Kyoto University*

²*Osaka Medical School*

INTRODUCTION: Research and development into several types of accelerator-based irradiation systems for boron neutron capture therapy (BNCT) is underway [1,2]. In the near future, BNCT using these newly developed irradiation systems may be carried out at multiple facilities across the world. Considering this situation, it is important that the estimations for dose quantity and quality are performed consistently among several irradiation fields, and that the equivalency of BNCT is guaranteed, within and across BNCT systems. Then, we are establishing the quality assurance and quality control (QA/QC) system for BNCT irradiation field.

As part of the QA/QC system, we are developing estimation method for neutron energy spectrum using Bonner sphere [3]. For our spectrometer using Bonner sphere, liquid such as pure water and/or boric acid solution is used as the moderator. A multi-layer concentric-sphere case with several sphere shells is prepared. The moderator and its diameter are changeable without entering the irradiation room, by the remote supply and drainage of liquid moderator in the several layers. For the detector, activation foils are remotely changed, or online measurement is performed using SOF (scintillator with optical fiber) detector containing boron, etc. [4]. The development of this remote-changeable Bonner-sphere spectrometer is reported.

METHODS: In the neutron energy spectrometry by Bonner-sphere and activation foils, the combinations of the moderator material and diameter should be previously decided and prepared. Of course, the more information can be obtained as the more moderators and detectors are prepared. However, the information number from those measured data is less than the combination number, because of the overlapped regions among the combinations. The selection is important, in which the more information number is obtained for the combination number.

The combination of moderator and detector is decided, for that the response functions cannot be approximated by the linear functions of the other response functions. The accuracy and precision for the spectrometry can be higher, because the independent information can be obtained from the measurement by the respective combinations.

We were developed the selection method, High Independence Selection (HIS) [5].

On the assumption of the application in a typical BNCT

irradiation field, the combination of the moderators for boron-10 concentration and diameter was optimized by HIS.

RESULTS: The optimized structure was selected by HIS as follows: three sphere shells such as 13, 18 and 20 cm in diameter, and three liquid moderators such as pure water, 0.028-wt% boron acid solution and 0.7-wt% boron acid solution, as shown in Fig.1.

CONCLUSION: We have a plan to make the remote-changeable Bonner-sphere spectrometer, based on the optimization result. Additionally, we have a plan to perform the spectrometry experiments at Kyoto University Reactor (KUR), etc., in order to confirm the efficacy of this spectrometer.

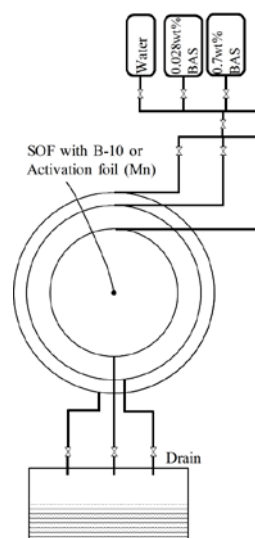


Fig. 1. Optimization for the structure of the remote-changeable Bonner-sphere spectrometer.

REFERENCES:

- [1] H. Tanaka *et al.*, Nucl. Instr. Meth. B **267** (2009) 1970-1977.
- [2] H. Kumada *et al.*, Appl. Radiat. Isot. **88** (2014) 211-215.
- [3] H. Ueda *et al.*, Appl. Radiat. Isot. **104** (2015) 25-28.
- [4] M. Ishikawa *et al.*, Radiat. Oncol. **11** (2016) 105(1-10).
- [5] H. Ueda, Doctoral Thesis (2016).

PR12-2 Basic Study on New Type of Neutron Spectrometer for Epi-thermal Energy Region

A. Uritani, N. Suda, K. Watanabe, S. Yoshihashi,
A. Yamazaki, H. Shimizu and Y. Sakurai¹

Graduate School of Engineering, Nagoya University
²Research Reactor Institute, Kyoto University

[3] K. Watanabe, Y. Kawabata, A. Yamazaki, A. Uritani,
T. Iguchi, K. Fukuda, T. Yanagida, Nuclear Instruments and Methods in Physics Research Section A, **802**, 1 (2015)

INTRODUCTION: Boron neutron capture therapy (BNCT) is one of the promising treatment methods for cancers such as brain tumors. The principle of BNCT was proposed by Locher [1] in 1939. In recent years, an accelerator-driven neutron source has been developed due to its simplicity of management. The C-BENS [2], the first accelerator-driven BNCT facility in the world, built at the Kyoto University Research Reactor Institute. This facility has already been in the clinical trial phase. In commissioning of these facilities, the irradiation field should be characterized in order to assure designed specifications, such as neutron intensity, the neutron energy spectrum and gamma-ray contamination. We are developing an optical fiber type neutron detector, which consists of a small Eu:LiCaAlF₆ scintillator, an optical fiber light guide and photomultiplier tube, for this purpose [3].

In this study, we are developing a new neutron energy spectrometer especially for epithermal neutrons using the optical fiber type detector. The spectrometer consists of some detectors surrounded by relatively small size moderators with various size and/or covered by various resonance foil absorbers. The small size moderators emphasize the energy response for epi-thermal region. In addition, the subtraction method using the resonance absorption foils also improves the epi-thermal energy response. In this paper, we evaluated the energy response of the designed detectors using Monte Carlo simulation code PHITS. We, additionally, carried out the detector tests at the Heavy Water Neutron Irradiation Facility of Kyoto University Research Reactor.

RESULTS: Figure 1 shows the energy responses of the designed detectors. As shown in Fig. 1, some detectors show narrow dips in the response function, corresponding to resonance absorption of each foil absorber. The subtraction method can extract narrow band energy response due to these dip components.

We fabricated the proto-type detector using the optical fiber type detector surrounded by a 5 mm thick polyethylene moderator and covered by a tungsten resonance filter and a cadmium thermal neutron shielding. The sensitivity of the fabricated detector was evaluated to be the order of 10⁻⁷ cm². This sensitivity level is adequate for characterization of the BNCT irradiation fields.

REFERENCES:

- [1] G. L. Locher: Am. J. Roentgenol **36**, 1 (1936).
[2] H. Tanaka, Y. Sakurai, M. Suzuki, S. Masunaga, T. Mitsumoto, K. Fujita, G. Kashino, Y. Kinashi, Y. Liu, M. Takada, K. Ono and A. Maruhashi, Applied Radiation and Isotopes, **69**, 1642 (2011).

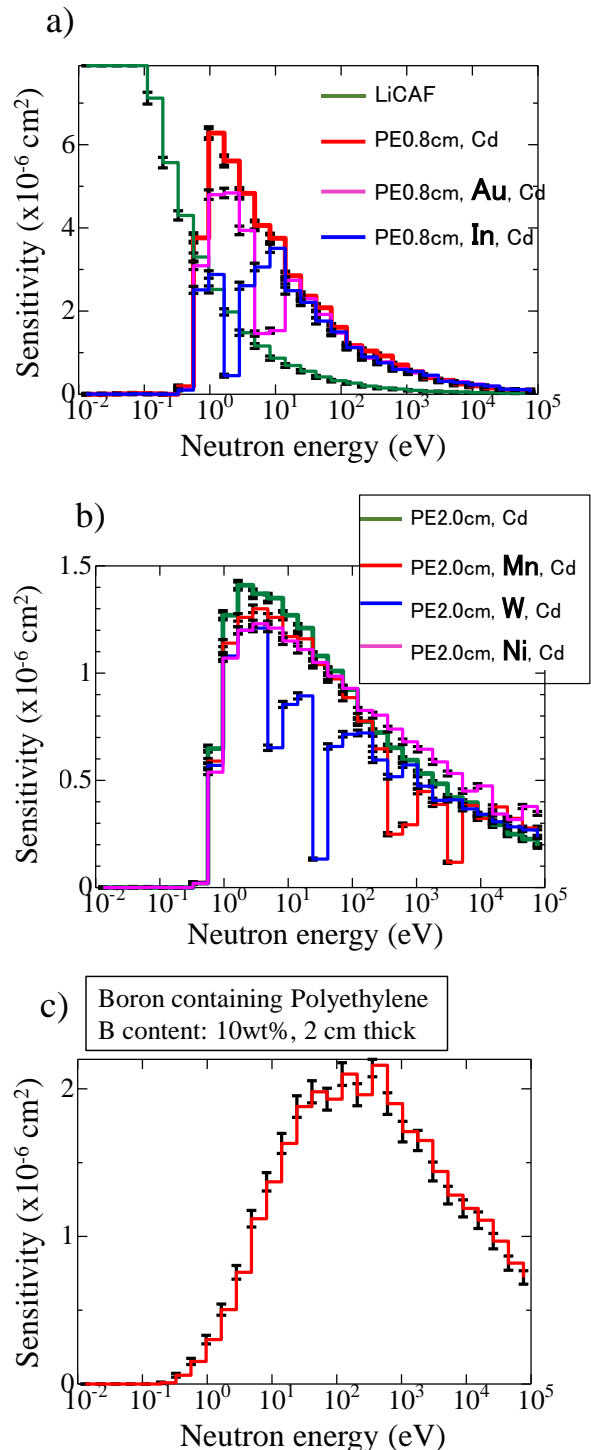


Fig. 1. Energy responses of designed detectors. a) Bare detector and detectors with 8 mm thick PE moderator and some resonance absorbers. b) detectors with 20 mm thick PE moderator and some resonance absorbers. c) detectors with 20 mm thick B-PE moderator.

M. Ishikawa, Y. Murayama, K. Baba¹, Y. Sakurai² and M. Suzuki²

Graduate School of Health Sciences, Hokkaido University

¹Graduate School of Biomedical Science and Engineering, Hokkaido University

²Kyoto University Research Reactor Institute

INTRODUCTION: In boron neutron capture therapy, absorbed dose is evaluated from boron concentration and thermal neutron flux in the tumor area. Conventionally, since gold activation method was used as an evaluation method of thermal neutron flux, absorbed dose could not be evaluated in real time. Therefore, our laboratory has developed a SOF detector (Scintillator with Optical Fiber Detector) to measure thermal neutron flux in real time [1, 2] and reported the usefulness of real-time measurement in clinical practice [3].

As shown in Fig. 1, the SOF detector consists of a small amount of plastic scintillator, a plastic optical fiber, a photo-multiplier tube, a charge pre-amplifier, a discriminator and a counter. The plastic scintillator BC490 is attached to the tip of the plastic optical fiber. A small amount of LiF powder (enriched 95% ⁶Li) is then painted over the plastic scintillator. The reactions between ⁶Li nuclei and thermal neutrons emit charged particles (alpha and triton) which produce scintillation photons in the plastic scintillator. The photon signals are relayed through an optical fiber to the Photon Counting Unit (Hamamatsu H7155) then converted into 30 nsec-width TTL pulse [1]. A paired-SOF method was used for gamma-ray compensation [2].

The SOF detector can measure thermal neutron flux in real time with very wide dynamic range, however, there is a report that output is decreased by long-term measurement under high thermal neutron flux [4]. Therefore, the purpose of this research is to improve the SOF detector system for enabling long-term stable measurement.

EXPERIMENTS: In this study, it is necessary to know the long-term change in measurement performance of the SOF detector. However, the research reactor at Kyoto University Reactor is not available for a long time, we have to calibrate the SOF detector. As shown in Fig. 2, pure thermal neutrons were irradiated to the SOF detector using the E-3 neutron guide tube facility, and conversion coefficients were calculated by comparing a thermal neutron flux evaluated by the gold foil.

RESULTS: A

A thermal neutron flux of the neutron beam from the E-3 neutron guide tube was evaluated using a 50 μm-thick gold foil. The evaluated thermal neutron flux at measured position was 2.65×10^5 [n/cm²/s], and the total thermal neutron fluence was calculated as 2.55×10^8 [n/cm²]. From this thermal neutron fluence, the conversion coefficient

of the SOF detector was determined to be 2.41×10^3 [n/cm²/counts]. For the future work, we will monitor the conversion coefficient change according to high thermal neutron flux irradiation to the SOF detector.

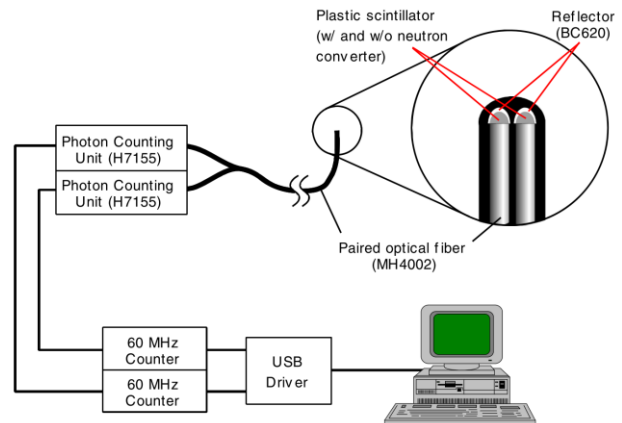


Fig. 1. Schematic illustration of SOF detector system. The SOF detector system consists of a small amount of plastic scintillator, a plastic optical fiber, a photo-multiplier tube, a charge pre-amplifier, a discriminator and a counter.



Fig. 2. Calibration geometry for the SOF detector using pure thermal neutrons from the E-3 neutron guide tube facility. The conversion coefficients were calculated by comparing a thermal neutron flux evaluated by the gold foil.

REFERENCES:

- [1] M. Ishikawa *et al.*, *Appl. Radiat. Isot.*, **61** (2004) 775–779.
- [2] M. Ishikawa *et al.*, *Nucl. Instr. and Meth., A* **551** (2005) 448–457.
- [3] M. Ishikawa *et al.* *Radiat. Oncol.*, **11:105** (2016) DOI: 10.1186.
- [4] M. Komeda *et al.* *Appl. Radiat. Isot.*, **67** (2009) S254-S25.

A. Nohtomi, R. Kurihara, G. Wakabayashi¹, Y. Sakurai² and T. Takata²

Graduate School of Medicine, Kyushu University
¹Atomic Energy Research Institute, Kindai University
²Research Reactor Institute, Kyoto University

INTRODUCTION: In our previous studies [1 - 5], the self-activation of iodine-containing scintillator had been successfully applied for detecting photo-neutrons around a high-energy X-ray radiotherapy machine. Absolute evaluation of neutron intensity is possible by the so-called activation analysis with online measurement. Especially, CsI scintillator is only slightly hygroscopic, and the light output is easily read out by a PD that does not need high-voltage power supply. The self-activation technique has been originally developed for the high sensitive neutron detection at a weak neutron field. In the present work, the applicability of commercially available CsI detectors were studied at rather intense neutron field like BNCT one of KUR irradiation facility for short time irradiation.

EXPERIMENTS: Two types of CsI detectors, Hamamatsu C12137 and Horiba PA1100 (Radi) were irradiated at Irradiation Rail Device of the Heavy Water Neutron Irradiation Facility with OO-0000F mode (1MW) [6]. The detectors were put at 1 m from the Bismuth Surface (thermal neutron flux : 5.1×10^7 n/cm²/s) during about 2 seconds, or at the entrance position of Rail Device during about 130 seconds. Two of Radis were covered with 1 mm-t Cd sheet or 5 mm-t B₄C silicon rubber sheet (70%).

RESULTS: Figure 1 shows a typical energy spectrum observed by C12137 just after the termination of 2 seconds irradiation at 1 m from the Bismuth Surface. In addition to continual spectrum of ¹²⁸I beta ray, a conversion electron peak of ^{134m}Cs (~140 keV) and a characteristic X-ray peak of ¹²⁸Te (~30 keV) can be clearly seen.

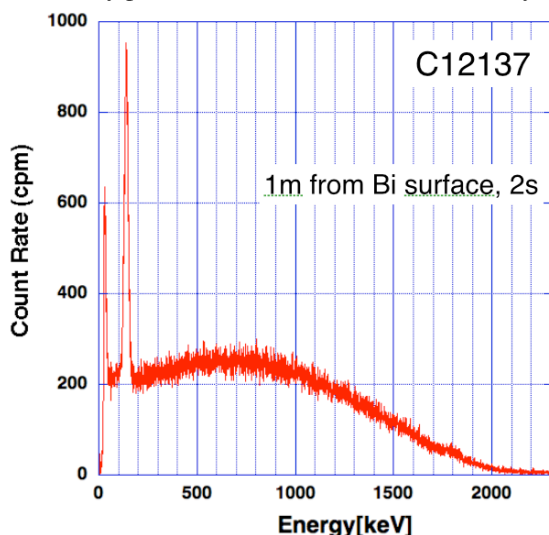


Fig. 1. Typical energy spectrum of CsI self-activation observed by C12137.

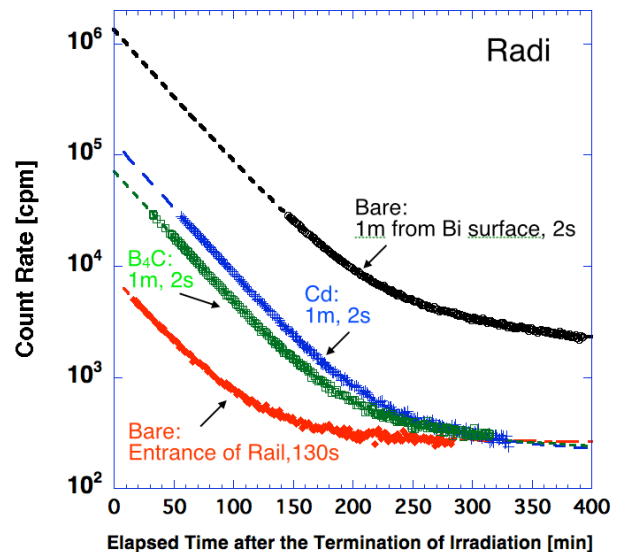


Fig. 2. Decay curves of count rate obtained by Radi for different irradiation conditions.

Decay curves of count rate obtained by Radis are plotted in Fig. 2. Acquired data for every 1 minute through bluetooth interface were fitted well with a combination of ¹²⁸I ($T_{1/2}=25$ min), ^{134m}Cs ($T_{1/2}=174$ min) and constant B.G. components. Then, initial count rate of ¹²⁸I were calculated to evaluate the initial activities. When Radis were put at 1m from the Bismuth Surface and irradiated about 2 seconds, the initial activity was 2.58×10^4 [Bq] for Bare (un-covered) Radi, 2.54×10^3 [Bq] for the Radi with Cd cover and 1.37×10^3 [Bq] for the Radi with B₄C cover. When a Bare (un-covered) Radi was put at the Entrance of Rail Device and irradiated about 130 seconds, the initial activity was evaluated to be 1.43×10^2 [Bq].

From the results mentioned above, it has been confirmed that those commercially available CsI detectors work properly for short time irradiation of intense neutron beam and are applicable to the self-activation method in BNCT field.

ACKNOWLEDGEMENT: This work was partially supported by JSPS KAKENHI Grant Number JP16K10320.

REFERENCES:

- [1] G.Wakabayashi *et al.*, Radiol. Phys. Technol., **8** (2015) 125-134.
- [2] A.Nohtomi and G.Wakabayashi, Nucl. Instr. and Meth., **A800** (2015) 6-11.
- [3] A.Nohtomi *et al.*, JPS Conf. Proc., **11** (2016) 050002.
- [4] A.Nohtomi *et al.*, Nucl. Instr. and Meth., **A832** (2016) 21-23.
- [5] S.Honda *et al.*, Nucl. Instr. and Meth., **A871** (2017) 148-153.
- [6] Y.Sakurai and T.Kobayashi, Nucl. Instr. and Meth., **A453** (2000) 569-596.

Neutron Beam Quality and dose Measurement of the Kyoto University Research Reactor Using Microdosimetric Technique

N. Ko, S. Endo², K. Tanaka², T. Kajimoto², M. Takada³,
T. Takata¹, Y. Sakurai¹ and H. Tanaka¹

Graduate School of Engineering, Kyoto University

¹*Institute for Integrated Radiation and Nuclear Science,
Kyoto University*

²*Quantum Energy Applications, Hiroshima University*
³*Applied Physics, National Defense Academy*

INTRODUCTION: The aim of BNCT is the local energy deposition of high LET particles to the target area. In addition to alpha particles and lithium ions generated from the boron-10 and thermal neutron interaction, protons and gamma rays are also present in the BNCT field. Microdosimetry is an effective tool to measure radiation in a mixed field. Using this technique, it is possible to derive the relative contribution of each radiation component. A tissue equivalent proportional counter (TEPC) measures energy deposition in a simulated micrometer scale volume comparable to that of a living cell. The TEPC uses material and gases that are essentially equivalent to human tissue in chemical composition. This paper presents the radiation beam quality measurements of the thermal and mixed mode irradiation of Kyoto University Reactor (KUR) that is used for both clinical and non-clinical studies, respectively.

EXPERIMENTS: The neutron single event spectrum was measured using the TEPC (LET 0.5 inch chamber, Far West Technology Inc.). To simulate a 1 μm diameter sphere, methane-based tissue equivalent gas was filled at a pressure of 74.5 hPa. The KUR heavy water neutron irradiation facility was operated at thermal, epithermal and mix mode irradiation. The TEPC was placed on top of the treatment couch in the center of the field, as shown in figure 1. Measurements were performed free-in-air and the beam on time for each irradiation was approximately 1 hour. Microdosimetric single event spectra was measured and the event and dose frequency spectra were calculated using the lineal energy, y , which is the deposited energy in an active volume of diameter divided by the mean chord length. Particle and Heavy Ion Transport code System (PHITS) version 2.88 was also used to calculate the microdosimetric spectrum.

RESULTS: Figure 2 shows the microdosimetric spectrum of the mix irradiation mode of KUR measured in air using the TEPC. The electron and proton edge were clearly visible at approximately 15 keV/ μm and 100 keV/ μm , respectively. Figure 3 shows the dose distribution spectrum measured with the TEPC. The major dose contributor was the proton component, having a lineal

energy between 20-100 keV/ μm , followed by the carbon ions at approximately 300 keV/ μm . The PHITS calculation showed similar results to the measured data. The y values below 10 keV/ μm were not obtained due to the high electrical noise of the system. Therefore, all of the gamma components could not be measured. Similar spectrum was obtained with the epithermal irradiation mode and comparison was made with previous experiment performed by Endo et.al [1].



Fig. 1. Image of the experimental set up inside the KUR irradiation room.

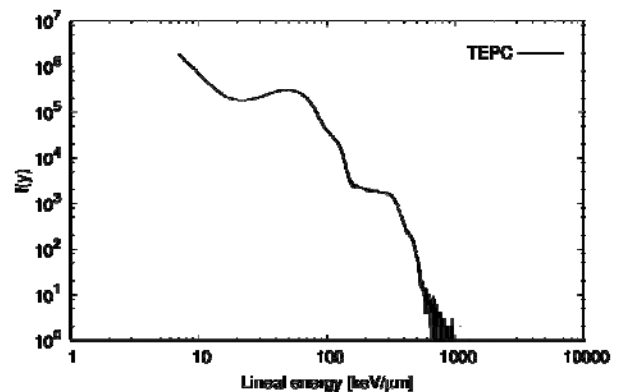


Fig. 2. Microdosimetric single event spectrum of $f(y)$ free in air for mix irradiation mode.

REFERENCE:

[1] S. Endo *et al.*, Radiat. Prot. Dosimetry, **110** (2004) 641-644.

Y. Sakurai, N. Ko¹, R. Uchida¹, T. Takata, H. Tanaka, T. L. Tran², J. Davis², S. Guatelli², A. Rozenfeld², N. Kondo, M. Suzuki

*Institute for Integrated Radiation and Nuclear Science,
Kyoto University*

¹*Graduate School of Engineering, Kyoto University*

²*Centre for Medical Radiation Physics, University of
Wollongong*

INTRODUCTION: Research and development into several types of accelerator-based irradiation systems for boron neutron capture therapy (BNCT) is underway [1,2]. In the near future, BNCT using these newly developed irradiation systems may be carried out at multiple facilities across the world. In contrast to conventional radiotherapy, the types of radiation present in BNCT consists of many distinct radiation components, each having a different biological weighting factor.

Microdosimetry is an effective dosimetry technique in a mixed radiation environment. Using this technique, it is possible to derive the relative contributions of different radiation modalities. The feasibility study of a novel 3D mesa bridge microdosimeter in BNCT [3], developed by University of Wollongong (UOW).

METHODS: The bridge microdosimeter is comprised of an array of 4248 individual silicon cells fabricated on a 10 μm thick n-type silicon-on-insulator substrate.

The performance of the microdosimeter was studied using Monte Carlo simulation. Different boron converter and silicon-on-insulator substrate thickness was modelled and the energy deposition within the detector was simulated using the Particle and Heavy Ions Transport Code System (PHITS). The T-deposit tally in PHITS was used to calculate the energy deposited per event inside the sensitive volume of the bridge microdosimeter. The lineal energy was calculated by dividing the deposited energy per event by the average chord length of the detector.

The clinical BNCT field at Kyoto University Reactor (KUR) using both thermal and epithermal irradiation modes were used in this study.

RESULTS: A thinner boron converter resulted in more reaction particles reaching the sensitive volume of the detector. Approximately double the number of particles reached the detector for a 1- μm thick boron converter as compared to a 0.5 mm thick boron converter. A peak at 120 $\text{keV}/\mu\text{m}$ was observed with both the 0.5mm and 1 μm boron converter and a peak at 200 $\text{keV}/\mu\text{m}$ was observed with no boron converter. A peak in the no converter spectrum arises from the boron p+ dopant in the device.

Figure 1 shows the microdosimetric spectrum obtained from the bridge microdosimeter for the KUR epithermal beam. The range of the alpha particles produced from BNCT is approximately 5 μm . For a 10- μm thick detector,

the alpha particle will come to a full stop inside the sensitive volume, resulting in an inaccurate lineal energy deposition. A 2- μm thick detector was simulated and tested. Results showed the lineal energy deposition was improved with the use of the 2- μm thick sensitive volume detector.

Simulation results showed that the thermal irradiation mode seemed the most appropriate mode to perform the measurements. This was due to the high thermal neutron flux, which resulted in high production of reaction particles, and lower epithermal and fast neutron flux, which resulted in lower recoil silicon particles produced.

CONCLUSION: The microdosimetric spectrum showed each particle can be separated by the use of the lineal energy. The simulation results show that this microdosimeter can be utilized as an effective tool for dosimetry in BNCT field. Experimental validation is planned using KUR.

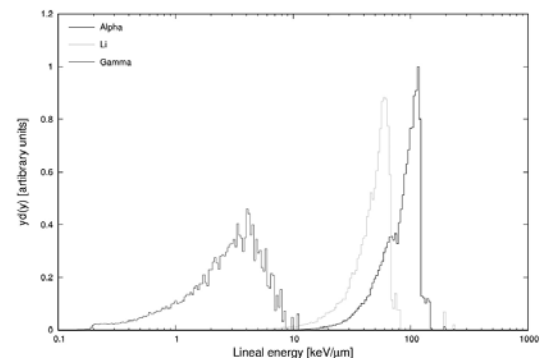


Fig. 1. Microdosimetric spectrum of the KUR epithermal beam generated by PHITS.

REFERENCES:

- [1] H. Tanaka *et al.*, Nucl. Instr. Meth. B **267** (2009) 1970-1977.
- [2] H. Kumada *et al.*, Appl. Radiat. Isot. **88** (2014) 211-215.
- [3] L. T. Tran *et al.*, IEEE Trans. Nucl. Sci. **62** (2015) 3027-3033.

R. Maruta, K. Tanaka, Y. Murakami, Y. Sakurai¹, T. Kajimoto, H. Tanaka¹, T. Takata¹ and S. Endo

Graduate School of Engineering, Hiroshima University
¹Research Reactor Institute, Kyoto University

INTRODUCTION: Evaluation of dose is required for quality assurance in the irradiation field used for boron neutron capture therapy. This study investigated the use of the MAGAT polymer gel detector in the QA by estimation of dose and position resolution.

EXPERIMENTS: The response of the MAGAT to dose was measured. The irradiation was performed by using Co gamma rays irradiation facility at Hiroshima University. The transverse relaxation rate (R_2) was determined using a 0.3T MRI scanner (AIRIS II comfort, Hitachi Medical Corp.) with a standards head coil. It is assumed that the difference in dose can be distinguished if signal intensity differs by 3 times standard deviation (SD). The parameters 'a' and 'b' in Fig.1 were estimated by measuring R_2 for regions with varied diameters. 'c' in Fig.1 was estimated from distance of R_2 decrease from the gel to its outside.

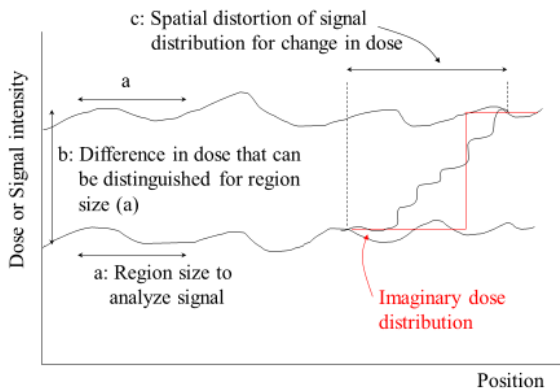


Fig. 1 Schematic drawing of dose and position resolution to be estimated.

RESULTS: As the diameters to be analyzed get smaller, dose resolution tends to decrease. On the other hand, one of the examples that dose resolution could be varied largely at smaller diameters is shown in Fig 2. The diameter of 'a' is required to be 3pixel (3.75mm) or more to distinguish the difference in dose.

Figure 3 shows the decrease of dose resolution associated with the decrease in R_2 at 3pixel diameters. 'b' in Fig.1 is estimated to be about 10-30%.

Figure 4 shows the decrease in R_2 through the gel (- about 6mm) and periphery (about 6mm-). It is estimated

that about 80% decrease in R_2 requires the distance by 2pixel (2.5mm, from 5mm to 7.5mm), and 6pixel (7.5mm, from 5mm to 12.5mm) is required for the decrease in R_2 from the gel to periphery region (considered as a convergence value). Therefore, 'c' is estimated to be about 2.5-7.5mm.

In conclusion, when the irradiation field has the region with low dose or high dose, it is estimated that the difference in dose by 10-30% can be distinguished for the region size of 8.75-18.75mm (7-15pixel).

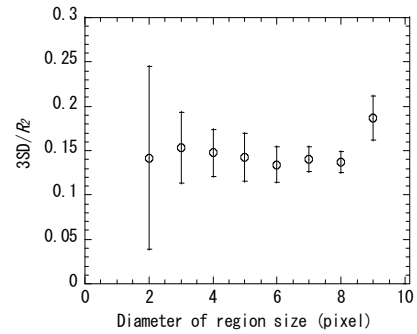


Fig. 2 Dose resolution dependence on diameter of region size to be analyzed signal.

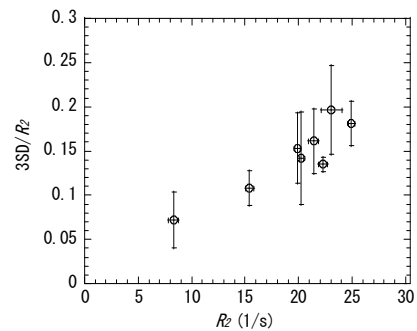


Fig. 3 Dose resolution dependence on signal intensity at 3pixel diameters.

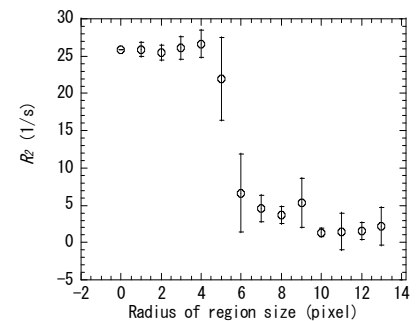


Fig. 4 Change in signal intensity through gel and periphery.

PR12-8 Study on the Development of Neutron Fluence Distribution Measurement Device Using Thermoluminescence of the Ceramic Plates

K. Shinsho, S. Yanagisawa, Y. Koba¹, G. Wakabayashi² and H. Tanaka³

Graduate School of Human Health Science, Tokyo Metropolitan University

¹ Center for Radiation Protection Knowledge, QST-NIRS

² Atomic Energy Research Institute, Kindai University

³ Institute for Integrated Radiation and Nuclear Science, Kyoto University

INTRODUCTION: BNCT (boron neutron capture therapy) is a next-generation cancer treatment that uses a boron compound and neutron irradiation to kill cancer cells selectively. Neutron fluence distribution measurement and the absorbed dose distribution measurement of tumors are required for planning improvement of the treatment precision of BNCT. We have studying TL gamma-ray detectors that primarily use Cr doped Al_2O_3 . [1,2] Luckily, we have also discovered that it has sensitivity toward neutrons, but now wish to increase this sensitivity. As boron has a high neutron cross section, we co-doped Al_2O_3 with Cr and B, in order to generate a higher sensitivity. We investigated the TL glow curves and the dose linearity for neutron and gamma mixed fields.

EXPERIMENTS: Low melting point Al_2O_3 of Chibaceramic MFG Co. LTD. which was composed of $\text{Al}_2\text{O}_3 > 99.5$ wt%, $\text{SiO}_2 < 0.10$ wt%, $\text{Fe}_2\text{O}_3 < 0.05$ wt%, $\text{Na}_2\text{O} < 0.10$ wt%, $\text{Cr} < 2$ ppm, $\text{Cd} < 1$ ppm, $\text{Pb} < 1$ ppm, $\text{Hg} < 1$ ppm was used. The bulk density of the plates was $3.7\text{g}\cdot\text{cm}^{-3}$. The dimensions used for the glow curve measurements were $10\text{ mm} \times 10\text{ mm} \times 1\text{ mm}$. The concentration of Cr_2O_3 in the present study was 0.05 wt% and the concentration of $^{10}\text{B}_2\text{O}_3$ was 0.1 wt%. The assumed irradiation fields are the standard thermal neutron irradiation mode, mixed neutron irradiation mode in KUR-HWNIF, with a power of 1MW. The glow curves were recorded from room temperature up to $400\text{ }^\circ\text{C}$ at a heating rate of $0.1\text{ }^\circ\text{C}\cdot\text{s}^{-1}$.

RESULTS: Fig. 1 shows the Glow curves of Al_2O_3 : 0.05 wt% Cr and Al_2O_3 : 0.05 wt% Cr, 0.1wt% B for neutron and gamma mixed fields. The Al_2O_3 : 0.05 wt% Cr and Al_2O_3 : 0.05 wt% Cr, 0.1wt% B glow curves were the same; the glow peaks were located at $305\text{ }^\circ\text{C}$. In the TL sensitivity, Al_2O_3 : 0.05 wt% Cr, 0.1wt% B was lower than Al_2O_3 :Cr. Although the B doping was not changed the trap state, it were generated lower the TL sensitivity. Fig. 2 shows the dose linearity for neutron and gamma mixed field of Al_2O_3 : 0.05 wt% Cr and Al_2O_3 : 0.05 wt% Cr, 0.1wt% B. Both TL phosphors were indicated the good linearity for irradiation time. Boron usage decreases sensitivity to gamma rays, but it is difficult to ascertain its sensitivity to neutrons. As a result, further studies will separate neutron and gamma ray.

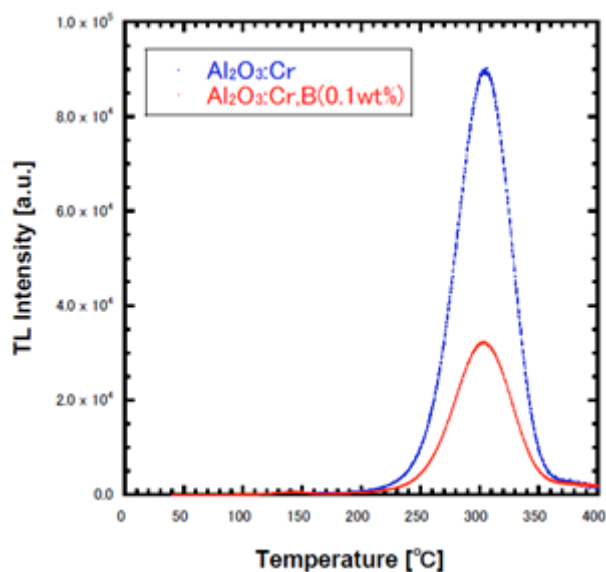


Fig. 1. Glow curves of Al_2O_3 : 0.05 wt% Cr and Al_2O_3 : 0.05 wt% Cr, 0.1wt% B for neutron and gamma mixed field..

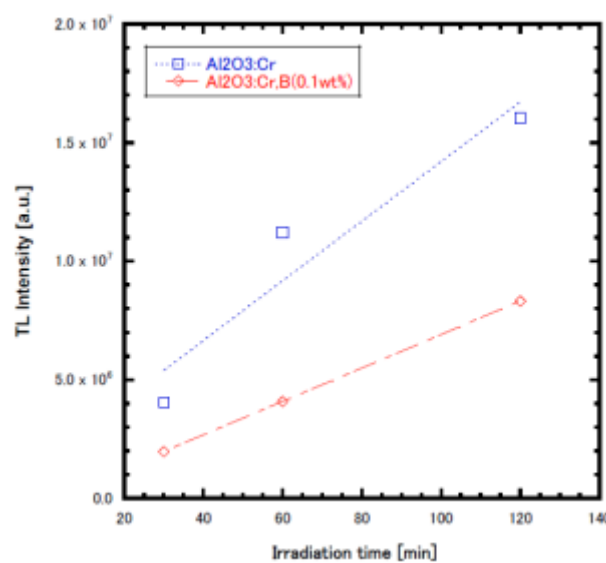


Fig. 2. Dose linearity for neutron and gamma mixed field of Al_2O_3 : 0.05 wt% Cr and Al_2O_3 : 0.05 wt% Cr, 0.1wt% B.

REFERENCES:

- [1] K. Shinsho *et al.*, Applied radiation and isotopes., **111** (2016) 117-123.
- [2] K. Shinsho *et al.*, Sensors and Materials., (2018) in press

PR12-9 The Study for Development and Application of Tissue Equivalent Neutron Dosimeter

M. Oita, T. Kamomae¹, T. Takada² and K. Sakurai²

Graduate School of Health Sciences, Okayama University

¹ Graduate School of Medicine, Department of Radiology, Nagoya University

² Research Reactor Institute, Kyoto University

INTRODUCTION: Recent years, the clinical application of boron neutron capture therapy (BNCT) has been started to make significant contributions to treatment for intractable cancer such as glioblastoma multiforme, superficial head and neck cancer and melanoma in Japan. In BNCT, the boron (n, α)-reaction of the isotope ¹⁰B has a high cross section toward thermal neutrons, and the produced alpha and lithium particles have a short range on the micrometer scale. However, the neutron spectrum always spans a broad energy range, which results in different dose distribution and biological effects in tissue. Therefore, there are some difficulties of neutron dosimetry in clinical practice.

A radiochromic film (RCF) is one of the most useful devices for the QA of radiotherapy equipment. The advantages of RCFs are their high spatial resolution, small energy dependence, tissue equivalence, and self-development without processing in a darkroom¹. A reflective-type RCF, e.g., GAFCHROMIC® EBT3, has been developed for qualitative dosimetry such as stereotactic irradiation (STI) and intensity modulated radiotherapy (IMRT)^{2,3}. In this work, the authors investigated the response of reflective-type RCF for neutron beam as a tissue equivalent dosimeter.

EXPERIMENTS: A reflective-type RCF, GAFCHROMIC® EBT3 (Ashland Inc., Wayne, NJ, USA) using the KUR neutron source was evaluated in this study. The RCFs were handled by the recommendation outlined in the American Association of Physicists in Medicine Task Group No. 55 report¹.

For irradiation, 1.0 × 1.0 cm² pieces of the RCF were placed at the depth of 1 cm-12 cm from the water equivalent phantom surface at central axis and peripheral (Fig.1). Also, the film was placed beneath a gold foil for neutron dosimetry. The RCF pieces were irradiated by the neutron source, respectively.

RESULTS: Fig.1 shows the geometry of irradiation of RCFs by the KUR neutron source. Fig.2 shows the change of pixel values of RCFs irradiated by the source. There was significance difference of pixel values of irradiated RCFs by the neutron source. The change of pixel value of RCF piece between 1 cm and 12 cm at central axis was 11864, while the value with the peripheral was

attenuated by 10807. Also, the value beneath the the gold foil was 23235. The central dose and peripheral dose converted by X-ray calibration of the RCF in the air were 237.2 cGy and 216.0 cGy, respectively. Besides neutrons, the RCFs were exposed to gamma rays coming from events taking place in the source itself and the surrounding moderator. Further analysis was needed of the response of RCFs with neutron spectrum and contributions of gamma rays using Monte Carlo simulation. However, the results suggested that the dosimetry using RCFs is important for a better knowledge of fast neutron flux distribution with the KUR neutron source. Moreover, it would be feasible for BNCT dosimetry in medical application.

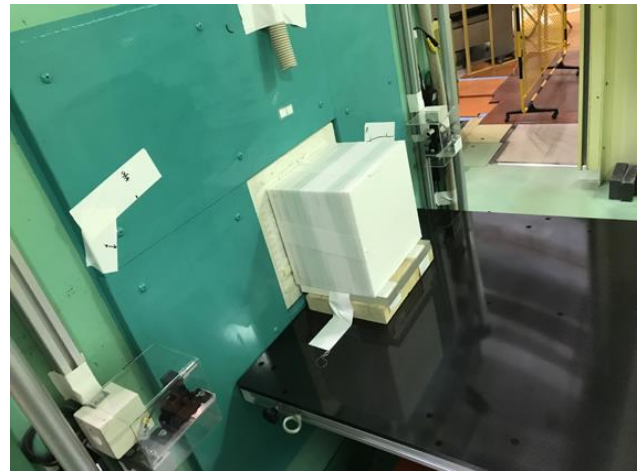


Fig. 1. The geometry of irradiation of RCFs by the KUR neutron source.

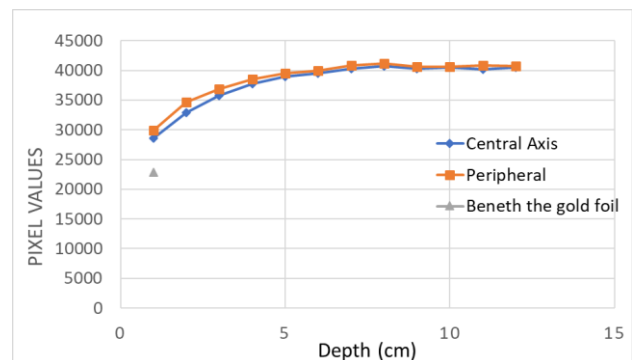


Fig. 2. The change of pixel values of the RCFs irradiated by the KUR neutron source.

REFERENCES:

- [1] Niroomand-Rad, Azam, *et al.* Medical physics **25** (1998) 2093-2115.
- [2] Borca, Valeria Casanova, *et al.* Journal of applied clinical medical physics **14** (2013).
- [3] Fiandra, Christian, *et al.* Medical physics **40** (2013).

PR12-10 Development and Evaluation of 3D Polymer Gel Dosimeter for the Measurement of dose Distribution in BNCT

S. Hayashi, Y. Sakurai¹, M. Suzuki¹, T. Takata and R. Uchida¹

Department of Clinical Radiology, Hiroshima International University

¹*Research Reactor Institute, Kyoto University*

INTRODUCTION: Polymer gel dosimeters have been investigated for the three-dimensional (3D) dose measurement of the complex conformal dose distributions in the clinical applications [1]. These devices utilize radiation-induced polymerization reaction of vinyl monomer in the aqueous gel matrix to preserve information about the radiation dose. The 3D absorbed dose distribution is deduced from the created polymer distribution measured by imaging modalities such as MRI and Optical CT.

Polymer gel dosimeter is also regarded as tissue equivalent to neutron beam because the components are mainly water and a small amount of other chemicals consisting of carbon, nitrogen and oxygen. A further advantage of polymer gel dosimeters is that the interaction with neutron could be controlled by addition of some compounds with neutron-capture-nuclei such as ¹⁰B and ⁶Li. It means that each dose component might be distinguished from complex dose due to various primary and secondary radiations by the variety of elemental composition.

In this work, the influence of ¹⁰B and ⁶Li on the dose-response of polymer gel dosimeters was investigated by thermal neutron beam and compared the results of Monte Carlo simulations.

EXPERIMENTS: We prepared three types of polymer gel dosimeter in this work: (1) standard MAGAT polymer gel dosimeter composed of water (87 wt.%), methacrylic-acid (5 wt.%), gelatin (8 wt.%) and 2 mM of Tetrakis (hydroxymethyl) phosphonium chloride, (2) MAGAT added with 5 mM of ⁶Li enriched (96 at.% ⁶Li) lithium sulfate and (3) 25 mM boric acid of natural isotopic composition. The dosimeters prepared were subdivided into quartz test tubes and placed at 2.5, 5.0 and 7.5 cm depths

in 10 cm × 10 cm × 10 cm cubic water phantom in order for the dosimeters to be irradiated with different neutron energy spectra.

The neutron irradiations were carried out using the epithermal neutron irradiation mode of Heavy Water Neutron Irradiation Facility at Kyoto University Reactor. The dosimeters were irradiated for 1 and 2 hours during 1 MW reactor operation at room temperature.

The read-out from the samples was performed using a 0.3 T MRI scanner (0.3 T AIRIS II Comfort, Hitachi medical) with a head coil the day after irradiation. A multiple spin-echo sequence was applied and the transverse relaxation rate $R_2 (=1/T_2)$ was obtained as the function of absorbed dose.

Monte Carlo simulations were performed using PHITS code. Absorbed dose for the dosimeters were calculated by energy deposition of each secondary charged particle. LET distributions of the absorbed dose were also calculated using T-LET tally of PHITS code. The measured values using gold activation foils and BeO TLDs were utilized to normalize the calculated neutron fluence and gamma-ray dose respectively. The dose-response curves were obtained and the relationship between dose-response characteristics and LET distributions was analyzed.

RESULTS: The response of the three types of dosimeter to ⁶⁰Co gamma-ray was almost identical. For neutron irradiations, the dose-response characteristics varied for different types of the dosimeter and neutron energy spectra. The relative efficiency of converting absorbed energy into the dosimeter response decreased monotonically up to one-fifth with increasing dose-mean LET. The more detailed analysis is underway.

(These results would be presented at 18th International Congress on Neutron Capture Therapy, 2018, ICNCT-18 in Taipei, Taiwan.)

REFERENCE:

[1] C. Baldock *et al.*, Phys. Med. Biol. **55** (2010) R1–63.

PR12-11 Establishment of Beam-quality Estimation Method in BNCT Irradiation Field using Dual Phantom Technique

Y. Sakurai, T. Takata, H. Tanaka, N. Kondo and M. Suzuki

Institute for Integrated Radiation and Nuclear Science, Kyoto University

INTRODUCTION: Research and development into several types of accelerator-based irradiation systems for boron neutron capture therapy (BNCT) is underway [1,2]. Many of these systems are nearing or have started clinical trials. Before the start of treatment with BNCT, the relative biological effectiveness (RBE) for the fast neutrons (over 10 keV) incident to the irradiation field must be estimated.

Measurements of RBE are typically performed by biological experiments with a phantom. Although the dose deposition due to secondary gamma rays is dominant, the relative contributions of thermal neutrons and fast neutrons are virtually equivalent under typical irradiation conditions in a water and/or acrylic phantom. Uniform contributions to the dose deposited from thermal and fast neutrons is based in part on relatively inaccurate dose information for fast neutrons.

The aim of this study is the establishment of accurate beam-quality estimation method mainly for fast neutrons by using two phantoms made of different materials, in which the dose components can be separated according to differences in the interaction cross-sections. The fundamental study of a “dual phantom technique” for measuring the fast neutron component of dose is reported [3].

METHODS: One phantom was filled with pure water. The other phantom was filled with a water solution of lithium hydroxide (LiOH) capitalizing on the absorbing characteristics of lithium-6 (Li-6) for thermal neutrons.

Monte Carlo simulations were used to determine the ideal mixing ratio of Li-6 in LiOH solution. Changes in the depth dose distributions for each respective dose component along the central beam axis were used to assess the LiOH concentration at 0, 0.001, 0.01, 0.1, 1 and 10 weight percent.

Simulations were also performed with the phantom filled with 10 weight percent $^6\text{LiOH}$ solution for 95%-enriched Li-6. A phantom was constructed containing 10 weight percent $^6\text{LiOH}$ solution based on the simulation results.

Experimental characterization of the depth dose distributions of the neutron and gamma-ray components along the central axis was performed at KUR Heavy Water Neutron Irradiation Facility using activation foils and thermo-luminescent dosimeters, respectively.

RESULTS: Simulation results demonstrated that the absorbing effect for thermal neutrons occurred when the LiOH concentration was over 1%. The most effective Li-6 concentration was determined to be enriched $^6\text{LiOH}$ with a solubility approaching its upper limit.

Experiments confirmed that the thermal neutron flux and secondary gamma-ray dose rate decreased substantially however the fast neutron flux and primary gamma-ray dose rate were hardly affected in the 10%- $^6\text{LiOH}$ phantom. It was confirmed that the dose contribution of fast neutrons is improved from approximately 10% in the pure water phantom, to approximately 50% in the 10%- $^6\text{LiOH}$ phantom.

CONCLUSION: The dual phantom technique using the combination of a pure water phantom and a 10%- $^6\text{LiOH}$ phantom provides an effective method for dose estimation of the fast neutron component in BNCT. Improvement in the accuracy achieved with the proposed technique results in improved RBE estimation for biological experiments and clinical practice.

ACKNOWLEDGMENT: This work was supported by JSPS KAKENHI Grant Number JP 16H05237.

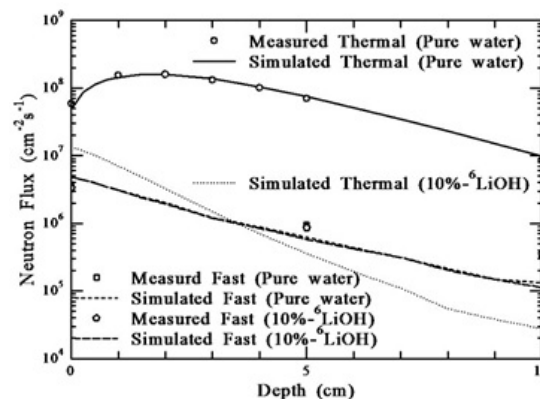


Fig. 1. Comparison between the measured and simulation results for the neutron-flux distributions in the pure water phantom and the 10%- $^6\text{LiOH}$ phantom.

REFERENCES:

- [1] H. Tanaka *et al.*, Nucl. Instr. Meth. B **267** (2009) 1970-1977.
- [2] H. Kumada *et al.*, Appl. Radiat. Isot. **88** (2014) 211-215.
- [3] Y. Sakurai *et al.*, Med. Phys. **42** (2015) 6651-6657.

H. Tanaka, K. Okazaki¹, T. Takata, Y. Sakurai and M. Suzuki

Institute for Integrated Radiation and Nuclear Science, Kyoto University

¹*Graduate School of Engineering, Kyoto University*

INTRODUCTION: In order to improve the quality of BNCT treatment, it is desired to measure the boron concentration during treatment of BNCT[1]. The boron concentration in the blood has been evaluated using prompt gamma rays or ICP. In these evaluation methods, boron concentration can not be obtained during irradiation.

Therefore, we are developing a system that can detect boron concentration distribution in real time by detecting prompt gamma rays of 478 keV caused by nuclear reaction between boron and thermal neutrons. Since the annihilation gamma ray of 511 keV exists as the background of the BNCT irradiation field, it is necessary to discriminate between 478 keV and 511 keV. In order to discriminate between these two energies, the energy resolution needs to be 6.5% or less.

We constructed a prompt gamma-ray imaging detector system combining 8×8 arrayed $\text{LaBr}_3(\text{Ce})$ scintillator and 8×8 MPPC array. We report the outline and the result of the characteristic test.

EXPERIMENTS: The size of the $\text{LaBr}_3(\text{Ce})$ scintillator is 50 mm x 50 mm x 10 mm and is divided into 8 x 8 arrays. The scintillator was set to an 8 x 8 array of MPPC.

The signal of 64 channels is amplified and shaped by the amplifier-shaper. Each analog signal was digitized by the ADC, and digital data was processed and stored by the PC. As a characteristic test, we tried to acquire the energy resolution and the two-dimensional distribution of 511 keV gamma ray using Na-22. In order to compare the performance of this system with arrayed scintillator, the same test was carried out for slab scintillators with the size of 50 mm x 50 mm x 10 mm.

RESULTS: For the arrayed scintillators, the energy resolution obtained from one pixel installed near the source was 7.6%, using gamma ray with Na-22 (Fig. 1). On the other hand, the energy resolution in each MPPC pixel of the non-arrayed scintillator was 6.6% on average.

One of the reasons that the energy resolution of arrayed scintillators is poor is that the peak at 511 keV is divided. The reason for the worse energy resolution is considered that the gain of each MPPC is not uniform. In

the next step, we have a plan to set the different bias for each MPPC in order to improve energy resolution.

Fig. 2 shows the measurement results of two-dimensional incident position of incident gamma rays acquired by a not arrayed scintillator. It was confirmed that a two-dimensional distribution can be acquired by this system.

In the future, we will measure the boron concentration of boron samples using thermal neutron beam at KUR guide tube.

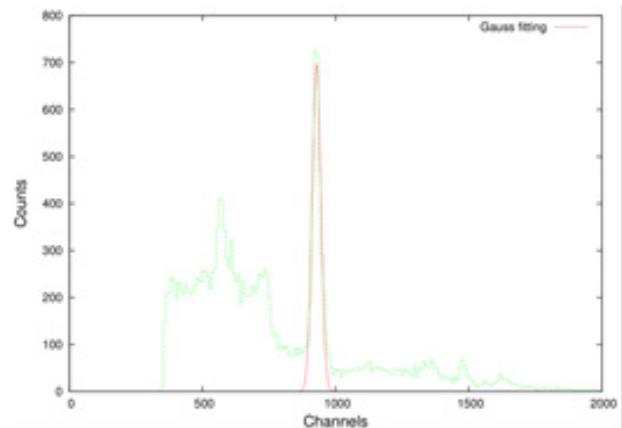


Fig. 1. The energy spectrum of gamma rays from Na-22.

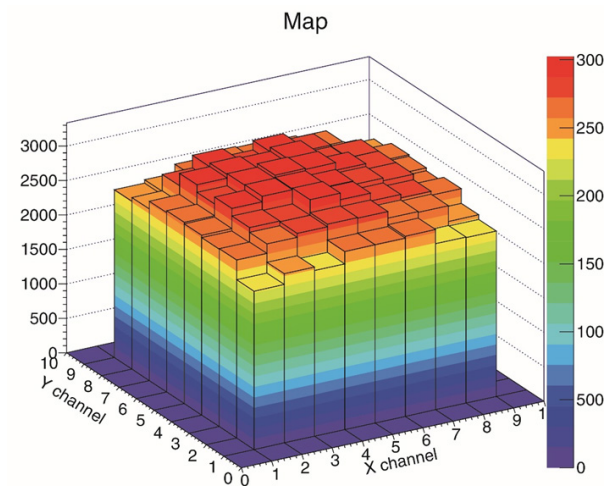


Fig. 2. Two-dimensional gamma rays image

REFERENCE:

[1]T. Kobayashi, *et al.*, *Medical Physics*, **27** (2000) 2124-2132.

S. Kurosawa^{1,2}, A. Yamaji¹, S. Kodama¹ and T. Horiai¹

¹ *New Industry Creation Hatchery Center, Tohoku University*

² *Faculty of science, Yamagata University*

INTRODUCTION: Neutron detection and imaging can find its application in various fields such as homeland security, crystallography, etc. [1, 2]. Up to now, ³He gaseous detectors have been used for neutron detection, because ³He has an unusually large cross-section for neutron capture (approximately 5300 barns for thermal neutrons) [3, 4]. However, the ³He sources are being depleted, and alternative suitable detection methods are required. BF₃ gas has been also used for a neutron detector. However, BF₃ gas has a big disadvantage since it is a toxic gas. On the other hand, neutron scintillator (solid state) is easy to handle to measure neutron.

To measure the neutron energy, Time-of-Flight (TOF) technique is required, and thus we need fast response scintillator. Some of halide scintillators show high light yield and fast decay time, however, most of them are hygroscopic. Therefore, we focused on the organic scintillator crystals, which showed fast decay time in the nano-second range and no hygroscopic nature.

However, conventional organic scintillators have low melting temperatures and would degrade when overheated. Therefore, we have developed organic crystals for neutron scintillators with high melting temperatures and fast decay times.

In this research, we have developed novel organic scintillators, and test some of their characteristics such as the light output and radiation hardness.

EXPERIMENTS: In this paper, p-terphenyl and trans-stilbene (as reference), crystals were grown by self-seeding vertical Bridgman method using an enclosed chamber [5]. Raw material powder was charged into a double glass ampoule and the atmosphere in the chamber was replaced with high purity nitrogen. The ampoule was heated by a resistance heater and pulled down slowly at the rate of 0.03-0.06 mm/min. The grown crystals looked transparent. We tested the radiation hardness for our samples in Co-60 Gamma-ray Irradiation Facility of KUR.

RESULTS: We irradiated these samples four times with gamma rays from Co-60, and the total dose was around 5 Gy. After each irradiation, we obtained pulse height spectra for these samples irradiated with gamma rays from a Cs-137 source. We evaluated the light output from the Compton edge in the pulse height spectra. As shown in Fig. 1, we found light output of trans-stilbene was degraded after Co-60 irradiation as the dose increased. On the other hand, p-terphenyl seems to keep the

light output even after 5 kGy (preliminary). In FY2018, also we would like to confirm the radiation harness for p-terphenyl and other novel organic scintillators.

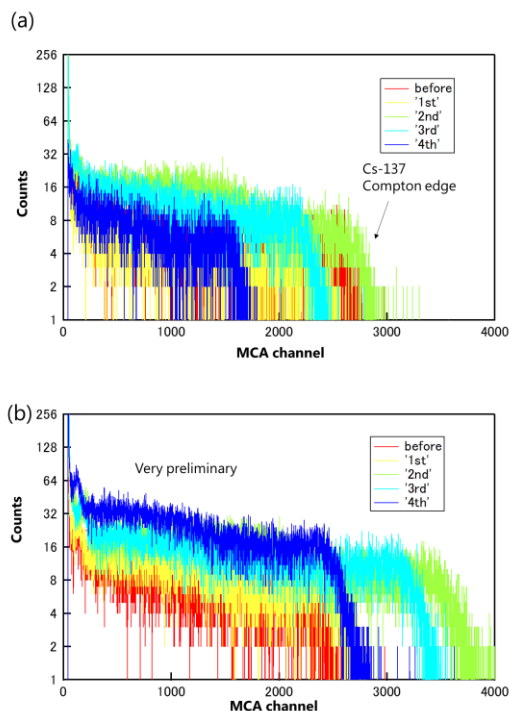


Fig. 1. Pulse height spectra of trans-stilbene (a) and p-terphenyl (b) measured under irradiation with gamma rays from Cs-137 before and after Co-60 irradiation.

REFERENCES:

- [1] M. P. Blakeley, P. Langan, N. Niimura and A. Podjarny, *Current Opinion in Structural Biology*, **18** (2008)593–600.
- [2] R. Chandra, G. Davatz, U. Gendotti and A. Howard, *Nuclear Science Symposium Conference Record (NSS/MIC)*, IEEE, (2010) 508 – 511.
- [3] G. F. Knoll, *Radiation Detection and Measurement* (John Wiley&Sons, Inc., New York 1979).
- [4] J. D. Parker, K. Hattori, H. Fujioka, M. Harada, S. Iwaki, S. Kabuki, Y. Kishimoto, H. Kubo, S. Kurosawa, K. Miuchi, T. Nagae, H. Nishimura, T. Oku, T. Sawano, T. Shinohara, J. Suzuki, A. Takada, T. Tanimori, K. Ueno, *Nuclear Instruments and Methods in Physics Research A*, **697**, (2013) 23–31.
- [5] A. Arulchakkaravarthi, P. Jayavel, P. Santharaghavan, P. Ramasamy, *J. Crystal Growth*, **234** (2002) 159-163.

T. Takata, H. Tanaka, Y. Sakurai and M. Suzuki

Research Reactor Institute, Kyoto University

INTRODUCTION: In boron neutron capture therapy (BNCT) irradiations carried out at Kyoto University Research Reactor, sitting position has been applied in many cases, considering flexibility of patient positioning and structural restriction of an irradiation facility. In some cases, there is difficulty in reproducing a patient position determined by a treatment planning process, which is related to a patient set-up error. Also, the sitting position is sometimes unstable, resulting in displacement from an initial set-up position during an irradiation period, which is related to patient motion. These set-up error and motion cause uncertainty in estimation of delivered dose.

Aiming to improve the dose estimation accuracy, we have been preparing a patient-position monitoring system using a real-time range sensing devices. An outline of the monitoring system and initial test operation are described.

MATERIALS AND METHODS: An outline of the monitoring system is shown in Fig. 1. The monitoring system consists of sensor devices and an analyzer. Kinect sensor (MICROSOFT CORPORATION, USA) including a real-time range camera based on a time-of-flight method, was used to track a patient position. A range sensor of the Kinect has the following specifications: a frame rate of 30 fps and an image size of 512x424. Two Kinect sensors were placed at a distance of a few meter from a patient and viewing the patient from different directions. Data acquired with the each range camera, which is a 2D range image showing a pixel-by-pixel distance map to surface points of objects from the camera, was transferred to the position analyzer. In the analyzer, 3D surface data of a patient and surrounding objects was constructed from a set of range images, and then stored as a point cloud data represented in an arbitrarily specified Cartesian frame, such as a frame parallel and perpendicular to a beam axis.

These data can be used for patient position monitoring not only by visual observation but also by quantitative evaluation. Also, displacement due to a set-up error and motion can be evaluated by comparing a position determined in a treatment planning system with a position measured by this system.

RESULTS: An initial test operation of the Kinect sensor was conducted. The sensor was placed at a distance of 200 cm from a reference object. It was confirmed that the indication of the distance was correctly displayed. However, the observed distance showed somewhat large time fluctuation in a range of ± 30 mm, which was considered as random noise. A moving averaging method was applied to reduce the fluctuation, and it was confirmed that the average over 100 frame could reduce the fluctuation

to < 5 mm. Also, it was confirmed that the analyzer could calculate 3D surface data from a set of range data and display a range image with a viewing axis parallel to a beam axis.

CONCLUSION: An outline of the monitoring system and initial test operation results were described. It was confirmed that the range sensing devices used in the system have sufficient accuracy and the position analysis can be correctly performed. The system can be expected to work effectively for monitoring a patient position. Functions to calculate a displacement are needed to evaluate a set-up error and motion, and are currently under development

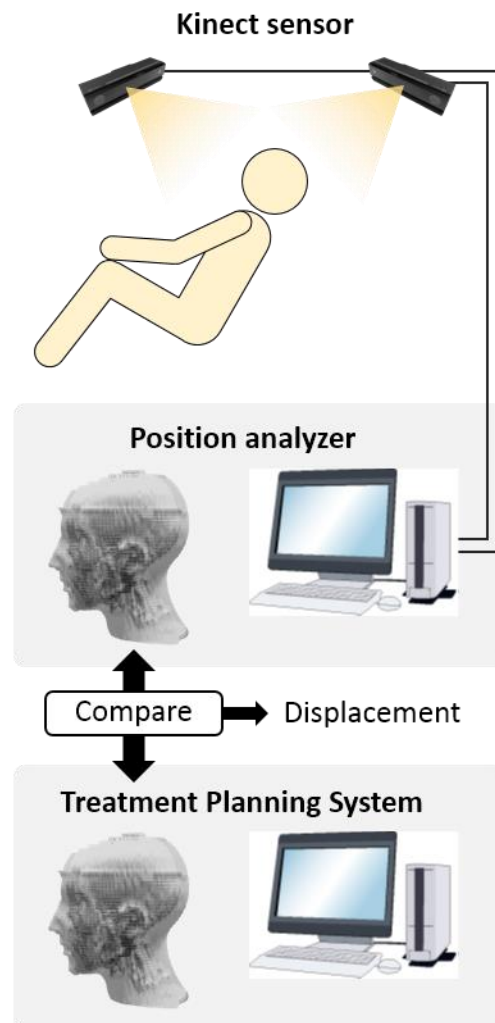


Fig. 1. An outline of the patient position monitoring system.

I-2. COLLABORATION RESEARCHES

- 1. Slow Neutron Physics and Neutron Scattering**
- 2. Nuclear Physics and Nuclear Data**
- 3. Reactor Physics and Reactor Engineering**
- 4. Material Science and Radiation Effects**
- 5. Geochemistry and Environmental Science**
- 6. Life Science and Medical Science**
- 7. Neutron Capture Therapy**
- 8. Neutron Radiography and Radiation Application**
- 9. TRU and Nuclear Chemistry**
- 10. Health Physics and Waste Management**
- 12. Others**

CO1-1 Morphological Control in PS-*b*-PI-*b*-PDMS Triblock Copolymer by Mixed-Solvent

M. Takenaka, YiChin Wang, H. Ogawa

Institute for Chemical Research, Kyoto University

Introduction

Various kinds of periodic morphologies in block copolymers have been extensively studied over decades. In addition, several researches have put emphasis toward complex systems, such as multiblock copolymers and non-linear block copolymers, and broaden the extent that various microdomain morphologies and different microdomain sizes can be accessed. In equilibrium state of strong segregation limit, the morphologies of block copolymers depend on only volume fraction of each constituent polymer and their architectures, and the synthesis process are very important to control their morphologies. In this study, we will demonstrate the tunability of the microdomain morphology in polystyrene-*block*-polyisoprene-*block*-polydimethylsiloxane (SID) triblock copolymer produced from its solution of mixed solvent of toluene and n-decane. By varying the weight ratio and the concentration of the mixed solvent, corresponding ordered microdomain morphologies such as spheres, hexagonally-packed cylinders, lamellae and OTDD structure could be easily formed in the polymer solution. Moreover, these ordered microdomain morphologies found in the solution can be preserved in thin bulk state.

Experimental Section

Polystyrene-*block*-polyisoprene-*block*-polydimethylsiloxane (coded as SID2) were used in this study. In order to control the morphologies by using mixed solvent, we employed toluene and n-decane. Toluene is selective to PS and PI while n-decane is selective to PDMS. Four SID2 polymer solutions with different weight mixing ratio (1/2, 1/1.5, 1/1.3, 1/1.2) of toluene/n-decane were prepared. The microdomain structures of SID2 triblock copolymers in the solution and in the bulk films cast from the corresponding solution were observed by SAXS.

Results and Discussion

The effects of different ratio between toluene and n-decane solvents on the microphase separation microdomain structures of SID2 triblock copolymer are demonstrated. Toluene prefers to stay in the PS phase while n-decane goes less into PS phase and more to the PI and PDMS phase. Figure 1 shows the mix solvent ratio dependence of SAXS profiles of different SID2 polymer solutions. The progressive addition of n-decane into toluene is found to induce a morphological transition, and various ordered microdomain structure is formed. Based on the SAXS result, at the mix weight ratio of 1/2 toluene/n-decane, the micro-separated structure is spheres in BCC lattice. The hexagonally-packed cylinder is observed as the mix ratio is 1/1.5 toluene/n-decane. Lamellar structure can be obtained if the mix ratio between toluene and n-decane is 1/1.3. For the toluene/n-decane ratio being 1/1.2, which is the most similar to that of pure toluene used in casting process, shows the identical

OTDD structure as observed in toluene-cast film.

Furthermore, the hexagonally-packed cylinders and the lamellae are persisted in the bulk state cast from the corresponding solutions, indicating the morphologies formed in the solution can be preserved down to cast bulk state. According to the results, mix-solvent can be used as a key technique for controlling and creating a variety of ordered microdomain structures in SID triblock copolymers.

Table 1. Molecular Characteristics of SID2

Code	$M_n (\times 10^4)$ ($\text{g} \cdot \text{mol}^{-1}$)	f_{PS}	f_{PI}	f_{PDMS}	M_w/M_n
SID2	3.24	0.29	0.43	0.28	1.05

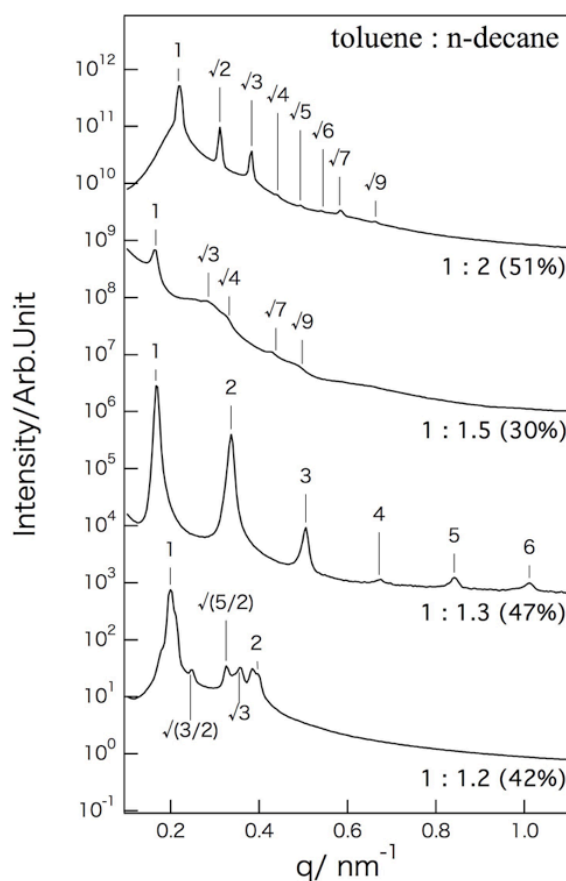


Figure 1 SAXS profiles of different ratio between toluene/n-decane for SID2 solution. The profiles are shifted vertically to avoid overlapping.

M. Yohda, K. Horiuchi, K. Hakamada, R. Inoue¹ and M. Sugiyama¹

Department of Biotechnology and Life Science, Tokyo University of Agriculture and Technology

¹ Institute for Integrated Radiation and Nuclear Science, Kyoto University

INTRODUCTION: HSPB5 (also called α B-crystallin) is a member of small heat shock proteins that are characterized by a conserved α -crystallin domain (ACD) [1]. HSPB family members are known to form both homo-oligomeric and hetero-oligomeric complexes with other HSPBs. These complexes exhibit high rates of subunits exchange, suggesting to play a key role in substrate recognition and chaperoning functions. The HSPB5 mutation, R120G, is associated with both cataract and adult onset myopathy. When expressed in cells, the R120G mutant is associated with formation of amyloid-like oligomeric structures [2]. *In vitro*, recombinant R120G mutant protein forms soluble oligomers that are larger and more polydisperse than the wild type [3]. The mutation is partly rescued by the mutation of C-terminal IPI sequence, the conserved C-terminal 'IxI/V' motif, which is known to be responsible for the interaction between dimeric units. In this study, we examined the oligomeric structures of HSPB5 variants, the wild type (HSPB5_WT), R120G mutant (HSPB5_R120G) and IPI mutant, in which IPI was replaced with AAA (HSPB5_IPI).

EXPERIMENTS: HSPB5 variants (HSPB5_WT, HSPB5_R120G, HSPB5_IPI) were expressed in *E. coli* and purified by hydrophobic chromatography with Phenyl Sepharose and size-exclusion chromatography with Superdex 200. The molecular weights of the oligomers of HSPB5 variants were analyzed by Size-exclusion chromatography - multiangle light scattering (SEC-MALS) using a multiangle light-scattering detector (MINI DAWN, Wyatt Technology) and also Native- PAGE. The oligomeric conformation of HSPB5 variants were also analyzed by small angle X-ray scattering using NANOPIX (RIGAKU)

RESULTS: By SEC-MALS, the molecular weights of the oligomers of HSPB5_WT and HSPB5_R120G determined to be 551kDa and 695kDa, respectively. The values are almost consistent with the results of Native PAGE. R120G appeared as a single band at the molecular weight of about 720 kDa. The wild type formed three bands with the molecular weights of approximately 480 kDa, 720 kDa and 960 kDa. Since the molecular mass of the monomer is about 20kDa, it is reasonable to think HSPB5_WT forms the canonical 24meric complex of 480 kDa, which seems to have a nature to interact to form a large dimer (960kDa). On the contrary, HSPB5_R120G does not take 24meric conformation, but exists as stable 36mer (720 kDa). The wild type partly takes the same oligomeric conformation. Therefore, HSPB5_WT chang-

es its oligomeric conformation between 24mer and 36mer, and HSPB5_R120G seems to lose the conformational change ability and stays at the 36meric conformation. The results of SAXS analyses are shown in Fig. 1 and 2. The profiles of diffraction indicate that HSPB5_R120G is the largest and HSPB5_IPI is the smallest (Fig. 1). Fig. 2 shows the Guinier plots. The estimated R_g values of HSPB5 variants are as follow. R_g (HSPB5_WT) = 75.9 ± 3.6 Å, R_g (HSPB5_R120G) = 87.2 ± 4.3 Å, R_g (HSPB5_IPI) = 85.9 ± 3.7 Å. Curiously, R_g of HSPB5_IPI is larger than that for HSPB5_WT.

We will further examine the oligomeric conformations of HSPB5 using various methods, SEC-MALS, SAXS, analytical ultracentrifuge and native mass spectrometry, and reveal the mechanism for the interaction with denatured proteins.

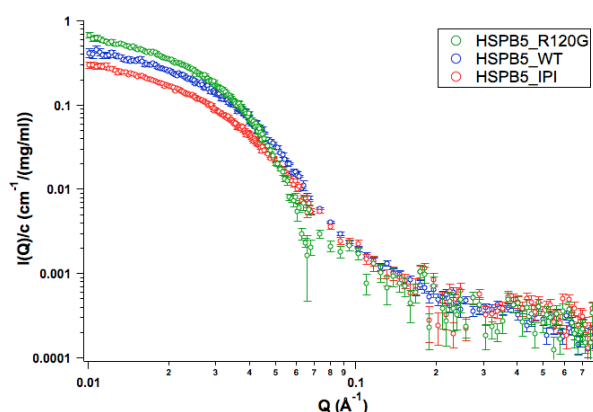


Fig. 1 SAXS profiles of HSPB5 variants

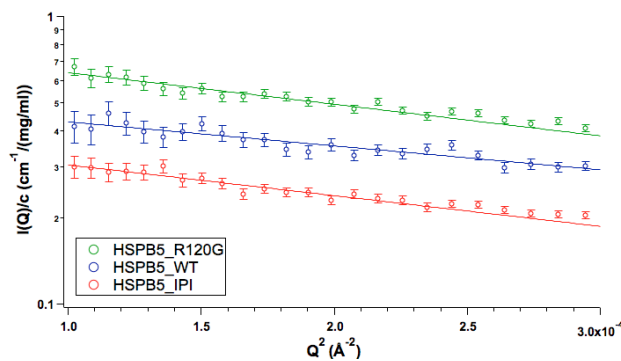


Fig. 2 Guinier plots of SAXS profiles

REFERENCES:

- [1] E. Basha *et al.*, Trends. Biochem. Sci., **37** (2012) 106–117.
- [2] A. Sanbe *et al.*, Proc. Natl. Acad. Sci. USA, **101** (2004) 10132–10136.
- [3] M.P. Bova *et al.*, Proc. Natl. Acad. Sci. USA, **96** (1999) 6137–6142.

CO1-3 Effect of Cancer Associated Histone Mutations in the Nucleosome Structure

Y. Arimura, H. Kurumizaka and M. Sugiyama¹
Faculty of Science and Engineering, Waseda University
¹Research Reactor Institute, Kyoto University

INTRODUCTION: In chromatin, the nucleosome is the repeating unit, which is composed of two molecules of histones H2A, H2B, H3, and H4. These histones form a histone octamer, and about 150 base-pair DNA was wrapped around it [1]. Currently, mutations in the histone genes have been identified in cancer cells [2-4]. These histone mutations may directly disturb the chromatin structure and function.

Interestingly, in human cancer cells, mutations in canonical histone genes have been identified [2,5,6]. These findings are very surprising, because the human genome contains the multiple canonical histone genes. Therefore, This indicates that just one mutation of the multiple histone genes may have impact in cells. However, the mechanism by which the cancer-associated mutations of canonical histones impact on the chromatin structure and function has not been studied yet.

In several cancer cells, the H3.1 mutations in genes have been found [6]. Among these mutations, mutations with amino acid substitution at the H3.1 Glu97 residue are frequently found in cancer cells [7,8]. Therefore, we focused on the H3.1 Glu97 to Lys (H3.1 E97K) mutation. We then study how the H3.1E97K mutation affects the solution structure of the nucleosome. To do so, we performed small angle X-ray scattering (SAXS) experiments.

EXPERIMENTS: Human histones H2A, H2B, H3, and H4 were bacterially produced, and were purified near homogeneity. The 145 or 146 base-pair DNA was also produced in bacterial cells, and was purified. The histone octamer was first reconstituted with the purified histones H2A, H2B, H3, and H4, and was purified by gel filtration column chromatography. The purified histone octamer was then mixed with the 145 base pairs of DNA, and the nucleosome was reconstituted by the salt dialysis method. After the nucleosome was reconstituted, the nucleosome was further purified by a native polyacrylamide gel electrophoresis, using Prep Cell apparatus. The purified nucleosome fractions were collected, and the samples were concentrated by a filter cartridge, and the debris was removed by centrifugation. We then performed the SAXS experiments with the nucleosome. For the nucleosome containing histone mutations, we introduced the corresponding mutation in the histone genes. The histone mutants containing the amino acid substitutions were produced in bacterial cells, and were purified by the same method as the wild-type histone proteins. We then reconstituted the histone octamer with the mutant and wild type histones, and the nucleosomes were reconstituted by the salt dialysis method. The histone H2A-H2B dimer and H3-H4 tetramer may also be used as materials for the

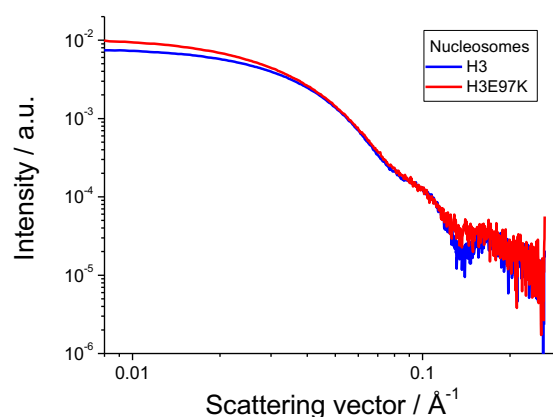


Fig. 1. SAXS profiles of the nucleosome containing H3E97K

nucleosome reconstitution by the salt dialysis method, if the histone mutation may affect the histone octamer formation.

RESULTS: As shown in Fig. 1, the SAXS curve was obtained with the nucleosome sample containing a histone mutation, and solution parameters of the nucleosome structure were estimated. A low resolution solution structure of the mutant nucleosome was obtained by Dummy atom modeling. The comparative study between solution structure and the X-ray structure of the mutant and wild type nucleosomes are underway.

REFERENCES:

- [1] K. Luger *et al.*, Crystal structure of the nucleosome core particle at 2.8 Å resolution. *Nature.*, **389** (1997) 251-260.
- [2] J. Schwartzentruber *et al.*, Driver mutations in histone H3.3 and chromatin remodelling genes in paediatric glioblastoma. *Nature.*, **482** (2012) 226-231.
- [3] G. Wu *et al.*, Somatic histone H3 alterations in pediatric diffuse intrinsic pontine gliomas and non-brainstem glioblastomas. *Nat Genet.*, **44** (2012) 251-253.
- [4] S. Behjati *et al.*, Distinct H3F3A and H3F3B driver mutations define chondroblastoma and giant cell tumor of bone. *Nat Genet.*, **45** (2013) 1479-1482.
- [5] C. Kandath *et al.*, Mutational landscape and significance across 12 major cancer types. *Nature.*, **502** (2013) 333-339.
- [6] I. Martincorena *et al.*, Somatic mutation in cancer and normal cells. *Science.*, **349** (2015) 1483-1489.
- [7] E. Cerami *et al.*, The cBio cancer genomics portal: an open platform for exploring multidimensional cancer genomics data. *Cancer Discov.*, **2** (2012) 401-404.
- [8] J. Gao *et al.*, Integrative analysis of complex cancer genomics and clinical profiles using the cBioPortal. *Sci Signal.*, **6** (2013) 1.

T. Sato, R. Sato, Y. Oba¹ and M. Sugiyama²

School of Integrated Design Engineering, Keio University

¹*Materials sciences Research Center, Japan Atomic Energy Agency*

²*Institute for Integrated Radiation and Nuclear Science, Kyoto University*

INTRODUCTION: Nanoparticles often show physical properties different from bulk materials. Onset of ferromagnetism in the nanoparticles is one of the most attractive phenomena. In particular, it has been reported that Au nanoparticles with clean surface show ferromagnetism, while bulk Au is diamagnetic [1]. This ferromagnetism is free from surface modification by protective agents, which highly affect the magnetism of Au and sometimes obscure size effects [2,3]. However, the origin of the Au nanoparticles with no protective agents is still unclear. Although the magnetization and the coercivity vary among the samples, the size effects are not properly discussed because it is difficult to quantify the size in the strongly agglomerated nanoparticles.

Small-angle X-ray scattering (SAXS) is a powerful means to quantitatively characterize and compare the nanostructures among the samples. Therefore, the nanostructures in the ferromagnetic Au nanoparticles were characterized using SAXS in this study.

EXPERIMENTS: The samples were prepared by a gas evaporation method. SAXS measurements were performed using a SAXS instrument with Mo K α radiation (Nano-viewer, RIGAKU) installed at the Institute for Integrated Radiation and Nuclear Science, Kyoto University. The characteristic X-ray emitted from Mo can penetrate heavy metals such as Au due to its high energy (17 keV). The sample-to-detector distance was 45 cm. During the SAXS measurements, the samples were put in vacuum to reduce the background scattering from air.

To measure low q region, an ultra-small-angle X-ray scattering (USAXS) instrument installed at the beam line BL19B2 in SPring-8 was also used [4]. Here, q is the magnitude of the scattering vector and is equal to $(4\pi/\lambda)\sin\theta$, where θ and λ are half the scattering angle and the wavelength of the incident X-ray. The energy of the incident X-ray was 18 keV. The obtained USAXS profiles were connected with the corresponding SAXS profiles. The analysis was carried out using the connected profiles.

RESULTS: Fig. 1 shows a typical scattering profile of the Au nanoparticles. The profile has a shoulder around $q=0.1 \text{ nm}^{-1}$. This indicates that the nanostructure is formed in the sample. The average diameter of the

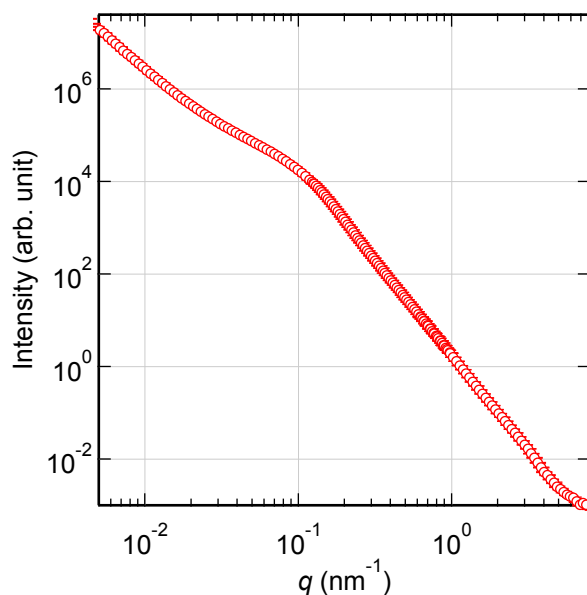


Fig. 1. Typical scattering profile of the Au nanoparticles with clean surface. The profile is composed of the USAXS ($q < 1 \text{ nm}^{-1}$) and SAXS ($q > 0.6 \text{ nm}^{-1}$) profiles. The intermediate region ($0.6 < q < 1 \text{ nm}^{-1}$) was measured using both USAXS and SAXS.

nanostructure is estimated to 51 nm using curve fitting analysis with the assumption that the nanoparticles are spherical. In the previous study [1], the Au nanoparticles with the average diameter of a few nm were observed using a transmission electron microscope (TEM). Therefore, the nanostructure observed using the SAXS and USAXS is the agglomerates of the Au nanoparticles. The clean surface of the Au nanoparticles probably induces the agglomeration of the Au nanoparticles.

The previous study reported the coercivity over 10 Oe even at room temperature. This is unrealistic value for the nanoparticles with the diameter of a few nm. Therefore, the formation of the agglomerates is probably related with this coercivity.

REFERENCES:

- [1] R. Sato *et al.*, *J. Magn. Magn. Mater.*, **393** (2015) 209-212.
- [2] P. Crespo *et al.*, *Phys. Rev. Lett.*, **93** (2004) 087204/1-4.
- [3] Y. Yamamoto *et al.*, *Phys. Rev. Lett.*, **93** (2004) 116801/1-4.
- [4] K. Osaka *et al.*, *AIP Conf. Proc.*, **1741** (2016) 030003/1-4.

F. Tokanai¹, R. Itoh², S. Ishizawa², T. Moriya¹, M. Takeyama¹, T. Sumiyoshi³, H. Kondo⁴, H. Sugiyama⁴, M. Hayashi⁴, T. Okada⁴, M. Hino⁵

¹Department of Physics, Yamagata University

²Graduate School of Science and Engineering, Yamagata University

³Graduate School of Science and Engineering, Tokyo Metropolitan University

⁴Electron Tube Division, Hamamatsu Photonics K.K.

⁵Research Reactor Institute, Kyoto University

INTRODUCTION: Neutron imaging is more useful than X-ray imaging for light elements in the sample such as hydrogen, lithium, boron, carbon, and nitrogen. Owing to their unique ability to probe inside samples, neutrons have been widely utilized for neutron radiography in various fields, including fundamental science, archaeology, and industry. A new beam line has recently been constructed at Japan proton accelerator research complex (J-PARC) for pulsed neutron imaging [1], and several compact accelerator-driven neutron sources are now available for non-destructive testing [2] or for boron neutron capture therapy (BNCT). High-resolution imaging capability with a moderate effective area is required in practical applications of neutron sources. We have been developed an optical imaging capillary plate (CP) gas detector for high-resolution neutron imaging [3]. The performance of the neutron imager was investigated using a cold neutron beam line CN-3 in Kyoto University Reactor (KUR)

EXPERIMENTS: Fig. 1 shows the experimental setup of the neutron gas scintillation imager (n-GSI). It consists of a thin layer of ^{10}B to convert neutron, a CP gas detector filled with a Ne-based gas mixture at 1 atm, mirror and lens optics, and a cooled CMOS camera system. CP has an effective diameter 25 mm and a thickness, individual hole diameter, and pitch of 300 μm , 50 μm , and 64

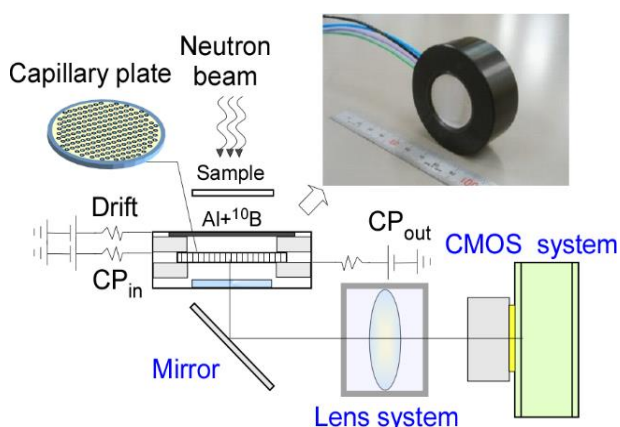


Fig. 1 Schematic view of n-GSI and experimental arrangement for the performance of neutron beams from KUR.

μm , respectively. The neutron wavelength of maximum intensity and total flux of the CN-3 guide tube were 2 \AA and 3.8×10^6 neutron $\text{cm}^{-2} \text{s}^{-1}$, respectively. The n-GSI system was placed 250 mm away from the downstream exit of the neutron guide. The neutrons were irradiated through a test chart made by using a Gd slit on a thin glass sheet.

RESULTS: Fig. 2 shows the neutron transmission image of the test chart obtained by n-GSI system. The exposure time was 300 s. The numerical number in Fig.2 indicates the width of the slit on the chart. The practical position resolution of n-GSI is estimated to be 200 μm for the neutron beam. To improve the position resolution, we have been currently developing a new n-GSI system.

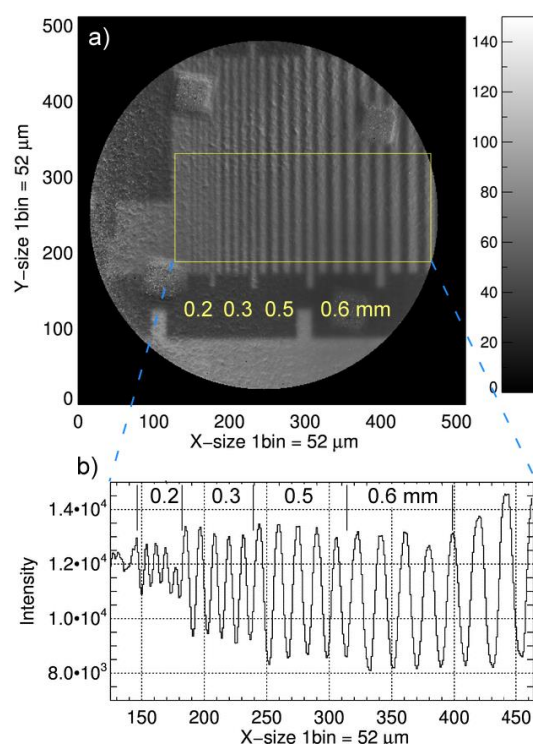


Fig. 2. a) Neutron image of a neutron test chart obtained by n-GSI system. The CP gas detector was filled with Ne (90%) + CF_4 (10%) at 1atm. b) the intensity projection on the x-axis for the yellow rectangular box in the neutron image.

REFERENCES:

- [1] T. Shinohara *et al.*, J. Phys.: Conf. Ser. **746** (2016) 012007K.
- [2] Y. Ikeda *et al.*, Nucl. Instr. and Meth., **833** (2016) 61-67.
- [3] T. Sumiyoshi *et al.*, Hamon **27** (1) (2017) 16-19.

K. Mori, R. Okumura, H. Yoshino, S. Sato¹, H. Hiraka²,
K. Iwase³, and A. Okumura⁴

*Institute for Integrated Radiation and Nuclear Science,
Kyoto University (KURNS)*

¹*High Energy Accelerator Research Organization (KEK)*

²*Neutron Science Center, Korea Atomic Energy Research
Institute*

³*Department of Materials and Engineering, Ibaraki Uni-
versity*

⁴*Graduate School of Engineering, Kyoto University*

INTRODUCTION: Neutron diffraction is a powerful tool to determine precisely the positions of light elements (e.g., hydrogen and lithium) in solids. This is the main reason why neutron powder diffractometers are critical for structural investigations of energy storage materials, for example, rechargeable lithium-ion batteries and hydrogen absorbing alloys. The B-3 beam port of Kyoto University Research Reactor (KUR) had long been used as a four-circle single-crystal neutron diffractometer (4CND). For the last decade, however, the 4CND was so old that its research activity on neutron science was quite low. Now, the compact multipurpose neutron diffractometer (CMND) is installed on the B-3 beam port of KUR.

SPECIFICATIONS: Fig. 1 shows the current state of the CMND. The CMND is equipped with a new beam shutter manufactured by the KURNS factory. In addition, the CMND has a wide space around the sample; therefore, we can easily install any other system. The neutron wavelength, λ , which is monochromatized by the (220) plane of a Cu single crystal (i.e., Cu monochromator), is 1 Å. To cover the detector area of $6^\circ \leq 2\theta \leq 150^\circ$, twenty-five ³He tube detectors (1/2 inch in diameter) are used (see Fig. 2), where 2θ is the scattering angle. A detector bank including the twenty-five ³He tube detectors is placed on an arm of the HUBER-440 goniometer. The distance from the Cu monochromator to the sample is approximately 2 m, and the distance from the sample to the detector is 1.2 m.

PRELIMINARY EXPERIMENTS: The preliminary neutron diffraction experiments were performed using a nickel (Ni) powder sample. Figs. 3(a) and (b) show the neutron powder diffraction data of Ni collected on the B-3 beam port and the X-ray powder diffraction data of Ni collected on the Laboratory X-ray diffractometer with a $\text{CuK}\alpha$ radiation, respectively. As shown in Fig. 3(a), we succeeded to observe several Bragg reflections of Ni. In particular, the Bragg reflections at the high Q region (corresponding to the high 2θ region) could be observed using the CMND, where Q is the magnitude of the scattering vector ($= 4\pi\sin\theta/\lambda$, where θ is half of the scattering angle, 2θ). The complementary use of neutron and X-ray diffraction is very useful for the structural investigations. Further improvements are now in progress.



Fig. 1. The compact multipurpose neutron diffractometer, installed at the B-3 beam port of KUR.



Fig. 2. Twenty-five ³He tube detectors (1/2 inch in diameter) on the detector bank.

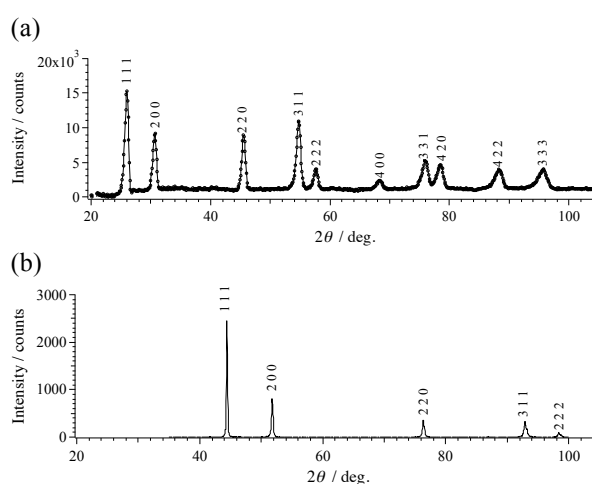


Fig. 3. Diffraction data of the nickel (Ni) powder: (a) neutron (B-3 beam port) and (b) X-ray ($\text{CuK}\alpha$ radiation), respectively.

CO1-7 Study of the Properties of Water and the Physiological Activation Phenomena by using High-Intensity Pulsed Coherent Radiation

S. Okuda, Y. Tanaka and T. Takahashi¹

Graduate School of Engineering, Osaka Prefecture University

¹Research Reactor Institute, Kyoto University

INTRODUCTION: The coherent transition radiation (CTR) from electron bunches of a linear accelerator (linac) has continuous spectra in a submillimeter to millimeter wavelength range corresponding to the terahertz (THz) frequency range. It is a picosecond pulsed light and hence, has extremely high peak-intensities compared with the other THz light sources. The light source system using the CTR from the electron beams of the 45 MeV L-band electron linac was established at Kyoto University Research Reactor Institute (KURRI) [1-3]. This CTR light source developed has been applied to absorption spectroscopy. Recently, the possibility of any nonlinear effects was found in the measurement of the absorption spectroscopy at KURRI.

The important application of the light source is the investigation of the biological effects of the CTR. The main purpose of the present work is the investigation of the biological effects of the high-intensity pulsed CTR.

EXPERIMENTAL METHOD: The electron linac at KURRI was used in the experiments. In most experiments the beam energy, macropulse length and the repetition rate are 42 MeV, 47 ns and 60 Hz, respectively. The experimental configurations for the absorption spectroscopy are schematically shown in Fig. 1. The output CTR light from a light source chamber was transported out from the accelerator room. The spectrum of the light after passing through the sample was measured with a Martin-Puplett type interferometer and a liquid-He-cooled silicon bolometer. The wavenumber resolution was 0.1 cm^{-1} . The incident light was divided to two parts with the same light intensity in the interferometer. In this system the absorption spectroscopy and the irradiation were carried out at the same time.

In the absorption spectroscopy the sample was located on the light path between the interferometer and the detector. The thickness of the liquid sample was about 100 μm , which was sandwiched with two anhydrous quartz plates 3 mm thick. The light was focused at a light collimator 8 mm ϕ in diameter located before the sample. The details of the methods for the measurements are described in ref. 2 and 3. The liquid samples used in the experiments were water, aqueous solutions of NaCl for the investigation of the basic behaviors of the absorbed light in the analysis of the biological effects by the irradiation of CTR.

In the irradiation experiments of the CTR several kinds of bacillus, human culture cell and microorganism were used. After the irradiation the physiological activation phenomena were investigated. The new system for observing the sample during the CTR irradiation experi-

ments is under preparation.

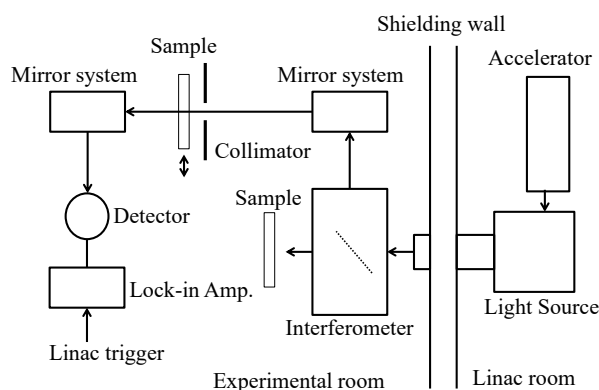


Fig. 1. Schematic diagram showing the configurations for absorption spectroscopy and irradiation experiments using the CTR

RESULTS AND DISCUSSION: The characteristics of the CTR light source were investigated, and the electron beam conditions and the experimental configurations were optimized. The light spectrum was sufficiently stable during the measurements within $\pm 2-3\%$ in a wavenumber range of 4-13 cm^{-1} . The spectrum had a peak at a wavenumber of about 7 cm^{-1} . If a band-pass light filter or a grating-type monochromator is used in order to avoid the influence of the main part of the spectrum around the peak the wavenumber range would be expanded to 2-35 cm^{-1} , which is determined by the specification of the detector. The intensity of light was estimated to be about 10^{-7} W/0.1%b.w. and was found to be sufficiently high even if it becomes 10^{-6} of the initial one after transmission through the sample due to absorption. The micropulse length of the CTR which corresponds to that of the electron beam from the linac was evaluated by the interferogram to be about 3 ps. Such a relatively short pulse length is due to the special bunching process in the optimized operational conditions of the linac. These results indicate that the peak light intensity in the micropulse is about 10^4 W. While the averaged CTR power is sufficiently low to induce thermal effects, the comparatively high peak power might cause any nonlinear effects.

In the irradiation experiments of CTR to investigate the biological effects the experimental conditions have been optimized. Preliminary results have been obtained by the CTR irradiation so far. 4 hours irradiation of CTR did not cause any effects on human fibroblast cells as the estimations of rate of living cells and rate of DNA segmentation.

REFERENCES:

- [1] T. Takahashi *et al.*, Rev. Sci. Instrum. **69** (1998) 3770.
- [2] S. Okuda and T. Takahashi, Infrared Phys. Technol. **51** (2008) 410.
- [3] S. Okuda and T. Takahashi, J. Jpn. Soc. Infrared Science & Technology 25 (2016) 49 (in Japanese).

M. Hino, T. Hosobata¹, T. Oda, H. Yoshinaga, S. Takeda¹, Y. Yamagata¹, H. Endo², N.L. Yamada² and Y. Kawabata

Institute for Integrated Radiation and Nuclear Science, Kyoto University (KURNS), Japan

¹*RAP, RIKEN, Japan*

²*IMSS, KEK, Japan*

INTRODUCTION: Progress of neutron optical devices is very significant. Recently we proposed promising fabrication method for aspherical focusing supermirror with metal substrate [1-4]. The metallic substrate is robust and ductile, to which able to fabricate steeply curved surface with high form accuracy. It is also applicable to use under high radiation irradiation and high-temperature filed, even at a place close to the neutron target and moderator. Furthermore, it is possible to fabricate a large focusing mirror by combining multiple segmented mirrors with mechanical fastening entailing the usage of screw holes and fixture tabs. The big problem was required surface roughness for neutron mirror. The roughness should be smaller than 0.3 nm for high- m supermirror coating. Here m is the maximum critical angle of the mirror in units of critical angle of natural nickel. By using electroless nickel-phosphorus (Ni-P) plating, we overcame the problem and are establishing fabrication process for aspherical focusing supermirror. In this study, we show a latest result for neutron focusing experiment with a couple of ellipsoidal supermirrors with metallic substrates.

EXPERIMENTS: We fabricated ellipsoidal metallic substrates with the Ni-P plating, based on the technology using ultrahigh precision cutting with correction processing, followed by mechanical precision polishing. The first precise manufacturing was conducted at a CNC machine for development of neutron optical devices at workshop of KURNS. The ultra-precise manufacturing, polishing and cleaning of the metallic substrate were conducted at RIKEN. The supermirror coating was conducted with KUR-IBS [5]. The neutron experiments were conducted at CN-3 beam line at KURNS and the BL06 (VIN ROSE) beam port at J-PARC MLF [6].

RESULTS: We fabricated a couple of $m=3$ NiC/Ti ellipsoidal supermirrors in which length of 900mm. The semi-major and semi-minor axes of the ellipsoidal supermirror were 1250 mm and 65.4 mm, respectively. The acceptable angle of the minor axis arc of the ellipsoidal supermirror is 20 degree. The two ellipsoidal supermirrors were placed between Φ 1mm pinhole and a two-dimensional position sensitive neutron detector as shown in Fig.1. The distances between the pinhole and the detector was 5 m and that between the two ellipsoidal supermirrors was 2.5m. Here Φ 10mm pinhole was placed 100 mm before the detector to reduce background neutrons. With the ellipsoidal mirrors, as shown in Fig 1(b), the intensity image was circular spot and the spot size was almost equivalent to that of the Φ 1mm pinhole. Without the mirrors, the intensity image was not clear

peak. Figure 1(c) shows TOF spectra with and without mirrors. Here the intensity without mirror was multiplied by 100 and that of wavelength 1nm or more was very little. On the other hand, the wavelength of peak intensity was longer than 1 nm because the available wavelength of neutrons reflected by the $m=3$ ellipsoidal supermirrors is longer than 1nm. It is possible to expand the available wavelength with higher- m supermirrors. In this study, it is clearly demonstrated that dramatically intensity gain for long wavelength neutrons reflected by the two $m=3$ ellipsoidal supermirrors.

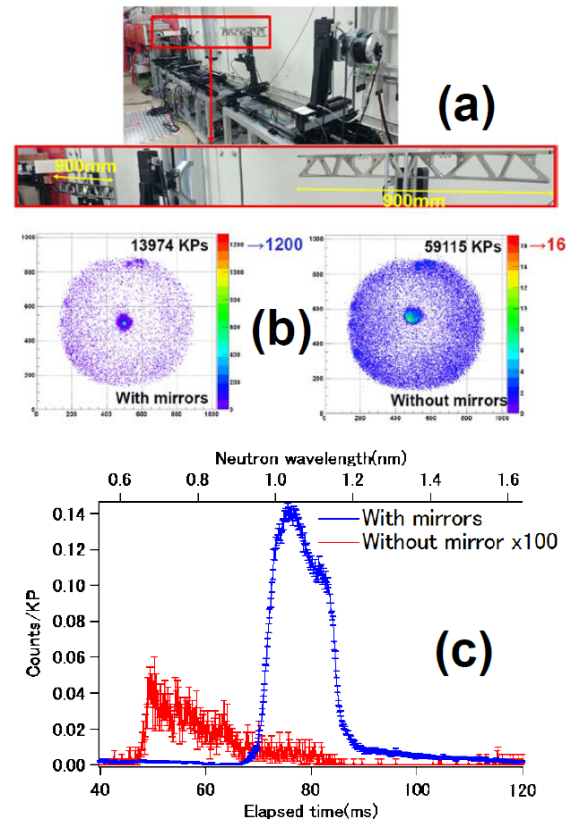


Fig. 1. (a) Photograph of the experimental setup for double ellipsoid neutron supermirrors at the BL06 at the J-PARC MLF. (b) Neutron intensity image at focal position with and without the ellipsoidal neutron supermirrors. (c) TOF spectra of neutrons reflected with and without the ellipsoidal neutron supermirrors. The intensity without mirror was multiplied by 100.

REFERENCES:

- [1] J.Guo, *et al.*, Optics Express 22(2014) 063108.
- [2] J.Guo, *et al.*, Review of Scientific Instruments 86(2015) 86(2015) 063108.
- [3] S.Takeda, *et al.*, Optics Express 24(2016) 12478.
- [4] T.Hosobata, *et al.*, Optics Express 25(2017) 20012.
- [5] M.Hino, *et al.*, Nucl. Instr. and Meth., **797**(2015) 265.
- [6] M.Hino, *et al.*, J. Nucl. Sci. Technol. 54(2017), 1223.

K. Tokunaga, M. Matsuyama¹, K. Araki, M. Hasegawa, K. Nakamura and Q. Xu²

Research Institute for Applied Mechanics, Kyushu University

¹*Hydrogen Isotope Research Center, University of Toyama*

²*Research Reactor Institute, Kyoto University*

INTRODUCTION: It is of importance to clarify phenomena of implantation, retention, diffusion and permeation of tritium on surface of the armor materials of the first wall/blanket and the divertor on fusion device from a viewpoint of precise control of fuel particles, reduction of tritium inventory and safe waste management of materials contaminated with tritium (T). Refractory metals such as tungsten (W) is potential candidate for an armor of the first wall and the divertor plate of the fusion reactor because of its low erosion yield and good thermal properties. The armor material will be subjected to heavy thermal loads in the steady state or transient mode combined with high energy neutron irradiation that will cause serious material degradation. In addition, high energy runaway electrons would bombard the armor materials along the equatorial plane in fusion device. It is considered that these cause radiation damage and enhance tritium retention. In the present works, T exposure experiments have been carried out on W samples which were irradiated by high energy electrons using LINAC in KURRI of Research Reactor Institute, Kyoto University to investigate effects of high energy electrons irradiation and microstructure on tritium retention of W. In this fiscal year, pure W and recrystallized W were irradiated by high energy electron beam. After that, positron annihilation experiment was carried out to identify the radiation defect. In addition, tritium exposure experiments have been carried out using a tritium (T) exposure device.

EXPERIMENTS: W samples used were ITER grade W (IG-W) and recrystallized W. In the case of IG-W, one was W sample (ITER grade W(1)) which the surface were manufactured to be oriented parallel to the rolling surface and rolling direction. The other W sample (ITER grade W(3)) which the surface were manufactured to be oriented perpendicular to the rolling surface and rolling direction. On the other hand, heat treatment was performed at 1800 °C for 1h at high vacuum to recrystallize IG-W. The sizes of W samples were 10mm x 10mm x 1mm. The surface of the both samples were polished to be mirrored. High energy electrons irradiation has been carried out using LINAC in KURRI of Research Reactor Institute, Kyoto University. An energy of electron irradiated was 10 MeV and DPA was 2.8×10^{-3} . Temperature during the irradiation was measured by thermocouples which was contacted with a backside of the W samples. After the electron beam irradiation, positron annihilation

experiment was carried out. In addition, T exposure experiments have been carried out using a T exposure device in University of Toyama. Pressure of the T gas was 1.3 kPa and T exposure was kept for 4 h. T concentration in the gas was about 5 %. Temperatures of pre-heating and T exposures were 100 °C. After the exposure to T gas, T amount retained in surface layers of the sample was evaluated by β -ray-induced X-ray spectrometry (BIXS) and imaging plate (IP) measurements.

RESULTS: Figure 1 shows amount of T measured by the IP measurement. In the case of non-irradiated samples, T retention of non-recrystallized samples is larger than that of recrystallized samples. These results indicated that some kinds of defects which can trap T decreased by the recrystallization. After the electron beam irradiation, amount of T of samples increases. In particular, in the case of the recrystallized samples, the amounts of T of electron beam irradiated samples are a few times of that of non-irradiated samples. Positron annihilation experiment indicated that the electron irradiation made life time of τ_2 small and intensity of I_2 increased. This result means that small defects were induced and concentration of the defects increased in the recrystallized sample by the electron irradiation. As a result, it is considered that these kinds of defects trap T. Quantitative evaluation is currently underway.

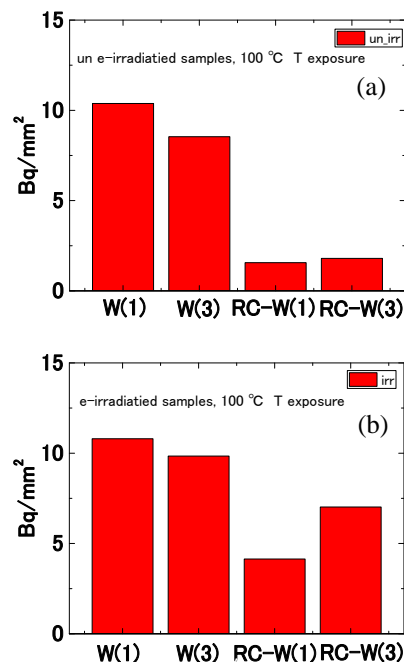


Fig. 1. Amount of tritium on before(a) and after(b) electron beam irradiation measured by IP measurement. RC-W(1) and RC-W(3) are recrystallized W(1) and W(3), respectively.

CO2-1 Study on Neutron Beam Pulse width Dependence in the Nuclear Fuel Measurement by the Neutron Resonance Transmission Analysis

F. Kitatani, H. Tsuchiya, Y. Toh, J. Hori¹, T. Sano¹, Y. Takahashi¹ and K. Nakajima¹

Research Group for Nuclear Sensing, Japan Atomic Energy Agency

¹Institute for Integrated Radiation and Science, Kyoto University

INTRODUCTION: As a non-destructive analytical technique for nuclear material in the field of nuclear security and nuclear nonproliferation, a neutron resonance transmission analysis (NRTA) attracts attention of researchers [1]. A large electron beam accelerator is generally used as a neutron source of a NRTA system so far. It is important to downsize a NRTA system when it is deployed at various facilities such as a reprocessing one [2]. For this aim, we have developed a compact NRTA system which utilizes a D-T neutron generator [3]. Its pulse width of 10 μ s is much longer than that of a large electron beam accelerator. It is necessary to understand the influence of pulse widths on the NRTA measurement. Therefore, we conducted the experiments of the simulated nuclear fuel pin samples to evaluate how the NRTA measurement is influenced by the pulse width of neutron beam.

EXPERIMENTS: Experiments were performed in KURNS-LINAC (Kyoto University, Institute for Integrated Radiation and Nuclear Science - Linear Accelerator). A sample changer was installed at the neutron irradiation line. A Li-6 detector was located at the position of approximately 7 m from the neutron source, and was utilized to measure neutrons which transmit through a sample. The simulated fuel pellet sample was made from metallic powders of Ag (around 1%) and Al (around 99%). Numbers in parentheses indicate weight ratio of each powder. The pellet size is about ϕ 6.5mm x t 10mm. The six pellets were put in a stainless case to simulate a fuel pin. The energy of the irradiation neutron is determined by a Time of Flight (TOF) technique. In addition to the sample, metallic plates of W and In were inserted in a neutron beam to investigate pulse width effects as well as to determine the neutron energy. The thicknesses of the W and In plates are 0.5mm and 0.2mm, respectively. In this work, we used three pulse widths of the neutron beam of 0.1, 1 and 4 μ s.

RESULTS: An example of a TOF spectrum measured is shown in Fig. 1. A resonance dip of ¹⁰⁹Ag at 5.19 eV is observed in the spectrum. The Ag resonance dip is able to measure in the other pulse widths. The resonance energies of ²³⁵U, ²³⁸U and ²³⁹Pu are around 5eV. Therefore, it is confirmed that NRTA can be utilized for the measurements of nuclear fuel materials in the fuel pin sample.

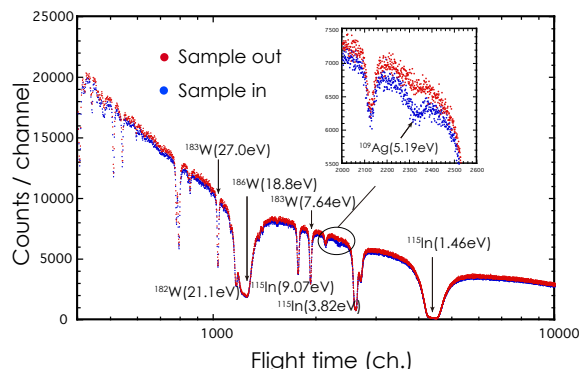


Fig. 1. TOF spectrum with pulse width 0.1 μ s

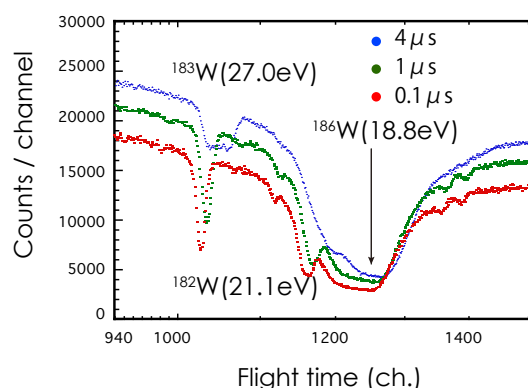


Fig. 2. The TOF spectra of individual pulse widths

Figure 2 shows the variation of TOF spectrum in the pulse width change. As can be seen, the dip of the TOF spectrum shifts towards low energy, with pulse width changed to a longer one. Resonance dips of ¹⁸²W and ¹⁸⁶W are not well separated in the 4 μ s spectrum. Furthermore, the ¹⁸³W resonance dip is strongly skewed in the 4 μ s spectrum. These mean that the resolution of the energy is worse with longer pulse width, and it would be difficult to apply a resonance analysis to the dips in the higher-energy region over approximately 20 eV with a longer pulse width of 4 μ s. In this work, we confirmed that neutron pulse width affected the NRTA measurement of the fuel pin sample. On the basis of this work, we will be able to quantify the effects of long-pulse width in a resonance analysis.

ACKNOWLEDGEMENTS: This research was implemented under the subsidiary for nuclear security promotion of MEXT.

REFERENCES:

- [1] J.W. Behrens *et al.*, Nucl. Tech. **67** (1984) 162.
- [2] H. Tsuchiya *et al.*, Plasma Fusion Res., **13** (2018) 2406004.
- [3] B.A. Ludewigt, LBNL-4426 (2011).

CO2-2 Measurement of Doppler Effect by Small Accelerator Neutron Source (II)

T. Sano, J. Hori, Jaehong Lee, Y. Takahashi, K. Nakajima, and H. Unesaki

Institute for Integrated Radiation and Nuclear Science, Kyoto University

INTRODUCTION: In order to reduce TRU, the research and technology development entitled as “TRU burning fast reactor cycle using uranium-free TRU metal fuel” have been started Japan at October 2014 [1]. The feature of the fast reactor is high content TRU and Zr without uranium in the fuel alloy so that additional TRU is not produced. On the other hand, uranium-free TRU metallic fuel leads to the reduction of the Doppler reactivity. Thus, the utilization of fuel alloy such as Mo and Nb instead of Zr is considered as one of the countermeasures [2]. As the Doppler effects depend on the magnitude of self-shielding at the resonances, it is important to verify the Doppler effects at each resonance of the fuel alloy (Mo or Nb) materials to evaluate the feasibility of the uranium-free TRU metallic fuel. Therefore, we have performed the measurement of the Doppler effects for Mo sample by Time-of-flight (TOF) method with the KURRI-LINAC pulsed neutron source since 2016 [4, 5].

EXPERIMENTS: We measured the Doppler effects of a Nb metal sample using a pulsed neutron source at the 46 MeV electron linac in the Integrated for Radiation and Nuclear Science, Kyoto University. In the experiment, neutron capture rates in the Nb sample at 300 K and 600 K were obtained by prompt gamma-ray measurement with the TOF method. The Nb sample was placed in the center of a heating device at a distance of 10 m from the Ta target. The surface temperature of the sample was observed by thermoelectric couple and controlled to be constant during the irradiation by a glass-heater. Two kinds of samples with different thickness of 1.0 mm^t and 3.0 mm^t were prepared to identify the neutron self-shielding effects for each resonance. Those samples had cross sections of 2.0×2.0 cm². The measurements with thick and thin samples, no sample (blank run) at 300 K were carried out. The experimental conditions are shown in table 1.

Table 1 Experimental conditions

Sample	Temperature (K)	Measurement time (h)
3.0 mm ^t	300	28.0
3.0 mm ^t	600	30.8
1.0 mm ^t	300	11.7
1.0 mm ^t	600	9.9
Blank	300	7.2

RESULTS: The measured TOF spectra with 1.0 mm^t and 3.0 mm^t Nb samples at 300K are shown in Fig. 1. The main resonances of Nb-93 were clearly observed in the energy range from 10 eV to 10 keV. For further anal-

ysis, counting statistics observed in TOF spectrum were improved by the JSF70 group structure [6] corresponding to the lethargy width of 0.25. Table 2 shows the absorption rate ratio of 3.0 mm^t sample by Doppler effect. The absorption rate ratio defined as the absorption rate at 600 K divided by it at 300 K was obtained for each energy group. As the results, the absorption rate ratio were $1.16 \pm 1.9\%$ at the 41th group, $1.09 \pm 2.3\%$ at the 42th group, $1.15 \pm 1.3\%$ at the 44th group, $1.04 \pm 1.6\%$ at the 46th group and $1.06 \pm 4.9\%$ at the 51th group.

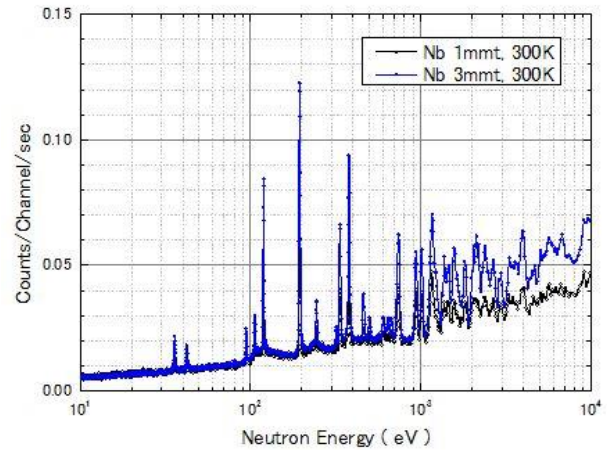


Fig1. Measured TOF spectrum

Table 2 Absorption rate ratio of 3.0 mm^t sample by Doppler effect

Energy group	Resonance (eV)	Absorption rate ratio
41	378.5	$1.16 \pm 1.9\%$
42	335.4	$1.09 \pm 2.3\%$
44	193.8	$1.15 \pm 1.3\%$
46	105.9, 119.1	$1.04 \pm 1.6\%$
51	35.9	$1.06 \pm 4.9\%$

This study is being performed under the contract with the Ministry of Education, Culture, Sports, Science and Technology of Japan (MEXT) in the framework of MEXT’s Nuclear System Research and Development Program.

REFERENCES:

- [1] K. Arie, *et al.*, Proc. of Global 2015, Sep. 20-24, Paris, France, Paper 5096, (2015).
- [2] K. Arie, *et al.*, Proc. of ICAPP 2014, Charlotte, USA, April 6-9, (2014).
- [3] Y. Nagaya *et al.*, JAERI1348, Japan Atomic Energy Research Institute, (2005).
- [4] T. Sano, *et al.*, Energy Procedia, 113C, 290-298, (2018).
- [5] T. Sano, *et al.*, KURRI Progress Report 2016, 28061, (2017).
- [7] M.Nakagawa, K. Tsuchihashi, JAERI 1294 (1984)

J. Hori, T. Sano, Y. Takahashi, D. Ito and K. Nakajima

*Institute for Integrated Radiation and Nuclear Science,
Kyoto University*

INTRODUCTION: A fast reactor system with trans-uranium (TRU) fuel containing minor actinides (MA) is considered as one of options for reduction the high-level radioactive waste from the nuclear power plants. It is important to test their integrity to confirm the fuel safety. Non-destructive nuclide assay is a key technology for nuclear material accountancy. Neutron Resonance Densitometry (NRD) is a non-destructive nuclide assay technique applicable to quantity nuclear materials in the fuel. For the TRU fuel having high radioactivity, a self-indication method [1] is adapted for the identification and quantification of nuclides in the fuels. In the self-indication method, an indicator consisting of the target nuclide is placed at the neutron beam downstream from a sample. The transmitted neutron thorough the sample can be measured indirectly by detecting the reaction products from the indicator with the neutron time-of-flight (TOF) method. The self-indicator is a transmission neutron detector that has high efficiency around the objective neutron resonance energies of the target nuclide, enabling us to quantify effectively the amount of resonance absorption of the target nuclide. Moreover, it is not easily affected by the decayed gamma-rays from the fuel. We carried out the quantitative examination of self-indication method for a nuclear material with highly enriched and depleted uranium-aluminum alloys.

EXPERIMENTS: The experiment was performed at the 46-MeV electron linear accelerator in Institute for Integral Radiation and Nuclear Science, Kyoto University. The linac was operated with a repetition rate of 300 Hz, a pulse width of 100 ns, a peak current of about 5 A, and an electron energy of about 35 MeV. We used a flight path in the direction of 135 degree with respect to the linac electron beam. A Cd sheet of 0.5 mm in thickness was also inserted into the TOF beam line to suppress overlap of low energy neutrons from the previous pulse due to the high frequency of the linac operation. A 4π $\text{Bi}_4\text{Ge}_3\text{O}_{12}$ (BGO) spectrometer was installed at the 12m flight path in the TOF beam line for the measurement of capture gamma rays from the indicator. A natural uranium sheet with the areal density of 7.36×10^{-3} (b) was used as a indicator. Five samples with different thickness were prepared by combining high enriched and depleted uranium-aluminum alloys. TOF measurements with and without samples were performed, respectively.

RESULTS: The TOF spectra with and without samples

are shown in Fig. 1. The resonances of ^{238}U were clearly observed at 6.67, 20.9, 36.7, 66.0, 80.7 and 103 eV. It can be seen that the reduction ratio of the resonance peak areas become larger as the areal density of ^{238}U increases. On the other hands, the relation curve between reduction ratio and the areal density was obtained by using Monte Carlo simulation for each resonance as shown in Fig. 2. As the results, the areal density of ^{238}U was obtained successfully by comparing the experimental reduction ratio with the estimated relation curves.

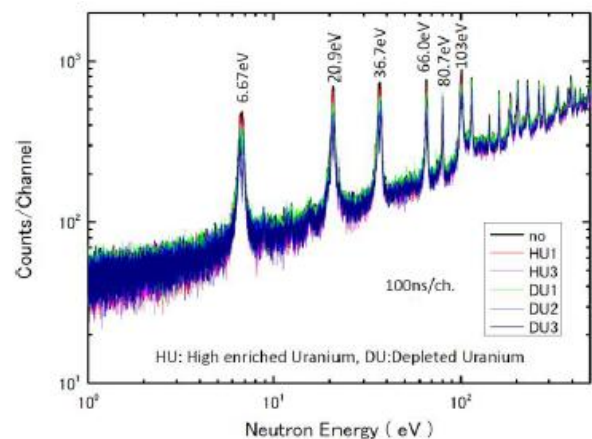


Fig.1 Comparison of TOF spectra with and without samples

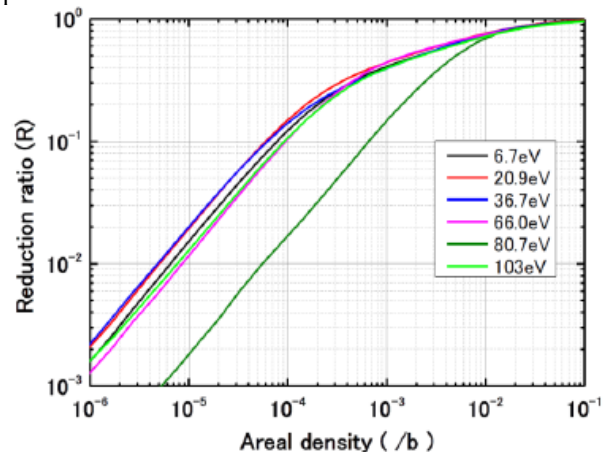


Fig.2 Relation between the reduction ratio and the areal density of the sample for each resonance of ^{238}U

Present study includes the result of “Development of Non-Destructive Methods Adopted for Integrity Test of Next Generation Nuclear Fuels” entrusted to the Kyoto University by the Ministry of Education, Culture, Sports, Science and Technology of Japan (MEXT).

REFERENCE:

[1] J. Hori *et al.*, EPJ Web of Conferences, **146** (2017) 09042 .

H. Tomita, T. Iguchi, K. Uema, K. Watanabe, T. Matsumoto¹, J. Kawarabayashi², E. Takada³, and J. Hori⁴

Graduate School of Engineering, Nagoya University
¹ National Institute of Advanced Industrial Science and Technology
² Tokyo City University
³ National Institute of Technology, Toyama College
⁴ Institute for Integrated Radiation and Nuclear Science, Kyoto University

INTRODUCTION: Identification of a hidden or shielded gamma radioactive sources and nuclear materials is required in anti-terrorism measures. We are developing passive and active gamma spectroscopy combined with gamma-ray imaging for these applications. Compton gamma imager can measure energy of incident gamma-ray and its direction to the detector. We applied a portable and 4π direction sensitive Compton imager [1-2] to identify ^{10}B sample by prompt gamma-ray with neutron irradiation at the pulsed neutron source at Kyoto University Institute for Integrated Radiation and Nuclear Science Linear Accelerator (KURNS-Linac).

EXPERIMENTS: Figure 1 shows an experimental setup at the pulsed neutron source. A 3D pixel array CdTe detector with 1440 ch. was used as a prototype of the 4π sensitive gamma-ray imager. The prototype CdTe detector was located at a distance of around 12 m from the neutron source. In our previous work based on Monte Carlo simulation using EGS5, the prototype Cd detector would be capable to identify a source position even if the gamma-ray energy emitted from the source is lower than 400 keV. A ^{10}B sample in an aluminum disk was irradiated by the pulsed neutron on the beam line.

RESULTS: Figure 2 shows a typical measured energy spectrum from the irradiated ^{10}B sample. Peaks corresponding to prompt gamma-ray of ^{10}B (478 keV) and ^{113}Cd (558, 651 keV etc.) appear clearly in the spectrum. Typical reconstructed image of ^{10}B prompt gamma-ray on a projection sphere around the prototype CdTe detector is shown in Fig.3. Note that ^{10}B was used in a shielding material surrounding the outlet of the pulsed neutron beam ($\theta=50^\circ$, $\varphi=0$) in this setup. Whereas the position of the ^{10}B sample ($\theta=-90^\circ$, $\varphi=0$) was localized by the prompt gamma-ray imaging, background events on the image were rather high due to interference of prompt gamma-rays from ^{113}Cd in the CdTe detector. To suppress the background in prompt gamma-ray analysis using the CdTe detector, we investigated shielding effect of a lithium fluoride tile to ^{10}B prompt gamma-ray used as a shielding material for thermal neutrons without any pro-

ductions of gamma rays by neutron absorption. One lithium fluoride tile was put in the front surface ($\theta = -90^\circ$ plane) of the detector. Even after passing through the lithium fluoride tile, the resolution of ^{10}B prompt gamma-ray image had same as that without the tile.

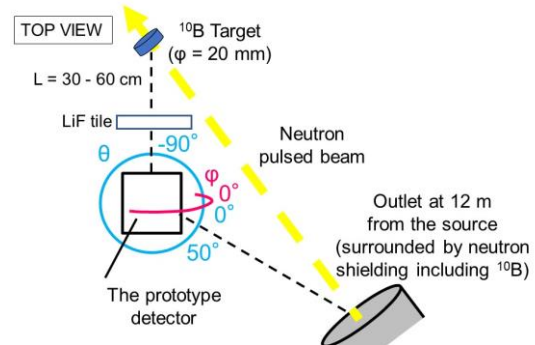


Fig. 1. Experimental setup at the pulsed neutron source.

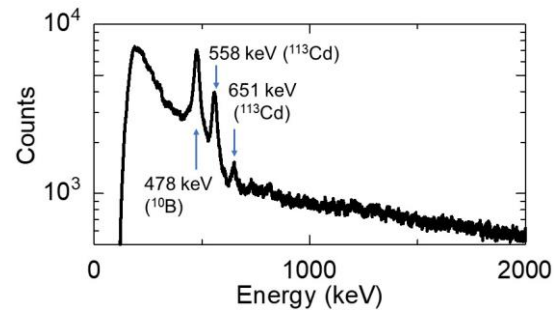


Fig. 2. Typical energy spectrum from the ^{10}B sample.

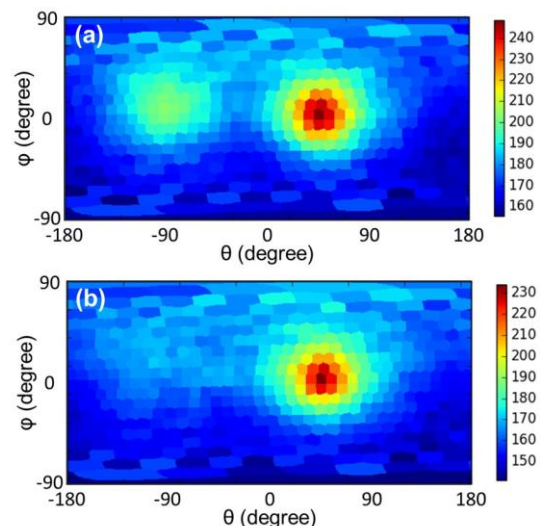


Fig. 3. Reconstructed images on the projection sphere (θ , φ), (a) with the ^{10}B sample and (b) with a dummy sample not including ^{10}B .

REFERENCES:

- [1] T. Takahashi, *et al.*, Proceedings ANIMMA, 1332, (2013).
- [2] Y. Fuwa *et al.*, JPS Conference Proceedings **11**, 070005 (2016).

CO2-5 Measurements of Epithermal Neutron Detector with a Boron Loaded Plastic Scintillator

T. Matsumoto, A. Masuda, H. Harano, H. Tomita¹ and J. Hori²

National Metrology Institute of Japan, National Institute of Advanced Industrial Science and Technology

¹Graduate School of Engineering, Nagoya University

²Institute for Integrated Radiation and Nuclear Science, Kyoto University

INTRODUCTION: Evaluation of neutron fluence and neutron dose equivalent for the epi-thermal neutron region is very important in work places with neutron sources or nuclear fuels as well as irradiation fields in a boron neutron capture therapy. In the present study, we have developed a precise epi-thermal measurement method that is not affected by nuclear reaction cross sections such as the $^{10}\text{B}(n,\alpha\gamma)$, $^3\text{He}(n,p)$ and $^6\text{Li}(n,\alpha)$ reactions. We experimentally evaluate the neutron detection system for absolute measurements of epi-thermal neutrons. The epi-thermal neutron detection system for absolute measurement is composed of a 50.8 mm diameter and 25.4 mm thick boron loaded plastic scintillation detector and two 50.8 mm diameter and 50.8 mm thick BGO scintillation detectors. In our previous experiments, a $^6\text{Li}^{\text{nat}}\text{Gd}^{10}\text{B}_3\text{O}_9:\text{Ce}+$ (LGB) scintillator was used as a boron containing scintillator. However, the LGB scintillator is not yet commonly used. In the present study, we tried to demonstrate epi-thermal neutron measurements using the neutron detection system with a boron loaded plastic scintillator that is commonly used.

EXPERIMENTS: A collimated neutron beam was obtained by the photo neutron reaction using a water-cooled tantalum target at the KURRI Linac [1]. Fig 1 shows the typical experimental arrangement. The boron loaded plastic scintillation detector was set at the center of beam line. The BGO scintillation detectors were placed on both side of the boron loaded plastic scintillation detector. For low energy neutrons, monoenergetic gamma rays with energy of 478 keV and alpha particles are produced in the plastic scintillation detector by the $^{10}\text{B}(n,\alpha\gamma)$ reaction. The alpha particles and a part of gamma rays are observed with the boron loaded plastic scintillator. The BGO scintillation detectors detects the rest of gamma rays. Characteristics of the neutron detection system were experimentally evaluated by means of the time-of-flight (TOF) method.

RESULTS: Fig.2 shows the two-dimensional plots of pulse heights of the boron loaded plastic scintillation detector and the BGO scintillation detector. In Fig.2, the area A indicates that

mono energetic gamma rays with 478 keV are detected by the BGO scintillation detector. In this case, the gamma rays produced by the $^{10}\text{B}(n,\alpha\gamma)$ reaction do not occur any reaction in the boron loaded plastic scintillator. On the other hand, the area B indicates that gamma rays are detected by the BGO scintillation detector after the Compton scattering reaction of the 478-keV gamma rays in the boron loaded plastic scintillator. We are developing a data analysis algorithm. The experimental results will be compared with experimental results of the previous studies.

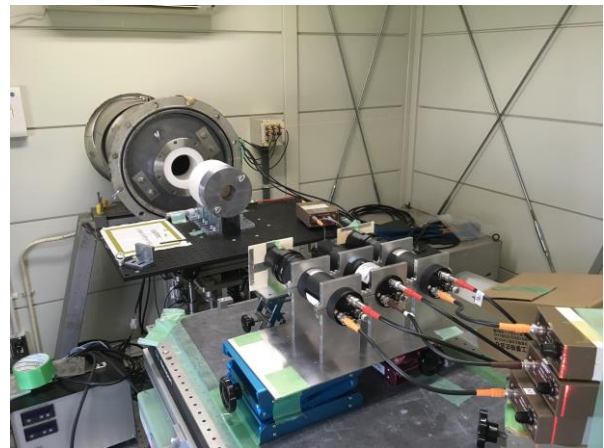


Fig. 1. Typical experimental arrangement in the KURRI linac facility.

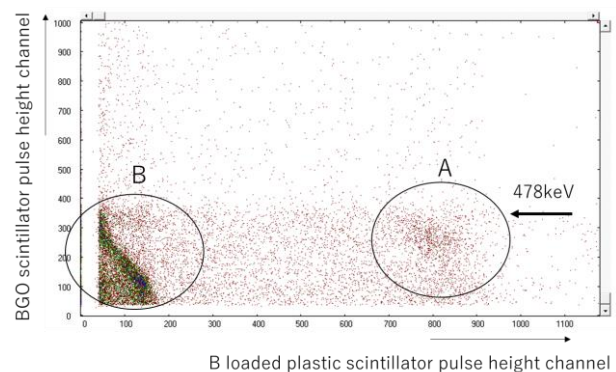


Fig. 2. Two-dimensional plots of pulse heights of the boron loaded plastic scintillation detector and the BGO scintillation detector.

REFERENCES:

[1] K. Kobayashi *et al.*, Annu. Rep. Res. Reactor Inst. Kyoto Univ. 22, 142 (1989).

This work was supported by JSPS KAKENHI(JP16K21679, JP16K09030).

CO2-6 Study of Isotope Separation via Chemical Exchange Reaction

R. Hazama, Y. Sakuma¹, T. Yoshimoto, H. Tatsubo, T. Fujii², T. Fukutani³, Y. Shibahara³

Graduate School of Human Environment, Osaka Sangyo University

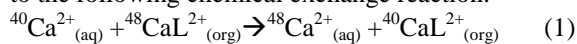
¹Research Laboratory for Nuclear Reactors, Tokyo Institute of Technology,

²Graduate School of Engineering, Osaka University

³Research Reactor Institute, Kyoto University

INTRODUCTION: By utilizing chemical separation method for calcium isotope effect in liquid-liquid extraction (LLE), an appropriate crown-ether (CE) can be used not only for separation of metal ions, but also for separation of isotope[1].

EXPERIMENTS: Isotopic enrichment occurs according to the following chemical exchange reaction:



where L represents macrocyclic polyether(18-crown-6). A 20 ml aqueous solution (3M CaCl₂) and 200 ml organic solution (0.07M DC18C6 in chloroform) were stirred by a magnetic stirrer for 60 m at room temperature and separated. This LLE was iterated six times (1–6)[2]. The large isotope effect with mass dependence was obtained by the back-extraction (BE) method [2]. However the Ca concentration was heavily degraded to the order of 10⁻⁶ after the six iteration/multistage LLE and this low mass content cannot be realized for the actual enrichment of Ca with a ton scale refinement. Thus we developed a new LLE procedure with maintaining the Ca concentration (partition factor) as much as possible and also keeping the separation factor as large as possible at the same time, which is shown in Fig. 1. It is well known that the relation between a separation factor and a partition factor is in a trade-off relationship. It is also noted that we can easily reuse the CE solution having Ca inside its cavity by detaching Ca via pure water only. By comparison, in the case of CE resin we are required to use high content (~9M) of HCl [3]. It is quite important that we can reuse the valuable CE easily and many times in terms of a cost-effective enrichment.

RESULTS: The Ca concentration in aqueous and organic phase for the new LLE procedure was measured by AAS. We can obtain about 20 % partition factor and its Ca transfer between two phases can be confirmed in Fig. 2, not to the other medium such as chloroform.

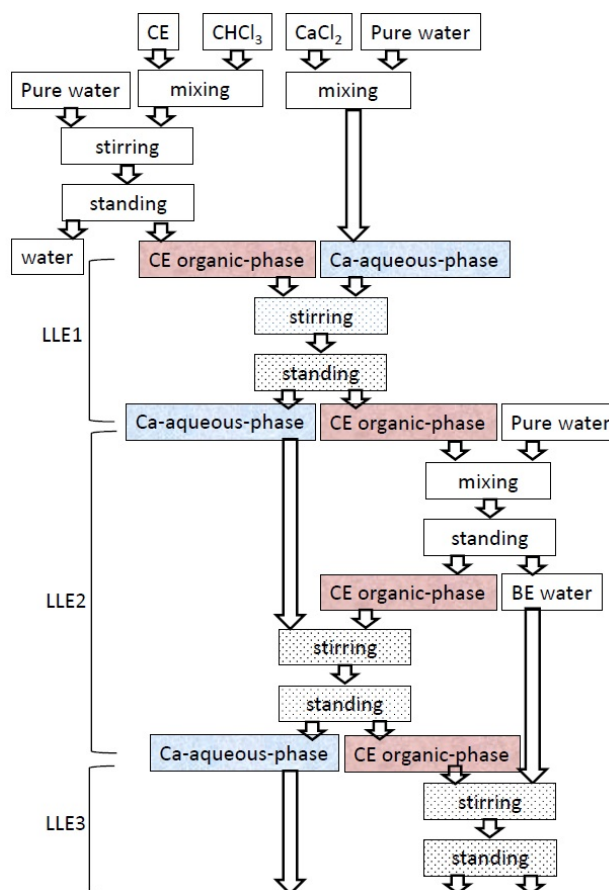


Fig 1. New LLE procedure with maintaining Ca concentration as much as possible and a separation factor at the same time, which allows to reuse CE via water only.

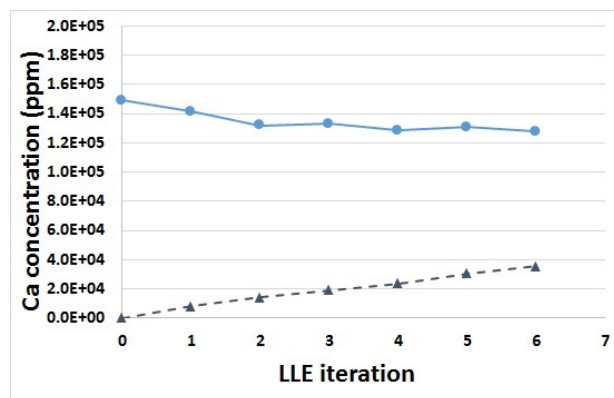


Fig 2. Ca concentration in aqueous phase (circle) and organic phase (triangle) for the process of LLE. Iteration is six times, zero is feed solution for CaCl₂ aqueous and crown-ether organic (CHCl₃) phase. : Preliminary.

REFERENCES:

- [1] B.E. Jepson *et al.*, J. Inorg. Nucl. Chem. **38**(1976)1175.
- [2] R. Hazama *et al.*, KURRI Progress Report 2016, 17.
- [3] K. Hayasaka *et al.*, Prog. in Nucl. Energy **50**(2008)510.

H. Ohta, Y. Nauchi, K. Nakamura and T. Sano¹

Nuclear Research Technology Laboratory,
Central Research Institute of Electric Power Industry

¹Institute for Integrated Radiation and Nuclear Science,
Kyoto University

INTRODUCTION: As an effort to improve the safety of light water reactors (LWRs), various concepts of “enhanced accident tolerant fuels and core components” are being developed in many countries. The Central Research Institute of Electric Power Industry (CRIEPI) has been developing an accident tolerant control rod (ATCR) to which the novel neutron absorbing materials including rare-earth sesquioxides (RE₂O₃) are applied¹. The ATCR improves the basic performance as a control rod such as the reactor shutdown margin and neutronic lifetime, and reduces the risk of re-criticality accident in any reactor conditions including severe accident (SA). For the ATCR candidate materials RE₂O₃-MO₂ (RE = Sm or Eu, M = Zr or Hf), a high temperature compatibility with iron or steel, which is a main component of current control rod cladding, and physicochemical stability under high temperature steam atmosphere were experimentally confirmed so far². Furthermore, a reactivity analysis in the representative LWRs revealed that these candidate materials have enough reactivity worth comparable to or higher than the conventional neutron absorbing materials B₄C or Ag-In-Cd alloy¹. In this study, the reactivity worths of RE₂O₃-MO₂ are measured to verify the analysis results in view of the importance of control rod functions such as power adjustment, shutdown and scram of reactor.

EXPERIMENTS: A critical core with thermal neutron spectrum (E3 core) was assembled in A-core of Kyoto University Critical Assembly (KUCA) as shown in Fig. 1. The unit cell of fuel assemblies is composed of a 93% enriched ²³⁵U-Al alloy fuel plate of 2"×2"×1/16" and 3 polyethylene plates of 2"×2"×1/8"/plate. An Al-holder that contains a mixed powder sample of RE₂O₃-MO₂ was loaded in the center of core and the reactivity worth of each sample was measured with the period method. Reactivity worth of each sample in E3 core was calculated using the continuous-energy Monte Carlo code MVP-3 with 2.58 billion neutron histories. The statistical error of reactivity calculation was less than 3pcm. The neutron cross section libraries were generated using JENDL- 4.0.

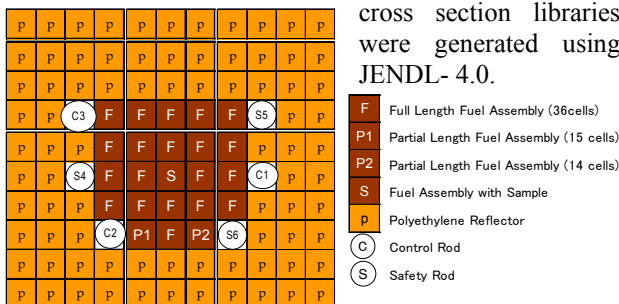


Fig. 1 Configuration of E3 core assembled in KUCA A-core.

RESULTS: The measurement results of reactivity for mixed powders of Sm₂O₃-MO₂ and Eu₂O₃-MO₂ are shown in Figs. 2 and 3, respectively. The self-shielding effect due to the strong neutron absorption of RE₂O₃ suppresses the change in reactivity worth even if excessive RE₂O₃ of 1.5-2.0g or more is loaded. Tables I and II summarize the differences between calculations (C) and measurements (E) of reactivity for Sm₂O₃-MO₂ and Eu₂O₃-MO₂, respectively. For all samples, the reactivity worth was predicted with high accuracy of less than 10pcm differences. From these results, validity of nuclear data of Sm, Eu, Zr and Hf in the thermal energy region was verified. As confirmed by the reactivity worth analysis in the representative LWRs¹, RE₂O₃-MO₂ is considered to be applicable as the alternative control materials.

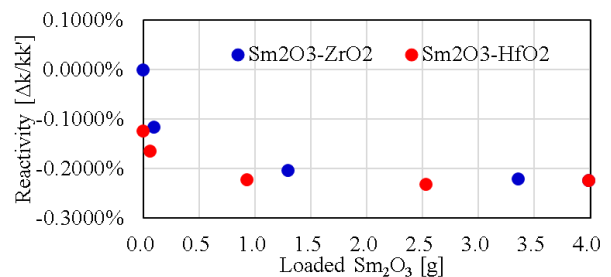


Fig. 2 Measurement results of reactivity for Sm₂O₃-ZrO₂ or Sm₂O₃-HfO₂.

Table I Differences between Calculations and Measurements (C-E) of Reactivity for Sm₂O₃-ZrO₂ or Sm₂O₃-HfO₂

Sm ₂ O ₃ [g]	0	0.058	0.93	2.5	0	0.093	1.3	3.4	4.0
HfO ₂ [g]	6.7	7.0	5.6	3.1	0	0	0	0	0
ZrO ₂ [g]	0	0	0	0	6.6	6.6	4.6	1.1	0
C-E [pcm]	6.4	8.6	5.8	2.9	3.4	3.2	-3.9	-2.3	3.4

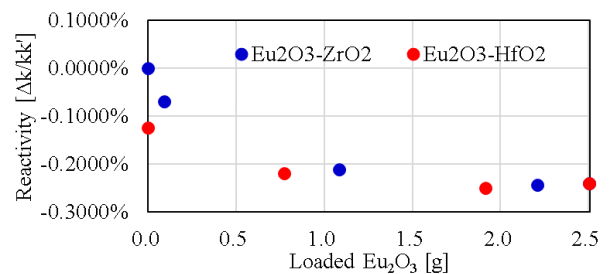


Fig. 3 Reactivity Measurement Results of Eu₂O₃-ZrO₂ or Eu₂O₃-HfO₂.

Table II Differences between Calculations and Measurements (C-E) of Reactivity for Eu₂O₃-ZrO₂ or Eu₂O₃-HfO₂

Eu ₂ O ₃ [g]	0	0.11	0.77	1.9	0	0.092	1.1	2.2	2.5
HfO ₂ [g]	6.7	6.5	4.6	1.0	0	0	0	0	0
ZrO ₂ [g]	0	0	0	0	6.6	6.6	4.6	1.1	0
C-E [pcm]	6.4	-	5.1	3.9	3.4	-1.4	-2.6	3.2	2.8

REFERENCES:

- [1] H. Ohta, *et al.*, TopFuel 2016, 17556 (2016).
- [2] K. Nakamura, *et al.*, AESJ 2017 spring meeting, 1106 in Japanese.

CO3-1 Basic Research for Sophistication of High-power Reactor Noise Analysis

S. Hohara, A. Sakon, K. Nakajima¹ and K. Hashimoto

Atomic Energy Research Institute, Kindai University

¹ Interdisciplinary Graduate School of Science and Engineering, Kindai University

INTRODUCTION: Reactor noise for high-power reactors were actively measured in the 1960's and 1970's. The major focuses of those researches were for the abnormality diagnosis or the output stabilization diagnosis, and almost researchers were in the field of system control engineering or instrumentation engineering. High-power reactor noise measurements for dynamics' analysis of reactivity change, reactivity feedback or reactor characteristics itself were few in the time (1960's and 1970's), because of the powerless measurement system. In this research, we plan to measure KUR's output with present-day measurement system and plan to analyze with several analysis methods. The results of this work will supply some knowledges and technics in the aspect of sophistication of reactor noise analysis or simulation methods.

In this year, we just started this research after 3years waiting for KUR's operation resuming. The experimental work was done in 30th January 2018. The allocated time for the experiment (that is consistent with the objective of this work) was only 1.5 hour, and the condition was far from what we hoped, because of the administrative problem and the following waiting experimental run (those were not of me!). However, some results were acquired from the bad-condition experiment, and I report those in this report paper.

EXPERIMENTS: In this experiment, the output signal was lined from the control console of KUR. The target signals were of the fission chamber #1 & #2. The signals were binarized in the control console as 4V/0.5 μ sec-TTL signals. The signal was measured by a time-series measurement system (HSMCA4106_LC: ANSeeN Inc.). A schematic view of the measurement is shown in Fig.1.

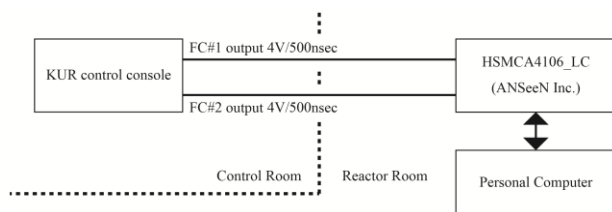


Fig. 1. Schematic view of the measurement.

The experimental condition is shown in Table.1. The allocated time for each condition was only 10 – 30 minutes, and the control rods were occasionally moved in the period of the measurements. (We requested NOT to move

the control rods in the measurements' period, however the request was rejected by the operation staff for the output adjustment.)

Table 1. Experimental condition

KUR power [W _{th}]	Measurement Time [sec]	FC#1 Position [%]	FC#2 Position [%]
20	700	14	19
1k	800	33	38
100k	1,800	51	62

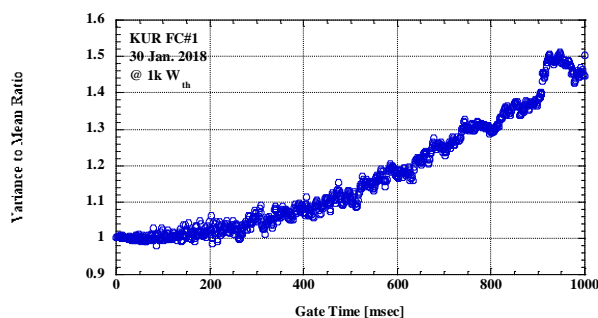


Fig.2. (a) Analyzed result of FC#1 for 1kW_{th} operation

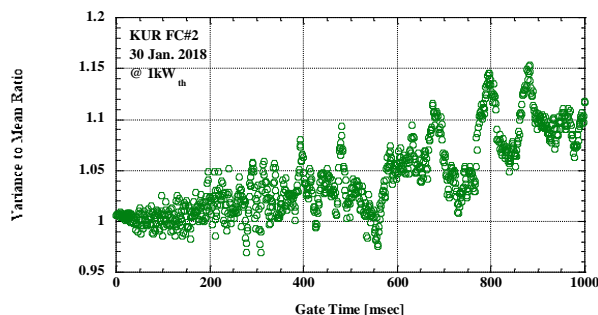


Fig.2. (b) Analyzed result of FC#2 for 1kW_{th} operation

RESULTS: Typical results of the experiments are shown in Fig.2 (a) and (b). Fig.2(a) shows an analyzed results of fission chamber #1 signal for 1kW_{th} operation with the Feynman- α analysis, and Fig.2(b) shows an analyzed results of fission chamber #2 signal for 1kW_{th} operation with the Feynman- α analysis. The vertical axis is the Variance to Mean Ratio, and the horizontal axis is the gate time. The analysis was done with the “bunching method”. The Variance to Mean Ratio increase with the gate time width expanding, and the ratio have fine structures. The increasing trend is estimated to be of the control rod moving, and the fine structures are estimated to be a characteristic of the “bunching method”. We are planning to apply another analysis method in the next experiments at KUR.

G. Chiba, M. Yamanaka¹ and C. H. Pyeon¹

Graduate School of Engineering, Hokkaido University

¹Institute for Integrated Radiation and Nuclear Science, Kyoto University

INTRODUCTION: Solution for the issue on the accumulation of minor actinides (MAs) from the operation of light water reactors (LWRs) has been proposed by reducing the amount of MA by the transmutation with high-energy neutrons before the disposal into underground. Among of MAs, nuclides of ^{237}Np and ^{241}Am constitute high radiotoxicity in the spent fuel from LWR and become a main target for the transmutation. For attaining the transmutation system, the accuracy of the nuclear data library of MA is regarded as quite important at a hard spectrum core because the accuracy influences the transmutation amount. However, the nuclear data library needs improvement for the MA and requires the accumulation of differential and integral experiments. Previous studies [1]-[3] were conducted for acquiring the fission reaction rate of ^{237}Np and ^{241}Am in integral experiments with thermal core. For the transmutation system, the experiment is also requisite in the high-energy neutrons. Accordingly, in this study, special attention was paid for the acquisition of $^{237}\text{Np}/^{235}\text{U}$ and $^{241}\text{Am}/^{235}\text{U}$ fission reaction rate ratios by the irradiation experiments with 14 MeV neutrons at the Kyoto University Critical Assembly (KUCA).

EXPERIMENTAL SETTINGS: For the irradiation experiments with 14 MeV neutrons, an irradiation hole was constituted in front of the tritium target at the KUCA-A core surrounding iron reflector, as shown in Fig. 1. ^{237}Np or ^{241}Am foil was set in the back-to-back (BTB) type double fission chamber with ^{235}U foil for normalization. By the insertion of objective foil (^{237}Np or ^{241}Am) and reference foil (^{235}U) closely into the BTB fission chamber and the irradiation at the same time, the fission counts could be regarded as the fission reaction rates under same neutron spectrum and flux. The results of the experiments were accumulated as an index of the fission reaction rate ratio of objective foil to reference foil. 14 MeV neutrons were prepared by the deuteron beam injection onto the tritium target. Deuteron accelerator was operated under 10 Hz of pulsed repetition, 80 μs of pulsed width and 0.1 mA of beam current. The irradiation time was for 2 hours.

RESULTS: The pulsed height distributions from the BTB fission chamber were obtained as shown in Fig. 2, and revealed very poor signals about fission reactions for all foils (discrimination channel between fission reactions and others: 125, 89 and 87 for ^{235}U , ^{237}Np and ^{241}Am , respectively). Although the effective signals indicating the fission reactions were very few, both fission reaction rate ratios were obtained in both foils, as shown in Table 1. Here, in the comparison of fission cross sections at 14

MeV neutrons between ^{235}U , ^{237}Np and ^{241}Am , the values are 2.053, 2.148 and 2.710 barns in JENDL-4.0. Thus, measured fission reaction rate ratio showed the possibility to be valid because the value of fission reaction rate ratio could be predicted near 1.0 from the division of fission cross section by $^{237}\text{Np}/^{235}\text{U}$ and $^{241}\text{Am}/^{235}\text{U}$. An improvement of 14 MeV neutron yield is needed to be higher measurement accuracy of MA irradiation experiments. Since spectrum indices of $^{37}\text{Np}/^{235}\text{U}$ and $^{241}\text{Am}/^{235}\text{U}$ fission reaction rate ratios were significantly obtained at 14 MeV neutrons in the experiments, numerical analyses are expected to be conducted to verify uncertainty of the MA cross sections in nuclear data library.

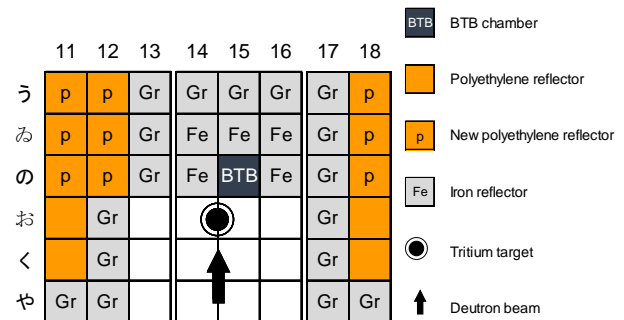


Fig. 1. Experimental settings of MA irradiation.

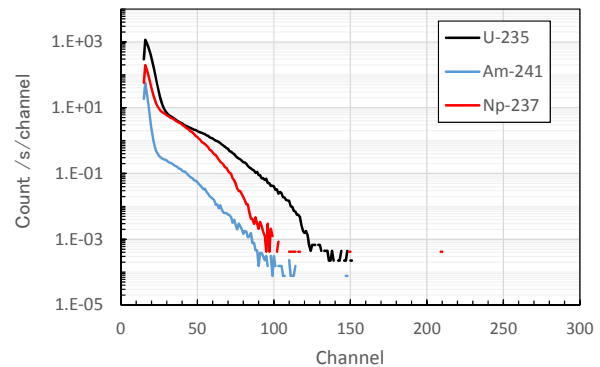


Fig. 2. Pulsed height from BTB fission chamber.

Table 1. $^{237}\text{Np}/^{235}\text{U}$ and $^{241}\text{Am}/^{235}\text{U}$ fission reaction rate ratios.

Nuclide	Fission reaction rate ratio to ^{235}U
^{237}Np	0.8141
^{241}Am	1.1501

REFERENCES:

- [1] H. Unesaki, *et al.*, J. Nucl. Sci. Technol., **37** (2000) 627-635.
- [2] H. Unesaki, *et al.*, J. Nucl. Sci. Technol., **38** (2001) 600-606.
- [3] T. Iwasaki, *et al.*, J. Nucl. Sci. Technol., **39** (2002) 920-923.

CO3-3 Neutronics of U-Fueled and Pb-Zoned Core in Accelerator-Driven System

C. H. Pyeon¹, M. Yamanaka¹, J. Gao² and C. Liu²

¹ Institute for Integrated Radiation and Nuclear Science, Kyoto University

² Institute of Nuclear Energy Safety and Technology, Chinese Academy of Sciences, China

INTRODUCTION: At the Kyoto University Critical Assembly (KUCA), the uranium (U)-fueled and lead (Pb)-zoned core (A(1/8"p60EUEU<1/8"Pb40p20EU EU>1/8"p60EUEU)) was newly comprised to evaluate the reactor characteristics of the accelerator-driven system (ADS), as shown in Fig. 1. In this core, two types of fuel rods were used for modeling the Pb-cooled reactor. The fuel rod containing Pb (f: 1/8"Pb40p20EUEU) was placed at the center region of the core and composed of 40 time repetition of a unit cell by 1/8" highly-enriched uranium (HEU) thick and 1/8"Pb thick plates sandwiched upper and lower parts by 10 time repetition of another unite cell by 1/8"HEU and 1/8"p plates. Further, the other fuel rod (F: 1/8"p60EUEU), composed of 60 time repetition of a unit cell by 1/8"HEU thick and 1/8"p (p: polyethylene moderator) thick plates, was used to surround the Pb-loaded fuel rods. In a series of ADS experiments, the subcriticality was varied by substituting the fuel rod for the polyethylene reflector, in order to provide deep subcriticality ranging between about 3,000 and 7,000 pcm; $k_{eff} = 0.97$ to 0.93).

EXPERIMENTS: The subcriticality measurement was carried out in the ADS experiment by the pulsed neutron source method with the use of 14 MeV neutrons (pulsed repetition 100 Hz, pulsed width 80 μ s and intensity 0.3 mA). The subcriticality was obtained by the α -fitting method, the Feynman- α method and the area ratio method, as shown in Table 1. From the results in Table 1, the BF₃#2 detector response revealed good agreement with reference result, and conversely BF₃#3 was compared with reference one, giving a large discrepancy caused by a closing location to 14 MeV neutron source. The irradiation experiment was carried out to obtain the reaction rate distribution with the use of indium (In) wire (1.5 mm diameter and 700 mm long) in the subcritical core together with 14 MeV neutrons. The deuteron accelerator was operated at pulsed repetition 100 Hz, pulsed width 80 μ s and intensity 0.3 mA for 1 hour. The ¹¹⁵In(*n*, γ)¹¹⁶In reaction rate distribution is shown in Fig. 2, demonstrating the thermal neutron flux information on normal fuel (F) and U-Pb zoned (f) core configuration.

CONCLUSION: The ADS experiments with 14 MeV neutrons were carried out in the KUCA A core (U-fueled and Pb-zoned core), and neutronics of U-Pb core were

investigated through the measurements of static and kinetic parameters in the reactor physics.

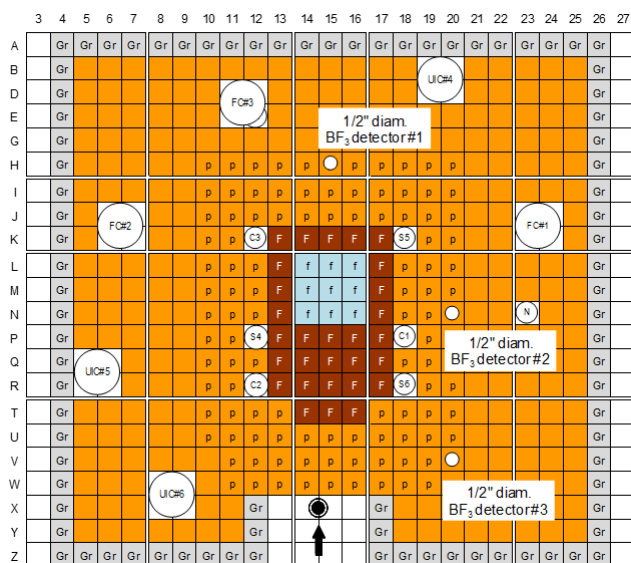


Fig. 1 Top view of configuration of U-fueled and Pb-zoned core.

Table 1 Result of subcriticality measurement in α -fitting method [pcm].

Reference (MCNP)	BF ₃ #1	BF ₃ #2	BF ₃ #3
3397 ± 13	3658 ± 167	3812 ± 198	4385 ± 1319
5032 ± 13	5252 ± 108	5285 ± 88	7230 ± 333
7491 ± 13	7626 ± 237	7613 ± 166	11326 ± 515

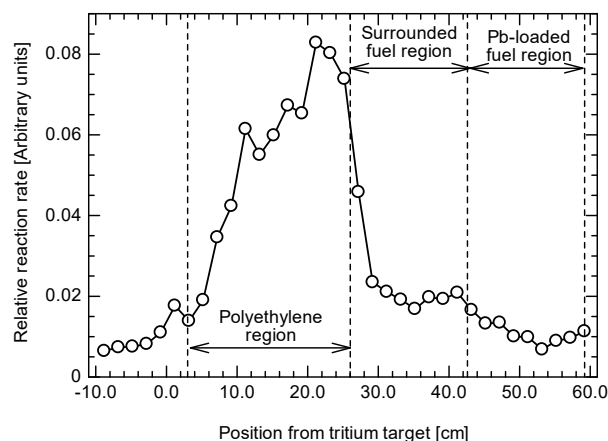


Fig. 2 Measured results of ¹¹⁵In(*n*, γ)¹¹⁶In reaction rates along (16, 17 – Z, L) in Fig. 1.

ACKNOWLEDGEMENT: This research was conducted under the collaboration research between INEST/CAS, China and Research Reactor Institute, Kyoto University.

Subcriticality Measurement by Advanced Rossi- α Fitting in Accelerator-Driven System

C. Kong, S. Yum, J. Jang, W. Lee, K. H. N. Nguyen, T. D. C. Nguyen, V. Dos, H. Kim, D. Lee, M. Yamanaka¹ and C. H. Pyeon¹

Department of Nuclear Engineering, Ulsan National Institute of Science and Technology (UNIST), Korea

¹*Institute for Integrated Radiation and Nuclear Science, Kyoto University*

INTRODUCTION: A new polyethylene-moderated A-core has been designed at Kyoto University Critical Assembly (KUCA) for a subcritical reactivity estimation experiment. UNIST students carried out the experiment to apply noise analysis methods for estimating the new core's subcriticality. Among the noise analysis methods, Rossi-alpha, Feynman-alpha, and advanced Rossi-alpha methods have been applied for subcriticality estimation. These three methods obtain a decay constant α using their fitting curve formulae and calculate a reactivity ρ from α using the delayed neutron fraction β and neutron generation time Λ . The β and Λ were given by an independent experiment carried by the KUCA professional staffs.

EXPERIMENTS: The core configuration is shown in Fig. 1. As shown in Fig. 1, "F" is a normal fuel assembly composed of uranium and polyethylene, "f" is a special fuel assembly composed of uranium, polyethylene, and lead, "p" is a polyethylene moderator assembly, "C1~C3" are control rods, "S4~S6" are safety rods, "FC#1~FC#3" are fission chambers, and "N" is an Am-Be neutron source located outside the core. The only difference between normal and special fuel assemblies is the presence of lead for the neutron spectrum control. The detector signals from the FC#1 has been used for analysis.

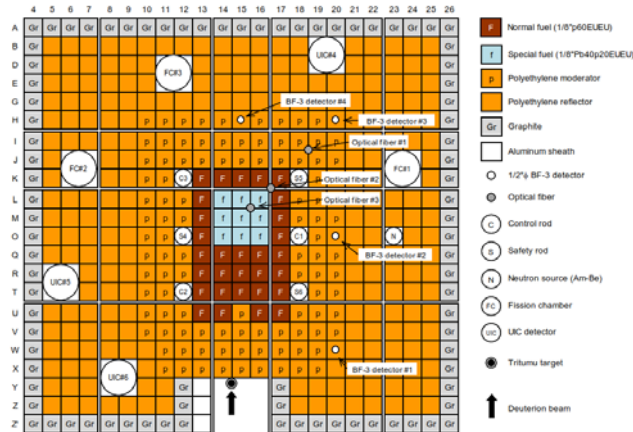


Fig. 1. KUCA core configuration

RESULTS: Table 1 summarizes the analysis results of the noise analysis methods using the FC#1's detector signals. The reference reactivities were provided by an independent experiment carried by the KUCA professional staffs. Figs. 2-4 show the Rossi-alpha, Feynman-alpha, and advanced Rossi-alpha fitting results.

Table 1. Analysis results using noise analysis methods

Method	Rossi-alpha	Feynman-alpha	Advanced Rossi-alpha
α	1766 ± 45	786 ± 45	1863 ± 17
ρ	-5028 ± 150	-1766 ± 151	-5351 ± 56
*Ref. ρ	-5211 ± 14	-1646 ± 40	-1646 ± 40
ρ error	-3.5 ± 2.9	7.3 ± 5.4	2.7 ± 0.9

*Reference ρ provided by the KUCA staff.

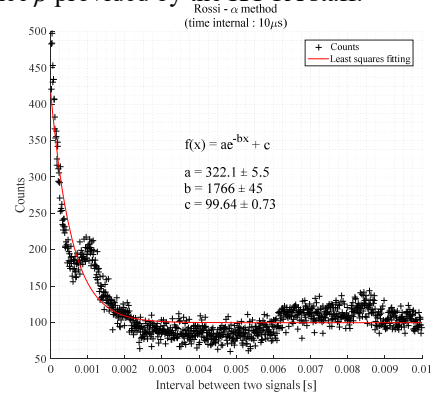


Fig. 2. Rossi-alpha fitting result

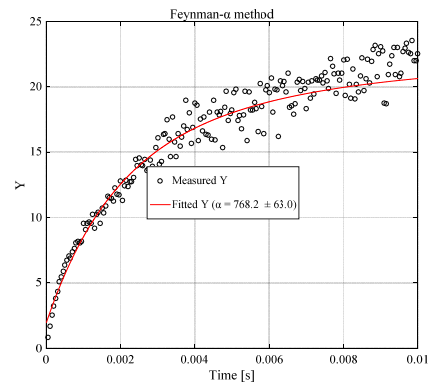


Fig. 3. Feynman-alpha fitting result

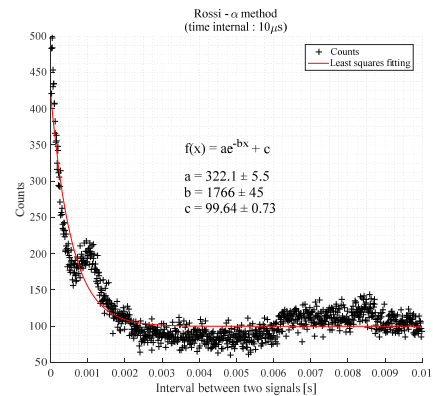


Fig. 4. Advanced Rossi-alpha fitting result

ACKNOWLEDGEMENT: This research was conducted under the collaboration research between UNIST, Korea and Research Reactor Institute, Kyoto University.

CO3-5 Measurement of Bismuth Sample Reactivity Worth in A-core of KUCA for ADS

M. Fukushima, A. Oizumi, K. Tsujimoto, M. Yamanaka¹ and C. H. Pyeon¹

Nuclear Science and Engineering Center, Japan Atomic Energy Agency

¹Institute for Integrated Radiation and Nuclear Science, Kyoto University

INTRODUCTION: The Japan Atomic Energy Agency (JAEA) has investigated neutronics of the accelerator-driven system (ADS) of a lead bismuth eutectic (LBE) cooled-tank-type core to transmute minor actinides discharged from nuclear power plants. For the design study of ADS [1], integral experimental data of nuclear characteristics of LBE is necessary to evaluate the error and uncertainty of cross sections of lead (Pb) and bismuth (Bi). This study aims to measure the Bi sample reactivity worth under the same conditions as the previous experiment for the Pb sample reactivity worth in FY2013 [2].

EXPERIMENTS: The Bi sample reactivity worth was measured by substituting Al plates for Bi ones in test fuel region at the critical state. Here, the reference configuration loaded with Al plates was constructed as the same one as the previous experiment for the Pb sample reactivity worth [2]. In the test fuel region, the number of test fuel assemblies was five, setting around the core central zone of (14, M), (15, L), (15, M), (15, O) and (16, M) as shown in Figure 1.

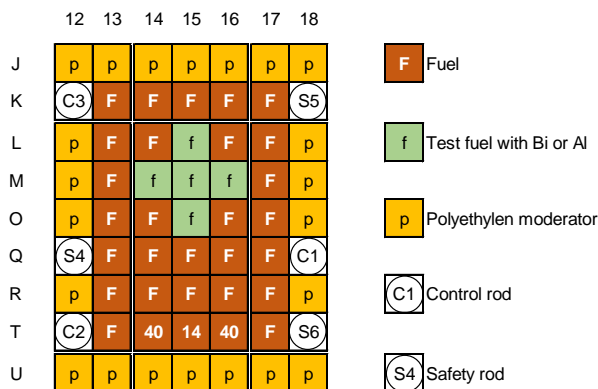


Figure 1 Core configuration of A-core of KUCA for Bi sample reactivity worth experiment

The patterns of Bi sample reactivity worth experiment were summarized in Table 1. In a total number of 40 unit cells of the central test region of fuel rod, two plates of Al (1/16") were substituted for two plates of Bi (1/16") per unit cell. This substitution is quite similar to that of the previous experiment except that the Bi plates were used instead of Pb ones. The Bi sample reactivity worth was

estimated through the difference of the excess reactivities between Al reference core and Bi core. In the experiment, the critical state was adjusted by maintaining the control rods in certain positions, and then the excess reactivity was deduced by the difference between the critical and super-critical states in the core. The experimental excess reactivity was obtained by combining with the reactivity worth of each control rod evaluated by the rod drop method and its integral calibration curve by the positive period method.

Table 1 Pattern of Bi sample reactivity worth experiment

Core	Test fuel region				
	(14,M)	(15,L)	(15,M)	(15,O)	(16,M)
Ref.	Al	Al	Al	Al	Al
Case 1	Bi	Al	Bi	Al	Bi
Case 2	Al	Bi	Bi	Bi	Al
Case 3	Bi	Bi	Al	Bi	Bi
Case 4	Bi	Bi	Bi	Bi	Bi

RESULTS: The Bi sample reactivity worth experiment was successfully carried out from the viewpoint of reproducibility of the previous Pb sample reactivity worth experiment [2], since measured excess reactivity of the Al reference cores for the Bi and Pb experiments were comparable in the same condition, as shown in Table 2. The absolute values of Bi sample reactivity worth were experimentally found to be less than those of Pb ones per equivalent volume. The analysis of the results is in progress. A comparative study on Bi and Pb sample reactivity worth would be available to assess qualitatively neutron characteristics of Pb-Bi coolant material in actual ADS experimental facility, with the combined use of experimental and numerical results.

Table 2 Comparison between the results of measured excess reactivities in Bi and Pb cores.

Core	Bi sample (pcm)	Pb sample (pcm) ^[2]
Ref.	87±1	92±5
Case 1	143±3	186±7
Case 2	165±3	202±8
Case 3	163±3	237±9
Case 4	171±3	248±9

Acknowledgement

This study is supported under the Innovative Nuclear Research and Development Program by the Ministry of Education, Culture, Sports, Science and Technology of Japan.

REFERENCES:

- [1] K. Tsujimoto, *et al.*, J. Nucl. Sci. Technol., **41**, 21-36 (2004).
- [2] C. H. Pyeon, *et al.*, J. Nucl. Sci. Technol., **53**, 602-612, (2016).

Y. Nauchi, S. Sato, M. Suzuki, H. Ohta, T. Sano¹ and H. Unesaki¹

Central Research Institute of Electric Power Industry

¹Research Reactor Institute, Kyoto University

INTRODUCTION: In Fukushima Dai Ichi nuclear power plant, so called fuel debris was formed. The fuel debris would be retrieved and enclosed in containers. For the efficient storage of the fuel debris, taking account of negative reactivity by capture reactions of stainless steel (Capture Credit) had been proposed [1]. That is based on the neutron induced gamma ray spectroscopy (NIGS) to obtain reaction rate ratio of the capture to the fission. Additionally, quantification of neutron capture reactions in ^{238}U is also desirable since $^{238}\text{U}(n,\gamma)$ is one of the most significant reactions in a system where low-enriched U is used. The reaction rate ratio of $^{238}\text{U}(n,\gamma)$ / fission would be of use to deduce the residual enrichment. In a zero-power critical system, the reaction rate could be obtained by detection of 0.278 MeV γ rays from β decay of ^{239}Np . However, for fuel debris, detection of the γ rays is not practical due to intense background γ rays from fission products (FP) such as $^{134,137}\text{Cs}$, ^{154}Eu , ^{144}Pr , and ^{106}Rh . Accordingly, we focused on prompt γ ray of 4.060 MeV from $^{238}\text{U}(n,\gamma)$ [2] since the energy is greater than highest one of long-lived FP γ rays. However, the emission of the 4.060 MeV γ ray is not evaluated in JENDL-4 [3] and the γ ray had never been detected in KUCA-C core where 93%- ^{235}U enriched U-Al fuel is loaded [4].

EXPERIMENTS: One of the noise for the measurements of 4.060 MeV γ ray is the prompt fission one, of which intensity is roughly proportional to the amount of ^{235}U . In order to enhance the signal to noise ratio, the average ^{235}U enrichment was reduced to 5.4 % in KUCA-A core by combined use of 93%- ^{235}U enriched U-Al with U- alloy plates of natural enrichment. In Fig. 1, the sub-critical set up of 5x5Al/8²p70EUDU is shown. The core was driven by a ^{252}Cf neutron source located center of the fuel. A HP-Ge detector of 20% relative efficiency is used for the γ ray measurement. In order to shield the detector from the neutron irradiation, 7 layers of polyethylene cells were also loaded. The measurement time was 2.5 h.

The overall measured spectrum is shown in Fig. 2. The most prominent peak is of 2.223 MeV γ ray from H(n, γ) reaction. In higher energy region, a photo-electric peak of 7.724 MeV γ rays from $^{27}\text{Al}(n,\gamma)$ reaction is prominent although count rates of its single and double escape peaks are larger. Between these peaks, continuum spectrum of prompt fission γ rays and small peaks are found. Using the peaks with those of prominent $^{27}\text{Al}(n,\gamma)$ peaks [5], the pulse height was calibrated. Then a peak spectrum of 4.060 MeV was identified. Since no peak is found in 4.571 MeV, the 4.060 MeV peak is of a photo-electric peak. No significant γ ray emission other than that from $^{238}\text{U}(n,\gamma)$ is reported in CapGam [5]. According to

JENDL-FPY/FPD-2011 [6], γ ray of 4.0617 MeV from ^{90}Rb generated by fission reactions may contribute to the peak of 4.060 MeV. However, the ^{238}U contribution is found greater than 91% in the peak by the count rates of another γ rays (4.135 MeV) from ^{90}Rb . Summarizing the results, we conclude detection of the 4.060 MeV γ ray from $^{238}\text{U}(n,\gamma)$ reaction is available for sub-critical systems of low-enriched U.

In the measured spectrum, several kinds of γ ray from fission products, such as, $^{88}\text{Br}(T_{1/2}=16.5\text{ s})$, $^{90}\text{Rb}(T_{1/2}=158\text{ s})$, $^{91}\text{Rb}(T_{1/2}=58\text{ s})$, $^{95}\text{Y}(T_{1/2}=10.3\text{ min})$, $^{97}\text{Y}(T_{1/2}=3.8\text{ s})$, $^{136}\text{Te}(T_{1/2}=17.5\text{ s})$ are observed. The intensity of them is known as a good indicator to infer ratio of fission nuclides [7]. Combining count rates of γ rays from those FPs, $^{238}\text{U}(n,\gamma)$, and prompt fission, nuclide densities inside the system might be inferred.

square cell: 5.53cm \times 5.53cm

yellow: polyethylene, red: fuel-cell(1/8" p72EUNU)

star: Cf-source, green: Pb-Bb(small perturbation)

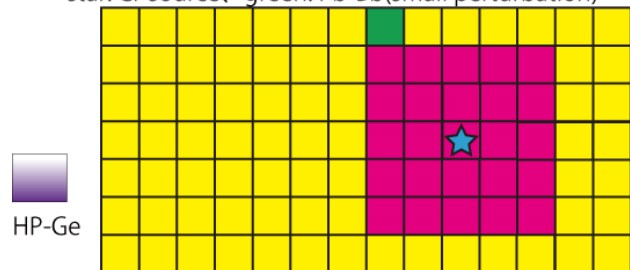


Fig.1 Horizontal geometry of fuel and detector.

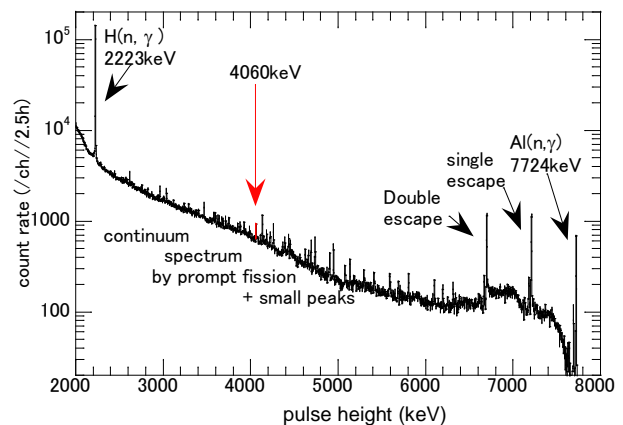


Fig.2 NIGS spectrum obtained in KUCA-C core.

REFERENCES:

- [1] Y. Nauchi *et al.*, JNST **52** (2015), 1074-1083.
- [2] G. L. Molnar *et al.*, NIM B **213** (2004), 389-393.
- [3] H. HAGURA *et al.*, Preprints Fall Meeting of Atomic Energy Society of Japan (2012), I28.
- [4] Y. Nauchi *et al.*, KURRI Progress Report 2012, VIII-II-1, CO3-7.
- [5] J. Tuli, <http://www.nndc.bnl.gov/capgam/>.
- [6] J. Katakura, JAEA-Data/Code 2011-025 (2011).
- [7] V. V. Mozin *et al.*, JNMM, **40** (2012), 78-87.

K. Watanabe, T. Endo, A. Uritani, A. Yamazaki, M. Yamanaoka¹ and C. H. Pyeon¹

Graduate School of Engineering, Nagoya University
²Research Reactor Institute, Kyoto University

INTRODUCTION: Neutron detection technology is one of the key issues in reactor physics experiments. Some specifications, such as the detection sensitivity, the dynamic range and the detector size, are required depending on purposes of experiments. A small size detector is quite useful because it can be easily inserted into a narrow space in an experimental reactor core and make little perturbation to a reactor. We are developing a new optical fiber type neutron detector, which can show a peak shape in a pulse height spectrum [1]. Since this type of detectors has only a small grain of a Eu:LiCaAlF_6 scintillator, its sensitivity is quite low. In order to improve the sensitivity, the number of scintillator grains should be increased. A wavelength-shifting fiber (WLSF) could be useful to collect uniformly scintillation photons from a large number of small scintillator grains. In this study, we fabricated a new optical fiber type neutron detector consisting of a small neutron scintillator and a WLSF connected to a clear optical fiber light guide. We, additionally, evaluated the response of the fabricated detector.

EXPERIMENTS: Figure 1 shows the photograph of the fabricated detector. The LiF/Eu:CaF_2 eutectic scintillators were used instead of the Eu:LiCaAlF_6 scintillator. This scintillator has high light yield comparable to the Eu:LiCaAlF_6 and higher Li content. Therefore, the sensitivity is expected to increase compared with the Eu:LiCaAlF_6 based detector. Hundreds of small LiF/Eu:CaF_2 scintillators were attached on the side surface of the WLSF with transparent resin. Scintillation photons are absorbed in a core of the WLSF, re-emitted as wavelength-shifted photons and then transferred in the core region of the WLSF. Since the attenuation length of the WLSF is not so long, the WLSF is connected with a clear optical fiber to effectively transmit wave-

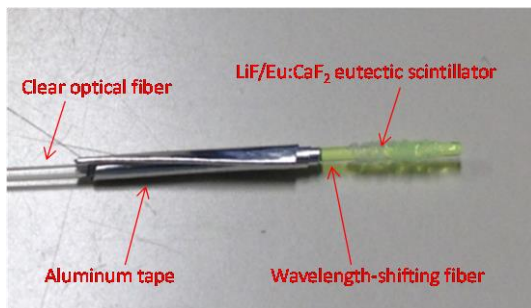


Fig. 1 Photograph of the fabricated optical fiber type neutron detector. The detector consists of small pieces of LiF/Eu:CaF_2 eutectic scintillators, a wavelength-shifting fiber connected with a clear optical fiber and a photomultiplier tube.

length-shifted photons to the photomultiplier tube. Signals from the photomultiplier tube was fed into a digital multichannel analyzer. In order to confirm basic operation of the fabricated detector, we irradiated it with neutrons emitted from a ^{252}Cf source and moderated by the polyethylene. We also tested the fabricated detector at Kyoto University Critical Assembly (KUCA).

RESULTS: Figure 2 shows the pulse height spectrum obtained from the fabricated detector when it was irradiated with ^{252}Cf neutrons. Although the scintillation photons were transmitted through an optical interface between the WLSF and the clear optical fiber, a clear peak shape corresponding to neutron events can be seen in the spectrum.

Finally, we confirmed a normal operation of the detector when it was placed in a core of the KUCA. Figure 3 shows the relationship of the signal count rate between the fabricated and the reference detector. The linear relationship was experimentally confirmed.

REFERENCES:

- [1] K. Watanabe, Y. Kawabata, A. Yamazaki, A. Uritani, T. Iguchi, K. Fukuda, T. Yanagida, Nuclear Instruments and Methods in Physics Research Section A, **802**, 1 (2015)

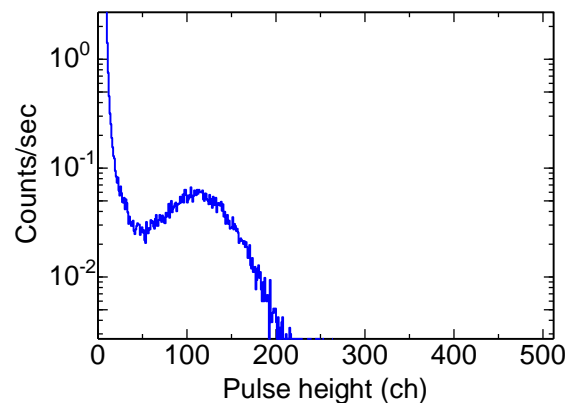


Fig. 2. Pulse height spectrum obtained from the fabricated detector.

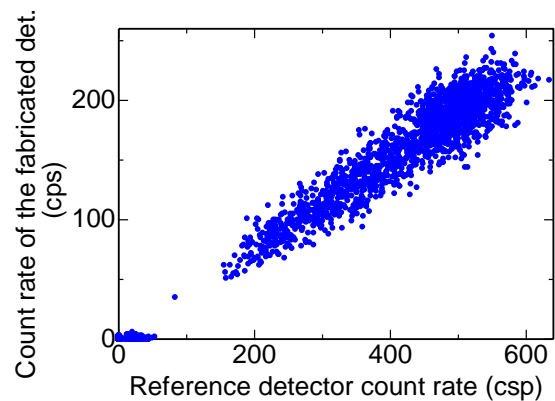


Fig. 3. Relationship of the signal count rate between the fabricated and the reference detector.

CO3-8 Measurement of Fundamental Characteristics of Nuclear Reactor at KUCA (II)

Y. Kitamura, T. Misawa, H. Shiga and Y. Igawa¹
Institute for Integrated Radiation and Nuclear Science,
Kyoto University
¹Graduate School of Energy Science, Kyoto University

ACKNOWLEDGEMENTS: This study was performed under the cooperation of the following researchers:

Y. Hayashi^{1,2}, S. Kano^{1,2}, Y. Shindo^{1,2}, S. Wada^{1,2}, M. Nakano^{1,3}, Y. Harada^{1,3}, Y. Morimoto^{1,4}, S. Takeo^{1,4}

¹International Research Institute for Nuclear Decommissioning

²Toshiba Corporation

³Mitsubishi Heavy Industries, Ltd.

⁴Hitachi-GE Nuclear Energy, Ltd.

INTRODUCTION: International Research Institute for nuclear Decommissioning (IRID) is developing criticality control techniques for fuel debris removal in Fukushima Daiichi nuclear power plant.

Sub-criticality monitoring system is to detect criticality approach for each step of debris removal operation by neutron noise analysis using Feynman-alpha method. A prototype of the sub-criticality monitoring system was tested to verify applicability on various sub-criticality measurement conditions.

Soluble and insoluble neutron absorbers are to prevent criticality of fuel debris. To prove ability of neutron absorption, reactivity worth was measured and compared to simulated prediction for each neutron absorbers.

EXPERIMENTS (Sub-criticality measurement):

Three H/U types of core condition corresponding to high (H/U235=322), middle (H/U235=107), and low (H/U235=54) were configured in KUCA B-core. Target k_{eff} varied from 0.7 to 0.95 by adjusting fuel bundle numbers for each H/U core condition. Three B-10 type neutron detectors connected to the prototype system were set in several horizontal distances from core. The distances varied from 0 to 60 [cm] with or without polyethylene between detectors and core. The prototype system, which is set in the control room of KUCA, acquired time list mode data of neutron pulse. A measuring time was about 30 minutes for each case. The time list mode data were analyzed by an off-line PC using Feynman-alpha method. Then, k_{eff} was evaluated from the analyzed prompt neutron decay ratio (α) and calculated prompt neutron life time.

RESULTS: The results are shown in Fig.1. The prototype system showed the measurement error of k_{eff} within almost 10% for the condition that the k_{eff} is above 0.7. It was found that H/U affected the measurement error relatively small. In contrast, the distance between core and detectors affected the measurement error large. The upper limit of measurable distance was found to be below 20 [cm] with polyethylene.

EXPERIMENTS (Reactivity worth measurement):

A representative H/U (H/U235=107) core was configured in KUCA-B core. Insoluble neutron absorbers (sintered metal/B₄C, B- and Gd-containing glass, Gd₂O₃ particles, liquid glass/Gd₂O₃ powder, and resin/Gd₂O₃ powder) were put in each Al cases (50×50×14 mm). The case was set in center of the core. Reactivity worth was measured by neutron source multiplication method. Soluble neutron absorber (sodium pentaborate) was also measured in the same way.

RESULTS: The results of insoluble neutron absorbers are shown in Fig. 2. C/E were 1.0~1.3 and show good agreement except for the Gd₂O₃ particles.

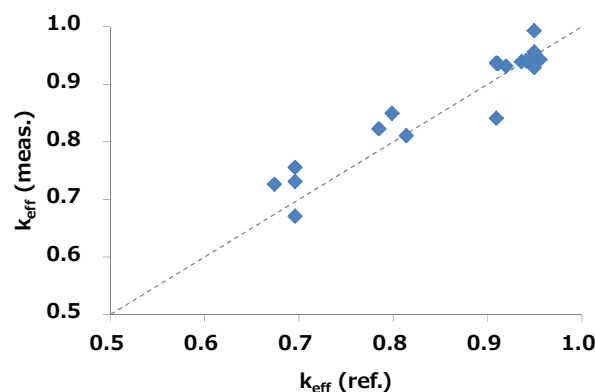


Fig.1 Comparison of measured and reference k_{eff} for sub-criticality monitoring

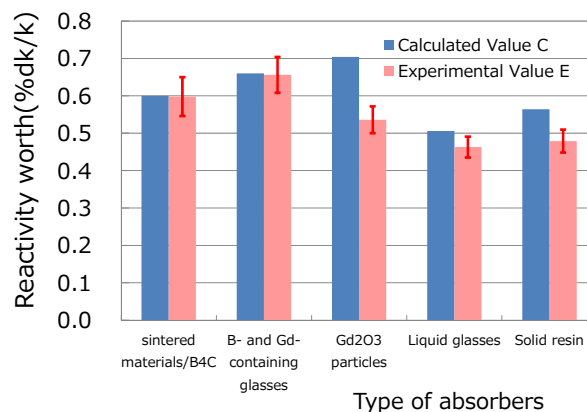


Fig.2 Comparison of measured and calculated reactivity worth for insoluble neutron absorber

REFERENCES:

- [1] T. Misawa *et al.*, "Measurement of Prompt Neutron Decay Constant and Large Subcriticality by the Feynman- α Method", Nuclear Science and Engineering, **104**, (1990) 53-65.
- [2] Y. Kitamura *et al.*, "Reactor Noise Experiments by Using Acquisition System for Time Series Data of Pulse Train", Journal of Nuclear Science and Technology, **36**, (1999) 653-660.

T. Misawa, Y. Kitamura, T. Shiga and Y. Igawa¹

Research Reactor Institute, Kyoto University

¹Graduate school of Energy Science, Kyoto University

INTRODUCTION:

Subcriticality monitoring system has to be used to detect criticality approach for each step of debris removal in Fukushima Daiichi nuclear power plant. For this purpose, International Research Institute for nuclear Decommissioning (IRID) is developing criticality control techniques for fuel debris removal based on neutron noise analysis using Feynman-alpha method. A prototype of the sub-criticality monitoring system was tested to verify applicability on various sub-criticality measurement conditions.

Usually, noise measurement has been carried out by detecting neutrons, however, gamma-ray detectors were also used in this experiments to analyze gamma-ray noise analysis.

EXPERIMENTS

Three H/U types of core condition corresponding to high (H/U235=322), middle (H/U235=107), and low (H/U235=54) were configured in KUCA B-core. Target k-eff varied from 0.7 to 0.95 by adjusting fuel bundle numbers for each H/U core condition. Three B-10 type neutron detectors connected to the prototype system were set in several horizontal distances from core. The distances varied from 0 to 60 [cm] with or without polyethylene between detectors and core. The prototype system, which is set in the control room of KUCA, acquired time list mode data of neutron pulse. A measuring time was about 30 minutes for each case. By detecting gamma-ray, LaBr₃ scintillation detectors whose energy resolution is much higher than a NaI(Tl) detector were used to discriminate gamma-ray emitted from certain gamma-ray source.

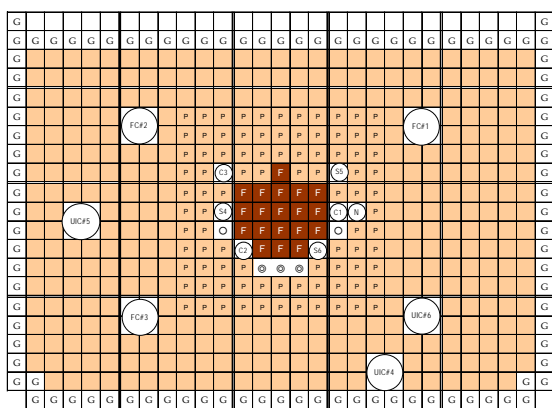


Fig.1 Core configuration of B-core

RESULTS: Figure 2 shows gamma-ray energy spectrum measured by a LaBr₃ detector at top of fuel assembly. It is found that gamma-ray emitted from neutron capture reaction of hydrogen is clearly discriminated from other gamma-ray.

Gamma-ray signal only from hydrogen capture reactions were acquired time list mode data acquisition system and analyzed according to normal Feynman-alpha method to obtain subcriticality. Figure 3 shows results of Y-value at low subcritical state (keff=0.95) and it can be fitted to theoretical formula based on Feynman-alpha method. Prompt neutron decay constant was 913.0 ± 360.1 (s⁻¹). On the other hand, prompt neutron decay constant obtained by neutron detection by a He-3 detector was 979.8 (s⁻¹), which means that gamma-ray noise analysis method can be used in subcriticality monitoring system. However, in large subcritical state (keff=0.7), measured Y-values were fairly scattered and cannot be fitted to theoretical formula.

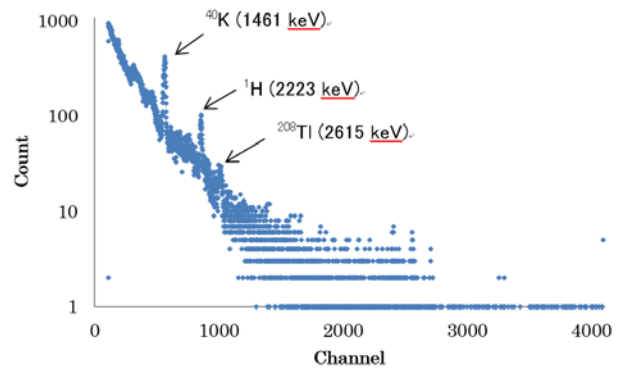


Fig.2 Gamma-ray energy spectrum by LaBr₃ detector

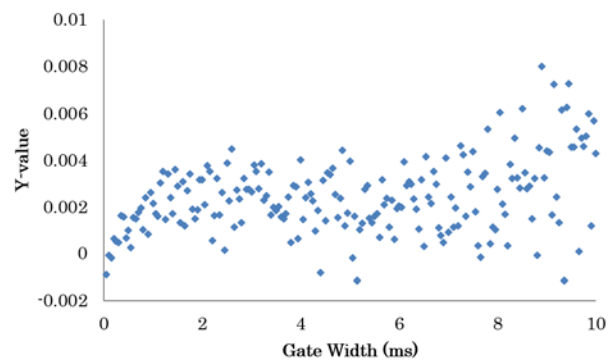


Fig.3 Results of Y-value by gamma-ray noise analysis

Y. Nagata, M. Sugimoto, M. Sugiyama¹, R. Inoue¹ and N. Sato¹

Graduate School of Science, Kyoto University

¹ Institute for Integrated Radiation and Nuclear Science, Kyoto University

INTRODUCTION: Helix is one of the simplest chiral motifs, being widely found in natural biomacromolecules, including DNA, RNA, proteins, and polysaccharides. Increasing attention has been paid to the structural control of artificial helical polymers because of their scientific and industrial applications for asymmetric catalysts, chiral stationary phase, and chiroptical materials. So far, we reported that single-handed helical poly(quinoxaline-2,3-diyl)s (PQXs) bearing chiral side chains exhibit solvent-dependent helix inversion,^{1,2} which can serve as effective scaffold for chirality-switchable catalysts³⁻⁷ and chiroptical materials.⁸⁻¹¹ For example, a PQX bearing chiral (*R*)-2-octyloxymethyl side chains (**2oct**) adopts right- or left-handed helical structures in tetrahydrofuran (THF) or 1,1,2-trichloroethane (1,1,2-TCE), respectively (Figure 1). It should be noted that the PQXs can exhibit a perfect solvent-dependent helix inversion between left-handed (>99%) to right-handed (>99%) structures, which is an unprecedented feature among various helical polymers. Therefore, it is urgent and essential issue to reveal the mechanism of the solvent-dependent helix inversion of the PQX for the development of advanced functional chiral materials. Furthermore, the solvent-dependent helix inversion can be a good educational example to understand the behavior of macromolecules. However, the detailed mechanism has been still unclear at this stage. In this study, we tried to reveal the detailed structure of **2oct** in solution by using small-angle X-ray scattering (SAXS) measurements.¹²

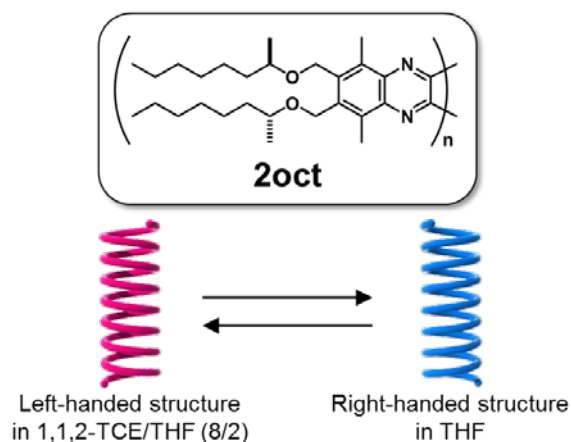


Figure 1. Structure of **2oct** exhibiting the solvent-dependent helix inversion

EXPERIMENTS and RESULTS: **2oct** was dissolved in tetrahydrofuran to measure the SAXS patterns by using the Rigaku NANOPIX SAXS/WAXS measurement system (Figure 2). Now we are trying to elucidate the detailed structure of **2oct** in solution from the SAXS pattern along with the theoretical calculations.

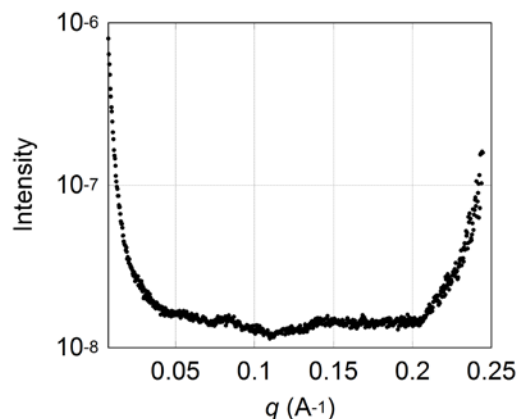


Figure 2. SAXS pattern of **2oct** dissolved in tetrahydrofuran.

REFERENCES:

- (1) Yamada, T.; Nagata, Y.; Sugimoto, M. *Chem. Commun.* **46** (2010) 4914-4916.
- (2) Nagata, Y.; Yamada, T.; Adachi, T.; Akai, Y.; Yamamoto, T.; Sugimoto, M. *J. Am. Chem. Soc.*, **135** (2013) 10104-10113.
- (3) Yamamoto, T.; Yamada, T.; Nagata, Y.; Sugimoto, M. *J. Am. Chem. Soc.*, **132** (2010) 7899-7901.
- (4) Nagata, Y.; Kuroda, T.; Takagi, K.; Sugimoto, M. *Chem. Sci.*, **5** (2014) 4953-4956.
- (5) Nagata, Y.; Nishikawa, T.; Sugimoto, M. *J. Am. Chem. Soc.*, **136** (2014) 15901-15904.
- (6) Ke, Y.-Z.; Nagata, Y.; Yamada, T.; Sugimoto, M. *Angew. Chem. Int. Ed.*, **54** (2015) 9333-9337.
- (7) Nagata, Y.; Nishikawa, T.; Sugimoto, M. *ACS Macro Lett.*, **5** (2016) 519-522.
- (8) Nagata, Y.; Nishikawa, T.; Sugimoto, M. *Chem. Commun.*, **50** (2014) 9951-9953.
- (9) Nagata, Y.; Takagi, K.; Sugimoto, M. *J. Am. Chem. Soc.*, **136** (2014) 9858-9861.
- (10) Nagata, Y.; Uno, M.; Sugimoto, M. *Angew. Chem. Int. Ed.*, **55** (2016) 7126-7130.
- (11) Nishikawa, T.; Nagata, Y.; Sugimoto, M. *ACS Macro Lett.*, **6** (2017) 431-435.
- (12) For SANS experiments; Nagata, Y.; Nishikawa, T.; Sugimoto, M.; Sato, S.; Sugiyama, M.; Porcar, L.; Mar-tel, A.; Inoue, R.; Sato, N. *J. Am. Chem. Soc.*, **140** (2018) 2722-2726.

Y. Oba, S. Abe¹ and M. Sugiyama²

Materials sciences Research Center, Japan Atomic Energy Agency

¹Research Institute for Electromagnetic Materials

²Institute for Integrated Radiation and Nuclear Science, Kyoto University

INTRODUCTION: Semiconductor nanocomposite thin films have attracted much attention due to their potential to quantum-dot solar cells [1,2]. They consist semiconductor nanocrystals embedded in the matrix of another semiconductor. The nanocrystals induce the quantum size effects and enhance conversion efficiency [3,4]. In addition, the semiconductor nanocomposite thin films can utilize a wide range of the solar spectrum for energy conversion because of the difference in the band gap between the nanocrystals and the matrix.

Since the quantum size effects are highly related to the size of the nanocrystals, the characterization and control of the size of the nanocrystals are crucial to develop high-efficiency materials. For the characterization of the nanostructures, small-angle X-ray scattering (SAXS) is a powerful means. Therefore, the SAXS measurements of the semiconductor nanocomposite thin films were performed.

EXPERIMENTS: The nanocomposite thin films were deposited on Si substrates by one-step synthesis techniques [1]. The nanocrystals are precipitated in the films during deposition. The thickness of the films and the substrates were around 1 μm and 0.5 mm. SAXS measurements were performed using a SAXS instrument with Mo $K\alpha$ radiation (Nano-viewer, RIGAKU) installed at the Institute for Integrated Radiation and Nuclear Science, Kyoto University. The characteristic X-ray emitted from Mo (17 keV) can penetrate the thicker substrates compared to that from Cu. The SAXS profiles were measured with two sample-to-detector distances of 45 and 160 cm to cover a wide q range. Here, q is the magnitude of the scattering vector and is equal to $(4\pi/\lambda)\sin\theta$, where θ and λ are half the scattering angle and the wavelength of the incident X-ray. During the SAXS measurements, the samples were put in vacuum to reduce the background scattering from air. The glassy carbon standard provided by the Argonne National Laboratory was used to calibrate the scattering intensity [5].

RESULTS: Fig. 1 shows a typical SAXS profile of the semiconductor nanocomposite thin film composed of the

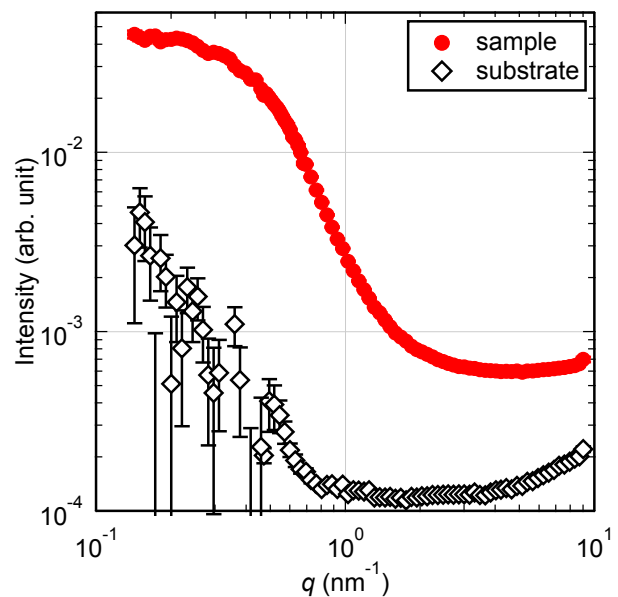


Fig. 1. SAXS profiles of a semiconductor nanocomposite thin film and a Si substrate.

PbTe nanocrystals and the ZnSe matrix [1]. The SAXS profile of the Si substrate is also shown in Fig. 1 for comparison. The SAXS profile of the sample shows a shoulder around $q=0.5 \text{ nm}^{-1}$. This indicates that the nanostructures are formed in the film. The diameter of the nanocrystals is estimated to be around a few nm using the Guinier plot [6]. Since the exciton Bohr radius of PbTe is 150 nm [7], the observed nanocrystals are small enough to induce the quantum size effects.

REFERENCES:

- [1] S. Abe, *Mater. Renew. Sustain. Energy*, **4** (2015) 18/1-7.
- [2] V. Arivazhagan *et al.*, *Appl. Phys. Lett.*, **102** (2013) 242110/1-4.
- [3] A. Nozik, *Physica E*, **14** (2002) 115-120.
- [4] M. Grätzel, *Inorg. Chem.*, **44** (2005) 6841-6851.
- [5] F. Zhang *et al.*, *Metal. Mater. Trans. A*, **41A** (2010) 1151-1158.
- [6] L. A. Feigin, *Structure Analysis by Small-Angle X-Ray and Neutron Scattering*, (Plenum Press, New York, 1987).
- [7] J. E. Murphy *et al.*, *J. Am. Chem. Soc.*, **128** (2006) 3241-3247.

CO4-3 Measurement of Electron Emission Properties of Field Emitter Array under Gamma-ray Irradiation

Y. Gotoh, T. Morito, Y. Handa, M. Nagao¹, T. Okamoto², N. Sato³, M. Akiyoshi⁴, and I. Takagi

Graduate School of Science, Kyoto University

¹National Institute of Advanced Industrial Science and Technology

²National Institute of Technology, Kisarazu College,

³Institute for Integrated Radiation and Nuclear Science, Kyoto University

⁴Radiation Research Center, Osaka Prefecture University

INTRODUCTION: Taking advantage of the high durability of vacuum electronic devices, we are developing a radiation tolerant compact image sensor with field emitter array [1]. In order to show the sufficient tolerance against gamma-ray irradiation, it is necessary to measure the performance of the device in radiation field. Especially, operation of field emitter array (FEA), which is the electron source of this device, should be confirmed to assure the performance of the image sensor. Since the FEA is operated in vacuum, it is necessary to develop a vacuum container which can maintain the interior pressure under 10^{-6} Pa. We have already reported the results of the preliminary experiments last year [2]. This year, non-evaporation getter (NEG) pump was attached to the vessel. In this report, we will describe the pressure in the vessel after encapsulating, and also the results of the measurement of electron emission properties of the FEA.

EXPERIMENTS: A vacuum vessel was prepared for the measurement of the electron emission properties of FEAs under the gamma-ray irradiation. The vessel had four ports: the ports were for a NEG pump, an all metal angle valve, glass tube in which the FEA is settled, and flange for the voltage and current inlet. Prior to the measurement, we have settled a vacuum gauge instead of the FEA in order to evaluate the attainable vacuum pressure inside the vessel. After pumping and activating the NEG pump (pumping speed of 100 L s^{-1} for hydrogen), the vessel could reach less than 10^{-7} Pa. Then a sample on which a dozen FEAs were mounted was installed in the vessel. The FEA measured in the present study was a single gate Spindt-type FEA with 1000 emission tips. Above the FEA, an anode electrode made of stainless steel, was positioned. The current-voltage (I - V) characteristics of the FEA were measured before, during, and after the gamma-ray irradiation to the FEA. A positive voltage of 200 V was given to the anode, and a negative lamp voltage to -70 V was applied to the emitter. The gate was grounded. The gamma-ray irradiation was performed at Co-60 Gamma-ray Irradiation Facility, Institute for Integrated Radiation and Nuclear Science, Kyoto University. The dose rate of irradiation was about 1 kGy h^{-1} . The irradiation continued for half an hour, and the I - V measurements were done every 5 min. After this series of

the measurement, the vacuum vessel was kept for several weeks. The pressure inside the vessel was examined from the pressure variation of another vacuum chamber to which the test tube was connected.

RESULTS: Throughout the experiments, the FEA showed a good electron emission properties and no serious deterioration was observed. Figure 1 shows the I - V characteristics before, during, and after the gamma-ray irradiation. The I - V curve obtained after the gamma-ray irradiation (red line) overlaps the curve obtained before the gamma-ray irradiation (black line). Constant current observed at the lower gate-emitter voltage is due to the leakage current because the anode was at a high voltage of 200 V. During the gamma-ray irradiation, the I - V curves showed little difference with those without irradiation. At a lower voltage, the leakage current increased (blue line). This would be probably due to the incident of electrons from glass tube or other part of the system under the gamma-ray irradiation. These results show that the FEA has tolerance against gamma-ray irradiation. It was found that the vacuum vessel maintained sufficient low pressure even after 2 month. More 2 month later, the FEA could be operated stably, which implies that the pressure inside the vessel was sufficiently low. It was found that the present system can evaluate the tolerance of the FEAs relatively long time.

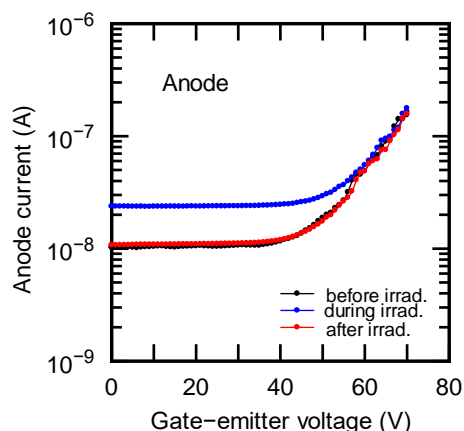


Fig. 1. Current-voltage characteristics of the FEA before and after the gamma-ray irradiation.

ACKNOWLEDGEMENTS

The present study was partially supported by Japan Society for the Promotion of Science, through a Grant-in-Aid for Scientific Research, KAKENHI 16H04631 and also by Futaba Electronics Memorial Foundation.

REFERENCES:

- [1] Y. Gotoh *et al.*, 2017 IEEE 30th International Vacuum Nanoelectronics Conference (2017) 104.
- [2] Y. Gotoh *et al.*, KURRI Progress Report 2016 (2017).

CO4-4 Evaluation of Unintentionally Doped Impurities in Silicon Carbide Substrates using Neutron Activation Analysis Technics

T. Makino, H. Yashima¹, S. Sekimoto¹ and T. Ohshima

Quantum Beam Science Research Directorate, National Institutes for Quantum and Radiological Science and Technology

¹*Kyoto Univ.*

INTRODUCTION: Silicon carbide(SiC) is regarded as a promising candidate for high power and high frequency electronic devices. For the high-performance device fabrication, it is necessary to develop the fabrication process of high quality substrates with low impurity content. However, unintentionally impurity of SiC in substrate have not been estimated quantitatively [1]. Therefore, we evaluated unintentionally doped impurities in SiC wafers by using neutron activation analysis technics.

EXPERIMENTS: Commercially available two pol types of SiC substrate (4H-SiC and 3C-SiC) were used for the evaluation. Moreover, two 4H-SiC substrates grown by different company were prepared (4H-SiC: A, 4H-SiC: B). Substrates were cut into 5 mm x 10 mm, and cleaning acetone with ultrasonic for 10 min. After the organic cleaning, samples were cleaned by nitro-hydrochloric acid (HCl:HNO₃=3:1) for 5 min. followed by hydrofluoric acid (50% HF) for 5min. Between the each treatment, samples were rinsed by de-ionized H₂O. To quantitative estimation of impurities, standard sample were prepared by using metallic solutions known contents of metals. These samples and standard samples were capsuled with polyethylene packs.

Capsuled samples were irradiated by neutrons for 1 hour at the KUR with 1MW. After the irradiation, gamma-ray spectra from activated impurity in substrate and standard samples were measured with high-purity Ge detectors.

RESULTS: Table 1 shows observed impurity nuclides and the order of concentrations. From 4H-SiC wafers, sodium, manganese, bromine, tungsten, were detected with the concentration of 10¹⁴~10¹⁵ /cm³. For 3C-SiC, arsenide was detected with the concentration of 10¹⁴ /cm³ additionally, while tungsten was not detected.

CONCLUSION: We obtained clear poly-type dependence of unintentionally doped impurities on SiC substrates. Moreover, slight deference was observed for concentration of some impurities for 4H-SiCs.

In future, we will carefully analyze the quantitative values of the concentration, and effects of the impurities for electric devices fabricated by the SiCs.

Table 1. Observed impurity nuclides and the order of concentrations from SiCs

Nuclide	Concentration [/cm ³]		
	4H-SiC: A	4H-SiC: B	3C-SiC
Na	3 x 10 ¹⁵	4 x 10 ¹⁵	3 x 10 ¹⁵
Mn	1 x 10 ¹⁴	8 x 10 ¹⁴	5 x 10 ¹⁴
As	ND	ND	2 x 10 ¹⁴
Br	2 x 10 ¹⁴	2 x 10 ¹⁵	4 x 10 ¹⁴
W	9 x 10 ¹⁴	3 x 10 ¹⁵	ND

REFERENCE:

[1] T. Ohshima *et al.*, *Matt. Sci. Forum* Vol. 556-557, 457-460.

Spectrum of Amino Acid in the Millimeter-wave Region using a Diode Detector

T. Takahashi

*Institute for Integrated Radiation and Nuclear Science,
Kyoto University*

INTRODUCTION: In recent years various types of coherent radiation emitted from a short bunch of relativistic electrons have attracted a considerable attention as a bright light source in the THz-wave and millimeter wave regions for the spectroscopic purpose. Coherent transition radiation (CTR), which is emitted from a boundary between two media, is one of such a coherent light source. CTR is usually utilized as a non-polarized light source, because the electric vector of transition radiation (TR) emitted from a metallic screen is axially symmetric with respect to the trajectory of an electron beam. The new system of the circularly polarized CTR using a pair of wire-grid radiators with the different polarization has been developed [1]. The significant point of my new technique is the use of linearly polarized CTR with the wire-grid radiator. With this technique the polarization degree is able to be controlled precisely. Circularly polarized light has been useful in the circular dichroism spectroscopy. In the previous report [2] spectra of some kinds of amino acid have been measured using linearly polarized CTR with a conventional bolometer over the wide wavelength range. In this report spectra in the millimeter-wave region has been investigated in detail with a diode detector.

EXPERIMENTAL PROCEDURES: The experiment was performed at the coherent radiation beamline [3] at the L-band linac of the Institute for Integrated Radiation and Nuclear Science, Kyoto University. The energy, the width of the macro pulse, and the repetition rate of the electron beam were 42 MeV, 100 ns, and 60 Hz, respectively. The average current of the electron beam was 3.5 μ A. The spectrum of CTR was measured by a Martin-Puplett type interferometer and a diode detector (DPX-10, Millitec Inc.) with a boxcar integrator. The schematic diagram of the experiment was shown in Fig.1.

RESULTS: Measured spectra of some kinds of amino acid, e.g., Phenylalanine, α -Alanine, and Tryptophan, are shown in Figs. 2. The identification of observed absorption is now in progress

REFERENCES:

- [1] T. Takahashi, *et al.*, KURRI-PR 2015 CO4-7.
- [2] T. Takahashi, *et al.*, KURRI-PR 2016 CO4-8.
- [3] T. Takahashi *et al.*, Rev. Sci. Instrum. **69** (1998) 3770.

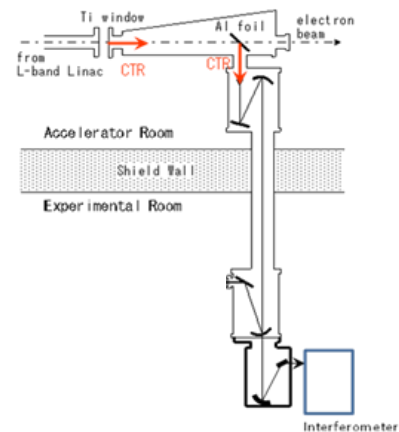


Fig.1 The schematic diagram of the experiment.

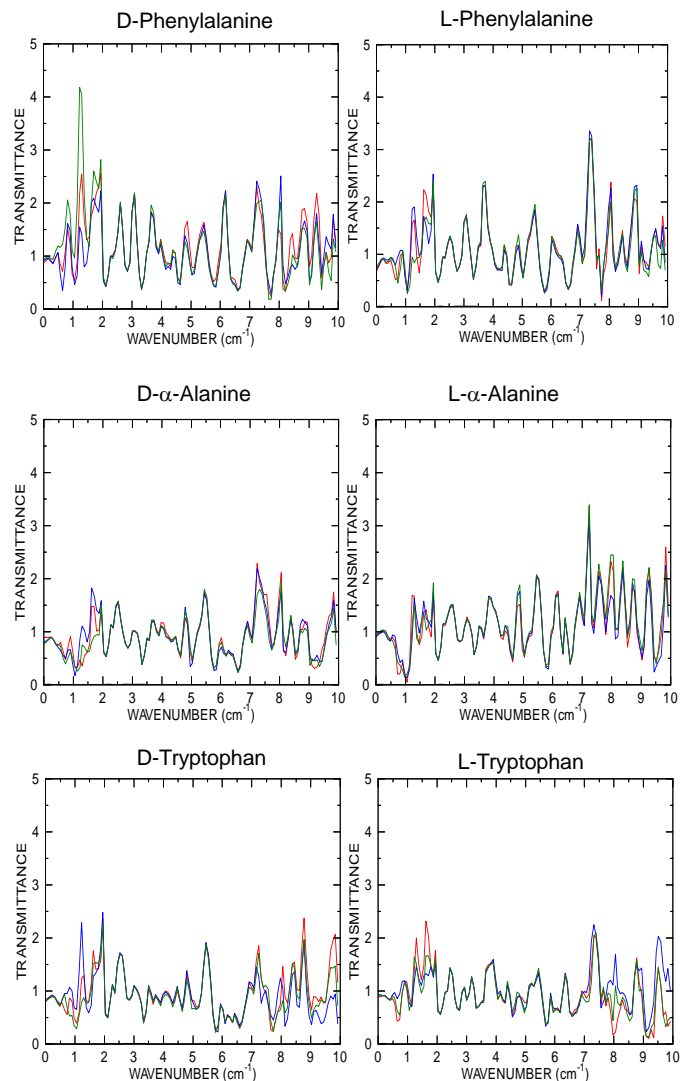


Fig.2 Spectra of some kinds of amino acid.

CO4-6 Correlation between Neutron Irradiation Damages and Hydrogen Isotope Retention

Y. Oya, A. Togari¹, M. Nakata¹, M. Zhao¹, Y. Iinuma² and R. Okumura²

Faculty of Science, Shizuoka University,

¹Graduate School of Science, Shizuoka University

²Research Reactor Institute, Kyoto University

INTRODUCTION: Li-based ceramic is one of the promising candidates for the tritium breeding materials in the D-T fusion reactor. Tritium is expected to be produced by the irradiation of neutron on Li atom to achieve the self-sustenance of D-T fusion reaction. It is important to understand the tritium breeding and desorption processes from the viewpoint of steady recovery of tritium. Recently, advanced composites such as $\text{Li}_2\text{TiO}_3\text{-Li}_4\text{SiO}_4$ materials are proposed [1] to combine the good chemical stability of Li_2TiO_3 and preferable tritium release property of Li_4SiO_4 . However, the neutron irradiation behavior and subsequent tritium release data on this new materials are scarce. In this study, neutron irradiation on the composite $\text{Li}_2\text{TiO}_3\text{-Li}_4\text{SiO}_4$ materials was carried out at KUR, and tritium release behavior was evaluated by thermal desorption spectroscopy (TDS) and liquid scintillation counter (LSC) measurement.

EXPERIMENTS: Composite $\text{Li}_2\text{TiO}_3\text{-Li}_4\text{SiO}_4$ with the Ti/Si ratio of 2.0 and 0.5, pure Li_2TiO_3 , and pure Li_4SiO_4 powders were prepared by solution combustion synthesis. The crystallite size of the powders is around 50 nm. The as-synthesized powders were annealed at 923 K for 2h at ambient atmosphere to remove the carbon and impurities. Thereafter, neutron irradiation on the samples was performed using the pneumatic tubes 2 (Pn-2) at KUR [2]. The thermal neutron flux was $2.75 \times 10^{13} \text{ n cm}^{-2} \text{ s}^{-1}$ and fluence was $9.9 \times 10^{16} \text{ n cm}^{-2}$. After irradiation, the samples were transferred to Shizuoka University to perform the tritium-TDS and LSC measurement.

RESULTS: Fig. 1 shows the tritium-TDS spectra of the neutron-irradiated samples with the heating rate of 30 K min^{-1} . Tritium is released at the temperature range of 400-1000 K. The pure Li_2TiO_3 shows a major desorption peak at 580 K and a sub-peak at around 680 K. The pure Li_4SiO_4 shows 4 peaks at different temperatures and it is noticed that compared with Li_2TiO_3 the tritium desorption starts at the lower temperature of 400 K. For the composite Ti/Si=2.0, tritium desorption started at 400 K which was also lower than that for pure Li_2TiO_3 , indicating that Li_4SiO_4 crystallites embedded in Li_2TiO_3 facilitated the tritium release from Li_2TiO_3 at lower temperature possibly due to high Li atom density in Li_4SiO_4 grains. For the composite Ti/Si=0.5, most tritium released at lower temperature below 600 K compared with pure Li_4SiO_4 . Fig. 2 shows tritium-TDS spectra of composite Ti/Si=2.0 at different heating rates. The tritium desorption was shifted

toward lower temperature side by decreasing heating rate. Three desorption peaks can be separated and activation energies for these peaks were obtained through the Arrhenius plot based on the peak shifting. For Peaks 1, 2 and 3, the activation energies were calculated to be 0.18, 0.20, 0.27 eV respectively, which were much lower than the conventional single phase breeders. It can be concluded that composite $\text{Li}_2\text{TiO}_3\text{-Li}_4\text{SiO}_4$ breeders combine the steady chemical stability of Li_2TiO_3 and enhanced tritium release behavior at lower temperature with decreased activation energy.

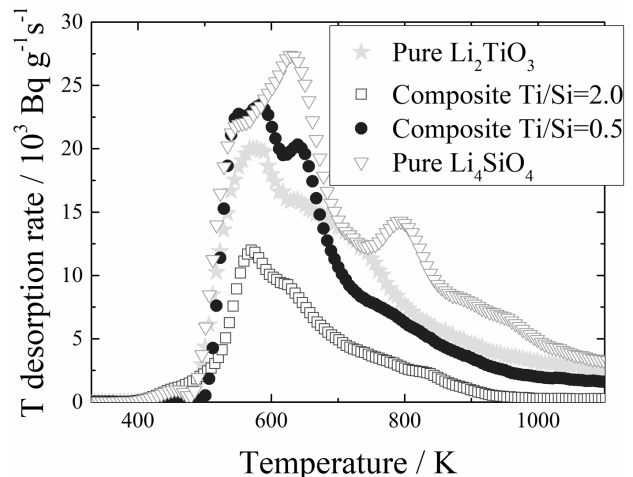


Fig. 1. Tritium-TDS spectra of the neutron irradiated materials with the heating of 30 K min^{-1}

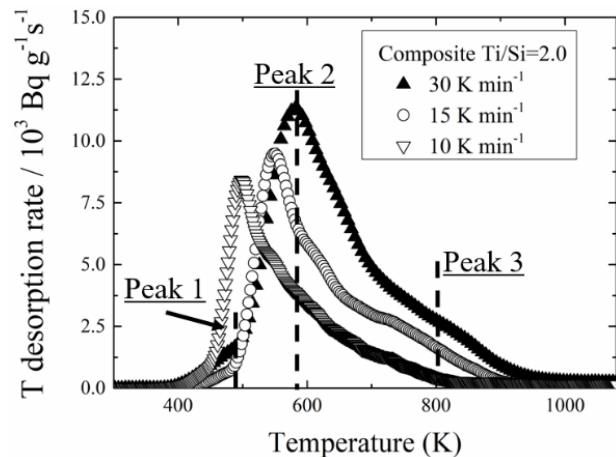


Fig. 2. Tritium-TDS spectra of composite Ti/Si=2.0 at different heating rates.

REFERENCES:

- [1] Q. Zhou, *et al.*, J. Eur. Ceram. Soc., **34** (2014)801-807.
- [2] M. Kobayashi, *et al.*, Fusion Eng. Des., **87**(2012) 475.

T. Awano and T. Takahashi¹

Faculty of Engineering, Tohoku Gakuin University
¹Research Reactor Institute, Kyoto University

INTRODUCTION: We have observed millimeter wave absorption bands of silver or cuprous iodides superionic conductive glasses in sub-terahertz region[1]. These bands are due to conducting ions because their frequency difference is coincident with the square root of the ratio of their atomic masses. On the other hand, these bands seem to be due to collective motion of the conductive ions because their frequencies are lower than those estimated from their ionic masses. However, the dynamics of the collective movement of ions is not clear yet.

Ionic liquids(ILs) are molten salts even at room temperature. It is interesting to compare ionic motion in ILs with those in superionic conducting glasses to making clarify influence of glass network upon the collective motion of ions.

Recently, we have found sub-terahertz absorption bands of ILs[2]. These bands disappear at low temperatures at which the IL is solid. Therefore, these bands are due to ionic movement. However, the thermal change of absorption spectra of these ILs were various. This difference seems to be due to the difference of the process of their phase transition to the solid states (crystal or glass).

In this study we have measured millimeter wave absorption spectra of 33 ILs to make clear the ionic movement from the temperature change of absorption spectra.

EXPERIMENTS: A fixed amount of ionic liquids (Tokyo Chemical Industry Co., Ltd.) were spread into filter paper. Transmission spectra of single and double papers with ionic liquids were measured at room temperature and low temperatures. Absorption spectra were obtained by subtraction of them. To confirmation, measurements were repeated twice or three times for each IL. Molecular dynamics simulation was executed using Gromacs 5.0.

RESULTS: Four types of the spectral change occurred at temperature above melting point or glass transition temperature. The intensities of the absorption bands in the ILs which are crystal in solid state showed rapid decrease at their melting points. On the other hand, those in ILs which are vitreous in solid state weakened and shifted gradually. Some others showed complicated change. The other type showed no absorption in this spectral range. Figures 1(a) - (d) show typical spectra of these four types. Figure 2(a) shows rotational velocity autocorrelation function of cation and anion in [C₂min][Tf₂N], and figure 2(b) shows temperature dependence of that of the anion obtained by the MD simulation. Observed sub-THz bands seems to be due to rotational motion of the ions

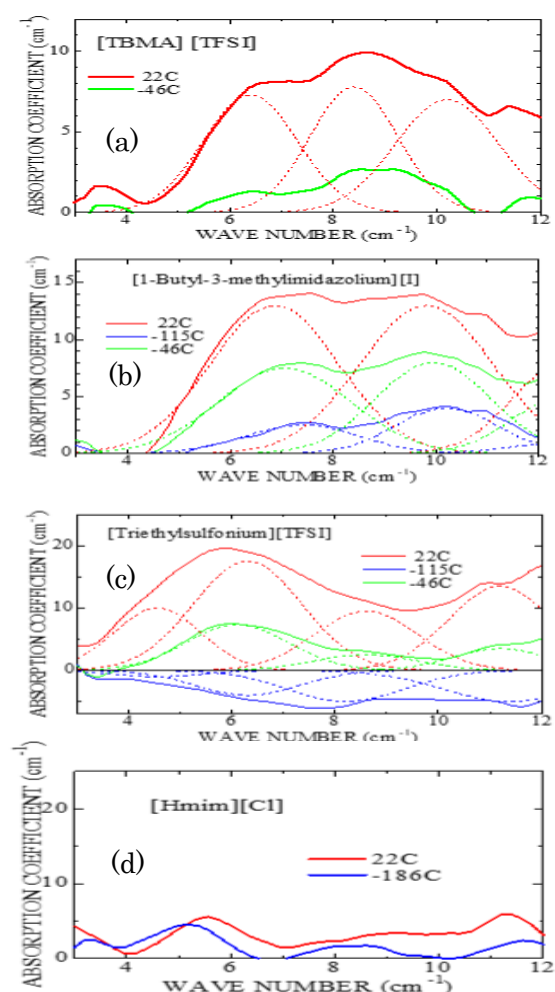


Fig. 1. Typical temperature dependence of absorption increment spectra of ionic liquids. The baseline is the absorption spectrum at 88 K.

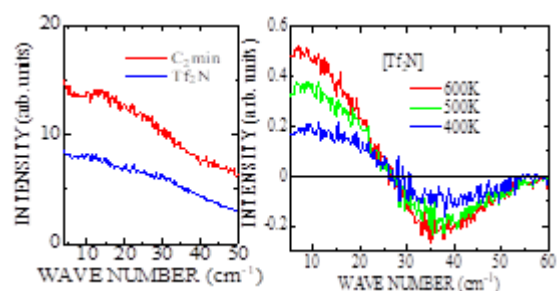


Fig. 2.(a) Rotational velocity autocorrelation function of the cation and anion at 300 K. (b) Increment spectra of anion against that at 300 K.

REFERENCES:

- [1] T. Awano and T. Takahashi, J. Phys. Soc. Jpn. **79** Suppl. A (2010) 118-121.
- [2] T. Awano, A. Shikoda and T. Takahashi, 21th International Conference on Solid State Ionics, (2017) IV-6 P.

CO4-8 The Correlation between Microstructural Evolution and Mechanical Property Changes in Neutron-irradiated Vanadium Alloys

K. Fukumoto, T. Onitsuka, Y. Tabata¹ and Xu Qiu²

RINE, Univ. of Fukui

¹Graduate school of Eng., Univ. of Fukui

²KUR, Kyoto Univ.

INTRODUCTION: Vanadium alloys are candidate materials for fusion reactor blanket structural materials, but the knowledge about the mechanical properties at high temperatures during neutron irradiation is limited and there are uncertainties that may have influenced the results such as the interstitial impurity content of specimens. Recently, material irradiation technology in a liquid metal environment was developed and irradiation experiments in various liquid metal environments can be performed for vanadium alloys. Environmental effects and irradiation effects for mechanical properties should be distinguished independently in order to understand the essential behavior of vanadium alloys during irradiation for fusion reactor application. The objective of this study is to investigate the mechanical properties and microstructural changes of the vanadium alloys, V-4Cr-4Ti alloys during neutron irradiation. In this study, tensile test was carried out for V-4Cr-4Ti and V-4Cr-4Nb alloys to investigate the effect of Ti addition in ternary alloy of V-Cr system.

EXPERIMENTS: The majority of test specimens for this study were prepared from V-4Cr-4Ti, V-3Fe-4Ti and V-4Cr-4Nb alloys. The tensile specimens had nominal gauge dimensions of 0.25mm(t) x 1.2mm(w) x 5mm(l). Before irradiation, all specimens were annealed in vacuum at 1000°C for 2hrs. The specimens were irradiated in Joyo in the temperature range from 450°C to 650 °C with total neutron dose from 0.47 to 2.1 x 10²⁶ n/m². In the previous study, the ratio of damage level, displacement per atom (dpa) to neutron dose in pure vanadium in Joyo MK-II was 2.5 x 10⁻²⁶ dpa/Φ_{tot}. The amounts of estimated damage level ranged from 1.2 to 5.3 dpa. Tensile tests were conducted at room temperature and 400°C with various strain rate ranged from 6.7x10⁻⁴ to 10⁻² to obtain the information of strain rate sensitivity at high temperature. SEM observation for fractography after tensile test was carried out in KUR, Kyoto University.

RESULTS: Tensile tests for V-4Cr-4Ti, V-3Fe-4Ti and V-4Cr-4Nb alloys were carried out at 400 °C at strain

rates between 6.7x10⁻⁴ and 6.7x10⁻¹/s. The strain-rate dependence was determined for the lower yield stress σ_{LYS}. From the general relationship between flow stress and strain rate, the strain rate sensitivity (SRS) parameter is defined as follows[1];

$$m = \frac{1}{\sigma} \frac{d\sigma}{d \ln \dot{\epsilon}} \quad (1)$$

When the flow stress σ rises with the increase of strain rate $\dot{\epsilon}$, i.e., $m > 0$, slip deformation is a thermally activated process. When $m < 0$, a barrier strength of obstacle against dislocation slip motion is weakened and leads to reduction of the flow stress, because increasing the strain rate decreases time available for solute diffusion to dislocations. Values of the SRS for the lower yield stress were determined for each irradiation condition and test temperature from a logarithmic fit to the lower yield strength data. Figure 1 shows the stress-strain curves for the irradiated V-4Cr-4Ti, V-4Cr-4Nb and V-3Fe-4Ti in this study. The data of SS-curves for three type alloys were so almost the same that V-3Fe-4Ti and V-4Cr-4Nb alloys had the larger irradiation hardening than V-4Cr-4Ti alloy. It indicates that the effect of Nb addition contributes to the larger irradiation hardening than that of Ti addition for V-Cr system. The value SRS of both V-4Cr-4Ti and V-4Cr-4Nb did not change so much that the contribution to impurity interaction for Ti atom and Ni atom might be the same.

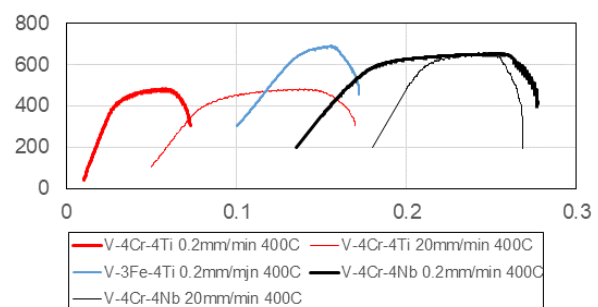


Figure 1 : The strain rate sensitivity (SRS) of lower yield stress dependence on the test temperature for the irradiated V-4Cr-4Ti alloy in this study and the previous data for V-4Cr-4Ti irradiated in HFBR [1].

Reference

[1] A. F. Rowcliffe, S. J. Zinkle and D. T. Hoelzer. J. Nucl. Mater., 283-287 (2000) 508-512

F. Hori, Y. Sumikura, A. Takano, K. Kanazawa, A. Iwase, K. Ohsawa¹, Q. Xu² and N. Abe²

Dept. of Quantum & Radiation Eng., Osaka Pref. Univ.

¹*Res. Inst. of Appl. Mech., Kyushu University*

²*Res. Reactor Inst., Kyoto University*

INTRODUCTION: We have been investigated radiation damage induced defects in intermetallic compound alloys, especially for B2 ordered Fe-Al alloys. Intermetallic compounds have good properties such as specific strength to weight ratio, oxidation resistance and strength in elevated temperature. However, the nature of basic defects in intermetallic compound alloys is not necessarily cleared yet. The reason why intermetallic compound alloys possibly include more than two types of vacancies, that is A-vacancy and B-vacancy in A-B compound alloy. It is difficult to distinguish these vacancies in any other experimental methods except for positron annihilation techniques. However, the amount of defect and the defect structure affects the various characteristic features, such as strength and electronic conductivity and so on. On the other hand, we have reported that vacancies introduced by electron irradiation strongly depend on incident electron energy because of their different threshold energy of displacement for each elemental atom. In Fe-Al alloys, we have shown that different energy of electron irradiation successfully produces different type of vacancy in Fe-Al alloys. In this study, we have tried to control the vacancy type induced by different energy of electron in another B2 ordered alloy system of Fe-Rh.

EXPERIMENTS: Fe-50%Rh alloy specimens with B2 structure were prepared by arc melting method. Sliced samples with the thickness of 0.5 mm were annealed at 1073 K for 3 h followed by quenched into water. These specimens were irradiated with 2 MeV electron to the fluence of 1×10^{17} and 1×10^{18} /cm² at JAEA-Takasaki and with 8 MeV electron to the fluence of 5×10^{17} and 1×10^{18} /cm² at KURRI, Kyoto University. In both cases, irradiations were carried out at about 330 K controlled by water flow system. After and before irradiation, samples were examined by X-ray diffraction, positron annihilation lifetime and coincidence Doppler broadening

measurements. The positron lifetime spectra were analyzed by using POSITRONFIT program.

RESULTS: As shown in Table 1, positron lifetime before irradiation was not single component, which has longer lifetime component. This fact reveals that thermally vacancy was not annealed out perfectly in this sample. Essentially, it is well known that vacancy type defects in Fe-Al alloy is hardly to remove even in stoichiometry. After 1×10^{18} /cm² electron irradiation, positron lifetime increases in both irradiation cases. However, it appears slight larger positron lifetime for 8 MeV irradiated sample than that for 2 MeV irradiation case. This difference may be caused by twice larger displacement cross section for Rh than that for Fe above 4 MeV electron irradiation (Fig.1).

Table 1 Positron lifetime in each sample.

	τ_1 (ps)	τ_2 (ps)
unirrad.	121	173
2MeV	122	181
8MeV	145	186

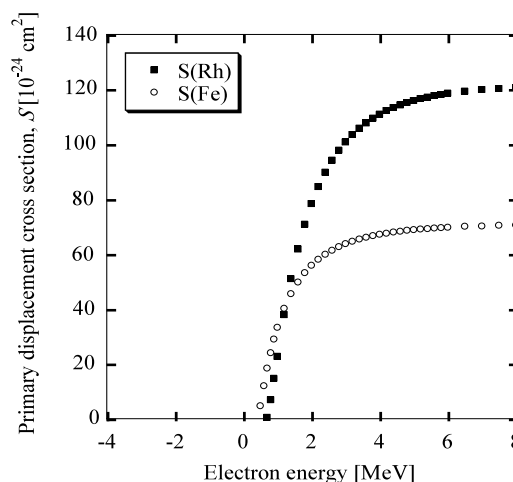


Fig. 1 Primary displacement cross section as a function of electron energy.

Acknowledgement

This work was supported by JSPS KAKENHI Grant-in-Aid for Scientific Research (B)-26289365.

CO4-10 Synthesis of Multi-component Metal Nanoparticles by γ -ray Irradiation Reduction Method

F.Hori, M.Tanaka, S.Toda, M.Tani, A.Iwase, K.Okitsu¹, T.Matsui², Y.Mizukoshi³ and Q.Xu⁴

Dept. of Engineering, Osaka Prefecture University

¹Dept. of Sustainable System Science, Osaka Prefecture University

²Center for Advanced Education of Entrepreneurship and Innovation, Osaka Prefecture University

³Institute of Materials Research, Tohoku University

⁴Research Reactor Institute, Kyoto University

INTRODUCTION: It is well known that metal nanoparticles (NPs) have some specific properties, which are not appeared in bulk materials such as catalytic activities, magnetic properties, electric conductivity and light absorption. These properties depend on its size, shape, structure, chemical composition and so on. They have many possibilities to applied for various industrial fields. However, it is not easy to fabricate multi elemental alloy NPs with controlling their size, shape and structure. Generally, many kinds of metal NPs commercially are synthesized by using chemical reaction method, which is not necessarily in water solution. Recent years, some reports show that it is possible to fabricate some metal NPs under irradiation reduction fields such as ultrasonic, solution plasma, electron beam, ion beam and gamma-ray [1]. We have been trying to synthesize various kinds of metal nanoparticles with size and shape controlled by gamma-ray irradiation reduction method. In this study, we have tried to synthesize pure Cu and Cu-Au multi component alloy NPs by gamma-ray irradiation.

EXPERIMENTS: Aqueous solution with a given concentration of copper complex ((CH₃COO)₂Cu·H₂O) with an additive of sodium dodecyl sulfate (SDS) and 8.5 vol% ethylene glycol. The solution was argon gas purged and sealed into polystyrene vessels. They were irradiated at about 300 K with 1.17 and 1.33 MeV gamma-rays from ⁶⁰Co radio active source at gamma irradiation facility in KURRI, Kyoto University. The total dose was fixed to 10 kGy with the dose rate of 2.0 kGy/h. After first irradiation, 1.0 mM gold complex (NaAuCl₄·2H₂O) was added and irradiated it with 10 kGy continuously. The shapes and the structures for all colloidal products were observed by TEM (JEM-2000FX and FEI-Titan) and energy dispersive X-ray spectrometry (EDS). Samples for TEM observations were made by

putting a drop of colloidal solutions on a carbon film with a Mo mesh and dried them in a vacuum. X-ray Photoelectron Spectroscopy (XPS) measurement at KEK-PF BL-27 has performed.

RESULTS:

Fig. 1 shows the TEM-EDS images for NPs formed in aqueous solutions after two second gamma-ray irradiation. This figure shows that Au-core and Cu-shell NPs are formed by this irradiation process. XPS result also shows existing of pure Cu metal in this NPs and it remains stable after 4 month (Fig. 2). On the other hand, UV-vis absorbance spectra shows only one absorption peak around 520 nm, which shows Au surface plasmon resonance. From these results, it can be concluded that Au-NPs covered with extreme thin Cu layers (at least one or two layers) were formed so that surface plasmon resonance of Au arises.

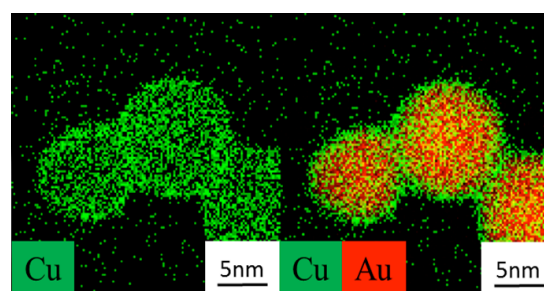


Fig.1 EDS images of synthesized nanoparticles after two steps gamma-ray irradiation reduction.

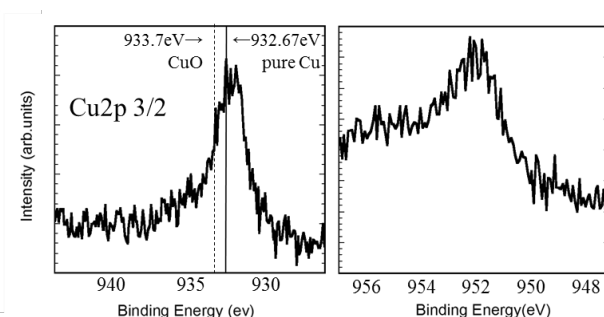


Fig. 2 XPS spectra of NPs exposed to air after two months.

Acknowledgement

This work was supported by JSPS KAKENHI Grant-in-Aid for Scientific Research (A)-15H02342. Authors would like to express cordial thanks to Dr. S.Tanaka and N.Taguchi for help of TEM-EDS measurements at AIST.

References

- [1] N.Taguchi and F.Hori *et al.*, Rad. Phys. Chem., **78** (2009) 1049-1053.

H. Ohta, Y. Nauchi, K. Nakamura and T. Sano¹

Nuclear Research Technology Laboratory,
Central Research Institute of Electric Power Industry

¹Institute for Integrated Radiation and Nuclear Science,
Kyoto University

INTRODUCTION: As an effort to improve the safety of light water reactors (LWRs), various concepts of “enhanced accident tolerant fuels and core components” are being developed in many countries. The Central Research Institute of Electric Power Industry (CRIEPI) has been developing an accident tolerant control rod (ATCR) to which the novel neutron absorbing materials including rare-earth sesquioxides (RE_2O_3) are applied¹. The ATCR improves the basic performance as a control rod such as the reactor shutdown margin and neutronic lifetime, and reduces the risk of re-criticality accident in any reactor conditions including severe accident (SA). For the ATCR candidate materials RE_2O_3 - MO_2 ($RE = Sm$ or Eu , $M = Zr$ or Hf), a high temperature compatibility with iron or steel, which is a main component of current control rod cladding, and physicochemical stability under high temperature steam atmosphere were experimentally confirmed so far². Furthermore, a reactivity analysis in representative LWRs revealed that these candidate materials have enough reactivity worth comparable to or higher than the conventional neutron absorbing materials B_4C or $Ag-In-Cd$ alloy¹. Since the control rods are arranged inside or very close to the operating core for a long period, the irradiation characteristics of the candidate materials are needed to be confirmed. In this study, the radioactivation characteristics of Sm_2O_3 , Eu_2O_3 and ZrO_2 , which are irradiated for short terms are measured toward the future long-term irradiation tests.

EXPERIMENTS: Irradiation experiment conditions are summarized in Table I. The powder of each material was packed in Al container with 8mm in diameter and 9.5mm in depth. The strong neutron absorbing materials, Sm_2O_3 and Eu_2O_3 were diluted with the powder of a neutronic inert material Al_2O_3 to reduce the self-shielding effect. For a preparation of ZrO_2 sample, highly pure Zr with impurity Hf of ~ 0.0055 wt% were used. Irradiation experiments were performed for 10 minutes or 4 hours using a pneumatic tube No.2 (Pn-2) in KUR operating at rated power 1MW. Then, gamma-ray emitted from each sample irradiated for 10 minutes were measured with an HP-Ge detector, and the induced radioactivities were evaluated. The samples irradiated for 4 hours are still cooled.

The detection efficiency of the HP-Ge detector applied in this study was calibrated with a multi-isotope mixed standard gamma-ray source in the range of 60keV to 1836keV, and the obtained curve is shown in Fig. 1.

Table I. Irradiation Experiment Conditions

	Sm_2O_3	Eu_2O_3	ZrO_2
Sample Specifications			
Container diameter	8mm	←	←
Container Height	9.5mm	←	←
Weight	2.38mg	0.425mg	1.105g
Diluent	Al_2O_3	←	-
Irradiation			
Position	Pn-2	←	←
Period	10min./4hr.	←	10min.

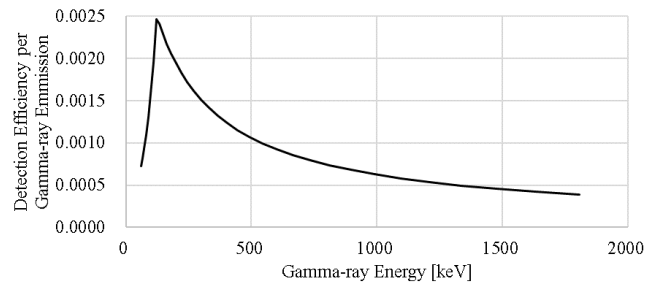


Fig. 1. Detection efficiency curve of HP-Ge detector.

RESULTS: For representative neutron absorption reactions of Sm, Eu and Zr as shown in following (1) - (5), gamma-ray intensities from the neutron absorption products were measured and the radioactivities of these samples at the end-of-irradiation were evaluated.

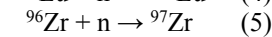
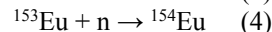
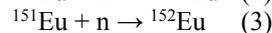
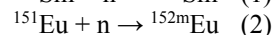
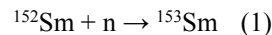


Table II summarizes the results of radioactivities evaluated from gamma-ray measurement, compared with predictions based on neutron absorption cross-sections for 0.025eV and thermal neutron flux in Pn-2 ($5.50E+12$ n/cm²·s). These results indicate that the radioactivation characteristics of Sm_2O_3 , Eu_2O_3 and ZrO_2 irradiated for 10 minutes are analytically predictable. Subsequently, the radioactivities of the other samples irradiated for 4 hours are also evaluated and longer-term irradiation test conditions will be discussed.

Table II Radioactivity of Sm_2O_3 , Eu_2O_3 and ZrO_2 irradiated for 10minutes

Sample isotope	Produced isotope	Half life	Radioactivity [Bq/gram-sample]	
			Measurement	Prediction
^{152}Sm	^{153}Sm	46.3 hr.	3.263E+9	2.577E+9
^{151}Eu	^{152m}Eu	9.3 hr.	2.458E+11	3.529E+11
^{151}Eu	^{152}Eu	13.3 yr.	3.727E+7	5.365E+7
^{153}Eu	^{154}Eu	8.8 yr.	4.646E+6	5.412E+6
^{96}Zr	^{97}Zr	16.8 hr.	7.951E+5	9.774E+5

REFERENCES:

[1] H. Ohta, *et al.*, TopFuel 2016 (2016) 17556 .

[2] K. Nakamura, *et al.*, AESJ 2017 spring meeting. 1I06 in Japanese.

CO4-12 Neutron Irradiation Effect of High-density MoO₃ Pellets for Mo-99 Production

Y. Suzuki, K. Nishikata, Y. Namekawa, A. Kimura,
A. Shibata, N. Nakamura, K. Tsuchiya,
T. Sano¹, Y. Fujihara¹, and J. Zhang¹

Department of JMTR, Japan Atomic Energy Agency
¹Research Reactor Institute, Kyoto University

INTRODUCTION: The research and development (R&D) has been carried out for the production of Molybdenum-99 (⁹⁹Mo) by the neutron activation method ((n, γ) method) from viewpoints of limited availability of high-enriched uranium, no-proliferation and nuclear security, and disposal of nuclear fissile materials. It is essential to improve the properties of Alumina (Al₂O₃) used widely as the ⁹⁹Mo/^{99m}Tc generator. In this study, two kinds of Al₂O₃ specimens were prepared, and molybdenum adsorption and technetium-99m (^{99m}Tc) desorption properties of these Al₂O₃ specimens were evaluated.

EXPERIMENTS: The MoO₃ pellets were fabricated by the cold pressing and sintering Method. Density of MoO₃ pellets was about 60%T.D. The MoO₃ pellet pieces (about 1.5 g) were irradiated in the Pn-2 of the KUR. Table 1 shows the irradiation conditions of MoO₃ pellets in the Pn-2. After the irradiation tests, the irradiated MoO₃ pellet pieces were dissolved with 6M-NaOH solution. Then, the Mo adsorption tests of the Al₂O₃ specimens were carried out with the sodium molybdate solution (10mg-Mo/mL at pH4) at RT. After the tests, each Al₂O₃ specimen adsorbing Mo was packed in the polypropylene column. The saline was flowed through in this column and the ^{99m}Tc was extracted from each Al₂O₃ specimen. In this test, the activities of ⁹⁹Mo and ^{99m}Tc in the solution were measured by the Gamma-ray spectrometer.

Table 1 Irradiation conditions of MoO₃ pellet pieces in Pn-2.

Items	Values
Thermal power	5 MW
Thermal neutron flux	$2.8 \times 10^{17} \text{ m}^{-2}\text{s}^{-1}$
Epithermal neutron flux	$1.1 \times 10^{16} \text{ m}^{-2}\text{s}^{-1}$
Fast neutron flux	$6.0 \times 10^{16} \text{ m}^{-2}\text{s}^{-1}$
Irradiation time	20 min.

RESULTS: Table 2 shows the activities of ⁹⁹Mo and ^{99m}Tc in the sodium molybdate solution after about 100 h from irradiation completion. The calculation value was evaluated by thermal neutron flux and correction by half time. In this experiment, the ratio of ^{99m}Tc and ⁹⁹Mo was about 0.95 except for the result of Run 1 and the ratio was almost the same as the ratio of calculation value. On the other hand, the ratios of calculation value and experimental value (C/E) of ⁹⁹Mo and ^{99m}Tc were about 0.456 and 0.448, respectively. In order to evaluate

⁹⁹Mo generation, it is necessary to take into account the ⁹⁸Mo absorption rate in epi-thermal and fast region. ^[1]

Table 2 Activities of ⁹⁹Mo and ^{99m}Tc in the sodium molybdate solution after about 100 h from irradiation completion.

	Run 1		Run 2			
			Specimen-1 (V-B-300)		Specimen-2 (Medical)	
	⁹⁹ Mo	^{99m} Tc	⁹⁹ Mo	^{99m} Tc	⁹⁹ Mo	^{99m} Tc
Calculation values* ¹ (MBq/g-MoO ₃)	4.49	4.35	4.49	4.35	4.49	4.35
Experimental values* ² (MBq/g-MoO ₃)	9.79	10.4	9.92	9.27	9.80	9.54

*1 : Calculation values by thermal neutron flux and correction by half time.

*2 : Measurement values by the γ-ray spectrometer.

Table 3 shows the result of ⁹⁹Mo adsorption amounts of Al₂O₃ specimens and ^{99m}Tc recovery rates from Al₂O₃ specimens. The Mo adsorption amounts of V-B-300 and medical Al₂O₃ were 83.1 and 24.3 mg-Mo/g-Al₂O₃, respectively. These values were almost the same as the values with un-irradiated Mo solution. It seems that the Mo adsorption properties were influenced to crystal structure and specific surface of Al₂O₃ specimens ^[2]. In the result of milking process, the ^{99m}Tc recovery property of V-B-300 was better than that of the medical Al₂O₃. On the other hand, the ^{99m}Tc recovery property was decreased for each milking.

Table 3 Results of ⁹⁹Mo adsorption amounts of Al₂O₃ specimens and ^{99m}Tc recovery rates from Al₂O₃ specimens

Items	Specimen-1 (V-B-300)	Specimen-2 (Medical)
⁹⁹ Mo adsorption amounts (Bq/g-Al ₂ O ₃) (mg-Mo/g-Al ₂ O ₃)	1.32×10^6 83.1	3.86×10^5 24.3
^{99m} Tc recovery rates in Milking		
1 st run	93.5 %	74.1 %
2 nd run	87.6 %	61.6 %
3 rd run	84.5 %	54.8 %

CONCLUSION: The MoO₃ pellets were irradiated in the Pn-2 at KUR, and ⁹⁹Mo adsorption/^{99m}Tc recovery properties of the Al₂O₃ specimens were evaluated with the solution of the irradiated MoO₃ pellets. The Mo adsorption amounts of V-B-300 and medical Al₂O₃ were almost the same as the values with un-irradiated Mo solution. In future, it is necessary to perform the detail evaluation of neutron flux in Pn-2 and ⁹⁹Mo adsorption/^{99m}Tc recovery properties of various Al₂O₃ specimens.

REFERENCES:

- [1] K. Nishikata, *et al.*, CO4-21, KURRI Progress Report 2013, (2013), P.242 .
- [2] Y. Suzuki, *et al.*, Transactions of the Materials Research Society of Japan, **43**(2018)73-80.

CO4-13 Reserch on Resonance Frequency Variation as Function of Exposure Radiation Dose

M. Kobayashi, T. Miyachi, S. Takechi¹, S. Fujita¹ and N. Konishi¹

Planetary Exploration Research Center, Chiba Institute of Technology

¹Graduate School of Engineering, Osaka City University

INTRODUCTION: In the previous studies, we have performed experiments that a piezoelectric element was irradiated with high intensity 400 MeV/n Xe beam at HIMAC of the National Institute of Radiological Sciences [1][2]. As a result, we found that when irradiating a very strong radiation to a piezoelectric element, its resonance frequency and anti-resonance frequency are shifted and also the impedance at the resonance frequency and anti-resonance frequency are changed by beam irradiation. In particular, it was found that the resonance frequency increases linearly with the irradiation amount.

Since the piezoelectric element is a crystalline material, it is considered that the crystal is damaged by the beam irradiation, and thus the characteristic parameter such as the resonance frequency has changed. Although it is considered to be some radiation damage, detailed mechanism such as its mechanism is not known. Radiation damage roughly includes damage due to ionization and non-ionization, but since ionized Xe beam has both ionization and non-ionizing effects, it is difficult to determine which effect mainly affects the piezoelectricity.

Therefore, in this study, we investigated the response of the piezoelectric parameter to energetic electron beam which has dominantly ionizing effect (less non-ionizing effect).

EXPERIMENTS: A piezoelectric element was placed in the beam line by KURRI-LINAC as an electron beam source. Before obtaining experimental data, we performed preliminary runs to find appropriate test set up and electron beam condition. The test piece of PZT element can be warmed by electron beam irradiation due to high intensity, the piece was air-cooled by a fan to keep the temperature lower than 100 °C otherwise the piezoelectricity can be quickly vanished due to high temperature. We monitored the temperature of the test piece and adjusted the beam current as beam intensity to be around 0.8 ~ 1.0 μ A not to heat it higher than 100 °C.

After fixing the test setup and beam condition, we had four runs to obtain experimental data.

RESULTS: Fig. 1 and Fig. 2 show changes of resonance frequency and anti-resonance frequency during electron beam irradiation with a constant beam current of 1.0 μ A. At 0 to 10 min of the elapse time, those frequencies changed rapidly because the PZT element temperature was changed by beam irradiation and then became stable after temperature achieved equilibrium. Even in stable temperature, those frequencies were slightly increased. Fig.3 shows only plots in thermal equilibrium period. The frequency was linearly increased with time, namely irradiation dose. That is the same trend as Xe

beam experiment. Xe beam experiments, however, did not show increase in anti-resonance frequency as this study. We will investigate quantitatively the experiment results in further analysis to compare with Xe beam results.

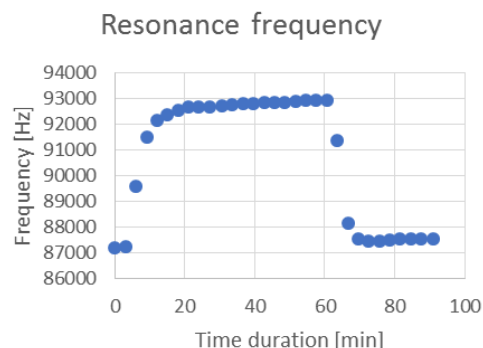


Fig.1 Resonance frequency change during electron beam irradiation with 1.0 μ A.

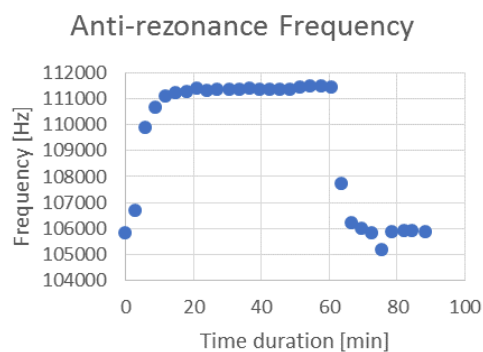


Fig.2 Anti-resonance frequency change during electron beam irradiation with 1.0 μ A.

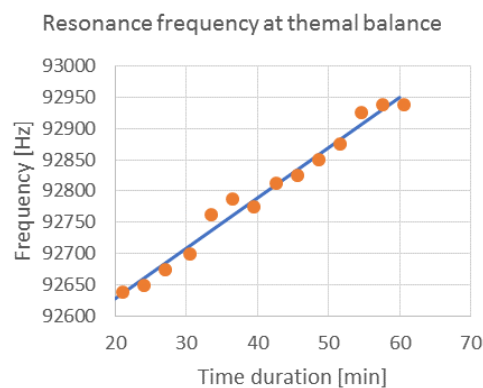


Fig. 3 Plots of frequency as function of time ranging 20 min to 60 min of Fig.1.

REFERENCES:

- [1] M. Kobayashi *et al.*, Japanese Journal of Applied Physics, **53** (2014) 066602 .
- [2] M. Kobayashi *et al.*, Japanese Journal of Applied Physics, **52** (2013) 126604.

CO4-14 Selection of Borosilicate Glass Composition for Neutron Irradiation Test

T. Nagai, A. Uehara¹ and T. Fujii²

Japan Atomic Energy Agency (JAEA)

¹Research Reactor Institute, Kyoto University

²Graduate School of Engineering, Osaka University

INTRODUCTION: A high-level radioactive liquid waste from a reprocessing process for spent nuclear fuels is processed into a solidified waste glass made by using a borosilicate glass as media. In our previous study [1], the neutron irradiation test of a borosilicate glass sample $19\text{Na}_2\text{O}-17\text{B}_2\text{O}_3-63\text{SiO}_2-\text{CeO}_2-\text{Y}_2\text{O}_3$ was carried out under the condition of 1000 kW for 10 min in KUR in 2014FY, and the structural change after the irradiation was observed slightly by using Raman spectrometry.

In this study, to understand the structural change of a borosilicate glass by a neutron irradiation in detail, the neutron irradiation test was carried out for 50 min in the Pn-2. The structural change of glass sample after the irradiation will be estimated in 2018FY. This is the intermediate report.

EXPERIMENTS: Before the irradiation test, the glass composition was selected to estimate a structural change accurately. As a result of the previous study [1], we thought that Li content in the sample would be increased by the $^{10}\text{B}(n,\alpha)^7\text{Li}$ reaction, and a connection of the Si-O bridging structure might be cut by the generated Li. To confirm the change of Raman spectrum by adding Li, $8\text{Li}_2\text{O}-11\text{Na}_2\text{O}-17\text{B}_2\text{O}_3-64\text{SiO}_2$ and $19\text{Na}_2\text{O}-17\text{B}_2\text{O}_3-63\text{SiO}_2$ were prepared, and their spectra were measured. As shown in Fig. 1, measured spectrum of $8\text{Li}_2\text{O}-11\text{Na}_2\text{O}-17\text{B}_2\text{O}_3-64\text{SiO}_2$ has a higher intensity around 1000cm^{-1} than the other. Therefore, it would be easy to estimate the structural change by applying a Li free borosilicate glass in this irradiation test.

With a consideration above-mentioned, two kinds of borosilicate glass, $17\text{Na}_2\text{O}-17\text{B}_2\text{O}_3-65\text{SiO}_2-\text{CeO}_2-\text{Y}_2\text{O}_3$ and $17\text{Na}_2\text{O}-28\text{B}_2\text{O}_3-54\text{SiO}_2-\text{CeO}_2-\text{Y}_2\text{O}_3$ were selected. The raw material reagents of SiO_2 , H_3BO_3 , Na_2CO_3 , CeO_2 , and Y_2O_3 were placed in an alumina crucible and were melted at 1150°C in an electric furnace. After the molten glass samples were solidified by cooling to room temperature, they were cut into thin plates.

In Dec. of 2017, the glass samples of thin plate were set in a polyethylene tube and were irradiated under the condition of 1000 kW for 50 min in the Pn-2 of KUR.

After the radioactivity of the samples is sufficiently attenuated, the Raman spectra of the glass sample will be measured by using a laser Raman spectrometer, NRS-3100 of JASCO in KUR in 2018FY.

RESULTS: On the selection of glass composition for the neutron irradiation test, Raman spectra of $8\text{Li}_2\text{O}-11\text{Na}_2\text{O}-17\text{B}_2\text{O}_3-64\text{SiO}_2$ and $19\text{Na}_2\text{O}-17\text{B}_2\text{O}_3-63\text{SiO}_2$ were measured by using a laser Raman spectrometer,

NRS-5100 of JASCO in JAEA as shown in Fig. 1.

The Raman spectrum of Si-O bridging structure of a silicate glass were in the wavenumber of $850-1200\text{cm}^{-1}$, and the peak positions of Raman shifts were different from the number of non-bridging oxygen, NBO, of the Si-O structure [2]. In this measurement of borosilicate glass, those Raman shifts were observed in $850-1250\text{cm}^{-1}$ and the measured spectra could be separated into Gaussian waves as shown in Fig. 1. The Raman peak of Q^4 structure without NBO appeared in $1140-1150\text{cm}^{-1}$, and those of Q^3 , Q^2 , and Q^1 structures with the NBO number = 1, 2, and 3 were in $1070-1090$, $1000-1020$, and $920-930\text{cm}^{-1}$ respectively. The peaks of Q^2 and Q^3 can be subdivided into plural by the Si-O-X connecting state, and only Q^3 in Fig. 1 was divided into 2 peaks of $\text{Q}^{3(1)}$ and $\text{Q}^{3(2)}$. When the change of Raman spectrum by adding Li, it can be observed that the peak heights of Q^4 , $\text{Q}^{3(1)}$ and $\text{Q}^{3(2)}$ decreased and those of Q^2 and Q^1 increased. These changes by a adding Li was similar to that by the neutron irradiation for 10 min in previous study [1].

This neutron irradiation effect can be confirmed clearly by measuring a Raman spectrum of the glass sample irradiated for 50 min.

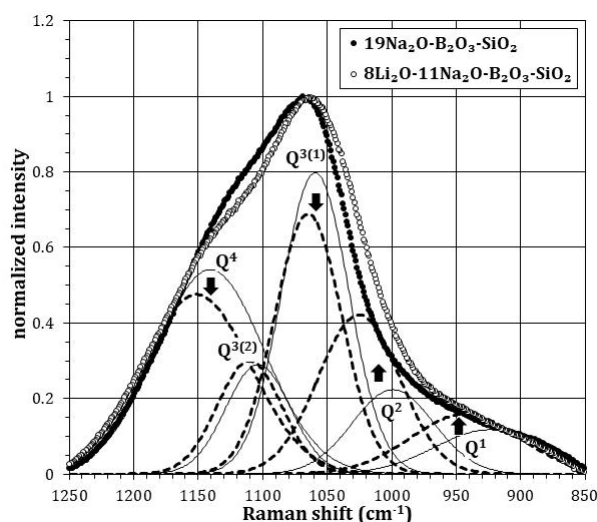


Fig. 1. Raman spectra of $8\text{Li}_2\text{O}-11\text{Na}_2\text{O}-17\text{B}_2\text{O}_3-64\text{SiO}_2$ (open circle, dashed lines) and $19\text{Na}_2\text{O}-17\text{B}_2\text{O}_3-64\text{SiO}_2$ (closed circle, fine lines) for selecting glass composition of neutron irradiation test.

REFERENCES:

- [1] T. Nagai, *et al*, 2009FY KURRI Progress Report, 2014 (2015) 26P11-4.
- [2] P. McMillan, *Am. Mineralogist*, **69** (1984) 622-644.

J. Yanagisawa, Q. Xu¹, A. Yabuuchi¹, K. Takamiya¹, and A. Kinomura¹

School of Engineering, The University of Shiga Prefecture

¹*Research Reactor Institute, Kyoto University*

INTRODUCTION: We have been reported that the high-energy (100 keV) focused gallium (Ga) ion beam (Ga FIB)-irradiated area of germanium (Ge) wafer surface was changed to porous structures with nanometer size (nano-porous structures) [1]. It is also found that the size and the shape of such nano-porous structures can be controlled by the FIB irradiation conditions, such as dwell time, ion beam current and total fluence of the FIB. Because such nano-porous structures have large specific surface area, an improvement of the efficiency of surface-related phenomena, such as photocatalytic action, can be expected. However, the formation of such nano-porous structures on whole area of a chip of a Ge wafer surface using FIB is difficult because of the small spot size of the FIB. Therefore, we have tried to form such nano-porous structures on the whole area of the Ge sample surfaces using the large-area ion implantation apparatus in this laboratory. In this system, the ion species used was argon (Ar) and the operation energy was 60 keV, which were different from the previous studies using the Ga-FIB at 90 – 100 keV.

The aim of the present study is to confirm the formation of the nano-porous structures on a whole area of Ge (110) surfaces by 60 keV Ar ion irradiation.

EXPERIMENTS: About 1 cm x 1 cm chip samples were prepared from a Ge (110) wafer by cleavage. After cleaning of them using ultrasonic bath, a corner part of each sample was covered by aluminum foil to prevent the ion irradiation.

Ion irradiation was performed using Ar ions at an energy of 60 keV. Ion irradiated area was 1.51 x 1.55 cm². Three kind of samples were prepared using the different ion current and total fluence, that is 0.6 μ A and 1 x 10¹⁶ cm⁻² (sample 1), 5 μ A and 5 x 10¹⁶ cm⁻² (sample 2), and 13 μ A and 1 x 10¹⁷ cm⁻² (sample 3), respectively.

After the ion irradiation, the change of the sample surface was firstly observed by an optical microscope. Then the surface morphology and the atomic composition of the surface were measured using the energy dispersive x-ray spectroscopy – scanning electron microscope (EDS-SEM) system (PHENOM PROX).

RESULTS and DISCUSSION: Figure 1 shows the optical microscope image of the surface of the sample 3 with the Ar ion fluence of 1 x 10¹⁷ cm⁻². It is found that the ion-irradiated area was obviously changed to dark. The darkness was increased with increasing the total fluence of the Ar ions (the result is not shown in this report).

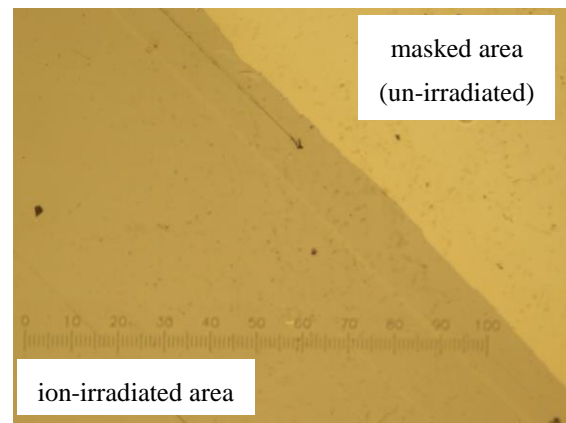


Fig. 1. Optical microscope image of ion-irradiated and un-irradiated area of Ge wafer surface (x200).

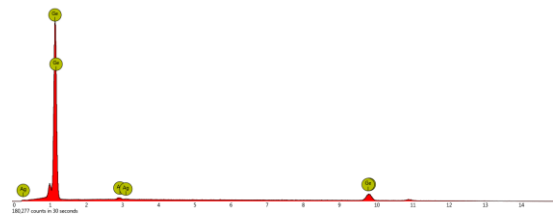


Fig. 2. EDS spectrum from the ion-irradiated area of the surface of sample 3.

One suspected reason for the darkness is the formation of a film of carbon-related materials, because of the temperature rise of the sample surface and/or other ion irradiated effects due to longer ion irradiation time and larger ion beam current (in case of sample 3, about 42 min. and 13 μ A, respectively). To confirm this, the atomic concentration of the ion-irradiated area of the sample 3 was measured using the EDS-SEM. The result is shown in Fig. 2. The atomic concentration was Ge : Ar = 97.8 : 2.2, no carbon was detected. Although the origin of Ar is not clear at present, this result indicates that at least the observed darkness of the ion-irradiated area is not due to the carbon-related materials, but is due to the formation of sub-micron structures, which change the reflectance ratio of the visible light, by the 60 keV Ar ion irradiation. In fact, lurking small structures were observed during the EDS-SEM observation of the ion-irradiated area.

CONCLUSION: 60 keV Ar ion irradiation was performed on whole area of Ge (110) surfaces. Although high-resolution SEM observation is necessary, the present result indicates that the formation of, at least, sub-micron (or nano-) structures can be obtained by the present ion irradiation conditions.

REFERENCE:

- [1] J. Yanagisawa, K. Takarabe, K. Ogushi, K. Gamo and Y. Akasaka, *J. Phys.: Condens. Matter* **19** (2007) 445002 (10pp).

Y. Kobayashi, T. Kubota, M. Saito, R. Masuda, M. Kurokuzu, S. Kitao and M. Seto

Institute for Integrated Radiation and Nuclear Science, Kyoto University

INTRODUCTION: On Mössbauer emission spectroscopy, the activated sample containing the Mössbauer-parent nuclei is used as a γ -ray source. The intensity of the emitted Mössbauer γ -ray from the sample is measured after transmitting a standard absorber as a function of the relative velocity of the source (sample) and the reference absorber. This technique allows for Mössbauer studies of samples containing relatively low amount of the Mössbauer nuclei e.g., low concentration dopants, thin films, surface of materials.

The purpose of this study is to demonstrate the production of ^{57}Co whose amount is sufficient for the ^{57}Fe -Mössbauer measurement using KURRI-LINAC. Here, ^{57}Co (half-life: 270 d) is the γ -ray source of ^{57}Fe Mössbauer spectroscopy. On KURRI-LINAC, we can produce radio isotopes by photonuclear reaction using the bremsstrahlung X-ray, which is emitted from the noble-metal target. By photonuclear reaction, we can produce ^{57}Co as daughter of ^{57}Ni (half-life: 35.6 h), which is produced by $^{58}\text{Ni}(\gamma, n)^{57}\text{Ni}$ reaction. ^{57}Co is also produced by $^{58}\text{Ni}(\gamma, p)^{57}\text{Co}$ reaction, though the cross section of this reaction is lower than (γ, n) reaction.

EXPERIMENTS: On the irradiation of KURRI-LINAC, the energy of electron beam was 31 MeV, and the current was 190 μA . The target to generate the bremsstrahlung X-ray was water-cooled Pt metal, and the irradiation sample was put on the downstream side of the target. The sample was natural Ni metal foil (8 mg), and the irradiation time was 24 hours. Because the natural abundance of ^{58}Ni is relatively high (68%), natural Ni was used for the source.

For Mössbauer spectroscopy measurement, we used conventional Mössbauer spectrometer, and the irradiated sample was attached on the velocity transducer. The reference absorber was $\text{K}_2\text{MgFe}(\text{CN})_6$, which shows a single peak spectrum on normal Mössbauer spectroscopy.

RESULTS: Figure 1 shows energy spectra of X-rays and γ -rays from the irradiated Ni. The γ -rays intensity from ^{57}Ni decreases with time; Instead, the γ -rays intensity from ^{57}Co increases as expected. Additionally, ^{61}Co ($^{62}\text{Ni}(\gamma, p)^{61}\text{Co}$, half-life: 1.65 h), ^{56}Ni ($^{58}\text{Ni}(\gamma, 2n)^{56}\text{Ni}$, half-life: 6.1 d) and ^{56}Co (daughter of ^{58}Ni , half-life: 77 d) were observed as minor radio isotopes [1]; these were ignorable on Mössbauer measurement.

Figure 2 shows the obtained Mössbauer spectrum. It shows sextet reflecting magnetism of Ni metal. The hyperfine magnetic field evaluated by the fitting of the spectrum was 26.7 T, which is consistent with the reported value of ^{57}Fe in Ni metal [2]. This result shows that enough amount of ^{57}Co for the Mössbauer measurement can be produced using KURRI-LINAC and the Mössbauer emission spectroscopy is potentially available for application studies. In the future, we will perform ^{67}Zn -Mössbauer spectroscopy using the established methodology. Additionally, we attempt to extract ^{57}Co from irradiated Ni sample by the chemical operation and utilize it for e.g., a tracer experiment.

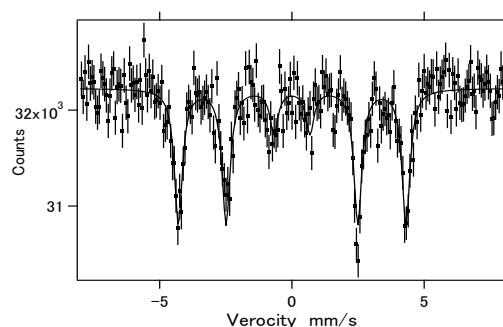


Fig. 2 Mössbauer spectrum obtained by using ^{57}Co source in Ni metal and $\text{K}_2\text{MgFe}(\text{CN})_6$ absorber at room temperature.

REFERENCES:

- [1] R. B. Firestone, in *Table of Isotopes*, 8th ed., edited by V. S. Shirley (Wiley, New York, 1996), Vol. 1.
- [2] C. E. Johnson, M. S. Ridout and T. E. Cranshaw, *Proc. Phys. Soc.*, **81** (1963) 107.

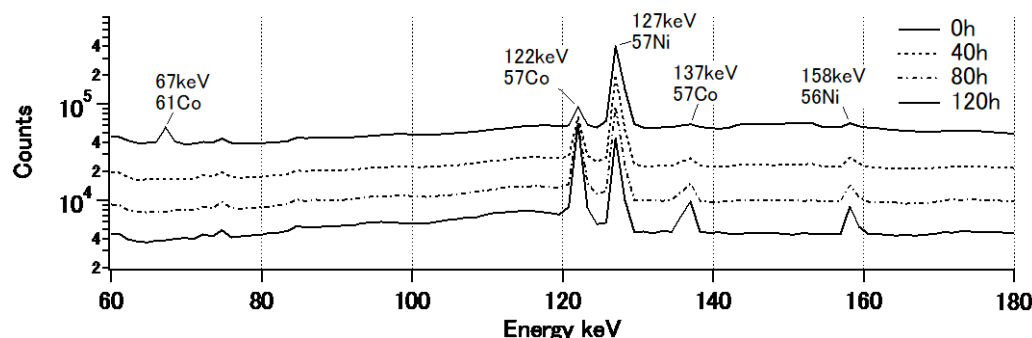


Fig. 1 Energy spectra of high-energy X-rays and γ -rays emitted from the Ni-foil source.

H. Sekimoto, Y. Haga¹ and A. Uehara²

Department of Physical Science and Materials Engineering, Faculty of Science and Engineering, Iwate University

¹*Department of Frontier Materials and Function Engineering, Graduate School of Engineering, Iwate University*

²*Research Reactor Institute, Kyoto University*

INTRODUCTION: It is well known that it is difficult to produce metallic calcium by the electrolysis of CaCl₂ based molten salt at high current efficiency. Because metallic calcium deposited on cathode is easily re-oxidized on anode due to the high solubility of metallic calcium in CaCl₂ molten salt. And chlorine gas generated on anode also easily reacted with metallic calcium. Recently, Lukasko and Murphy developed an interesting technique that metallic calcium is once recovered as Sn-Ca alloy by the electrolysis of CaCl₂-KCl molten salt and then the Sn-Ca alloy is electrorefined to pure metallic calcium at high current efficiency [1]. The feed of calcium in their technique is CaCl₂. This study is a progress of their process to change the feed to CaO. In this study, electro-winning of metallic calcium as calcium-tin alloy from CaCl₂-KCl-CaO molten salt using liquid tin cathode was investigated.

EXPERIMENTS: All electrochemical experiments were carried out in an argon filled glove box, where the vapor pressure was controlled below 10 ppm. Metallic tin, CaCl₂, KCl, and CaO were weighed and put in an alumina crucible, which was then set in a vertical electric furnace. The sample was heated at 1000 K to prepare CaCl₂-65 mass%KCl molten containing 0 – 2.0 mass% of CaO and liquid tin. Then, tungsten wire inserted in an alumina tube was immersed in the metallic tin and a graphite rod inserted in a silica tube was immersed in the CaCl₂-KCl molten salt. Galvanostatic electrolysis using 2 electrodes of tin cathode and graphite anode was carried out at -0.4 A for 2 hours. After the electrolysis, W wire and graphite rod were removed and the sample was cooled to be solidified. The concentration of calcium in tin cathode was determined by ICP-OES to evaluate the cathode current efficiency.

RESULTS: Figure 1 shows temporal changes of the terminal voltage during galvanostatic electrolysis experiments for the CaCl₂-KCl molten salt containing various concentrations of CaO. Figure 2 shows the variation of cathode current efficiency to the initial concentration of CaO in the CaCl₂-KCl molten salt. The terminal voltage for the CaO concentration of 0 mass% corresponds a decomposition voltage of CaCl₂. The initial terminal voltage for the molten salt containing 0.5 – 2.0 mass% of CaO was lower than that for the molten salt containing 0 mass% of CaO and that increased with time, which means that anode reaction was an evolution of CO₂ or

formation of CO₃²⁻ ion and CaO was consumed by electrolysis. The current efficiency was decreased with the increase of initial CaO content. After electrolysis, considerable amount of powdery carbon was confirmed in the molten salt whose initial CaO concentration was 1.0 mass% and 2.0 mass%. It is thus considered that the low current efficiency for the molten salt of high CaO content is due to a reduction of CO₃²⁻ ion to C on cathode or reaction of metallic calcium in tin cathode with CO₃²⁻ ion to form C.

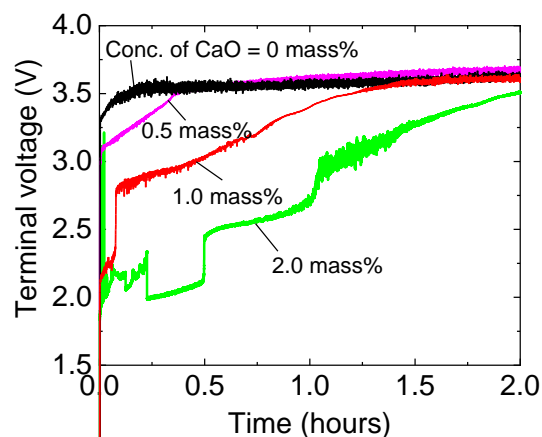


Fig. 1 Temporal change of the terminal voltage during electrolysis for the CaCl₂-KCl molten salt containing various concentration of CaO at 1000 K.

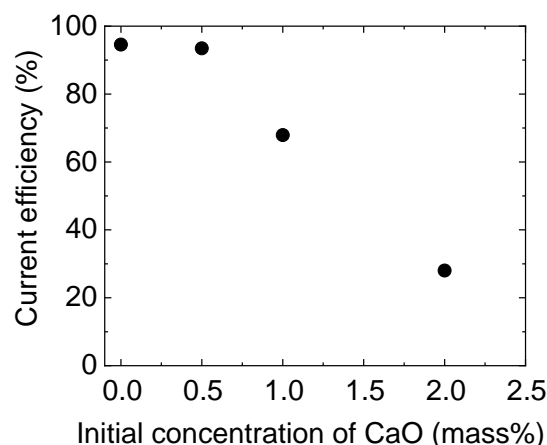


Fig. 2 Variation of cathode current efficiency to the initial concentration of CaO in the CaCl₂-KCl molten salt.

REFERENCE:

[1] J.J.Lukasko and J.E.Murphy: Report of Investigations (1990) RI9315.

S. Kitao¹, M. Kobayashi¹, T. Kubota¹, M. Saito¹,
R. Masuda¹, H. Ishibashi², S. Hosokawa² and M. Seto¹

¹Research Reactor Institute, Kyoto University

²Graduate School of Science, Kyoto University

INTRODUCTION:

The Mössbauer spectroscopy is one of the most powerful methods for investigation of electronic states, magnetic properties, chemical properties, and so on. A remarkable feature of this method is to extract the information of the specific isotope. This feature is effective to understand the essential properties of the materials, even with complex components. However, this method has a difficulty in obtaining and managing of the radioactive sources. Although about one hundred of Mössbauer energy levels are known, research activities in Mössbauer studies so far are quite limited, except ⁵⁷Fe and ¹¹⁹Sn. It is partly because commercially available sources at present are only ⁵⁷Co and ^{119m}Sn for the Mössbauer spectroscopy of ⁵⁷Fe and ¹¹⁹Sn, respectively.

On the contrary, at the Kyoto University Reactor(KUR), various short-lived isotopes can be obtained by neutron irradiation. We have already been performing Mössbauer spectroscopy of some isotopes, such as ¹²⁵Te, ¹²⁹I, ¹⁹⁷Au, by obtaining ^{125m}Te, ^{129m}Te or ^{129m}Te, ^{197m}Pt, respectively. Moreover, complementary short-lived isotopes can be produced by high-energy γ -ray irradiation at the electron linear accelerator(KUR-LINAC). The main purpose of this research is to increase the number of applicable Mössbauer spectroscopy by producing effective Mössbauer sources to apply various researches.

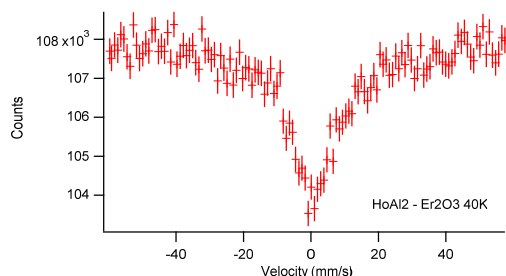


Fig. 1. ¹⁶⁶Er-Mössbauer spectrum of Er₂O₃ at 40K using ¹⁶⁶Ho source in HoAl₂ irradiated at KUR.

EXPERIMENTS AND RESULTS:

(1) ¹⁶⁶Er Mössbauer spectroscopy

The 80.56keV level of ¹⁶⁶Er is known as one of useful levels for Er-Mössbauer spectroscopy. ¹⁶⁶Ho with a half-life of 26.8 hours can be used as a Mössbauer source. It is obtainable by neutron irradiation of natural Ho, which has 100% abundance of ¹⁶⁵Ho. One of candidates for the source material is HoAl₂[1]. A HoAl₂ was synthesized by arc-melting of Ho and Al metals. The neutron irradiation was performed by pneumatic tube(Pn)

for 5 minutes at 1MW operation of KUR. The 80.56keV γ -rays from ¹⁶⁶Ho source are well resolved by using a CeBr₃ scintillation counter. The ¹⁶⁶Er-Mössbauer spectrum of Er₂O₃ at the temperature of 40K by using ¹⁶⁶HoAl₂ source is shown in Fig. 1. The obtained spectra shows expected single-line spectrum. This proved the effectiveness of the ¹⁶⁶Er-Mössbauer spectroscopy by using thus obtained source. Since HoAl₂ shows ferromagnetic order at 27K, the HoAl₂ source should not be used at the temperature of lower than about 40K.

(2) ¹⁶¹Dy Mössbauer spectroscopy

The 25.5keV level of ¹⁶¹Dy is known as the most useful level for Dy-Mössbauer spectroscopy. As for the Mössbauer source, ¹⁶¹Tb with a half-life of 6.88days is effectively usable. Since ¹⁶¹Gd becomes ¹⁶¹Tb in β -decay process with a half-life of 3.7 minutes, ¹⁶¹Tb source is obtainable by neutron irradiation of ¹⁶⁰Gd. Since natural Gd contains 21.86% abundance of ¹⁶⁰Gd, natural Gd is usable by waiting a few days for decay of a by-product of ¹⁵⁹Gd with a half-life of 18.48 hours. A Gd-Mg alloy is used as a source material[2]. The neutron irradiation was performed by Pn for 1 hour at 5MW operation of KUR. The expected ¹⁶¹Dy Mössbauer spectra were obtained successfully by using a Xe proportional counter.

Alternatively, ¹⁶¹Tb can be produced through (γ , p) reaction by high-energy γ -ray irradiation of ¹⁶²Dy at KUR-LINAC. The γ -rays are produced by electron irradiation of water-cooled Pt converter. In use of natural Dy, some by-products are inevitable. For an attempt, we obtained a ¹⁶¹Tb source by irradiation of a Dy metal using KUR-LINAC for 3 days. A Ge solid state detector is used to resolve the 25.5keV γ -rays. The ¹⁶¹Dy-Mössbauer spectrum of DyF₃ at room temperature using ¹⁶¹Tb source in Dy metal is shown in Fig. 2. Since expected spectrum was obtained, the results shows the effectiveness of this method.

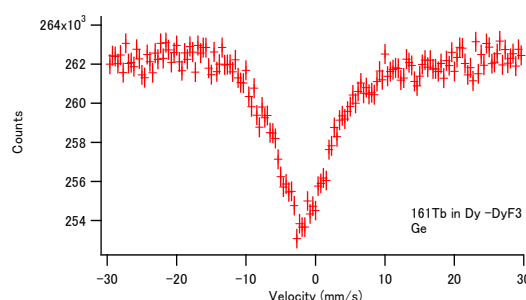


Fig. 2. ¹⁶¹Dy-Mössbauer spectrum of DyF₃ at room temperature using ¹⁶¹Tb source in Dy metal obtained at KUR-LINAC.

REFERENCES:

- [1] R. L. Cohen and J. H. Wernick, Phys. Rev. **134** (1964) B503.
- [2] G. J. Bowden, D. St. P. Bunbury, J. M. Williams, Proc. Phys. Soc. **916** (1967) 12.

Y. Kobayashi, Mariola Kadziolka-Gaweł¹, Damian Plažuk¹ and M. Seto

Institute for Integrated Radiation and Nuclear Science, Kyoto University

¹*Department of Organic Chemistry, Faculty of Chemistry, University of Łódź, Poland*

INTRODUCTION: Organogold complexes have attracted considerable interest in the last decades mainly due to their rich structural chemistry, involving Au-Au interactions (aurophilicity), luminescent properties, catalytic and biological activity. Gold(I) complexes of the type L-Au-X are known to form dimers, oligomers or polymers. In some cases, these complexes undergo ligands scrambling leading to two new ionic gold(I) species L₂Au and AuX₂. Among a variety of such complexes special attention has been paid to gold(I) acetylides [1]. Some Au acetylides which have COC≡CAu structure cause ligands scrambling, but which have C≡CAu structure do not cause ligands scrambling. It is considered that this difference comes from the steric structure of the complexes. However, it is also said that the Au-Au bonding in the oligomer and the electronic state of Au cause the difference. We measured ¹⁹⁷Au Mossbauer spectra of Au acetylides to elucidate origin of the ligands scrambling.

EXPERIMENTS: Three Au acetylides were synthesized: #1: (FcCCAuPEt₃), #2: ((FcCOCC)₂AuAu(PEt₃)₂) and #3: (FcCOCCAuPEt₃) [2,3]. The detailed structures of these complexes were studied by X-ray diffraction and ³¹P{¹H} NMR.

¹⁹⁷Au Mössbauer measurement was conducted using a constant-acceleration spectrometer with a NaI scintillation counter. The ¹⁹⁷Au γ-ray source (77.3 keV) was obtained from ¹⁹⁷Pt (half-life; 18.3 hrs) generated by irradiation of neutron to 98%-enriched ¹⁹⁶Pt metal foil using KUR. The γ-ray source and samples were cooled to 16 K, and the spectra were recorded in a transmission geometry. The isomer shift value of a gold foil was referenced to 0 mm/s.

RESULTS: Figure 1 shows ¹⁹⁷Au Mössbauer spectra of the Au acetylides. The amount of sample #3 was less than other samples, thus the absorption is small, and the distortion of the background line is larger than other spectra. The spectrum of #2 contains two components which relate to two different Au local surroundings. The spectra of #1 and #3 shows simple doublet. The values of isomer shift (IS) and quadrupole splitting (QS) are typical for AuL₂ type complexes [4]. If there is strong interaction between Au atoms in adjacent complexes, the IS values and QS values become near the values of four-coordinated Au atoms, which is smaller than typical values of AuL₂. However, such decreases

of IS and QS are not observed. This result shows that the strong interaction between Au atoms do not exist. The difference of the ligands scrambling is not caused by the electronic state of Au.

On X-ray diffraction study, the formation of wire-like structures on COC≡CAu complexes. This structure is commonly on ligands-scrambling complexes. The steric structure is main factor of the ligands scrambling on these Au acetylides.

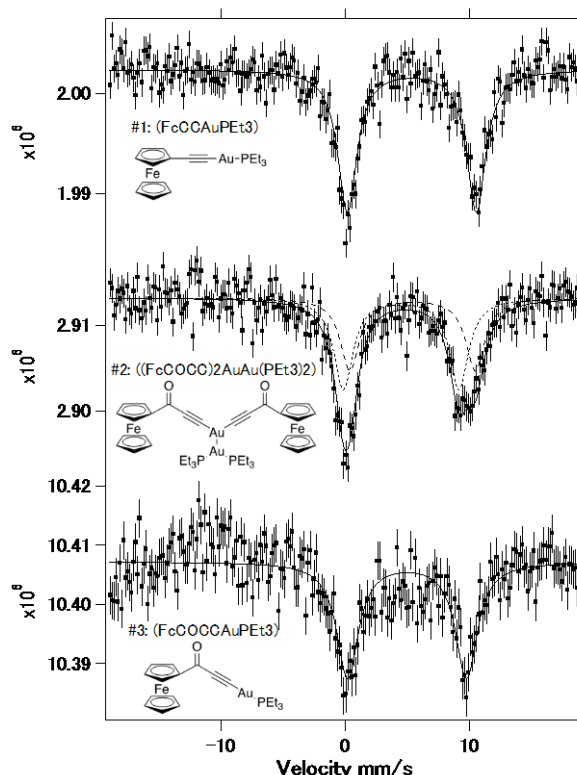


Fig. 1 ¹⁹⁷Au Mössbauer spectra of the Au acetylides at 16K.

REFERENCES:

- [1] J. Carlos Lima and L. Rodríguez, *Chemical Society Reviews*, **40** (2011) 5442-5456.
- [2] R. Flamholz, D. Plažuk, J. Zakrzewski, R. Métivier, K. Nakatani, A. Makal and K. Woźniak, *RSC Advances*, **4** (2014) 31594-31601.
- [3] D. Plažuk and J. Zakrzewski, *Journal of Organometallic Chemistry*, **694** (2009) 1802-1806.
- [4] G. J. Long, in *Mössbauer spectroscopy applied to inorganic chemistry*, Springer, 1984, pp. 7-26.

A. Kawaguchi and Y. Morimoto

KURNS, Kyoto University

INTRODUCTION: We have reported interacted structures between iodine (polyiodide ions, I_n^{m-} , m, n : integer, $n \neq 1$) and polymers.[1] While polyiodide ions (and their counter-ions) are prepared as solutes in aqueous solution, they can be diffused into various polymeric matrix. Such structures and procedures are expected to introduce novel functionality and wide applications to polymeric materials with easy operation.[2]

For some hydrophilic polymers, diffusion of polyiodide from their aqueous solutions advances very quickly; since, in some matrix such as polyamide-6 (PA6), ionic diffusion into crystallite region or "diffusion-induced" orientation are also observed during doping operation at room temperature, as phenomena, iodine-doped polymers can be regarded as "pseudo solvents" for ionic diffusion.[3,4] These results suggest that coordination between iodine and polymers is dynamic and pliable and activated process and that previous existence of polyiodide ion drastically enhances posterior ionic diffusion in polymers. Such posterior diffusion means can be applied for functionalization for matrices with arbitrary shape or size, occasionally, beyond hydrophobicity.

EXPERIMENTS: Samples are industrial products of micron-sized particles, which designed for ACF (anisotropic conduction film) or spacer with 2 or 5 mm diameters; they are synthesized as spherical particles of acryl resin showing fine-controlled dispersion of diameter. Some particles are products grafted with polystyrene (PS) on their spherical surface. [5]

These matrixes were "iodine-doped" by immersing in I_2 -KI(aq) or I_2 - NH_4I (aq) (0.1-3.0N) for more than one week. For secondary doping of Ag^+ , each samples were immersed in $AgNO_3$ (aq) (0.1-2.0M) for a few days. All operation were done at room temperature (c.a. 25°C).

For observation for section of spherical particles, transmission electron microscopy (TEM) was used for sliced matrixes of the particles molded in epoxy resin.

RESULTS: One of noteworthy points is the samples have chemically hydrophobic materials of acrylic resin or grafted surface with PS, which powder actually show very low affinity with water or ordinary aqueous solutions. Nevertheless, process with the polyiodides aqueous solutions can easily introduce iodine on "(1st iodine doping" and following Ag^+ ion on "secondary doping"; coloring with inner-diffused polyiodide (brown) or inner-precipitated AgI (light yellow) had been achieved in a few days or less. (Figure 1) And, TEM observation for the section of the sample after "Ag-secondary doping" with $AgNO_3$ (aq) indicates that (1)precipitation of AgI grains advances in inner region of the micro particle, that (2)precipitation region is not exposed on surface of the particles; there is intermediate region between the surface

of the spherical particles and region where AgI grains are grown up. (Figure 2) In the intermediate region, either polyiodide ions or precipitated AgI grains hardly exist. These results means that, (1)even for hydrophobic particle, polyiodide ions can be diffused from each aqueous solution, that (2) Ag^+ ion can be also diffused into the hydrophobic micro particle from the $AgNO_3$ (aq), and that (3)AgI grains which have precipitated through diffusion of Ag^+ into the particles dissolve to external environment of the particles with advance of "Ag secondary doping". Such behavior is qualitatively similar to results in iodine doping and "Ag secondary doping" for other hydrophobic polymers: polyethylene (PE), polypropylene (PP), SERB elastomers, and "silicone rubber" tubes, previously reported.[6] While the intermediate region may be obstacle for plating on surface of the particles, it should be functionalization on the surface of hydrophobic materials.

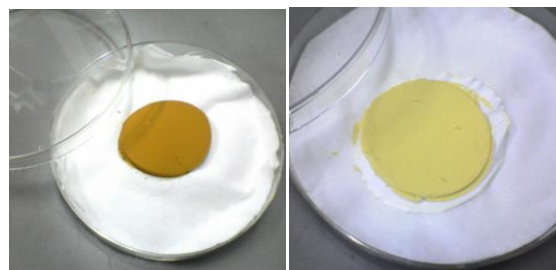


Fig.1: left: powder of micro particle after iodine-doping with polyiodide aqueous solution; right: next, the powder treated with $AgNO_3$ (aq).

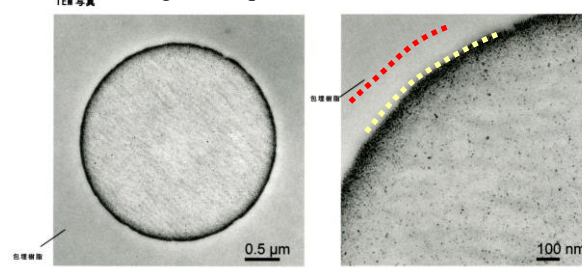


Fig.2: TEM observation for section of micro particle after "Ag-secondary doping" with $AgNO_3$ (aq); either polyiodide ions or AgI exist hardly at intermediate region between spherical surface of micro particle (red, dotted line) and region of AgI precipitation (yellow, dotted line).

ACKNOWLEDGMENTS: These results are researched with Dr. Gotoh (Shinshu Univ.) and his staff and are partially funded by NEDO.[5]

REFERENCES:

- [1] A. Kawaguchi, *Polymer*, **35** (1994) 3797-3798.
- [2] patent. JPN-5444559 (2014).
- [3] KAWAGUCHI Akio, et.al., *SPring-8 User Exp. Rep.* **5** (2000A) (2000) 354-354.
- [4] A.Kawaguchi, *Polym.Prep.Jpn.*, **62** (2013) 5116-5117.
- [5] "Projects for Practical Use from Innovation" sponsored by NEDO (2007-2009).
- [6] A. Kawaguchi, et.al., *KURRI Prog.Rep.*2015 (2016) 79-79.

Study on Metal Surface Wettability Enhanced by Radiation Induced Surface Activation

T. Hazuku, T. Ihara, R. Taguchi, S. Morooka¹, T. Miyoshi¹, H. Abe², S. Kano², T. Takamasa³, D. Ito⁴ and Y. Sai-to⁴

Tokyo University of Marine Science and Technology

¹Waseda University

²The University of Tokyo

³National Institute of Technology, Toyama College

⁴Research Reactor Institute, Kyoto University

INTRODUCTION: A supercritical water-cooled reactor (SCWR) is one of the 4th generation nuclear reactors, which is based on the light water reactor technology and the thermal power generation technology [1]. The system is simple, compact and high thermal efficiency. Therefore, it is considered to have high safety and economic performance. On the other hand, radiation induced surface activation (RISA) phenomenon enhances metal surface wettability, boiling heat transfer and anticorrosive effects by the electrical interaction between the base material and the surface of oxidized film [2]. It implies that RISA phenomenon can contribute the much higher performance of SCWR and improve the safety features.

This study is mainly aimed at evaluations of the RISA effect on metal surface wettability at high temperatures and pressures.

EXPERIMENTS: Figure 1 shows a schematic diagram of the apparatus for contact angle measurement at high temperatures and pressures. A specimen was placed at the center of the pressure vessel. A water droplet was supplied on the specimen from the bottom. A high speed video camera with backlighting from a plate light photographed the water droplet on the specimen. The image of water droplet were recorded into a personal computer and the contact angle, an indicator of macroscopic wettability, was measured by image-processing. The stainless-304 and the PNC1520 which is considered as a potential material in the SCWR were used as the base test materials. Three kinds of specimens: (1) bare metals before gamma-ray irradiation, (2) bare metals after gamma-ray irradiation and (3) metals with an oxidized film surface after gamma-ray irradiation were prepared for measurements of contact angles. The oxidized film on the base metal was made by submerging the metal in an autoclave for 60 hours under a supercritical condition with temperature of 380°C. The integrated irradiation dose of 60-Co gamma-ray was approximately 770 kGy.

RESULTS: Figure 2 compares the measured contact angles of water droplets on metals before gamma-ray irradiation, after gamma-ray irradiation and metals with oxidized film after gamma-ray irradiation. Although the surface wettability on the bare metals at room temperature conditions was drastically improved due to the RISA effect as is the results confirmed in the previous studies

[2], insignificant wettability improvement was confirmed under high temperatures over 290°C even after gamma-ray irradiation.

On the other hand, it was confirmed that the surface wettability on the stainless-304 with oxidized film was improved due to RISA even under high temperatures. The wettability enhancement due to RISA effect is basically considered to be occurred by formation of hydrophilic domain like a hydroxyl on the oxidized film. The present results reveal that the formation efficiency of hydrophilic domain on the metals with the stable oxidized film may be much higher than that on the bare metals. The effect of oxidization of metals on RISA effect will be evaluated in detail in the future study.

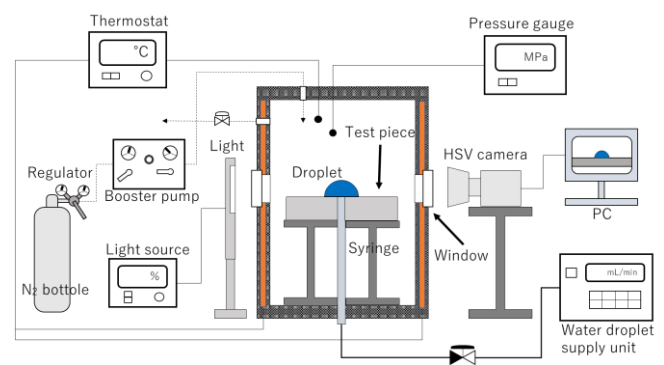


Fig. 1. Apparatus

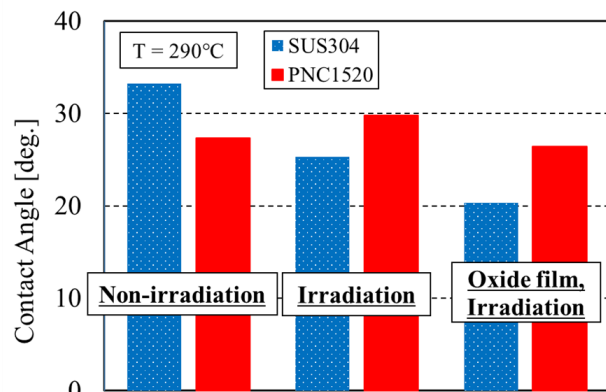


Fig. 2. Comparison of measured contact angles

REFERENCES:

- [1] Y. Oka and H. Mori, Supercritical pressure light water cooled reactor, Springer (2014).
- [2] T. Takamasa, *et al.*, Development of high-performance nuclear reactor technology by radiation induced surface activation effect "Improvement of in-furnace heat transfer and corrosion prevention technology using surface active effect by irradiation, Journal of Atomic Energy Society of Japan, Vol.49, No.1 (2007) 45-50 [in Japanese].

CO4-22 Characterization of Heterogeneous Nanostructures Formed in Stainless Steel using Small-Angle Scattering

Y. Todaka, N. Adachi, Y. Oba¹ and M. Sugiyama²

Department of Mechanical Engineering, Toyohashi University of Technology

¹Materials Sciences Research Center, Japan Atomic Energy Agency

²Institute for Integrated Radiation and Nuclear Science, Kyoto University

INTRODUCTION: Stainless steel is one of the most important materials and widely utilized as basic a structural material. Recent study has reported that heavy plastic deformation such as heavy cold rolling and high-pressure torsion (HPT) produce characteristic heterogeneous nanostructures composed of shear bands and nano-sized twins in the stainless steels [1]. These nanostructures can satisfy both high strength and high ductility. Furthermore, increases the strength of these nanostructured stainless steels increases with thermal ageing. However, the complicated heterogeneous nanostructures make it difficult to detect the origin of the strengthening using electron microscopes.

Small-angle X-ray scattering (SAXS) is a powerful means to quantitatively characterize and compare the nanostructures between the samples. From the comparison of the samples before and after ageing, SAXS can analyze the change in the nanostructures. Therefore, we perform the SAXS measurements of the heterogeneous nanostructures formed in the stainless steels in this study.

EXPERIMENTS: A typical austenitic stainless steel JIS SUS316LN was chosen as the sample. HPT straining was conducted to form the heterogeneous nanostructures. SAXS measurements were performed using a SAXS instrument with Mo K α radiation (Nano-viewer, RIGAKU) installed at the Institute for Integrated Radiation and Nuclear Science, Kyoto University. The characteristic X-ray emitted from Mo can penetrate steels. The sample-to-detector distance was 43 cm and 160 cm. During the SAXS measurements, the samples were put in vacuum to reduce the background scattering from air. A silver behenate and a glassy carbon were measured as the standard materials [2].

RESULTS: Fig. 1 shows SAXS profiles of the HPT-strained SUS316LN. Scattering intensities are clearly observed in the q range between 0.12 and 9 nm⁻¹. Here, q is the magnitude of the scattering vector. The intensity at around $q < 1$ nm⁻¹ shows difference. This indicates the change in the nanostructures roughly larger than 6 nm. It can be expected that significant increase by the

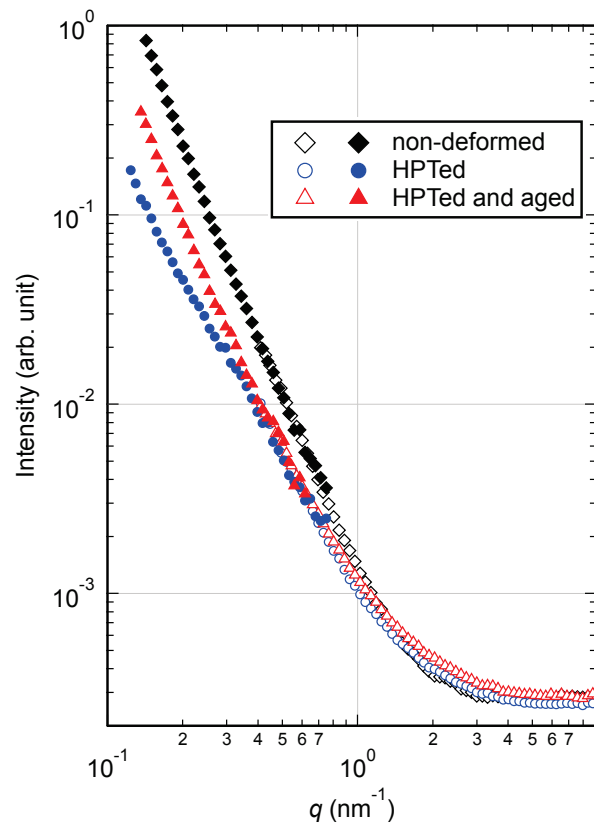


Fig. 1. SAXS profiles of the HPT-strained SUS316LN. Diamonds, triangles, and circles indicate the non-deformed sample, the HPT-strained sample, and the HPT-strained and aged sample, respectively.

thermal aging is given by nano-sized precipitates. The detailed structure of the nano-sized precipitate is still unknown. In order to analyze the chemical composition of the nanostructures, small-angle neutron scattering (SANS) experiments will be performed in the near future.

REFERENCES:

- [1] H. Miura *et al.*, *Scr. Mater.*, **133** (2017) 33-36.
- [2] F. Zhang *et al.*, *Metal. Mater. Trans. A*, **41A** (2010) 1151-1158.

CO4-23 Research on Spin Density Wave in Mixed Anion Layered Compounds, $\text{Sr}_2\text{VFeAsO}_{3-\delta}$

Y. Tojo, T. Nakamura, H. Fujioka, M. Matoba, S. Kitao¹, M. Seto¹ and Y. Kamihara

Department of Applied Physics and Physico-Informatics,
Faculty of Science and Technology, Keio University
¹Research Reactor Institute, Kyoto University

INTRODUCTION: The discovery of high temperature iron-based superconductors in Mixed Anion Layered Compounds (MALC) [1] has triggered the search on the new superconducting materials. Much attention has been devoted to the newly developed superconductors with Fe-square lattices. In 2009, a family of superconducting layered iron pnictides was reported; $Ae_2M\text{FePnO}_3$ with a perovskite-type layered local structure of $Ae_2\text{MO}_3$, where Ae denotes an alkaline-earth metal, M denotes Sc, Ti, Cr, V or another transition metals, and Pn denotes P or As. [2] Among these compounds, $\text{Sr}_2\text{VFeAsO}_{3-\delta}$ has attracted attention as a practical superconducting material because of its large upper critical magnetic fields [3]. The crystal structure of $\text{Sr}_2\text{VFeAsO}_{3-\delta}$ is described as a tetragonal lattice with FeAs carrier conducting layers sandwiched by $\text{Sr}_2\text{VO}_{3-\delta}$ perovskite-related carrier-blocking layers. $\text{Sr}_2\text{VFeAsO}_{3-\delta}$, which has been reported with nominal chemical compositions, shows superconducting transitions at $T_c^{\text{onset}} \leq 37.2$ K [3] under ambient pressure and at $T_c^{\text{onset}} = 46.0$ K [4] under high pressure. In this work, we unveil magnetic phases and superconducting phase in an iron-based superconductor with a thick-blocking layer of a perovskite-related transition metal oxide, $\text{Sr}_2\text{VFeAsO}_{3-\delta}$.

EXPERIMENTS: Polycrystalline samples were prepared via a two-step solid-state reaction using dehydrated SrO , FeAs , V_2O_5 , and V as starting materials. The phase purity and lattice constants of the resulting powders were examined by powder X-ray diffraction (XRD) (Rigaku; RINT2500Ultra18) using $\text{Cu K}\alpha$ radiation from a rotating anode. ^{57}Fe Mössbauer spectra (MS) were obtained using conventional equipment with ^{57}Co source from 2.5 K to 300 K. [5] The ^{57}Fe MS were measured for $\delta = 0.124$, 0.232, 0.237, 0.267, 0.509, and 0.631 samples. IS values of each sample are determined relative to that of $\alpha\text{-Fe}$ at room temperature.

RESULTS: Electronic and magnetic properties of ^{57}Fe in $\text{Sr}_2\text{VFeAsO}_{3-\delta}$. (a) Temperature (T) dependences of isomer shifts (IS), quadrupole splitting (QS) and full width at half maximum (FWHM) for $\text{Sr}_2\text{VFeAsO}_{3-\delta}$ samples with $\delta = 0.124$ (open circle), 0.232 (open square), 0.237 (open triangles), 0.267 (closed triangles), 0.509 (red closed circles), and 0.631 (closed squares). The QS and FWHM values of the samples with $\delta = 0.267$, 0.509, and 0.631 are written only when the spectrum is a doublet. The black lines in all plots indicate standard deviations. $\sqrt{\langle B_{\text{int}}^2 \rangle}$ are obtained from the distributions of the internal fields (B_{int}) of the samples with $\delta = 0.267$, 0.509, and 0.631 exhibiting antiferromagnetic ordering of Fe

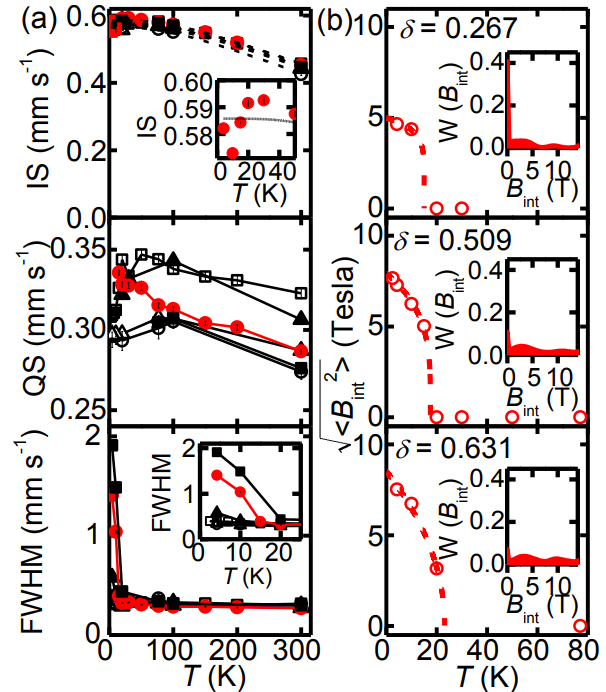


Fig. 1. Electronic and magnetic properties of ^{57}Fe in $\text{Sr}_2\text{VFeAsO}_{3-\delta}$. (a) Temperature (T) dependence of isomer shift (IS), quadruple splitting (QS), and full width half maxima (FWHM) for $\delta = 0.124$ (open circle), 0.232 (open square), 0.237 (open triangles), 0.267 (closed triangles), 0.509 (red closed circles), and 0.631 (closed squares). (b) $\sqrt{\langle B_{\text{int}}^2 \rangle}$ versus T for $\delta = 0.267$, 0.509, and 0.631. Insets show histograms of B_{int} distributions for each sample at 4.2 K. Figs are reprinted from Ref. 6.

sub-lattice at temperatures $< T_N$. The red dashed lines are fitted lines, obtained by the formula

$$\sqrt{\langle B_{\text{int}}^2 \rangle} = B_0 \left(1 - \frac{T}{T_N}\right)^\alpha \quad \text{for } 0 \leq T/T_N \leq 1$$

with $\alpha = 0.5$. Details results and discussions have been reported in ref. 6.

REFERENCES:

- [1] H. Hiramatsu and Y. Kamihara, in Transparent oxides as active electronic materials and their applications, edited by H. Hosono and M. Hirano (CMC publishing, Tokyo, 2006), p. 71-93, Layered compounds (in Japanese).
- [2] H. Ogino, *et al*, Supercond. Sci. Technol., **22** (2009) 085001.
- [3] X. Zhu, *et al*, Phys. Rev. B **79**, 220512 (2009).
- [4] H. Kotegawa, *et al*, J. Phys. Soc. Jpn., **78** (2009) 123707.
- [5] S. Kitao, *et al*, J. Phys. Soc. Jpn., **77** (2008) 103706.
- [6] Y. Tojo, *et al*, arXiv:1802 (2018) 03907.

K. Sugita, M. Mizuno, H. Araki, A. Yabuuchi¹ and A. Kinomura¹

Graduate School of Engineering, Osaka University

¹Institute for Integrated Radiation and Nuclear Science, Kyoto University

INTRODUCTION: The alloy design has been conventionally performed by choosing a base metal and adding suitable elements to achieve desired properties. Over the last decade, a new type of multicomponent alloys called as “high entropy alloys”, which include equiatomic / near-equiatomic proportion of constituent elements, have been proposed by Yeh et al. [1-3]. They often show simple solid solution structures at high temperature due to high configurational entropy of mixing for a random solid solution. High entropy alloys have been reported to have the following promising properties of practical interest, such as high strength combined with ductility, high fracture toughness, excellent oxidation and corrosion resistance. “Sluggish diffusion” kinetics is believed to be a main contributor to these properties. Therefore it has also created fundamental interest for atomic diffusion in a multiprincipal element matrix, and the diffusion kinetics in high entropy alloys has been actively investigated by diffusion couple method and tracer-diffusion method.

In this work, we contribute to a debate about hypothetical sluggish diffusion phenomena in high entropy alloys by investigating the vacancy migration behavior in a CoCrFeMnNi alloy during the isochronal annealing after electron-irradiation.

EXPERIMENTS: Metal pieces of Co, Cr, Fe, Mn and Ni with 99.9% up purity were added together in equiatomic proportions to produce Co₂₀Cr₂₀Fe₂₀Mn₂₀Ni₂₀ alloy ingots by arc melting followed by homogenization at 1373 K for 24 h. Fe₄₀Cr₁₅Ni₄₅ alloy ingots were also prepared for comparison. The alloy ingots were cut into square plate specimens with dimensions of 10 × 10 × 0.5 mm³. The specimens were subjected to strain relief annealing at 1373K for 10 h and then rapidly cooled to prevent secondary phase precipitation and to stabilize single-phase FCC structures. The specimens in water flow were exposed to 8 MeV electron beam irradiation for 1 h in KURRI-LINAC. The irradiation damage was evaluated at (1.3 - 1.8) × 10⁻⁴ dpa. In order to investigate the thermal stability of vacancies, the electron irradiated specimens were subjected to the subsequent isochronal annealing for 1 at 373-593K.

Positron lifetime measurements were carried out by using a digital oscilloscope system with photomultiplier tubes mounted with BaF₂ scintillators, having a time resolution (FWHM) of 180 ps. The positron lifetime measurements require data acquisition for approximately 12 hours with a Na-22 positron source of 0.6 MBq activity in order to

acquire 3 million counts in the positron lifetime spectrum. The measured spectra were analyzed using the programs RESOLUTION and POSITRONFIT Extended.

RESULTS: Mean positron lifetime in the electron-irradiated CoCrFeMnNi and CrFeNi specimens after isochronal annealing is shown in Fig.1. The positron lifetime spectra of as-irradiated CoCrFeMnNi and CrFeNi specimens shows a clear splitting into two exponential components with the longer lifetime values of 185-195 ps. This indicates that a part of positrons are trapped by monovacancies and relatively small vacancy clusters produced during the electron beam irradiation. After the subsequent isochronal annealing, the mean positron lifetime is observed to decrease sharply around 473K. This can be attributed to the decrease in vacancy concentrations triggered by the free vacancy-migration. It demonstrates the vacancy migration enthalpy in the CoCrFeMnNi high entropy alloy is very similar to that in the CrFeNi alloy. These results indicates that the “sluggish diffusion” hypothesis is not supported in a CoCrFeMnNi high entropy alloy at least in view of vacancy migration behavior.

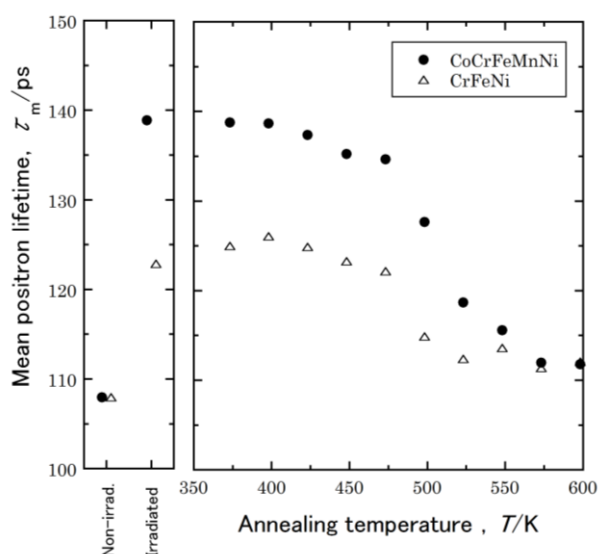


Fig. 1 Mean positron lifetime in the electron-irradiated CoCrFeMnNi and CrFeNi alloys after isochronal annealing.

REFERENCES:

- [1] C. Y. Hsu, J. W. Yeh, S. K. Chen, T. T. Shun: Metall. Mater. Trans. **35A**, (2004), 1465.
- [2] J. W. Yeh, S. K. Chen, S. J. Lin, J. Y. Gan, T. S. Chin, T. T. Shun, C. H. Tsau, S. Y. Chang: Adv. Eng. Mater., **6** (2004) 299.
- [3] J. W. Yeh: Ann. Chim. Sci. Mat., **31** (2006) 633.

H. Tsuchida^{1,2}, D. Ueda², S. Konishi² and Q. Xu²¹Quantum Science and Engineering Center, Kyoto University²Department of Nuclear Engineering, Kyoto University³Institute for Integrated Radiation and Nuclear Science, Kyoto University

INTRODUCTION: Studies on radiation damage in materials are of technical importance for developing radiation-resistant materials used in an irradiation environment [1,2]. In this work, we investigated radiation damage in polymers. The purpose of this study is to understand a fundamental nature of radical-related radiation damage. Gamma-ray irradiated polystyrene was analyzed using positron Age-MOMentum Correlation (AMOC) technique. The AMOC combines positron lifetime and annihilation gamma-ray Doppler-broadening spectroscopy by correlated measurements of the positron age and the Doppler shift of one of the annihilation quanta. In this analysis, we developed a new system, $\beta^+\text{-}\gamma$ coincidence-based AMOC.

EXPERIMENTS: The irradiation experiments were performed at Co-60 gamma-ray irradiation facility at KURNS. Polystyrene with a thickness of 2 mm was used as a sample. The sample was irradiated with the gamma-rays at two different doses of 30 and 300-kGy at room temperature. Position annihilation analysis was carried out at our facility, where we developed AMOC system combined with $\beta^+\text{-}\gamma$ coincidence positron lifetime spectroscopy. The positron source used was Ge-68.

RESULTS: Fig. 1 shows AMOC spectrum (correlation between the energy of annihilation gamma-rays and the positron lifetime) for the sample irradiated at dose of 300-kGy. Long-lifetime components (above 1 ns) correspond to positron annihilation characteristic on formation of positronium (Ps) in open volume defects of materials. Namely, self-annihilation of para-Ps has a lifetime of 0.12 ns, whereas pick-off annihilation of ortho-Ps has typically a lifetime of 0.5–5.0 ns.

Based on observed spectra, we obtained time dependent line-shape parameter S . Fig. 2 shows the results for the samples irradiated at two different doses of 30 and 300-kGy. The S parameter gradually decreases in the time range below 1 ns, in which self-annihilation of para-Ps mainly occurs. With increasing dose, the values of S are reduced. This reduction is attributed to the damage accumulation. In the result for the sample irradiated at 300-kGy, the S increases in the range above 1 ns, and becomes maximum around 3.5 ns. This result may be related to the pick-off annihilation of ortho-Ps originating from interactions with radical-related damage. To determine this observation, we will perform further research for identification of radical-related damage by electron

spin resonance (ESR) method.

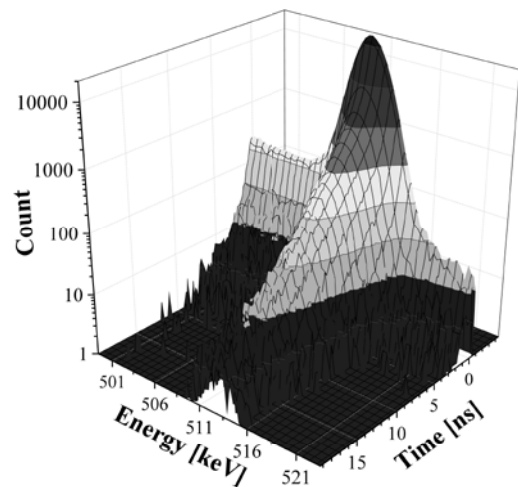


Fig. 1. AMOC spectrum for polystyrene irradiated with Co-60 gamma-rays at dose of 300-kGy.

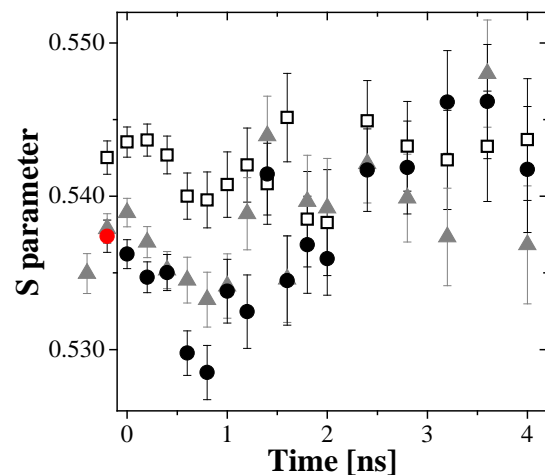


Fig. 2. Line-shape parameter S as a function of time (positron age) for gamma-ray irradiated polystyrene at various doses: \square un-irradiated, \blacktriangle 30-kGy, and \bullet 300-kGy.

REFERENCES:

- [1] H. Tsuchida *et al.*, Jpn. J. Appl. Phys. Conf. Proc., **2** (2014) 011103.
- [2] H. Tsuchida *et al.*, Mater. Res. Express, **3** (2016) 055201.

H. Yokota, S. Jitsukawa, S. Nakamura¹, S. Kitao², Y. Kobayashi², M. Saito³, R. Masuda³ and M. Seto²

Graduate School of Science, Chiba University

¹*Department of Physics, Teikyo University*

²*Research Reactor Institute, Kyoto University*

INTRODUCTION: As the strong demands of the miniaturization of devices, controlling more than two order parameters at the same time is the key factor to open up the new possibility for designing the novel applications. Multiferroics are the most promising candidates for this usage since they possess more than two ferroic properties in the same phase [1-4]. Especially, cross-control of magnetization and polarization by electric and magnetic fields provides a great potential. In spite of their attractive properties, most of multiferroics exhibit their properties at low temperature, which make us difficult to realize the devices using multiferroics. Recent progress on thin film fabrications is changing this situation and now we are able to obtain material which cannot be realized as a bulk form. Hexagonal rare earth ferrites (h-REFeO₃), which we are interested in, are one of the examples and this series of materials are only obtained as thin film or nano particle form. In the case of bulk, orthorhombic perovskite structure becomes a stable state. Therefore not so many reports on h-REFeO₃ has have been reported so far. Recently, room temperature multiferroic properties have been reported in hexagonal LuFeO₃ thin film and this class of materials has been receiving an attention [5-9]. We succeeded to fabricate h-ErFeO₃ thin film by using a pulsed laser deposition technique and investigated its physical properties by various methods. We confirmed that h-ErFeO₃ thin film was epitaxially grown and it exhibits ferroelectricity at room temperature. The superconducting quantum interference device (SQUID) measurements disclosed that the magnetization shows the discrepancy between zero field cooling (ZFC) and field cooling (FC) processes under a weak magnetic field. Below the magnetic transition temperature of 120 K, it shows an apparent magnetic hysteresis loop indicating the weak ferromagnetic property of h-ErFeO₃ thin film. The Mössbauer spectroscopy clarified that the Fe ions are in the high-spin Fe³⁺ state and we proposed a possible magnetic structure of Fe ion[10]. Although our previous experiments elucidated ferroelectric and weak ferromagnetic properties of h-ErFeO₃ thin film, there are still some ambiguities of this material. The Mössbauer spectroscopy is very powerful technique and provides abundant knowledge about a magnetic and electronic state concerning the targeted nuclides in compounds. In spite of its efficiency, most of the Mössbauer studies are limited on ⁵⁷Fe or ¹¹⁹Sn ion and not many reports exist on rare earth ions. The purpose of our study is to establish the Mössbauer spectroscopy on rare earth Er ion and apply this technique on h-ErFeO₃ thin film.

EXPERIMENTS: HoAl₂ was irradiated for 5 minutes at 1MW power at KUR and used as γ -source. Er₂O₃ powder and h-ErFeO₃ thin films were used as samples and the measurements were carried out at 40 K. CeBr₃ Scintillation counter was used as a detector.

RESULTS: Figure 1 shows the Mössbauer spectrum of Er₂O₃ powder. It exhibits a typical paramagnetic behavior. It suggests that we succeeded to measure the Mössbauer spectrum for rare earth Er element. On the other hand, our trial on h-ErFeO₃ thin films is very difficult to obtain enough intensity an SN ratio to discuss about its magnetic properties. Further trial using a stronger γ -intensity or Er radioactive enrich sample is needed.

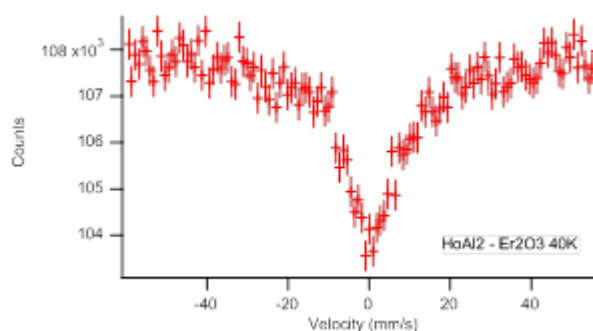


Fig. 1. Mössbauer spectrum of Er₂O₃ powder measured at 40 K

REFERENCES:

- [1] H. Schmid, *Ferroelectrics* **162** (1994) 317-338 .
- [2] T. Kimura, T. Goto, H. Shintani, K. Ishizaka, T. Arima, and Y. Tokura, *Nature* **426** (2003) 55.
- [3] Fiebig, *J. Phys. D: Appl. Phys.*, **38** (2005) R123-R152 .
- [4] G. Catalan and James F. Scott, *Adv. Mater.*, **21** (2009) 2463–2485 .
- [5] A. R. Akbashev, A. S. Semisalova, N. S. Perov, and A. R. Kaul, *Appl. Phys. Lett.*, **99** (2011) 122502.
- [6] Y. K. Jeong, J.-H. Lee, S.-J. Ahn, S.-W. Song, H. M. Jang, H. Chio, and J. F. Scott, *J. Ame. Chem. Soc.*, **134** (2012) 1450 .
- [7] Y. K. Jeong, J.-H. Lee, S.-J. Ahn, and H. M. Jang, *Chem. Mat.*, **24** (2012) 2426 .
- [8] H. Iida, T. Koizumi, Y. Uesu, K. Kohn, N. Ikeda, S. Mori, R. Haumont, P.-E. Janolin, J.-M. Kiat, M. Fukunaga, and Y. Noda, *J. Phys. Soc. Jpn.*, **81** (2012) 024719.
- [9] W. Wang, J. Zhao, W. Wang, Z. Gai, N. Balke, M. Chi, H. N. Lee, W. Tian, L. Zhu, X. Cheng, D. J. Keavney, J. Yi, T. Z. Ward, Paul C. Snijders, H. M. Christen, W. Wu, J. Shen, and X. Xu, *Phys. Rev. Lett.*, **110** (2013) 237601 .
- [10] H. Yokota, T. Nozue, S. Nakamura, H. Hojo, M. Fu-kunaga, P. E. Janolin, K. M. Kiat and A. Fuwa, *Phys. Rev. B*, **92** (2015) 054101.

Dose Response and Mechanism of Radiophotoluminescence Phenomenon Induced by γ -ray Irradiation in Cu-doped Glass

R. Hashikawa, Y. Fujii, A. Kinomura¹, T. Saito¹,
A. Okada², T. Wakasugi² and K. Kadono²
Graduate School of Science and Technology,
Kyoto Institute of Technology

¹Institute for Integrated Radiation and Nuclear Science,
Kyoto University

²Faculty of Materials Science and Engineering,
Kyoto Institute of Technology

INTRODUCTION: Radiophotoluminescence is a phenomenon in which photoluminescence is induced in materials by the exposure to ionizing radiation. It is well known that Ag-activated phosphate glass exhibits strong radiophotoluminescence, in which the intensity of the induced luminescence is proportional to the absorbed dose. Then the Ag-activated phosphate glass is practically used as a personal dosimeter [1]. However, there are few studies on the radiophotoluminescence behaviors of glasses other than the Ag-activated glass [2]. We have been interested to the luminescence properties of Cu-doped materials and explored new glasses exhibiting radiophotoluminescence with high performance. Here, we present the photoluminescence in a Cu-doped aluminoborosilicate glass induced by the γ -ray irradiation and the mechanism for the enhancement of the luminescence.

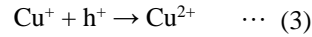
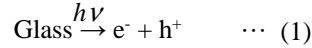
EXPERIMENTS: A Glass with the composition, $25\text{Na}_2\text{O} \cdot 25\text{Al}_2\text{O}_3 \cdot 10\text{B}_2\text{O}_3 \cdot 40\text{SiO}_2$ (mol%) (ABS25), was prepared from raw materials, NaNO_3 , Al_2O_3 , B_2O_3 , SiO_2 , CuO , by the conventional melting-cooling method. The batch mixtures with CuO were melted at 1600°C for two hours using a Pt crucible. The concentration of Cu was 0.005 mol% for 100 mol% of glass. The prepared glass was annealed at 660°C and cut to the size of $15 \times 15 \text{ mm}^2$ and 1 mm in thickness. Both sides of the glass were optically polished.

The γ -ray irradiation experiments were performed with 60Co γ -ray at the Co-60 Gamma-ray Irradiation Facility at Institute for Integrated Radiation and Nuclear Science, Kyoto University. The irradiation dose was represented as absorbed dose for water.

RESULTS: Figure 1 shows the photoluminescence spectra of the 0.005 mol% Cu-doped glass irradiated by the γ -ray with various dose. Increasing the absorbed dose, the intensity of the luminescence band at 2.5 eV (500 nm), assigned to the $3d^94s^1 \rightarrow 3d^{10}$ transition, was increased. Figure 2 shows the relationship of the integrated intensity of the luminescence against the absorption dose. The excellent linearity between 40 Gy and 1.1×10^3 Gy of the absorbed dose was observed. At the absorbed dose below 40 Gy and above 1.1×10^3 Gy, the luminescence intensities were deviated to higher and lower sides of the line, respectively.

It is expected that the exposure of the Cu-doped glass to the ionizing radiation induces the fol-

lowing reactions in it. The eq. (1) shows the generation of electron-hole pairs. The generated electrons and holes are trapped at Cu^{2+} and Cu^+ ions through eq. (2) and (3), respectively.



When the absorbed dose is small, the effect of eq. (3) suppressing the increase of the amount of Cu^+ can not be negligible. Then the intensity of the photoluminescence was deviated to the higher side from the line. On the other hand, increasing the absorption dose beyond 1.1×10^3 Gy, the reaction of the electron capture expressed by eq. (2) reached the saturation. Then, the intensity of the photoluminescence deviated to the lower side from the line.

More quantitative investigations relating the absorbed does, and the amount of the generated electron-hole pairs, Cu^+ , and Cu^{2+} are planned in the near future.

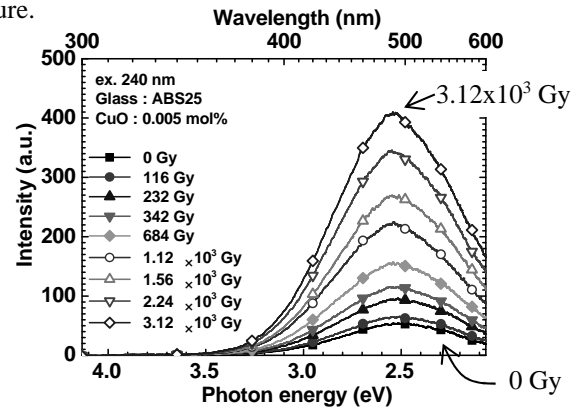


Fig. 1. Emission spectra of ABS25 doped with 0.005 mol% CuO at various absorbed doses.

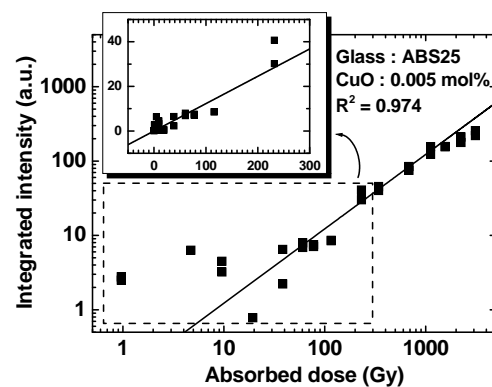


Fig. 2. Plot of integrated intensity of emission spectra versus the absorbed dose of ABS25 doped with 0.005 mol% CuO.

REFERENCES:

- [1] Y. Miyamoto *et al.*, Radiat. Meas., **46** (2011) 1480-1483.
- [2] R. K. Parajuli *et al.*, Key. Eng. Mat., **698** (2016) 163-170.

R. Okazaki and S. Sekimoto¹

Department of Earth and Planetary Sciences, Kyushu University

¹*Research Reactor Institute, Kyoto University*

INTRODUCTION: In order to elucidate the origin and evolution of planetary materials, it is important to determine the chemical composition and age of specific minerals and microscopic portions, such as impact melt pockets, CAIs (Ca- and Al-rich Inclusion), and chondrules. The major chemical composition of microscopic regions or dust particles can be analyzed with generally-used analytical instruments (e.g., EMPA, electron microprobe analyzer), whereas it is difficult to measure abundances of trace elements and isotopic compositions. Combination of EMPA, INAA, and noble gas analysis are one of the best way to determine chemical and isotopic compositions of as many elements as possible. For example, mineral chemistry such as Fe content in olivine and pyroxene can be determined by EMPA at first by using a one-side-polished section, which will be followed by INAA for trace element (e.g., Pt) analysis, and finally Ar isotopes will be determined to date Ar-Ar age of the sample. This analytical method is useful for limited samples without any substitution, such as anomalous meteorite material, extraterrestrial dust particles (micrometeorites) and spacecraft-returned samples.

As a first step, we have selected the standard samples with similar size and weight to extraterrestrial microgram samples for INAA and Ar-Ar dating. Next, we have established a sample container and a handling method to minimize loss and contamination of the samples. These works have been conducted through our research projects at KURRI.

EXPERIMENTS: In this work, neutron irradiation was applied to several tens to several hundred micron-sized (0.1 to 10 microgram) rock fragments recovered from meteorites (Allende CV3 chondrite, Holbrook L6 chondrite, and Agoult and HAH262 eucrites), terrestrial rocks and minerals (JB-1, orthoclase, and wollastonite), Pt-Ir alloy, and an NIST glass standard (SRM610). Each of the sample particles was placed in a conical dimple ($\phi 1$, depth ~ 0.5 mm) of a sapphire disk ($\phi 5.5$, 1.5 mm thick), and covered with a sapphire disk ($\phi 5.5$, 0.3 mm thick). Each of the sapphire container was wrapped with pure aluminum foil. These Al-wrapped containers were stacked and sealed in the Hydro capsules to perform neutron irradiation. After irradiation, the samples were moved to non-irradiated glass container with similar dimension from the sapphire one in order to reduce the radioactivity from the sapphire containers and Al foil.

Gamma ray measurements for short halflife nuclides

were performed promptly after collection of the samples. Allende and JB-1 were used as reference standard of the INAA. Noble gas isotopes in orthoclase samples were measured by using a mass spectrometer at Kyushu university. These INAA and noble-gas analyses were conducted as a project adopted in 2014 (No. 25066, PI: S. S.). In this project in 2017 (No. 29008, PI: R. O.), only neutron irradiation has been carried out in 2018 Jan. Noble gas analysis will be done in this summer.

RESULTS: Fig. 1 shows the Co and Ni concentrations in some fragments collected from Holbrook L6 chondrite. The Hol-2G and -3C plot on the tie line defined by iron meteorites, chondrite components, and bulk chondrite data (Fig. 1). Electron microscope observation revealed that these two samples contain Fe-Ni metal and/or troilite (FeS). In contrast, Hol-13G contains neither metal or troilite, and its Ni content was below than the detection limit of INAA.

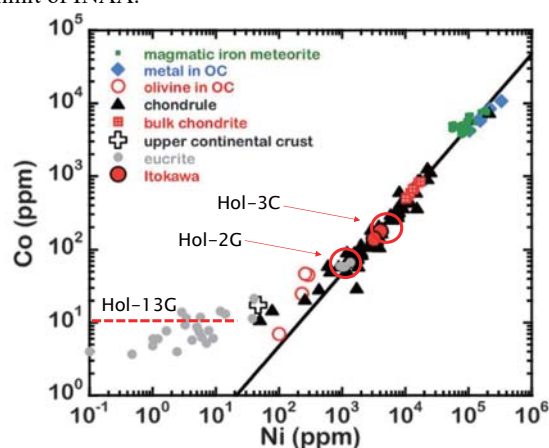


Fig. 1. Co and Ni concentrations in Holbrook and other extraterrestrial samples ([1]).

The concentration of Ir was determined to be 4.44 ± 0.38 wt% ($n=5$) by using ~ 5 μg of in Pr-Ir alloy samples, which is in good agreement with the reference value of 5 wt%.

Minor and trace element concentrations in SRM610 were around 300-400 ppm with relatively small deviations, but are lower than reference values of ~ 500 ppm [2]. Exceptionally, Ni and Zn concentrations were ~ 1000 -1400 ppm, which is due to interference from other elements (possibly Eu) contained in SRM610. Hence, SRM610 is not suited for INAA.

REFERENCES:

- [1] M. Ebihara *et al.*, *Science*, **333** (2011) 1119-1121.
- [2] A. B. E. Rocholl *et al.*, *Geostandards Newsletter*, **21** (1997) 101-114.

O. Ishizuka, S. Sekimoto¹, R. Okumura¹, H. Yoshinaga¹,
T. Fujii²

Geological Survey of Japan, AIST

¹*Institute for Integrated Radiation and Nuclear Science,
Kyoto University*

²*Graduate School of Engineering, Osaka University*

INTRODUCTION: Submarine volcanic rocks are known to give K-Ar ages different from their true eruption ages in some cases. This is due to the existence of excess ^{40}Ar in the rapidly quenched glass or Ar loss and K remobilization caused by reaction with seawater or hydrothermal fluids. Capability of evaluating these effects makes stepwise-heating analysis in $^{40}\text{Ar}/^{39}\text{Ar}$ dating particularly useful for dating submarine volcanics.

We conducted a research cruise KS-17-15 in November, 2017 to achieve robust tectonic reconstruction of the evolving Philippine Sea Plate for the period immediately before and after subduction initiation at ~ 52 Ma to form the Izu-Bonin-Mariana arc, which is one of the “typical” intra-oceanic island arc. This cruise successfully recovered igneous rocks from the Kita-Daito Basin, which is one of the major oceanic basins in the oldest part of the Philippine Sea Plate. Here we report the first preliminary $^{40}\text{Ar}/^{39}\text{Ar}$ age obtained from the igneous rock recovered during this cruise.

EXPERIMENTS: Samples were wrapped in an aluminum foil packet and the packets were piled up in a pure aluminum (99.5% Al) irradiation capsule (9 mm diameter and 30 mm long). The irradiation capsule was partitioned into 3 compartments to minimize the uncertainty of the sample positions at irradiation. The irradiation capsule was wrapped with 0.5 mm-thick Cd-foil before irradiation. The capsule was irradiated for 2 hours at 5MW in Hyd facility of KUR on January 18, 2018. Analyses were conducted using $^{40}\text{Ar}/^{39}\text{Ar}$ geochronology facility at the Geological Survey of Japan/AIST following the analytical procedure described in [1].

For the experiments described here, 5 mg of sample was analysed. Due to alteration of poorly-crystallized part of groundmass, the sample was treated at 100°C on hot plate with stirrer in 6N HCl for 30 minutes and then 6N HNO₃ for 30 minutes to remove possible alteration products (clays and carbonates) prior to irradiation. This procedure effectively separated and concentrated fresh plagioclase in groundmass and of microphenocryst. After this acid treatment, the separates were examined under binocular microscope before packed for irradiation.

RESULTS: One basaltic sample recovered from the western part of the Kita-Daito Basin was dated. The Kita-Daito Basin, separating the Amami Plateau and the Daito Ridge, has a thin crust of 4 to 6 km based on seismic structure, and was inferred to be a backarc ocean crust [2]. No

age data have been obtained from this basin to constrain its age of formation.

The analysed sample was recovered by dredging operation. This dredge was conducted on the steep NE-facing slope of a 1000m-high irregular-shaped bathymetric high in the westernmost part of the Kita-Daito Basin (Fig. 1). The dredge arrived at bottom at a water depth of 5399 m. Total 5 kg of samples were recovered. Major rock types are polymictic breccia and cpx-ol basalt lava clasts. These breccia samples are mainly composed of cpx-ol basalt, px basalt and pl-phyric basalt. The dated sample (D1R3) is cpx-phyric basalt with groundmass containing abundant plagioclase.

Stepwise heating procedure of $^{40}\text{Ar}/^{39}\text{Ar}$ dating was applied for this sample. Fig. 2 shows age spectrum for this analysis. This sample gave a plateau age of 41.00 ± 0.09 Ma comprising of 69.1% of released gas. This age plateau consists of 19 steps out of 31 steps. The plateau age shown here is still temporary age because flux monitor measurement has not been completed yet. However, the data strong implies that formation of the Kita-Daito Basin is younger than the neighboring Amami Plateau and Daito Ridge, and also postdate the subduction initiation of the Izu-Bonin-Mariana arc. This new result is crucial for tectonic reconstruction of the Philippine Sea area.

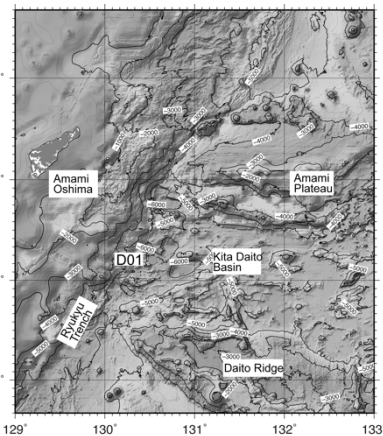


Fig. 1 Locality of the dated sample.

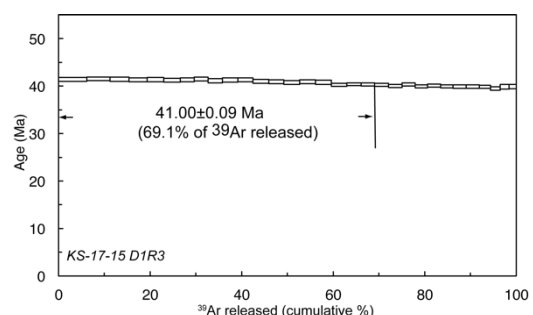


Fig. 2 Age spectrum for the basalts from the Kita-Daito Basin.

REFERENCES:

- [1] O. Ishizuka *et al.*, *Earth Planet. Sci. Lett.*, **481** (2018), 80-90.
[2] A. Nishizawa *et al.*, *Earth Planets Space*, **66**:25 (2014).

H. Sumino, K. Shimodate, K. Sudo, S. Kishi, M. Koike, T. Kagoshima, T. Yamaguchi, R. Okumura¹ and S. Sekimoto¹

University of Tokyo

¹ Institute for Integrated Radiation and Nuclear Science, Kyoto University

INTRODUCTION: An extinct nuclide ^{129}I ($T_{1/2} = 15.7$ million years) is known to have lived in the early stage of solar system formation. As ratio of ^{129}I to stable isotope ^{127}I in the solar system decreased with time, formation ages of individual meteorites can be estimated if we determine $^{129}\text{I}/^{127}\text{I}$ ratios for the meteorites. Because all ^{129}I trapped in a meteorite now has completely decayed to stable isotope ^{129}Xe , present $^{129}\text{Xe}^*/^{127}\text{I}$ ratio, where $^{129}\text{Xe}^*$ is excess of ^{129}Xe over primordial Xe component such as Q-Xe [1], is equivalent to $^{129}\text{I}/^{127}\text{I}$ ratio at the meteorite formation. In the I-Xe dating method, meteorites and an age standard meteorite are irradiated with neutrons in a nuclear reactor to convert ^{127}I to $^{128}\text{Xe}^*$, and then $^{129}\text{Xe}^*/^{128}\text{Xe}^*$ ratios are measured for the meteorites [2]. Time span of formation age “ Δt ” after formation of the standard meteorite is expressed as;

$$\Delta t = (1/\lambda) \times \ln \left[\left(\frac{^{129}\text{Xe}^*/^{128}\text{Xe}^*}_{\text{std}} \right) / \left(\frac{^{129}\text{Xe}^*/^{128}\text{Xe}^*}_{\text{sample}} \right) \right].$$

Brecciated meteorites record impact events occurred on their parent planetesimals, where meteoroids bombarded surface materials producing rock fragments and soils which finally solidified to rocks with brecciated structure. The impact fragmentation would have continued before and after dissipation of dense solar nebular in the early solar system. Some brecciated meteorites are known to have very high concentrations of solar He and Ne, but other brecciated ones do not contain. The solar noble gases are derived from solar wind which was implanted within 1 μm of regolith particles on the surface of the parent bodies of the meteorites. We measured noble gas compositions and I-Xe ages for several brecciated meteorites and found out that meteorites showing old I-Xe ages are solar gas free, but those with younger ages are enriched in solar gases. This may constrain timing of dissipation of solar nebula, which could be determined experimentally by I-Xe dating and noble gas analysis for brecciated meteorites [3]. Here we report a new I-Xe data of the NWA2139 meteorite, which is classified as LL6 chondrite with brecciated texture.

EXPERIMENTS: The light-colored and dark-colored fragments of the NWA2139 meteorite and age standard meteorite, Shallowater, weighing ca. 20 mg each were irradiated with neutrons in the long-term irradiation plug of KUR reactor. After cooling down for several months noble gas isotopes in the samples were analyzed using a modified-VG3600 mass spectrometry system at the Graduate School of Arts and Sciences, the University of

Tokyo [4]. Non-irradiated meteorites were also measured for noble gases with a modified-VG5400 noble gas mass spectrometer at the University of Tokyo.

RESULTS: Isotopic ratios $^{129}\text{Xe}/^{132}\text{Xe}$ plot against $^{128}\text{Xe}/^{132}\text{Xe}$ in Fig. 1 for both NWA2139 and Shallowater meteorites. The data points for Shallowater with 4563.3 ± 0.4 Ma (Ma = million years ago) absolute age [5] plot on a straight line, showing perfect closure to I-Xe system. Contrary to the Shallowater data points, those for the dark-colored fragment of NWA2139 do not show a linear trend and plot around the trapped Q-Xe [1]. This would result from almost complete resetting of I-Xe system caused by a heavy shock event occurred after the extinction of ^{129}I . This is consistent with that the sample does not show a presence of solar noble gases. The light-colored fragment of NWA2139 yielded I-Xe age of 4512 ± 12 Ma. Although this age postdates the dissipation of solar nebula inferred from a relationship between I-Xe ages and solar noble gas concentrations for other brecciated meteorites [3], the NWA2139 light-colored fragment does not contain detectable amounts of solar noble gases. This can be explained by (1) the sample was not exposed to the solar wind on the surface of its parent body, or (2) solar noble gases were degassed by a shock event, which could be milder than that the dark-colored fragment experienced as the I-Xe system of the light-colored fragment has not been completely reset.

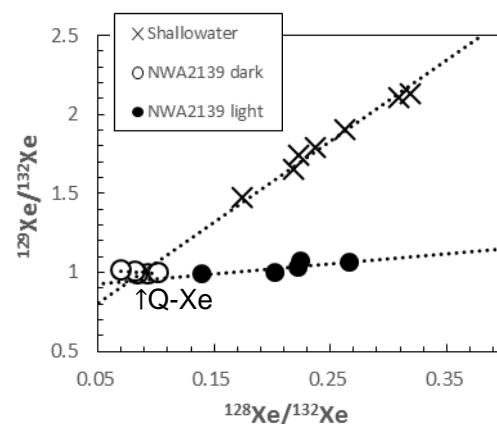


Fig. 1. Plot of $^{129}\text{Xe}/^{130}\text{Xe}$ vs. $^{128}\text{Xe}/^{130}\text{Xe}$ for NWA2139 and Shallowater meteorites.

REFERENCES:

- [1] H. Busemann *et al.*, *Meteorit. Planet. Sci.*, **35** (2000) 949–973.
- [2] P.M. Jeffrey and J.H. Reynolds, *J. Geophys. Res.*, **66** (1961) 3582–3583.
- [3] K. Bajo, Ph.D. Thesis, Univ. Tokyo (2010).
- [4] N. Ebisawa *et al.*, *J. Mass Spectrom. Soc. Jpn.*, **52** (2004) 219–229.
- [5] J.D. Gilmour *et al.*, *Meteorit. Planet. Sci.*, **41** (2006) 19–31.

Clear Descent of Antimony(Sb) Concentration in Atmospheric Aerosol Observed at Sakai, Osaka from 1995 to 2017

N. Ito, A. Mizohata, R. Okumura¹ and Y. Iinuma¹

Radiation Research Center, Osaka Prefecture University,
¹Research Reactor Institute, Kyoto University

Antimony(Sb) is a poison element and can be found in the aerosols collected on the urban area as a trace element in the coarse particle (might be affected from brake pads) and fine particle (might be affected from burning of plastics). To study a characteristic of Sb on the aerosols in the urban area, we have observed the size distribution of Sb in the aerosols at Sakai since 1995. Here we report the yearly change in concentration from which result reveal the clear descent in Sb concentration.

We have collected the aerosol by Andersen Sampler, collecting the aerosols on 9 particle size ranges (>11, 7.0-11.0, 4.7-7.0, 3.3-4.7, 2.1-3.3, 1.1-2.1, 0.65-1.1, 0.43-0.65, <0.43 μ m) with one week sampling period. The aerosols were collected on the polyethylene sheet for each sampling stages except for the final stage that uses Teflon filter to filter the smallest particles. The concentration of Sb were measured by neutron activation analysis using Kyoto University Reactor, measuring

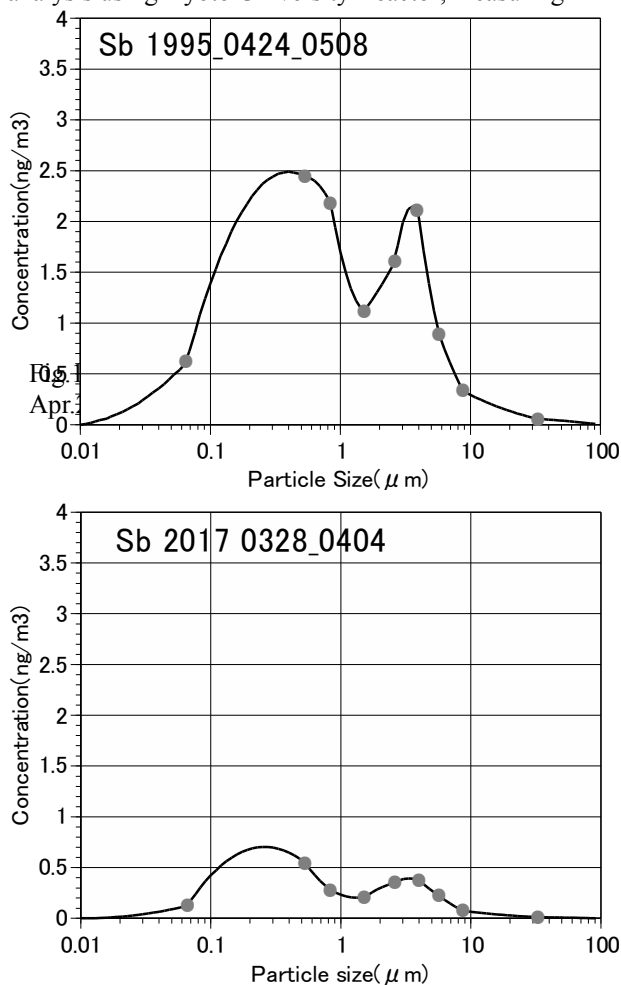


Fig.1 Size distribution of Sb observed in 1995 Apr.24-May08 and 2017 Mar.28-Apr04 at Sakai

gamma ray (1691 keV) from ¹²⁴Sb activated in PN2 line with 2 hour irradiation of thermal neutron.

Results of size distribution (Fig.1) observed in 1995 Apr.24-May08 and 2017 Mar.28-Apr04 show that Sb occurs in coarse and fine particles on the affect of particles from soils and brake pad for coarse particles and from plastic burning for fine particles. Result of two size distribution (1995 Apr and 2017 Mar) of Sb for 22 years interval reveal the clear descent in concentration.

Result of Sb concentration change (coarse : d > 2.1 μ m, fine: d < 2.1 μ m) in year of 1995, 1996, 1997, 1998, 1999, 2000, 2012, 2017 are drawn on the Fig.2. From 1998 concentrations of Sb in coarse and fine particles have descended clearly on the decrease with 2ng/m³ in 1995 -1997 to 0.5ng/m³ in 2017 for coarse particles, 6 ng/m³ in 1995-1997 to 1 ng/m³ in 2017 for fine particles. We suggest that reduction of exhausted matter from incinerator that were controlled by government direction caused the clear descent of Sb concentration in recent 20 years.

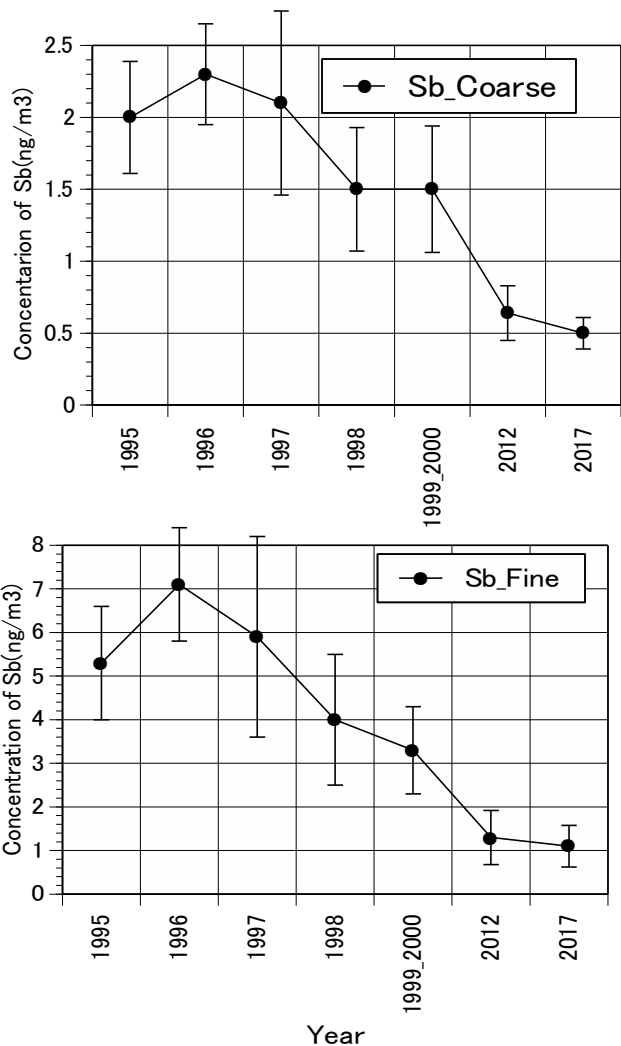


Fig.2 Change of Sb in 1995, 1996, 1997, 1998, 1999, 2000, 2012 and 2017 in coarse and fine particles at Sakai.

CO5-5 A Study on the Sedimentary Environment of Tokyo-Bay Sediments under Hypoxia Using Instrumental Neutron Activation Analysis

M. Matsuo¹, K. Shozugawa¹, Y. Mihara¹, M. Komori^{1,2}, R. Okumura³, Y. Iinuma³ and K. Takamiya³

¹Graduate School of Arts and Sciences, The University of Tokyo

²Environmental Research Institute of Yokohama

³Research Reactor Institute, Kyoto University

INTRODUCTION: Hypoxia is water mass with little dissolved oxygen (DO) [1]. It has been a big problem particularly in inner bay such as Tokyo Bay. To understand and solve the problem, it is important to know when or where hypoxia occurred. However, the data of water quality in Tokyo Bay are absolutely lacking. Therefore, we attempted to estimate the redox environment of Tokyo-bay sediments under hypoxia, assuming that the effect of past hypoxia could be preserved as a difference in concentrations and/or chemical states of elements in the sediments.

To estimate the sedimentary environment related to redox conditions, various elements have been used. For example, Fe and Mn are used because their various chemical states on Eh-pH diagrams have become clear [2]. And U is used for the evaluation of weak reductive conditions because the redox potential of U(VI)/U(IV) is between Mn(IV)/Mn(II) and S(VI)/S(-II) [3]. In this study, sediment cores were collected from Tokyo Bay and concentrations of Fe, Mn, U, Th, and Ce in sediments were analyzed by instrumental neutron activation analysis (INAA).

EXPERIMENTS: We collected sediment cores off the coast of Yokohama (flat seafloor) and Makuhari (flat seafloor and dredged trench) in Tokyo Bay. All cores were cut in the vertical direction at 2 cm intervals in the laboratory. Then, the samples were desalted by centrifugation with pure water washing three times and dried at 105 °C.

Approximately 30 mg of sediments were packed in double polyethylene film bags to perform INAA. All samples were irradiated with neutrons at the pneumatic tube, Kyoto University Research Reactor. Three types of gamma-ray measurement were carried out corresponding to half-lives of elements. For analysis of Mn, samples were irradiated for 10 seconds at 1 MW, and then gamma-ray was measured for 600 seconds by Ge detector after 600 seconds cooling. Regarding U, samples were irradiated for 20 minutes at 1 MW or 4 minutes at 5 MW, and then gamma-ray was measured for 1200 seconds after 3-5 days cooling. Regarding Fe, Th and Ce, samples were irradiated for 20 minutes at 1 MW or 4 minutes at 5 MW, and the measuring time of gamma-ray was for 10800 seconds after 2-4 weeks cooling.

RESULTS: Analysis of redox sensitive elements in the sediments was done by INAA method. As a result, the concentration of Mn was low in the dredged trench off Makuhari, whereas there was no significant difference in

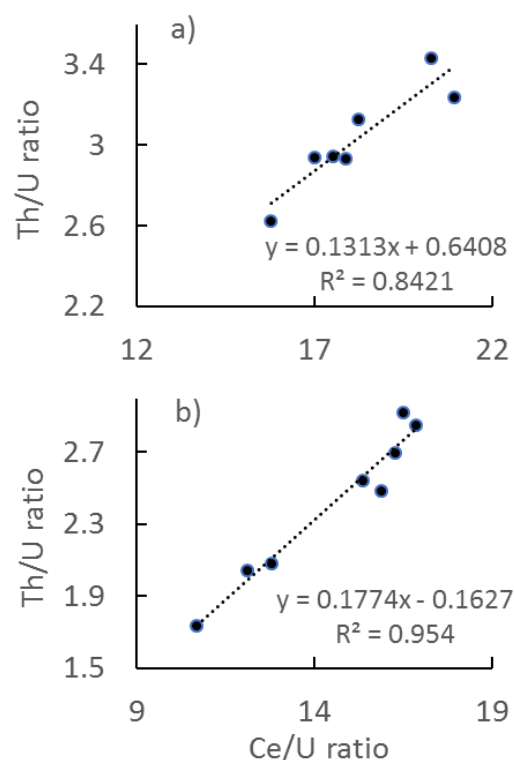


Fig. 1. Th/U-Ce/U plots in the sediments collected from (a) flat seafloor off Yokohama and (b) dredged trench off Makuhari.

Fe. It is well-known that the concentrations of both Fe and Mn in sediments increase when condition of seawater is oxidative. However, we note that Mn precipitates under more oxidative conditions. Therefore, it is estimated that the oxidation-reduction potential in the dredged trench remained to the extent that Fe precipitation occurred but no Mn precipitation occurred.

In addition, we plotted the relations between Th/U and Ce/U ratios, and they are shown in Figure 1. The values of Th/U and Ce/U ratios at each site existed in different places on a same line. This fact indicates that the sediments cannot be the mixture of two or more sources which have different Th/U and Ce/U ratios. Therefore, it is thought that the fact is caused by redox conditions. As a result, it was found that the magnitude of the reductive environment increased in the order of flat seafloor off Yokohama < flat seafloor off Makuhari < dredged trench off Makuhari. This trend was in good agreement with water quality data and estimation results from chemical states of iron measured by ⁵⁷Fe Mossbauer spectroscopy.

REFERENCES:

- [1] R.J. Diaz *et al.*, *Science*, **321** (2008), 926-929.
- [2] D.G. Brookins, in *Eh-pH diagrams for geochemistry* (Springer-Verlag, 1988).
- [3] D.R. Turner, M. Whitfield and A.G. Dickson, *Geochim. Cosmochim. Acta*, **45** (1981), 855-881.

H. Hashizume, A. Uehara¹, S. Fukutani², K. Fujii and T. Ando

National Institute for Materials Science

¹National Institute of Radiological Science

²Institute for Integrated Radiation and Nuclear Science, Kyoto University

INTRODUCTION: Tritium is one of radioactive elements. Its half-time is about 12 years. Since the amount of yield of tritium which is formed in a nuclear reactor is a very little, generally, tritium does not affect the environment. However, in the serious trouble of the Fukushima 1 Nuclear Power Station, a huge amount of tritium was formed and tritium had been included in water. Since water including tritium is almost the same characteristics as water without tritium, it is almost impossible to remove tritium from water. For that reason, the water contaminated by tritium has been accumulated. We have to find out new methods to remove tritium from water, eargently. Koyanaka and Miyatake (2015) found out that about 30% amounts of tritium in water including tritium was caught by manganese oxide for about 20 min [1]. Hashizume et al. (2016) investigated that tritium was discriminated in the formation of a hydroxide from an oxide in water including tritium. When the reaction of magnesia with water including tritium resulted in magnesium hydroxide, a small amount of tritium as a hydroxyl group was caught in the formation of magnesium hydroxide [2]. About 2% of tritium was removed from water including tritium. Since the decomposition temperature of magnesium hydroxide is more than 300 °C, tritium would be captured in magnesium hydroxide and would not remove from magnesium hydroxide at around room temperature.

As anther possible removal of tritium, we investigate the ionic exchange of tritium in water and hydrogen in a hydroxide and the change of amount of ionic exchange of tritium to the contact time with hydroxide and water with tritium.

EXPERIMENTS: The hydroxides used were magnesium, calcium and aluminum hydroxide ($Mg(OH)_2$, $Ca(OH)_2$ and $Al(OH)_3$). We used water including tritium, which is prepared in Institute for Integrated Radiation and Nuclear Science, Kyoto University. The hydroxide, which weighed 2 g, and 10 cm³ of water including tritium were put in the glass bottle with stopper. For the investigation of the ionic exchange, the shaking time was changed from 1 to 18 hours. After shaking, supernatant was separated from suspension by filtering. The supernatant and the initial solution were diluted by the liquid scintillator, that is 20 cm³ of the liquid scintillator was added in 1 cm³ of supernatant or initial solution. The mixed solution was measured by a scintillation detector (Packard, Liquid Scintillation Analyzer). We estimated the removal of tritium (R %).

$$R=100 \cdot (C-C_0)/C_0 \cdot W$$

where C, C₀ and W are concentration of supernatant and initial solution (Bq) and weight (g), respectively.

RESULTS: The removal of tritium to the shaking time is shown in Fig. 1. The removal by $Mg(OH)_2$ and $Ca(OH)_2$ rises as the increase of shaking time. The removals by $Mg(OH)_2$ and $Ca(OH)_2$ are finally almost constant. In the case of $Mg(OH)_2$, The removal is increasing until 5 h of the shaking time. After 5 h, the removal is almost constant, that is about 1.0 %. In the case of $Ca(OH)_2$, the removal reaches the plateau within about 3 h of the shaking time. The removal of the plateau is about 0.6 %. On the other hand, in the use of $Al(OH)_3$, tritium hardly exchanged with hydrogen in $Al(OH)_3$. Although we do not know the reasons why hydrogen in $Al(OH)_3$ is not exchanged with tritium, the crystal structure of $Al(OH)_3$ is different from that of $Mg(OH)_2$ or $Ca(OH)_2$. $Mg(OH)_2$ belongs to a trigonal system and it has a three-fold rotation axis. $Ca(OH)_2$ belongs to a hexagonal system and it has a six-fold rotation axis. The trigonal system is very similar to the hexagonal one. However, the crystal system of $Al(OH)_3$ is monoclinic. The crystal system of $Al(OH)_3$ is different from that of $Mg(OH)_2$ or $Ca(OH)_2$, though those three hydroxides show the sheet structure. The similarity of crystal systems of $Mg(OH)_2$, $Ca(OH)_2$ and $Al(OH)_3$ might cause the different removals of tritium of three ionic exchange materials.

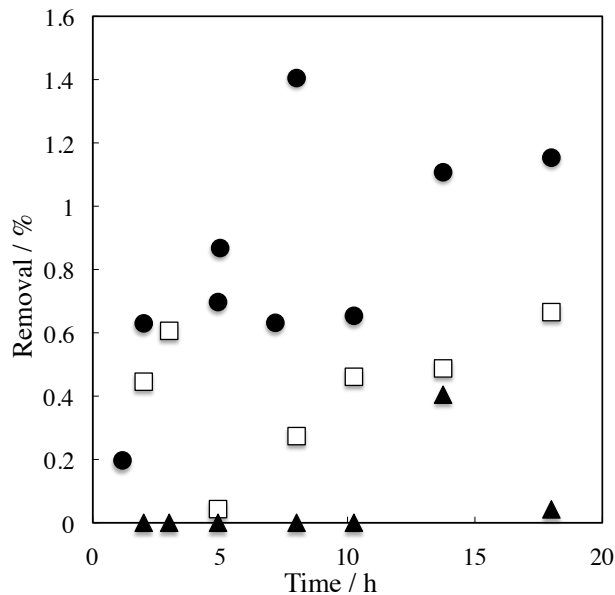


Fig.1 removal of tritium from water depending on shaking time by the ionic exchange to use magnesium hydroxide (●), calcium hydroxide (□), aluminum hydroxide (▲).

REFERENCES:

- [1] H.Koyanaka & H. Miyatake, *Separation Science Technology*, **50** (2015) 2142-2145.
- [2] H.Hashizume *et al.* Tokugann 2016-135839 (2016) (Japanese patent in Japanese).

CO5-7 Determination of Abundance of Rare Metal Elements in Seafloor Hydrothermal Ore Deposits by INAA Techniques-4: Evaluation of Analytical Accuracy

J. Ishibashi, Y. Tada¹, S. Kawaguchi¹, K. Yonezu²,
R. Okumura³, H. Yoshinaga³ and K. Takamiya³

Department of Earth and Planetary Sciences, Faculty of Science, Kyushu University

¹*Department of Earth Resources Engineering, Faculty of Engineering, Kyushu University*

³*Research Reactor Institute, Kyoto University*

INTRODUCTION: To meet recent increased demand for rare metal elements as mineral resources, high sensitive multi-element analysis becomes more important as geochemical tools for mineral exploration. Instrumental neutron activation analysis (INAA) has the advantage of non-destructive analysis, which eliminates possible failings to exclude concentrate of elements included in specific mineral poorly soluble during acid digestion. We have conducted preliminary studies using mineralized samples collected from active seafloor hydrothermal fields, with a view to confirm and extend the range of application of this technique. Here, we report evaluation for analytical accuracy of INAA techniques, using reference ore materials.

EXPERIMENTS: We conducted a series of analysis of “Certified Reference Materials” which are provided by Natural Resource Canada. Samples were irradiated at Pn-3 (thermal neutron flux = 4.8×10^{12} n/cm²/sec at 1 MW) for 3 minutes. The gamma ray activity was measured twice; 2 minutes measurement after 4-20 minutes cooling, and 10 minutes measurement after about 4 hours cooling. Content of each nuclide was calculated by comparison of gamma ray intensities between samples and artificial standard materials which contain known amount of Mn.

RESULTS: Analytical results of the Certified Reference Materials, CCU-1d, WMA-1a, CH-4, and DS-4 are listed in Table 1. Nuclides used for the determination of elemental content are listed with their energies and half-life in minutes. We conducted at least two runs to check the accuracy. Content of elements is shown together with one sigma deviations for counting the peak intensity of the gamma ray spectra. The determined contents are basically agreed with the literature values (which are reported as informational values, provisional values, or certified values in the document provided by Natural Resource Canada).

Table 1 Analytical results of “Certified Reference Materials” provided by Natural Resources Canada. Results of two runs (the cooling time is denoted in parentheses) are listed to check the accuracy. Content of elements is shown with one sigma deviation for counting the peak intensity. Digits expressed in blankets are certified values reported for the Reference Materials.

Element (unit)	Al (wt%)	V (ppm)	Cu (ppm)	In (ppm)	Mn (ppm)
Nuclide	Al-28	V-52	Cu-66	In-116m	Mn-56
energy (kev)	1779	1434	1039	1097	846
half-life (min.)	2.24	3.75	5.10	54.1	154
CCU-1d	[0.19]	[no data]	[239000]	[7.0]	[99.4]
Run-1 (1331s)	-	-	70400±600	23.9±0.8	87.8±3.0
Run-2 (11172s)	-	-	-	19.8±1.0	92.7±1.4
WMA-1a	[1.35]	[140]	[13400]	[0.2]	[600]
Run-1 (235s)	1.00±0.05	90.4±1.4	3410±43	-	511±5
Run-2 (796s)	1.10±0.02	90.4±1.4	3640±66	-	568±5
CH-4	[7.73]	[87]	[2000]	[no data]	[430]
Run-1 (758s)	8.06±0.05	92.9±4.1	650±53	-	398±6
Run-2 (13203s)	-	-	-	-	410±4
DS-1	[4.48]	[147]	[27.1]	[no data]	[437]
Run-1 (568s)	4.45±0.03	146±3	-	-	420±6
Run-2 (705s)	4.67±0.04	151±4	-	-	443±6

Bar marks indicate too small peak intensity of the gamma ray spectrum.

N. Hirano, H. Sumino¹ and S. Sekimoto²

Center for Northeast Asian Studies, Tohoku University

¹ Graduate School of Arts and Sciences, University of Tokyo

² Research Reactor Institute, Kyoto University

INTRODUCTION: Petit-spot volcanoes, erupted on NW Pacific plate, provide direct information on the asthenosphere and the lithospheric deformations below the NW Pacific because their magma originates from the asthenosphere and ascends along the concavely flexed zone prior to the outer-rise along the trench [1][2]. Similar volcanoes have been reported at subduction zones worldwide (e.g., the Japan, Tonga, Chile, and Java trenches) [1][2][3][4][5].

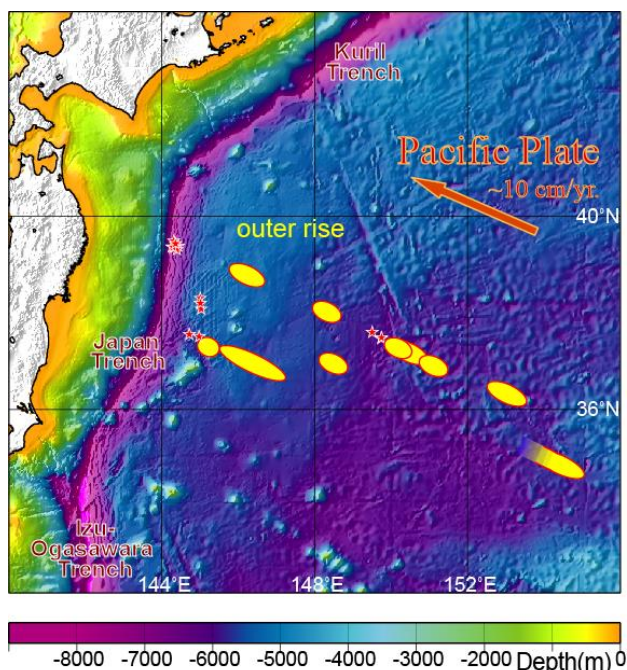


Fig. 1. Bathymetric map of offshore NE Japan [9]. Recognized sites of petit-spot volcano are known as red stars. Yellow ellipses show eruptive portions estimated by previously reported Ar-Ar ages of lavas [1][2] and constant plate motion of the present day (thick brown arrow) (10.29 cm/yr [10]).

Recent researches into the geochemistry and petrography of petit-spot lavas indicate that the conventional subducting lithospheric theories require some revision in terms of the nature of subducting lithospheric and asthenospheric materials (e.g., heterogeneous asthenosphere and the presence of a higher geothermal gradient than the conventional model) [6][7][8]. Most of lava samples do not contain phenocrysts in spite of their differentiated compositions, implying the fractionations in

the magma chamber in lithosphere where the high levels of CO₂ contents of lavas must occur the lithospheric contamination by carbon-rich melt during magma ascent [8][11]. More recently, Sato et al. reported the primitive (low Si and high CO₂) composition for two example of volcanoes which erupt atop of outer rise (Fig. 1) and unusually include olivine phenocrysts [12]. As tectonic stress field atop outer rise is quite different from that of lithosphere below previously reported petit-spots (more than 20 volcanoes), lithospheric deformation must control their geochemical compositions and carbon emissions. We, therefore, conduct to determine the eruption ages of volcano using Ar-Ar dating to understand their eruptive site and tectonic reconstructions.

EXPERIMENTS: Radiometric Ar-Ar dating is commonly used to determine the ages of submarine lavas, because the traditional K-Ar dating is impossible to remove the alteration part of rocks [13]. After the rock-samples, crushed to 100-500 μm grains, they were irradiated by neutrons in a reactor to produce ³⁹Ar from ³⁹K during a few hours. During the irradiation, samples were packed with EB-1 biotite flux monitors [14], K₂SO₄ and CaF₂ as correcting factors in an aluminum capsule. Then, radiogenic ⁴⁰Ar, daughter nuclide of radioactive ⁴⁰K and parent, ³⁹Ar instead of ⁴⁰K, were simultaneously analyzed using a mass-spectrometer with an extraction technique of multi-step heating of approximately every 50 to 100 °C between 500 to 1500 °C.

RESULTS: The irradiations of sample in KUR were done in January, 2018. We are going to analyze the irradiated samples after cooling, awaiting future determinations.

REFERENCES:

- [1] N. Hirano *et al.*, *Science*, **313** (2006), 1426-1428.
- [2] N. Hirano *et al.*, *Basin Res.*, **20** (2008), 543-553.
- [3] N. Hirano *et al.*, *Geochem. J.*, **47** (2013), 249-257.
- [4] R. Taneja *et al.*, *Gondwana Res.*, **28** (2014), 391-406.
- [5] N. Hirano *et al.*, *Marine Geol.*, **373** (2016), 39-48.
- [6] J. Yamamoto *et al.*, *Geology* **42** (2014), 967-980.
- [7] S. Pilet *et al.*, *Nature Geosci.* **9** (2016), 898-903.
- [8] S. Machida *et al.*, *Nature Comm.* **8** (2017), 14302.
- [9] D. T. Sandwell, and W. H. F. Smith, *J. Geophys. Res.*, **102** (1997), 10039-10050.
- [10] A. E. Gripp, and R. G. Gordon, *Geophys. Res. Lett.*, **17** (1990), 1109-1112.
- [11] S. Okumura, and N. Hirano, *Geology*, **41** (2013), 1167-1170.
- [12] Y. Sato *et al.*, *Int'l. Geol. Rev.* (2017), in press.
- [13] I. McDougall and T. M. Harrison, in *Geochronology and Thermochronology by the ⁴⁰Ar/³⁹Ar Method*, (Oxford, New York, 1988).
- [14] N. Iwata, Ph.D. Thesis, Tokyo Univ. (1998).

CO5-9 Basic Study on Radiation-induced Luminescence from Natural Mineral

H. Fujita, M. Nagaoka, T. Saito¹

*Nuclear Fuel Cycle Engineering Laboratories, JAEA
1Research Reactor Institute, Kyoto University*

INTRODUCTION: It is well known that dielectric materials such as natural quartz exposed to ionizing radiation emit thermoluminescence (TL) and optically stimulated luminescence (OSL). OSL is a well-established tool for measuring radiation doses in unfired sediments [1]. It has features in common with TL which has long been used in measuring radiation doses [2]. Both TL and OSL dosimetry with white mineral do not need to be specially installed in advance, prior to dose estimation.

Quartz is an excellent material for use in dosimetry, because of its almost ubiquitous availability including an accidental place. Feldspar is an extensive ternary family of minerals appropriate for OSL and TL dosimetry as they display a strong luminescence and are quite common in the Earth's formation, although it has anomalous fading effects which could decay OSL-related luminescence signals.

However, the detailed emission mechanisms of TL and OSL from natural minerals such as quartz and feldspar are not yet clear. In this study, the emission mechanisms of TL and OSL were investigated in conjunction with various radiation-induced phenomena after annealing treatments of quartz samples, involving TL, OSL and electron spin resonance (ESR) measurements.

EXPERIMENTS: Natural quartz were sieved to adjust the grain sizes ranging from 150 – 250 μm in a diameter after extracted from surface soil with conventional method [3]. The quartz samples were annealed at 800 °C for 24 hours in an electric furnace, to make luminescence signals strong. In addition, one part of the annealed quartz samples were treated with supercritical water. Both of the annealed and the treated samples were irradiated a dose of 20 kGy with ⁶⁰Co source (10.09 kGy/h at center position) at liquid nitrogen temperature at Kyoto University Research Reactor Institute (KURRI). The irradiated samples were measured by an ESR spectrometer (Jeol Ltd., JES-TE 200) at -196 °C. All preparations were carried out under dim red light.

After the ESR measurements, all samples were kept to measure luminescence signals in a dark room. TL (Red-TL and Ultraviolet-TL) and OSL were measured by a JREC automated TL/OSL-reader system.

RESULTS: The ESR signals of Al centers as hole-trapped centers and Ti centers ($[\text{TiO}_4/\text{H}^+]^0$, $[\text{TiO}_4/\text{Li}^+]^0$ and $[\text{TiO}_4/\text{Na}^+]^0$) as electron-trapped centers were detected in the annealed and treated quartz samples as before. Both signals showed similar shapes. Moreover, in ESR spectra of the treated sample sampled in one point, small two signals caused by atomic hydrogen were found. However, this signals should be confirmed the reproducibility at future experiment.

The OSL signals were measured at three times for each sample. The OSL decay curves of both samples had similar shapes but different intensities corrected by each sample weight. The OSL intensity of the treated sample was higher than the OSL intensity of the annealed sample. From the result, OSL intensity could be increased by the supercritical water reaction.

The Ultraviolet-TL (UVTL) signals were measured at three times for each sample. The UVTL glow curves of both samples had similar shapes but different intensities corrected by each sample weight. The UVTL intensity of the annealed sample was higher than the UVTL intensity of the treated sample. From the result, UVTL intensity could be decreased by the supercritical water reaction but as opposite effect comparing with the OSL.

The Red-TL (RTL) signals were measured at three times for each sample. The RTL glow curves of both samples had similar shapes and similar intensities corrected by each sample weight. From the result, RTL intensity could not be influenced by the supercritical water reaction.

The results of ESR, OSL, UVTL and RTL were not difference between quartz samples collected at two places.

In this research, the luminescence emission mechanism could not be identified.

Second experiment was scheduled in February of 2018 but was canceled by preparation of personnel changes. Therefore, during the Visiting Researchers Program an experiment was done using Co-60 Gamma-ray Irradiation Facility.

REFERENCES:

- [1] Huntley, D. J., *et al.*, Nature, **313** (1985) 105-107.
- [2] McKeever, S. W. S., Cambridge University Press, Cambridge, (1985) 103-105.
- [3] Fujita, H., *et al.*, Radiat. Meas., **46** (2011) 565-572.

CO5-10 Trace Amounts of Halogens (Cl, Br and I) in Andesite and Basalt Reference Materials

S. Sekimoto, N. Shirai¹ and M. Ebihara¹

Research Reactor Institute, Kyoto University

¹Graduate School of Science, Tokyo Metropolitan University

INTRODUCTION: Accurate and reliable data of halogen abundance have been rarely reported for terrestrial samples, such as andesite and basalt materials. Since halogens differ in volatility from element to element, their content and relative abundance are highly informative when discussing the petrogenesis of such samples. Recently, we have improved the radiochemical neutron activation analysis (RNAA) procedure for trace amounts of halogens (Cl, Br and I) [1]. In this study, our RNAA was applied to one andesite and three basalts materials that are available in U.S. Geological Survey (USGS) and then, our RNAA values were compared with the literature values.

EXPERIMENTS: Trace amounts of Cl, Br and I in the one andesite (AGV-2) and three basalts (BCR-2, BHVO-2, and BIR-1a) were determined by RNAA. The RNAA procedure is described elsewhere [1-2]. Those samples were repeatedly analyzed more than two times.

Table 1: Cl, Br and I contents in USGS andesite and basalts materials analyzed by RNAA in this study and from the Literature

(^a Not reported. ^b Number of analysis was two. ^c IC (Ion chromatography) and ICPMS were coupled with pyrohydrolysis. ^d Analytical methods for individual data were Spark-source Mass Spectrometry, Neutron Activation Analysis, Ion Selective Electrodes, Ion Chromatography, etc.)

Sample	Cl (mg kg ⁻¹)	Br (mg kg ⁻¹)	I (mg kg ⁻¹)	Method ^c	Ref.
AGV-2	72.8 ± 2.7	0.101 ± 0.007	0.197 ± 0.038	RNAA	[2]
	75 ± 3	- ^a	-	IC	[3]
	-	0.107-0.145 ^b	0.007 ± 0.001	ICP-MS	[3]
	61 ± 3	-	-	IC	[4]
BCR-2	112 ± 1	0.144 ± 0.008	0.082 ± 0.022	RNAA	[2]
	98 ± 8	-	-	IC	[3]
	-	0.157-0.175 ^b	0.017 ± 0.004	ICP-MS	[3]
	89 ± 6	-	-	IC	[4]
	101	-	-	XRF	[5]
BHVO-2	104 ± 4	0.240 ± 0.013	0.307 ± 0.050	RNAA	[2]
	150 ± 21	-	-	IC	[3]
	-	0.269-0.277 ^b	0.016 ± 0.002	ICP-MS	[3]
	81 ± 11	-	-	IC	[6]
	-	0.29 ± 0.10	0.020 ± 0.012	ICP-MS	[6]
89 ± 7	-	-	IC	[4]	
BIR-1a	5.64 ± 0.43	0.039 ± 0.012	0.041 ± 0.009	RNAA	[2]
BIR-1	26 ± 6	<2	-	<i>Compiled values</i> ^d	[7]
	44	-	-	IC	[3]
	-	0.065 ± 0.026	0.014 ± 0.002	ICP-MS	[3]

RESULTS: Our RNAA data for AGV-2, BCR-2, BHVO-2, and BIR-1a were consistent with previously published data for Cl and Br but not for I [3, 4, 6]. Iodine values measured by RNAA for these reference materials (RM) are higher by factors of 3 to 10 compared those measured by pyrohydrolysis and ICP-MS analysis. We suggest that I may be partially lost during slow evaporation and concentration of pyrohydrolysis solutions prior to mass spectrometry. From a detailed comparison in Cl values between RNAA and IC coupled with pyrohydrolysis, it can also be seen that IC values tend to be lower than the RNAA values (Fig. 1), because Cl may not always be quantitatively extracted from basaltic and andesitic RM during pyrohydrolysis. Sekimoto and Ebihara (2013) reported similar discrepancies for Br and I in sedimentary RM.

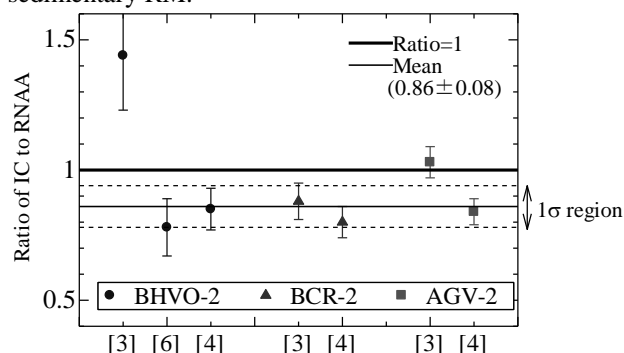


Fig. 1. Concentration ratios of Cl between RNAA values and IC values.

REFERENCES:

- [1] S. Sekimoto and M. Ebihara, *Anal. Chem.*, **85** (2013) 6336-6341.
- [2] S. Sekimoto and M. Ebihara, *Geostand. Geoanal. Res.*, **41** (2017) 213-219.
- [3] A. Michel and B. Villemant, *Geostand. Newslett.*, **27** (2003) 163-171.
- [4] Q. Wang *et al.* *Geostand. Geoanal. Res.*, **34** (2010) 175-183.
- [5] D. Hanano *et al.* *Geochem. Geophys. Geosy.*, **11** (2010) Q01004, 1-22.
- [6] H. Balcone-Boissard *et al.* *Geostand. Geoanal. Res.*, **33** (2009) 477-485.
- [7] E.S. Gladney and I. Roelandts, *Geostand. Newslett.*, **12** (1988) 63-118.

CO5-11 Application of Neutron Activation Analysis to Micro Gram Scale of Solid Samples

S. Sekimoto, N. Shirai¹ and M. Ebihara¹

Research Reactor Institute, Kyoto University

¹ Graduate School of Science, Tokyo Metropolitan University

INTRODUCTION: Instrumental neutron activation analysis (INAA) is often used in cosmochemistry, where meteorites are the objects for INAA. Chondritic meteorites (chondrites) and iron meteorites contain relatively high contents of Co and Ir compared with those in the earth crust. As Co and Ir have high sensitivity in INAA, they can be good markers for the identification of such extraterrestrial materials. In NAA of chondrites, a few tens mg of specimen is commonly used. For such a case, a few hundred $\mu\text{g kg}^{-1}$ of Ir and a few hundred mg kg^{-1} of Co can be reliably determined. When an extremely small size (e.g., micro gram) of samples such as micrometeorites recovered on the Earth surface and tiny particles returned from extraterrestrial asteroids are to be analyzed by INAA, the conventional INAA procedure used for a few tens mg is not suitable. For such tiny samples, neutron irradiation with high neutron flux and long irradiation time (namely, high neutron dose) is required. Recently we have presented the INAA procedure for micro gram scale of solid samples [1]. In this report, one typical example for the application of the proposed procedure is shown with limited scientific discussion. For the meteoritic grain sample, here, a chunk of the Kilabo (LL6) chondrite was crushed and a single piece was picked.

RESULTS: Instrumental NAA results of the Kilabo piece are summarized in Table 1. Since the weight of this piece is less than 1 mg and cannot be weighed, elemental concentrations are not given.

The Kilabo sample analyzed in this study is a small silicate piece. Therefore, its chemical composition cannot be the same as that of the bulk Kilabo meteorite. As no mineralogical and petrological information is available for the Kilabo piece sample, the detailed cosmochemical discussion cannot be developed. Here, only Ni and Co contents are concerned. Cobalt and Ni are known to behave similarly cosmochemically [2] as well as geochemically. Both elements tend to be hosted in metals in ordinary chondrites like Kilabo. Figure 1 shows the relationship between Co/Fe and Ni/Fe ratios for the Kilabo piece. In addition, data for CI chondrite [3], LL6 chondrite (bulk) [4] and metal separate of LL6 and L6 chondrites [5] are also shown for comparison. The solid line represents the Co/Ni ratio of CI chondrite, on which the Kilabo piece sample is placed along with LL6 bulk and metal samples. This suggests that the Kilabo piece contains a tiny metal grain inside. A similar chemical

characteristic was observed in tiny silicate grains recovered from the asteroid Itokawa by the Hayabusa spacecraft [6]. Their Co/Fe and Ni/Fe ratios are similar to those of the Kilabo piece, falling on the CI line as seen in Fig. 1.

As the Co/Ni ratio in the Kilabo piece is chondritic, the kilabo piece might contain 0.5-0.6 pg of Ir if we assume that the Ir/Co and Ir/Ni ratios in the Kilabo piece are equal to those in CI chondrite [3]. Although only an upper limit was derived for the Kilabo piece, it is clear that Ir is depleted in the tiny metal grain that the Kilabo piece contains. From the view point of Ir-depletion, Kilabo and Itokawa grains thus appear alike.

Table 1 Elemental contents in Kilabo

Sm	0.38 ± 0.04 pg	Cr	4.60 ± 0.04 ng
La	2.6 ± 0.3 pg	Ni	14.5 ± 0.3 ng
Sc	22.2 ± 0.4 pg	Au	0.62 ± 0.03 pg
Fe	0.576 ± 0.007 μg	Zn	1.4 ± 0.1 ng
Na	7.93 ± 0.12 ng	Ir	< 0.068 pg
Co	0.589 ± 0.008 ng		

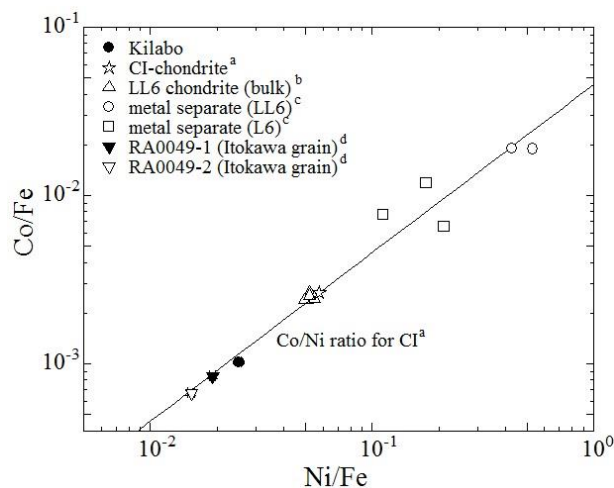


Fig. 1. Correlation between Co/Fe and Ni/Fe ratios in several astromaterials (^a[3], ^b[4], ^c[5], ^d[6])

REFERENCES:

- [1] S. Sekimoto *et al.*, J Radioanal Nucl Chem., **307** (2016) 1757-1764.
- [2] J.T. Wasson Meteorites-Their Record of Early Solar-System History, W. H Freeman and Company, New York (1985).
- [3] E. Anders & N. Grevesse, Geochim Cosmochim Acta., **53** (1989) 197-214.
- [4] G.W. Kallemeyn *et al.*, Geochim Cosmochim Acta., **53** (1989) 2747-2767.
- [5] P. Kong & M. Ebihara, Geochim Cosmochim Acta., **61** (1997) 2317-2329.
- [6] M. Ebihara *et al.*, Science, **333** (2011) 1119-1121.

K. Mukai, T. Fujimori, K. Oshita, S. Fukutani¹ and S. Takahashi²

Department of Environmental Engineering, Graduate School of Engineering, Kyoto University

¹ *Research Reactor Institute, Kyoto University (KURRI)*

² *Graduate School of Agriculture, Ehime University*

INTRODUCTION: Studies on extractable organohalogenes (EOX, X=Cl, Br) have indicated that there are many unidentified organochlorine/bromine compounds (OHCs) in the environment [1, 2]. Some of these unidentified compounds have bioaccumulation potential and toxicity like persistent organic pollutants (POPs), but little is known about how much of EOX can have POP-like properties and which environment is an important source or sink of unidentified POP-like OHCs. In general, molecular weights of POP-like OHCs are below 1000. Thus, EOX in this fraction can be indicator for potential amounts of POP-like OHCs.

In this study, we used gel permeation chromatography (GPC) to separate EOX into low-molecular-weight EOX (EOX-L) and high-molecular-weight EOX (EOX-H). We compare the results in various samples and discuss which environment has high potential of POP-like OHCs including unidentified compounds.

EXPERIMENTS: Natural forest soils are collected from O, A, B layers at Mt. Yatsugatake and Tango Peninsula in Kyoto. Soil standard samples are taken from The Japan Society for Analytical Chemistry (JSAC) standard reference material 0422 (0–3 cm depth) and 0421 (3–10 cm depth). They are both collected at forest near a municipal solid waste incinerator (MSWI). Sediment and Finless porpoise blubber were samples studied in previous studies [3, 4]. House dust came from the NIST standard reference materials 2585. Urban particulate matter is taken from the NIST standard reference material 1648a. MSWI bottom ash and MSWI fly ash was taken from the JSAC standard reference materials 0512 and 0511 respectively.

Samples (5 g for soils and sediment, 2 g for house dust, ash and blubber, 0.5 g for urban particulate matter) were extracted by ultra-sonic extraction method using three different solvents; acetone/hexane (1:1) 10 mL, hexane 10 mL and toluene 10 mL. Three fractions were combined and reduced to 10 mL by rotary evaporation followed by washing for inorganic Cl and Br removal. Then extracts were applied to GPC. The first fraction is EOX-H and the second fraction is EOX-L. Each fraction was used for neutron activation analysis. 2 mL was put in a polyethylene (PE) bag and dried up under normal temperature and pressure. Samples were irradiated for 5 min with a thermal neutron flux of $2.0\text{--}2.4 \times 10^{13} \text{ cm}^{-2} \cdot \text{s}^{-1}$ at KURRI. ^{38}Cl ($t_{1/2} = 37.18 \text{ min}$, $E_{\gamma} = 1642, 2168 \text{ keV}$) and ^{80}Br ($t_{1/2} = 17.6 \text{ min}$, $E_{\gamma} = 616 \text{ keV}$) were measured by

using a Ge semiconductor detector for 60 s.

RESULTS: Results are shown in Fig. 1. In order to evaluate the POP-like potencies, we focus on EOX-L below. Comparing to the natural forest soil, EOCl-L is similar in soils and sediment, while EOBr-L is 3.6 times higher in sediment. This indicates that the sediment is contaminated by synthetic brominated compounds from industries. EOCl-L in house dust, and ash samples are about 2–3 times higher, and EOBr-L in house dust is 47-fold higher than those of forest soils. In finless porpoise blubber, EOCl-L is 6.7 times higher and EOBr-L is 17 times higher than natural forest soil. This is explained by the bioaccumulation properties of POP-like OHCs. In urban particulate matter, even higher concentrations of EOX-L are observed; 27 times higher EOCl-L and 112 times higher EOBr-L (compared to natural forest soil), suggesting that urban particulate matter is extremely important reservoir of OHCs.

We showed the potential of POP-like organochlorine compounds are high in urban particulate matter, house dust, fly ash, and finless porpoise blubber; and the potential of POP-like organobromine compounds is high in sediment, urban particulate matter, house dust, and finless porpoise blubber. Further researches are expected toward these environmental matrices.

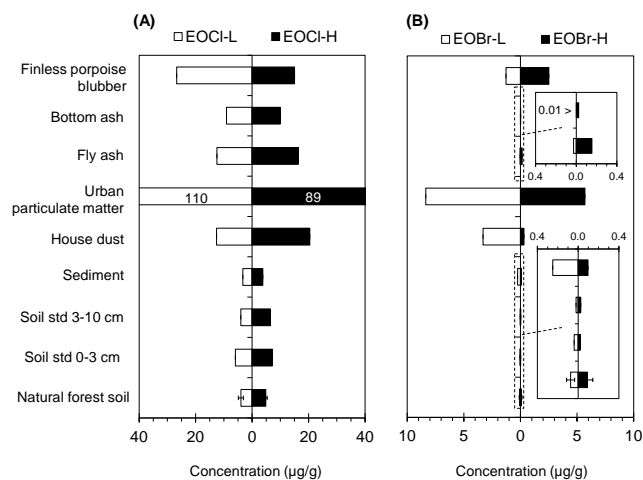


Fig. 1. (A) Concentrations of EOCl-L and EOCl-H. (B) Concentrations of EOBr-L and EOBr-H.

REFERENCES:

- [1] K. Kannan *et al.*, *Environ. Sci. Technol.*, **33** (1999) 1004-1008.
- [2] Y. Wan *et al.*, *Environ. Sci. Technol.*, **44** (2010) 6068-6073.
- [3] S. Takahashi *et al.*, *Chemosphere.*, **64** (2006) 234-244.
- [4] S. Takahashi *et al.*, *Organohalogen Cmpds.* **67** (2005) 430-433.

CO5-13 Chemical Compositions of Chromitite Reference Materials (CHR-Bkg and CHR-Pt+)

N. Shirai, S. Sekimoto¹ and M. Ebihara

Department of Chemistry, Tokyo Metropolitan University

¹Institute for Integrated Radiation and Nuclear Science, Kyoto University

INTRODUCTION: Chromitite is mostly composed of chromite (FeCr₂O₄), which plays an important role for behavior of PGE during igneous processes [e.g., 1]. Ultramafic and mafic samples have positive correlations between Cr, and Os, Ir and Ru, implying that these four elements are partitioned into the same minerals [1]. Partition coefficients of Os, Ir and Ru between chromite and silicate melt are higher than those of Rh, Pd and Pt [2]. As chromite is known to be resistant to most acid, complete digestion of rock samples including chromite is essential for reliable determination of PGE when analytical methods accompanying acid digestion such as ICP-MS. It has been getting common to use ICP-MS for the determination of PGE in rock samples. The commonly used digestion techniques are NiS fire-assay and acid digestion in Carius tube and a high pressure asher (HPA-S) for the determination of PGE in rock samples. A major concern in ICP-MS of PGE in rock samples has been whether NiS fire-assay can completely dissolve chromite or not. Komatiite samples were analyzed by both NiS fire-assay and Carius tube digestion and it was found that PGE values obtained from NiS fire-assay are systematically lower than those from Carius tube digestion [2]. In the later studies, komatiite samples were analyzed by using both NiS fire-assay and acid digestion in Carius tube or HPA-S, and it was demonstrated that two analytical results are not distinguishable from each other [3]. In the previous studies [2,3], different samples of different amounts were analyzed. In the comparison of the two analytical results, the sampling bias could become a critical problem. Therefore, the same samples of GPt-5 were analyzed by using different analytical methods (INAA and NiS fire-assay combined with ICP-MS) in order to solve the sampling bias problem [4]. Iridium was determined by INAA, while Ru, Rh, Pd, Ir and Pt values were obtained by using INAA. Iridium values obtained by INAA and ICP-MS were consistent with each other and it was concluded that NiS fire-assay can completely digest chromite. Other chromitite reference mate-

rials (CHR-Bkg and CHR-Pt+) are analyzed in order to obtain a additional evidence whose NiS fire-assay can release all PGE from chromite. In this paper, INAA results are presented.

EXPERIMENTS: Two chromitite reference samples (CHR-Bkg and CHR-Pt+) were analyzed by INAA. Neutron irradiation was performed in Institute for Integrated Radiation and Nuclear Science, Kyoto University. The Sc, Cr, Fe, Co, Ni, Zn and Ir concentrations were determined after the 4 h irradiation. For quantification, JB-1a, a basaltic geochemical reference powder issued by the Geological Survey of Japan, was used as a calibration standard. Literature values of Jochum et al. [5] were used. In addition, the Smithsonian Institution Allende meteorite powder and Ir-doped filter paper were irradiated for the determination of the Ni and Ir concentrations. The Ni value of the Smithsonian Institution Allende meteorite powder was taken from Kallemeyn and Wasson [6] and Kallemeyn et al. [7].

RESULTS: The measurement results of CHR-Pt+ and CHR-Bkg are summarized in Table 1. Mean values and relative standard deviations (RSDs) along with the literature values [8] are also shown. Our mean values for CHR-Pt+ and CHR-Bkg are consistent with literature values [8] within 15%. It is noted that there is a large variation of Ir values (RSD; 50%) in CHR-Bkg. This large variation of 50% for Ir is due to the sample heterogeneity. In consideration that RSD for other elements are less than 3%, it is likely that Ir alloy or PGE alloy are heterogeneously distributed in CHR-Bkg.

REFERENCES:

- [1] P. Page *et al.*, Chem. Geol., **302-303** (2001) 3-15.
- [2] I. S. Puchtel and M. Humayun, Geochim. Cosmochim. Acta, **65** (2001) 2979-2993.
- [3] D. Savard *et al.*, Geostand. Geoanal. Res., **34** (2010) 281-291.
- [4] R. Akhter *et al.*, Geochem. J., **50** (2016) 179-185.
- [5] K. P. Jochum *et al.*, Geostand. Geoanal. Res., **40** (2016) 333-350.
- [6] G. W. Kallemeyn and J. T. Wasson, Geochim. Cosmochim. Acta, **45** (1981) 1217-1230.
- [7] G. W. Kallemeyn *et al.*, Geochim. Cosmochim. Acta, **53** (1986) 2747-2767.
- [8] K. Govindaraju, Geostand. Newslett., **18** (1994) 1-158.

Table 1. Measurements results for three CHR-Pt+ (A-C) and CHR-Bkg (D-F) samples obtained by INAA.

Element	Unit	CHR-Pt+					Literature value ^d	CHR-Bkg					Literature value ^d
		This work ^a			Mean ^b	RSD ^c		This work ^a			Mean ^b	RSD ^c	
		A	B	C				D	E	F			
Sample mass	mg	53.5	52.1	49.3			64.0	55.8	65.2				
Sc	ppm	3.81±0.03	3.84±0.03	3.81±0.03	3.82±0.02	0.5	5.57±0.02	5.46±0.02	5.37±0.02	5.47±0.10	1.8		
Cr	%	11.8±0.2	12.1±0.2	11.9±0.2	11.9±0.1	1.2	13.91	18.7±0.3	18.1±0.3	17.9±0.3	18.2±0.4	2.1	19.88
Fe	%	8.56±0.08	8.73±0.09	8.48±0.09	8.59±0.13	1.5	9.379	9.62±0.08	9.33±0.08	9.26±0.08	9.40±0.19	2.0	9.701
Co	ppm	185±2	190±2	186±2	187±2	1.3	177	192±1	186±1	185±1	188±4	2.1	167
Ni	ppm	5310±40	5540±40	5190±40	5340±180	3.3	5862	1830±10	1750±20	1760±10	1780±40	2.2	2006
Zn	ppm	205±7	214±8	216±8	212±6	2.8	192	234±7	229±7	231±7	231±2	1.0	205
Ir	ppb	5690±40	5940±40	6770±50	6130±570	9.3	6200	43.6±1.7	100±3	46.7±2.1	63.4±31.7	50	28

^aErrors quoted for A to F are due to counting statistics (1 s) in gamma-ray spectrometry.

^bMean values of replicate analyses with their standard deviations (1s).

^cRelative standard deviations (in % for 1 s).

^dGovindaraju (1994).

CO5-14 Fission Track Dating and Thermal History of Hydrothermally Altered Rock Sample

H. Ohira and A. Takasu

Department of Geoscience, Shimane University

INTRODUCTION: Fission track (FT) dating was carried out to estimate ages and cooling history of hydrothermally altered rock sample from the Tsuchihashi mine, Bizen City, Okayama Prefecture. The mine yields high grade clay minerals used as raw materials for refractories and ceramics. Original rock of the mine is Cretaceous pyroclastic rock, and is thought to be strongly altered to form clay deposit, by hydrothermal activity following the eruption of pyroclastic rocks and Caldera Formation. In the mine area, several clay zones such as pyrophyllite, sericite and kaolinite, develops in response to conditions of hydrothermal fluid infiltrated [1]. Sericite vein sample which develops in sericite ore zone was collected. Occurrence of the vein implies the vein formed at the latest stage of hydrothermal activity. The depositional age of the original pyroclastic rock is thought to be 82.4 ± 0.6 Ma by U-Pb zircon dating [1], and the period of hydrothermal activity is estimated by K-Ar dating for clayey rock samples (74.2 ± 1.8 Ma \sim 77.8 ± 1.7 Ma) [2].

EXPERIMENTS: Rock sample was crashed, sieved and fraction less than 0.3mm in grain size was separated. Heavy minerals were concentrated using conventional method of heavy liquid and magnetic separator. Zircons were mounted in PFA Teflon, and then polished to reveal a complete internal surface, and was etched in a NaOH-KOH eutectic melt at 225°C [3] for 13-17 hours. Samples were irradiated at pneumatic tube of graphite facility (Tc-pn) of Kyoto University Reactor (KUR). After irradiation, external detectors (mica) were etched in 46% HF at 25°C for 6-7 minutes (for mineral mounts) and for 20-50min (for NIST-SRM612 glass). FT density was measured at 1000 \times magnification with a dry objective.

RESULTS: Despite of more than 150 grains used for experiments, almost grains were uncountable because of its significantly high spontaneous track density. Instead, only 24 grains which show clearly visible tracks due to relatively lower FT density were successfully measured. FT age was 74.1 ± 2.5 Ma. The obtained FT age is nearly 8Ma younger than U-Pb age previously reported (82.4 ± 0.6 Ma [1]). The discordant between the two ages is probably attributable to the difference of closure temper-

ature of each dating method. Closure temperature of U-Pb and FT methods are thought to be 800°C < [4] and 230°C < [5], respectively. The FT age from the sericite vein is probably indicates the period when the sericite vein formed by hydrothermal activity, and then cooled below 230°C during the latest cooling stage. Fluid inclusion data of secondary inclusion arrays in quartz phenocryst from the mine show relatively wide range of homogenization temperature ($270\sim 310^\circ\text{C}$), suggesting that the temperature condition of hydrothermal alteration was completely exceeded the closure temperature of FT dating method. Assuming that the hydrothermal activity began immediately after the deposition of original pyroclastic rock and continued to form the sericite vein, the gap of ages (nearly 8Ma) may indicate the duration of hydrothermal fluid circulation following volcanic activity of this area.

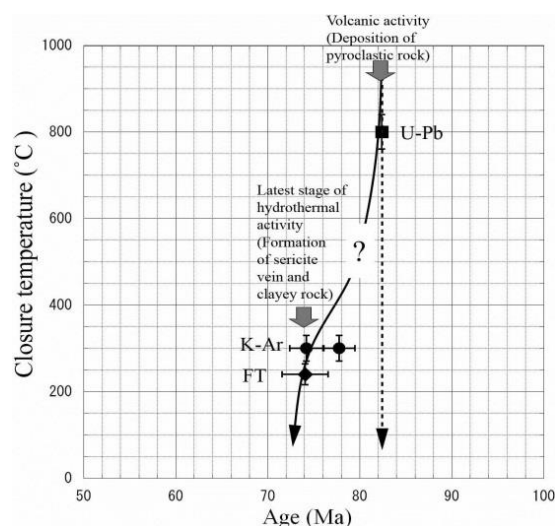


Fig.1 Preliminary estimated cooling history (solid line) of hydrothermally altered rock sample (sericite vein), from the Tsuchihashi mine.

- [1] Sato D., Yamamoto T. and Takagi T., 2016, Geology of the Banshu-Ako district. Quadrangle Series, 1:50000, Geological Survey of Japan, AIST, 68p (in Japanese with English abstract).
- [2] Motomiya H., Kitagawa R. and Nishido H., 2000, Clay Science (Nendo Kagaku) **40**, 46-53.
- [3] Gleadow A.J.W. *et al.*, 1976, Earth and Planetary Science Letter, **33**, 273-276.
- [4] Cherniak, D.J. and Watson, E.B., 2000, Chemical Geology, **172**, 5-24.
- [5] Hasebe N. and Tagami T., 2001, Tectonophysics **331**, 247-267.

H. Hyodo¹, K. Sato² and H. Kumagai³

¹Research Institute of Natural Sciences,
Okayama University of Science

²Department of Applied Chemistry and Biochemistry,
National Institute of Technology, Fukushima College

³Research Center for Marine Resources,
Japan Agency for Marine-Earth Science and Technology

INTRODUCTION: Acasta gneiss is known as the oldest rock (ca. 4.0 Ga) by U-Pb zircon SHRIMP dating [1]. The thermal history of the rock seems to be complicated [2] because it shows much younger age (1.9 Ga) in apatite U-Pb method [3], hornblende and biotite in K-Ar method (unpublished results).

K-Ar system is more susceptible to external disturbance compared to U-Pb system. On the other hand, if a zircon grain acts as a solid guard for its inclusions against such disturbance, the inclusions may keep the primary K-Ar system when they are formed, and may provide some insights on the precambrian atmosphere. Variety of inclusions might behave separately, but average behavior could be determined from the experiment. Several zircon grains from Acasta gneiss were selected to determine the ⁴⁰Ar/³⁹Ar age of such inclusions.

EXPERIMENTS: Experimental procedure is the same as described as previous studies on single grain datings. Rock samples were crushed, and sieved in #25-100 mesh. After ultrasonic cleaning in distilled water, single mineral grains were handpicked. The zircon grains were irradiated in the KUR for 22 hours at 1 MW and subsequently 6 hours at 5MW. The total neutron flux was monitored by 3gr hornblende age standard [4], [5], which was irradiated in the same sample holder. In the same batch, CaSi₂ and KAlSi₃O₈ salts were used for interfering isotope correction. A typical J-value was $(1.183 \pm 0.009) \times 10^{-2}$. In stepwise heating experiment, temperature of a mineral grain was measured using infrared thermometer whose spatial resolution is 0.3 mm in diameter with a precision of 5 degrees. The amount of argon isotopes in inclusions seems to be small. In some cases when grain sizes are too small for the analyses, multiple (3-5) grains were heated under defocused beam in order to increase the sample size. Extracted argon isotopes were measured using the custom made mass spectrometer [5].

RESULTS: One of ⁴⁰Ar/³⁹Ar age spectra of zircon grains were illustrated in Fig. 1. Since the average grains sizes are normally 100-200 microns, four grains were heated together. The temperature control was difficult for the milky to transparent grains particularly at higher temperatures. The laser power was increased rapidly above 800 degrees to fuse the grain. The grains do not release much argon isotopes below 1000 degrees in most cases. This behavior suggests heat resistant nature of the zircon

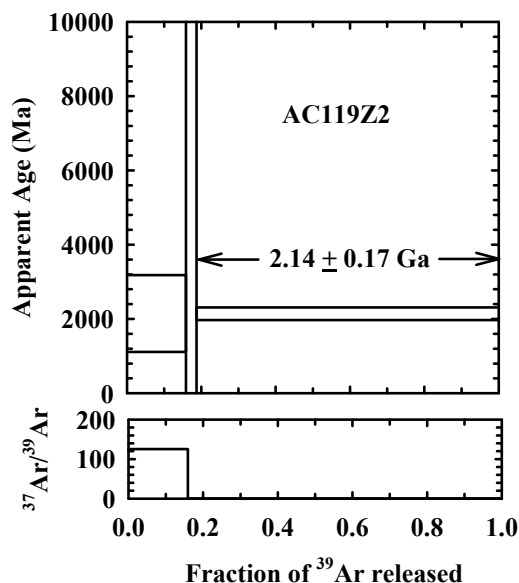


Fig. 1. ⁴⁰Ar/³⁹Ar age spectra of zircon from Acasta gneiss. The error seems to be large due to the small amount of ³⁹Ar, but it indicates an age close to the age reported from other potassium minerals.

grains. The plateau age obtained here are slightly older than the average age of hornblende and biotite in the Acasta gneiss, but apparently much younger than the U-Pb age. The similar behavior is confirmed in another sample. This seems to be consistent in terms of closure temperature if we assume that closure temperature of potassium minerals in the zircon is higher than those of hornblende and biotite. The number of analyses is too few to make a solid conclusion, but the results suggest that the Acasta gneiss suffered from relatively high temperature metamorphism above 500°C.

Inclusions in the zircon possibly have a variety of mixture including fluid inclusion and initial argon from the ancient environment. It is impossible to separate each contribution, but the average behavior seems to give consistent results.

REFERENCES:

- [1] S.A. Bowring and I.S. Williams, *Contributions to Mineralogy and Petrology*, **134** (1999) 3–16.
- [2] T. Iizuka *et al.* *Precambrian Research* **153** 179-208.(2007).
- [3] Y. Sano, *et al.* *Geochimica Cosmochimica Acta* **63** (1999) 899–905.
- [4] J.C. Roddick, *Geochim. Cosmochim. Acta* **47** (1983) 887-898.
- [5] H. Hyodo, *Gondwana Research* **14** (2008) 609-616.

Y. Shibahara, S. Fukutani, T. Kubota, T. Shibata¹,
M. Yoshikawa²

Research Reactor Institute, Kyoto University

¹Graduate School of Science, Hiroshima University

²Institute for Geothermal Sciences, Kyoto University

INTRODUCTION: For the analysis of radionuclide which was released on the accident of Fukushima Dai-ichi Nuclear Power Plant, we have studied the applicability of the mass spectrometry, especially thermal ionization mass spectrometry (TIMS). Our study has focused on Cs, Sr, U and Pu as target of the analysis by TIMS. In this study, we discussed the applicability of the isotopic analysis of Cs by the comparison of our results with the literature data.

EXPERIMENTS: Cs was recovered from the standard reference materials of IAEA-373 and IAEA-156, the environmental sample obtained in Fukushima prefecture and the natural uranium irradiated at KUR. The standard reference materials are the environmental samples contaminated by the accident of Chernobyl Nuclear Power Plant. The ¹³⁷Cs concentration of them corrected on 11 Mar 2011 was 2.4×10^{-12} g/g for IAEA-373 and 4.7×10^{-14} g/g for IAEA-156 respectively. The concentration of ¹³⁷Cs of the environmental sample obtained in Fukushima prefecture was about 2.6×10^{-10} g/g (corrected on 11 Mar 2011). The irradiation of the natural uranium (10 mg) was performed with the neutron flux of 5.5×10^{12} n/s cm² and the irradiation time of 3 hours. By using ORIGEN-II code [4], the amount of the ¹³⁷Cs generated by this irradiation was estimated at 7.4×10^{-11} g. Cs was recovered according to the recovery scheme [1-3]. After the preparation of the samples for the isotopic ratio analysis of Cs, the Cs isotopic ratio ($= {}^{135}\text{Cs}/{}^{137}\text{Cs}$) was analyzed by TIMS.

In the analysis of Cs by TIMS, a thermal ionization mass spectrometer (TRITON-T1, Thermo Fisher Scientific) with a rhenium single filament system was used. The Cs sample prepared for the TIMS analysis was loaded onto a rhenium filament with a TaO activator. Because of the loading amount of Cs (max. 1×10^{-12} g), the mass spectrometry was conducted with a secondary electron multiplier detector and the peak jump method [1-3].

RESULTS: Figure 1 shows the mass spectra of Cs recovered from the standard reference material of IAEA-373 and the environmental sample obtained in Fukushima prefecture. We found the clear difference in the beam intensity of ¹³⁵Cs compared with that of ¹³⁷Cs. We obtained the ¹³⁵Cs/¹³⁷Cs ratio of ca. 0.50 for the standard reference material of IAEA-373, and ca. 0.36 for the environmental sample obtained in Fukushima prefecture: these values are corrected on 11 Mar. 2011.

Figure 2 shows the comparison of the ¹³⁵Cs/¹³⁷Cs ratio observed in our study with that of the literature data for the sample of IAEA-156 and the environmental sample

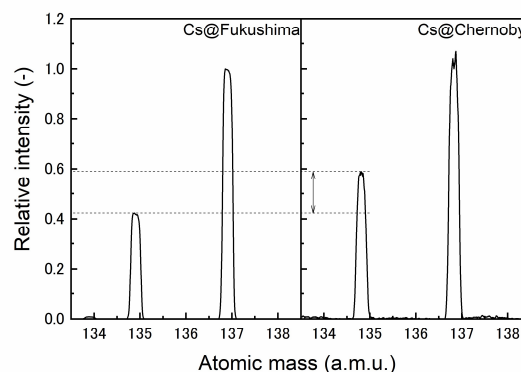


Fig. 1 Mass spectra of Cs recovered from environmental sample. Cs@Fukushima: Cs was recovered from the environmental sample obtained Fukushima prefecture. Cs@Chernobyl: Cs was recovered from standard sample of IAEA-373.

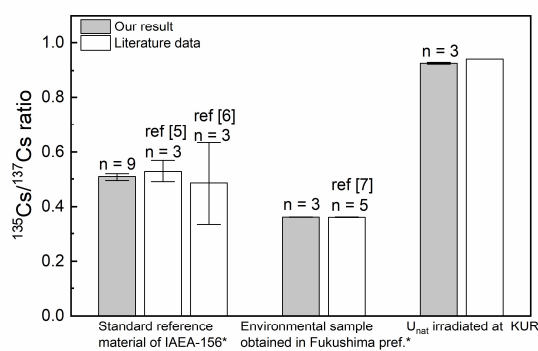


Fig. 2 Comparison ¹³⁵Cs/¹³⁷Cs ratio observed in our study [1-3] and literature data [5-7]. Error bar means $\pm 2\sigma$.

[5-7] and the calculation results by using the ORIGEN-II code for the sample recovered from the irradiated uranium [4]. Although the statistical precision was not excellent because of the low concentration of the radioactive Cs in the environmental sample, we found that the ¹³⁵Cs/¹³⁷Cs ratio observed in our study shows the agreement with the literature data and also shows the linear correlation with the literature data as follows;

$$Y = (1.00 \pm 0.01) \times X, R^2 = 1.000 \text{ or}$$

$$Y = (-0.01 \pm 0.01) + (1.03 \pm 0.04) \times X, R^2 = 1.000.$$

where X and Y mean the isotopic ratio of ¹³⁵Cs/¹³⁷Cs of our study and the literature data, respectively.

REFERENCES:

- [1] Y. Shibahara *et al.* J. Nucl. Sci. Technol. 2014, 51, 575-579.
- [2] Y. Shibahara *et al.* Radiological issues for Fukushima's revitalized future. Springer. 2016. 33-46.
- [3] Y. Shibahara *et al.* J. Nucl. Sci. Technol. 2017, 54, 148-166.
- [4] S. B. Ludwig *et al.* ORNL/TM-11018. ORNL. 1989.
- [5] M. S. Snow *et al.* J. Environ. Radioact. 2016, 151, 258-263.
- [6] J. Zheng *et al.* Anal. Chem. 2016, 88, 8772-8779.
- [7] J. A. Dunne *et al.* Talanta. 2017, 174, 347-356.

CO5-17 Characteristics of Calcite Thermoluminescence and Its Use for Age Estimate

N. Hasebe, K. Miura¹, M. Ogata, U. Uyangaa¹, K. Kinugawa¹ and R. Hayasaka¹

Institute of Nature and Environmental Technology, Kanazawa University

¹*Graduate School of Natural Science and Technology, Kanazawa University*

INTRODUCTION: Luminescence dating observes the natural accumulated radiation damage caused by radioisotopes such as U and Th as the form of glow after stimulation by heating or lightening. Thermally stimulated luminescence from calcite shows strong red emission. When thermoluminescence (TL) characteristics of calcites are examined using both of natural occurring and synthetic calcite, their response to the various radiations depends on minor chemistry (Fe, Mg, Mn and Sr). After establishment of empirical relationship between impurity concentration and luminescence efficiency for each radiation, the calcite collected from Philippines was dated.

EXPERIMENTS: First, the mineral species of the samples were examined by XRD measurement and it turned out to be calcite. Then luminescence emission from calcite was measured by the luminescence reader MOSL-22, and dose was estimated by the external x-ray source, whose dose rate is calibrated as 0.1 Gy/sec with quartz. The glow curve was compared to that of calcite from other origin. Chemical compositions were measured by LAICPMS to estimate annual dose and luminescence efficiencies.

RESULTS: The emission curve shows high emission at around 360 °C, and the response to radiation is small (or insignificant)(Fig.1). This feature is very different from TL curve from ordinary calcite (Fig. 2), but similar to that of aragonite. Most of the emission around 360°C is not due to radiation damage accumulated in the natural environment, but rather due to filling traps through the mineral growth from the start. To find out the reason for this calcite having a different trap nature from ordinal calcite, examination of crystallinity estimated from XRD data, trace element concentration from LAICPMS data, and effect by sample preparation methods, was carried out, but no clear interpretation was possible. Based on the geological observation where samples were collected, the calcite analyzed here could be contaminated with more organic carbon (although, measured samples did not contain much of H₂O₂ solubles) than other ordinal calcite. The unusual emission might be caused from this contamination.

To extract TL originated from the radiation induced traps, peak separation was performed to eliminate the influence

of the peak from the high temperature side which is the light emission derived from the original trap fill. Accumulated dose was calculated by using the signal of 200 to 280 °C derived from radiation damage by the Multi aliquot additive dose method (Aitken, 1985). As a result, all the measured sample show dates much older than 100,000 years. However, these samples are precipitated from current alkaline water flow, and are expected to be in a relatively young age (around 2000 to 10000 years), suggested by the ¹⁴C age of carbonate and organic matter collected in the area. It is considered that part of traps responsible for peaks existing at 200 to 280°C was also filled originally, but not by radiation. In order to measure the accumulated dose more accurately, further research on identification of the precise peak position of this sample and emission existed just after the crystal precipitation is necessary.

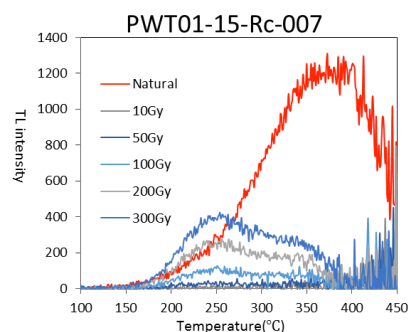


Fig. 1. Example of natural (red line) and artificial (others) TL glow curve.

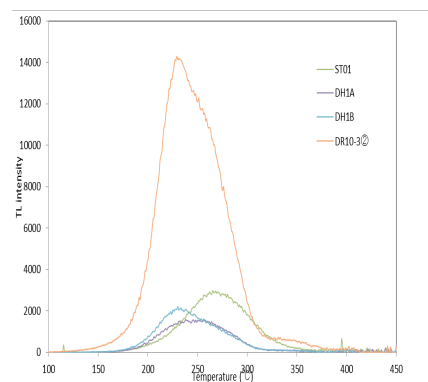


Fig. 2. Example of natural TL glow curve from ordinary calcite.

CO5-18 Studies on the Binding Mechanism and Stoichiometry of Mercury Atoms in an Organomercury Lyase from Smear Solution by an *in-cell* Radioactivation Analysis

K. Takamiya and Y. Morimoto

Institute for Integrated Radiation and Nuclear Science, Kyoto University

INTRODUCTION: The organomercury lyase (MerB) catalyzes the protonolysis of the carbon-mercury bonding and produces an ionic mercury and hydrocarbon. The ionic mercury [Hg(II)] is immediately reduced to less reactive mercury [Hg(0)] by a mercuric reductase (MerA). The MerB enzyme has three active amino acids in an active site, and they hold stoichiometrically one Hg atom by Cys-SH or Asp-COOH / Hg-C bonding. We have determined the tertiary structure of the enzyme at atomic resolution, and considered a pathway of Hg compound via solution. And other research point, structure based mercury capture system will be proposed to decrease toxic mercury in the environment. It is available for non-energetic mercury detox by use of bacterial bio-remediation. In the evaluation of mercury recover from solution or cultivation medium, radioactivation analysis is available rather than an ICP-mass spectroscopy in particular intact cell analysis. We have checked and pre-evaluated mercury content in a standard mercury solution by a measurement of γ -ray after irradiation of neutron in the KUR.

EXPERIMENTS: Cultivation of over-expression system of the *E.coli* (BL21-DE3) and sampling procedures are shown in the figure 1.

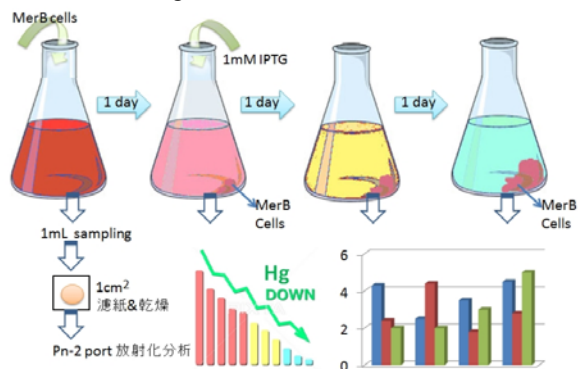


Fig.1 A schematic drawing of cultivation of the *E.coli* harboring MerB and medium sampling to radioactivation analysis

In a cultivation of the *E.coli*, minimum medium based on the ILL deuterium lab was used to keep surplus reagents away from bacterium growth. Several millimolar mercury reagent (Hg_2I_2 , CH_3HgI , C_2H_5HgCl , CH_3HgCl , $HgNO_3/H_2O$, $HgCl_2$, $HgCl$ and $Hg(CH_3COO)_2$) solutions are prepared and used. Neutron irradiation was carried out at Pn-2 port at the KUR operated by 5MW.

RESULTS and DISCUSSION: In the enzyme structure an Hg atom is found at active site¹⁾ in the CH_3HgCl additive preparation and is stoichiometrically held as one Hg-atom (Fig.2), a dimer enzyme has two Hg atoms. And also there is no CH_3HgCl compound, it suggests that Hg atom is isolated by bond-braking between Hg-C.

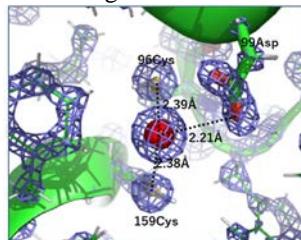


Fig.2 An Hg atom held by three amino acids. Electron densities are presented by case.

The enzyme prepared by the previous minimum medium cultivation and purification has enough activity to donate proton into the Hg compound and protonolysis Hg-C bonding.

In a radioactivation analysis by neutron irradiation, it is essential how limit of under concentration of Hg atoms in the enzyme or solution. Since in the structural analysis the CH_3HgCl is suitable for enzymatic activity and structural stability, its solution is used as standard solution with three kinds of concentration of 5mM, 0.5mM and 0.05mM. Filter papers (1 x 1 cm) soaked by 500 μ L of each solution are used for evaluation of γ -ray. A decay of the Hg is led by the following process (Fig.3).

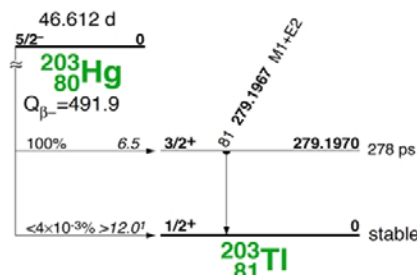


Fig.3 A typical scheme of ^{203}Hg decay in a $^{202}Hg(n,\nu)$ reaction.

The γ -ray spectrometry was carried out by the Canberra GC 4020 Ge- detector within two weeks. Neutron exposure time was 60 seconds at 5MW reactor operation.

A high concentration (5mM) sample out of three solutions gives an efficient γ -ray within error of 1%, but other two concentrations have large errors under the same condition in the case of 5mM solution. We have obtained information of the irradiation time over 60 seconds for 0.5 and 0.05mM concentration solutions and precise evaluation of the mercury content is now still going.

REFERENCE:

- 1) A study of preparation and structural analysis of the organomercury lyase for a neutron diffraction experiment. Y.Morimoto and A.Kita, Annual meeting of the KURRI 2017

H. Kurumizaka and M. Sugiyama¹
 Faculty of Science and Engineering, Waseda University
¹Research Reactor Institute, Kyoto University

INTRODUCTION: In eukaryotic cells, genomic DNA is compacted and accommodated in the nucleus. To do so, the DNA must be formed a highly compacted structure, called chromatin. The fundamental unit of chromatin is the nucleosome, in which histones H2A, H2B, H3, and H4 are protein components. Two of each of histones form an octamer, containing two copies of each H2A-H2B and H3-H4 dimers, and approximately 150 base pairs of DNA are tightly bound to this histone core [1].

In cells, nucleosomes are extremely stable, but they have to be dynamic to promote DNA functions, such as repair, replication, recombination, and transcription [2,3]. Especially, nucleosomes are slide and reposition along genomic DNA by spontaneous and/or enzymatic remodeling processes [4,5]. It has been known that the nucleosome remodeling is an essential process for transcription, DNA repair, and replication. Intriguingly, a nucleosome repositioned by the remodeling process collides with a neighboring nucleosome [6,7]. This nucleosome collision forms the intermediate structure, called “overlapping dinucleosome” [6,7]. The overlapping dinucleosome may also be formed by another mechanism such as a DNA-sequence-directed nucleosome positioning, if two positioning DNA sequences for nucleosomes are located in close proximity enough to form the overlapping dinucleosome on the genomic DNA [6,7]. However, the structure of the overlapping dinucleosome has remained elusive.

We previously determined the crystal structure of the overlapping dinucleosome. In the overlapping dinucleosome structure, two nucleosomes are collided, and one H2A-H2B dimer is released. Consequently, the canonical octasome nucleosome containing a histone octamer and the unusual hexasome containing a histone hexamer are associated with new interactions between two nucleosomes [8]. This finding suggested that, in the overlapping dinucleosome, the octasome and hexasome moieties may dynamic interact each other. However, it has not been reported the dynamic property of the overlapping dinucleosome, so far. Therefore, in the present study, we reconstitute the overlapping dinucleosome in vitro, and studied its dynamic property in solution by small angle X-ray scattering (SAXS) method.

EXPERIMENTS: Human histones H2A, H2B, H3, and H4 were bacterially produced, and were purified near homogeneity. The 250 base-pair DNA was also produced in bacterial cells, and was purified. Then, the overlapping dinucleosome was reconstituted by a salt-dialysis method.

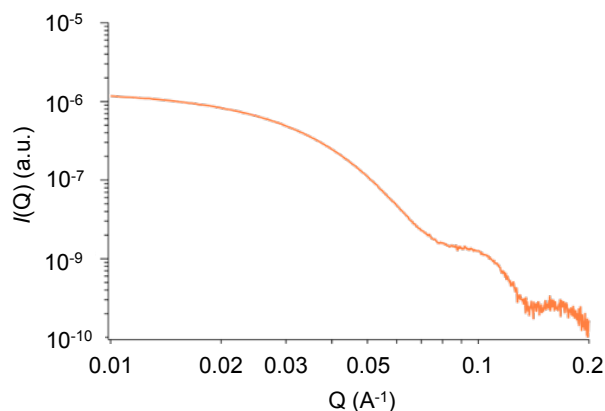


Fig. 1. SAXS profiles of the overlapping dinucleosome

The reconstituted overlapping dinucleosome was further purified by a native polyacrylamide gel electrophoresis. The purified overlapping dinucleosome samples were concentrated with a cartridge filter, and the debris was removed by centrifugation. We then performed the SAXS experiments.

RESULTS: As shown in Fig. 1, the SAXS curve was obtained, and solution parameters of the overlapping dinucleosome structure were estimated. A low resolution solution structure of the overlapping dinucleosome was obtained by Dummy atom modeling. The comparative study between solution structure and the X-ray structure of the overlapping dinucleosomes are underway.

REFERENCES:

- [1] K. Luger *et al.*, Crystal structure of the nucleosome core particle at 2.8 Å resolution. *Nature.*, **389** (1997) 251-260.
- [2] B. Li *et al.* The role of chromatin during transcription. *Cell.*, **128** (2007) 707-719.
- [3] R. Kornberg *et al.* Twenty-five years of the nucleosome, fundamental particle of the eukaryote chromosome. *Cell.*, **98** (1999) 285-294.
- [4] M. Bruno *et al.*, Histone H2A/H2B dimer exchange by ATP-dependent chromatin remodeling activities. *Mol. Cell.*, **12** (2003) 1599-1606.
- [5] P. Becker *et al.*, ATP-dependent nucleosome remodeling. *Annu Rev Biochem.*, **71** (2002) 247-273.
- [6] N. Ulyanova *et al.*, Human SWI/SNF generates abundant, structurally altered dinucleosomes on polynucleosomal templates. *Mol Cell Biol.*, **25** (2005) 11156-11170.
- [7] M. Engholm *et al.*, Nucleosomes can invade DNA territories occupied by their neighbors. *Nat Struct Mol Biol.*, **16** (2009) 151-158.
- [8] D. Kato *et al.*, Crystal structure of the overlapping dinucleosome composed of hexasome and octasome. *Science.*, **356** (2017) 205-208.

M. Koyama, R. Inoue¹, W. Nagakura, M. Sugiyama¹ and H. Kurumizaka

Division of Advanced Science and Engineering, Waseda University

¹Research Reactor Institute, Kyoto University

INTRODUCTION:

In the eukaryotic nucleus, genomic DNA binds to histone proteins to form the chromatin structure. The fundamental unit of the chromatin structure is the nucleosome, in which about 150-base-pairs of DNA are wrapped around the histone octamer, containing two molecules of each of four core histones (H2A, H2B, H3, and H4) [1, 2]. Although the nucleosome is the major structural unit of chromatin, it is also known that the structures different from the conventional nucleosome can be formed under specific conditions. For example, when four core histones are mixed with a 250-base-pair DNA fragment, which is longer than the mono-nucleosomal DNA (150-base-pairs) but shorter than the di-nucleosomal DNA (300-base-pairs), the structure called ‘overlapping dinucleosome’ is formed [3]. The overlapping dinucleosome is the structure, in which the DNA is wrapped continuously around the histone octamer (containing two H2A-H2B dimers and two H3-H4 dimers) and hexamer (containing one H2A-H2B dimer and two H3-H4 dimers) [3]. It is assumed that these structures such as overlapping dinucleosome are also formed on the genomic DNA *in vivo*, playing key roles in regulating the genome function.

The fission yeast *S. pombe* is a unicellular eukaryote that has a simple genome but shares many characteristics of the chromatin organization with higher eukaryotes such as human. Furthermore, *S. pombe* is readily manipulated in the laboratory. Therefore, *S. pombe* is useful as a model organism to study chromatin structure and function. Recently, we established a system to purify *S. pombe* four canonical histones, and reconstituted the *S. pombe* nucleosome *in vitro* [4]. Furthermore, the biochemical and biophysical assays revealed that the *S. pombe* nucleosome possesses unstable nature, and its DNA ends are flexible, as compared to the canonical human nucleosome [4]. In this study, we reconstituted the *S. pombe* overlapping dinucleosome *in vitro*, and measured its small angle X-ray scattering profiles to analyze its structural properties.

EXPERIMENTS: The *S. pombe* overlapping dinucleosome was reconstituted *in vitro*, by mixing a 250-base-pair DNA fragment with *S. pombe* four canonical core histones (SpH2A, SpH2B, SpH3, SpH4). The reconstituted overlapping dinucleosome was further purified by polyacrylamide gel electrophoresis using the Prep Cell apparatus (BioRad). The purified sample was concentrated using a Millipore concentrator (Mw cutoff of 30,000). After filtration,

the sample was used for the SAXS measurement. SAXS experiments were performed with NANOPIX (Rigaku).

RESULTS: SAXS profiles of the *S. pombe* and human overlapping dinucleosomes are shown in Fig. 1. The *S. pombe* overlapping dinucleosome appeared to have a stretched structure, as compared to the human overlapping dinucleosome. A Guinier plot of the data for the *S. pombe* overlapping dinucleosome is shown in Fig. 2. The straight line represents the least-square fitting for the data. This result revealed that the gyration radius (R_g) of the *S. pombe* overlapping dinucleosome is $62.8 \pm 1.2 \text{ \AA}$, which is larger than that of the human canonical overlapping dinucleosome ($R_g = 58.4 \pm 1.2 \text{ \AA}$).

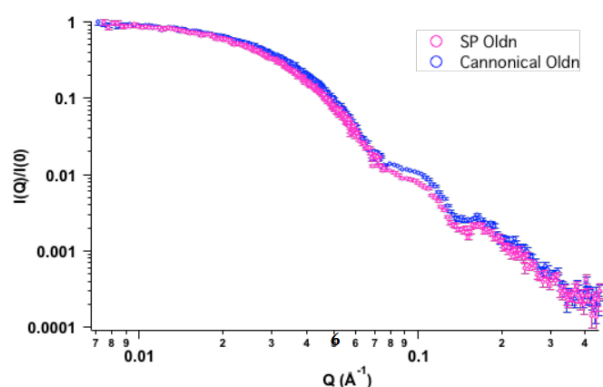


Fig. 1. SAXS profiles of the *S. pombe* (magenta) and human (blue) overlapping dinucleosomes.

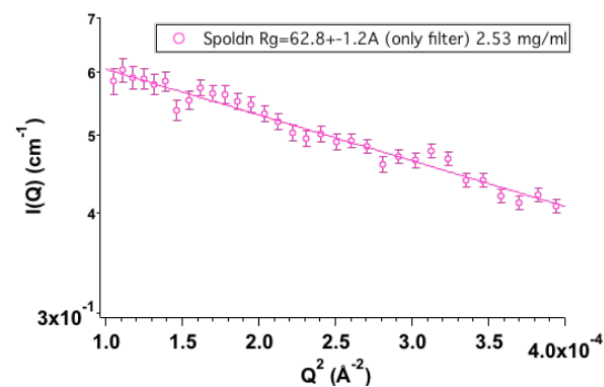


Fig. 2. A Guinier plot of the *S. pombe* overlapping dinucleosome.

REFERENCES:

- [1] K. Luger *et al.*, Nature, **389** (1997) 251-260.
- [2] M. Koyama and H. Kurumizaka, J. Biochem., **163** (2018) 85-95.
- [3] D. Kato *et al.*, Science, **356** (2017) 205-208.
- [4] M. Koyama *et al.*, Biochem. Biophys. Res. Commun., **482** (2017) 896-901.

E. Hibino, R. Inoue¹, M. Sugiyama¹, J. Kuwahara², K. Matsuzaki and M. Hoshino

Graduate School of Pharmaceutical Sciences, Kyoto University

¹Research Reactor Institute, Kyoto University

²Faculty of Pharmaceutical Sciences, Doshisha Women's University

INTRODUCTION: The expression of genes is controlled in a temporally and spatially coordinated manner, and this precise regulation is accomplished by the interactions of a variety of transcriptional factors.

The promoter-specific transcription factor Sp1 plays a primary role in the regulation of more than 100 genes. Sp1 specifically recognizes the GC-rich consensus sequence, and binds to these promoter regions to increase the transcriptional levels of target genes. Sp1 contains two Q-domains in the middle of the molecule, and three zinc fingers at the C-terminus. Although the structures of Zn-finger motifs were revealed by high-resolution NMR spectroscopy, structural details on other regions including the two Q-domains have yet to be elucidated.

The fourth-element of the general transcriptional factors, TAF4, is involved in the interactions with cellular transcriptional activators. Sequence analyses revealed that TAF4 possesses two highly conserved domains, CI and CII, as well as four Q-domains in the center of molecule. Whereas the X-ray structures are reported for CI and CII domains, only limited information is available on the structures of the four Q-domains although these Q-domains are involved in interactions with a number of gene-specific transcriptional activators, such as Sp1.

Here, we report the structural details of two Q-domains in Sp1 and four in TAF4, which are important for the interaction between these proteins.

EXPERIMENTS: The glutamine-rich fragment proteins of Sp1 (Sp1-QA, -QB, -QBn, -QBc), and TAF4 (TAF4-Q12, -CI, -Q34) were constructed as fusion protein with ubiquitin. The proteins were expressed and purified as described previously [1].

CD spectra were measured on a Jasco J-820 spectropolarimeter. An assembling cell composed of a pair of quartz plates with a 0.1-mm path length, was used to record spectra between 250 and 190 nm at a protein concentration of 50 μ M at 25°C.

SAXS measurements were performed with the spectrometer installed at BL-10C of Photon Factory with a PILATUS 2M detector. The two-dimensional data were converted into a one-dimensional curve by a circulation average and the scattering profile, $I(q)$, of the protein was then obtained.

NMR experiments were performed on a Bruker Avance 600 spectrometer with triple-resonance probe. A typical ¹H-¹⁵N HSQC experiments were performed at protein concentration of 50 mM. The solvent conditions used were 20 mM sodium acetate (pH 5.0), and 10% D₂O. The chemical shift value was referenced to DSS.

RESULTS: We first measured the far-UV CD spectra of Q-domain fragment proteins of Sp1 and TAF4. All the spectra showed a large minimum at ~200 nm, suggesting that neither protein has rigid secondary structures. Next, we measured ¹H-¹⁵N HSQC spectra for each fragment proteins. We found that the chemical shift dispersion was

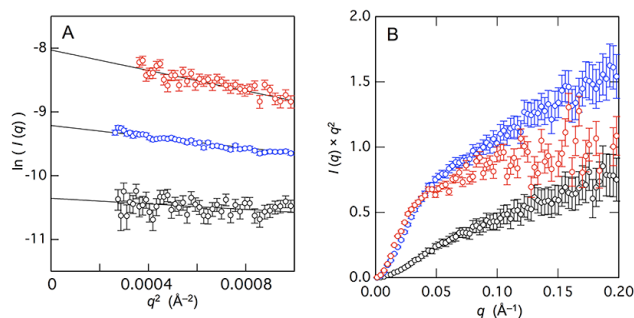


Fig. 1. The Guinier (A) and Kratky (B) plots of small-angle X-ray scattering of Sp1-QA (black), Sp1-QB (blue), and TAF4N/C (red) shown in open circles. The lines in (A) indicate the results of linear curve fitting for the data within the Guinier-region.

very poor and all the peaks were appeared within a narrow region between 7.6 and 8.6 ppm. We also analyzed the overall shape of the molecules by the small-angle X-ray scattering. The analysis of Guinier plots revealed that the proteins were largely expanded. Furthermore, the Kratky plots did not show any clear peak, suggesting that the molecules lack globular shape but are rather chain-like conformation. All these analyses (CD, NMR and SAXS) indicate that the Q-domains of Sp1 and TAF4 are categorized as the intrinsically disordered proteins (IDPs), which lack rigid secondary and tertiary structures under the physiological conditions.

In order to examine whether the isolated Q-domains (Sp1-QA and QB) interact with the central part of TAF4 (TAF4N/C, containing all four Q-domains), the ¹H-¹⁵N HSQC spectra were measured for ¹⁵N-Sp1-QA and ¹⁵N-Sp1-QB in the absence and presence of unlabeled TAF4N/C. In the case of ¹⁵N-Sp1-QA, any change in the spectra was observed even in the presence of three-fold molar excess amount of unlabeled TAF4N/C. On the other hand, the intensity of several peaks in ¹⁵N-Sp1-QB was significantly decreased by the addition of equimolar amount of TAF4N/C. We also analyzed the change in the chemical shift value upon the interaction in detail, and found that the binding site for TAF4N/C is located in the C-terminal region of Sp1-QB molecule. The results also suggested that the interaction between these proteins did not accompany with the significant conformational change in the molecules. This finding is not explained by the “coupled folding and binding mechanism”, a widely accepted interaction mode for the IDPs and their ligands. The interaction between Sp1-QB and TAF4 might represent a novel binding mode for the IDPs.

REFERENCES:

- [1] E. Hibino *et al.*, *Protein Sci.*, **25** (2016) 2006-2017.
- [2] E. Hibino *et al.*, *Protein Sci.*, **26** (2017) 2280-2290.

Study of Localization Estimation of Abasic Sites in DNA Exposed to Radiomimetic Chemicals and ^{60}Co γ -rays

K. Akamatsu, N. Shikazono and T. Saito¹

Radiation DNA Damage Research Group, Kansai Photon Science Institute, National Institutes for Quantum and Radiological Science and Technology (QST)

¹Research Reactor Institute, Kyoto University

INTRODUCTION:

DNA lesions induced by ionizing radiation and chemicals can cause mutation and carcinogenesis. In particular, “clustered damage” site, that is a DNA region with multiple lesions within one or two helical turns, is believed to hardly be repaired. This damage is considered to be induced, *e.g.*, around high-LET ionizing radiation tracks. However, detail of the damage is not known. We have already developed a method for estimating degree of localization of abasic sites (APs) in DNA using Förster resonance energy transfer occurred between different fluorescence probes (“hetero-FRET” using Alexa350 and Alexa488) [1]. The results showed that $^{12}\text{C}^{5+}$ beam produced close APs within a track: the apparent distance calculated was approximately 17 base pairs [2]. This finding indicates that *direct radiation effect* of $^{12}\text{C}^{5+}$ beam near the Bragg peak produces clustered DNA damage. We have recently applied the method to DNA in a cell-mimetic radical scavenging condition. However, there are some problems of the complex protocol and of the sensitivity due to the low extinction coefficient of Alexa350. We have, therefore, developed “homo-FRET” occurred between two or more Alexa488 molecules. We will obtain magnitude of FRET also from “fluorescence anisotropy” of homo-FRET between Alexa488 molecules. The new protocol using homo-FRET [3] enables us to estimate DNA damage localization without any enzymes and improves sensitivity to detect a clustered damage.

EXPERIMENTS:

● Sample preparation and irradiation

The plasmid DNA digested by Sma I was used (linear form). The DNA was dissolved to be 0.1 g/L in 0.2 M Tris-HCl buffer (pH 7.5) which is a cell-mimetic condition in relation to radical scavenging capacity. Twenty microliters of the DNA solution was transferred to a microtube (0.5-mL size), and was irradiated with ^{60}Co γ -rays (LET: ~ 0.2 keV/ μm ; Kyoto University Research Reactor Institute: KURRI) as a standard radiation source. Moreover, the DNA solution was treated with so-called “radiomimetic” chemicals: MMS (methylmethanesulfonate, an alkylating agent) and NCS (neocarzinostatin, an antibiotic).

● Preparation of fluorophore-labeled irradiated DNA and the FRET observation

The damaged sample DNA (10 μL in water) and 10 μL of 100 mM Tris-HCl (pH 7.5) were mixed in a microtube. Two microliters of Alexa488/DMSO was added to the DNA solution and was incubated for 24 h at 35°C.

The fluorophore-labeled DNA was purified by ethanol-precipitation followed by ultrafiltration. The fluorescence anisotropy was measured at 525 nm (ex. 470 nm).

The anisotropy, $\langle r \rangle$, is defined as follows:

$$\langle r \rangle = \frac{I_{VV} - G \cdot I_{VH}}{I_{VV} + 2G \cdot I_{VH}},$$

where I_{VV} is the fluorescence intensity when the excitation and emission polarizers are both vertically oriented. I_{VH} is one when the excitation/emission polarizers are vertically/horizontally oriented. G is the grating factor defined as I_{HV}/I_{HH} .

RESULTS AND DISCUSSION:

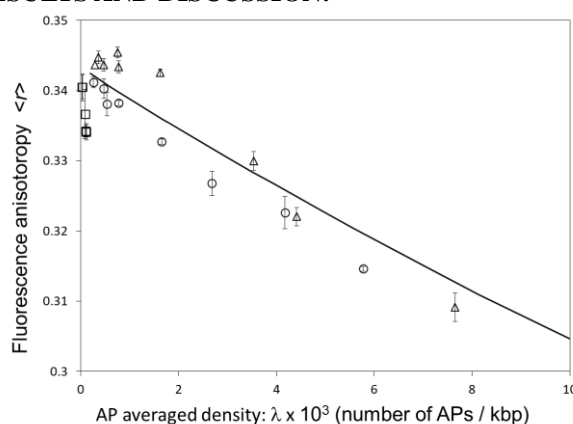


Fig. 1. Relationship between AP averaged density and fluorescence anisotropy for ^{60}Co γ -rays (o), MMS (Δ), and NCS (\square). The solid line indicates a theoretical curve when APs are randomly distributed.

In general, fluorescence anisotropy decreases with increasing FRET [4]. As shown in Fig.1, we found that the relationship differed significantly among MMS, NCS, and ^{60}Co γ -rays. At lower AP density, MMS-inducing APs seemed to not be closely distributed, whereas NCS-induced APs were remarkably clustered. In contrast, the AP clustering by the γ -rays was similar to, but potentially more likely to occur than, random distribution. Here, we conclude that these radiomimetic chemicals are *not* radiomimetic at least in AP distribution. Now we apply the method to DNA irradiated with a variety of heavy ion beams such as He, C, and Fe, under cell-mimetic condition.

REFERENCES:

- [1] K. Akamatsu, N. Shikazono, *Anal. Biochem.*, **433** (2013) 171-180.
- [2] K. Akamatsu, N. Shikazono, and T. Saito, *Radiat. Res.*, **183** (2015) 105-113.
- [3] K. Akamatsu, N. Shikazono, *Anal. Biochem.*, **536** (2017) 78-89.
- [4] L. W. Runnels, and S. F. Scarlata, *Biophys. J.*, **69** (1995) 1569.

CO6-5 SAXS Study on the Structure of Prefibrillar Intermediates for the Formation of Insulin B Chain Amyloid Fibrils

N. Yamamoto, T. Akai, E. Chatani, R. Inoue¹, K. Morishima¹ and M. Sugiyama¹

Graduate School of Science, Kobe University

¹Research Reactor Institute, Kyoto University

INTRODUCTION: Amyloid fibrils are a form of protein aggregates with fibrous morphology and β -sheet-rich structure. Because of their deep association with a numerous number of diseases such as Alzheimer's disease and Creutzfeldt-Jacob disease, finding strategies for preventing aggregation is quite important from a perspective of the onset of above-mentioned diseases.

The formation of amyloid fibrils typically follows a nucleation-dependent polymerization, and a one-step nucleation has widely been accepted as the simplest scheme. On the other hand, various types of oligomers have been identified in the time domain of nucleation. This observation invokes the necessity of considering multi-step nucleation as another principle mechanism of amyloid nucleation, in which the formation of metastable prefibrillar intermediate species plays an important role [1].

We are attempting direct observation of such species, and recently, the formation of prefibrillar intermediates has been found in an insulin-derived peptide (insulin B chain) [2]. In this study, to elucidate structural properties of the prefibrillar intermediates, small-angle X-ray scattering (SAXS) measurements have been performed in combination with dynamic light scattering (DLS) experiments. Furthermore, we have analyzed changes in SAXS profiles after the addition of fibrinogen, a protein which has been revealed to function as the inhibitor of B-chain fibrillation [3].

EXPERIMENTS: Insulin B chain was dissolved in 50 mM Tris-HCl buffer at a concentration of 1.4 mg/ml, and was then put in a 1-mm path-length quartz cell. After 2-hour incubation at 25 °C to form the prefibrillar intermediate, the small angle X-ray scattering (SAXS) pattern was collected with NANOPIX (Rigaku Corporation, Japan) equipped with HyPix-6000. A Cu K- α line (MicroMAX-007HF) was used as a beam source, which was further focused and collimated with a confocal multilayer mirror (OptiSAXS). The camera length was set to 1.326 m and the range of the scattering vector q was from 0.0005 to 0.24 \AA^{-1} . In the structural analysis of the prefibrillar intermediate in the presence of fibrinogen, the prefibrillar intermediate formed by incubating 1.4 mg/ml insulin B chain for 2 hours was mixed with fibrinogen at a final concentration of 3.5 mg/ml and then subjected to the SAXS measurement.

RESULTS: Fig. 1 shows SAXS profiles of the prefibrillar intermediate of B chains and the complex of B chain

and fibrinogen. The slope of the log-log plot of the scattering profile of the prefibrillar intermediate (circles) was close to -1 , indicating that the prefibrillar intermediate has a rod-like structure. The analysis of cross-section plot suggested the approximate base radius of ~ 33 \AA , and by using a diffusion coefficient determined by the DLS measurement, the length of the prefibrillar intermediate was estimated to be $\sim 2,700$ \AA on the basis of Broersma's relationship, where a diffusion coefficient of a rod-like molecule is described by a function of the length and base radius. This result suggests that the peptide molecules of insulin B chain associated into rod-like prefibrillar intermediates in an early stage of the reaction. Preliminary time lapse monitoring of the amyloid formation reaction is now ongoing to investigate detailed time evolution of conformational development from monomers towards mature amyloid fibrils via the rod-like prefibrillar intermediate species.

As for the prefibrillar intermediate-fibrinogen complex, the slope of the log-log plot of the scattering profile (squares) was also close to -1 , suggesting that the rod-like intermediate structure was kept even after the addition of the fibrinogen. The base radius and length of this complex form was calculated to be ~ 74 \AA and $\sim 2,900$ \AA , respectively. A slight increase of the base radius has provided a possible picture that a layer of fibrinogen is formed on the surface of the prefibrillar intermediates, shedding light on the inhibitory mechanism of fibrinogen on the B chain amyloid fibril formation.

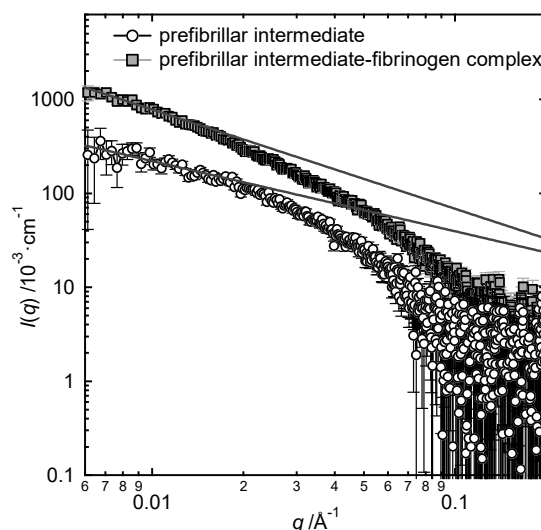


Fig. 1. One-dimensional SAXS profiles of the prefibrillar intermediate of insulin B chain (circles) and its complex with fibrinogen (squares).

REFERENCES:

- [1] E. Chatani and N. Yamamoto, *Biophys. Rev.*, **10** (2018) 527-534.
- [2] N. Yamamoto *et al.*, *Sci. Rep.*, **8** (2018) 62.
- [3] T. Akai, Master's Thesis, Kobe Univ. (2017).

CO6-6 Possible Involvement of Aspartyl L-to-D Isomerization of Cell Adhesion Molecule-1 Shedding Products in Neurodegeneration

A. Ito and N. Fujii¹

Department of Pathology, Kindai University Faculty of Medicine

¹Research Reactor Institute, Kyoto University

INTRODUCTION: Cell adhesion molecule 1 (CADM1) is a member of the immunoglobulin superfamily mediating intercellular adhesion. It is expressed in epithelial cells, such as lung alveolar and renal tubular cells, and widely in neurites of the central and peripheral nervous systems. CADM1 is enzymatically shed at the extracellular domain near the cell membrane. This phenomenon called ectodomain shedding is accelerated under some pathological conditions. In the lung of patients with pulmonary emphysema, a degenerative lung disease, CADM1 ectodomain shedding is increased in alveolar cells, and the resulting shedding products accumulate within the cells, then causing apoptosis [1,2]. This event appears to be involved in alveolar destruction, a hallmark feature of emphysema [1]. As CADM1 shedding occurs in nerves, it may be also involved in degeneration and/or apoptosis of neurons. Neuronal degeneration and apoptosis are common features of diseases caused by elevation of the intraluminal pressure, such as glaucoma and ventricular hydrocephalus.

EXPERIMENTS:

(1) A water pressure-loadable two-chamber culture system was originally devised by connecting a 60-cm-long plastic cylinder to the upper chamber in a water-proof manner [3,4]. This system can reproduce pathological conditions of the intraluminal pressure elevation. When cells are cultured in this system, they are to receive static medium-water pressure ranging up to 55 cmH₂O.

(2) Dorsal root ganglion neurons from C57BL/6 mouse neonates were cultured in the system, and were loaded with various degrees of water pressure for 1 to 3 days, when the neurons were sprouting many neurites to form elaborate neuritic networks.

(3) Protein was extracted from the resulting neuritic networks, and was subjected to Western blot analyses using an anti-CADM1 antibody.

(4) The resulting neuritic networks were also double stained with CADM1 immunofluorescence and mitochondrial labeling using the Mitotracker dye.

RESULTS:

(1) The intracellular product of CADM1 ectodomain shedding (C-terminal fragment, CADM1-CTF) was increased in a manner dependent on the loaded water pressure.

(2) The more the loaded water pressure was, the less elaborate the neuritic networks were [Fig. 1]. In addition, the neurites became rough and course in their surface, and CADM1 immunostain signals were punctate [Fig. 1].

Some punctate CADM1 signals were colocalized with Mitotracker dye stains, which were also punctate or drop-like [Fig. 1].

(3) These results suggest that CADM1-CTF might preferentially aggregate with each other and might inhibit neuritic extension and cause neuritic degeneration.

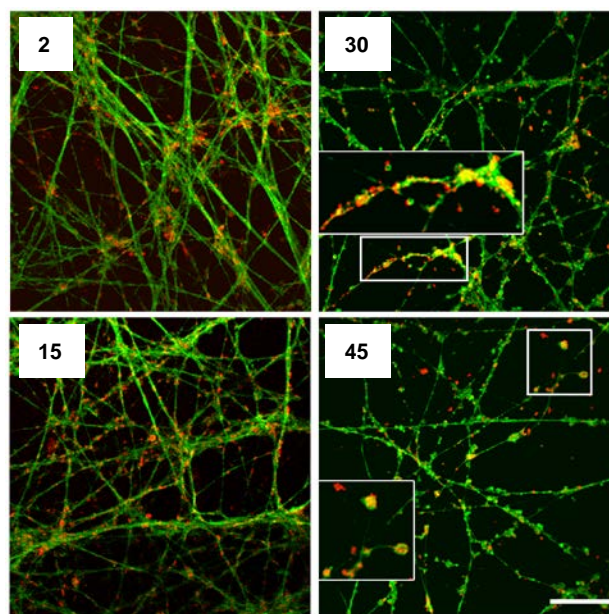


Fig. 1. Double staining of neuritic networks with CADM1 immunofluorescence (green) and mitochondrial labeling (red). Neuritic networks were developed for 3 days under the water pressure indicated (cmH₂O).

PERSPECTIVES:

CADM1-CTF contains an amino acid region very rich in aspartyl residues, *i.e.*, ADDAADAD. These aspartyl residues may be isomerized to D-form, because they are surrounded by alanine residues that have a small side chain. This D-isomerization may be a cause of molecular aggregation of CADM1-CTF in neurites, and thereby neuritic degeneration possibly through interfering with neuritic mitochondrial function. Future studies to prove this hypothesis will open a new avenue leading to better understanding of neurodegeneration caused by internal pressure elevation.

REFERENCES:

- [1] T. Mimae *et al.*, Thorax, **69** (2014) 223-231.
- [2] M. Hagiyaama *et al.*, J. Biomed. Sci., **22** (2015) 67.
- [3] A. Yoneshige *et al.*, Mol. Neurobiol., **54** (2017) 6378-6390.
- [4] M. Hagiyaama *et al.*, Front. Physiol., **8** (2017) 997.

H. Yagi, Y. Yunoki, K. Morishima¹, N. Sato¹, R. Inoue¹, and M. Sugiyama¹

Graduate School of Pharmaceutical Sciences, Nagoya City University,

¹Institute for Integrated Radiation and Nuclear Science, Kyoto University

INTRODUCTION: The central oscillator that generates the circadian rhythm in the cyanobacterium comprises only three proteins—KaiA, KaiB, and KaiC. Through interactions among these proteins in the presence of ATP, KaiC undergoes phosphorylation and dephosphorylation cycles with the period of 24 h, which proceeds *in vitro* without daylight oscillation, indicating that the internal clock mechanism can be autonomous irrespective of transcriptional and translational feedback systems. Although the formation of several complexes, such as KaiA-KaiC, KaiB-KaiC, and KaiA-KaiB-KaiC oscillated in a circadian manner, their stoichiometry or the detailed structures remains to be elucidated. Herein, in order to understand the oscillation mechanism mediated by the clock protein complex, we characterized the complexes by using native mass spectrometry (nMS), nuclear magnetic resonance (NMR) spectroscopy and small angle scattering analysis.

EXPERIMENTS: The expression and purification of clock proteins, KaiA, KaiB and KaiC were performed according to methods previously described [1]. Small angle X-ray scattering (SAXS) pattern was collected with NANOPIX (Rigaku Corporation, Japan) equipped with HyPix-6000. A Cu K- α line (Mi-cro MAX-007HF) was used as a beam source, which was further focused and collimated with a confocal multilayer mirror (OptiSAXS). The camera length was set to 1.326 m and the range of the scattering vector q was from 0.007 to 0.24 \AA^{-1} . Deuterium-assisted small angle neutron scattering (SANS) experiments were performed using the D22 instrument installed at the Institut Laue-Langevin (ILL), Grenoble, France.

RESULTS:

KaiB-KaiC complex

The nMS titration data showed that the proteins formed a complex exclusively in a 6:6 stoichiometry, indicating that KaiB bound to the KaiC hexamer with strong positive cooperativity. The inverse contrast-matching SANS measurement indicated that the disk-shaped arrangement of the KaiB subunits on the outer surface of the KaiC ring, which also serves as the interaction site for SasA, a histidine kinase that operates as a clock-output protein in the

regulation of circadian transcription. These data suggest that cooperatively binding KaiB competes with SasA with respect to interaction with KaiC, thereby promoting the synergistic release of this clock-output protein from the circadian oscillator complex.

KaiA-KaiC complex

KaiC binds 12 ATP to form a hexamer and possesses ATPase related to autokinase and autophosphatase activities. Herein, we characterized changes in structure and the KaiA-binding affinity of KaiC depending on its nucleotide state resulting from ATP hydrolysis. In this study, we controlled the nucleotide state using non-hydrolysable ATP analog (AMPPNP). The nMS analyses indicated that a KaiC hexamer formed with AMPPNP exhibits a lower affinity to KaiA in comparison with that formed with ATP. The data indicated that ATP hydrolysis in the KaiC hexamer promotes its interaction with KaiA presumably through KaiC's conformational change in KaiA binding region. In the SAXS experiment, the overall structural change was not observed upon ATP hydrolysis (Fig. 1). It has been reported that KaiA interacts with flexible C-terminal region on KaiC. Indeed, our NMR data indicated that the C-terminal region underwent structural change depending on ATP hydrolysis, and moreover was involved in interaction with KaiA.

On the basis of these data, we conclude that ATP hydrolysis in the KaiC hexamer causes its conformational changes in the KaiA-binding site, endowing it with high-affinity for KaiA. These findings provide mechanistic insights into the circadian periodicity in cyanobacteria.

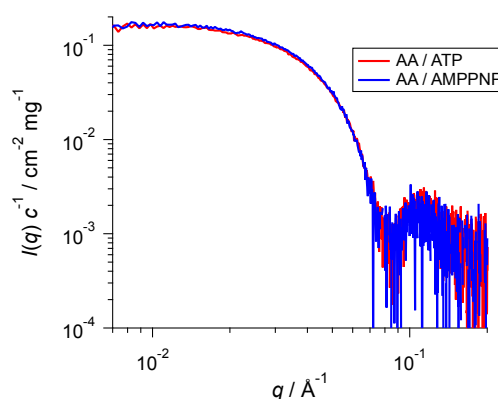


Fig. 1. The SAXS profiles of dephosphorylated mutant KaiC hexamers formed with ATP (red) and AMPPNP (blue).

REFERENCE:[1] M. Sugiyama *et al.*, *Sci. Rep.*, Article number: 35567 (2016).

CO6-8 Measurement of Transmittance Spectra of a Human Calcified Aorta Tissue in the Sub-Terahertz Region

N. Miyoshi and T. Takahashi¹

Department of Molecular Chemistry, Kyoto Institute of Technology

¹Institute for Integrated Radiation and Nuclear Science, Kyoto University

INTRODUCTION: The LINAC (Electron linear accelerator) technology in the millimeter- and terahertz-waves had been unique and had been used as a coherent synchrotron light source in the Institute for Integrated Radiation and Nuclear Science of Kyoto university (KURNS) to observe the transmittance spectra of a human calcified aorta tissue as a collaborate study. The absorption spectra in the sub-terahertz region had been not so clear for the raw tumor tissue although Ashworth-PC. *et al.* [1] had reported for the excised human breast cancer by a terahertz pulsed spectroscopy observed at 320 GHz, which was estimated a longer relaxation time component of the induced electricity for water molecules [2-3] in the raw tumor tissue for three years at the linear analysis.

We estimated what kind of water molecules become dominant in the viable and necrotic cancer regions by the different measurement method as an aim of 2D mapping study comparing with the pathological staining H&E imaging. In the results, it is considered that the molecule of the water presented in the necrotic area will be different one of the normal tissue, which looks to be near closed one of free water in the necrotic area at 600 GHz (the fast relaxation time) which was reported by Dr. H. Yada [3] beside of 4-5 THz. The other components at 200-400 GHz were also presented in the raw tumor tissues as un-known components [2], which was very interesting ones about the water molecules in the necrotic environment.

EXPERIMENTS: (1) Instrument of Near-field in Terahertz Region: The photograph of the instrument was shown in Fig. 1. Mark-A: Pre-probe Wiston cone; 50-10mm diameter, Length=60mm; the irradiate diameter=0.775mm; Mark-B: The concentrate light probe (diameter=3mm). The instrument was developed by Dr. T. Takahashi [4] for the transmittance measurements.

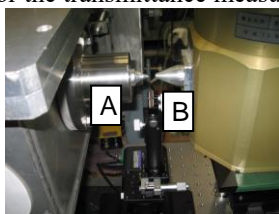


Fig. 1. The near field area of sample holder position.

(2) Sample Preparation: A calcified aorta blood vessel wall tissues were supplied by pathological autopsy. The sample tissues were dried with air in the room temperature as Fig. 2.

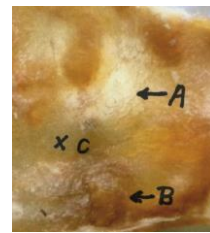


Fig. 2. The sample photograph of a human calcified aorta blood vessel wall tissue supplied from an autopsy. (A: calcified; B: cholesterol; C: normal blood vessel wall tissues)

RESULTS:

The transmittance spectra of the sample tissue for each points A, B and C were measured as shown in Fig. 3.

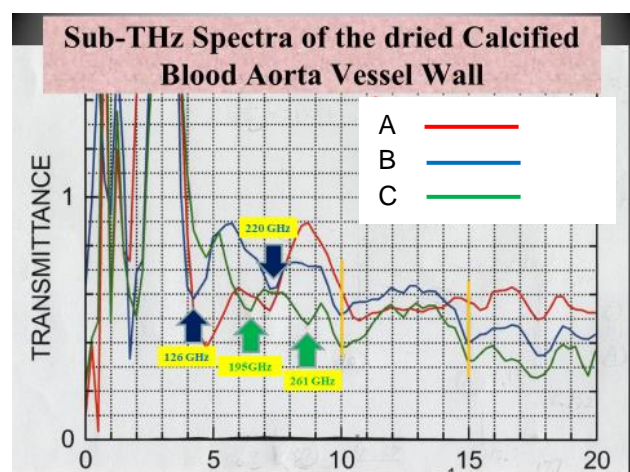


Fig. 3. Sub-THz spectra of the dried calcified blood aorta vessel wall.

(A: calcified; B: cholesterol; C: normal)

In the results, the absorbance of the dried tissue at 195 and 261 GHz were observed in the calcified area (included of PO₄ components), and the absorption peaks of 125, 220 GHz were observed in the cholesterol (included of C-H and C-H₂ components) adhesion area.

In the both areas, it was observed the absorption peaks at 300 and 450 GHz also.

In future, it will be needed more measurements and analysis of these spectra.

REFERENCES:

- [1] Phillip C. Ashworth *et al.*, Optics Express, **17** (2009) 12444-12454.
- [2] Toshiko Fukasawa, *et al.*, Phys. Rev. Lett., **95** (2005) 197802.
- [3] Hiroyuki Yada, *et al.*, Chem. Phys. Lett., **464** (2007) 166-170.
- [4] T. Takahashi, *et al.*, J. Phys.: Conf. Ser. **359** (2012) 012016-1-4.

T. Saito

*Institute for Integrated Radiation and Nuclear Science,
Kyoto University*

INTRODUCTION: There are various environments in nature, and organisms have evolved diversely to be able to adapt to most of these environments. Some organisms can survive in environments that are considered extremely severe by our common sense. Elucidation of the adaptive mechanisms of organisms to severe environments can provide meaningful information about the evolution and diversity of whole organisms. Some bacteria, known as radioresistant bacteria, have extremely high resistance to ionizing radiation [1]. Their resistance to such extreme conditions makes radioresistant bacteria an interesting area in research. In order to elucidate the mechanisms underlying this radioresistance, it is important to study the organisms' defense mechanisms at a molecular level against external stress. However, the study of these organisms in nature can be very challenging, as the knowledge on their genetic and biochemical properties is still inadequate. In this study, generation of radioresistant *Escherichia coli* cells by an experiment on the adaptive evolution to gamma rays was attempted. In this experiment, the following steps were performed: gamma-ray irradiation of *E. coli* cells whose genetic and biochemical properties are well known, growth of surviving cells, and irradiation of the grown cells.

EXPERIMENTS: Evaluation of the sensitivity of *E. coli* cells to gamma rays: *E. coli* K-12 cells were grown to the early log phase in LB medium at 37°C at 200 rpm. One milliliter of culture was centrifuged at 4000 × *g* at 20°C for 10 min. The supernatant was discarded and the pellet was suspended in 1 mL of PBS(-). The cell suspension was irradiated with gamma rays at a dose rate of 21 Gy/min at room temperature. Gamma irradiation was carried out at the Co-60 Gamma-ray Irradiation Facility of the Institute for Integrated Radiation and Nuclear Science, Kyoto University. The gamma-irradiated cell suspension was diluted appropriately with PBS(-), plated on LB agar, and incubated at 37°C for 12 hr. Colonies were counted, colony forming units were determined, and survival rates were calculated.

Selection with gamma rays: A single colony of *E. coli* K-12 clone cells was suspended in LB medium and grown to the early log phase at 37°C at 200 rpm. The cell suspension was prepared as described above. The cell suspension was irradiated with the 1% survival dose of

gamma rays at a dose rate of 21 Gy/min at room temperature. One milliliter of gamma-irradiated cell suspension was inoculated in 100 mL LB medium and grown to the early stationary phase at 37°C at 200 rpm. Glycerol stock was prepared and stored at -80°C. This protocol was repeated with cells from the glycerol stock grown to the early log phase.

RESULTS: In order to generate *E. coli* cells radioresistant to gamma rays by adaptive evolution, which were used as the selection pressure, *E. coli* cells were irradiated with a 1% survival dose of gamma rays, and the surviving cells were grown. The 1% survival dose of the surviving cell population to the same radiation was evaluated, and the cell population was once again irradiated with the 1% survival dose. An increasing trend in radioresistance of the *E. coli* cell population was observed when the experiment was repeated six times. The *E. coli* cell population with 3.4-fold resistance to gamma rays compared to the cells without selection was obtained by repeating the experiment eight times (Fig. 1). However, no further increase in radioresistance was observed in the *E. coli* cell population when the experiment was repeated ten times (Fig. 1). These results indicate that an evolutionary plateau exists in the process of adaptive evolution of *E. coli*, when gamma rays are used as selection pressure. Further studies should be conducted to generate *E. coli* cells resistant to higher doses of gamma rays by additional repetitions of the selection cycle and to analyze the genetic and biochemical properties of the resulting *E. coli* cells. These experiments will be required to further understand the biological defense mechanisms of radioresistant bacteria to ionizing radiation.

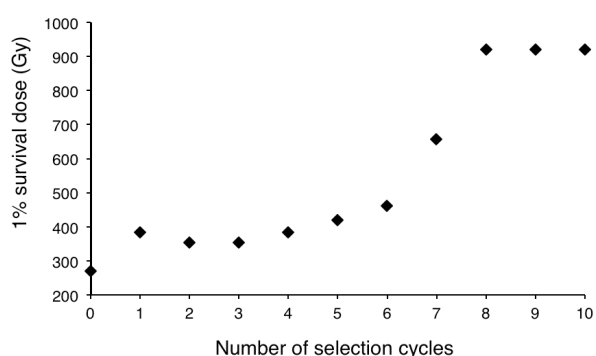


Fig. 1. One percent survival doses of *E. coli* cell populations to gamma rays evaluated at each selection cycle.

REFERENCE:

[1] T. Saito, *Viva Origino*, **30** (2007) 85–92.

M. Yagi-Utsumi, R. Inoue¹, N. Sato¹, M. Sugiyama¹ and K. Kato

Institute for Molecular Science, National Institutes of Natural Sciences

¹*Institute for Integrated Radiation and Nuclear Science, Kyoto University*

INTRODUCTION: Recent bioinformatic analyses identified proteasome assembly chaperone-like proteins, PbaA and PbaB, in archaea. PbaB forms a homotetramer and functions as a proteasome activator, whereas PbaA does not interact with the proteasome despite the presence of an apparent C-terminal proteasome activation motif [1, 2]. The C-terminal $\alpha 6$ helices of the PbaB tetramer show tentacle-like structures that project from the core domain, whereas the corresponding C-terminal helical segments of a PbaA pentamer are packed against the core. These structural features may explain the distinct proteasome-binding capabilities of PbaA and PbaB, although the conformational difference may be due to different modes of crystal packing.

In this study, we characterized the quaternary structure of PbaA in solution by small-angle X-ray scattering (SAXS) and high-speed atomic force microscopy (HS-AFM). Moreover, we attempted to endow PbaA with proteasome-binding activity by mutational modifications of its C-terminal segment based on our structural data and examined the structural impact of the mutations using biophysical techniques.

EXPERIMENTS: The expression and purification of *P. furiosus* PbaA, PbaB and the 20 S proteasome were performed according to methods previously described [1, 2]. Three constructs encoding PbaA–PbaB chimeric proteins were created by replacing the C-terminal segment of PbaA with that of PbaB. SAXS experiments were performed with NANOPIX (Rigaku) at 20°C. X-rays from a high-brilliance point-focused X-ray source (MicroMAX-007HF) were focused and collimated with a confocal multilayer mirror (OptiSAXS) and low parasitic scattering pinhole slits (ClearPinhole). The scattered X-rays were detected using a two-dimensional semiconductor detector (HyPix-6000). The SAXS pattern was converted to a one-dimensional scattering profile, and then standard corrections were applied for initial beam intensity, background scattering and buffer scattering. X-ray crystal structure analyses of PbaA, HS-AFM, and the proteasome activation assay were also performed.

RESULTS: We revealed that PbaA forms a homopentamer predominantly in the closed conformation with its

C-terminal segments packed against the core domains (Fig. 1), in contrast to the PbaB homotetramer with projecting C-terminal segments. This prompted us to create a novel proteasome activator based on a well-characterized structural framework. We constructed a panel of chimeric proteins comprising the homopentameric scaffold of PbaA and C-terminal segment of PbaB and subjected them to proteasome-activating assays as well as SAXS and HS-AFM. The results indicated that the open conformation and consequent proteasome activation activity could be enhanced by replacement of the crystallographically disordered C-terminal segment of PbaA with the corresponding disordered segment of PbaB [3]. Moreover, these effects can be produced just by incorporating two glutamate residues into the disordered C-terminal segment of PbaA, probably due to electrostatic repulsion among the negatively charged segments. Thus, we successfully endowed a functionally undefined protein with proteasome-activating activity by modifying its C-terminal segment.

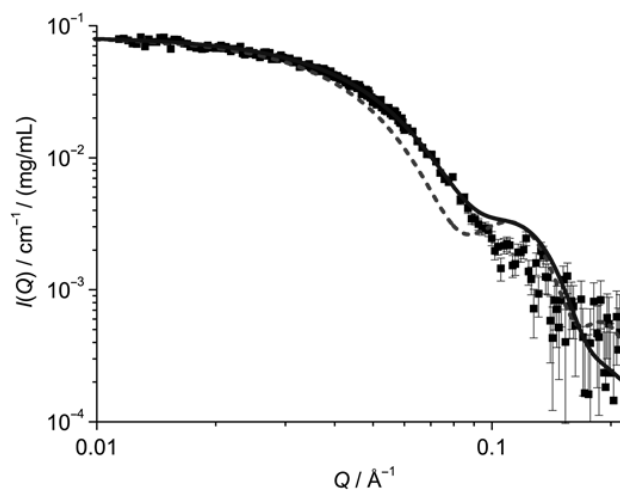


Fig. 1. The SAXS profile calculated from the crystal structures of the closed conformation of PbaA (solid line) and the open conformation of PbaA (dashed line), along with the experimentally obtained profile (black square).

REFERENCES:

- [1] K. Kumoi *et al.*, PLoS ONE, **8** (2013) e60294.
- [2] A. Sikdar *et al.*, Biochem. Biophys. Res. Commun., **453** (2014) 493-497.
- [3] M. Yagi-Utsumi *et al.*, Protein Eng. Des. Sel., **31** (2018) 29-36.

S. Fujiwara, K. Morishima¹, T. Matsuo, F. Kono, T. Chatake¹, R. Inoue¹ and M. Sugiyama¹

Quantum Beam Research Science Directorate, National Institutes for Quantum and Radiological Science and Technology

¹*Research Reactor Institute, Kyoto University*

INTRODUCTION: Proteins are constantly fluctuating under the influence of thermal fluctuations of surrounding solvent molecules. These fluctuations, or the dynamics, of the proteins are known to be indispensable to the structural changes that enable the proteins to function [1]. Full understanding of the molecular mechanisms of the functions of the proteins thus requires understanding of the dynamics as well as the structures of the proteins.

The dynamics of the proteins spans from the fluctuations of the polypeptide side chains through motions of the disordered segments in the polypeptide chains and the domain motions to diffusion of the entire protein [2]. Elucidating how the dynamics at these different levels are related to each other is important to elucidate the relationship between the dynamics and the structures.

Quasielastic neutron scattering (QENS) provides a tool to directly measure the dynamics of the proteins. We have noticed that QENS contains information on the segmental motions and the domain motions as well as the diffusion of the entire molecules and the local motions of the side chains [3,4]. Although the local motions can be separated, attempts to separate the segmental and domain motions from the diffusion of the entire molecules have not been made because both contribute to the broadening of the elastic peak. To separate the contribution of the segmental and domain motions, the information on the diffusion of the entire molecules is required. Dynamic light scattering (DLS) provides this information. From the DLS measurements of the protein solutions, the translational diffusion coefficients can be estimated. Since the DLS measurements can be carried out under the condition similar to the QENS measurements, DLS and QENS are well suited as the complementary measurements.

EXPERIMENTS: As part of the project measuring the dynamics at the different structural levels of the proteins, we carried out the DLS measurements of protein solutions. We employed ribonuclease (RNase) A as a typical globular protein (the folded state). We also prepared the molten-globule (MG) and unfolded states of RNase A as samples with different degrees of the segmental motions. The measurements were carried out using a system consisting of a 22 mW He-Ne laser (wavelength 632.8 nm), an avalanche photodiode mounted on a static/dynamic compact goniometer, ALV/LSE-5003 electronics and an ALV-5000 correlator.

RESULTS: Figure 1 shows an example of the decay

time distributions of the folded, MG, and unfolded states of RNase A, obtained by the CONTIN analysis [5]. The distributions with a single peak indicate that the solution in each state is monodisperse.

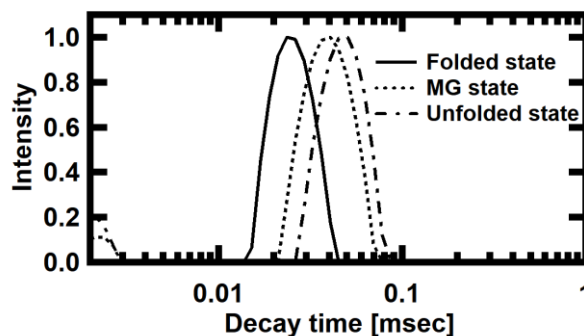


Figure 1. Example of the decay time distributions of RNase A. The distributions at the scattering angle of 90 degrees are shown.

Figure 2 shows the Q ($= (4\pi n_0/\lambda)\sin\theta$, where n_0 is the refractive index, λ is the wavelength, and 2θ is the scattering angle) dependences of the decay rates (the inverse of the decay time). These curves are well fit with straight lines, from the slopes of which the translational diffusion coefficients can be estimated.

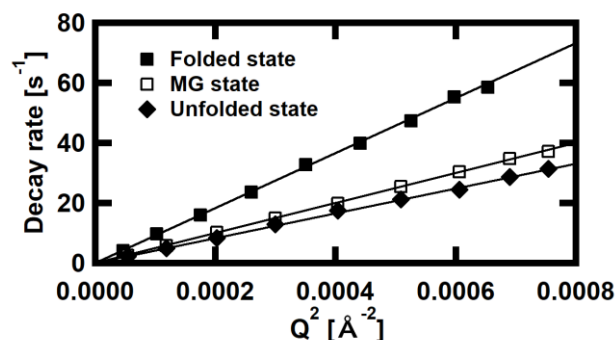


Figure 2. The Q -dependences of the decay rates. The linear fits to the curves are shown.

The translational diffusion coefficients of the folded, MG, and unfolded states were found to be $9.1 \times 10^{-7} \text{ cm}^2/\text{s}$, $5.0 \times 10^{-7} \text{ cm}^2/\text{s}$, and $4.2 \times 10^{-7} \text{ cm}^2/\text{s}$, respectively. These values provide the important information on the extraction of the contribution of the segmental and domain motions in the QENS spectra.

REFERENCES:

- [1] G. Zaccai, *Science*, **288** (2000) 1604-1607.
- [2] K. Henzler-Wildman *et al.*, *Nature*, **450** (2007) 964-972.
- [3] S. Fujiwara *et al.*, *PLOS ONE*, **11** (2016) e0151447.
- [4] S. Fujiwara *et al.*, *J. Phys. Chem. B*, **121** (2017) 8069-8077.
- [5] S.W.A. Provencher, *Comp. Phys. Comm.*, **27** (1982) 213-227.

CO6-12 Characterization of Conformational Deformation-coupled Interaction between Immunoglobulin G1 Fc Glycoprotein and a Low-affinity Fcγ Receptor

S. Yanaka, R. Yogo¹, R. Inoue², N. Sato², M. Sugiyama², and K. Kato

Institute for Molecular Science, National Institutes of Natural Sciences

¹*Graduate School of Pharmaceutical Sciences, Nagoya City University*

²*Institute for Integrated Radiation and Nuclear Science, Kyoto University*

INTRODUCTION: A recently developed integrative approach combining varied types of experimental data has been successfully applied to three-dimensional modelling of larger biomacromolecular complexes. Deuteration-assisted small-angle neutron scattering (SANS) plays a unique role in this approach by making it possible to observe selected components in the complex. It enables integrative modelling of biomolecular complexes based on building-block structures typically provided by X-ray crystallography. In this integrative approach, it is important to be aware of the flexible properties of the individual building blocks.

EXPERIMENTS: Here we examine the ability of SANS to detect a subtle conformational change of a multidomain protein using the Fc portion of human immunoglobulin G (IgG) interacting with a soluble form of the low-affinity Fcγ receptor IIIb (sFcγRIIIb) as a model system. The IgG-Fc glycoprotein was subjected to SANS in the absence and presence of 75%-deuterated sFcγRIIIb, which was matched out in D₂O solution.

RESULTS: Inverse contrast-matching technique enabled selective observation of SANS from IgG-Fc, thereby detecting its subtle structural deformation induced by the receptor binding (Fig.1). The SANS data were successfully interpreted by considering previously reported crystallographic data and an equilibrium between free and sFcγRIIIb-bound forms. Our SANS data thus demonstrate the applicability of SANS in the integrative approach dealing with biomacromolecular complexes composed of weakly associated building blocks with conformational plasticity.

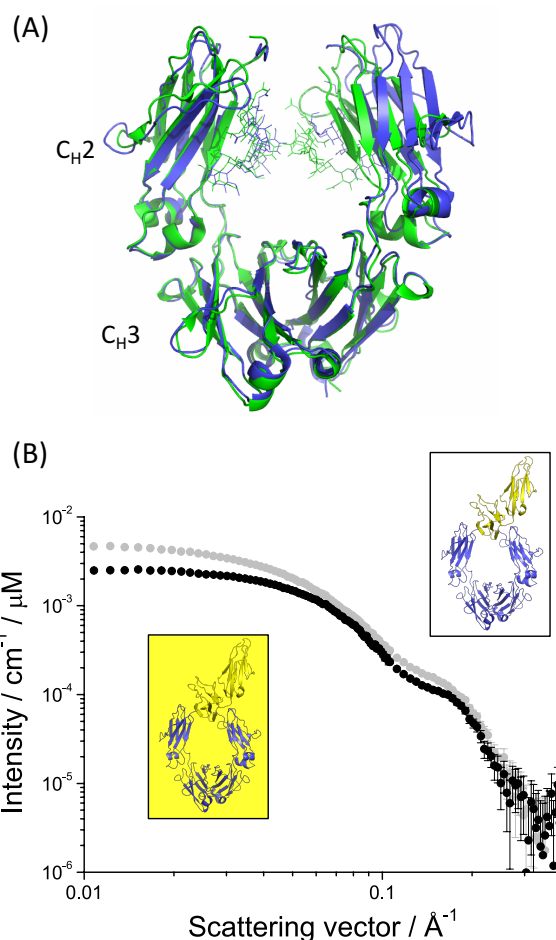


Fig. 1. structural deformation of IgG-Fc induced by the receptor binding

(A) Superposition of crystal structures of Fc in free (PDB code 3AVE) and sFcγRIIIb-bound states (PDB code 1T89).

(B) SANS profiles for Fc in the presence of non-deuterated sFcγRIIIb (gray circles) and Fc in the presence of 75%-deuterated sFcγRIIIb (black circles) in 99.8% D₂O. Graphical models illustrate deuteration (colored gray) of solvent and protein based on the crystal structure of the Fc-sFcγRIIIb complex (PDB code 1T89)

REFERENCE:

[1] R. Yogo *et al.*, *Biochem. Biophys. Rep.* **12** (2017) 1-4.

H. Nakagawa, T. Saio^{1,2}, M. Sugiyama³ and R. Inoue³

Materials Science Research Center, Japan Atomic Energy Agency

¹Graduate School of Chemical Sciences and Engineering, Hokkaido University

²Department of Chemistry, Faculty of Science, Hokkaido University

³Research Reactor Institute, Kyoto University

INTRODUCTION: In structural biology, precise de-termination of three-dimensional structures of proteins has been focused, and the structures with an atom-ic-resolution have given solid platforms to understand their biological functions. Recently, the idea of structural biology has extended beyond the static structural information with atomic resolution, in order to cover more complex and dynamical structures at different levels of space and time resolution. SAXS measurement can observe the solution structure of flexible protein under the physiological conditions [1].

MurD (UDP-N-acetylmuramoylalanine--D-glutamate ligase) is a typical multi-domain protein (Fig.1), which is one of the ATP-driven Mur ligases that are responsible for peptidoglycan biosynthesis. The crystal structure of MurD has been determined, but the ATP-bound form is not determined.

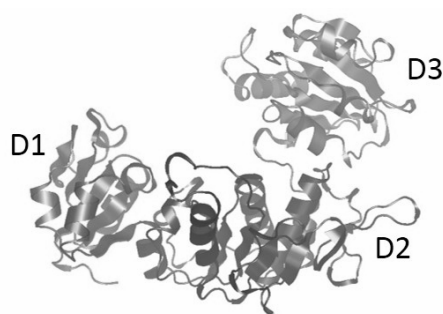


Fig. 1. Multi-domain protein, MurD, which are composed of three domains, D1, D2 and D3.

EXPERIMENTS: MurD were expressed in E. coli strain BL21 (DE3). Small angle X-ray scattering (SAXS) were measured for MurD in ATP-unbound and bound states at the concentration of 5, 10, 20 and 50 mg/ml. The

buffer conditions were 20 mM Tris-HCl at pH=7.2. For the sample of ATP-bound states, AMP-PNP and MgCl₂ were added at the concentration of 2 mM and 5 mM, respectively.

RESULTS: SAXS profiles of MurD were successfully obtained for ATP-bound and unbound states. At the higher concentrations, the inter-particle interaction effects were observed in the profiles. And it was found that under 10 mg/ml, the effect can be negligible. As shown in Fig. 2, SAXS profiles are different between ATP-bound and unbound states, indicating the structural change by ATP binding. The previous NMR measurement predicted that the domain orientation of MurD is changed by ATP binding [2]. And our preliminary MD simulation shows the ATP-dependent structural and motional change of MurD domain, and these results should be consistent with the NMR results. The comparison of the SAXS profiles with the results of the NMR and MD simulation are in progress.

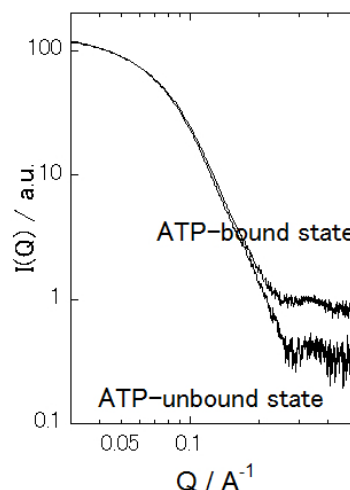


Fig. 2. SAXS profiles in ATP-bound and unbound states of MurD at the concentration of 10 mg/ml.

REFERENCES:

- [1] J. Trehwella *et al.*, Acta Cryst. **D73** (2017) 710-728.
 [2] T. Saio *et al.*, Sci. Rep., **5** (2015) 16685.

CO6-14 Production of Medical Radioisotopes Using Electron Linear Accelerator

S. Sekimoto, T. Ohtsuki

Research Reactor Institute, Kyoto University

INTRODUCTION: A shortage in the supply of ^{99}Mo resulting from the shutdown of reactors used for its production is a global problem. Because ^{99}Mo is an indispensable source of $^{99\text{m}}\text{Tc}$, which is used in nuclear medicine to make diagnoses using techniques such as scintigraphy and single photon emission computed tomography (SPECT), a stable supply of ^{99}Mo is vital. Therefore, production of ^{99}Mo by using neutrons or protons generated in accelerators has been investigated [1–3]. To separate $^{99\text{m}}\text{Tc}$ from ^{99}Mo produced by an accelerator, methods based on sublimation, solvent extraction, and ion-exchange column chromatography have been examined and developed [2,4–6]. In addition, Gopalakrishna et al. have reported the preparation of ^{99}Mo by the $^{100}\text{Mo}(\gamma, n)$ reaction using bremsstrahlung photons [6], followed by conventional solvent extraction using methyl ethyl ketone (MEK) and zirconium (Zr) molybdate gel to separate $^{99\text{m}}\text{Tc}$. According to the regulations of the Japanese pharmacopeia, the extraction using organic materials and the gel method using heavy metal elements such as Zr are not approved for the $^{99\text{m}}\text{Tc}$ -separation methods. Additionally, it is also difficult and impractical to use the sublimation method, which requires complicated and/or large scale devices for the mass-production of pure $^{99\text{m}}\text{Tc}$.

In this work, we carried out the production of ^{99}Mo by the $^{100}\text{Mo}(\gamma, n)$ reaction using bremsstrahlung photons generated in an electron linear accelerator (LINAC), a technique that has not been investigated significantly in Japan. The amounts of ^{99}Mo produced at several electron energies (E_e) were examined.

EXPERIMENTS: Powdered molybdenum oxide of about 20 mg ($^{100}\text{MoO}_3$, 99.01% isotopic enrichment, ISOFLEX, USA) was sealed in a high-purity aluminum foil and shaped into a pellet of 10 mm diameter. Each pellet stacked between the gold foils was enclosed in a quartz tube. The gold foils (10 mm $\phi \times 0.02$ mm thickness) were used as a fluence monitor for bremsstrahlung photons. The stacked samples in the quartz tube were irradiated by bremsstrahlung photons generated by a platinum converter (2 mm thickness) and cooled with running tap water. The irradiation was carried out using the LINAC at the Kyoto University Research Reactor Institute (KURRI). For five $^{100}\text{MoO}_3$ pellets, the accelerator was operated for 5 min with electron energies (E_e) of 21, 25.5, 32, 35, and 41 MeV and mean currents of 60, 44, 90, 34, and 36 μA , respectively. After the irradiation, the five $^{100}\text{MoO}_3$ pellets were weighed and resealed in new (non-irradiated) aluminum foil pieces that were shaped into pellets of 10 mm diameter for γ -ray counting.

The γ rays of ^{99}Mo (740 keV) produced by the $^{100}\text{Mo}(\gamma, n)$ reaction in the irradiated $^{100}\text{MoO}_3$ pellet were measured using a Ge detector at KURRI. Measurements of 400–20,000 s were repeated several times within a

week. The irradiated $^{100}\text{MoO}_3$ pellets were placed at the appropriate distance from the Ge detector surface to maintain a dead time of <10%. The activity of the ^{99}Mo produced in each irradiated $^{100}\text{MoO}_3$ pellet was estimated from the counting efficiency that was obtained from the radioactivity of the mixed standard sources.

RESULTS: The measured activities of ^{99}Mo produced by the $^{100}\text{Mo}(\gamma, n)$ reaction using bremsstrahlung photons, which were generated at E_e 's of 21, 25.5, 32, 35, and 41 MeV at the LINAC, are shown in Fig. 1. The irradiation time, beam current of electrons, and amount of target material ($^{100}\text{MoO}_3$) were normalized to 5 min, 100 μA , and 10 mg, respectively. Generally, the activity of ^{99}Mo increases as the E_e increases. The amount of ^{99}Mo produced by the $^{100}\text{Mo}(\gamma, n)$ reaction has not previously been reported, an exception being the values for E_e of 25 and 35 MeV reported by Sabelnikov et al. [7] and Mang'era et al. [5], respectively. These values can be compared with those obtained by us. By comparing these values, we found an inconsistency between our values and those of the literature that have been normalized to the same irradiation time, beam current of electrons, and amount of target material used in our experiments. The literature values were higher than ours at E_e 's of 25 and 35 MeV by a factor of 2–3. This inconsistency can be explained by the differences in the experimental systems, e.g., converters

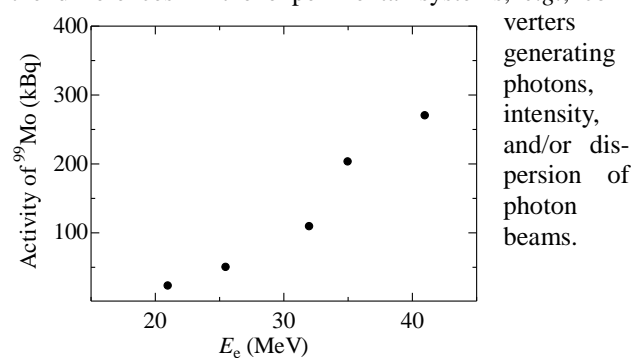


Fig. 1. Activity of ^{99}Mo produced using electron linear accelerator

REFERENCES:

- [1] Y. Nagai *et al.*, J. Phys. Soc. Jpn., **82** (2013) 064201.
- [2] Y. Nagai *et al.*, J. Phys. Soc. Jpn., **83** (2014) 083201.
- [3] K. Nakai *et al.*, Proc. Jpn. Acad. Ser. **B** **90** (2014) 413–421.
- [4] M. Kawabata *et al.*, J. Phys. Soc. Jpn., **84** (2015) 023201.
- [5] K. Mang'era *et al.*, J. Radioanal. Nucl. Chem., **305** (2015) 79–85.
- [6] A. Gopalakrishna *et al.*, J. Radioanal. Nucl. Chem., **308** (2016) 431–438.
- [7] A.V. Sabel'nikov *et al.*, Radiochemistry, **48** (2006) 19–194.

CO6-15 Characterization of Resonance Hybrid of Fe-bound Oxygen in Myoglobin

K. Hasegawa, M. Saito¹, M. Seto¹, Y. Kobayashi¹, T. Ohta², S. Yanagisawa², T. Ogura², Y. Yamamoto, T. Shibata, S. Neya³ and A. Suzuki⁴

Department of Chemistry, University of Tsukuba

¹ Research Reactor Institute, Kyoto University

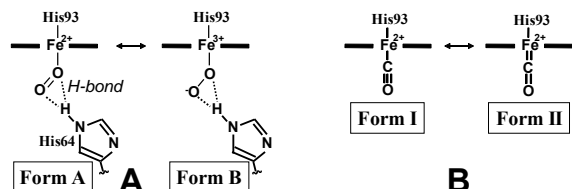
² Graduate School of Life Science, University of Hyogo

³ Graduate School of Pharmaceutical Sciences, Chiba University

⁴ Department of Materials Engineering, Nagaoka National College of Technology

INTRODUCTION: Oxygen (O₂) affinity of myoglobin (Mb) is regulated through heme electronic structure as well as heme environment furnished by nearby amino acid residues. We found that the intrinsic reactivity of heme Fe atom in the protein is affected by the electron density of the heme Fe atom (ρ_{Fe}) in a manner that the O₂ affinity decreases with decreasing the ρ_{Fe} .¹ This finding could be interpreted in terms of the effect of a change in the ρ_{Fe} on the resonance between Form A \leftrightarrow Form B of oxyMb (Scheme 1A). In this study, we measured Mössbauer spectra of oxyMbs reconstituted with Proto, Meso, 3,8-DMD, 7-PF, and 2,8-DPF (oxyMb(Proto), oxyMb(Meso), oxyMb(3,8-DMD), oxyMb(7-PF), and oxyMb(2,8-DPF), respectively) (Figure 1). These heme cofactors differ in the numbers of CF₃, CH₃, and C₂H₅ side chains, and the substitution of strongly electron-withdrawing trifluoromethyl (CF₃) group(s), as side chain(s) of heme cofactors, causes large and stepwise alterations of the heme electronic structure. The formal charges of heme Fe atom in Forms A and B are +2 and +3, respectively (Scheme 1A), and hence the effect of changes in the ρ_{Fe} , due to the chemical modifications of the heme cofactors, on the resonance between Form A \leftrightarrow Form B could be analyzed through the resonance hybrid of the formal charge of heme Fe atom reflected in the quadrupole splitting (QS) determined by the Mössbauer spectra.

EXPERIMENTS: Iron-⁵⁷Fe (95 atom %, Merck) was used to prepare ⁵⁷Fe-enriched heme cofactors. ApoMb was prepared from sperm whale Mb, using the standard procedure, and reconstituted with ⁵⁷Fe-labelled heme cofactors. 2 mM oxyMbs in 50 mM potassium phosphate buffer, pH 7.40, were cooled in liquid nitrogen bath. The Mössbauer measurements were performed at 3-6 K.



Scheme 1. Resonance between the two canonical forms A and B of the Fe-O₂ fragment in oxyMb (A) and that between forms I and II of the Fe-CO fragment in carbon monoxide (CO) adduct of the protein (B). In (A), the formal charges of heme Fe atom in Forms A and B are +2 and +3, respectively. In (B), the resonance is affected by the electron density of the heme Fe atom (ρ_{Fe}).

RESULTS: The Mössbauer spectra of oxyMbs reconstituted with ⁵⁷Fe-labeled native and some chemically-modified heme cofactors (Figures 1) indicated that the heme cofactors are ranked as 2,8-DPF < 7-PF \approx Proto < 3,8-DMD < Meso, in order of increasing QS, although their isomer shifts were similar to each other. The determined QS values correlated well with the stretching frequencies of Fe-bound CO (ν_{CO}) of carbon monoxide (CO) adducts of the proteins (Figure 2). Since the ν_{CO} value is recognized as a sensitive index for the ρ_{Fe} (Scheme 1B),² the plots in Figure 2 confirmed a close relationship between the ρ_{Fe} and the resonance hybrid of the Fe-O₂ fragment (Scheme 1A), which underlays the electronic control of the heme Fe reactivity.

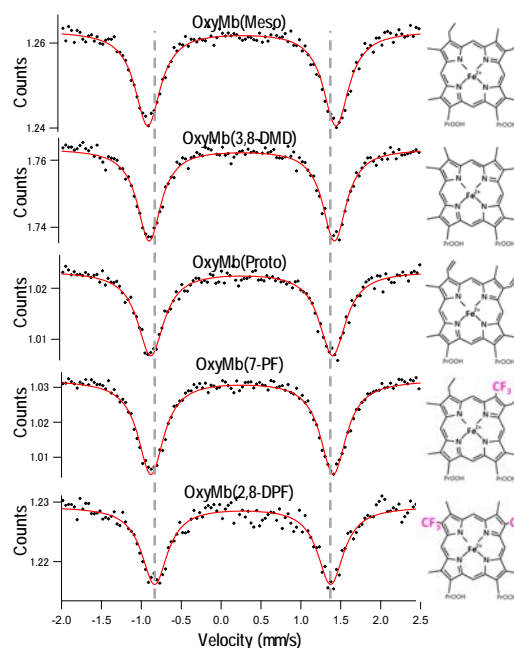


Figure 1. Mössbauer spectra of oxyMbs reconstituted with ⁵⁷Fe-labeled native and chemically-modified heme cofactors at 6 K.

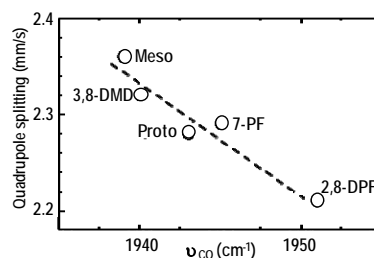


Figure 2. Plots of the quadrupole splittings against the ν_{CO} values of the proteins.

REFERENCES:

- [1] T. Shibata, D. Matsumoto, R. Nishimura, H. Tai, A. Matsuoka, S. Nagao, T. Matsuo, S. Hirota, K. Imai, S. Neya, S. Suzuki, and Y. Yamamoto, *Inorg. Chem.*, **51**, (2012) 11955–11960.
- [2] R. Nishimura, T. Shibata, H. Tai, I. Ishigami, T. Ogura, S. Nagao, T. Matsuo, S. Hirota, K. Imai, S. Neya, A. Suzuki, and Y. Yamamoto, *Inorg. Chem.*, **52**, (2013) 3349–3355.

CO6-16 Potential of Boron Neutron Capture Therapy (BNCT) for Metastatic Bone: Study with Human Breast Cancer-bearing Animal Model

T. Fujimoto, T. Andoh¹, R. Satani¹, M. Suzuki², Y. Sakurai², T. Takata², H. Tanaka² and H. Ichikawa²

Hyogo Cancer Center,
Department of Orthopedic Surgery
¹Faculty of Pharmaceutical Sciences and Cooperative
Research Center of Life Sciences,
Kobe Gakuin University
²Institute for Integrated Radiation and Nuclear Science,
Kyoto University

INTRODUCTION: In recent years, advances in chemotherapy for the treatment of cancer has markedly improved the prognosis of cancer patients. On the other hand, a remarkable increase in the number of cases of metastatic bone cancer has been evident, necessitating the introduction of new methods for treatment of the disease. Bone is vital/essential for supporting the body, in particular when cancer metastasizing to limb bones induces pathological fractures, a drastic decrease in the activity of daily life (ADL) and worsens the quality of life (QOL). Therefore, when metastasis to limb bones reaches the stage of impending fracture, preventive osteosynthesis is carried out for preventing pathological fractures. Nonetheless, since this procedure does not remove the tumor, postoperative radiotherapy for the entire surgical site is requisite for about 2 months — a very invasive procedure, especially for end-stage cancer patients. Therefore, in this study, a newly created human breast cancer-bearing animal model was used to investigate whether BNCT, a minimally invasive and non-surgical procedure, can control bone metastases.

EXPERIMENTS: All animal experiments were carried out according to the regulations of the Animal Care and Use Committee.

(1) Tumor cell line: Human breast cancer cell line MDA-MB-231-luc was cultured in Leibovitz's L-15 with fetal bovine serum in a 5% CO₂ humidified incubator at 37°C.

(2) Producing bone metastasis in the human breast cancer-bearing animal model: MDA-MB-231-luc cells suspended in Matrigel® were transplanted into the tibia of the left hind leg of nude mice. Eight weeks thereafter, the formation of a tumor was confirmed by micro-CT scans.

(3) BNCT in vivo: The mice were divided into two groups.

Under anesthesia and through the femoral vein, the BNCT group and the control group were administered BPA-Fr (24 mg 10B/kg) and saline, respectively. After an interval of 90 min, and according to the biodistribution data of 10B in this animal model as previously described

[1], thermal neutrons (1 MW) were irradiated for 60 min onto the left hind leg of the mice under anesthesia in the heavy water facility at KURRI. Nine weeks after the irradiation, the left hind leg of the animals was observed by imaging techniques. The mice were then terminated and tissue specimens collected immediately and stained with hematoxylin-eosin (HE) for histological analysis.

RESULTS: Imaging studies before BNCT disclosed two type of bone metastasis in the femur: 1) a pathological fracture had already occurred [Fig. 1A] and 2) the tumor was present in the intact femur. The physical dose (Gy) absorbed by the tumor and skin of the BNCT group was 5.0 Gy and 2.0 Gy, respectively. Nine weeks after the irradiation, no abnormality was macroscopically observed in the epidermis at the irradiated site. Imaging analysis revealed tumor shrinkage in metastatic foci in the type-2 BNCT group. Conversely, pathological studies of the type-1 BNCT group disclosed an increase in the tumor mass at the irradiation site [Fig. 1B]. No shrinkage of the tumor mass was observed in the control group. The results suggested that when a pathological fracture occurs, the tumor diffuses to the surroundings of the fracture site through blood, and the tumor is less likely to take up boron at BPA administration; also, that BNCT has no effect on pathological fractures. Therefore, the administration of a boron preparation including BSH may be needed for accumulation in the surrounding tumor cells when a pathological fracture is present.

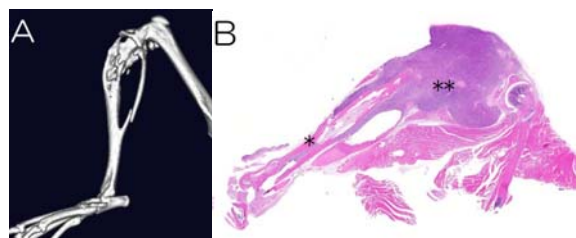


[Fig. 1] A; 3D-CT image of the pathological fracture of left tibia 5days after BNCT.

B; HE staining of left side of mouse model. The pathological study demonstrated the tumor mass extending from the intramedullary to the surface of the tibia. *: cortex of tibia, **: tumor.

REFERENCE:

[1] Biodistribution of p-borono-L-phenylalanine in human breast cancer-bearing bone metastasis animal model for BNCT. T. Fujimoto *et al.* KURRI Progress Report 2016, PR6-2.

CO6-17 Preparation of F1Fo-ATP Synthase as a Whole Body Complex from Bovine Heart for Structural Analysis by Cryo-electron Microscopy and X-ray Crystallography

C. Jiko, A. Uehara, C. Gerle¹, and Y. Morimoto

*Institute for Integrated Radiation and Nuclear Science,
Kyoto University*

¹*Institute for Protein Research, Osaka University*

INTRODUCTION: The mitochondrial F type ATP synthase functions as a mammalian energy transducer for the homeostasis of the living cell. It not only produces ATP to over 90 % during respiration (Boyer, An-nu.Rev.Biochem.,1997), but also plays an important role in the architecture of the inner membrane (Davies et al., PNAS, 2012) and apoptosis cascade (Giorgio et al., PNAS, 2013). In addition, lack of the enzyme may lead to diseases in neuropathology and metabolic disorders. However, to date neither the reaction mechanism of the ATP nor rotational motion of the enzyme is understood in detail, since the tertiary structure of the enzyme has not been clarified at atomic resolution.

Structural analyses of the F-ATP synthase have been going on for over 50 years and lead to two Nobel prizes until now, but they are restricted to the soluble F1 domain and subcomplexes by X-ray crystal structure analysis (Walker, Biochem. Soc. Tran., 2013). There is no report of an intact F-ATP synthase complex. On the other hand, cryo-electron microscopy (cryo-EM) has become a powerful tool for a structure analysis of large macromolecular complexes and can be used as a checking method of purified samples for crystallographic studies. It is essential that a highly homogeneity of the samples should be led to a suitable crystal even a huge and multi-domain complex, an external form and population from them should be verified before set-up crystallization and function analyses. We have prepared the F1Fo ATP synthase complex as a whole body and a dimer forming from bovine heart, and crystallized them. A selection of detergents at a preparation step and application of the GraDeR method for cryo-EM are very useful for the future research. Here, we report a preparation steps of F1Fo ATP synthase in this institute and show TEM images from the prepared samples in order to determine purities of them by use of Mo- or Uranium acetate (Ac-U)- treatment.

EXPERIMENTS: Bovine heart was obtained just after slaughter at Nishinomiya field, and their mitochondria was isolated by the red-green separation process under ultracentrifugation steps with use of the buffer, 40mM HEPES-Na(pH7.4). A density gradient by ultracentrifugation supplied a red component containing the enzymes (Fig.1).

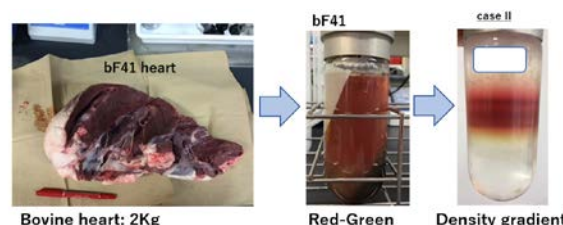


Fig.1 Preparation step from bovine heart to enzyme component

TEM images of the prepared enzyme were obtained by the Hitachi HT7800 operated by 80kV, 10 μ A at the Institute for Protein Research, Osaka University. Ac-U solution after re-batch uranyl reagent was prepared in the restricted hot-lab area in our institute under the conductor and nuclear guidelines.

RESULTS and DISCUSSION: TEM images (Fig.2) under Ac-U stain clearly shows enzyme forms monomer, dimer or tetramer with high contrast, other Mo-stain shows poorly formation of the enzyme. The later could not lead us to decide how preparation steps are suitable for cryo-EM and crystallization.

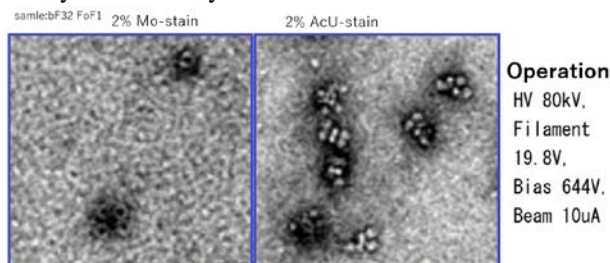


Fig.2 Typical TEM images of the whole enzyme, left: Mo stain, right: uranyl acetate staining.

As seen in the micrograph of the negatively stained purified F1Fo-ATP synthase complexes, the dimeric shape of the complex is well preserved. In addition, a monodisperse distribution, crucial for both 3D crystallization and cryo-EM, is observed.

K. Kimura, T. Mori, T. Takata¹, Y. Sakurai¹, H. Tanaka¹, and K. Takamiya¹

Fujita Corporation

¹*Research Reactor Institute, Kyoto University*

INTRODUCTION: Concrete is very useful material for all of aspects for construction, including infrastructure, office building, and facilities. In addition, concrete for radiation shield is also commonly used in nuclear power plants and radiation related facilities, because of inexpensively, durability, and flexibility. However, once those facilities start to operation, the concrete for the shield are affected by the radiation ray from the operating radiation source in the facilities and activated. For the above situation, low activation concrete [1]-[4] is the one of the way to solve the problem. Especially, boron neutron capture therapy (BNCT) should be effective facilities to apply the low activation concrete, because accelerator based BNCTs, including Cyclotron-based BNCT Epi-thermal Neutron Source (C-BENS) [5], have been developed by several groups in the world right now. Compared to irradiation facilities for X-ray and charged-particle radiation therapy, the neutron yield is much higher at BNCT facility. Thus, the activation of concrete, which is a main structure material of the irradiation facility, becomes an issue from the viewpoints of radiation exposure of medical workers, and the decommissioning of the facility. One of the objects for this research is intended to perform the characteristic estimation of the materials for activation reduction and to confirm its usability at BNCT facility. In 2016, characteristic estimation of a neutron shielding material covering concrete wall surfaces was performed by using an Am-Be neutron source in the same manner in 2014 and 2015 [6], [7], because Kyoto University Reactor (KUR) was not operated. After the re-operation of KUR, we restarted to make the data base for low activation concrete.

METHODS: More than 3000 of raw material for low activation concrete and ordinary concrete were gathered from all over the Japan and oversea, including hundreds of raw materials newly corrected during the period of KUR shut down. Several tens of the materials were chosen among the material stock library shown Fig.1. These materials were crushed to certain size (typically under 1mm or less), and were packed for 0.1 to 0.3 g with special treatment for the irradiation in KUR Pn-2 facility. After the irradiation with 5 to 60 minutes and with the

certain cooling period, these samples were measured by Ge detector one by one. The quantity of the target elements, which were selected by former investigations as Co, Cs, Sc, Fe, and Eu [1]- [4], in each sample were estimated by the comparison of the standard material in the same package for the irradiation.

CONCLUSION: A trial experiment for establishment of material data base for low activation design method by neutron activation analysis with KUR has been conducted from 2017. More than several tens of raw materials were irradiated in KUR and were waited to estimate the target elements, which are important for activation in the concrete shield. These new data enable to support existing data base and introduce the effective low activation shielding design for the BNCT facility as well as other radiation related facilities.

REFERENCES:

- [1] M. Kinno, *et al.*, Journal of Nuclear Science and Technology, Vol. **39**, No.12, 1275-1280, 2002.
- [2] K. Kimura, *et al.*, Proceedings of 8th International Conference on Radiation Shielding, vol. 1, pp.35-42, ANS inc, Arlington, USA, 1994.
- [3] M. Kinno, *et al.*, ANS Radiation Protection and Shielding Conference, pp.673-678, Spokane, USA, 2002.
- [4] K. Kimura, *et al.*, Proc. of Int. conf. on nuclear Engineering (ICONE16), Florida, USA, May 11-15, (2008) 48484.
- [5] H. Tanaka *et al.*, Nucl. Instr. Meth. B **267** (2009) 1970-1977.
- [6] Y. Sakurai, T. Takata *et al.*, KURRI Progress Report 2015 (2016) 97.
- [7] T. Takata, *et al.*, KURRI Progress Report 2016 (2017) 98.

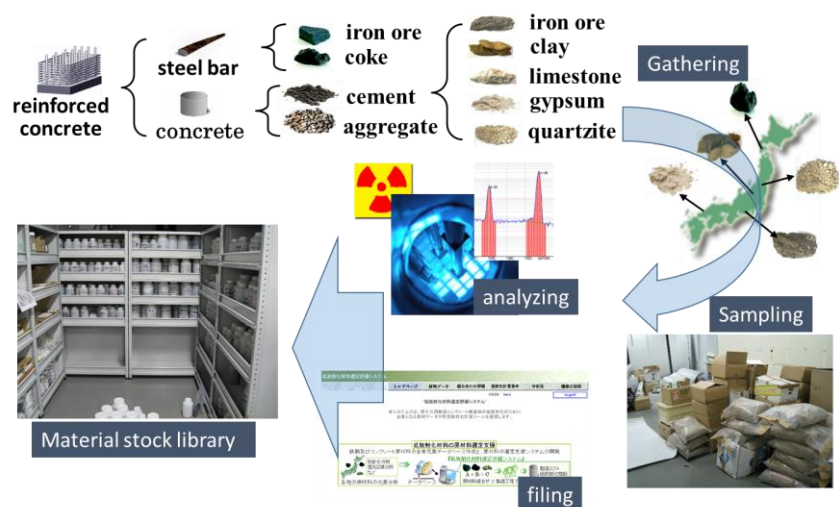


Fig. 1. Data based materials and stock library for low activation concrete.

CO7-2 The Feasibility Study of Eu:LiCaF Neutron Detector for an Accelerator-based BNCT

D. Nio, K. Sakasai, T. Nakamura, H. Nakashima
K. Takamiya¹, S. Tanaka² and H. Kumada²,

Japan Atomic Energy Agency

¹ Kyoto University Research Reactor

² University of Tsukuba

INTRODUCTION: The stability of neutron flux intensity at an accelerator-based BNCT facility is relatively worse than that at a reactor-based one. Therefore, it is necessary to measure the neutron flux precisely in real-time to optimize the patient's exposure dose for the accelerator-based BNCT. However, the neutron flux is so intense (about 10^9 (n/cm²/s)) that the real-time measurement has not been realized yet. Hence we tried to measure the neutron flux with a small detector using a Eu:LiCaF scintillator [1] on the tip of optical fibers, as shown Fig.1. We have carried out some experiments to check the followability and the linearity of the detector to the reactor power at KUR.



Fig. 1 Detector coupled with the optical fiber.

EXPERIMENTS: The experiments were performed at the KUR-SLY where the maximum neutron flux of about 10^{12} (n/cm²/s) is available at the bottom when the reactor power is 1MW [2]. Figure 2 shows the experimental setup for the measurement. The optical output from the Eu:LiCaF scintillator through the optical fibers was properly converted to an electric signal and counted with the counting units. Prior to the measurement, the detector was put into the plastic bottle and loaded to the bottom of the KUR-SLY by two threads. Figure 3 shows the loading of the detector into the KUR-SLY. The measurement was carried out during the power-up of the reactor.

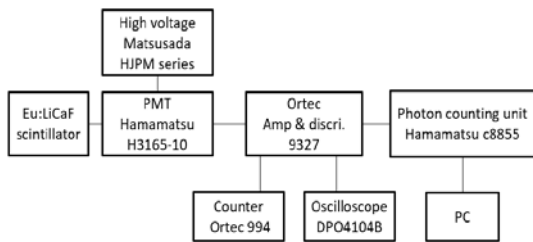


Fig. 2 Experimental setup.

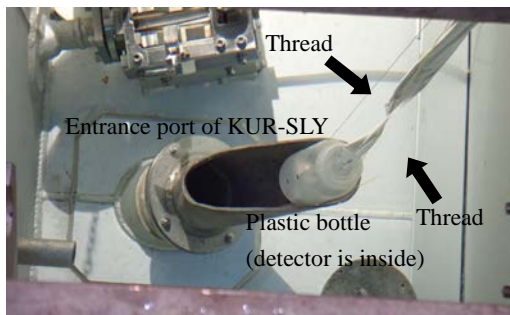


Fig. 3 Loading of the detector into the KUR-SLY.

RESULTS: Figure 4 shows the measured counting rate of the detector during the power up from 20 W to 1 kW. Also shown is a reactor power, where the both counting rate and reactor power were normalized at the average of the maximum values. As the followability to the reactor power from 20 W to 1 kW, the counting rate agrees with the reactor power. Figure 5 shows the counting rate as a function of the reactor power. We can see the good linearity of the counting rate to the reactor power.

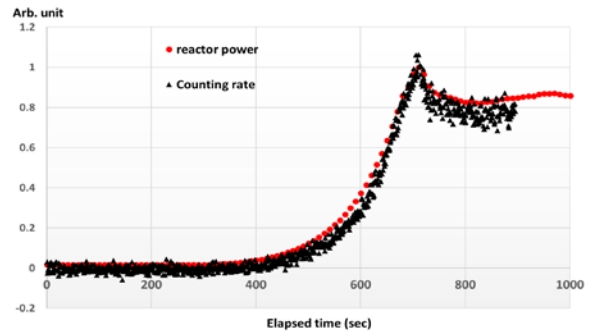


Fig. 4 Detector counting rate and reactor power

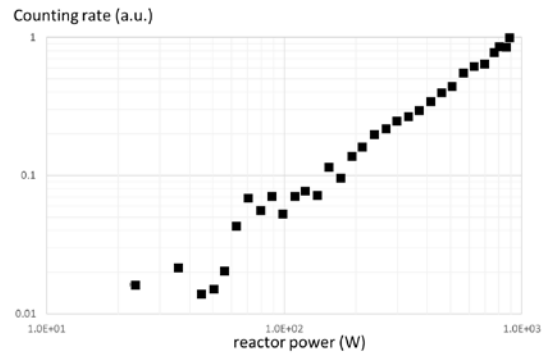


Fig. 5 Counting rate as a function of reactor power

CONCLUSIONS: A small detector using a Eu:LiCaF scintillator has been tested at the KUR-SLY experimental port. The counting rate from the detector has a good linearity and followability to the reactor power from 20 W to 1kW. Based on the results, we are planning to conduct another experiment at the KUR-SLY with a modified experimental setup.

In addition, we will investigate the influence of Cerenkov radiation of which wavelength spreads from 400 nm to 750 nm. Since the scintillation peak of the Eu:LiCaF is about 370 nm, the influence of the Cerenkov radiation should be estimated.

REFERENCES:

- [1] N. Kawaguchi., Doctor Thesis, Tohoku University, <http://hdl.handle.net/10097/56580>
- [2] KUR-SLY <http://www.rii.kyoto-u.ac.jp/JRS/>

CO7-3 Development of *closo*-Dodecaborate-Conjugated Serum Albumins as Novel Boron Delivery Carriers to Tumor for BNCT

H. Nakamura¹, S. Kikuchi¹, K. Kawai^{1,2}, S. Ishii^{1,2}, S. Sato¹, and M. Suzuki³

¹ Laboratory for Chemistry and Life Science, Institute of Innovative Research, Tokyo Institute of Technology

² School of Life Science and Technology, Tokyo Institute of Technology

³ Research Reactor Institute, Kyoto University

INTRODUCTION: Boron neutron capture therapy (BNCT) has been attracting growing interest as one of the minimally invasive cancer therapies. The accelerator-based BNCT is now undergoing phase II clinical study for the treatment of brain tumor and head and neck cancer patients using L-BPA in Japan.

We focused on a serum albumin as a nano biocarrier. Albumin is known to accumulate in malignant and inflamed tissues due to enhanced permeability and retention (EPR) effect. We developed maleimide-functionalized *closo*-dodecaborate (MID; Figure 1) for conjugation to bovine serum albumin (BSA).[1] In this paper, we examined confirmation of BSA-MID conjugation by western blot analysis and SEM image analysis.

EXPERIMENTS:

Conjugation of MID to BSA and Western blot analysis
BSA (0.1 mM) was reacted with MID (1.0 mM) to BSA in PBS (50 μ L) at ambient temperature for 1h. The mixture was subjected to SDS-polyacrylamide gel electrophoresis (PAGE), transferred to polyvinylidene difluoride (PVDF) membrane (GE Healthcare, Buckinghamshire, UK), and immunoblotted with anti-MID antibody.

E-SEM analysis of MID-albumin conjugates

The morphology of MID-albumin conjugates was measured by FE-SEM (Hitachi SEM S-5500, Tokyo, Japan) at an accelerating voltage of 5.0 kV. Dried MID-albumin conjugates were placed on double-side carbon tape and then sputter-coated with gold-palladium in an argon atmosphere using a Hummer I sputter coater (Anatech Ltd. St. Alexandria, VA, USA).

RESULTS: The conjugation reactions of MID to BSA were carried out in PBS buffer (pH 7.4) at room temperature for 1 h and the resulting MID-albumin conjugates were detected by Western blot analysis using anti-MID antibody. MID was conjugated to BSA not only at SH free Cys residue but also at an amino group of Lys residue. In general, common maleimide compounds do not react with a nucleophilic amino group of Lys residue that is protonated under physiological conditions (pH 7.4). In the case of MID, MID contains negatively charged boron

cluster in the molecule associated with sodium counter cations. In the local environment in proteins, the protonated amino group of Lys is probably deprotonated with the negatively charged boron cluster to induce the nucleophilicity. Therefore, the Michael reaction proceeded between the amino group of Lys residue and the maleimide moiety of MID.[2,3]

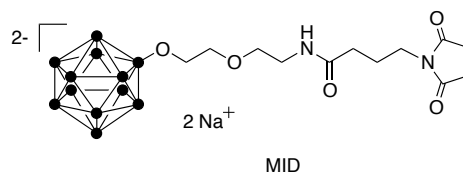


Fig. 1. Structures of maleimide-functionalized *closo*-dodecaborate (MID)

Nanoparticles albumin-bound technology using high-pressure homogenizers has been used to make albumin nanoparticles of 100–200 nm. In particular, Abraxane® was reported to form albumin-paclitaxel nanoparticles with a mean particle size of 130 nm. In the current study, a self-assembly method was used to make BSA-MID nanoparticles. As shown in Figure 3, albumin-MID conjugates were found to be almost spherical with size distribution from 36 to 52 nm in diameter by field-emission scanning electron microscopy (FE-SEM) analysis.

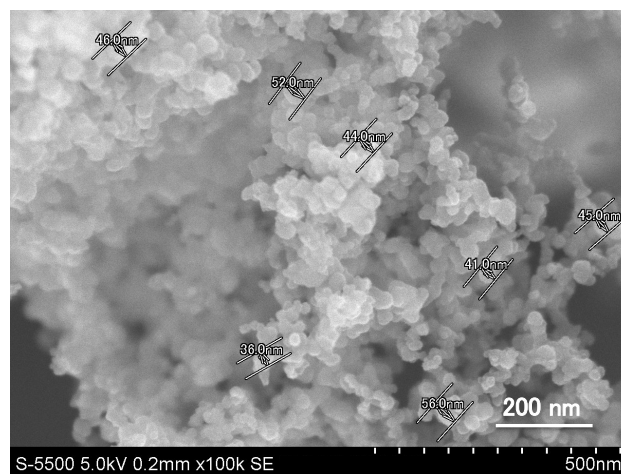


Fig. 2. FE-SEM images of albumin-MID conjugates.

REFERENCES:

- [1] S. Kikuchi, *et al.*, J. Control. Release, **237** (2016) 160-167.
- [2] H. Nakamura, Isotope News, **753** (2017) 2-7.
- [3] H. Nakamura, BIO Clinica., **32**, (2017) 669-703.

R. Ubagai, W. Kurosawa, K. Matsumoto, Y. Suga, Y. Kitahara, Y. Sakurai¹, K. Mouri¹, D. Novriana¹, M. Yanagawa², T. Nomoto³, N. Nishiyama³, R. Terai⁴, S. Dowaki⁴, T. Nagasaki⁴, H. Yanagie¹, H. Takahashi⁵, H. Tanaka⁶, Y. Sakurai⁶, K. Ono⁶ and M. Suzuki⁶

Institute for Innovation, Ajinomoto Co., Inc.

¹Niigata University of Pharmacy and Applied Life Sciences

²Obihiro University of Agriculture and Veterinary Medicine

³Tokyo Institute of technology

⁴Graduate School of Engineering, Osaka City University

⁵Graduate School of Engineering, The University of Tokyo

⁶Research Reactor Institute, Kyoto University

INTRODUCTION: The principle of cancer cell destruction in boron neutron capture therapy (BNCT) is due to the nuclear reaction between ¹⁰B and thermal neutrons to release alpha-particles (⁴He) and lithium-7 ions (⁷Li) after delivery of ¹⁰B atoms to cancer cells selectively. The ⁴He kills cells in the range of 10 μm from the site of ⁴He generation, so the BNCT is prospective as low invasive cancer therapy.

Many clinical studies has been performed using *p*-boronophenylalanine (¹⁰BPA) and sodium borocaptate (¹⁰BSH) as neutron capture agents. These boron compounds show superior selective tumour accumulation property, but low tumour retentivity, so administration several hours before the radiation and persistent administration are necessary for effective BNCT. We already had reported that boron cluster conjugated polymer which had tumour selectivity and retentivity showed the anti-tumour effects by BNCT in tumour bearing mice [1].

In this study, we synthesized the novel derivative of boron cluster conjugated polymer, and evaluated the anti-tumour effects by BNCT.

EXPERIMENTS: We prepared the tumour bearing mice model after injection of CT26 mouse colorectal cancer cells (3 x 10⁶ cells) into the right femoral region subcutis of the female Balb/c mice. Nine days after tumour inoculation, boron cluster conjugated polymer BN2017 (17.1 mg[¹⁰B]/kg) as tested compound, fructose chelate of ¹⁰BPA 300 mg/kg (14.4 mg[¹⁰B]/kg), or ¹⁰BSH 100 mg/kg (57 mg[¹⁰B]/kg) as a positive control was dissolved in saline and administrated by tail vein injection under anesthesia in CT26 mouse tumour bearing models (each group n=3).

To evaluate the selective accumulating tendency of boron compound, we measured ¹⁰B concentration in tumour, normal liver tissue, kidney tissue, or blood after 2 hours injection in the group of ¹⁰BPA and ¹⁰BSH, or after 2 and 24 hours injection in the group of BN2017. We firstly treated ashing. Briefly, the twenty to fifty mg weighted tissues except the blood after freeze crushing, and 0.1mL of blood were heated at one hour by 50°C,

followed at two hour by 90°C, in each 60% nitric acid water solution. After filtration of insoluble matter, we diluted ashing samples to 20 times with ion exchanged water and assayed quantity of ¹⁰B atoms using ICP-MS.

RESULTS: As shown in Figure 1, it was suggested that the BN2017 has high tumor retentivity, because the intratumoral boron concentration increased, and blood boron concentration decreased in the manner of time course until 24 hours in the BN2017 administrated group.

Concerning to the comparison of the boron concentration in ¹⁰BPA or ¹⁰BSH group 2 hours after injection, and in BN2017 group 24 hours after injection, the intratumoral boron concentration of the BN2017 group was higher than the groups of ¹⁰BPA or ¹⁰BSH administrated, and it exceeded 50 ppm. The boron concentrationratio in tumor / blood (T/B) between ¹⁰BPA or ¹⁰BSH and BN2017 was equivalent, but hopefully, it is expected that the T/B ratios in BN2017 group increase 24 hours after administration by the changes of concentration in Fig. 1.

Therefore, it is expected that BN2017 can be a novel practical boron compound characterized with selective accumulation activity, intratumoral retentivity, and high T/B ratio by administrating on an appropriate timing.

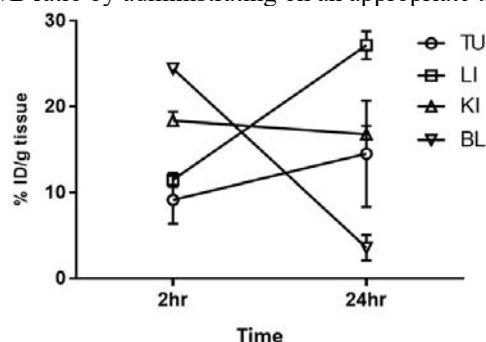


Fig. 1. Tissue distribution profiles of BN2017 (n =3, 17.1 mg[¹⁰B]/kg). (TU: tumor, LI: liver, KI: kidney, BL: blood)

Table 1. Boron level (ppm) in each tissue of tumor-bearing mice after injecting BPA, BSH and BN2017.

	Boron level (ppm)		
	BPA (2 hr after i.v. administration)	BSH (2 hr after i.v. administration)	BN2017 (24 hr after i.v. administration)
Tumor	13.2	13.3	55.4
Liver	4.4	35.5	102
Kidney	10.4	25.4	63.2
Blood	4.3	29.6	13.7
Tumor/blood ratio	3.1	0.45	4.0

REFERENCE:

[1] P. Mi, *et al.*, J. Control. Release. **254** (2017) 1-9.

N. Kamitani, Y. Kawata, Y. Sakurai¹, M. Suzuki¹ and J. Hiratsuka

Department of Radiation Oncology, Kawasaki Medical School

²*Research Reactor Institute, Kyoto University*

INTRODUCTION: Advanced head and neck carcinoma (AHNC) and recurrent head and neck cancer (RHNC) are often radio-/chemo-resistant and show extensive growth, requiring a wide resection including surrounding normal tissues. To avoid severe impairment of head and neck structures, it is necessary to explore new treatment for AHNC. Mishima first proposed employing BNCT for malignant melanomas utilizing the specific melanin synthesis activity of melanoma cells¹⁾. Kato et al.²⁾ began BNCT using both BSH and BPA for recurrent parotid gland carcinoma for the first time and reported excellent preliminary results. On the basis of the encouraging results of their pioneering clinical trial, our many years' experience with melanoma BNCT and the trend toward emphasizing the quality of life after treatment, we also began treating our patients with BNCT using BPA alone^{3,4)}.

BPA is known as a renally excreted drugs and have been reported no toxicity before. Sometimes the inflammation of the urinary bladder is occurred after undergoing BNCT, cause of BPA forming crystals damaging urinary mucosa. Therefore, hydration after BNCT is recommended as soon as possible.

This report is a summary of severe adverse effect that developed acute renal failure after BNCT in 2017.

EXPERIMENTS: Two RHNC patients developed acute renal failure after BNCT. One is nasal cancer and the other is oropharynx cancer, they have no medical history of renal dysfunction. The last medical examination including blood tests was one week before BNCT date and they were conformed no abnormality in renal function such as serum creatinine (Scr) <1.0 mg/dL and estimate glomerular filtration rate (eGFR) >65. The day of BNCT, physical conditions of patients seemed no change from the one presented in the last examination. BPA was dripped administered to the patients according to schedule, and BNCT was undergoing without difficulties. After starting neutron irradiation, the blood boron level at second period was announced and found that the level is higher than one at second period that never expected usually. Although blood boron level at the end of BNCT is less than one at second period in general, in these cases, the opposite result was shown.

In the following day of BNCT, patients were developing anuria, and blood test showed higher Scr (>4.0 mg/dL) and lower eGFR (<20) than before treatment. A computed tomographic scanning (CT) of patients' abdomen was taken immediately and found many small high ab-

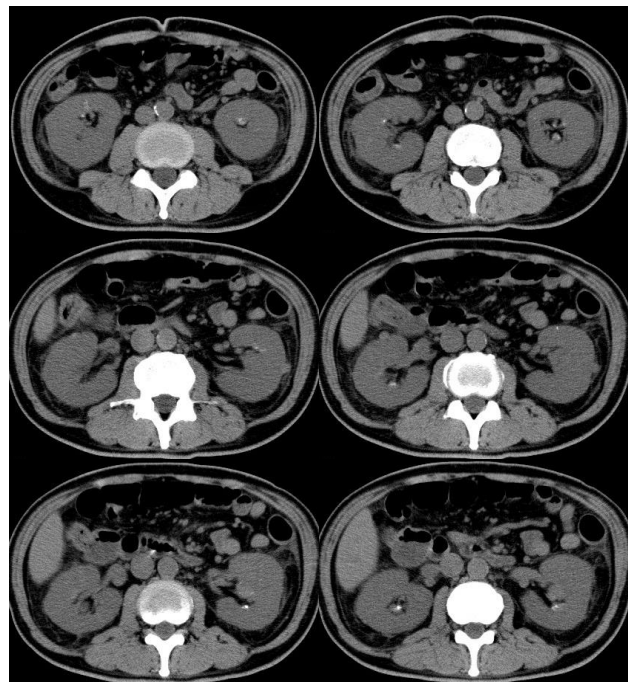


Figure 1. Crystals of BPA depositing kidney.

sorption range in kidney (Fig. 1). The further examination determined that small lesions deposit on renal calyx are crystals of BPA, and patients turned to acute renal failure. The cause of acute renal failure was not only postrenal failure by BPA crystals but also based on appearance of prerenal failure such as severe dehydration which was induced by tumor preventing oral intake or molecular targeted drugs associated diarrhea. Patients were rehydrated by an intravenous drip and used diuretic drugs, for four to five days later, levels of Scr and eGFR were improved to normal range. Hemodialysis for salvation was considered at first but never went at this time.

RESULTS: Patients with poor oral intake have possibility of complicating an acute renal failure after BNCT. To hydrate adequately before/after BNCT will help to prevent severe renal dysfunction from patients.

REFERENCES:

- [1] Y Mishima. Neutron capture treatment of malignant melanoma using 10B-chlorpromazine. *Pigment Cell Res.*, **1**(1973) 215-221.
- [2] I Kato, *et.al.* Effectiveness of BNCT for recurrent head and neck malignancies. *Applied Radiation and Isotopes* **61** (2004) 1069-1073.
- [3] T.Aihara, *et al.* First clinical case of boron neutron capture therapy for head and neck malignancies utilizing 18F-BPA PET. *Head and Neck* **28** (2006) p850-855.
- [4] T.Aihara, *et al.* BNCT for advanced or recurrent head and neck cancer. *New Challenges in Neutron capture therapy.* : 2010 25-29.

CO7-6 Boron Neutron Capture Therapy Combined with Early Successive Bevacizumab Treatments for Recurrent Malignant

S-I. Miyatake¹, H. Shiba, S. Kawabata, T. Kuroiwa², N. Kondo, Y. Sakurai, M. Suzuki³, and K. Ono⁴

¹Cancer Center, Osaka Medical College
²Department of Neurosurgery, Osaka Medical College
³Faculty of Engineering, Toyama University
⁴Research Reactor Institute, Kyoto University

INTRODUCTION: Recurrent malignant gliomas (RMGs) are difficult to control, and no standard protocol has been established for their treatment. At our institute, we have often treated RMGs using a form of tumor-selective particle radiation called boron neutron capture therapy (BNCT). However, despite the cell-selectivity of BNCT, brain radiation necrosis (BRN) may develop and cause severe neurological complications and sometimes death. This is partly due to the full-dose X-ray treatments usually given earlier in the treatment course. To overcome BRN following BNCT, recent studies have used bevacizumab (BV). We herein used extended BV treatment beginning just after reactor-based BNCT to confer protection against or ameliorate BRN, and evaluated; the feasibility, efficacy, and BRN control of this combination treatment.

MATERIALS and METHODS: Two cohorts were included in this study. The first cohort was treated with BNCT between June 2013 and May 2014, followed by successive BV treatments. The second cohort was treated with BNCT between August 2017 and December 2017, followed by successive BV treatments. The first cohort is composed of 7 patients with RMGs (4 grade 4 and 3 grade 3 cases). The second cohort was composed of 6 patients with RMGs (5 grade 4 and 1 grade 3 cases). They were followed-up to April 2018. The Kyoto University Reactor did not work between these 2 cohorts due to renovation.

RESULTS: Median overall survival (OS) and progression-free survival (PFS) after combination treatment were 15.1 and 5.4 months, respectively in the 1st cohort. Median OS and PFS in the second cohort was not reached. The OS data was compared with the class of recursive partitioning analysis (RPA) for RMG as advocated by Carson et al. in a 2007 article in the Journal of Clinical Oncology[1]. RPA classification is the stratified prognosis grouping as shown in Fig. 1. In the 1st cohort, in one case, uncontrollable brain edema occurred and ultimately led to death after BV was interrupted due to meningitis. In 2 other cases, symptomatic aggravation of BRN occurred after interruption of BV treatment. No BRN was observed during the observation period in the other cases. CTCAE grade 2 and 3 proteinuria occurred in two cases and necessitated the interruption of BV treatments. In the second cohort, no apparent BRN and adverse event occurred. Totally 11 cases' OS in both cohorts were compared using JCO's RPA classification. Nine out of 11 cases showed longer OS in comparison with corresponding JCO's RPA classes (Table 1). Representative MR images of Case 7 were shown in Fig. 2 and 3.

CONCLUSION: BNCT followed by BV treatments well-prevented or well-controlled BRN with prolonged OS and acceptable incidence of adverse events in our patients with RMG.

Fig. 1 RPA in JCO (Carson et al. in a 2007 article in the Journal of Clinical Oncology[1].)

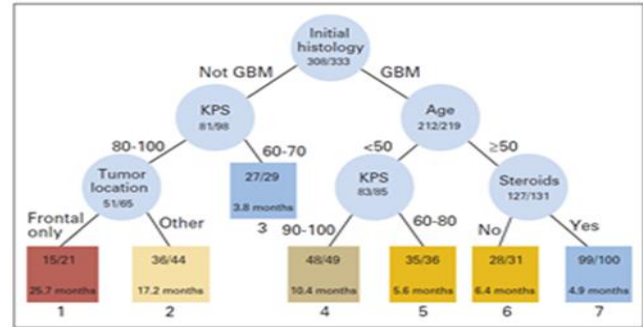


Fig. 2 Case 7 periodic change of MRI

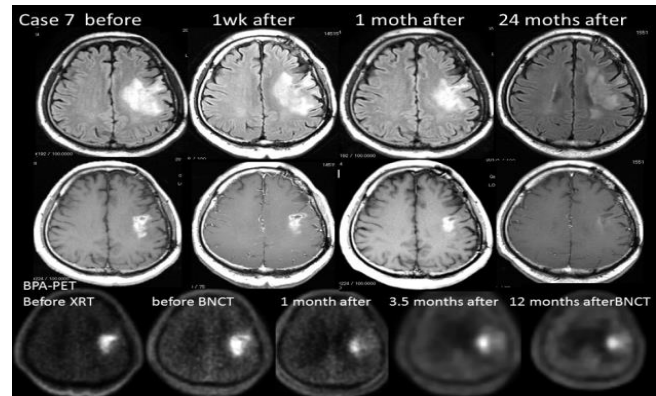


Fig. 3 Worsening of brain radiation necrosis in Case 7 After discontinuation of BV



Table 1

	WHO grade	RPA*1	mOSin JCO*2	OS*3	PFS*4	AE*5
Cohort 1						
case 1	4	7	4.9	15.1	3.1	PU*6 grade1
case 2	4	3	3.8	7.5	5.4	-
case 3	3	2	17.2	38	19.5	PU grade2
case 4	3	1	25.7	57(alive)	NP*7	PU grade1
case 5	4	7	4.9	11	5	-
case 6	4	7	4.9	4.4	NA*8	meningitis
case 7	3	3	3.8	47(alive)	47	PU grade3
cohort 2						
case 8	3	3	3.8	8(alive)	4.7	PU grade3
case 9	4	7*9	4.9	8(alive)	N8	
case 10	4	7'	4.9	6(alive)	3.7	
case 11	4	5	5.6	6(alive)	NP	
case 12	4	5	5.6	55	3	
case 13	4	7'	4.9	6(alive)	NP	

*1RPA :recursive partitioning analysis
 *2 mOSinJCO:median overall survival in J Clin Oncol[1]
 *3OS :overall survival from BNCT
 *4PFS :progression free survival assessed by RANO criteria
 *5AE :adverse event
 *6PU :proteinuria
 *7NP :no progression
 *8NA :not applicable
 *9 7' RPA 7': recurrence after BV treatment

REFERENCE:

[1] Carson KA et al., J Clin Oncol 25 (2007) 2601-2606.

CO7-7 Research on Pretreatment or Concomitant Drug to Augment Therapeutic Effect of BPA-BNCT

M. Suzuki and H. Tanaka
Research Reactor Institute, Kyoto University

Introduction

We have reported that high dose of L-phenylalanine preloading reduce the uptake of L-4-dihydroxy-borylphenylalanine (L-BPA) in the brain relative to the tumor leading to the increase of BPA accumulation ratio of tumor to brain. The aim of this study is to search another pre-treatment drug to reduce L-BPA uptake in the normal organs especially in the dose-constraint organ in BPA-BNCT.

In this study, the measurement of boron concentration in the tumor and normal tissues is essential component. The boron concentrations in the tissues are measured by prompt gamma ray spectroscopy (PGA) and inductively coupled plasma atomic emission spectroscopy (ICP-AES). In the both methods, the sample volume to measure the boron concentration is greater than 300-500 mg. To get the blood greater than 500 mg, the mice should be sacrificed. To monitor the change of the boron concentration in the blood after the administration of boron compound at one mouse, it is important to measure the boron concentration in the blood less than 1 to 10 mg.

We developed a new device to measure the boron concentration in the blood less than 1 mg. In this report, we present preliminary results of the experiments using the new device.

Materials and methods

New device

We have developed a device which has eight well (<10 μ l) with upper side made by CR-39 film on the plate. CR 39 film is a particle track detector.

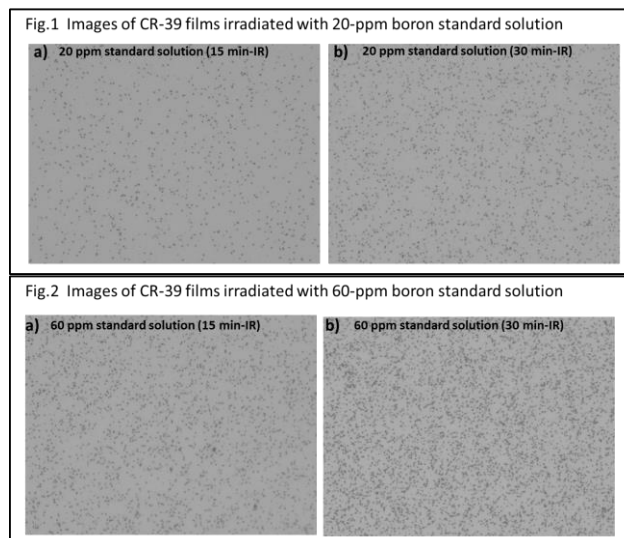
Experimental protocols

The aim of the preliminary experiment is to optimize the irradiation condition for the standard curve to measure the boron concentration. Boron-containing standard solutions of 20, 40, 60 and 80 ppm were applied into 8 wells at the volume less than 10 μ l on the four devices, separately. The devices were irradiated with thermal neutron beam in two conditions of 1.1×10^{12} n \cdot cm $^{-2}$ and 2.2×10^{12} n \cdot cm $^{-2}$, respectively. After irradiation, the devices was etched by a 6N NaOH solution for 1 h at 65 $^{\circ}$ C. The etched pits were observed by a microscope with a magnification of 40 times. The number of pits was counted automatically using the software installed in the analyzing system of the microscope. The average of pit

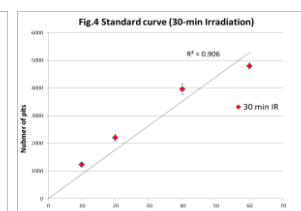
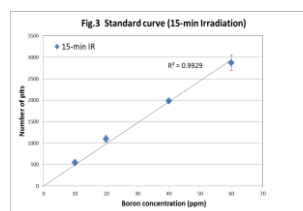
number was calculated after the smallest and the largest pit numbers were excluded.

Results

Figures 1 and 2 show the images of CR-39 films irradiated with 20 ppm boron standard solution for 15 min and 60 ppm boron standard solution for 30 min. Visually, the density of pit was increased in proportion to boron concentration and irradiation time (neutron intensity).



Figures 3 and 4 show the standard curve yielded by two irradiation conditions (15-min and 30-min irradiation). The curve obtained by 15-min irradiation show a remarkable agreement with linear approximation ($r^2=0.9929$). The curve obtained by 30-min irradiation shows poor agreement with linear approximation compared with that by 15-min irradiation ($r^2=0.906$) due to overlaps of pits by combination of 60-ppm solution and intensity of 2.2×10^{12} thermal neutron fluence.



We will repeat the experiments to optimize the irradiation condition and use this new device for measurement of boron concentrations in small sample size less than 1-10 mg.

M. Suzuki, H. Tanaka, Y. Sakurai, N. Kondo, Y. Tamari and T. Takata

Research Reactor Institute, Kyoto University

Introduction

Boron neutron capture therapy (BNCT) has been applied mainly for the treatment of locally recurrent malignant brain tumors or head and neck cancers in the irradiated region. The outcomes of the clinical BNCT studies on BNCT for both tumors have been reported to be promising in some studies.

Clinical trials using accelerator-based (AB)-BNCT system are currently in progress. Since the AB-BNCT system is much compact compared with a research reactor, the system can be installed in the existing medical institutes. The AB-BNCT system in the hospital is available to more patients suffering from malignant tumors compared with the BNCT system using research reactor. Lung cancer, breast cancer and hepatic tumors including hepatocellular carcinoma and multiple metastatic tumors are more common than malignant brain tumors and head and neck tumors.

In this study, for BNCT to apply more common cancer such as lung cancer, breast cancer and hepatic tumors, the effect of BNCT irradiation on normal organs including lung and liver was investigated. These normal tissues are irradiated in the treatment of lung cancer, breast cancer and hepatic tumors with BNCT. Kyoto University Research Reactor (KUR) reworked at the end of August following the long period of operation stopping. Therefore, the research on the effect of BNCT on the normal lung is still ongoing and that on the normal liver just started. The preliminary results of the study on normal lung not liver were reported.

Materials and methods

Experimental animals

Twelve- to thirteen-week-old female C3H/He mice were used for this study. All procedures for animal experiments were carried out in accordance with the regulations of Kyoto University Research Reactor Institute regarding animal care and handling.

Experimental protocols

In this study, the radiobiological effectiveness of high linear energy transfer (LET) irradiation by $^{10}\text{B}(n,\alpha)^7\text{Li}$ reaction on normal lung tissues is investigated in comparison to that of X-ray.

Three types of irradiation carried out in this study were as follows, X-ray irradiation, thermal neutron beam irradiation and BNCT-irradiation using p-boronophenylalanine-fructose complex (BPA-F). In each irradiation, the whole lung was irradiated with

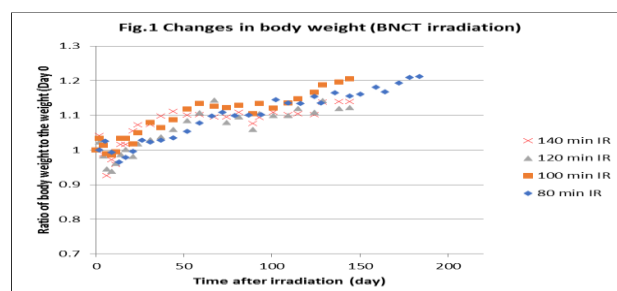
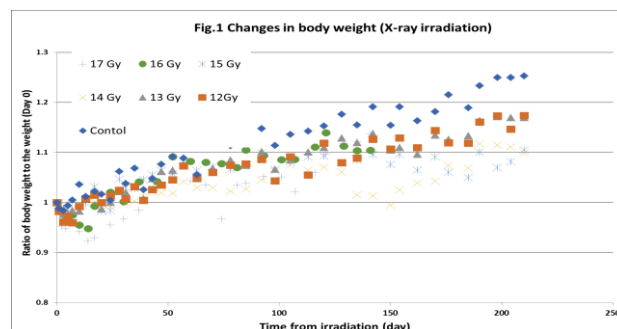
shielding other part of the body. In X-ray-irradiation, anesthetized mice were confined in 1mmPB box with 25x20 mm-sized window. The whole thoracic put within the window was irradiated with 150keV X-ray at 1.16 Gy min^{-1} . In thermal neutron beam irradiation, mice was held within a specially designed acrylic cage at the flux of $3.73\text{E}+10 \text{ cm}^{-2}\cdot\text{min}^{-1}$. LiF tiles (50-mm thick) were used to shield parts of the body other than the chest. In BNCT-irradiation, BPA-F was subcutaneously injected in each mouse at the dose of 500 mg/kg. Irradiation was started at two hours after the injection of BPA-F. Eight- to nine mice were used for each data point.

At two or three days' intervals during two months from the irradiation and weekly intervals after two months, the mice were weighted and carefully observed.

Results

In X-ray treatment, mice were irradiated with a single dose (12 to 17 Gy). In BNCT treatment, mice were sorted in four groups (80, 100, 120 and 140 min-duration groups). Thermal neutron beam irradiation had not been carried out due to less allocation of the experiment.

Figures 1 and 2 shows the changes in body weight after irradiation in the X-ray irradiation group and BNCT irradiation group.



One or two mice died at 3 to 6 months after irradiation in 15,16, and 17 Gy X-ray irradiation groups. Survival time in the each treatment group will be analyzed.

S. Satoh, K. Mori¹, Y. Yoshino¹, M. Sakaguchi, T. Seya, T. Otomo and H. Oshita

Accelerator Laboratory, KEK

¹ Research Reactor Institute, Kyoto University

INTRODUCTION: In this research, we are developing two-dimensional position sensitive detector [1] and neutron scintillator detector [2] for neutron scattering experiments. We are also developing alternative detectors for a ³He gas detector. In this fiscal year, a detector system combining neutron scintillator and wavelength shift fiber, which was a fundamental research, was verified.

A ZnS/⁶LiF (ZnS) scintillator, which is most frequently used in neutron scintillators, has low gamma ray sensitivity with high light emission amount. However, because of an opaque scintillator, it is not made thick and has low detection efficiency. Because lights shining inside are difficult to emit outside, there are many attenuated small signals, which make a bad characteristic in a pulse height analyze (PHA) distribution. In order to solve these problems, we developed a fiber multilayer ZnS (FMZ) detector and evaluated effects of it.

EXPERIMENTS: Experiments of the FMZ detector were carried out using the B-3 beam line. A neutron efficiency of up to four sheets of ZnS which are sandwiched by five planes of wavelength shift fiber was evaluated. The efficiency compared to a standard ³He detector was determined. An effect of both sides receiving of ZnS scintillator was also evaluated.

RESULTS: Figure 1 shows the neutron detection efficiency of the multilayer ZnS scintillator. The lines of 0.45 mm thick ZnS, 0.25 mm thick ZnS and these calculations are drawn. These lines of the ZnS are very good fitting with the calculated lines, assuming that the efficiency of the 0.45 mm thick is 33% and the 0.25 mm thick is 23%, respectively. The neutron detection efficiency of four sheets of the 0.45 mm thick has been obtained 82%, and the efficiency of the 0.25 mm thick has been obtained 64%.

Figure 2 shows a PHA distribution of both sides and single side receiving-lights of the 0.25 mm thick ZnS. It was confirmed that the PHA distribution of the opaque scintillator improves on the both sides receiving than on the single side receiving. The detection efficiency improved by 27%, and a clear bulge appeared in the PHA distribution.

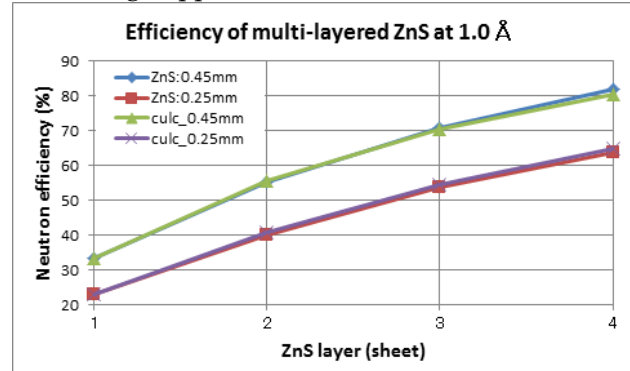


Fig. 1. Neutron detection efficiency of multi-layered ZnS scintillator.

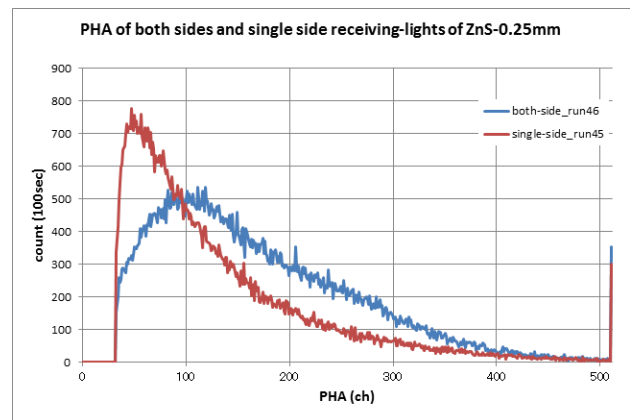


Fig. 2. PHA distributions of both sides and single side receiving-lights of a ZnS scintillator.

REFERENCES:

- [1] S. Satoh, Development of wide area detector for the 2012 model of the ⁶Li time analyzer neutron detector system, *in UCANS-V 2015* DOI 10.1393/ncc/i2015-15197-7.
- [2] S. Satoh, Fiber multilayered ZnS position-sensitive neutron detector with high detection efficiency, *in ICNS2017* DOI 10.1016/j.physb.2018.03.011.

CO8-2 Multi-element Analysis of Cultivated Oysters by Neutron Activation Analysis

M. Fukushima, A. Chatt¹, T. Maeda

Faculty of Science and Engineering, Ishinomaki Senshu University

¹ Trace Analysis Research Centre, Department of Chemistry, Dalhousie University

INTRODUCTION: Japanese cultivated oysters were collected from six different locations in Ishinomaki Bay in 2015 May. To study any possible seasonal variation, oyster samples were also collected every month from April to September from one of these cultivation areas. Bioaccessible trace element levels in soft tissues of oysters were also estimated by using an AOAC method.

EXPELIMENTAL: To study locational variation of trace elements, cultivated oysters were collected from six different bays in 2015 May; Takenoura Bay, Shizugawa Bay, Nagatsura-Hama, Ogatsu Bay, Ohishi-Hama, and Obuchi Bay in Miyagi Prefecture. Also, to study seasonal variation, one year old and two years old oysters were collected every month from April to September in 2015 from Higashimatsushima. Soft tissues were separated from shells of 5 oysters, washed with tap water, separated into gills, mantles, muscles, and hepatopancreas. Each organ was freeze dried, pulverized, and irradiated for 1 h in the Kyoto University Reactor, Japan. Gamma-ray spectra of the irradiated samples were recorded after one-month decay for 20-30 min using a Ge detector system. Levels of Ag, Co, Cr, Fe, Rb, Sc, Se, and Zn were obtained using ^{110m}Ag, ⁶⁰Co, ⁵¹Cr, ⁵⁹Fe, ⁸⁶Rb, ⁴⁶Sc, ⁷⁵Se, and ⁶⁵Zn, respectively. The instrumental neutron activation analysis (INAA) method used was validated using NIST 1566b Oyster Tissue, NIST SRM 1573a Tomato Leaves, and NRCC TORT-1 Lobster Hepatopancreas certified reference materials.

Bioaccessible trace element levels in soft tissues of oysters were also estimated by using an AOAC method. Briefly, about 1 g of dried oyster soft tissue powders was incubated with α -amylase, protease, and amyloglucosidase one after another. Water soluble dietary fiber was filtered from the undigested residue after adding ethanol, and both fractions were analyzed by INAA.

RESULTS: Three SRMs and one CRM were analyzed and data for two materials are shown in Table 1.

Table 1. Analysis of SRM and CRM.

Element	NIST SRM 1573a Tomato Leaves (mg/kg)		NRCC TORT-1 Lobster Hepatopancreas (mg/kg)	
	This work	Agency values	This work	Agency values
Ag	---	0.017*	9.82±1.03	---
Co	0.57±0.05	0.57±0.02	0.38±0.02	---
Cr	1.90±0.15	1.99±0.06	2.4±0.4	2.4±0.6
Fe	365±40	368±7	180±17	186±11
Se	---	0.054±0.003	6.86±0.5	6.88±0.4
Zn	29.7±4.1	30.9±0.7	160±2	177±10

* reference value.

All the results agreed well with agency values.

Mass fractions obtained for hepatopancreas from six different bays are shown in Fig. 1.

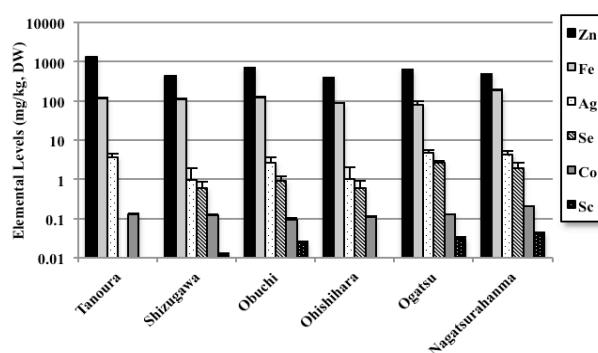


Fig.1 Mass fractions of elements in hepatopancreas from six different bays.

From all the results for hepatopancreas, mantle, gill, and muscle, Zn level was high in oysters from Tanoura and Fe was high in Nagatsura-Hama. Seasonal variations of total and bioaccessible Zn levels in oyster soft tissues are shown in Fig. 2. Both of 12 and 25 month old oysters were collected in July and total levels showed peak in July. July is mating season in Tohoku district. When the amount of Zn in whole soft tissues were calculated, it showed peak in June and decreased in July. Soft tissue weight decreased drastically in July, and it might be the reason that Zn level showed peak in July. Bioaccessible level of Zn was not same as total level and almost proportional to total levels in all seasons.

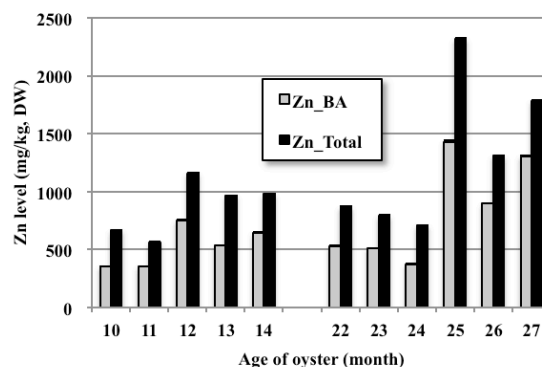


Fig. 2. Seasonal variations of total and bioavailable level of Zn in soft tissues from Higashimatsushima.

This tendency was same for Fe, Ag, and Sc. Se showed different tendency.

Conclusions: Eight selected trace elements in oyster soft tissues and separately in hepatopancreas, gill, mantle, and muscle were obtained by INAA. Seasonal and locational variation were observed for several elements.

CO8-3 First Result of Neutron Imaging at Reactor with Neutron Flat Panel Detector

T. Fujiwarwa and M. Hino¹

National Metrology Institute of Japan, National Institute of Advanced Industrial Science and Technology

¹Research Reactor Institute, Kyoto University

INTRODUCTION: Neutron imaging is powerful tool for observing inside an object without destructing the object. Although neutron imaging (neutron radiography) is one of the most traditional uses of neutrons, still there are rooms for improvement. Here, we report on the first neutron imaging result at reactor with our new neutron imaging detector based on Thin-Film-Transistor (TFT) technology, the neutron Flat Panel Detector. nFPD is tested at neutron beam port at KUR, and succeed in taking fine neutron image and 3D computed tomography (CT).

EXPERIMENTS: Experiments were held in CN-3 port at Kyoto University Reactor [1]. At this facility, approximately $20 \times 100 \text{ mm}^2$ size cold neutron beam is available. Fig. 1 shows the outlook of the nFPD. The volume of the detector is remarkably compact and thin compared to the conventional neutron imagers. The size of this detector improves the flexibility for placing and it will be a great advantage for installation to various experiments. Meanwhile, nFPD only requires 5V (4W) single power supply, and simply connected to PC with USB cable. The detector has effective area with 512×512 pixels (200 mm pixel size).

In this experiment, we took various radiographs and 3D CT was performed with automated turntable.

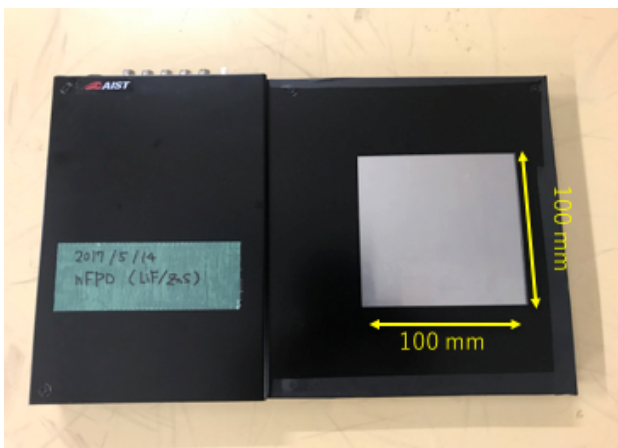


Fig. 1. Outlook of nFPD with $100 \times 100 \text{ mm}^2$ effective area. For the neutron converter, 320 mm thick LiF/ZnS(Ag) scintillator was used.

RESULTS: First, simple neutron imaging capability of nFPD was tested with Gd coated test chart developed at

PSI [2]. As shown in Fig. 2, fine neutron radiograph was obtained. Fine structures less than $300 \mu\text{m}$ can be observed. From this result, spatial resolution of our nFPD is estimated as $200 \mu\text{m}$.

Neutron CT was performed with automated turntable. The sample used here is an aluminum plate with screw holes and screwed with various material screws. Using this setup, the scanning sample was rotated in 1° pitch, and 360 images were obtained for 360° radiosopic image. The 3D image was reconstructed from those images by a filtered back-projection algorithm. The reconstructed 3D image is shown in Fig. 3. Fine structure of M4 screws can be clearly seen, and in addition, CT value of the objects agrees to theoretical neutron cross-section (Aluminum < Steel (Fe) < Plastics (Hydrogen)). Time for total scanning was less than 60 minutes.

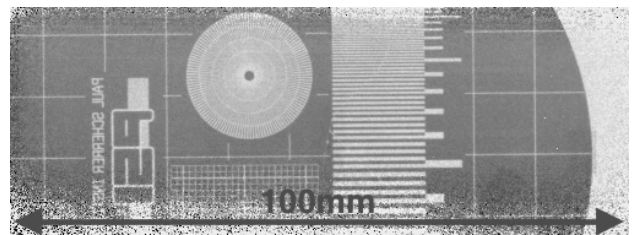


Fig. 2. Obtained neutron radiography of fine-structured Gd chart with nFPD. Integrating time was 5s at 1 MW operation. Fine patterns can be clearly observed.

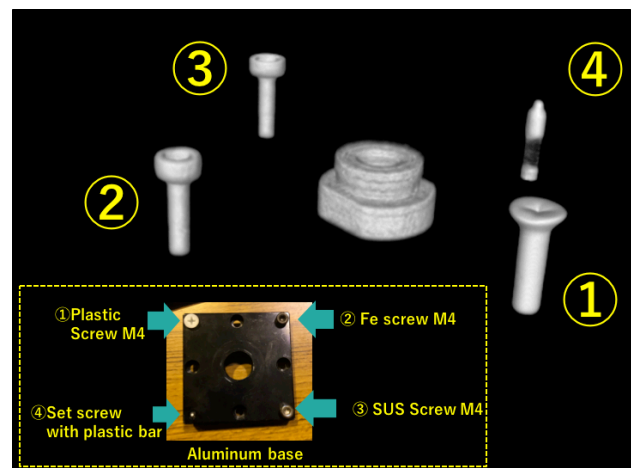


Fig. 3. Reconstructed 3D CT image of aluminum plate with various screws. Plastic screws and steel screws can be clearly seen while Aluminum part is almost transparent.

REFERENCES:

- [1] Y. Kawabata *et al.*, *Physica B* **311** (2002) 106.
- [2] K.-U. Hess *et al.*, *Geosphere* **7** 6. (2011) 1294–130.

Development of Neutron Source and Neutron Detector for Non-destructive Assay of Nuclear Materials

Y. Takahashi, Y. Kiyonagi¹, J. Hori, T. Sano, D. Ito, H. Unesaki, K. Nakajima, T. Kamiyama², K. Mochiki³, N. Hagura³ and S. Satou⁴

*Institute for Integrated Radiation and Nuclear Science,
Kyoto University,*

¹*Nagoya University,*

²*Hokkaido University,*

³*Tokyo City University,*

⁴*High Energy Accelerator Research Organization*

INTRODUCTION: The Kyoto University Research Reactor Institute electron linac, KURRI-LINAC, has been used for executing a project to develop methodology for the integrity evaluation of nuclear fuels, named the N-DeMAIN (Development of Non-Destructive Methods Adapted for Integrity test of Next generation nuclear fuels) project in Japan. As a non-destructive method, the neutron resonance transmission analysis was adopted for the identification and the quantification of nuclide in the fuels. Furthermore, determination of temperature distribution in the fuels based on Doppler broadening was also planned as well as traditional transmission imaging.

To obtain accurate data by these methods, high quality neutron beam regarding neutron flux, time resolution and spatial resolution is required. In order to satisfy the neutron beam quality required to successfully execute the experiments described above, the design of the neutron source, especially the moderator, reflector and collimator, should be improved and optimized. In this project, a target-moderator-reflector system (TMRS) and a beam collimator system have been redesigned to obtain the highest intensity and good spatial resolution with the use of simulation calculation. Then, the neutron source system including moderator and reflector was newly developed. The neutron beam line is placed at an angle of 135° with respect to the electron beam line and the collimator in 12 m beam line was also re-arranged. The characteristic of the TMRS was investigated experimentally.

EXPERIMENTS: A water-cooled photo-neutron target was set at the center of the neutron source system located in the target room. To enhance the neutron flux in thermal and epi-thermal regions, the size of the moderator of polyethylene was 5 cm thickness and 15 cm square. The collimators of polyethylene with 10% boron of 20 cm thickness were set at following positions; 15, 10 cm in inner diameter at 3, 9 m from the target, respectively. The conditions of the accelerator were as follows: average beam current was about 100 μ A, frequency was 50 Hz and pulse width was 4 μ s. For the evaluation of the spatial resolution of the TMRS, the dysprosium (Dy) foil transfer method was adopted in this study. The 6 Gd₂O₂S ceramic plates of 1 cm square and B₄C markers as shown in Fig. 1 are placed on the neutron beam line while shifting the position by 10 cm intervals. The Dy foil (110 mm width, 160 mm height, 0.1 mm thickness) was set at the

end the Gd plate. The Dy foil was activated by the neutron passed through Gd plate and the Dy foil emitted beta ray. The beta ray emitted from Dy foil was transferred a neutron imaging plate and we obtained neutron imaging indirectly. After the Gd plate experiment, the neutron imaging with BPI and SI indicators was measured by Dy foil transfer method.

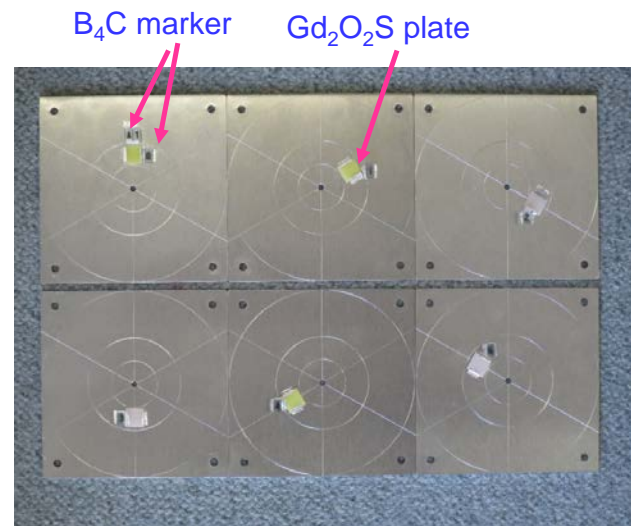


Fig. 1 Gd plates and B₄C marker for Dy foil transfer method

RESULTS: The results of neutron imaging by Dy foil transfer method are shown in Fig. 2. The modulation transfer function (MTF) on the results of Gd plate was well and it was found that the TMRS has good L/D. The boron point can be observed in BPI indicator and the 50 μ m line is visible in SI indicator. From the results, it was found that we can obtain the enough neutron flux and our system is available for a neutron imaging with good spatial resolution.

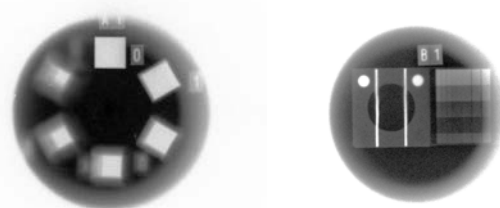


Fig.2 Results of neutron imaging by Dy foil transfer method
(left: Gd₂O₂S ceramic plates, right: Indicators)

Present study includes the result of “Development of Non-Destructive Methods Adapted for Integrity test of Next generation nuclear fuels” entrusted to the Kyoto University by the Ministry of Education, Culture, Sports, Science and Technology of Japan (MEXT)

CO8-5 Integral Test for the Development of Nondestructive Methods Adopted for Integrity Test of Next Generation Nuclear Fuels (N-DeMAIN)

K. Nakajima, J. Hori, T. Sano, Y. Takahashi, H. Unesaki, D. Ito, T. Kamiyama¹, H. Hasemi¹, K. Mochiki², N. Hagura², Y. Kiyonagi³, K. Koike⁴ and S. Satoh⁵

Research Reactor Institute, Kyoto University
¹ Graduate School of Engineering, Hokkaido University
² Faculty of Engineering, Tokyo City University
³ Graduate School of Engineering, Nagoya University
⁴ R-Tech Corporation
⁵ Institute of Material Structure Science, KEK

INTRODUCTION: TRU fuels containing MA will be used in a fast reactor system to reduce the high-level waste by the transmutation of long-lived minor actinides. It is important to test their integrity to confirm the fuel safety, however, such fuels have high radioactivity and high decay heat, thus the conventional techniques would be difficult to use. Therefore, we launched a new project, which named as “N-DeMAIN” (Development of Non-Destructive Methods Adopted for Integrity Test of Next Generation Nuclear Fuels) in 2014, in order to develop the NDA techniques for Next generation fuels, i.e., TRU fuels containing MAs. In the project, the neutron resonance transmission analysis (NRTA) with the time-of-flight (TOF) measurement is adapted for the identification and quantification of nuclides in the fuels. In addition, the determination of temperature distribution in the fuels based on Doppler-effect and neutron imaging are conducted.

In the present study, we have performed the following measurements using the KURRI-LINAC as the integral test: 1) Isotopic imaging of the sample containing a minor actinide and a long-lived fission product, 2) Geometry measurement by neutron beam and X-ray, 3) Temperature measurement using the Doppler effect.

EXPERIMENTS and RESULTS:

1) Isotopic imaging of the sample containing a minor actinide and a long-lived fission product: By selecting the specified resonance region in the TOF spectrum of a sample, we can obtain the 2D imaging of the isotope corresponding to the specified resonance. We have obtained the 2D imaging of the samples containing a minor actinide, ²³⁷Np, and a long-lived fission product, ⁹³Zr, by the NRTA using the THIN-GEM detector. The samples are oxide powder of ⁹³Zr and ²³⁷Np, and they were encapsulated in aluminum disk-shaped containers with 30mm diameter. Those samples have radioactivities, 47MBq for ⁹³Zr and 26MBq for ²³⁷Np. In addition to the samples, the indium foil was measured for the reference. As shown in Fig.1, the 2D imaging of the samples is not clear when the all neutrons were detected, however, the shape of ²³⁷Np can be observed by selecting the 0.49-eV resonance region in the TOF spectrum. Thus, it was confirmed that this technique would be applicable for the TRU fuel imaging with the high radioactivity.

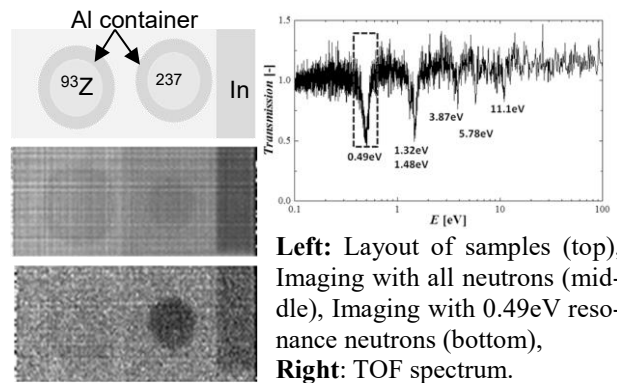


Fig.1. Result of 2D imaging for ²³⁷Np.

2) Geometry measurement by neutron beam and X-ray: Since the X-ray imaging has a high spatial resolution, the obtained imaging data were combined with the neutron imaging which has a low resolution to improve the spatial resolution. The nuclide identification was performed by neutron imaging. As shown in Fig. 2, we succeeded in reconstructing synergy imaging by using X-ray and neutron imaging data.

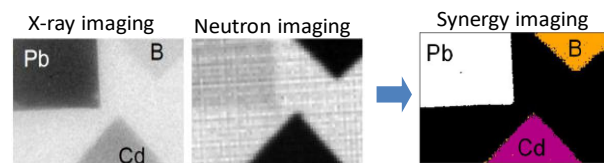


Fig.2. Synergy imaging for 2D-sample.

3) Temperature measurement using the Doppler effect: The temperature rise of a sample causes the Doppler broadening of the resonance peak, then, we can evaluate the temperature change by observing the change of resonance reactions. Because the TRU fuel containing MAs has high decay heat, it is important to monitor the fuel pellet temperature and keeps it to the proper range during the storage. Then, we tried to develop the nondestructive method to monitor the fuel pellet temperature. In the experiment, the temperature of a cylindrical Ta sample (10mmφ×30mm) was controlled up to 350°C using the sample heating device. The transmitted neutrons were measured with the THIN-GEM detector. It was found that the ratios of resonance count ratios for high temperature to room temperature tend to decrease with temperature rise in the rate of about 0.01%/K as shown, and it was indicated that the change of temperature might be evaluated using the change of the ratio.

SUMMARY: Through the integral test, it was confirmed that the developed techniques satisfy our requirements.

ACKNOWLEDGMENT: Present study is performed under the entrustment to the Kyoto University by the Ministry of Education, Culture, Sports, Science and Technology of Japan (MEXT).

T. Sasaki, R. Goto, T. Saito¹, T. Kobayashi, D. Matoba and A. Uehara¹

Graduate School of Engineering, Kyoto University
¹Research Reactor Institute, Kyoto University

INTRODUCTION: The randomly cross-linked heterogeneous and macromolecule properties of humic substances (HSs) as natural organic matter would be influenced by radiation, in soils, sediments, and natural waters. When the HS in underground water contacts with a radioactive waste package at repository site, the chemical property of HS should be altered by gamma irradiation and the ability of complex formation may be decreased. The acid dissociation constant and the apparent formation constant of radionuclides with HS changes depending on the solution conditions such as pH, metal and HS concentrations, and ionic strength. In the present study, the HS samples irradiated by Co-60 gamma-ray source were characterized by potentiometric titration.

EXPERIMENTS: The gamma-ray irradiation was performed in the gamma-ray irradiation facility in Kyoto university research reactor institute (KURRI) with TBq ⁶⁰Co source. Aqueous solution of Aldrich humic acid abbreviated to HS (Sigma-Aldrich Co.) sealed into glass vessels without air removing were set at positions of 1 kGy/h for high dose rate. The applied doses were 0 - 500 kGy by controlling the irradiation period between 0 - 500 h. The initial concentration of proton-exchanging sites C_R in meq/g for HS is known value. Each sample solution containing 1 meq/dm³ of HS was prepared by dissolving the solid humic substance in 0.1 M NaOH and then 0.1 M HClO₄ to neutralize alkali solution. The ionic strength was controlled by 0.1 M NaClO₄. After irradiation, the solution pH values were slightly decreased, then the pH was readjusted to ca. 8. On the other hand, no pH shift has been observed under no gamma-irradiation condition.

The titration was conducted using an automatic titrator, equipped with a microburette, combination glass electrode, and polyethylene centrifuge tubes in a water bath at 298 ± 0.5 K under a nitrogen gas atmosphere. A combined glass electrode was used to measure the pH, and the reference electrode was filled with a mixed solution of 3.6 M NaCl and 0.4 M NaClO₄ in order to prevent precipitation of KClO₄ at the junction of the electrode and the solution. The calibration of the glass electrode for conversion of the millivolt readings into pH was conducted with a blank titration using 0.1 M HClO₄ and 0.05 M NaOH + 0.05 M NaClO₄ standard solutions. The millivolt readings of the glass electrode were compared with $-\log[H^+]$ (= pH) calculated from the added NaOH concentration assuming NaOH was completely dissociated under the titration conditions.

RESULTS: The experimental titration of HS at $I = 0.1$ (NaClO₄) was conducted from an initial pH of ca. 2.5 to 10.5. As shown in Fig. 1, the fitted values of (R⁻) increased with increasing pH_c. These curves showed no clear point of neutralization, which suggested polyelectrolytic properties and heterogeneity of functional groups for each binding site.

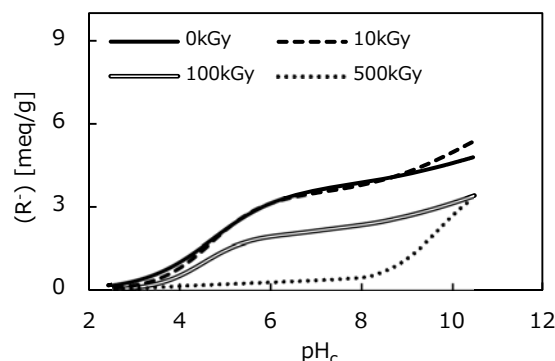


Fig. 1 Irradiation dose effect on the the total carboxylic and phenolic group concentrations of HS, (R⁻).

The plots as a function of pH_c were fitted by non-linear least-squares fitting analysis according to Eqs. (1) and (2).

$$[R^-] = 10^{-pH_c} - 10^{(pH_c - pK_w)} - \frac{c_{Na}V_{ini} + c_{Na}V_{add} - c_{ClO_4}V_{ini} - c_{ClO_4}V_{add}}{V_{ini} + V_{add}} \quad (1)$$

$$[R^-] = (R^-)^j \quad (2)$$

where c_{Na} and c_{ClO_4} are the concentrations of sodium and perchlorate ions in the initial test solution, c'_{Na} and c'_{ClO_4} are the concentrations of the titrant solutions, V_{ini} is the initial volume, V_{add} is the added titrant volume. At a given I , the $[R^-]$ in eq/dm³ is defined by the sum of two dissociated functional groups of HS (R^-) in meq/g and j g dissolved in V mL solution. The fitted curves reproduced the experimental data well, and some general parameters of acid dissociation [1] could be determined as summarized in Table 1.

Table 1 Fitted parameters for HS

Dose	C^{W_1}	C^{W_2}	$\frac{\log K_1}{1 - m_1}$	$\frac{\log K_2}{1 - m_2}$	m_1	m_2
kGy	meq/g	meq/g				
0	3.56	2.82	4.70	10.84	0.42	0.71
500	0.29	3.83	3.78	9.70	0.47	0.24

REFERENCE:

[1] Kirishima, A., Ohnishi, T., Sato, N., Tochiyama, O.: *Talanta*, **79** (2009) 446.

T. Kobayashi, S. Nakajima, P. Wang, T. Sasaki and A. Uehara¹

Graduate School of Engineering, Kyoto University
¹Research Reactor Institute, Kyoto University

INTRODUCTION: Safety assessment of radioactive waste disposal requires to predict the solubility limit of radionuclides under relevant repository conditions. Isosaccharinic acid (ISA), a degradation product of cellulose found in low- and intermediate-level radioactive waste, is known to form strong complexes with radionuclides [1]. Therefore, ISA has been considered to potentially enhance the solubility of radionuclides, which possibly affects the safety assessment of radioactive waste disposal. Although several literatures have investigated the interaction of ISA with radionuclides, uranium is one of the elements, on which only very few studies have proposed the dominant ISA complexes and their formation constants. Under reducing geochemical conditions in the repository system, tetravalent state (U(IV)) is the most relevant oxidation state for uranium. Due to the strong hydrolysis reaction, U(IV) easily precipitates as sparingly soluble amorphous hydrous oxide (UO₂(am, hyd)) in the neutral to alkaline pH range [2]. The formation of soluble U(IV)-ISA complex potentially increases the apparent solubility of uranium, which can mobilize uranium in the repository system. In the present study, we focused on the solubility of U(IV) in the presence of ISA at hydrogen ion concentrations (pH_c) of 6–12 and total concentration of ISA ([ISA]_{tot}) of 10⁻³ to 10⁻¹ mol/dm³ (M). Based on the solid phase analysis and slope analysis of the solubilities, dominant U(IV)-ISA complex was revealed, and the formation constant was determined by the thermodynamic analysis of the solubility data.

EXPERIMENTS: Calcium isosaccharinate (Ca(ISA)₂) was synthesized from α-lactose and converted to NaISA stock solution. A stock solution of U(IV) was electrochemically prepared by reducing 0.06 M uranyl nitrate. Portions of concentrated NaOH solution was then added into the U(IV) stock solution to precipitate amorphous U(IV) hydrous oxides (UO₂(am, hyd)). The precipitate was washed several times and finally suspended in 20 mL of 1 mM Na₂S₂O₄ solution at around pH_c = 10. Sample solutions at specific pH_c and [ISA]_{tot} were prepared by an undersaturation method. Before adding a portion of suspended stock solution of UO₂(am, hyd) to each sample tube, pH_c was adjusted using HCl/NaOH and [ISA]_{tot} was adjusted by appropriate amount of NaISA stock solution. The ionic strength (*I*) of each sample solution was set to *I* = 0.5 using the 5 M NaCl stock solution. The sample solutions kept in polypropylene tubes were placed in glass bottles and stored under the Ar atmosphere to avoid the

oxidation of U(IV) during the experiment. After aging a given period, the pH_c was measured and supernatant was filtrated through 10 kDa membranes. U(IV) concentration in the filtrate was determined by ICP-MS and solid phase was examined by XRD after drying the samples.

RESULTS: U(IV) solubility after 3–10 weeks in the presence of 10⁻³–10⁻¹ M ISA was measured in the pH_c range of 6–12 after ultrafiltration through 10 kDa membranes. A steady state was confirmed to be achieved within 3 weeks. In the presence of ISA with a concentration higher than 10^{-2.1} M, U(IV) solubility was found to be higher in comparison with systems in the absence of ISA, depending on the pH_c and ISA concentration. U(IV) solubility was observed to be almost constant against pH_c at pH_c 6–12, indicating that four OH⁻ ions are involved in the U(IV)-ISA complex, provided that UO₂(am, hyd) is the solid phase. The slope of U(IV) against [ISA]_{tot} at around pH_c 7.2 and 10.0 was approximately 2, indicating that two ISA molecules were involved in the formation of the U(IV)-ISA complex. It is noted that no significant peak except that of NaCl(cr) was observed in the XRD patterns of the solid phase, suggesting that the initial UO₂(am, hyd) was not transformed during the experiment. The formation of U(IV)-ISA complex was then described by the equation; U⁴⁺ + 4OH⁻ + 2ISA⁻ ⇌ U(OH)₄(ISA)₂²⁻. Taking the U(IV)-ISA complex formation constant (β₁₄₂), hydrolysis constants of U(IV) (β_{1m}) [3], and solubility product of UO₂(am, hyd) (K_{sp}) [3] into account, U(IV) solubility ([U(IV)]) can be described as

$$[U(IV)] = [U^{4+}] + \sum_m [U(OH)_m^{4-m}] + [U(OH)_4(ISA)_2^{2-}]$$

The solubility data in the neutral to alkaline pH range were analyzed to determine the complex formation constants β₁₄₂ in the least squares fitting analysis. The formation constant was determined to be log β₁₄₂ = 50.8 ± 0.1. The increase of the U(IV) solubility in the presence of ISA was quantitatively well explained by the formation of U(OH)₄(ISA)₂²⁻.

REFERENCES:

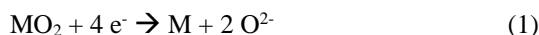
- [1] Hummel W *et al.* Chemical Thermodynamics of Compounds and Complexes of U, Np, Pu, Am, Tc, Se, Ni and Zr with Selected Organic Ligands. Elsevier, North-Holland, Amsterdam (2005).
- [2] Baes C. F., Mesmer R. E. The Hydrolysis of Cations. John Wiley & Sons, New York (1976).
- [3] Guillaumont R *et al.* Update on the Chemical Thermodynamics of Uranium, Neptunium, Plutonium, Americium and Technetium. Elsevier, North-Holland, Amsterdam (2003).

CO9-3 Electronic Absorption Spectra of Tellurium in LiCl-KCl Eutectic Melt

Y. Sakamura, T. Murakami, K. Uozumi and A. Uehara¹

Central Research Institute of Electric Power Industry
¹Research Reactor Institute, Kyoto University

INTRODUCTION: The electrolytic reduction technique in LiCl-Li₂O melts has been developed for pyrochemical reprocessing of spent oxide fuels. At the cathode, actinide oxides are reduced to their metals:



where M denotes actinides such as U and Pu. Similar to oxygen, chalcogen fission products such as Se and Te are dissolved into the melt in the form of divalent anion.

Recently, the authors have been studied electrochemical behaviors of Na₂Se and Na₂Te in LiCl-KCl eutectic melt to extract Se and Te from molten salts [1,2]. It was indicated that the deposition of Te proceeded in two steps at the anode: the oxidation of Te²⁻ to Te₂²⁻ occurred followed by the oxidation of Te₂²⁻ to Te, which was similar to the electrochemical behaviors of S [3] and Se [1]. To verify the redox mechanism of Te, a spectroscopic study was conducted in this study. The absorption spectra of Na₂Se in LiCl-KCl melt have been already reported [4].

EXPERIMENTS: LiCl-KCl-Na₂Te mixture (Te: 0.51 wt%) was prepared by heating a quartz crucible containing LiCl-KCl eutectic (59:41 mole ratio, Aldrich-APL) and Na₂Te (99.9% purity, Alfa Aesar) at 773 K.

LiCl-KCl eutectic (4.077 g) was loaded in a rectangular cylinder quartz cell (10 x 10 mm) used for absorption spectrometry and heated to 723 K in an electric furnace. The experimental apparatus was previously described in detail by Nagai et al. [5] The following steps were carried out and then the absorption spectrum of the melt was measured by using an UV/Vis/NIR spectrophotometer (V-570, JASCO).

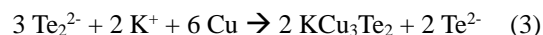
- (1) 0.118 g of the LiCl-KCl-Na₂Te mixture was added.
- (2) 0.064 g of the LiCl-KCl-Na₂Te mixture was added.
- (3) 0.099 g of the LiCl-KCl-Na₂Te mixture was added.
- (4) 0.030 g of Te (99.9999% purity, Nilaco) in an Al₂O₃ tube was immersed in the melt.
- (5) The Te was removed from the melt.
- (6) A Cu rod (φ2 mm) was immersed in the melt.

RESULTS: Fig. 1 shows absorption spectra of the melt during the steps (1)-(4). The absorption peak at ~500 nm corresponding to Te²⁻ ions was increased by adding the LiCl-KCl-Na₂Te mixture (steps (1)-(3)). The Te concentration in the melt after step (3) was determined to be 0.027 wt% by ICP-AES analysis. After Te was added into the melt by step (4), the absorption peak remarkably increased within 1.0 h, which was visually confirmed as shown in Figs. 2a and 2b. The Te concentration in the melt after 1.5 h immersion of the Te was 0.039 wt%. In addition, the peak position was slightly shifted to the shorter wavelength. Therefore, it was suggested that

about 40% of Te²⁻ was reacted with Te to form Te₂²⁻.



After the Cu rod immersion (step (6)), the absorption peak gradually decreased and the melt turned light brown as shown in Fig. 2c. The Te concentration in the melt was decreased to 0.017 wt% after the Cu rod was immersed for 2.0 h, which might be due to the deposition of KCu₃Te₂ [2].



The results of this spectroscopic study are considered to be consistent with the results of the electrochemical measurement [2]. However, the mass balance of Te in the melt should be examined in detail in future work.

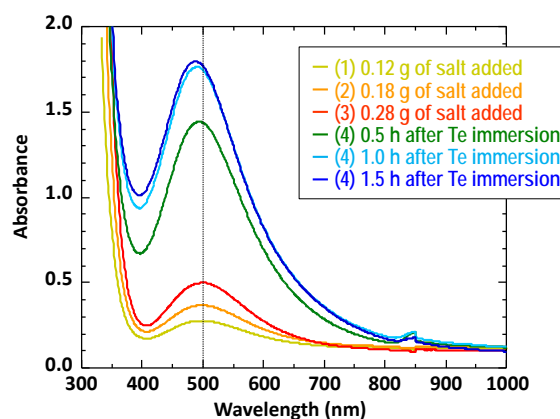


Fig. 1 Absorption spectra of LiCl-KCl-Na₂Te melt during steps (1)-(4).

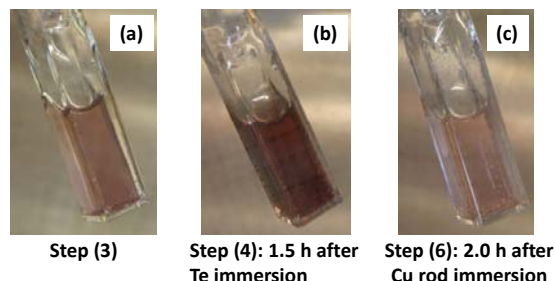


Fig. 2 The quartz cell containing LiCl-KCl-Na₂Te melt after steps (3), (4) and (6).

REFERENCES:

- [1] Y. Sakamura, T. Murakami and K. Uozumi, Proc. The 48th Symposium on Molten Salt Chemistry, p. 1, Niigata Univ., Japan, Nov. 24-25, 2016, in Japanese.
- [2] Y. Sakamura, T. Murakami and K. Uozumi, Proc. The 49th Symposium on Molten Salt Chemistry, p. 84, Kansai Univ., Japan, Nov. 30 - Dec. 1, 2017, in Japanese.
- [3] D. Warin, Z. Tomczuk and D.R. Vissers, J. Electrochem. Soc., **130** (1983) 64-70.
- [4] Y. Sakamura, T. Murakami, K. Uozumi, A. Uehara and T. Fujii, KURRI Progress Report 2016, p. 15, 2017.
- [5] T. Nagai, T. Fujii, O. Shirai and H. Yamana, J. Nucl. Sci. Technol., **41** (2004) 690-695.

CO9-4 Solvent Extraction of Uranium(VI) from Concentrated Calcium Chloride to Organic Solution

A. Uehara^{1*}, T. Fujii², T. Nagai³ and Y. Okamoto⁴

¹ Research Reactor Institute, Kyoto University

² Graduate School of Engineering, Osaka University

³ Nuclear Fuel Cycle Engineering Lab., Japan Atomic Energy Agency

⁴ Material Sciences Research Center, Japan Atomic Energy Agency

INTRODUCTION: The extraction distribution of trivalent actinides and lanthanides between tri-butyl phosphate (TBP) and nitric acid solutions has been studied [1] and their extraction behavior has been systematically elucidated. When the concentrated electrolyte solutions such as calcium nitrate hexahydrate were used as an aqueous solution, distribution of lanthanide ions were enhanced because of the water-deficiency by which we can expect magnified appearance of ligand solvation and hydration [2,3]. We have reported that the coordination structure of UO_2^{2+} in concentrated CaCl_2 determined by X-ray absorption fine structure (XAFS) analyses changed significantly depended on the concentration of Cl^- [4]. In this study, extraction behavior of UO_2^{2+} depended on the concentration of CaCl_2 as well as H^+ was compared with the local structure of UO_2^{2+} in those solvents.

EXPERIMENTS: Solvent extraction experiments, concentrated CaCl_2 containing uranyl ion was used as aqueous solution, and dodecane containing TBP was used as organic solution. After equilibrium was attained, two phases were separated, and concentration of uranyl ion was measured by using absorption spectrometer. X-ray absorption fine structure XAFS measurement was performed at BL27B beam line in KEK. Sample solution was sealed in polyethylene bag. For the analysis of XAFS spectra, Win XAS 3.1 and FEFF 8 was used.

RESULTS: In the present report, effect of H^+ in concentrated CaCl_2 on the coordination number and bond distances of UO_2^{2+} determined by XAFS was investigated based on the results of the solvent extraction of UO_2^{2+} in the electrolyte by TBP. These figures show that the coordination numbers of Cl and H_2O to UO_2^{2+} were plotted as a function of H^+ concentration ratio. Here, total concentration of Cl^- was adjusted to be 13 M by adding water or CaCl_2 . In the absence of H^+ , about two Cl and two H_2O coordinate to UO_2^{2+} equatorial sphere to be $\text{UO}_2\text{Cl}_2(\text{H}_2\text{O})_2$ whereas five H_2O coordinate to UO_2^{2+} in 1 M HClO_4 aqueous solution [4]. Two water molecules coordinated to UO_2^{2+} was exchanged by two TBP to be extracted into organic phase as $\text{UO}_2\text{Cl}_2(\text{TBP})_2$ resulted in higher extraction percentage. When H^+ concentration increases, coordination number of H_2O significantly decreased to one, and that of Cl slightly increased to three. It was suggested that the uranyl ion forms tri-chloro complex, which is ionic species, at high concentration of

H^+ would be formed. The extraction percentage decreased because of the ionic formation in aqueous phase.

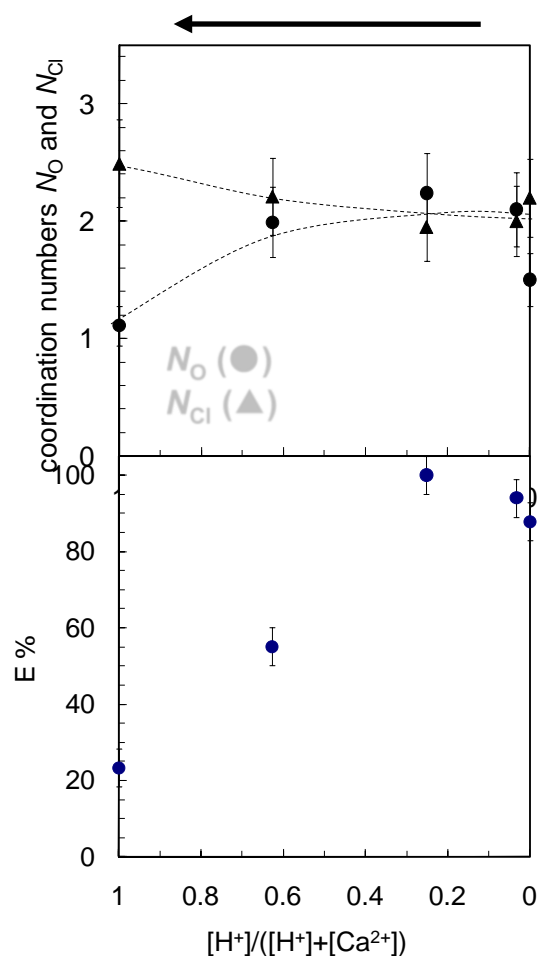


Figure 1. Coordination number of Cl and H_2O to UO_2^{2+} equatorial sphere calculated based on the R-space after Fourier transform. Extraction percentage of UO_2^{2+} between various H^+ concentration in 12 M Cl electrolyte and 0.2 M tributyl phosphate in dodecane.

REFERENCES:

- [1] G.F. Best, et al., *J. Inorg. Nucl. Chem.* **12** (1959) 136-140.
- [2] E. Akatsu, et al., *Anal. Chim. Acta.* **62** (1972) 325-335.
- [3] H. Yamana, et al., *J. Alloys Comp.* **271-273** (1998) 707-711.
- [4] A. Uehara, et al., *NEA/NSC/DOC 15* (2009) 197-203.

* Present address: National Institute of Radiological Sciences, National Institute for Quantum and Radiological Science and Technology

N. Sato, A. Kirishima, D. Akiyama, S. Kimuro, A. Nagatomo, T. Sasaki¹, T. Kobayashi¹, S. Sakamoto¹, D. Harumoto¹, A. Uehara², K. Takamiya² and T. Fujii³

Institute of Multidisciplinary Research for Advanced Materials, Tohoku University

¹ Graduate School of Engineering, Kyoto University

² Research Reactor Institute, Kyoto University

³ Graduate School of Engineering, Osaka University

INTRODUCTION:

After the LOCA of Fukushima Daiichi NPS, the melted core reacted with coolant at high temperature forming fuel debris containing fuel and structural materials such as zirconium. Under high temperature condition in the pressure vessel, several kinds of FPs and TRU were possibly released into the cooling water mixed with seawater and the air from the melted core and its fine debris. Information on the radionuclide behavior in fuel debris and surface seawater will be helpful to analyze the forthcoming analysis data about the contents of minor FPs and TRU in contaminated water, and to manage associated secondary wastes. First, the simulated fuel debris composed of uranium and zirconium oxides with main structural materials such as steel and concrete was prepared by heat treatment in reductive or oxidative conditions. Then the dissolution behavior of typical gamma-ray fission products and neutron activated nuclides as well as uranium in solid solutions was investigated by neutron irradiation and following leaching in the non-filtrated seawater. Dissolution behavior of MA was also studied by the used of MA doped simulated fuel debris.

EXPERIMENTAL:

Several types of $\text{UO}_2\text{-ZrO}_2$ solid solution samples with different Zr concentration were prepared by heat treatments under reducing and oxidizing atmospheres. The sample was vacuum-sealed in quartz tube and irradiated for 20 min using the pneumatic transferring system (Pn-2) at KUR. For reducing the high radioactivity of short-lived nuclides, the sample was left for a given period, and then suspended in 30 ml of deionized water. After the aging time in the atmospheric condition at R.T., a 10 mL of supernatant was transferred to new sample tube after filtration with 0.45 μm (Advantec) or 10 kDa (Microcon, Millipore) membranes, followed by evaporation of the solution at 363 K in order to prepare a solidified point-like gamma source. For MA doped sample, similar preparation techniques were applied by using U_3O_8 powder doped with ^{237}Np , ^{243}Am . Gamma- and alpha ray spectrometry were performed using a Ge detector (GMX15P4, Ortec) and Si-detector (7401, Camberra) to determine the nuclides leached.

RESULTS:

Figure 1 shows the typical γ -ray spectrum of the UO_2 sample after thermal neutron irradiation at KURRI. The γ -ray peaks from FP nuclides, Cs-137, Ba-140, Zr-95, I-131, and Ru-103 were observed.

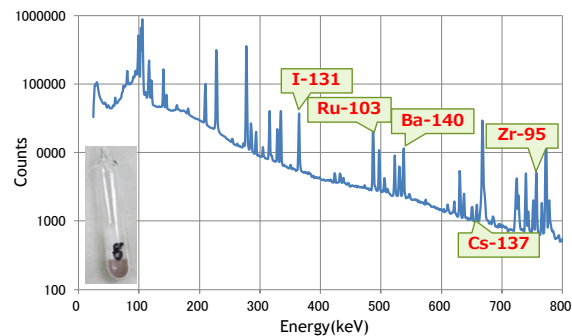


Fig.1 γ -ray spectrum of the uranium oxide sample after neutron irradiation at KURRI.

The leaching ratio of FPs for MCCI debris ($\text{UO}_2\text{-CaCO}_3\text{-SiO}_2$ component), which was prepared at 1200 °C under an aerobic condition of 2% oxygen + Ar, was determined. The UO_2 was partly oxidized to U_3O_8 , and CaUO_4 (cubic), CaUO_4 (trigonal), Ca_3UO_6 were formed with increasing the initial Ca/U ratio. One example of the leaching ratio was shown in Figure 2. The r_M values for all of FPs were higher than uranium, probably due to the facilitation of Ca leaching from the debris.

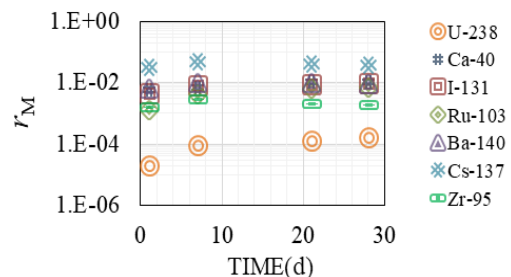


Fig.2 The leaching ratio r_M of oxidized MCCI debris.

The leaching ratio of Pu and Am was suppressed in the very low extent (0.02 % or less). The leaching of Am is expected to be suppressed to very low extent regardless of the oxidation state of Am in the solid phase since the solubilities of both Am(III) and Am(IV) are very low at the pH of seawater. The R_U value was about 0.1 % during the leaching test. From this result, it is considered that the uranium dissolution from the simulated fuel debris was governed by the solubility limitation of $\text{UO}_3 \cdot 2\text{H}_2\text{O}(\text{cr})$, $\text{UO}_3 \cdot 2\text{H}_2\text{O}(\text{am})$ or maybe their intermediate phase as discussed in our previous study [1].

REFERENCE:

- [1] T. Sasaki, Y. Takeno, A. Kirishima, N. Sato, J. Nucl. Sci. Technol., **53** (2016) 303-311.

CO9-6 Search for the Vacuum Ultraviolet Photons from $^{229\text{m}}\text{Th}$ Reacted with HF Gas

Y. Yasuda, Y. Kasamatsu, Y. Shigekawa, T. Ohtsuki¹,
K. Takamiya¹, A. Shinohara

Graduate School of Science, Osaka University
¹Research Reactor Institute, Kyoto University

INTRODUCTION: Thorium-229m is the extremely low energy isomeric state in ^{229}Th and the excitation energy was reported to be 7.8 ± 0.5 eV [1]. The energy corresponds to vacuum ultraviolet photon ($\lambda = 160$ nm). Because of the low excitation energy, $^{229\text{m}}\text{Th}$ is expected to change the decay mode: internal conversion or gamma-ray transition, depending on its chemical condition. Recently, it was reported that the $^{229\text{m}}\text{Th}$ neutral atom decays by internal conversion with a half-life of 7 μs , and that the $^{229\text{m}}\text{Th}^{2+}$ ion in the isolated system decays with a half-life of longer than 60 s [2, 3]. It suggests that $^{229\text{m}}\text{Th}^{2+}$ ion may decay by mainly gamma-ray transition (photon emission). However, the photons from $^{229\text{m}}\text{Th}$ have never been observed; photon detection for $^{229\text{m}}\text{Th}$ would provide valuable information to elucidate the interesting decay mechanism of $^{229\text{m}}\text{Th}$. To observe the photons, in this study we performed following experiments: First, we prepared $^{229\text{m}}\text{Th}$ as recoil products (high valence $^{229\text{m}}\text{Th}^{2+}$ ions). Subsequently, $^{229\text{m}}\text{Th}$ ions were directly reacted with hydrogen fluoride gas. Since the lowest binding energy of the outermost electron in ThF_4 is 8.3 eV [4] which is larger than the $^{229\text{m}}\text{Th}$ excitation energy, 7.8 eV, it is expected that $^{229\text{m}}\text{Th}$ is not able to decay by internal conversion. Finally, the $^{229\text{m}}\text{Th}$ sample was subjected to the photon detection.

EXPERIMENTS: In the previous experiment [5] performed in the similar manner, disturbing photon emission from the daughter nuclides of ^{233}U and ^{232}U was observed. Therefore, in this study, we purified ^{233}U by anion-exchange method using HCl solution and then, immediately prepared electrodeposited ^{233}U sample. To obtain $^{229\text{m}}\text{Th}$ ions as recoil products, the ^{233}U sample was set in the Collection Apparatus for Recoil Products (CARP) [6]. The schematic diagram of CARP is shown in Fig. 1. In collecting $^{229\text{m}}\text{Th}$ ions, He gas or He/HF mixture gas were guided into the CARP and the required voltage was applied to guide $^{229\text{m}}\text{Th}$ ions onto the copper plate. After $^{229\text{m}}\text{Th}$ was collected for several hours, the copper plate was taken and set in the photon detection chamber to perform photon detection. In the photon detection, we used the photomultiplier tube (PMT, HAMAMATSU R6836), which detects 4-10 eV photons. The PMT was cooled to about 10°C and set in vacuum.

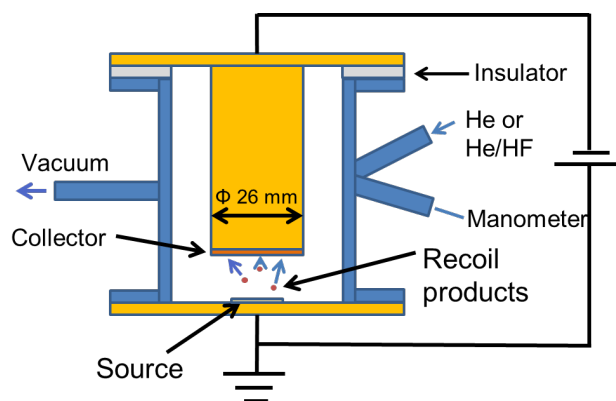


Fig. 1. Schematic diagram of CARP. Recoil products are stopped in the gas and are guided onto the collector (Cu plate) by the voltage applied between the source and the collector.

RESULTS: As a result, disturbing photon emission observed in the previous experiment [5] became negligibly small. In the previous experiment [5], decaying photon emission was observed for both the samples: collected under He gas and the sample under He/HF gas. Under He gas, $^{229\text{m}}\text{Th}$ recoils are considered to be soon neutralized and therefore the nuclide decays by internal conversion (no photons), which contradicts the result. Thus, we concluded that the observed photons originate from β -ray emitting daughter nuclides (Cherenkov) not from $^{229\text{m}}\text{Th}$. In this study using fresh ^{233}U , by contrast, no significant photons were detected for the ^{229}Th sample collected under He gas. This result means that the influence of the daughter nuclides (disturbing photon emission) was removed; we achieved low background ultraviolet photon detection for $^{229\text{m}}\text{Th}$ sample. However, for ^{229}Th sample collected under He/HF mixture gas, photon emission was also not observed. Under the present experimental conditions, $^{229\text{m}}\text{Th}$ ions might not be reacted with HF gas sufficiently. Highly charged ion is easily and rapidly oxidized in air. Pure fluorine gas should be used although it is difficult.

REFERENCES:

- [1] B. R. Beck *et al.*, LLNL-PROC-415170 (2009).
- [2] L. von der Wense *et al.*, *Nature* **533** (2016) 47-51.
- [3] B. Seiferle *et al.*, *Phys. Rev. Lett.*, **118** (2017) 042501.
- [4] N. Trautmann, *J. Alloys Compd.*, **213/214** (1994) 28.
- [5] Y. Yasuda *et al.*, *KUR Progress Report* **2016** (2017) 98.
- [6] Y. Shigekawa *et al.*, *Rev. Sci. Instrum.*, **87** (2016) 053508.

CO9-7 Investigation of Coprecipitation with Sm Hydroxide Using KUR Multitracer

Y. Kasamatsu, M. Nagase, Y. Shigekawa, N. Kondo, E. Watanabe, H. Ninomiya, K. Takamiya¹ and A. Shinohara

Graduate School of Science, Osaka University

¹*Research Reactor Institute, Kyoto University*

INTRODUCTION: Chemistry researches on actinide and transactinide elements at the uppermost end of the periodic table are very important in inorganic chemistry. Owing to strong relativistic effect on the electronic shells of heavy elements, their chemical properties would be unique in the periodic table. It is, however, difficult to perform chemical experiment with heavy actinide and transactinide elements because these atoms must be produced at accelerators using heavy-ion induced nuclear reactions with low production rates. Furthermore, these elements have short half-lives. Thus, we need to establish new experimental methods or apparatuses specified for these elements. For such a purpose, it is important to perform fundamental chemical experiments (with and without apparatuses) using the lighter elements whose chemical properties are known.

We previously reported the coprecipitation method with Sm hydroxide for heavy elements [1]. Indeed, suitable experimental condition for element 104, Rf, was successfully determined through fundamental experiments using homologues of Rf: Zr, Hf, and Th [2]. In the previous coprecipitation experiment [1], multitracer produced by spallation reaction of Ta in RIKEN was used to investigate the coprecipitation properties of various elements. In this work, precipitation properties of the elements contained in KUR multitracer were studied. The KUR multitracer was produced by neutron-induced fission reaction of ²³⁵U. Thus, the product nuclides are different from those in RIKEN multitracer. We expect to obtain complementary data by this experiment.

EXPERIMENTS: The KUR multitracer sample was prepared by irradiating thermal neutrons on UO₂ powder which is mixed with RbCl at KUR [3]. Fission products implanted in NaCl were dissolved in 0.01 M HCl and were separated from the UO₂ powder by a suction filtration. A portion of the sample was subjected to γ -ray measurement by a Ge detector, and count rates of γ -ray

peaks and their time dependences were measured.

In the precipitation experiment, 20 μ L (20 μ g) of Sm standard solution (1 M HNO₃) was added into the multitracer solution. After mixing it, 2 mL of basic solution was added to generate hydroxide precipitate. In the present experiment, we used dilute NH₃ solution, concentrated NH₃ solution, 0.1, 1, 6, and 12 M NaOH solutions as the basic solutions to observe the dependence of the precipitation yield on the concentration of the basic solution. Subsequently, the solution was stirred for 10 s and was soon filtrated with a polypropylene membrane filter. To check the complete precipitation of the samples, precipitate samples with stirring for 10 min after adding the basic solution were also prepared. The samples were then dried on heater at 100 degree C and were assayed for γ -ray measurements. Supernatant solutions were evaporated to dryness and were also subjected to measurements. The coprecipitation yields were determined from the results of the γ -ray measurements.

RESULTS: The product nuclides were identified from the γ -ray energies and the half-lives. To obtain correct precipitation yields, we exclude the nuclides whose decays are affected by their parent or daughter nuclide from the analysis of the coprecipitation yield. Especially, the ⁹¹Sr and ¹⁵¹Pm nuclides are of great importance for the establishment of the experimental method: Sr is comparative data for element 102, No, and Pm is near to Sm in the periodic table (Radioactive isotopes of Sm were not observed in both RIKEN and KUR multitracer). The coprecipitation experiment was succeeded and now the data are under analysis. The coprecipitation yields would be shown later.

REFERENCES:

- [1] Y. Kasamatsu *et al.*, *Appl. Radiat. Isot.* **118** (2016) 105-116.
- [2] Y. Kasamatsu *et al.*, *J. Nucl. Radiochem. Sci.* **14** (2014) 7-11.
- [3] K. Takamiya *et al.*, *J. Nucl. Radiochem. Sci.*, **1** (2000) 81-82.

M. Nogami, K. Dohi, S. Nakamura and N. Sato¹

¹Faculty of Science and Engineering, Kindai University
²Research Reactor Institute, Kyoto University

INTRODUCTION: It is of great importance to develop resins with selectivity to uranium(VI) species in nitric acid media. As a part of this purpose, we have previously investigated the change in chemical structure and adsorptivity to metal ions of a cyclic monoamide resin consisting of poly-*N*-vinyl- ϵ -caprolactam (VEC) with a 7-membered ring and polyvinylpyrrolidone (PVPP), another cyclic monoamide resin with a 5-membered ring by γ -ray irradiation in HNO_3 . The manner of structure change in these two resins has been found basically identical, namely, starting from the cleavage of the monoamide ring by the addition of oxygen atom originating from HNO_3 , followed by the formation of chain monoamides by the continuous addition of oxygen. These compounds have multiple coordinative oxygen atoms, but the change in the adsorptivity has been found different resulting probably from the number of atoms in the ring[1-3]. For these two resins, the functional carbonyl groups are located relatively close to the main polymer chain. In the present study, a resin consisting of 1-(4-vinylbenzyl)piperidin-2-one (VBPP) was newly synthesized. It has a 6-membered cyclic piperidine ring with a spacer between the functional carbonyl group and the main polymer chain. γ -Ray irradiation in HNO_3 was performed to this resin to reveal the change in chemical structure and adsorptivity.

EXPERIMENTS: VBPP was synthesized by reacting piperidin-2-one with copolymer beads of chloromethylstyrene and divinylbenzene by following the literature[4]. γ -Ray irradiation to VBPP was carried out using 6 M HNO_3 similarly to the earlier study (max. 0.95 MGy)[1]. The irradiated VBPP was separated from the supernatant liquid and washed using distilled water to avoid further degradation by HNO_3 . Adsorptivities of the irradiated VBPP to metal ions at equilibrium were obtained by a batch method. Samples of the conditioned resin (wet 0.15 g) and 3 cm³ of 0.1 - 6 M HNO_3 solutions containing 1 mM Pd(II), Zr(IV), or Mo(VI) were shaken at 298K in a thermostatic shaking bath for 24 h. After shaking, samples of the supernatant were taken and the concentrations of the metal ions were measured using ICP-OES. Adsorptivities were evaluated by the distribution ratio, K_d .

RESULTS: Adsorptivities of VBPP irradiated in 0.1 M HNO_3 at various dose to the examined metal ions are shown in Fig. 1. The K_d values for Re(VII) are found decreased with increasing dose. On the other hand, those for Pd(II) and Zr(IV) are found decreased with increasing dose. These tendencies were also observed for

the samples with the other examined HNO_3 concentrations. It has been revealed that the irradiated VEC and PVPP showed increasing adsorptivities to Pd(II) and Zr(IV), and these are in accordance with the results in this study.

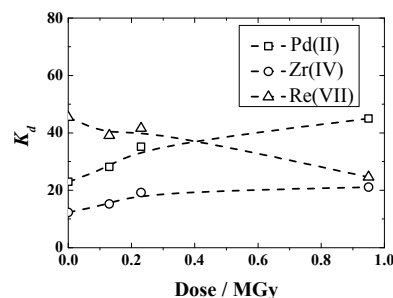


Fig. 1. Adsorptivity of VBPP irradiated in 0.1 M HNO_3 at various dose to metal ions in HNO_3

For the IR spectra of irradiated VBPP, a new peak generated at around 1730 cm⁻¹ probably attributed to a carboxyl group. In addition, no water-soluble degraded compounds were observed for the supernatant liquid separated from the irradiated VBPP by ¹H and ¹³C NMR analyses.

The above results indicate that the structure change in VBPP by γ -ray irradiation in HNO_3 occurred mainly in piperidine ring similarly to those for PVPP and VEC and that the “spacer” part underwent little influence (Fig. 2). Water-soluble degraded compounds were observed for PVPP and VEC, e.g., oxalic acid for PVPP and succinic acid for VEC, respectively. The reason why such compounds were not generated in VBPP is unclear so far.

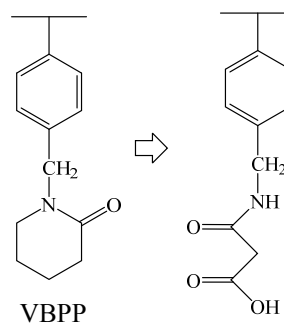


Fig.2. Expected major route of change in chemical structure of VBPP by γ -ray irradiation in HNO_3

REFERENCES:

- [1] N. Miyata *et al.*, KURRI Progress Report 2010 (2011) 258.
- [2] M. Nogami *et al.*, J. Radioanal. Nucl. Chem., **296** (2013) 423-427.
- [3] T. Nishida *et al.*, KURRI Progress Report 2013 (2014) 295.
- [4] M. Nogami *et al.*, Prog. Nucl. Energy, **50** (2008) 462-465.

CO9-9 Electrochemical Behavior of Zirconium in Molten Chloride Coexisting Fluoride and Oxide to Develop Processing Nuclear Fuel Debris

T. Emori, T. Sato, H. Matsuura^{1,2}, A. Uehara³

Graduate School of Engineering, Tokyo City University

¹ Faculty of Engineering, Tokyo City University

² Atomic Energy Research Laboratory, Tokyo City University

³ Research Reactor Institute, Kyoto University

INTRODUCTION: In order to develop processing nuclear fuel debris caused by nuclear accident of the Fukushima Daiichi Nuclear Power Plants with huge earthquake and tsunami 2011, We proposed selective fluorination and molten salt electrolysis to separate uranium from nuclear fuel debris. Process scheme is as follows; 1) selective fluorination; UF_4 was fluorinated from nuclear fuel debris using HF[1], 2) selective dissolution; UF_4 was dissolved in molten bath and 3) molten salt electrolysis; uranium ions were reduced in molten bath, and uranium metal or oxide was deposited on electrode. However coexisted zirconium can be fluorinated with uranium and zirconium oxide will be remained at the upstream process. Therefore, electro-reduction of uranium cannot be made because standard redox potential of zirconium is more positive than uranium. Zirconium electrochemistry due to the presence fluoride ions and oxide should be investigated to reduce zirconium concentration in molten bath.

EXPERIMENTS: All the electrochemical experiments using molten LiCl-KCl have been performed in an electric furnace which is built inside a glove box filled with on argon atmosphere using an electrochemical analyzer. Electrochemical analysis has been performed according to both Cyclic voltammetry and differential pulsed voltammetry by using the electrodes as follows: working electrode: tungsten, counter electrode: glassy carbon and reference electrode: silver wire dipped in molten LiCl-KCl + AgCl inside the borosilicate tube. Silica glass was used as a crucible. To observe the oxide addition effect, 0 and 10 times amount of Li_2O to the concentration of zirconium (0.1 mol%) was added to the molten bath. Constant-voltage and constant-current electrolysis has been carried out during 2000 sec to obtain a sample of characterization for SEM/EDX and XRD by using the electrodes as follows: cathode: tungsten, anode and reference electrode: silver wire dipped in molten LiCl-KCl + AgCl inside the borosilicate tube. All measurements have been performed at 823.15 K. Sweep rate was 50 mV/s and sweep potential range was -0.2 to -1.7(V vs. Ag/AgCl).

RESULTS AND DISCUSSION: As shown in Fig. 1, cyclic voltammetry of cathodic sweeps and anodic sweeps was observed mainly zirconium reduction peaks and oxidation peaks[2]. Increasing current density from -0.8 (V vs. Ag/AgCl) and reduction potential of Zr^{4+}/Zr^{2+} was observed at -1.4 to -1.0 (V vs. Ag/AgCl). Reduction potential of Zr^{2+}/Zr^0 was also observed at -1.6(V vs. Ag/AgCl). The potential of zirconium reduction to metal was not negatively shifted, while, the potential of zirconium to divalent was negatively shifted and the current of zirconium to divalent further decreasing by increasing measurement cycle. It was considered that structure of zirconium ions complex was changed by addition of oxide. Furthermore, this fact suggested that the substance with poor electrical conductivity such as ZrO might be deposited on the electrode. In the constant current electrolysis, it was confirmed that a difference in the voltage change was observed to compare containing Li_2O sample and Li_2O free sample. In the case of Li_2O free sample, the current increases or decreases drastically. It can be expected that zirconium ions concentration in molten bath decreases and the behavior of deposition of zirconium metal changes according to formula of $ZrCl_4 + 2Li_2O = ZrO_2 + 4LiCl$ [3].

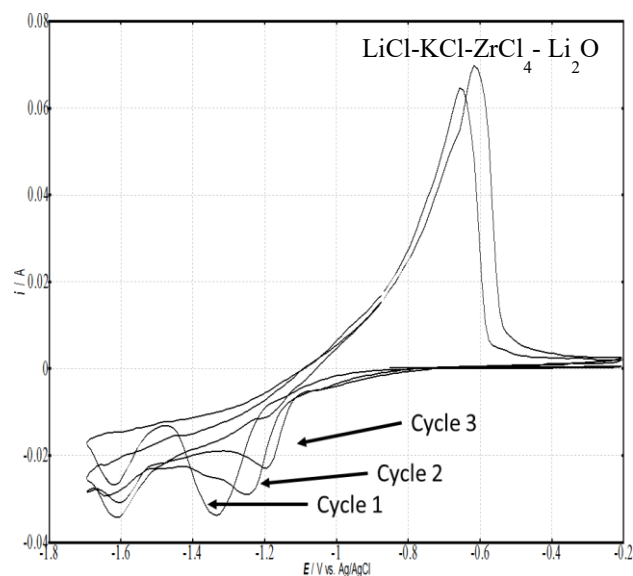


Fig.1 CV for molten LiCl-KCl containing 0.1 mol% $ZrCl_4$ and containing 1 mol% Li_2O

REFERENCES:

- [1] T. Ono, N. Sato, A. Nezu, T. Uchiyama, H. Matsuura, *ECS, Trans.*, **75**, 87, 2016
- [2] M. Iizuka, CRIEPI Report T98001, 23, 1998
- [3] Y. Sakamura, T. Kato, M. Kurata, H. Moriyama, CRIEPI Report T96073, 7, 1997

M. Yoneda, Y. Shimada, D. Setouchi, R. Kato, S. Fukutani¹ and M. Ikegami¹

Faculty of Engineering, Kyoto University

¹Institute for Integrated Radiation and Nuclear Science, Kyoto University

INTRODUCTION: The procedure to the final disposal of the waste polluted with radioactive Cs in Fukushima is far from well established. In carrying out a middle storage of the polluted waste and its final disposal, it is necessary that behaviors of radioactive Cs in the wastes are clarified and a realistic method is suggested to estimate leakage of radioactive Cs to the environment in future to establish the safe disposal method of the waste. This study developed the theoretical equation to estimate the result of Cs elution test of incineration ash containing soil and proposed a practical method to get the parameter in the equation on site.

THEORY AND EXPERIMENT: Based on Langmuir type competitive adsorption theory, and assuming the existence of three types of adsorption sites for Cs in soil, which are So type: exchangeable adsorption site mainly on organic matter; Ss type: exchangeable adsorption site mainly in clay matrix; and Sf type: almost unchangeable adsorption site in soil called frayed edge site. Then, adsorbed Cs is expressed by the following equations:

$$[Cs-S] = [Cs-So] + [Cs-Ss] + [Cs-Sf] \tag{1}$$

$$[Cs-So] = [So_{max}] b_{Cs-So} [Cs^+] / (1 + \sum_i b_{i-So} [M_i]) \tag{2}$$

$$[Cs-Ss] = [Ss_{max}] b_{Cs-Ss} [Cs^+] / (1 + \sum_i b_{i-Ss} [M_i]) \tag{3}$$

$$[Cs-Sf] = [Sf_{max}] b_{Cs-Sf} [Cs^+] / (1 + \sum_i b_{i-Sf} [M_i]) \tag{4}$$

where,

[Cs⁺]: concentration of Cs⁺ in eluate (meq/mL)

[M_i]: concentration of cation i in eluate (meq/mL)

[Cs-S] : adsorbed Cs to solid phase in soil (meq/g)

[Cs-So], [Cs-Ss], [Cs-Sf]: adsorbed Cs to So type, Ss type, and Sf type adsorption site (meq/g) .

Considering the practical situation of incineration ash containing soil, the elution ratio E_{Cs} (%) by standard heavy metal elution test of Ministry of Environment is expressed by the following equation:

$$E_{Cs} = 100 / (1 + (a/R)RIP/[K^+]) \tag{5}$$

where,

a: weight containing (or mixture) ratio of soil in incineration ash,

R: weight ratio of incineration ash and eluate,

[K⁺]: concentration of K⁺ in eluate (meq/mL).

The efficiency of Equation (5) is considered by the following experiment:

A quantity of Cs is added to Refuse Derived Fuel (RDF) , then it is mixed with a certain amount of forest soil, then it is incinerated at 500 degree C for three hours, and then it is eluted by the method of elution test of Ministry of Environment.

RESULTS AND DISCUSSION: The elution ratio estimated by equation (5) is compared with observed value in Fig.1. It shows that equation (5) can well estimate the elution ratio of Cs from incineration ash containing soil, when the soil mixture ratio is not small. Equation (5) also shows that it is not necessary to measure the soil mixture ratio a and the concentration of K⁺ respectively, but it is enough to measure the value of a/[K⁺]. We also showed that the ratio of a/[K⁺] can be estimated from the ratio of Si and K measured by a portable XRF instrument:

$$a/[K^+] = (M_K R) / (1000 r_{Si} ([K/Si] - r_K / r_{Si})) \tag{6}$$

where,

M_K: atomic mass of K,

r_{Si}: weight ratio of Si in soil,

r_K: weight ratio of K in clay matrix

[K/Si]: weight ratio of K and Si measured by XRF.

It is expected that elution ratio of each sample can be estimated on site using XRF measurement and equation (5) and (6).

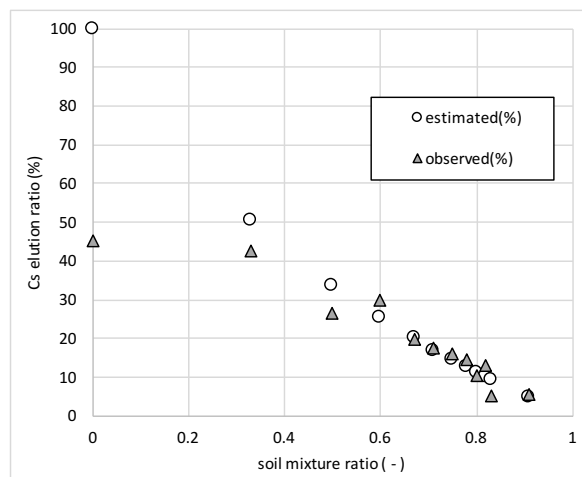


Fig.1 Comparison of estimated and observed elution ratio of Cs from incineration ash depending on its soil mixture ratio.

CO10-2 Ethnographic Study of Radiation Regulation for Victims Living in a Low Dose Radiation Field post National Decontamination Act in Fukushima

M. Takagaki, K. Uno and SI, Masunaga¹

Louis Pasteur Center for Medical Research

²Institute for Integrated Radiation and Nuclear Science, Kyoto Univ

INTRODUCTION: In FY 2017, we interviewed the scientists of IIRNS about the responsibilities of science on Fukushima nuclear accident, and heard precious opinions. We sincerely appreciate them for their many suggestive comments. In particular, the necessity of ethnography on regulation of radiation dose was discussed. Therefore, this time we analyzed the numerical values of environmental radioactivity in Fukushima Iitate village and feelings of villagers from long-term investigation and summarized it in this report as ethnography of radiation regulation.

Many of the villagers who had gone back to home in Iitate were elderly. The reason for many villagers to return home while they know that their village is still contaminated with low dose radiation was a sense of unity with previous living for agriculture. Elderly people who can only find living in the village life have returned home while they also aware of the radiation hazard after national decontamination act.

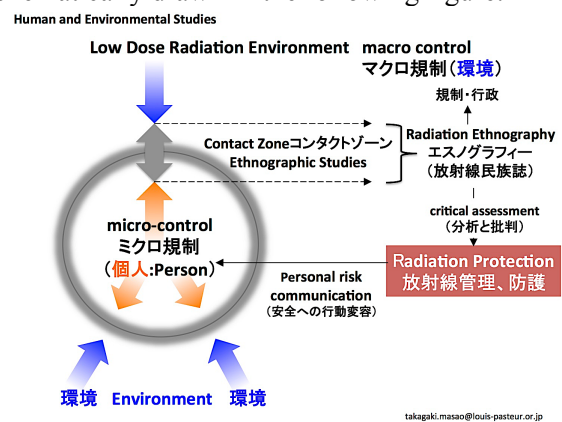
NARRATIVE: Mrs. S who came back to Sasu says that *in our refuge where my husband and I have been evacuated, even when our children and grandchildren who live outside the prefecture come to visit there are no places to sleep for a narrow floor. Because it was canceled evacuation on June 2017, we decided to return to the living home in Iitate to greet the grandchildren in a large house. Although it is not good that grandchildren stay for about two or three days in low dose radiation field but we think that 2-3 days exposure might be safe for their radiation protection. There is one other reason to return. Since I had been always listening to grandpa and grandma's narratives of hardship for building our house and keeping farm in Iitate village, we thought that it was quite natural for us to protect our homes then we decided to go back to our village.*

NARRATIVE: Mr. N who came back to Ohkura says that *after returning home, we made vegetables by putting compost in the decontaminated hothouse. There is unfortunately 100-200Bq in the vegetables experimentally grown there. But most of all that I want to do is to contact with the soil. When I am cleaning the flowerbeds and giving fertilizer and fertilizer, I forget about worries and anger, I feel very calm. It is mysterious. Fear for low dose radiation hazard does not leave from my head and the bottom of my heart. However happiness to make vegetables and flowers in Iitate that I could not do for seven years so far surpass my fear. Even after decontamination, we know radioactivity still*

remains in the soil. However, we thought that we would not be relieved at the refuge at all, we decided to return as a place to relax.

The villagers will come back to their villages by giving priority to their living although they know the risk of the low-level radiation environment. Scientist's explain to the villagers about the risk of low level radiation for the purpose of literacy for radiation protection might not be effective anymore. Many other narratives will be handed over Takagaki's second doctoral thesis due to space limitations.

DISCUSSION: A contact zone between macro control (environment) and micro control (person) is schematically drawn in the following figure.



It is difficult for villagers whose communities are damaged to act collectively (Hannah Arendt, 1906.10.14. - 1975.12.4.). Meanwhile, it seems that the bio-politics that encourages villagers to go home in the low-level radiation environment seems to have further divided the community through villagers' management and enclosure (Michel Foucault, 1926.10.15. - 1984.6.25.).

When the evacuation direction was canceled on June 2017, because the community was further divided by being left to the free will of the villagers rather than the joint return, group activities became difficult in subsequent litigation activities. As pointed out by Arendt, collective activities will be difficult unless the group becomes monolith once again.

We scientists are forced to simply restrict with numerical values of radiation when doing radiation protection, but in reality the radiation contamination should be carefully managed by taking into consideration the thought of the victims lurking in various ways in the contact-zone.

Acknowledgments: I would like to thank the scientists at IIRNS who gave us suggestive many comments on a several hours interview and also thank the villagers of Iitate Village who accepted interview willingly for more than several years. This study is financially supported by JSPS grant (No.17K18536).

CO12-1 Profile measurements of Coherent Cherenkov Radiation Matched to the Circular Plane at KURNS-LINAC

N. Sei, T. Takahashi¹

Research Institute for Measurement and Analytical Instrumentation, National Institute of Advanced Industrial Science and Technology

¹*Institute for Integrated Radiation and Nuclear Science, Kyoto University*

INTRODUCTION: In order to generate an intense light beam in the terahertz (THz) region, we proposed coherent Cherenkov radiation matched to circular plane wave (CCR-MCP) using a hollow conical dielectric [1]. Cherenkov radiation concentrates on the surface of a cone with the Cherenkov angle [2]. Because it was difficult to converge the Cherenkov radiation, it was not used as a THz-wave source based on electron accelerators. In the scheme of the CCR-MCP, the CCR generated on the inner surface of the hollow conical dielectric is entirely reflected from the conical surface and the CCR phase is matched to the basal plane. Then, the CCR-MCP beam is easy to transport for applied experiments. We have already observed the CCR-MCP beam and measured its radiation power. In this fiscal year, we measured two-dimensional distributions of the CCR-MCP beam in the experimental room.

EXPERIMENTS: We performed the experiments of the CCR-MCP with an L-band linac at Kyoto University Institute for Integrated Radiation and Nuclear Science. High-density polyethylene was used as a material for the hollow conical dielectric. The observation of hollow structure peculiar to the CCR-MCP beam is easier as the inner diameter of the hollow conical dielectric is larger. However, the intensity of the CCR-MCP beam decreases as the inner diameter increase, and the inner diameter was set to be 10 mm. When the bottom of the hollow conical dielectric was small, the CCR-MCP beam was spread by diffraction at the experimental room. Therefore, the length of the hollow conical dielectric was set to be 80 mm, which was the maximum value that the CCR-MCP beam could be transported to the experimental room.

An aluminum collimator with the length of 150 mm and the inner diameter of 8 mm was set in front of the hollow conical dielectric so that the electron beam did not collide with the hollow conical dielectric. In order to avoid generation of coherent transition radiation, a kapton film with a thickness of 50 μm was located at 0.4 m from the hollow conical dielectric and the electron beam and the CCR-MCP beam were separated by it. The CCR-MCP beam was transported to the experimental room and emitted from a monochromator without a diffraction grating to the air. This beam was converted into a parallel beam by a spherical concave mirror. It was focused by another spherical concave mirror and measured by a Si bolometer. We installed an aperture with a diame-

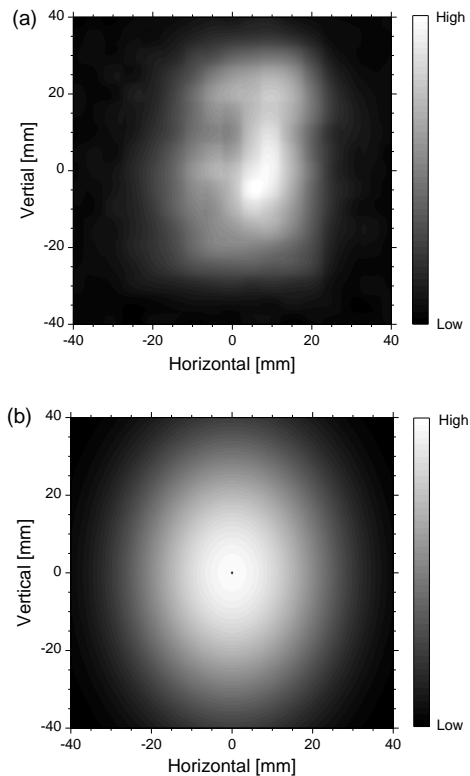


Fig. 1 Measured (a) and calculated (b) two-dimensional distributions of the CCR-MCP.

ter of 10 mm, which was set on an X-Y axis translation stage, at the parallel beam, and measured the two-dimensional distribution of the CCR-MCP beam.

RESULTS: The measured two-dimensional distribution of the CCR-MCP beam is shown in Fig. 1(a). It is noted that the hollow structure, which the radiator has, disappears at the observation point due to the diffraction. Because the short-focus concave mirror is used instead of a toroidal mirror to make a parallel beam, the profile of the CCR-MCP beam is an ellipse with the short axis in the horizontal direction. Fig. 1(b) shows the two-dimensional distribution of the CCR-MCP beam calculated for the hollow conical dielectric with the length of 80 mm. The measured standard deviations are about 20% smaller than the calculated ones. However, we note that both the measured profile and the calculated profile have a similar, shorter axis in the horizontal direction. We plan to measure the two-dimensional distribution of the CCR-MCP beam near the hollow conical dielectric.

REFERENCES:

- [1] N. Sei *et al.*, Phys. Lett. A **379** (2015) 2399.
- [2] T. Takahashi *et al.*, Phys. Rev. E **62** (2000) 8606.
- [3] N. Sei and T. Takahashi, Sci. Rep. **7** (2017) 17440.

K. Shinoda and Y. Kobayashi¹

*Department of Geosciences,
Graduate School of Science, Osaka City University*

¹*Research Reactor Institute, Kyoto University*

INTRODUCTION: The ^{57}Fe Mössbauer spectroscopy have been widely used to analyses of $\text{Fe}^{2+}/\text{Fe}^{3+}$ ratio and Fe^{2+} ratio between non-equivalent crystallographic sites of Fe bearing minerals. Fe ions in non-magnetic minerals such as olivine, pyroxene, mica show doublet peaks due to quadrupole splitting in Mössbauer spectra. The quadrupole splitting results from an interaction between the nuclear quadrupole moment and the electric field gradient (EFG) due to electrons around the nucleus. In general, while an Fe^{3+} ion occupying octahedral sites results in the quadrupole splitting as narrow as about 0.5mm/s, quadrupole splitting of Fe^{2+} results in the wider quadrupole splitting about 2mm/s. Mössbauer peaks have Lorentzian shapes, Lorentzian peaks are characterized by 4 variables, (1) isomer shift (IS), (2) quadrupole splitting (QS), (3) line width (LW) and (4) intensity ratio (IR). Doublet peaks of Mössbauer spectra are usually analysed by least square fitting (LSQ) raw data with allowing 4 variables to vary independently. Separation of doublet peaks due to Fe^{2+} and Fe^{3+} of mixed valence of iron minerals can be easily done, because wide QS of Fe^{2+} and narrow QS of Fe^{3+} do not overlap. Therefore, the most probable values of 4 variables can be converging, even if four variables are allowed to vary independently during LSQ. On the other hand, Fe^{2+} ions occupying two non-equivalent sites such as M1 and M2 sites in pyroxene give two kinds of doublet peaks of closely overlapping. In the measurements of Mössbauer spectra of thin sections of a single crystal, a constraint on the intensity ratio of quadrupole splitting is important during data fitting. Intensity ratio due to Fe^{2+} (Fe^{3+}) occupying a crystallographic site can be calculated from an EFG tensor of the site. The determination of EFG tensor is important to calculate intensity ratio. To compare an experimentally determined EFG tensor with the crystal structure is important for theoretically calculating EFG tensors. The EFG tensor can be experimentally determined from intensity tensor measured by Mössbauer spectra of single crystal. Zimmermann (1975, 1983) proposed the formulation of EFG tensor from intensity tensor and an example of monoclinic crystal. In this study, Zimmermann's method was applied to aegirine

($\text{NaFeSi}_2\text{O}_6$), in which Fe^{3+} occupies M1 site of pyroxene structure in order to determine EFG tensor of aegirine.

EXPERIMENTS and RESULTS: A single crystal of aegirine was used for this study. Six crystallographically oriented thin sections were prepared by measuring X-ray diffraction using precession camera. Thin sections #1 and #2 are normal to b^* and parallel to (110) cleavage plane, respectively, which are mounted on 1mm ϕ holed Al plate. Thin section #3 normal to a^* -axis was mounted on Goniometer and adjusted b^* -axis to dial (horizontal) direction by X-ray diffraction. Thin sections #4 and #5 normal to b^* -axis were mounted on Goniometer as c^* and a -axes to dial, respectively. Thin section #6 is normal to c^* -axis. In this study, Cartesian coordinate ($X Y Z$) is set as $X//c^*$, $Y//a$, $Z//b^*$ in order to set b -axis as Z and set a , b , c -axes as right-handed system, where a , b , c are real and a^* , b^* , c^* are reciprocal lattice vectors of aegirine. Mössbauer measurements were carried out in transmission mode on a constant acceleration spectrometer with an Si-PIN semiconductor detector (XR-100CR, AMPTEK Inc.) and multi-channel analyzer of 1024 channels. A 3.7GBq $^{57}\text{Co}/\text{Rh}$ of 4mm ϕ in diameter was used as γ -ray source. An ^{57}Fe -enriched iron foil was used as velocity calibrant. The two symmetric spectra were folded and velocity range was $\pm 5\text{mm/s}$. Thickness corrections of raw spectra were done by transmission integral method of Mosswin program. According to Zimmermann (1975, 1983), intensity and local EFG tensors is determined. As the results, three components of Electric Field Gradient (EFG) tensor of Fe^{3+} in M1 site of aegirine were (-0.218(5), 0.214(5), 0.004(10)). Asymmetric parameter η was nearly equal to 1. The principal axes of EFG tensor of aegirine are almost oriented to a^* , b , c -axes. While V_{xx} axis is determined to orient b -axis, V_{yy} and V_{zz} axes were not fixed along a^* or c -axes.

REFERENCES

- Zimmermann, R. (1983) The intensity tensor formulation for dipole transitions (e.g. ^{57}Fe) and its application to the determination of EFG tensor. *Advances in Mössbauer spectroscopy* (Thosar, B.V. Ed.). pp.273-315, Elsevier Scientific Publishing Co. Amsterdam.
- Zimmermann, R. (1975) A method for evaluation of single crystal ^{57}Fe Mössbauer spectra ($\text{FeCl}_2 \cdot 4\text{H}_2\text{O}$). *Nuclear Instruments and Methods*. 128, 537-543.

T. Miura¹, R. Okumura², Y. Inuma², S. Sekimoto² and K. Takamiya²

¹National Metrology Institute of Japan, AIST

²Research Reactor Institute, Kyoto University

INTRODUCTION: National Metrology Institute of Japan (NMIJ) is responsible for developing certified reference materials and for establishing the traceability of SI (The International System of Units) on chemical metrology in Japan. To establish SI traceability, the primary method of measurements should be applied to the characterization of the certified reference materials. Recently, neutron activation analysis using comparator standard is recognized as a potential primary ratio method [1]. Despite the potential of neutron activation analysis as primary ratio method, the evaluation of the measurement uncertainty is required in any analysis. In general, there are three main components of uncertainty in neutron activation analysis, that is, sample preparation uncertainty, neutron flux homogeneity, and gamma ray measurement uncertainty. Usually, flux monitor is used to correct the neutron flux in-homogeneity. However, although the flux monitor can correct the neutron flux variation using the count rate of the known amount of the monitor nuclide, it does not reflect the neutron flux of the actual sample. The most practical method to eliminate neutron flux in-homogeneity and to improve gamma ray measurement uncertainty is an internal standard method [2-4]. For the development of primary inorganic standard solution as national standard, the purity of starting material has to be determined. The high purity Ti metal was candidate starting material for preparation of titanium standard solution as national standard of Japan. The several trace analytical methods including neutron activation analysis, were used for purity determination of the high purity Ti metal. In this study, we presented that capability of instrumental neutron activation analysis for determination of Cl, Br, and I in high purity Ti metal.

EXPERIMENTS: The high purity Ti metal was purchased from Sumitomo Metal Mining Co. Ltd. The informative purity value of the Ti metal was 99.9 %. The calibration solution of Cl was prepared from NMIJ primary standard solution. The In solution for the internal standard for Cl was prepared from NMIJ primary standard solution. The calibration solution of Br was prepared from NMIJ primary standard solutions. The Au solution for the internal standard for Br was prepared from a high purity metal.

The Iodine standard solution was prepared from NMIJ primary standard solution. The In solution for the internal standard for Iodine was prepared from NMIJ primary standard solution. Three hundred mg of the Ti metal samples were used for Cl and I analysis. On the other hands, one gram of Ti metal sample was used for Br analysis. The neutron irradiations were performed by KUR (Kyoto University Research Reactor) Pn3 (thermal neutron flux: $4.7 \times 10^{12} \text{ cm}^{-2} \text{ s}^{-1}$) for 15 min. For the determination of Br in the Ti metal samples, the neutron irradiation were performed using KUR TCPn (thermal neutron flux: $8.0 \times 10^{10} \text{ cm}^{-2} \text{ s}^{-1}$, 12 h) for 12 h. The γ ray measurement system consisted of a Canberra GC4070-7500 Ge detector and a Laboratory Equipment Corporation MCA600

RESULTS: In this experiment, Cl, Br and I in the high purity Ti metal sample could not be detected even by using instrumental neutron activation analysis. Therefore, the upper limit of Cl, Br and I in the high purity Ti metal sample were estimated from the count rates of energy region of gamma rays emitted by each radioactive nuclide. The estimated upper limit of Cl, Br, and I were <1 mg/kg, <0.02 mg/kg and <0.1 mg/kg, respectively.

Impurity elements in high purity Ti metal sample were determined by multiple analysis methods such as instrumental neutron activation analysis, ICP-MS, combustion infrared spectrometry and so on. By subtracting the total value of impurity elements from 100%, the purity of the Ti metal sample was determined to be $(99.973 \pm 0.0013) \%$.

REFERENCES:

- [1] R.Greenberg, P. Bode, E. De Nardi Fernandes, *Spectrochim. Acta B*, **66** (2011) 193-241.
- [2] T. Miura, K.Chiba, T. Kuroiwa, T. Narukawa, A.Hioki, H. Matsue, *Talanta*, **82** (2010) 1143-1148.
- [3] T. Miura, H. Matsue, T. Kuroiwa, *J. Radioanal. Nucl. Chem.*, **282** (2009) 49-52.
- [4] T. Miura, R. Okumura, Y. Inuma, S. Sekimoto, K. Takamiya, M. Ohata, A.Hioki, *J. Radioanal. Nucl. Chem.*, **303** (2015) 1417-1420.

T. Takatsuka, K. Hirata, Y. Iinuma¹, R. Okumura¹ and K. Takamiya¹

National Metrology Institute of Japan, National Institute of Advanced Industrial Science and Technology

¹Research Reactor Institute, Kyoto University

INTRODUCTION: Hafnium oxide is utilized as high-*k* dielectric films for semiconductor devices in order to attain the higher performance. The device fabrication process should be in precise control of the thickness of thin (typically a few nm) dielectric films. However, the accurate measurements of the thickness in length unit are getting laborious, possibly caused by the atomic fluctuation at the interface layers. We aimed to quantify hafnium in hafnium oxide films in weight unit, instead of in length, by means of isotope dilution-neutron activation analysis (ID-NAA) [1].

EXPERIMENTS: Hafnium oxide films were deposited on 4-inch Si wafers by magnetron sputtering. The target thickness was set to 4 nm. The homogeneity in thickness over the wafer was estimated less than 2% of standard deviation. The prepared wafers with the films were cut into 10 mm × 10 mm pieces for the measurements.

The procedure for ID-NAA has two sequences of an isotope dilution (ID) and a reverse-ID to ensure traceability to the SI units; the latter sequence was performed to determine the hafnium concentration in a spike solution by referring to a hafnium standard. The spike solution was prepared by dissolving ¹⁷⁴Hf-enriched hafnium oxide in a HNO₃ + HF aqueous solution, and by diluting to a proper concentration. For calibrating the amounts of hafnium, a working standard solution was prepared by diluting NIST SRM 3122 gravimetrically. For the ID analysis, small amounts of the spike solution was dropped onto each hafnium oxide sample using a polyethylene pipette (HfO₂+Sp), while the spike solution or standard solution was dropped separately onto each piece of cleaned filter paper (Sp or STD), as shown in Fig. 1. The hafnium contents of the droplets were determined by weighing the polyethylene pipettes before and after every dropping. For the reverse-ID analysis, the spike and standard solutions were dropped onto one piece of filter paper (Sp+STD).

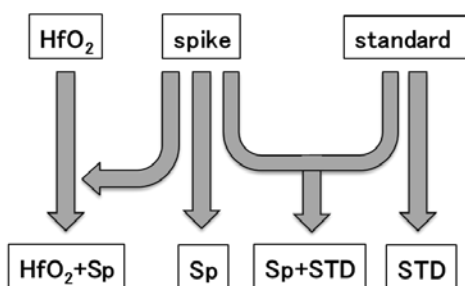


Fig. 1. Sample preparation for ID-NAA.

All the samples were sealed up separately in clean polyethylene bags, followed by being stacked in a polyethylene container for the neutron irradiation. The irradiation was performed for 4 hours with a $5.5 \times 10^{12} \text{ cm}^{-2} \cdot \text{s}^{-1}$ thermal neutron fluence rate at Pn-2 in the Kyoto university research reactor (KUR). The gamma-ray activity of each sample was measured by a high-purity germanium detector (CANBERRA) with an energy resolution around 2.0 keV and a relative efficiency of 40% at 1333 keV.

RESULTS: As shown in Fig. 2, several peaks are found in the gamma-ray spectrum, and most of the large peaks were due to the hafnium isotopes generated during the neutron irradiation. The peaks at 343 keV and 482 keV were selected to calculate the gamma-ray intensity ratio of ¹⁷⁵Hf to ¹⁸¹Hf for the samples. The integrated peak areas were converted into the counting rates at the end of the irradiation, taking into account of the radioactive decay and the dead time of the measuring system [2]. The amounts of hafnium in the hafnium oxide samples were calculated from the intensity ratios based on a formula reported in Ref. 1. The obtained amounts are 3.54 μg and 3.47 μg for two measured samples. Dividing the hafnium amounts by measured sample surface areas, the area densities are calculated to be 3.62 μg·cm⁻² and 3.58 μg·cm⁻². The resultant average is 3.60 μg·cm⁻², which agrees with the previous results of 3.68 μg·cm⁻² and 3.60 μg·cm⁻² obtained by NAA with an internal standards.

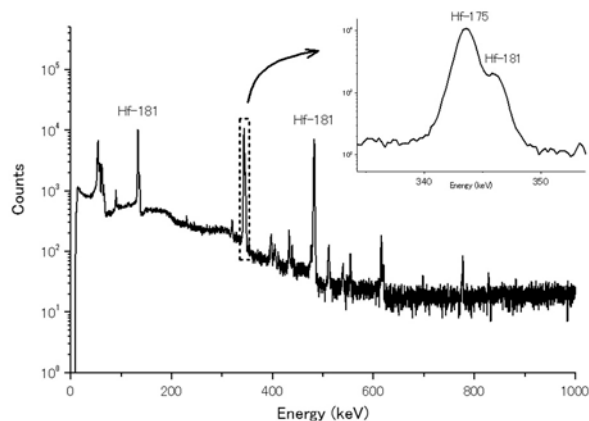


Fig. 2. Gamma-ray spectrum of hafnium oxide film + spike solution (HfO₂+Sp).

REFERENCES:

- [1] C. Yonezawa *et al.*, *Anal. Chem.*, **55** (1983) 2059-2062.
- [2] G. Gilmore and J. D. Hemingway, *Practical gamma-ray spectrometry* (John Wiley & Sons, Chichester, 1995).

CO12-5 The Structure of the DN-polymers under Different Temperature and Humidity

T. Tominaga, N. Sato¹, R. Inoue¹ and M. Sugiyama¹

Neutron Science and Technology Center, CROSS

¹ Institute for Integrated Radiation and Nuclear Science, Kyoto University

INTRODUCTION: Biocomposite systems have distinct hierarchical structures on the molecular, nanoscopic, microscopic, and macroscopic scales [1]. Synthetic materials polymerized from monomers are good mimics of biocomposites, and promise the creation of new materials.

We reported the fabrication of porous polymeric materials, namely, double-network polymers (DN-polymers) exhibiting unique mechanical properties against humidity change [2]. The DN-polymers were xerogels prepared from double-network hydrogels (DN-hydrogels) [3] consisting of two kinds of hydrophilic polymers with a crosslinker.

Previously we investigated static structures of dried-state DN-polymers by determining their porosity from nitrogen adsorption isotherms and mercury intrusion techniques. Besides, the morphologies of the DN-polymers were observed by scanning electron microscopy and laser microscopy. We showed that the DN-polymers formed a continuous porous network with diameters ranging from 1.7 nm to more than 100 μm [4]. Three classes of hierarchical porous structure were identified. Small pores (diameter 1.7–10 nm) were present within the walls of mid-sized pores (diameter 60 nm), and the mid-sized pores resided in the walls of large pores (diameter 4 μm). Recently we also found that unique mechanical properties are not only room temperature but also temperature dependence. Therefore, we study the structure of the DN-polymers under temperature and humidity controlling atmosphere. The length scale ξ of $3 < \xi \text{ nm} < 160$, which covers a network of hierarchical structure more than approximately 20 nm and inside the first class of hierarchical structure composing a linear polymer chains less than approximately 20 nm is measured in this study using SAXS.

EXPERIMENTS: The samples were prepared by DN-hydrogels [3] from 2-acrylamido-2-methylpropane sulphonic acid sodium salt (NaAMPS) and acrylamide (AAm) crosslinked with N, N'-methylenebisacrylamide (MBAA). Sheet-shaped DN-hydrogels were frozen and dried in a freeze-dryer unit, yielding the sheet-shaped freeze-dried DN-polymers [2,4].

Flow-humidity controlling system was developed for this SAXS measurements by mixing dried and humid nitrogen gas. Sensirion humidity sensors were used for controlling and monitoring temperature and humidity. The temperature from 5 to 80 dC was controlling by a Partier system. we compared dried condition and a constant moisture concentration (approximately 0.05 g/cm³). Cu-SAXS (RIGAKU Nanopix) available at Institute for Integrated Radiation and Nuclear Science, Kyoto University was used.

RESULTS: Preliminary results are shown in Fig. 1. The SAXS profiles were divided by a profile at low temperature 5dC. Although details are not understood, these figures are clarified differences of tendencies between different humidity and temperature.

Compared to temperature dependence of wet and dried

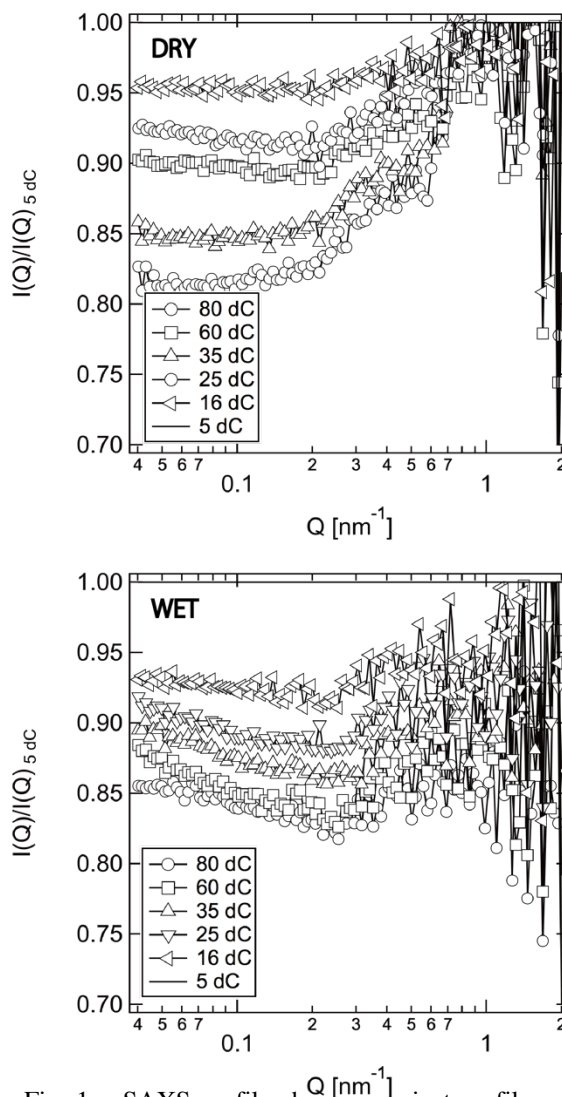


Fig. 1. SAXS profile changes against profiles of 5 dC under dried and wet conditions.

local structure of high-Q ($>20 \text{ nm}$) is quite different. Under the dried state, the local structure is fixed, no structure change against temperature difference, however under the wet state, the local structure can expand with a kind of similarity. This indicates that the mobility of inner structure of the first hierarchical structure composing a linear polymer chains against humidity is quite different. Further careful analysis would be required.

REFERENCES:

- [1] B.-L. (Editor) Su, C. Sanchez, X.-Y. (Editor) Yang, eds., *Hierarchically Structured Porous Materials*, (Wiley-VCH Verlag GmbH & Co. KGaA, Weinheim, 2011.)
- [2] T. Tominaga *et al.*, ACS Macro Lett. **1** (2012) 432–436.
- [3] J.P. Gong *et al.*, Adv. Mater. **15** (2003) 1155–1158.
- [4] T. Tominaga *et al.*, Polymer **108** (2017) 493e501

CO12-6 Electron Induced Noise on Avaranche Photodiode for Ganymede Laser Altimeter of Jovian Icy Satellite Exploerer

M. Kobayashi, O. Okudaira, M. Fujii¹, T. Takahashi² and N. Abe²

Planetary Exploration Research Center, Chiba Institute of Technology

¹*FAM science Co., Ltd.*

²*Research Reactor Institute, Kyoto University*

INTRODUCTION: The Ganymede Laser Altimeter (GALA) as part of the JUICE (Jovian Icy Satellite Explorer) payload is one of the instruments focusing on aspects related to the presence and characterizations of subsurface water oceans [1][2]. For the first time the time-variability of the global figure of a moon due to tides exerted by Jupiter will be detected by altimetry measurements.

GALA is a laser ranging instrument that measures time-of-flight of a transmitted laser pulse from the instrument on the spacecraft and the returned pulse from the surface of Ganymede. The returned laser pulse must consist of tiny amount of photons and high sensitive optical sensor is required to be used for light detection. The returned laser pulse reflects terrain slope and flatness, therefore the shape of the returned pulse is needed to be measured and recorded. In case of GALA, the receiver unit consists of a telescope, a back-end optics unit, an optical sensor, an analog electronics module and a range finder module. For optical sensor and the front-end electronics, we adopted an optical receiver module which contains an avalanche photo diode (hereafter APD) and a trans-impedance amplifier as front-end electronics in one package, which is manufactured by Excelitas Technologies, Montreal in Canada. The APD module is customized for our purpose based on one of their commercial APD modules, LLAM-1060-R8BH.

In case of GALA, we use the APD as an optical sensor converting optical return pulse to electrical signal while the APD is also sensitive to incident ionizing radiation. Ionizing radiation can induce hole-electron pairs in the depression layer of APD and the APD outputs electrical signal. Induced signals by ionizing radiation in orbit may affect light detection as false signals, called radiation noise. Jupiter has a strong magnetosphere and previous studies revealed that energetic electrons are trapped in the magnetosphere and major component among the other ionizing radiation like proton and the other energetic ion. The APD will be shielded up against to the Jovian radiation environment however some of electrons can penetrate the shield into the APD.

In this study, we used KURRI-LINAC as an electron beam source to emulate electrons irradiating the APD to investigate how energetic electron induces signals and interferes the returning laser pulse signal.

EXPERIMENTS: As device under test, we used an engineering module (EM) of APD module customized for GALA (GALA APD). The EM has the same performance as the flight module of GALA APD but before quality conformance inspection test for JUICE environment condition.

We performed twenty one runs of the LINAC and electrons was accelerated to six different energies for irradiation to the DUT, 5, 10, 20, 30 and 40 MeV. Irradiation angle is changed to be 0° (straight forward), 30°, 45°, 60°, 90° (right beside) and 180° (backward). The output signals of the trans-impedance amplifier in APD module were recorded with a digital oscilloscope.

RESULTS: Incident electron on the APD sensor induces a signal of short pulse, typically both rise and fall time are 2nsec. The pulse shape is not changed by the incident electron energy while the pulse shape is slightly broaden when the incident angle is large, 2-3nsec for incident angle of 60deg.

Pulse height of the signal induced by electrons has variation ranging 150 mV to higher when the responsivity of the APD sensor is about 700kV/W. For any energies and incident angles of electrons, the most events of the induced signal has pulse heights of 150mV to 300mV.

For backward irradiation, the APD module as DUT does not output any signals induced by irradiated electrons when the electron energy is 5MeV or lower. Apparently a structure on the back of the APD sensor in the module shields against incoming radiation.

CONCLUSIONS: We conclude that radiation induced noise on GALA APD in orbit does not significantly affect the performance of GALA. We will have radiation induced noise on GALA APD signal in orbit, however, the rate of occurrence is low (the incident rate of electron hit on the APD sensor is low), and the radiation induced noise hardly degrade SNR of the stop pulse because the pulse shape is different from the stop pulse rather similar to the start pulse. If a radiation induced noise has larger pulse height than power supplies voltages, it affect the signal baseline to be unstable but the radiation induced noise does not have such large pulse height as that.

REFERENCES:

- [1] H. Hussmann *et al.*, European Planetary Science Congress 2017, held 17-22 September, 2017 in Riga Latvia, **11** (2017) id. EPSC2017-567.
- [2] H. Hussmann *et al.*, 19th EGU General Assembly, EGU2017, proceedings from the conference held 23-28 April, 2017 in Vienna, Austria., **19** (2017) 16366.

M. Aoki, N. Abe¹, F. Morimoto², D. Nagao, Y. Nakatsugawa³, H. Natori⁴, T.M. Nguyen⁵, Y. Seiya², T. Takahashi¹, N. Teshima² and K. Yamamoto²

School of Science, Osaka University

¹*Research Reactor Institute, Kyoto University*

²*Faculty of Science, Osaka City University*

³*Institute of High Energy Physics, China*

⁴*Institute for Basic Science, Korea*

⁵*University of Science and Technology Da Nang City*

INTRODUCTION: There has been no observations related to a charged-lepton flavor violation (CLFV) process such as $\mu \rightarrow e \gamma$, μ -e conversion, τ -CLFV decays and so on up to now. Based on this fact, the charged-lepton flavor is assumed to be conserved a priori in the Standard Model of particle physics (SM). However, it is rather natural not to be conserved in most of the models beyond SM (BSM). Any discoveries or improvements of the upper limit on the branching ratio of CLFV processes provide very important information to BSM. DeeMe is one of experiments that aim to search for CLFV with μ -e conversion in nuclear field [1]. It uses high-power high-purity pulsed proton beam from J-PARC RCS. The detector of DeeMe should be operational after $\mathcal{O}(\mu\text{s})$ from a burst of particles (100 GHz/mm²). We successfully developed such a detector with high-voltage switching technique [2]. It is very important to evaluate the performance of the detector before we start the physics data taking at J-PARC MLF.

EXPERIMENTS: Measurement of detection efficiency for the newly developed DeeMe detector was performed at KURRI. Figure 1 shows the experimental setup placed at the exit of the electron LINAC at KURRI. The beam size was shaped to 2 cm \times 2 cm by a collimator, and the high-voltage switching multi-wire proportional chamber (MWPC) was placed in between two plastic-scintillation counters (TC1 and TC2). The timing of the MWPC high-voltage switch was synchronized to the electron gun timing (25 Hz) so that the MWPC is sensitive to the coming charged particles only during 6

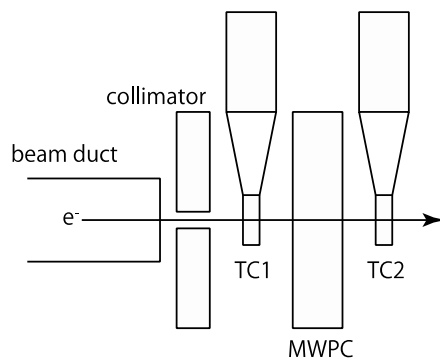


Fig. 1 Experimental Setup

μs in every 40 ms. A heater voltage of the electron gun of the LINAC was adjusted to reduce the number of electrons hitting the MWPC being only a few per pulse. Signal waveforms from MWPC were recorded with Fast ADCs. Signals from TC1 and TC2 were also recorded with another Fast ADC. Waveform data were obtained with several different conditions of the electron gun timings and electron intensities.

In the off-line analysis, the recorded waveforms from TC1 and TC2 were scanned to find hits in coincidence. In the case that there was the coincidence hit in TC1 and TC2, the waveforms from MWPC were scanned to find the hits at the same timing. The MWPC efficiency was calculated by taking a ratio between the number of MWPC hits and that of the TC1-TC2 coincidence hits.

RESULTS: Figure 2 shows the efficiency as a function of hit timing. The efficiency of this high-voltage switching MWPC is more than 98% after 1.3 μs from the gate of the high-voltage switching. This efficiency is sufficiently high as a charged-particle detector for DeeMe experiment.

Mode24.Paget (DeeMe.02.Reconstruction)

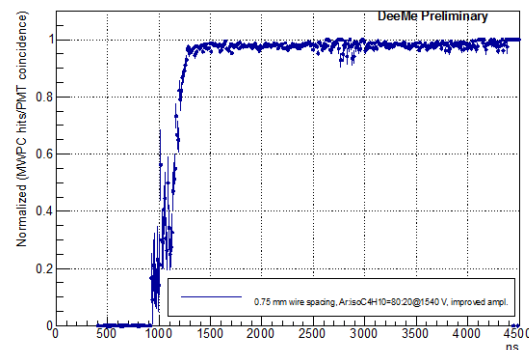


Fig. 2 Efficiency of the high-voltage switching MWPC as a function of time. Time origin corresponds to the time of high-voltage gate.

REFERENCES:

- [1] N. Teshima on behalf of the DeeMe Collaboration, "DeeMe experiment to search for muon to electron conversion at J-PARC MLF", in proceedings of NUFAC conference PoS (NuFact2017) 109 (2018).
- [2] H. Natori, et al., "A fast high-voltage switching multiwire proportional chamber", Prog. Theor. Exp. Phys. 2017(2) 023C01 (2017).

Influence of Submerged Condition and Soil on the Cadmium and Arsenic Concentration of Brown Rice

T. Inamura, D. Tojou, S. Fukutani¹ and K. Takamiya¹

Graduate School of Agriculture, Kyoto University

¹*Institute for Integrated Radiation and Nuclear Science, Kyoto University*

INTRODUCTION: Cadmium and arsenic concentration of brown rice are influenced by submerged condition of a paddy field which paddy rice grew. However, the Cd and As concentration of brown rice fluctuate by the growth environment except the submerged condition [1]. We examined the influence of the submerged condition to the Cd and As concentration of brown rice using the different paddy field soil.

EXPERIMENTS: The “Senshou” cultivar, which is Tropical-Japonica and upland rice, was used in this study. The soil (a) with the high concentration of Cd and As and the soil (b) with the low those concentration were used for cultivation of the upland rice. Four submerged treatments were carried out: treatment 3 (always keeping flooded) to treatment 0 (always keeping no flooded). The brown rice gathered at maturity stage was dried at 70°C for 48 h. The dried brown rice was crushed with an agate mortar, and the crushed sample was digested by microwave digestion. The Cd and As concentration of the digested solution of brown rice was determined using inductively coupled plasma-mass spectrometry (ICP-MS).

RESULTS: Influence of submerged condition and soil on the cadmium and arsenic concentration of brown rice are shown in Fig. 1. The Cd and As concentration in brown rice were influenced by those concentrations in the soil regardless of intensity of submerged treatment. The tendency that Cd concentrations increased and As concentration decreased when flooding strength decreased was detected in both soil. These results indicated that the submerged condition is able to be estimated by two-dimensional distribution of the Cd and As concentration of brown rice regardless of the both concentration of paddy soil.

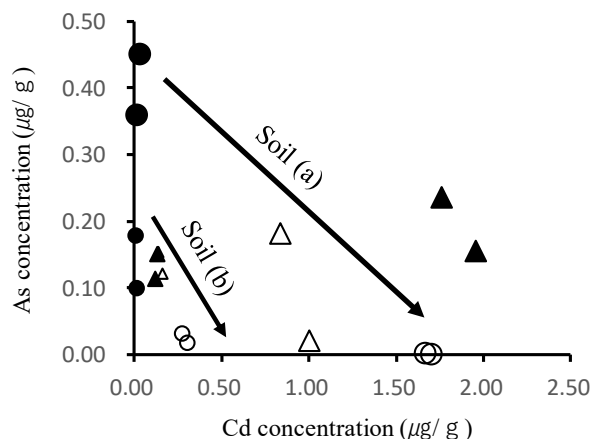


Fig. 1, Influence of submerged condition and soil on the cadmium and arsenic concentration of brown rice.

●, ▲, △ and ○ indicate the submerged treatment levels of 3 (always keeping flooded), 2, 1 and 0 (always keeping no flooded), respectively.

REFERENCE:

[1] T. Inamura *et al.*, *Jap. J. Crop Sci.*, **75** (2006) 273-280.

T. Kubota, S. Fukutani, Y. Shibahara and T. Ohta¹

*Institute for Integrated Radiation and Nuclear Science,
Kyoto University*

¹*Central Research Institute of Electric Power Industry*

INTRODUCTION: Radioactive tracers are a useful tool for the investigation on the fate and migration of various elements in the environment [1]. In particular carrier free radionuclides, without naturally occurring isotopes, are important for the study on the migration of trace elements in living organisms without any chemical toxicity. Carrier free tracers can be produced through (γ , p) reaction. In this report we produced the radioactive tracers (^{43}K and ^{136}Cs), which are planned to be applied for the investigation on the migration of potassium and ^{137}Cs in glasses and trees.

EXPERIMENTS: ^{43}K and ^{136}Cs were produced from calcium and barium, respectively. Target materials used were calcium chloride dihydrate and barium chloride dihydrate. Each material was dried up in a quartz test tube and then encapsulated in quartz under vacuum. The sample material was irradiated with high-energy photons, which was generated by the bombardment of Pt with electrons of 30 MeV, for 20 hours at the KURRI-LINAC [2]. Potassium and cesium were purified by a carbonate precipitation method from the target sample immediately after irradiation. The target sample was dissolved with H_2O and the resulting solution was equally divided into two polyethylene centrifugation tubes. This solution was added with 3 M ammonium carbonate to remove calcium and barium as precipitate [3]. After centrifugation the supernatant was transferred to a glass beaker and heated to dryness in order to remove HN_4Cl . Finally, ^{43}K and ^{136}Cs were dissolved into 1 M HCl.

RESULTS: Target materials, calcium and barium, were sufficiently removed by the precipitation method in Fig. 1 and 2. This method showed that the recovery ratio and decontamination factor of alkali metal was 0.9 and 10^5 , respectively. From the calcium target strontium as impurity and ^{47}Sc as decay product of ^{47}Ca were also removed. In the barium target ^{129}Cs produced simultaneously was one of major gamma emitters; however, this nuclide can be ignored after cooling for 2 weeks due to its short half-life of 1.34 d. The induced radioactivity of other cesium nuclides, ^{132}Cs , ^{134}Cs , and ^{137}Cs , was low enough not to disturb radioactivity measurements. Radioactive tracers, ^{43}K and ^{136}Cs , suitable for in vivo experiments were produced and will be applied for plant and animal experiments in future work.

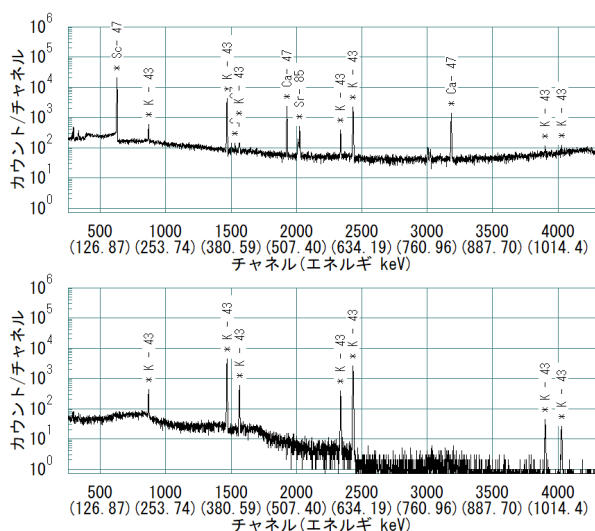


Fig. 1. Gamma-ray spectra of ^{43}K before (upper) and after (lower) purification.

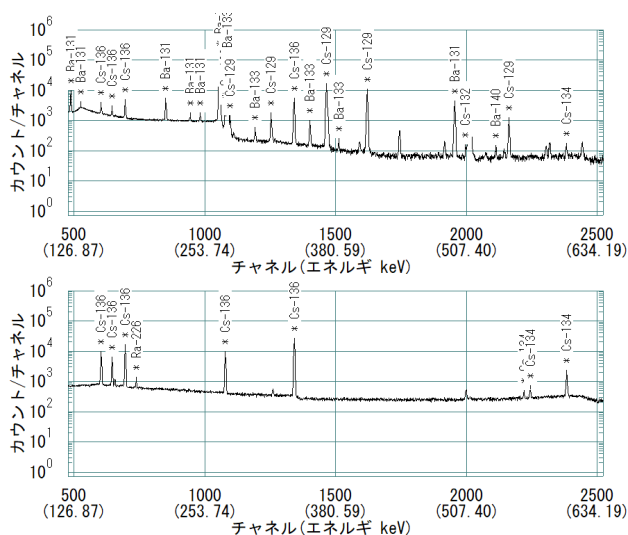


Fig. 2. Gamma-ray spectra of ^{136}Cs before (upper) and after (lower) purification.

REFERENCES:

- [1] T. Kubota *et al.*, J. Radioanal. Nucl. Chem. **296** (2013) 981-984.
- [2] T. Kubota *et al.*, KURRI Progress Report 2011 (2012) 286.
- [3] T. Kubota *et al.*, KURRI Progress Report 2016 (2017) 19.

H. Masui, A. H. Kafi, J. C. Javier, T. Tumenjargal, M. Cho and K. Takamiya¹

Laboratory of Spacecraft Environment Interaction Engineering, Kyushu Institute of Technology

¹Research Reactor Institute, Kyoto University

INTRODUCTION: Kyushu Institute of Technology (Kyutech) has been developing nano satellites since 2010. Kyutech’s main concern is the environmental testing. As a part of environmental testing, the radiation testing is also important. Since 2012, Kyutech has tested the radiation test using ²⁵²Cf in Kyoto University Research Reactor Institute. Currently, Kyutech are developing many cubesats and a standard bas system. The development of standard bas system has many advantages such as improvement of reliability, short delivery and the achievement of mission-oriented satellite development. For the next generation bus system, Kyutech suggest a back plane type configuration^[1]. To improve the accessibility and flexibility of backplane type configuration, we decided to introduce Complex Programmable Logic Device (CPLD) as a new device to back plane. The advantage of CPLD is that the signal wiring can be changed by changing the program without changing the hardware. Field Programmable Gate Array (FPGA) also has the same characteristics as CPLD, but it differs from FPGA in that the power consumption of CPLD is small. The CPLD will be installed to cubesat project of BIRDS-3 and will be demonstrated on orbit. The backplane installed CPLD needs a high reliability because the backplane needs to operate without error until deorbiting. The purpose of this test is to evaluate the tolerance of CPLD for SEE. This document reports the detail of testing and test results of CPLD.

EXPERIMENTS: Figure 1 shows the experimental setup. Two CPLDs were installed to vacuum chamber at the same time and a total four CPLDs were tested. A model number of CPLD tested was LC4256ZE5TN144C manufactured by Lattice Semiconductor,. Inputs and outputs of the CPLD are connected each other and its functions are confirmed by sending and receiving data between the input and the output. The data transferring was checked with a serial communication of RS232 via PC. Figure 2 shows the CPLD tested. The package of CPLD was removed for the heavy ion exposure from ²⁵²Cf source. ²⁵²Cf source was mounted on XYZ stage and the position of ²⁵²Cf was controlled from outside and was moved above CPLDs. In the test, Single Event latch-up (SEL) current was also measured by oscilloscope and digital acquisition (DAQ).

RESULTS: Table 1 shows the summary of test results for four CPLDs. A nominal current of CPLD is 7 mA. When SEL occurs, increasing current consumption was observed in all CPLDs. Although SEL was observed, the function of CPLD as data transferring was never lost. The

maximum SEL current was 37mA for all samples, and no difference was observed with respect to the maximum SEL current. However, in term of the probability of SEL occurrence, a large difference was observed. Especially, there was a big difference between sample 2 and 4. Improvement of statistical performance by longer test will be a future subject. From the viewpoint of satellite system, the characteristic that CPLD does not hang even when SEL occurs is very important. However, whether to take measures against current increase should be discussed because the current increasing due to SEL of the CPLD is much smaller than that of typical microprocessors and the implement of reset system for the CPLD induces the complexity of system.

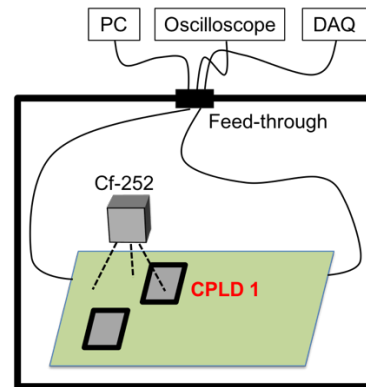


Fig. 1 Test setup

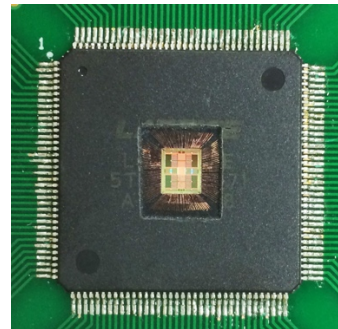


Fig. 2 Test article (CPLD decapped)

Table 1 Summary of test results

CPLD sample ID	Exposure time, hr	Number of SEL, -	Range of SEL current, mA
1	2	4	17 to 34
2	1	5	18 to 34
3	2	6	19 to 34
4	1	1	34

REFERENCE:

[1] S. Busch *et al.*, The 4S Symposium (2016).

CO12-11 Growth of Adsorbed Additive Layer for Further Friction Reduction Confirmed by Multi-Analytical Methods Including Neutron Reflectometry

T. Hirayama, Y. Sasaki¹ and M. Hino²

Dept. of Mechanical Eng., Doshisha University

¹Dept. of Mechanical Eng., Graduate School of Doshisha University

²Institute for Integrated Radiation and Nuclear Science, Kyoto University

INTRODUCTION: Understanding the state of the boundary lubrication layer formed by additive molecules and its role is an important research topic because the formation of a boundary layer greatly affects the coefficient of friction under boundary lubricated conditions. Typical models of the boundary lubrication layer are Hardy's monolayered model and Allen's multilayered model, and the conflict between them has resulted in a 'monolayer-multilayer controversy'. Actually, the most important issue is boundary layer sustainability, so the formation model, monolayer or multilayer, may be not so important. However, for a deeper understanding of the formation process, obtaining information on the actual interface is quite useful. Recent advances in interfacial analyzers have enabled physical/chemical information related to the structure of the boundary layer to be obtained through various *in-situ* analyses. This report shows the 'growing' behaviour of an adsorbed additive layer onto metal surface due to high pressure by means of NR with in conjunction with the result obtained through cross-sectional imaging by FM-AFM we already published before [1]. It also discusses the relationship between the structure of the adsorbed layer and its coefficient of friction as measured by AFM with a SiO₂ colloidal probe.

EXPERIMENTAL RESULTS: The reflectivity profiles from the target interface are shown in Figure 1. The substrate we selected was Cu-coated Si block. The profiles in PAO (bottom) were drawn with decoupling for the profile in PAO with deuterated palmitic acid (d-PA) (middle) and with centuplicating for profile in PAO with d-PA at 3.0 MPa (top) for clear viewability, though the maximum values of reflectivity in all of original profiles were 1. The optimum fitting lines based on Parratt's theory are also shown. In comparison of reflective profiles for PAO (bottom) and PAO with d-PA (middle), the reflectivity profiles are obviously slightly different: the fringe interval in the profile for PAO with d-PA is clearly narrower than in the profile for PAO. Fitting based on Parratt's theory showed that the adsorbed additive layer on the Cu surface was about 1.4 nm thick and that the density of the additive in the layer was almost the same as that of pure deuterated palmitic acid. It means that a monolayer of palmitic acid molecules was formed on the Cu surface with high grafting density which is almost the same as that of pure palmitic acid. In addition, further fitting operation revealed that the

thickness the adsorbed additive layer grew up to be 5.9 nm under high pressure. These results suggest that using high pressure can make the additive layer thicker.

The coefficients of friction measured with the colloidal probe AFM under various loads are shown in Figure 2. It shows that when pure hexadecane was used, the coefficient of friction was 5% lower after pre-scratching than in the non-scratched area because the surface was made smoother by the pre-scratching due to the running-in effect. When hexadecane with palmitic acid was used, on the other hand, the coefficient of friction was 12% lower after pre-scratching than in the non-scratched area even though the running-in effect became smaller than that in the case without palmitic acid because the surface profile in area A did not change. This higher reduction ratio of coefficient of friction for the case with acid is expected to be caused by the change in additive layer formation due to the pre-scratch treatment. These results and those of the previous structural analysis show that an adsorbed layer easily grows into a multilayer under tribological conditions and that the growth of the layer contributes more greatly to a reduction in the coefficient of friction.

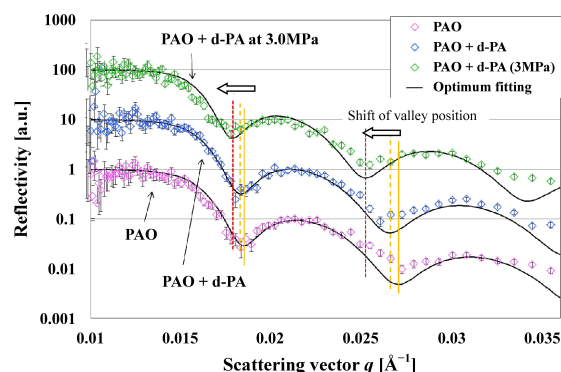


Fig. 1 Reflectivity profiles obtained from the interface in PAO (bottom), in PAO with deuterated palmitic acid (d-PA) (middle), and in PAO with d-PA at 3.0 MPa (top).

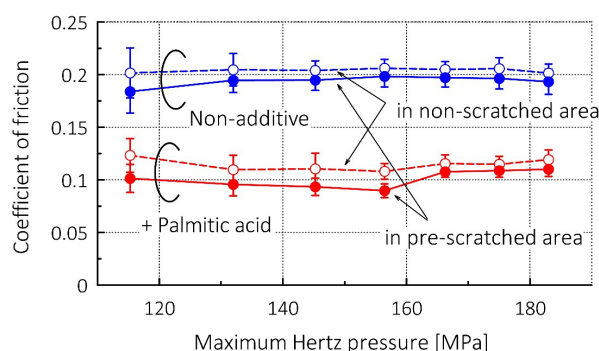


Fig. 2 Coefficients of friction measured with SiO₂ colloidal probe in hexadecane without/with palmitic acid in pre-scratched area and outside area.

REFERENCE:

[1] T. Hirayama *et al.*, *Lungmuir*, **33(40)** (2017) 10492.

T. Miyazawa and Y. Tanaka¹*School of Materials and Chemical Engineering, Tokyo Institute of Technology*¹*Department of Metallurgy and Ceramics Science, Tokyo Institute of Technology*

INTRODUCTION: A lot of studies of precipitation phenomena in metallic materials for increasing a strength and stability of microstructure were carried out with TEM (Transmission electron microscope) observation. On the other hand, recently, small angle X-ray scattering (SAXS) method with using synchrotron X-ray has been received attention as an investigation method of the precipitates dispersed in the metallic materials[1,2]. The SAXS profiles can be analyzed the size and shape of precipitates. However, most studies about metallic materials with SAXS method assumed the precipitate shape is sphere. Only the size of precipitates was estimated from the SAXS profiles. In this study, both of the shape and size of precipitates in Cu alloys aged for various conditions were estimated to investigate the usability of the SAXS measurement.

EXPERIMENTS: The specimens were cut from plates of a Cu-2.15mass%Ni-0.49mass%Si alloy and Cu-1.31mass%Co-0.69mass%Fe alloy. These specimens were solution-treated at 1323 K for 1 h, quenched into water. After that, Cu-Ni-Si alloy specimens were aged at 973 K and Cu-Co-Fe alloy specimens were aged at 923 K for various times. After aging, Ni₂Si particles having ellipsoidal shape and CoFe particles having flattened rectangular shape are dispersed in Cu matrix, respectively[3,4]. Thin foils for SAXS measurement about 200 μm thickness were prepared from these aged specimens by mechanical polishing. The SAXS measurements were carried out in BL19B2 at SPring-8. That beam line has the two measurement conditions such as the SAXS with camera length equal to 3.1 m and the USAXS (Ultra SAXS) with the camera length equal to 41.6 m to acquire wide q range scattering profiles. The incident X-ray energy is 30 keV.

RESULTS: Figure 1 shows the scattering profiles measured from the Cu alloy specimens. All scattering profiles are constituted of SAXS and USAXS profiles. The profiles acquired from as-quenched specimens indicate the decrease as a function of scattering vector q . The SAXS profiles from ellipsoid and rectangular particles has the broadening shoulder which is proportion to $q^{-3}q^{-1}$ [5]. Convex shoulder parts exist on scattering profiles measured from the aged specimens. The convex shoulders are shifting from low q region to high q region and broadening with increasing the aging time in Cu-Ni-Si alloy. That means the size and shape anisot-

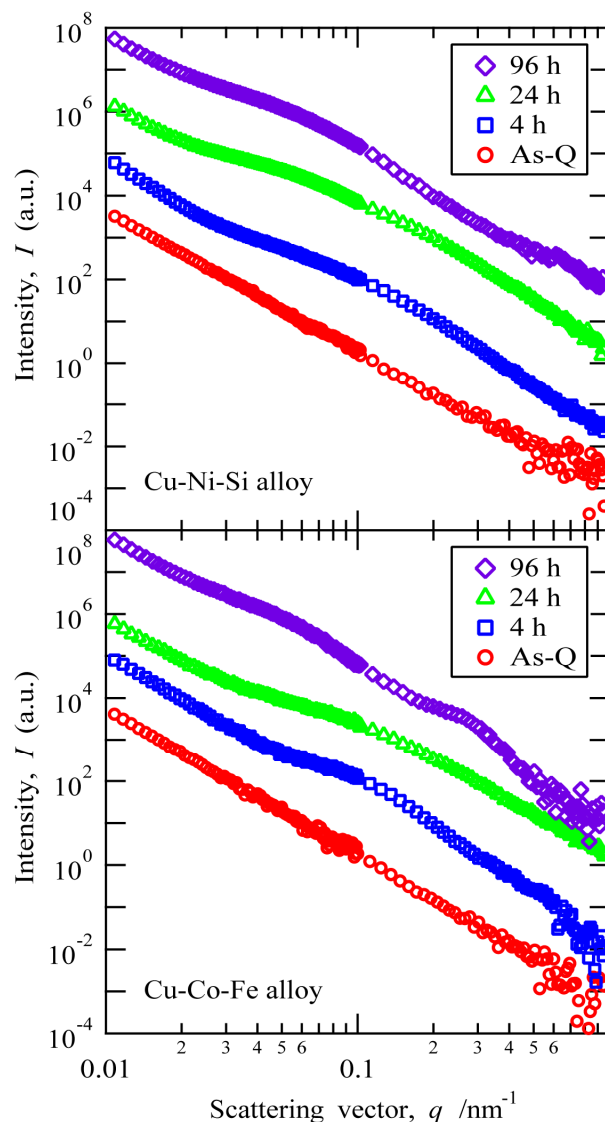


Fig. 1. The scattering profiles of Cu-Ni-Si alloy and Cu-Co-Fe alloy.

ropy of the Ni₂Si particles increases with the increase of aging time. Similarly, in Cu-Co-Fe alloy, the convex shoulders move from low q region to high q region with increasing the aging time and shoulder broaden occurs. The CoFe particles also grow and the shape anisotropy changes with the increase of aging time.

REFERENCES:

- [1] Y. Takahashi, *et al.*, *Mater. Trans.*, **48** (2007) 101-104.
- [2] Y. Oba, *et al.*, *ISIJ International*, **52** (2012) 457-463.
- [3] C. Watanabe, R. Monzen, *J. Mater. Sci.*, **46** (2011) 4327-4335.
- [4] C. Kanno, *et al.*, *Phil. Mag. Lett.*, **90** (2010) 589-598.
- [5] J. S. Pedersen, *Adv. Col. and Inter. Sci.*, **70** (1997) 171-210.

Y. Yanagisawa, T. Chatake¹, T. Saito¹, K. Morishima¹, R. Inoue¹ and M. Sugiyama¹

Faculty of Pharmaceutical Sciences, Chiba Institute of Science

¹Institute for Integrated Radiation and Nuclear Science, Kyoto University

INTRODUCTION: Natto is a Japanese traditional fermented food made from soybeans by *Bacillus subtilis natto*. *Bacillus subtilis natto* produces various biologically active substances, which contribute to health. In addition, *Bacillus subtilis natto* is one of high-resistance bacteria. We took two biophysical approaches to *Bacillus subtilis natto*; structural study of macromolecular complexes containing vitamin K₂, and irradiation study of *Bacillus subtilis natto*.

(1) Although vitamin K₂ is water-insoluble, *Bacillus subtilis natto* produces a large amount of water-soluble macromolecular complex containing vitamin K₂ (hereafter natto-MK-7). While natto-MK-7 is already commercially available as supplement, its structural information is poor. In the present study, natto-MK-7 was investigated through the combination of size-exclusion chromatography and dynamic light scattering (SEC-DLS), which was developed at Institute for Integrated Radiation and Nuclear Science, Kyoto University (KURNS).

(2) *Bacillus subtilis natto* takes two states; spores and vegetative cells. So far, it is well known that the spores has high radiation resistivity. In the present study, radiation resistivity of vegetative cells were measured using Co-60 gamma-ray at Co-60 Gamma-ray Irradiation Facility of KURNS.

EXPERIMENTS: (1) *Bacillus subtilis natto* was cultured in liquid medium. The cultured medium was centrifuged to remove precipitants, and its supernatant was concentrated by ultracentrifuge membrane. Natto-MK-7 was isolated from the concentrated medium. The repetition of ion-exchange chromatography was carried out to obtain purified natto-MK-7. SEC-DLS was carried out using HiPrep 16/60 Sephacryl S-300 HR on AKTA prime FPLC system and a system consisting of a 22 mW He-Ne laser ($\lambda = 632.8$ nm), an avalanche photodiode mounted on a static/dynamic compact goniometer, ALV/LSE-5003 electronics and an ALV-5000 correlator.

(2) Glycerol stock of the clone *Bacillus subtilis natto* was pre-incubated overnight, and was inoculated in LB medium. After a few hour, 600-nm optical density (OD₆₀₀) of the medium reached in the range of 0.4~1.0. The medium was centrifuged with 1,000 g for 10 minutes. After centrifugation, the supernatant was removed, then the precipitant was suspended in PBS(-) buffer. Seven samples were prepared, and irradiated with gamma rays at a dose of 0, 25, 50, 75, 100, 200, and 400 Gy at a dose rate of 24 Gy/min. After the irradiation, each liquid medium was diluted by PBS(-) medium, and plated. Colony forming units were counted after 6-hour incubation at

42 °C.

RESULTS: (1) As shown in Fig. 1, the chart of size-exclusion chromatography was clarified from SEC chart (refer to Fig. 1(a)). The frequencies of decay time from Fr. 1 and Fr. 4, which were purified from SEC are shown in Fig. 1 (b). The peak hydrodynamic radii from Fr.1 is much larger than that evaluated from monomeric form of natto-MK-7. On the other hand, natto-MK-7 mainly possesses the monomeric form in Fr. 4. It can be concluded that SEC-DLS contributes to observe pure monomeric form of natto-MK-7 having polymeric forms in nature.

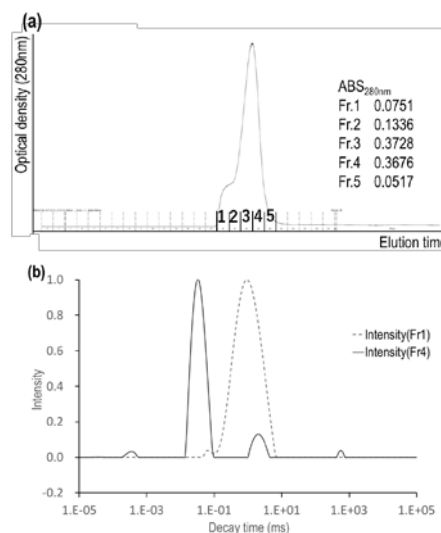


Fig. 1. The result of SEC-DLS of natto-MK-7. (a) The SEC chart, (b) the particle-size distribution of the Fr. 1 and 4, respectively.

(2) Fig. 2 shows the survival fraction curve of *Bacillus subtilis natto* against Co60-gamma ray. In this experiment, *Bacillus subtilis natto* shows radiation resistivity to low radiation dose (0~50 Gy), and an exponential decay of survival fraction was observed after 50 Gy dose. The resistivity to low radiation dose observed in this irradiation experiment is larger than those observed in *E. Coli* in previous studies. On the other hand, the exponential decay is comparable with those of *E. Coli*. Further experiments are necessary to confirm the present results.

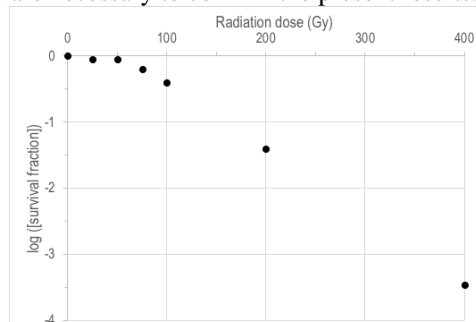


Fig. 2. The radiation survival fraction curve of *Bacillus subtilis natto*.

II. PUBLICATION LIST
(APRIL 2017 – MARCH 2018)

1. Slow Neutron Physics and Neutron Scattering

Papers

Weak-beam scanning transmission electron microscopy for quantitative dislocation density measurement in steels
Yoshida Kenta, Shimodaira Masaki, Toyama Takeshi, Shimizu Yasuo, Inoue Koji, Yoshiie Toshimasa, Milan Konstantinovic J., Gerard Robert, Nagai Yasuyoshi
Microscopy **66(2)** (2017) 120-130.

Crystal structure of Pr₃MgNi₁₄D_x studied by in situ neutron diffraction
K. Iwase, K. Mori, N. Terashita, S. Tashiro, T. Suzuki
Inorganic Chemistry **56** (2017) 6933-6937.

A Neutron Detector with Submicron Spatial Resolution using Fine-grained Nuclear Emulsion
Naganawa N., Awano S., Hino M., Hirose M., Hirota K., Kawahara H., Kitaguchi M., Mishima K., Nagae T., Shimizu H.M., Tasaki S., Umemoto A.
Physics Procedia **88** (2016) 224-230.

Mechanical synthesis and structural properties of the fast fluoride-ion conductor PbSnF₄
F. Fujisaki, K. Mori, M. Yonemura, Y. Ishikawa, T. Kamiyama, T. Otomo, E. Matsubara, T. Fukunaga
J. Solid State Chemistry **253** (2017) 287-293.

Towards a high-resolution TOF-MIEZE spectrometer with very cold neutrons
T. Oda, M. Hino, M. Kitaguchi, H. Filter, P. Geltenbort, Y. Kawabata
Nuclear Instruments and Methods in Physics Research Section A **860** (2017) 35-41.

Development of precision elliptic neutron-focusing supermirror
Hosobata Takuya, Yamada Norifumi L., Hino Masahiro, Yamagata Yutaka, Kawai Toshihide, Yoshinaga Hisao, Hori Koichiro, Takeda Masahiro, Takeda Shin, Morita Shin-ya
Optics Express **17** (2017) 20012.

Salting-out and salting-in effects of amphiphilic salt on cloud point of aqueous methylcellulose
Nishida Koji, Morita Hideyuki, Katayama Yutaka, Inoue Rintaro, Kanaya Toshiji, Sadakane Koichiro, Seto Hideki
Process Biochemistry **59** (2017) 52-57.

Role of molecular weight in shish-kebab formation during drawing by small-angle neutron and X-ray scatterin
Kanaya Toshiji, Murakami Momoko, Maede Tadahiko, Ogawa Hiroki, Inoue Rintaro, Nishida Koji, Matsuba Go, Ohta Noboru, Takata Shin-ichi, Tominaga Taiki, Suzuki Jun-ichi, Han Young-Soo, Kim Tae-Hwan
Polymer Journal **49(12)** (2017) 831-837.

Supermirror neutron guide system for neutron resonance spin echo spectrometers at a pulsed neutron source
Hino Masahiro, Oda Tatsuro, Yamada Norifumi L., Endo Hitoshi, Seto Hideki, Kitaguchi Masaaki, Harada Masahide, Kawabata Yuji
Journal of Nuclear Science and Technology **54(11)** (2017) 1223-1232.

Materials and Life Science Experimental Facility(MLF) at J-PARC. II – Neutron Scattering Instruments –
K. Nakajima, Y. Kawakita, S. Itoh, J. Abe, K. Aizawa, H. Aok, H. Endo, M. Fujita, K. Funakoshi, W. Gong, M. Harada, S. Harjo, T. Hattori, M. Hino, T. Honda, A. Hoshikawa, K. Ikeda, T. Ino, T. Ishigaki, Y. Ishikawa, H. Iwase, T. Kai, R. Kajimoto, T. Kamiyama, N. Kaneko, D. Kawana, S. Ohira-Kawamura, T. Kawasaki, A. Kimura, R. Kiyonagi, K. Kojima, K. Kusaka, S. Lee, S. Machida, T. Masuda, K. Mishima, K. Mitamura, M. Nakamura, S. Nakamura, A. Nakao, T. Oda, T. Ohhara, K. Ohishi, H. Ohshita, K. Oikawa, T. Otomo, A. Sano-Furukawa, K. Shibata, T. Shinohara, K. Soyama, J. Suzuki, K. Suzuya, A. Takahara, S. Takata, M. Takeda, Y. Toh, S. Torii, N. Torikai, N.L. Yamada, T. Yamada, D. Yamazaki, T. Yokoo, M. Yonemura, H. Yoshizawa
Quantum Beam Science **1(3)** (2017) 9.

Effect of Mg substitution on crystalline structure and hydrogenation of Gd₄ MgNi₁₉
K. Iwase, N. Terashita, K. Mori, S. Tashiro, T. Suzuki
Int. J. Hydrogen Energy **43** (2018) 1675-1680.

Proceedings

Development of a Sealed-type Capillary Plate Gas Detector for Neutron Imaging

H. KONDO, H. SUGIYAMA, M. HAYASHI, T. OKADA, F. TOKANAI, R. ITO, S. ISHIZAWA, Y. INOMATA, K. SUZUKI, S. TASAKI, M. HIROSE, M. HINO, R. HANAYAMA, T. SUMIYOSHI
Conference on Laser Energy Science / Laser and Accelerator Neutron Sources and Applications 2017, Yokohama, Japan (Apr. 18-21, 2017).

Development of high spatial resolution cold/ultra- cold neutron detector using fine-grained nuclear emulsion

N. Naganawa, S. Awano, M. Hino, M. Hirose, H. Kawahara, M. Kitaguchi, K. Mishima, T. Nagae, H. M. Shimizu, S. Tada, S. Tasaki, .A. Umemoto
3rd KMI International Symposium on Quest for the Origin of Particles and the Universe (KMI2017), PoS(KMI2017) 077, Nagoya, Japan (Jan. 5-7, 2017).

Precision Mechanical Design of 900 mm Long Ellipsoidal Neutron-focusing Supermirror for VIN ROSE at J-PARC/MLF

Takuya Hosobata, Masahiro Hino, Hisao Yoshinaga, Toshihide Kawai, Hitoshi Endo, Yutaka Yamagata, Norifumi L. Yamada, Koichiro Hori, Tatsuro Oda and Shin Takeda
International Conference on Neutron Optics (NOP2017), JPS Conf. Proc., Nara, Japan (July 5-8, 2017).

Fundamental physics activities with pulsed neutron at J-PARC (BL05)

Kenji MISHIMA, Shogo AWANO, Yasuhiro FUWA, Fumiya Goto, Christopher C. Haddock, Masahiro Hino, Masanori Hirose, Katsuya Hirota, Sei Ieki, Sohei Imajo, Takashi Ino, Yoshihisa Iwashita, Ryo Katayama, Hiroaki Kawahara, Masaaki Kitaguchi, Ryunosuke Kitahara, Jun Koga, Aya Morishita, Tomofumi Nagae, Naoki Nagakura, Naotaka Naganawa, Noriko Oi, Hideyuki Oide, Hidetoshi Otono, Yoshichika Seki, Daiichiro Sekiba1, Tatsushi Shima, Hirohiko M. Shimizu, William M. Snow, Naoyuki Sumi, Hirochika Sumino, Satomi Tada, Kaoru Taketani, Seiji Tasaki, Tatsuhiko Tomita, Atsuhiko Umemoto, Takahito Yamada, Satoru Yamashita, Mami Yokohashi, Tamaki Yoshioka
International Conference on Neutron Optics (NOP2017), JPS Conf. Proc. Nara, Japan (July 5-8, 2017).

Observation of 400-kHz TOF-MIEZE Signals

Tatsuro Oda, Masahiro Hino, Hitoshi Endo, Norifumi L. Yamada, Yuji Kawabata, Hideki Seto
International Conference on Neutron Optics (NOP2017), JPS Conf. Proc. Nara, Japan (July 5-8, 2017).

Development of High Spatial Resolution Cold/Ultra-Cold Neutron Detector Using Nano Imaging Tracker

S. Tada, S. Awano, M. Hino, K. Hirota, H. Kawahara, M. Kitaguchi, K. Mishima, N. Naganawa, H. M. Shimizu, S. Tasaki, A. Umemoto
International Conference on Neutron Optics (NOP2017), JPS Conf. Proc. Nara, Japan (July 5-8, 2017).

Development of new neutron mirrors for measuring the neutron electric dipole moment

Ryo Katayama, Kenji Mishima, Satoru Yamashita, Masaaki Kitaguchi, Tamaki Yoshioka, Yoshichika Seki, Masahiko Mitsushashi, Masahiko Sugihara, Masahiro Hino, Eiichiro Watanabe, Daiju Tsuya, Mikiko Saito, Norifumi Yamada
International Conference on Neutron Optics (NOP2017), JPS Conf. Proc. Nara, Japan (July 5-8, 2017).

A focusing test of a multiple segmented ellipsoidal neutron-focusing mirror for a mini-focusing type SANS instrument

Ryo Katayama, Kenji Mishima, Satoru Yamashita, Masaaki Kitaguchi, Tamaki Yoshioka, Yoshichika Seki, S. Takeda, T. Hosobata, Y. Yamaagata, M. Hino, T. Oda, H. Endo, N.L. Yamada, S. Morita, M. Furusaka
International Conference on Neutron Optics (NOP2017), JPS Conf. Proc. Nara, Japan (July 5-8, 2017).

材料照射とその評価技術の高度化(研究計画・構想)

木野村 淳, 藪内 敦

Proceedings of the Project Meeting on "Construction of the basis for the advanced materials science and analytical study by the innovative use of quantum beam and nuclear sciences" Kumatori, Japan (Dec. 15, 2017) 34.
(in Japanese)

KUR 低速陽電子ビームラインの陽電子強度向上のための改良

藪内 敦, 木野村 淳

Proceedings of the Project Meeting on "Construction of the basis for the advanced materials science and analytical study by the innovative use of quantum beam and nuclear sciences" Kumatori, Japan (Dec. 15, 2017) 37.
(in Japanese)

材料照射ターゲットの高精度化と照射研究への寄与

木野村 淳, 藪内 敦, 外山 健, 鬼塚 貴志

Proceedings of the Project Meeting on "Construction of the basis for the advanced materials science and analytical study by the innovative use of quantum beam and nuclear sciences" Kumatori, Japan (Dec. 15, 2017) 42. (in Japanese)

KURにおける量子ビームを用いたナノ構造研究

杉山正明, 井上倫太郎, 佐藤信治, 守島 健

Proceedings of the Project Meeting on "Construction of the basis for the advanced materials science and analytical study by the innovative use of quantum beam and nuclear sciences" Kumatori, Japan (Dec. 15, 2017) 49. (in Japanese)

多元素メスアバウー分光法による物質・生命科学研究の展開

瀬戸 誠

Proceedings of the Project Meeting on "Construction of the basis for the advanced materials science and analytical study by the innovative use of quantum beam and nuclear sciences" Kumatori, Japan (Dec. 15, 2017) 1. (in Japanese)

パルス中性子源における中性子共鳴スピンエコー分光法の研究/

Study on the Neutron Resonance Spin Echo Spectroscopy at Pulsed Neutron Sources

Tatsuro Oda

Proceedings of the 52th KURRI Scientific Meeting. Kumatori, Japan (Jan. 25-26, 2018) 11-13. (in Japanese)

X線・中性子反射率法による潤滑界面の平均構造評価の試み /

A trial for Structural evaluation of lubrication interface by X-ray and neutron reflectometry

Masahiro Hino, Nozomu Adachi, Yoshikazu Todaka, Yojiro Oba, Tomoko Hirayama

Proceedings of the 52th KURRI Scientific Meeting. Kumatori, Japan (Jan. 25-26, 2018) 21. (in Japanese)

J-PARC/MLF BL06 中性子共鳴スピンエコー分光器群(VINROSE)と中性子集光ミラー開発の現状 3 /

Current status of development of VIN ROSE and neutron focusing mirrors III

Masahiro Hino, Tatsuro Oda, Hisao Yoshinaga, Hitoshi Endo, Norifumi L Yamada, Takuya Hosoda, Shin Takeda, Hidetoshi Kawai Yutaka Yamagata, Hideki Seto Yuji Kawabata

Proceedings of the 52th KURRI Scientific Meeting. Kumatori, Japan (Jan. 25-26, 2018) 22. (in Japanese)

多元素メスパウアー分光法の開発の現状 /

Present Status of Development in Multi-Element Mossbauer Spectroscopy

Shinji Kitao, Yasuhiro Kobayashi, Takumi Kubota, Makina Saito, Ryo Masuda, Masayuki Kurokuzu, Hiroki Ishibashi, Shuichi Ho- sokawa and Makoto Seto

"Proceedings of the 52th KURRI Scientific Meeting" Kumatori, Japan (Jan. 25-26, 2018) 31. (in Japanese)

サイズ排除クロマトグラフィー小角 X 線散乱(SEC-SAXS)システムの立ち上げ /

Start-up of SEC-SAXS system

Rintaro Inoue, Toshiyuki Chatake, Nobuhiro Sato, Ken Morishima and Masaaki Sugiyama

Proceedings of the 52th KURRI Scientific Meeting. Kumatori, Japan (Jan. 25-26, 2018) 47. (in Japanese)

X線小角散乱による大豆タンパク質の凝固過程の追跡 /

Coagulation process of soy bean protein as revealed by small-angle X-ray scattering

Nobuhiro Sato, Rintaro Inoue, Ken Morishima, Masaaki Sugiyama, Yuki Higashino and Reiko Urade

Proceedings of the 52th KURRI Scientific Meeting. Kumatori, Japan (Jan. 25-26, 2018) 48. (in Japanese)

小角中性子散乱を用いた高分子主鎖の溶媒依存性反転の機構解明 /

Elucidation of the mechanism of the solvent-dependent helix inversion using small-angle neutron scattering

Yuuya Nagata, Tsuyoshi Nishikawa, Michinori Sugimoto, Sota Sato, Masaaki Sugiyama, Lionel Porcar, Anne Martel, Rintaro Inoue and Nobuhiro Sato

Proceedings of the 52th KURRI Scientific Meeting. Kumatori, Japan (Jan. 25-26, 2018) 52. (in Japanese)

転写因子 Sp1 と TAF4 の相互作用の分子機構 /

Molecular mechanism of interaction between transcriptional factors Sp1 and TAF4

Emi Hibino, Rintaro Inoue, Masaaki Subiyama, Jun Kuwahara, Katsumi Matsuzaki and Masaru Hoshino
Proceedings of the 52th KURRI Scientific Meeting. Kumatori, Japan (Jan. 25-26, 2018) 54. (in Japanese)

パルス中性子イメージングによる鉛ビスマス固液相構造の可視化 /

Visualization of lead-bismuth phase structure using pulsed neutron imaging

Daisuke Ito, Hiroataka Sato, Yasushi Saito, Takenao Shinohara

Proceedings of the 52th KURRI Scientific Meeting. Kumatori, Japan (Jan. 25-26, 2018) 58. (in Japanese)

疎水性内包ミセルのキャラクタリゼーション /

Characterization of Hydrophobe-Uptake Micelle

Ken Morishima

Proceedings of the 52th KURRI Scientific Meeting. Kumatori, Japan (Jan. 25-26, 2018) 62. (in Japanese)

Reviews

中性子散乱の原理と中性子全散乱によるガラス・非晶質物質の構造解析

小野寺陽平, 福永俊晴

セラミックス **52** (2017) 330-336. (in Japanese)

中性子回折によるリチウムイオン伝導ガラスの構造研究

森 一広

まてりあ **56** (2017) 443-447. (in Japanese)

中性子を利用した $\text{Li}_2\text{S-P}_{255}$ 系リチウムイオン伝導体の構造およびイオン伝導経路の可視化

森 一広, 米村雅雄, 福永俊晴

日本結晶学会誌 **59** (2017) 230-237. (in Japanese)

原子炉中性子源

日野正裕, 川端祐司

日本中性子科学会誌 **27** (2017) 155-154. (in Japanese)

2. Nuclear Physics and Nuclear Data

Papers

A Simple and Practical Correction Technique for Reactivity Worth of Short-Sized Samples Measured by Critical-Water-Level Method

Kitamura Yasunori and Fukushima Masahiro

Nuclear Science and Engineering **186(2)** (2017) 168-179.

Experimental fission study using multi-nucleon transfer reactions

Nishio Katsuhisa, Hirose Kentaro, Léguillon Romain, Makii Hiroyuki, Orlandi Riccardo, Tsukada Kazuaki, Smallcombe James, Chiba Satoshi, Aritomo Yoshihiro, Tanaka Shouya, Ohtsuki Tsutomu, Tsekhanovich Igor, Petrache Costel M., Andreyev Andrei

EPJ Web of Conferences **146** (2017) 04009.

Theory of Feynman-alpha technique with masking window for accelerator-driven systems

Kitamura Yasunori, Misawa Tsuyoshi

Annals of Nuclear Energy **103** (2017) 470-479.

Applicability of the two-angle differential method to response measurement of neutron-sensitive devices at the RCNP high-energy neutron facility

Masuda Akihiko, Matsumoto Tetsuro, Iwamoto Yosuke, Hagiwara Masayuki, Satoh Daiki, Sato Tatsuhiko, Iwase Hiroshi, Yashima Hiroshi, Nakane Yoshihiro, Nishiyama Jun, Shima Tatsushi, Tamii Atsushi, Hatanaka Kichiji, Harano Hideki, Nakamura Takashi

Nuclear Instruments and Methods in Physics Research Section A **849** (2017) 94-101.

- Simultaneous measurement of neutron-induced fission and capture cross sections for ^{241}Am at neutron energies below fission threshold
Hirose K., Nishio K., Makii H., Nishinaka I., Ota S., Nagayama T., Tamura N., Goto S., Andreyev A.N., Vermeulen M.J., Gillespie S., Barton C., Kimura A., Harada H., Meigo S., Chiba S., Ohtsuki T.
Nuclear Instruments and Methods in Physics Research Section A **856** (2017) 133-138.
- Effect of helium irradiation on deuterium permeation behavior in tungsten
Uemura Yuki, Sakurada Shodai, Fujita Hiroe, Azuma Keisuke, Zhou Quilai, Hatano Yuji, Yoshida Naoaki, Watanabe Hideo, Oyaizu Makoto, Isobe Kanetsugu, Shimada Masashi, Buchenauer Dean, Kolasinski Robert, Chikada Takumi, Oya Yasuhisa
Journal of Nuclear Materials **490** (2017) 242-246.
- Nondestructive Inspection System for Special Nuclear Material Using Inertial Electrostatic Confinement Fusion Neutrons and Laser Compton Scattering Gamma-Rays
Ohgaki H., Daito I., Zen H., Kii T., Masuda K., Misawa T., Hajima R., Hayakawa T., Shizuma T., Kando M., Fujimoto S.
IEEE Transactions on Nuclear Science **64(7)** (2017) 1635-1640.
- Modification of the yellow luminescence in gamma-ray irradiated GaN bulk single crystal
Torita Y., Nishikata N., Kuriyama K., Kushida K., Kinomura A., Xu Q.
Journal of Physics: Conference Series **864** (2017) 012016.
- Neutron capture cross section measurements of $^{131,153}\text{Eu}$ using a pair of C_6D_6 detectors
J. Lee, J. Hori, K. Nakajima, T. Sano, S. Lee
Journal of Nuclear Science and Thecnology **54** (2017) 1046-1057.
- Improving nuclear data accuracy of ^{241}Am and ^{237}Np capture cross sections
Gašper Žerovnik, Peter Schillebeeckx, Danie l Cano-Ott, Marian Jandel, Jun-ichi Hori, Atsushi Kimura, Matthias Rossbach, Alain Letourneau, Gilles Noguere, Pierre Leconte, Tadafumi Sano, Mark A Kellett, Osamu Iwamoto, Anatoly V Ignatyuk, Oscar Cabellos, Christoph Genreith, Hideo Harada
EPJ Web of Conferences **146** (2017) 1135.
- Influence of the neutron transport tube on neutron resonance densitometry
F. Kitatani, H. Tsuchiya, J. Takamine, J. Hori, T. Sano
EPJ Web of Conferences **146** (2017) 9032.
- Method to Reduce Long-lived Fission Products by Nuclear Transmutations with Fast Spectrum Reactors
Chiba Satoshi, Wakabayashi Toshio, Tachi Yoshiaki, Takaki Naoyuki, Terashima Atsunori, Okumura Shin, Yoshida Tadashi
Scientific Reports **7** (2017) 13961.
- Neutron capture cross section measurements of ^{120}Sn , ^{122}Sn and ^{124}Sn with the array of Ge spectrometer at the J-PARC/MLF/ANNRI
A. Kimura, H. Harada, S. Nakamura, Y. Toh, M. Igashira, T. Katabuchi, M. Mizumoto, J. Hori
EPJ Web of Conferences **146** (2017) 11031.
- Non-destructive assay of nuclear materials using a self-indication method
J. Hori, T. Sano, Y. Takahashi, J. Lee, H. Unesaki, K. Nakajima
EPJ Web of Conferences **146** (2017) 9042.
- On prediction accuracy of neutronics parameters of accelerator-driven system
Chiba Go, Endo Tomohiro, Rooijen Wilfred van, Pyeon Cheol Ho
EPJ Web of Conferences **146** (2017) 09005.
- Research and development for accuracy improvement of neutron nuclear data on minor actinides
H. Harada, O. Iwamoto, N. Iwamoto, A. Kimura, K. Terada, T. Nakao, S. Nakamura, K. Mizuyama, M. Igashira, T. Katabuchi, T. Sano, Y. Shibahara, Y. Takahashi, K. Takamiya, C. H. Pyeon, S. Fukutani, T. Fujii, J. Hori, H. Yashima
EPJ Web of Conferences **146** (2017) 11001.

Effect of wall wettability condition on drift-flux parameters in lead–bismuth two-phase flow in circular and annular bubble columns

Ariyoshi Gen, Inatomi Ryota, Ito Daisuke, Saito Yasushi
Journal of Nuclear Science and Technology **55(3)** (2017) 239-253.

Role of Multichance Fission in the Description of Fission-Fragment Mass Distributions at High Energies

Hirose K., Nishio K., Tanaka S., Léguillon R., Makii H., Nishinaka I., Orlandi R., Tsukada K., Smallcombe J., Vermeulen M. J., Chiba S., Aritomo Y., Ohtsuki T., Nakano K., Araki S., Watanabe Y., Tatsuzawa R., Takaki N., Tamura N., Goto S., Tsekhanovich I., Andreyev A. N.

Physical Review Letters **119(22)** (2017) 222501.

Core geometry for recriticality prevention against CDA in sodium-cooled fast reactor

Suetomi Eiichi, Nakano Satoshi, Takezawa Hiroki, Takaki Naoyuki

Energy Procedia **131** (2017) 45-52.

Systematic effects on cross section data derived from reaction rates in 2 reactor spectra and a re-analysis of ^{241}Am reactor activation measurements

G. Zerovnik, P. Schillebeeckx, B. Becker, L. Fiorito, H. Harada, S. Kopecky, V. Radulovi, T. Sano

Nuclear Instruments and Methods in Physics Research Section A **877** (2018) 300-313.

In-gas-cell laser spectroscopy of the magnetic dipole moment of the $N \approx 126$ isotope ^{199}Pt

Y. Hirayama, M. Mukai, Y. X. Watanabe, M. Ahmed, S. C. Jeong, H. S. Jung, Y. Kakiguchi, S. Kanaya, S. Kimura, J. Y. Moon, T. Nakatsukasa, M. Oyaizu, J. H. Park, P. Schury, A. Taniguchi, M. Wada, K. Washiyama, H. Watanabe, and H. Miyatake

Phys. Rev. C **96** (2017) 014307.

Proceedings

Time-resolved analysis of Cerenkov light from positron emitter as a new probe to high-precision measurement of nuclear reaction cross section

T. Masuda, J. Kataoka, M. Arimoto, M. Takabe, T. Nishio, S. Hatori, K. Kume, T. Hasegawa, K. Matsushita, S. Yamamoto, T. Inaniawa, T. Toshito

Proceedings of the 113th JSMP in a Supplement Issue of the Japanese Journal of Medical Physics. Yokohama, Japan (Apr. 13-16, 2017) 45.

Evaluation of Sample-dependent Background at the KURRI-LINAC using a Time-of-Flight Method

J. Lee, J. Hori, T. Sano, K. Nakajima

Proceeding of Reactor Physics Asia 2017. China (Aug. 24-25, 2017) 74.

Current Status of Nuclear Data Measurement at the KURRI-LINAC

J. Hori

Proceeding of the 2016 Symposium on Nuclear Data. Tsukuba, Ibaraki, Japan (Nov.17-18, 2017) 23.

軽水炉燃料の燃焼中の反応度における不確かさの定量化に関する研究/

Study on uncertainty quantification of reactivity during burnup in LWR fuel

奥村 晋太郎, 千葉 豪

"Proceedings of 6th Reactor Physics Workshop (RPW 2017)" Kumatori, Japan (Nov.29-30, 2017) 29. (in Japanese)

未臨界積分法・外挿法によるドル単位未臨界度測定/

Measurement of subcriticality in dollars using integral and extrapolation method

遠藤知弘, 野中 朝日

"Proceedings of 6th Reactor Physics Workshop (RPW 2017)" Kumatori, Japan (Nov.29-30, 2017) 42. (in Japanese)

中性子雑音法を用いた気泡を含む水流の通過時間測定に対する時間依存モンテカルロシミュレーション/

Time-Dependent Monte Carlo Simulation for Transit Time Measurement of Bubbly Water Flow with Neutron Noise Technique

高山直毅, 長家康展, 山本俊弘

"Proceedings of 6th Reactor Physics Workshop (RPW 2017)" Kumatori, Japan (Nov.29-30, 2017) 53. (in Japanese)

次世代高速炉の核設計における燃焼核特性評価の解析条件の検討/

Investigation of the Core Neutronics Analysis Conditions for Evaluation of Burnup Nuclear Characteristics of Next-Generation Fast Reactors

滝野一夫

"Proceedings of 6th Reactor Physics Workshop (RPW 2017)" Kumatori, Japan (Nov.29-30, 2017) 60. (in Japanese)

地層処分場に対する中性子・ γ 線放射線場総合解析コードの開発/

Development of Calculation Code for Neutron and Gamma ray field analysis on Geological repository

Daiki Maeda, Naoto Aizawa, Tomohiko Iwasaki

"Proceedings of 6th Reactor Physics Workshop (RPW 2017)" Kumatori, Japan (Nov.29-30, 2017) 73. (in Japanese)

JENDL-4.0に基づくCASMO5/TRACE/PARCSを用いたSPERT-III実験解析・不確かさ評価/

Analysis and Uncertainty Quantification of the SPERT-III Experiments Using CASMO5/TRACE/PARCS with JENDL-4.0 Library

Tatsuya FUJITA and Tomohiro SAKAI

"Proceedings of 6th Reactor Physics Workshop (RPW 2017)" Kumatori, Japan (Nov.29-30, 2017) 92. (in Japanese)

同位体を利用した先進科学の創出

大槻 勤, 沖 雄一, 高宮幸一, 関本 俊

Proceedings of the Project Meeting on "Construction of the basis for the advanced materials science and analytical study by the innovative use of quantum beam and nuclear sciences" Kumatori, Japan (Dec.15, 2017) 75. (in Japanese)

陽電子ビームを用いた空孔型欠陥研究—金属材料における原子空孔/

Studies of vacancy-type defects using positron beams-Atomic vacancies in metals

Atsushi Yabuuchi

"Proceedings of the 52th KURRI Scientific Meeting" Kumatori, Japan (Jan.25-26, 2018) 5-7. (in Japanese)

中性子照射ウラン酸化物からの核種溶出挙動 /

Leaching behavior of elements from neutron-irradiated various uranium oxides

Shunichi Sakamoto, Takayuki Sasaki, Taishi Kobayashi, Daisuke Akiyama, Akira Kirishima and Nobuaki Sato

"Proceedings of the 52th KURRI Scientific Meeting" Kumatori, Japan (Jan.25-26, 2018) 29. (in Japanese)

鉛ビスマス気泡塔内のポイド率計測および乱流モデルを用いた数値解析に関する研究 /

Research on measurement of void fraction in lead-bismuth bubble column and numerical analysis using turbulent model

Gen Ariyoshi, Ryota Inatomi, Daisuke Ito, Yasushi Saito

"Proceedings of the 52th KURRI Scientific Meeting" Kumatori, Japan (Jan.25-26, 2018) 35. (in Japanese)

二流体モデルによる鉛ビスマス気液二相流動特性の予測 /

Prediction of flow characteristics in lead bismuth two-phase flow with two fluid model

Keisuke Maeda, Gen Ariyoshi, Daisuke Ito, Kei Ito, Yasushi Saito

"Proceedings of the 52th KURRI Scientific Meeting" Kumatori, Japan (Jpn. 25-26, 2018) 36. (in Japanese)

α 壊変反跳核 ^{229}mTh のガス反応試料からの真空紫外光測定 /

Vacuum ultraviolet photon detection for ^{229}mTh reacted with He/HF mixture gas

Yuki Yasuda, Yoshitaka Kasamatsu, Yudai Shigekawa, Atsushi Shinohara, Koichi Takamiya, Tsutomu Ohtsuki, Toshiaki, Mitsugashira

"Proceedings of the 52th KURRI Scientific Meeting" Kumatori, Japan (Jpn. 25-26, 2018) 38. (in Japanese)

化学交換法における同位体分別研究 /

Study of Isotope Separation via Chemical Exchange Reaction

Ryuta Hazama, Takaaki Yoshimoto, Yoichi Sakuma, Toshiyuki Fujii, Satoshi Fukutani, Yuji Shibahara

"Proceedings of the 52th KURRI Scientific Meeting" Kumatori, Japan (Jpn. 25-26, 2018) 56. (in Japanese)

混相界面運動の数値解析 /

Numerical simulation of multi-fluid interface in motion

Kei Ito

"Proceedings of the 52th KURRI Scientific Meeting" Kumatori, Japan (Jpn. 25-26, 2018) 61. (in Japanese)

Intense Negative Muon Facility with MERIT ring for Nuclear Transmutation

Yoshiharu Mori, Akihiro Taniguchi, Yasutoshi Kuriyama, Tomonori Uesugi, Yoshihiro Ishi, Masayuki Muto, Yuka Ono, Hidefumi Okita, Akira Sato, Michikazu Kinsho, Yasuhiro Miyake, Masahiro Yoshimoto and Kota Okabe
JPS Conf. Proc. **21** 011063 (2018).

3. Reactor Physics and Reactor Engineering

Papers

Experimental Benchmarks on Kinetic Parameters in Accelerator-Driven System with 100 MeV Protons at Kyoto University Critical Assembly

C. H. Pyeon, M. Yamanaka, T. Endo, W. F. G. van Rooijen and G. Chiba
Ann. Nucl. Energy **105** (2017) 346-354.

A Feasibility Study of Solid Core for Fast Reactor Experiments with Low-Enriched Uranium Fuels at Kyoto University Critical Assembly

S. H. Kim, C. H. Pyeon, A. Ohizumi, M. Fukushima, K. Tsujimoto and H. Unesaki
Prog. Nucl. Energy **100** (2017) 60-70.

Analysis of the KUCA ADS Benchmarks with Diffusion Theory

W. F. G. Rooijen, T. Endo, G. Chiba and C. H. Pyeon
Prog. Nucl. Energy **101** (2017) 243-250.

Benchmarks of Subcriticality in Accelerator-Driven System Experiments at Kyoto University Critical Assembly

C. H. Pyeon, M. Yamanaka, S. H. Kim, T. M. Vu, T. Endo, W. F. G. van Rooijen and G. Chiba
Nucl. Eng. Technol. **49** (2017) 1234-1239.

Improvement and performance evaluation of the perturbation source method for an exact Monte Carlo perturbation calculation in fixed source problems

H. Sakamoto and T. Yamamoto
Journal of Computational Physics **345** (2017) 245-259.

Experimental study on interfacial area transport of two-phase bubbly flow in a vertical large-diameter square duct

Shen Xiuzhong, Sun Haomin, Deng Baoqing, Hibiki Takashi, Nakamura Hideo
International Journal of Heat and Fluid Flow **67** (2017) 168-184.

Measurement of the neutron capture cross section of ⁹⁹Tc using ANNRI at J-PARC

Katabuchi Tatsuya, Mizumoto Motoharu, Igashira Masayuki, Terada Kazushi, Kimura Atsushi, Nakamura Shoji, Nakao Taro, Iwamoto Osamu, Iwamoto Nobuyuki, Mizuyama Kazuhito, Harada Hideo, Hori Jun-ich, Kino Koichi
EPJ Web of Conferences **146** (2017) 11050.

Neutron production in deuteron-induced reactions on Li, Be, and C at an incident energy of 102 MeV

Araki Shouhei, Watanabe Yukinobu, Kitajima Mizuki, Sadamatsu Hiroki, Nakano Keita, Kin Tadahiro, Iwamoto Yosuke, Satoh Daiki, Hagiwara Masayuki, Yashima Hiroshi, Shima Tatsushi
EPJ Web of Conferences **146** (2017) 11027.

Coupling Sjostrand and Feynman Methods in Prompt Neutron Decay Constant Analyses

A. Talamo, Y. Gohar, F. Gabrielli, A. Rineiski and C. H. Pyeon
Prog. Nucl. Energy **101** (2017) 299-311.

Time-dependent Monte Carlo simulations for neutron noise in void-containing water flow

T. Yamamoto
Progress in Nuclear Energy **101** (2017) 270-278.

A Preliminary Study on Applicability of Artificial Neural Network for Optimized Reflector Designs

S. H. Kim, T. M. Vu and C. H. Pyeon
Energy Procedia **131** (2017) 77-85.

Measurement of Doppler Effect for Metallic Fuel Alloy

T. Sano, J. Hori, H. Unesaki, Y. Takahashi, A. Hara, K. Nakajima
Energy Procedia **131C** (2017) 292-298.

Thermal-hydraulic Feasibility Study of a Convex shaped Fast Reactor Core
Chitose Keiko, Mochizuki Hiroyasu, Takaki Naoyuki
Energy Procedia **131** (2017) 86-93.

Undersize solute element effects on defect structure development in copper under electron irradiation
Sato Y., Yoshiie T., Arai S.
Philosophical Magazine **8** (2017) 646-672.

Kinetics Solution with Iteration Scheme of History-Based Neutron Source in Accelerator-Driven System
S. H. Kim, M. Yamanaka and C. H. Pyeon
Ann. Nucl. Energy **112** (2018) 337-353.

Eigenvalue sensitivity analysis capabilities with the differential operator method in the superhistory Monte Carlo method
T. Yamamoto
Annals of Nuclear Energy **112** (2018) 150-157.

Reaction Rate Analyses of Accelerator-Driven System Experiments with 100 MeV Protons at Kyoto University Critical Assembly
C. H. Pyeon, T. M. Vu, M. Yamanaka, T. Sugawara, H. Iwamoto, K. Nishihara, S. H. Kim, Y. Takahashi, K. Nakajima and K. Tsujimoto
J. Nucl. Sci. Technol. **55** (2018) 190-198.

Proceedings

Nuclear Data-Induced Uncertainty Quantification of Neutron Multiplication Factor and Prompt Neutron Decay Constant for Pb-Bi loaded ADS Benchmark Problems at KUCA
T. Endo, G. Chiba, W. F. G. van Rooijen, M. Yamanaka and C. H. Pyeon
Proc. Int. Conf. Mathematics & Computational Methods Applied to Nucl. Sci. & Eng. (M&C2017) Jeju, Korea (Apr.16-20, 2017) 1-8.

Implementation of Fuel Depletion Sensitivity Calculation Capability into a Deterministic Reactor Physics Code System CBZ for Accelerator-Driven Sub-System Multi-Cycle Burnup Calculations
G. Chiba, W. F. G. van Rooijen, T. Endo and C. H. Pyeon
Proc. Int. Conf. Mathematics & Computational Methods Applied to Nucl. Sci. & Eng. (M&C2017) Jeju, Korea (Apr.16-20, 2017) 1-8.

Benchmarks of Subcriticality in Accelerator-Driven System at Kyoto University Critical Assembly
C. H. Pyeon, M. Yamanaka, S. H. Kim, T. M. Vu, T. Endo, W. F. G. van Rooijen and G. Chiba
Proc. Int. Conf. Mathematics & Computational Methods Applied to Nucl. Sci. & Eng. (M&C2017) Jeju, Korea (Apr.16-20, 2017) 1-5.

Study on the Technology for Enhancing Element Value by Neutron Transmutation in Light Water Reactors
Hiroki Takezawa and Naoyuki Takaki
Transactions of the American Nuclear Society. San Francisco (June 11-15, 2017) 1013.

Measurement of two-phase flow pressure drop in a simulated debris bed
Milka Nava, Daisuke Ito, Yasushi Saito, Mitsuhiro Aoyagi, Kenji Kamiyama, Tohru Suzuki
Proceedings of the 25th International Conference on Nuclear Engineering. Shanghai, China (July 2-6, 2017).

Axial flow characteristics of bubbly flow in a vertical large-diameter square duct (Paper No.: NURETH-17-20863)
X. Shen, H. Sun, B. Deng, T. Hibiki, H. Nakamura
Proceeding of the 17th International Topical Meeting on Nuclear Reactor Thermal Hydraulics (NURETH-17) Xi (sept.3-8, 2017).

Two-phase flow measurements in a simulated debris bed
Daisuke Ito, Milka Nava, Yasushi Saito, Mitsuhiro Aoyagi, Kenji Kamiyama, Tohru Suzuki
Proceedings of the 17th International Topical Meeting on Nuclear Reactor Thermal Hydraulics. Shanghai, China (sept.3-8, 2017).

Experiments on gas entrainment phenomena due to free surface vortex induced by flow passing beside stagnation region -Development of evaluation method for vortex cavitation onset behavior in sodium-cooled fast reactor
T. Ezure, K. Ito, M. Tanaka, H. Ohshima, Y. Kameyama, T. Kunugi
Proceedings of the 17th International Topical Meeting on Nuclear Reactor Thermal Hydraulics. Shanghai, China (sept.3-8, 2017).

Preliminary manufacturing studies of the KUCA LEU conversion fuels
B. Stepnik, C. Coullomb, J. Allenou, G. Foti, C. Rontard, H. Unesaki, J. Morman, J. Stevens
RERTR2017- 38th International Meeting on Reduced Enrichment for Research and Test Reactors. Chicago, USA (Nov.12-15, 2017).

Neutronic and Safety Analysis of KUCA Wet Core using LEU Fuel
Hironobu Unesaki and Tsuyoshi Misawa
RERTR2017- 38th International Meeting on Reduced Enrichment for Research and Test Reactors. Chicago, USA (Nov.12-15, 2017).

Impact of Fuel Heterogeneity on Neutronic Characteristics of U-Mo Dispersion LEU Fuel
Hironobu Unesaki and Tadafumi Sano
RERTR2017- 38th International Meeting on Reduced Enrichment for Research and Test Reactors Chicago, USA (Nov.12-15, 2017).

東芝臨界実験装置(NCA)での炉物理実習
Satoshi Wada, Tsukasa Sugita, Kenichi Yoshioka, Kouji Hiraiwa
Proceedings of 6th Reactor Physics Workshop (RPW 2017). Kumatori, Japan (Nov.29-30, 2017) 72. (in Japanese)

Present Status of Kyoto University Research Reactor, KUR
Ken Nakajima
18th IGORR (International Group on Research Reactors) Conference Sydney, Australia (Dec.4-8, 2017).

Outline of the development of Nondestructive Methods Adopted for Integrity Test of Next Generation Nuclear Fuels (N-DeMAIN)
Ken Nakajima, Takashi Kamiyama, Koh-ichi Mochiki, Yoshiaki Kiyonagi, Kou Koike, Setsuo Satoh
International Symposium on Radiation Detectors and Their Uses (ISR2018). Tsukuba, Ibaraki, Japan (Jan.23-26, 2018).

燃料集合体チャンネルボックス内気泡拡散現象の実験研究 /
Experimental study on bubble dispersion phenomena in gas-liquid two-phase flows in a fuel assembly channel box
Xiuzhong Shen and Takashi Hibiki
"Proceedings of the 52th KURRI Scientific Meeting" Kumatori, Japan (Jpn. 25-26, 2018) 23. (in Japanese)

液膜センサの開発と二相流計測への応用 /
Development of liquid film sensor and its application to two-phase flow measurement.
Takahiro Matsushita, Daisuke Ito, Kei Ito, Yasushi Saito
"Proceedings of the 52th KURRI Scientific Meeting" Kumatori, Japan (Jpn. 25-26, 2018) 46. (in Japanese)

UPDATE OF NEUTRONIC ANALYSIS OF KUCA DRY CORE USING LEU FUEL
G. ALIBERTI, J.A. MORMAN, J.G. STEVENS, T. SANO, H. UNESAKI, T. MISAWA, B. STEPNIK
European Research Reactor Conference RRFM 2018. Munich, Germany (Mar.11-15, 2018).

Reviews

京都大学研究用原子炉 KUR の状況
中島健
放射化学 **36** (2017) 1-7. (in Japanese)

大学における研究炉の現状と課題

中島健

エネルギーレビュー**38** (2018) 38-41. (in Japanese)

4. Material Science and Radiation Effects

Papers

Crystal structure of the overlapping dinucleosome composed of hexasome and octasome

Kato Daiki, Osakabe Akihisa, Arimura Yasuhiro, Mizukami Yuka, Horikoshi Naoki, Saikusa Kazumi, Akashi Satoko, Nishimura Yoshifumi, Park Sam-Yong, Nogami Jumpei, Maehara Kazumitsu, Ohkawa Yasuyuki, Matsumoto Atsushi, Kono Hidetoshi, Inoue Rintaro, Sugiyama Masaaki, Kurumizaka Hitoshi

Science **356(6334)** (2017) 205-208.

Microstructural Evolution and Changes in Mechanical Property of Irradiated Fe-0.6Cu Alloy under Uniaxial Tension Stress in Reactor

Q. Xu and J. Zhang

Radiat. Eff. Defects Solids **172** (2017) 305-312.

Microstructure and Deuterium Retention after Ion Irradiation of W-Lu₂O₃ Composites

J.S. Lin, L.M. Luo, Q. Xu, X. Zan, X.Y. Zhu, Y.C. Wu

J. Nucl. Mater. **490** (2017) 272-278.

Simulation of the Effect of Volume Size Factor of Solute Atoms and Their Clusters on One Dimensional Motion of Interstitial Clusters in Ni Binary Alloys

K. Sato, Q. Xu, T. Yoshiie

Comput. Mater. Sci. **132** (2017) 1-5.

Study of fission using multi-nucleon transfer reactions

Nishio Katsuhisa, Hirose Kentaro, Mark Vermeulen, Makii Hiroyuki, Orlandi Riccardo, Tsukada Kazuaki, Asai Masato, Toyoshima Atsushi, Sato Tetsuya K., Nagame Yuichiro, Chiba Satoshi, Aritomo Yoshihiro, Tanaka Shouya, Ohtsuki Tsutomu, Tsekhanovich Igor, Petrache Costel M., Andreyev Andrei

EPJ Web of Conferences **163** (2017) 00041.

Structure and Rheology of Wormlike Micelles Formed by Fluorocarbon-Hydrocarbon-Type Hybrid Gemini Surfactant in Aqueous Solution

Morishima Ken, Sugawara Seiya, Yoshimura Tomokazu, Shibayama Mitsuhiro

Langmuir **33(24)** (2017) 6084-6091.

Fast x-ray detector system with simultaneous measurement of timing and energy for a single photon

Masuda T., Okubo S., Hara H., Hiraki T., Kitao S., Miyamoto Y., Okai K., Ozaki R., Sasao N., Seto M., Uetake S., Yamaguchi A., Yoda Y., Yoshimi A., Yoshimura K.

Review of Scientific Instruments **88(6)** (2017) 063105.

Investigation of W-B Behavior during Short Transient Events by Laser Irradiation

H.Y. Chen, L.M. Luo, X. Zan, Q. Xu, X.Y. Zhu, Y.C. Wu

Fusion Eng. Des. **121** (2017) 130-136.

Mesoscopic Structural Aspects of Ca²⁺-Triggered Polymer Chain Folding of a Tetraphenylethene-Appended Poly(acrylic acid) in Relation to Its Aggregation-Induced Emission Behavior

Morishima Ken, Ishiwari Fumitaka, Matsumura Satoko, Fukushima Takanori, Shibayama Mitsuhiro

Macromolecules **50(15)** (2017) 5940-5945.

Synchrotron radiation Mössbauer spectroscopy for ⁶¹Ni nanoparticles

Ryo Masuda and Makoto Seto

SPring-8 Research Frontier 2016 (2017) 72-73.

The Influence of Dislocation and Hydrogen on Thermal Helium Desorption Behavior in Fe9Cr Alloys

T. Zhu, S.X. Jin, Y.H. Gong, E.Y. Lu, L.G. Song, Q. Xu, L.P. Guo, X.Z. Cao, B.Y. Wang

J. Nucl. Mater. **495** (2017) 244-248.

D₂ Retention and Microstructural Evolution during He Irradiation in Candidate Plasma Material W-La₂O₃ Alloy
Q. Xu, X.Y. Ding, L.M. Luo, M. Miyamoto, M. Tokitani, J. Zhang, Y.C. Wu
J. Nucl. Mater. **496** (2017) 227-233.

Quantitative Evaluation of Hydrogen Atoms Trapped at Single Vacancies in Tungsten using Positron Annihilation Lifetime Measurements: Experiments and Theoretical Calculations
K. Sato, A. Hirosako, K. Ishibashi, Y. Miura, Q. Xu, M. Onoue, Y. Fukutoku, T. Onitsuka, M. Hatakeyama, S. Sunada, T. Yoshiie
Journal of Nuclear Materials **496** (2017) 9-17.

Spin state and electronic environment of iron in basaltic glass in the lower mantle
Maeda Fumiya, Kamada Seiji, Ohtani Eiji, Hirao Naohisa, Mitsui Takaya, Masuda Ryo, Miyahara Masaaki, McCammon Catherine
American Mineralogist **102(10)** (2017) 2106-2112.

Synchrotron radiation-based quasi-elastic scattering using time-domain interferometry with multi-line gamma rays
Saito Makina, Masuda Ryo, Yoda Yoshitaka, Seto Makoto
Scientific Reports **7(1)** (2017) 12558.

⁵⁷Fe and ¹¹⁹Sn Mossbauer study of SrSnO_{3-δ} doped with Fe and Sb under external magnetic fields
Kiyoshi Nomura, Shigeo Suzuki, Yuya Koike, Atsushi Okazawa, Yasuhiro Kobayashi, Masashi Kaneko
Hyperfine Interactions **238** (2017) 70.

Comparison of reductive nanoparticle preparation using plasma and ultrasound irradiation in aqueous solution
Mizukoshi Yoshiteru, Hori Fuminobu, Okitsu Kenji
Japanese Journal of Applied Physics **57(1)** (2017) 0102A5.

Effect of silica nanoparticle filler on microscopic polymer α-relaxation dynamics
Saito Makina, Mashita Ryo, Kishimoto Hiroyuki, Masuda Ryo, Yoda Yoshitaka, Seto Makoto
Hyperfine Interactions **238** (2017) 99.

Evolution of synchrotron-radiation-based Mössbauer absorption spectroscopy for various isotopes
Seto Makoto, Masuda Ryo, Kobayashi Yasuhiro, Kitao Shinji, Kurokuzu Masayuki, Saito Makina, Hosokawa Shuich, Ishibashi Hiroki, Mitsui Takaya, Yoda Yoshitaka, Mibu Ko
Hyperfine Interactions **238** (2017) 78.

Quasielastic Neutron Scattering Study of Microscopic Dynamics in Polybutadiene Reinforced with an Unsaturated Carboxylate
R. Mashita, R. Inoue, T. Tominaga, K. Shibata, H. Kishimoto and T. Kanaya
Soft Matter **13** (2017) 7862.

Thickness dependence of Morin transition temperature in iridium-doped hematite layers studied through nuclear resonant scattering
Mibu Ko, Mikami Kazuaki, Tanaka Masaaki, Masuda Ryo, Yoda Yoshitaka, Seto Makoto
Hyperfine Interactions **238** (2017) 92.

Gliadins from wheat grain: an overview, from primary structure to nanostructures of aggregates
Urade Reiko, Sato Nobuhiro, Sugiyama Masaaki
Biophysical Reviews 2017.

Novel Methods for Prevention of Hydrogen Embrittlement in Iron
Q. Xu and J. Zhang
Sci. Rep. **7** (2017) 16927.

⁵⁷Fe nuclear resonant inelastic scattering of Fe_{1.1}Te
Kurokuzu Masayuki, Kitao Shinji, Kobayashi Yasuhiro, Saito Makina, Masuda Ryo, Mitsui Takaya, Yoda Yoshitaka, Seto Makoto
Hyperfine Interactions **239** (2018) 9.

⁶¹Ni synchrotron-radiation-based Mössbauer absorption spectroscopy of Ni nanoparticle composites
Masuda Ryo, Kobayashi Hirokazu, Aoyama Yoshimasa, Saito Makina, Kitao Shinji, Ishibashi Hiroki, Hosokawa Shuichi, Mitsui Takaya, Yoda Yoshitaka, Kitagawa Hiroshi, Seto Makoto
Hyperfine Interactions **239** (2018) 11.

Deuterium Trapping at Vacancy Clusters in Electron / Neutron-Irradiated Tungsten Studies by Positron Annihilation Spectroscopy

T. Toyama, K. Ami, K. Inoue, Y. Nagai, K. Sato, Q. Xu, Y. Hatano
J. Nucl. Mater. **499** (2018) 464-470.

Experimental investigation of the glass transition of polystyrene thin films in a broad frequency range

Inoue Rintaro, Kanaya Toshiji, Yamada Takeshi, Shibata Kaoru, Fukao Koji
Physical Review E **97**(1) (2018) 12501.

Microstructure and Performances of W-TiC-Y₂O₃ Composites Prepared by Mechano-Chemical and Wet-Chemical Methods

J.S. Lin, Y.C. Hao, L.M. Luo, M.L. Zhao, Q. Xu, X. Zan, X.Y. Zhu, Y.C. Wu
J. Alloy Com. **732** (2018) 871-879.

Preparation and Properties of Fine-Grained and Ultrafine-Grained W-TiC-Y₂O₃ Composite

J.S. Lin, L.M. Luo, K. Huang, X. Zan, Q. Xu, J.Q. Liu, X.Y. Zhu, J.G. Cheng, Y.C. Wu
Fusion Eng. Des. **126** (2018) 147-155.

Preparation of TiC-Doped W-Ti Alloy and Heat Flux Performance Test under Laser Beam Facility

J. Shi, L.M. Luo, S. Wang, W.Q. Pan, Q. Xu, X. Zan, X.Y. Zhu, J.G. Cheng, Y.C. Wu
Fusion Eng. Des. **126** (2018) 79-86.

Repair Behavior of He⁺-Irradiated W-Y₂O₃ Composites after Different Temperature-Isochronal Annealing Experiments

G. Yao, X.Y. Tan, L.M. Luo, X. Zan, J.Q. Liu, Q. Xu, X.Y. Zhu, Y.C. Wu
Nucl. Instr. & Meth. in Phys. Res. B **415** (2018) 82-88.

Structural Relaxation and Viscoelasticity of a Higher Alcohol with Mesoscopic Structure

Yamaguchi Tsuyoshi, Saito Makina, Yoshida Koji, Yamaguchi Toshio, Yoda Yoshitaka, Seto Makoto
The Journal of Physical Chemistry Letters **9**(2) (2018) 298-301.

Thermal Shock Behavior of W-ZrC/Sc₂O₃ Composites under Two Different Transient Events by Electron and Laser Irradiation

H.Y. Chen, L.M. Luo, X. Zan, Q. Xu, K. Tokunaga, J.Q. Liu, X.Y. Zhu, J.G. Cheng, Y.C. Wu
J. Nucl. Mater. **499** (2018) 248-255.

Transient Thermal Shock Behavior of W-Zr/Sc₂O₃ Composites Prepared via Spark Plasma Sintering

H.Y. Chen, L.M. Luo, X. Zan, Q. Xu, K. Tokunaga, J.Q. Liu, D.G. Liu, X.Y. Zhu, J.G. Cheng, Y.C. Wu
Fusion Eng. Des. **126** (2018) 44-50.

Elucidating the Solvent Effect on the Switch of the Helicity of Poly(quinoxaline-2,3-diyl)s: A Conformational Analysis by Small-Angle Neutron Scattering

Nagata Yuuya, Nishikawa Tsuyoshi, Sugimoto Michinori, Sato Sota, Sugiyama Masaaki, Porcar Lionel, Martel Anne, Inoue Rintaro, Sato Nobuhiro
Journal of the American Chemical Society **140**(8) (2018) 2722-2726.

Measurement of nuclear resonant scattering on ⁶¹Ni with fast scintillation detector using proportional-mode silicon avalanche photodiode

Inoue Keisuke, Kobayashi Yasuhiro, Yoda Yoshitaka, Koshimizu Masanori, Nishikido Fumihiko, Haruki Rie, Kishimoto Shunji
Nuclear Instruments and Methods in Physics Research Section A: Accelerators, Spectrometers, Detectors and Associated Equipment **880** (2018) 87-91.

Microstructure and Damage Behavior of W-Cr Alloy under He Irradiation

K. Huang, L.M. Luo, X. Zan, Q. Xu, D.G. Liu, X.Y. Zhu, J.G. Cheng, Y.C. Wu
J. Nucl. Mater. **501** (2018) 181-188.

Nuclear resonant scattering experiment with fast time response: Photonuclear excitation of ^{201}Hg
Yoshimi A., Hara H., Hiraki T., Kasamatsu Y., Kitao S., Kobayashi Y., Konashi K., Masuda R., Masuda T., Miyamoto Y., Okai K., Okubo S., Ozaki R., Sasao N., Sato O., Seto M., Schumm T., Shigekawa Y., Stellmer S., Suzuki K., Uetake S., Watanabe M., Yamaguchi A., Yasuda Y., Yoda Y., Yoshimura K., Yoshimura M.
Physical Review C **97**(2) (2018) 024607.

Proceedings

京大原子炉におけるメスバウアー分光の現状/

Present Status of Mössbauer Spectroscopy in Kyoto University Reactor

S. Kitao, Y. Kobayashi, T. Kubota, M. Saito¹, R. Masuda, M. Kurokuzu, H. Ishibashi, S. Hosokawa and M. Seto
Proceedings of the Specialists' Meeting on "Nuclear Spectroscopy and Condensed Matter Physics Using Short-Lived Nuclei IV" Kumatori, Japan (Dec.20-21, 2017) (2018) 1-4. (in Japanese)

重い電子化合物 $\text{SmT}_2\text{Al}_{20}$ (T: 遷移金属) における Sm 価数と磁性/

Sm Valence States and Magnetic Properties in Heavy Fermion Compounds $\text{SmT}_2\text{Al}_{20}$ (T: transition metals)
Investigated by ^{149}Sm Synchrotron-Radiation-Based Mössbauer Spectroscopy

S. Tsutsui, J. Nakamura, Y. Kobayashi, S. Amagasa, Y. Yamada, M. K. Kubo, M. Mizumaki, Y. Yoda, A. Yamada, R. Higashinaka, T. D. Matsuda and Y. Aoki
Proceedings of the Specialists' Meeting on "Nuclear Spectroscopy and Condensed Matter Physics Using Short-Lived Nuclei IV" Kumatori, Japan (Dec.20-21, 2017) (2018) 34-39. (in Japanese)

双安定性を示す Hofmann-like 高分子錯体/

Hofmann-like Coordination Polymers with Bi-stable States

T. Kitazawa, M. Sekiya and M. Takahashi

Proceedings of the Specialists' Meeting on "Nuclear Spectroscopy and Condensed Matter Physics Using Short-Lived Nuclei IV" Kumatori, Japan (Dec.20-21, 2017) (2018) 40-44. (in Japanese)

鉄混合原子価錯体における連結異性と電荷移動相転移に及ぼす効果のメスバウアー分光研究/

Study of the Linkage Isomerization and Its Influence on the Charge Transfer Phase Transition for Iron Mixed-Valence Complexes by Means of Mössbauer Spectroscopy

N. Kojima

Proceedings of the Specialists' Meeting on "Nuclear Spectroscopy and Condensed Matter Physics Using Short-Lived Nuclei IV" Kumatori, Japan (Dec.20-21, 2017) (2018) 45-52. (in Japanese)

スピネル型化合物中 Cd-111 の核スピン緩和

W. Sato, S. Komatsuda and Y. Ohkubo

Proceedings of the Specialists' Meeting on "Nuclear Spectroscopy and Condensed Matter Physics Using Short-Lived Nuclei IV" Kumatori, Japan (Dec.20-21, 2017) (2018) 53-55. (in Japanese)

量子ビーム実験と構造モデリングによるリン酸塩ガラスのネットワーク構造解析/

Network structure for anomalous thermal expansion coefficients in binary zinc phosphate glass

Yohei Onodera

"Proceedings of the 52th KURRI Scientific Meeting" Kumatori, Japan (Jan. 25-26, 2018) 8-10. (in Japanese)

各種固液界面分析手法による金属基板への実用添加剤の吸着構造解析 一水中におけるカルボン酸ナトリウムの吸着構造およびナノトライボロジー特性 /

Interfacial Structure of Actual Additives in Lubricant on Metal Substrate Analyzed by Multi-Analytical Methods - Adsorption Behaviour and Nanotribological Property of Sodium Carboxylates on Fe Substrate in Water

Naoki Akamatsu, Ryohei Okada, Tomoko Hirayama, Takashi Matsuoka, Hidetoshi Sakamoto, Hideaki Hattori, Masahiro Hino

"Proceedings of the 52th KURRI Scientific Meeting" Kumatori, Japan (Jan. 25-26, 2018) 24. (in Japanese)

B2 型金属間化合物中の異なる欠陥種への水素捕獲 /

Hydrogen trapping of defects in B2 type intermetallic compound alloys

Yuga Sumikura, Akihiro Iwase, Xu Qiu, Kazuhito Ohsawa, Yuichi Saitoh, Fuminobu Hori

"Proceedings of the 52th KURRI Scientific Meeting" Kumatori, Japan (Jan. 25-26, 2018) 27. (in Japanese)

天然腐植物質の錯生成能に及ぼすガンマ線照射効果 /

Effect of gamma-radiation on complex formation of natural organic matter with metal ions

ryohei Goto, Takeshi Saito, Uehara Akihiro, Taishi Kobayashi, Takayuki Sasaki

"Proceedings of the 52th KURRI Scientific Meeting" Kumatori, Japan (Jan. 25-26, 2018) 28. (in Japanese)

平面波コヒーレントチェレンコフ放射における放射強度の誘電体長依存性の研究 /

Study of dependence of radiation power on the dielectric length for coherent Cherenkov radiation matched to circular plane wave

Norihiro Sei and Toshiharu Takahashi

"Proceedings of the 52th KURRI Scientific Meeting" Kumatori, Japan (Jan. 25-26, 2018) 33. (in Japanese)

γ 線照射還元法を用いた Cu ナノ粒子合金化による耐酸化性向上に関する研究 /

Synthesis of Cu nanoparticles stabilized by alloying under gamma-ray irradiation field.

Motoaki Tanaka, Shintaro Toda, Masaumi Tani, Akihiro Iwase, Yoshiteru Mizukoshi, Noboru Taguchi, Shingo Tanaka, Toshiyuki Matsui, Xu Qiu, Fuminobu Hori

"Proceedings of the 52th KURRI Scientific Meeting" Kumatori, Japan (Jan. 25-26, 2018) 39. (in Japanese)

Zr(IV)-有機酸の錯生成に及ぼす官能基の影響 /

Effect of functional groups on complex formation of Zr(IV)-Organic acids

Peng Wang, Taishi Kobayashi, Takayuki Sasaki, Akihiro Uehara

"Proceedings of the 52th KURRI Scientific Meeting" Kumatori, Japan (Jan. 25-26, 2018) 40. (in Japanese)

原子炉中性子によって生じる DNA 損傷分析 /

DNA damage induced by nuclear plant neutron

Hiroaki Terato, Yuka Tokuyama, Kanae Mori, Toshiro Matsuda, Hiroki Yamanishi

"Proceedings of the 52th KURRI Scientific Meeting" Kumatori, Japan (Jan. 25-26, 2018) 42. (in Japanese)

硝酸溶液からのパラジウムの溶媒抽出特性 /

Solvent extraction behavior of palladium from nitric acid solutions

Yuta Araki, Misaki Morita, Takahiro Kawakami, Akihiro Uehara, Satoshi Fukutani, Yasuhiro Tsubata, Tatsuro Matsumura, Chizu Kato, Toshiyuki Fujii

"Proceedings of the 52th KURRI Scientific Meeting" Kumatori, Japan (Jan. 25-26, 2018) 43. (in Japanese)

ジグリコールアミド化合物を用いた硝酸溶液からのロジウムの溶媒抽出 /

Solvent extraction of rhodium from nitric acid solutions by using diglycolamide

Misaki Morita, Yuta Araki, Takahiro Kawakami, Akihiko Uehara, Satoshi Fukutani, Yasuhiro Tsubata, Tatsuro Matsumura, Chizu Kato and Toshiyuki Fujii

"Proceedings of the 52th KURRI Scientific Meeting" Kumatori, Japan (Jan. 25-26, 2018) 44. (in Japanese)

IL-6 による放射線抵抗性獲得は γ 線照射後のミトコンドリア由来酸化ストレスを抑制する /

Acquisition of radioresistance by IL-6 treatment is caused by suppression of oxidative stress derived from mitochondria after γ -irradiation

Yuki Tamari, Genro Kashino, Hiromu Mori

"Proceedings of the 52th KURRI Scientific Meeting" Kumatori, Japan (Jan. 25-26, 2018) 67. (in Japanese)

5. Geochemistry and Environmental Science

Papers

Applicability of source scaling relations for crustal earthquakes to estimation of the ground motions of the 2016 Kumamoto earthquake

Irikura Kojiro, Miyakoshi Ken, Kamae Katsuhiro, Yoshida Kunikazu, Somei Kazuhiro, Kurahashi Susumu, Miyake Hiroe

Earth, Planets and Space **69(1)** (2017).

Fukushima-1 and Chernobyl: Comparison of Radioactivity Release and Contamination

Imanaka, T.

Genetics, Evolution and Radiation (2017) 225-236.

- Use of different surface covering materials to enhance removal of radiocaesium in plants and upper soil from orchards in Fukushima prefecture
Sato Mamoru, Akai Hiroko, Saito Yuichi, Takase Tsugiko, Kikunaga Hidetoshi, Sekiya Nobuhito, Ohtsuki Tsutomu, Yamaguchi Katsuhiko
Journal of Environmental Radioactivity **S0265-931X (17)** (2017) 30235-30237.
- A rapid method for accurate determination of ^{241}Am by sector field inductively coupled plasma mass spectrometry and its application to Sellafield site soil samples
Wang Z.T., Zheng J., Imanaka T., Uchida S.
Journal of Analytical Atomic Spectrometry **32(10)** (2017) 2034-2040.
- GPS 連動型放射線自動計測システム —KURAMA/KURAMA-II の開発と運用—
谷垣 実
電気学会誌 **137** (2017) 600-608. (in Japanese)
- Interpreting the deposition and vertical migration characteristics of ^{137}Cs in forest soil after the Fukushima Dai-ichi Nuclear Power Plant accident
Kang Seongjoo, Yoneda Minoru, Shimada Yoko, Satta Naoya, Fujita Yasutaka, Shin In Hwan
Environmental Monitoring and Assessment **189(8)** (2017) 384.
- Desorption of radioactive cesium by seawater from the suspended particles in river water
Onodera Masaki, Kirishima Akira, Nagao Seiya, Takamiya Kouichi, Ohtsuki Tsutomu, Akiyama Daisuke, Sato Nobuaki
Chemosphere **185** (2017) 806-815.
- Bioaccessibility of Fukushima-Accident-Derived Cs in Soils and the Contribution of Soil Ingestion to Radiation Doses in Children
Takahara Shogo, Ikegami Maiko, Yoneda Minoru, Kondo Hitoshi, Ishizaki Azusa, Iijima Masashi, Shimada Yoko, Matsui Yasuto
Risk Analysis **37(7)** (2017) 1256-1267.
- Collision-induced post-plateau volcanism: Evidence from a seamount on Ontong Java Plateau
T. Hanyu, MLG, Tejada, K. Shimizu, O. Ishizuka, T. Fujii, J. Kimura, Q. Chang, R. Senda, T. Miyazaki, Y. Hirahara, BS. Vaglarov, KT. Goto, A. Ishikawa
Lithos **294-295** (2017) 87-96.
- 大阪平野における長周期地震動
上林宏敏
日本建築学会近畿支部耐震構造研究部会シンポジウム「大振幅地震動に対する設計と地震対策の最新動向」
(2017) 1-10. (in Japanese)
- 土壤の放射性セシウム捕捉ポテンシャル(RIP)測定法についての検討/
Study on the measurement method of Radiocaesium Interception Potential (RIP) of a soil
Maiko Ikegami, Ryohei Shimomura, Satoshi Fukutani, Hendra Adhi Pratama, Yoko Shimada, Minoru Yoneda
Symposium on Soil and Groundwater Contamination and Remediation (2017) 397-402. (in Japanese)
- Measuring apparent dose rate factors using beta and gamma rays, and alpha efficiency for precise thermoluminescence dating of calcite
OGATA Manabu, HASEBE Noriko, FUJII Naoki, YAMAKAWA Minoru
Journal of Mineralogical and Petrological Sciences **112(6)** (2017) 336-345.
- Effects of Radiation from Contaminated Soil and Moss in Fukushima on Embryogenesis and Egg Hatching of the Aphid *Prociphilus oriens*
Akimoto Shin-ichi, Li Yang, Imanaka Tetsuji, Sato Hitoshi, Ishida Ken
Journal of Heredity **109(2)** (2018) 199-205.

Progress toward Rice Seed OMICS in Low-Level Gamma Radiation Environment in Iitate Village, Fukushima
Rakwal Randeep, Hayashi Gohei, Shibato Junko, Deepak Saligrama A, Gundimeda Seetaramanjaneyulu, Simha Upendra, Padmanaban Arunkumar, Gupta Ravi, Han Sang-Ik, Kim Sun Tae, Kubo Akihiro, Imanaka Tetsuji, Fukumoto Manabu, Agrawal Ganesh Kumar, Shioda Seiji
Journal of Heredity **109(2)** (2018) 206-211.

Identification and temporal decrease of ¹³⁷Cs and ¹³⁴Cs in groundwater in Minami-Soma City following the accident at the Fukushima Dai-ichi nuclear power plant
Shizuma Kiyoshi, Fujikawa Yoko, Kurihara Momo, Sakurai Yushi
Environmental Pollution **234** (2018) 1-8.

Lifecycle of palladium in Japan: for setting clearance levels of ¹⁰⁷Pd
Takahashi Tomoyuki, Iwata Kayoko, Tanaka Sota, Takashima Naoki, Ikawa Tomoyuki, Takahashi Sentaro
Journal of Nuclear Science and Technology (2018).

Proceedings

科研費共同研究の概要と、ウラル核惨事、ウインズケール火災事故、ウラジオストク原潜臨界事故の顛末/
The nuclear disaster in Ural, the fire accident at the Windscale reactor and the submarine criticality accident near Vladivostok
Imanaka T.
Proceedings of the Meeting on Investigation of Various Nuclear Disasters in the World Tokyo, Japan (Nov. 12, 2017) 1-10. (in Japanese)

マーシャル諸島米核実験の「その後」～核災害からの「再生」・「復興」はあるのか～/
The U.S. nuclear testings in the Marshall Islands and thereafter: Impossibility to "Reconstruct" and "Recover" after nuclear disasters
Takemine S.
Proceedings of the Meeting on Investigation of Various Nuclear Disasters in the World Tokyo, Japan (Nov. 12, 2017) 11-19. (in Japanese)

フランス核実験が残した問題：放射能と被害者補償/
The problem of liability and redress in the French nuclear testing aftereffects : Recent developments
Mashimo T.
Proceedings of the Meeting on Investigation of Various Nuclear Disasters in the World Tokyo, Japan (Nov. 12, 2017) 20-31. (in Japanese)

住民の核実験に対する認識について ～セミパラチンスク地区における質問票調査とインタビューより/
Recognition or awareness of inhabitants toward nuclear test - by the survey of questionnaire and interview in the Semipalatinsk area
Hirabayashi K.
Proceedings of the Meeting on Investigation of Various Nuclear Disasters in the World Tokyo, Japan (Nov. 12, 2017) 32-43. (in Japanese)

旧ソ連核実験によるセミパラチンスク核被害者に対する社会的保護法の概要
Takemine S., Kawano N., Muldagaliyev T., Apsalikov K.
Proceedings of the Meeting on Investigation of Various Nuclear Disasters in the World Tokyo, Japan (Nov. 12, 2017) 43-55. (in Japanese)

ABCC と米原子力委員会の被ばく者調査/
Medical research activities of Hibakusha by ABCC and USAEC
高橋博子/Hiroko Takahashi
Proceedings of the Meeting on Investigation of Various Nuclear Disasters in the World Tokyo, Japan (Nov. 12, 2017) 56-59. (in Japanese)

放射線の継世代(遺伝的)影響研究の現状と問題点ー核被害者次世代の人権を考えるー/
The present situation and problems of the research on trans-generational effect of radiation - considering the human rights of the second and future generation of radiation victims
Furitsu K.
Proceedings of the Meeting on Investigation of Various Nuclear Disasters in the World Tokyo, Japan (Nov. 12, 2017) 60-69. (in Japanese)

"チェルノブイリ事故後 30 年のナロージチ村における 1 年間の食品放射能汚染と内部被ばくのコホート調査/
Annual research of ¹³⁷Cs concentration in foodstuff and human body of the population cohort in Narodichi after 30
years from the Chernobyl accident"

Kimura S.

Proceedings of the Meeting on Investigation of Various Nuclear Disasters in the World Tokyo, Japan (Nov. 12,
2017) 70-74. (in Japanese)

誰が、どのように原子力事故を収束したか？～チェルノブイリ・東海村・福島現場で～/

Nanasawa K.

Proceedings of the Meeting on Investigation of Various Nuclear Disasters in the World Tokyo, Japan (Nov. 12,
2017) 75-84. (in Japanese)

英国の核災害時緊急事態対応体制から学ぶ/

Revising the Japanese nuclear emergency preparedness and response: Lessons learnt from the system of the United
Kingdom

Shindo M.

Proceedings of the Meeting on Investigation of Various Nuclear Disasters in the World Tokyo, Japan (Nov. 12,
2017) 85-90. (in Japanese)

米国核廃棄物問題の現状/

The current nuclear legacy issues in the US

Tamayama T.

Proceedings of the Meeting on Investigation of Various Nuclear Disasters in the World Tokyo, Japan (Nov. 12,
2017) 91-102. (in Japanese)

台湾の原子力政策の転換過程～「フクシマ・エフェクト」はどう作用したのか～/

Nuclear Energy Policy Change in Taiwan : Exploring the Fukushima Effect on Politics and Society

Suzuki M.

Proceedings of the Meeting on Investigation of Various Nuclear Disasters in the World Tokyo, Japan (Nov. 12,
2017) 103-118. (in Japanese)

大気エアロゾル金属成分の粒径別濃度 /

Size distribution of concentration of metal elements in atmospheric aerosols

Norio Ito, Akira Mizohata, Yuto Inuma, Ryo Okumura

"Proceedings of the 52th KURRI Scientific Meeting" Kumatori, Japan (Jan. 25-26, 2018) 25. (in Japanese)

原発事故後の昆虫類に対する放射線影響評価:カイコを利用した被ばく実験と線量評価 /

Effects of radiation on the insects after a nuclear power plant accident: Exposure experiments and dose assessments
using the Silk- worm Bombyx mori

Sota Tanaka, Tadatoshi Kinouchi, Tomoyuki Takahashi, Daisuke Maki, Hiroki Tanaka, Akihiro Nohtomi, Sentaro
Takahashi

"Proceedings of the 52th KURRI Scientific Meeting" Kumatori, Japan (Jan. 25-26, 2018) 30. (in Japanese)

水中のトリチウムと水酸化物中の水素のイオン交換 /

Ion exchange between tritium in aqueous solution and hydrogen in some hydroxides

Hideo Hashizume, Akihiro Uehara, Satoshi Fukutani, Kazuko Fujii, Toshihiro Ando

"Proceedings of the 52th KURRI Scientific Meeting" Kumatori, Japan (Jan. 25-26, 2018) 34. (in Japanese)

粘土鉱物中のセシウムに与えるシデロホアの影響/

The effect of siderophore on cesium in clay minerals

Tatsuki Kimura, Satoshi Fukutani, Maiko Ikegami

"Proceedings of the 52th KURRI Scientific Meeting" Kumatori, Japan (Jan. 25-26, 2018) 45. (in Japanese)

Development and Current Status of a Carborne gamma-ray Survey System, KURAMA-II

Minoru Tanigaki, Ryo Okumura, Koichi Takamiya, Nobuhiro Sato, Yasuhiro Kobayashi, Hirofumi Yoshino,
Hisao Yoshinaga, Akihiro Uehara

"Proceedings of the 14th International Congress of the International Radiation Protection Association" Cape Town,
South Africa (May 9-13, 2016) 1818-1825.

Books

Environmental Remediation Technologies for Metal-Contaminated Soils
S. Mizutani, M. Ikegami, H. Sakanakura, Y. Kanjo
Springer Japan 2017.

原子力安全基盤科学3 放射線防護と環境放射線管理

高橋千太郎 (第 1.2.4 章、コラム 2 執筆), 高橋知之 (第 3 章執筆), 谷垣実 (第 1.4 章執筆), 木梨友子 (コラム 5 執筆), 八島 浩 (コラム 9 執筆), 佐藤信浩 (コラム 12 執筆), 中村秀仁 (コラム 13 執筆) (in Japanese)

Reviews

大阪－京都の地下水の水質問題と処理方策 一色度、アンモニア等

藤川陽子

環境技術 **46** (2017) 254-261. (in Japanese)

放射化学的中性子放射化分析法による堆積岩標準試料中の微量ハロゲン元素の精密な定量

関本俊

ISOTOPE NEWS **754** (2017) 26-31. (in Japanese)

「環境の分析技術・データ解析・モデル化講座」開始にあたって

藤川陽子

環境技術 **47(2)** (2018) 107-108. (in Japanese)

6. Life Science and Medical Science

Papers

ナットウキナーゼとメナキノン-7の構造研究/

Structural studies of nattokinase and lincnaquinone-7

柳澤泰任, 太田さくら, 足立達美, 内藤佐和, 須見洋行, 齊藤剛, 茶竹俊行

テンペ研究会誌 **13** (2017) 7-13. (in Japanese)

Crystal structure of octocoral lectin SLL-2 complexed with Forssman antigen tetrasaccharide

Kita Akiko, Jimbo Mitsuru, Sakai Ryuichi, Morimoto Yukio, Takeuchi Ryota, Tanaka Hiroshi, Takahashi Takashi, Miki Kunio

Glycobiology **8** (2017) 696-700.

Inhibitory effects of local anesthetics on the proteasome and their biological actions

Bahrudin Udin, Unno Masaki, Nishio Kazuya, Kita Akiko, Li Peili, Kato Masaru, Inoue Masashi, Tsujitani Shunichi, Murakami Takuto, Sugiyama Rina, Saeki Yasushi, Obara Yuji, Tanaka Keiji, Yamaguchi Hiroshi, Sakane Isao, Kawata Yasushi, Itoh Toshiyuki, Ninomiya Haruaki, Hisatome Ichiro, Morimoto Yukio

Scientific Reports **7(1)** (2017) 5079.

Peroxide Activation for Electrophilic Reactivity by the Binuclear Non-heme Iron Enzyme AurF

Park Kiyoungh, Li Ning, Kwak Yeonju, Srnc Martin, Bell Caleb B., Liu Lei V., Wong Shaun D., Yoda Yoshitaka, Kitao Shinji, Seto Makoto, Hu Michael, Zhao Jiyong, Krebs Carsten, Bollinger J. Martin, Solomon Edward I.

Journal of the American Chemical Society **1396(20)** (2017) 7062-7070.

Lifestyle Changes and Oxidative Stress in a High-incidence Area of Amyotrophic Lateral Sclerosis in the Southwestern Kii Peninsula, Japan

Kihira Tameko, Okamoto Kazushi, Sakurai Iori, Arakawa Yuya, Wakayama Ikuro, Takamiya Koichi, Okumura Ryo, Iinuma Yuhto, Iwai Keiko, Kokubo Yasumasa, Yoshida Sohei

Internal Medicine **56(12)** (2017) 1497-1506.

Manifestation of osteoblastic phenotypes in the sarcomatous component of epithelial carcinoma and sarcomatoid carcinoma

Takashima Yasutoshi, Murakami Teppei, Inoue Takao, Hagiya Man, Yoneshige Azusa, Nishimura Syunji, Akagi Masao, Ito Akihiko

Tumor Biology **9(6)** (2017) 101042831770436.

Structural and biochemical analyses of monoubiquitinated human histones H2B and H4
Machida Shinichi, Sekine Satoshi, Nishiyama Yuuki, Horikoshi Naoki, Kurumizaka Hitoshi
Open Biology **6** (2017) 160090.

Ligation-Dependent Picosecond Dynamics in Human Hemoglobin As Revealed by Quasielastic Neutron Scattering
Fujiwara Satoru, Chatake Toshiyuki, Matsuo Tatsuhito, Kono Fumiaki, Tominaga Taiki, Shibata Kaoru, Sato-Tomita Ayana, Shibayama Naoya
The Journal of Physical Chemistry B **34** (2017) 8069-8077.

New method for estimating clustering of DNA lesions induced by physical/chemical mutagens using fluorescence anisotropy
K. Akamatsu, N. Shikazono, T. Saito
Analytical Biochemistry **536** (2017) 78-89.

2017 Publication guidelines for structural modelling of small-angle scattering data from biomolecules in solution: an update
J. Trehwella, A. P. Duff, D. Durand, F. Gabel, J. M. Guss, W. A. Hendrickson, G. L. Hura, D. A. Jacques, N. M. Kriby, A. H. Kwan, J. Perez, L. Pollack, T. M. Ryan, A. Sali, D. Schneidman-Duhovny, T. Schwede, D. I. Svergun, M. Sugiyama, J. A. Tainer, P. Vachette, J. Westbrook, and A. E. Whitten
Acta Crystallographica Section D **73** (2017) 710-728.

Complementation of aprataxin deficiency by base excision repair enzymes in mitochondrial extracts
Çağlayan Melike, Prasad Rajendra, Krasich Rachel, Longley Matthew J., Kadoda Kei, Tsuda Masataka, Sasanuma Hiroyuki, Takeda Shunichi, Tano Keizo, Copeland William C., Wilson Samuel H.
Nucleic Acids Research **45**(17) (2017) 10079-10088.

Proton pump inhibitors have pH-dependent effects on the thermostability of the carboxyl-terminal domain of voltage-gated proton channel Hv1
Zhao Qing, Zuo Weiyan, Zhang Shangrong, Zhang Yongqiang, Li Chuanyong, Li Shu Jie
European Biophysics Journal (2017).

Selective cytotoxicity of the anti-diabetic drug, metformin, in glucose-deprived chicken DT40 cells
Kadoda Kei, Moriwaki Takahito, Tsuda Masataka, Sasanuma Hiroyuki, Ishiai Masamichi, Takata Minoru, Ide Hiroshi, Masunaga Shin-ichiro, Takeda Shunichi, Tano Keizo
PLOS ONE **9** (2017) e0185141.

Structure and function of the intermembrane space domain of mammalian F₀F₁ ATP synthase
Fischer, N., Beilsten-Edmands, V., Chorev, D., Hauer, F., Jiko, C, Shimada, S., Shinzawa, Itoh, K., Robinson, C., Stark, H., and Gerle, C.
BioRxiv (2017) 193045.

Design of an X-band electron linear accelerator dedicated to decentralized Mo⁻⁹⁹/Tc^{-99m} supply: From beam energy selection to yield estimation
J. Jang, M. Yamamoto, M. Uesaka
Physical Review Accelerators and Beams **20** (2017) 104701.

Effect of Tirapazamine, Metformin or Mild Hyperthermia on Recovery from Radiation-Induced Damage in Pimonidazole-Unlabeled Quiescent Tumor Cells
Masunaga Shin-ichiro, Tano Keizo, Sanada Yu, Sakurai Yoshinori, Tanaka Hiroki, Suzuki Minoru, Kondo Natsuko, Watanabe Tsubasa, Takata Takushi, Maruhashi Akira, Ono Koji
World Journal of Oncology **8**(5) (2017) 137-146.

Modest Static Pressure Can Cause Enteric Nerve Degeneration through Ectodomain Shedding of Cell Adhesion Molecule 1
Yoneshige Azusa, Hagiwara Man, Inoue Takao, Tanaka Tomonori, Ri Aritoshi, Ito Akihiko
Molecular Neurobiology **54**(8) (2017) 6378-6390.

Identification of heteromolecular binding sites in transcription factors Sp1 and TAF4 using high-resolution NMR spectroscopy
E. Hibino, R. Inoue, M. Sugiyama, J. Kuwahara, K. Matsuzaki and M. Hoshino
Protein Science **26** (2017) 2280-2290.

RAZA: A Rapid 3D z-crossings Algorithm to segment electron tomograms and extract organelles and macromolecules

Ali, R. A., Mehdi, A. M., Rothnagel, R., Hamilton, N. A., Gerle, C., Landsberg, M. J., & Hankamer, B
Journal of Structural Biology **200** (2017) 73-86.

Characterization of conformational deformation-coupled interaction between immunoglobulin G1 Fc glycoprotein and a low-affinity Fcγ receptor by deuteration-assisted small-angle neutron scattering

R. Yogo, S. Yanaka, H. Yagi, A. Martel, L. Porcar, Y. Ueki, R. Inoue, N. Sato, M. Sugiyama and K. Kato,
Biochemistry and Biophysics Reports **12** (2017) 1-4.

Identification of D-amino acid-containing peptides in human serum

Ha S, Kim I, Takata T, Kinouchi T, Isoyama, Suzuki M, Fujii N*
PLOS ONE **12** (2017) e0189972-e0189972.

ALC1/CHD1L, a chromatin-remodeling enzyme, is required for efficient base excision repair

Tsuda Masataka, Cho Kosai, Ooka Masato, Shimizu Naoto, Watanabe Reiko, Yasui Akira, Nakazawa Yuka, Ogi Tomoo, Harada Hiroshi, Agama Keli, Nakamura Jun, Asada Ryuta, Fujii Haruna, Sakuma Tetsushi, Yamamoto Takashi, Murai Junko, Hiraoka Masahiro, Koike Kaoru, Pommier Yves, Takeda Shunichi, Hirota Kouji
PLOS ONE **11** (2018) e0188320.

Conversion of functionally undefined homopentameric protein PbaA into a proteasome activator by mutational modification of its C-terminal segment conformation

Yagi-Utsumi Maho, Sikdar Arunima, Kozai Toshiya, Inoue Rintaro, Sugiyama Masaaki, Uchihashi Takayuki, Yagi Hirokazu, Satoh Tadashi, Kato Koichi
Protein Engineering, Design and Selection **31(1)** (2018) 29-36.

Disruption of Hif-1α enhances cytotoxic effects of metformin in murine squamous cell carcinoma

Sanada Yu, Sasanuma Hiroyuki, Takeda Shunichi, Tano Keizo, Masunaga Shin-ichiro
International Journal of Radiation Biology **94(1)** (2018) 88-96.

Measurement of nuclear reaction cross sections by using Cherenkov radiation toward high-precision proton therapy

Masuda Takamitsu, Kataoka Jun, Arimoto Makoto, Takabe Miho, Nishio Teiji, Matsushita Keiichiro, Miyake Tasuku, Yamamoto Seiichi, Inaniwa Taku, Toshito Toshiyuki
Scientific Reports **8(1)** (2018) 2570.

Solution scattering approaches to dynamical ordering in biomolecular systems

Bernadó Pau, Shimizu Nobutaka, Zaccai Giuseppe, Kamikubo Hironari, Sugiyama Masaaki
Biochimica et Biophysica Acta (BBA) - General Subjects **1862(2)** (2018) 253-274.

Proceedings

京大炉における蛋白質の重水素化の取り組み及び最近の研究成果

井上倫太郎, 佐藤信浩, 守島 健, 杉山正明

Proceedings of the Project Meeting on "Construction of the basis for the advanced materials science and analytical study by the innovative use of quantum beam and nuclear sciences" Kumatori, Japan (Dec. 15, 2017) 53. (in Japanese)

量子ビーム小角散乱法を用いた食品タンパク質凝集体のナノ構造解析

佐藤信浩

Proceedings of the Project Meeting on "Construction of the basis for the advanced materials science and analytical study by the innovative use of quantum beam and nuclear sciences" Kumatori, Japan (Dec.15, 2017) 62. (in Japanese)

超遠心分析を用いたタンパク質溶液構造研究

守島 健, 井上倫太郎, 酒巻祐介, 佐藤信浩, 杉山正明

Proceedings of the Project Meeting on "Construction of the basis for the advanced materials science and analytical study by the innovative use of quantum beam and nuclear sciences" Kumatori, Japan (Dec.15, 2017) 68. (in Japanese)

自発的アミノ酸修飾が関与する加齢性白内障発症機構の解明/

Spontaneous Modifications of Asp Residue Caused Lens Protein Insolubilization

Takumi Takata

"Proceedings of the 52th KURRI Scientific Meeting" Kumatori, Japan (Jan. 25-26, 2018) 1-4. (in Japanese)

有機水銀分解酵素の中性子解析のための最小培地試料作成と構造解析/

A Study of preparation and structural analysis of the organomercury lyase for a neutron diffraction experiment
Yukio Morimoto and Akiko Kita
“Proceedings of the 52th KURRI Scientific Meeting” Kumatori, Japan (Jan. 25-26, 2018) 19. (in Japanese)

対数増殖期における納豆菌のガンマ線耐性/

Radiation resistance with gamma rays of *Bacillus subtilis* natto in a logarithmic growth phase
Toshiyuki Chatake, Takeshi Saito, Yasuhide Yanaiswa
“Proceedings of the 52th KURRI Scientific Meeting” Kumatori, Japan (Jan. 25-26, 2018) 21. (in Japanese)

グルコサミン型 BNCT 用ホウ素キャリアーの設計・合成と機能評価 /

Design, synthesis and functional evaluation of boron carriers for BNCT bearing glucosamine scaffold
Hiroki Ueda, Taiki Itoh, Yasuhiro Sawamoto, Tomohiro Tanaka, Shin Aoki
“Proceedings of the 52th KURRI Scientific Meeting” Kumatori, Japan (Jan. 25-26, 2018) 26. (in Japanese)

超好熱性アーキアの補酵素 A 生合成経路に固有の酵素群の構造解析 /

Structure analysis of enzymes required for the distinct CoA production pathway in hyperthermophilic archaea.
Akiko Kita, Asako Kishimoto, Takahiro Shimosaka, Takuya Ishibashi, Hiroya Tomita, Yuusuke Yokooji, Tadayuki Imanaka, Haruyuki Atomi, and Kunio Miki
“Proceedings of the 52th KURRI Scientific Meeting” Kumatori, Japan (Jan. 25-26, 2018) 32. (in Japanese)

超遠心分析を用いたタンパク質溶液構造研究 /

Analytical Ultracentrifugation for Structural Research of Protein Solutions
Ken Morishima, Yusuke Sakamaki, Rintaro Inoue, Nobuhiro Sato, Masaaki Sugiyama
“Proceedings of the 52th KURRI Scientific Meeting” Kumatori, Japan (Jan. 25-26, 2018) 49. (in Japanese)

マルチドメイン蛋白質の溶液構造解析に関する研究 /

Solution structure of multi-domain protein
Hiroshi Nakagawa, Tomohide Saio, Masaaki Sugiyama, Rintaro Inoue
“Proceedings of the 52th KURRI Scientific Meeting” Kumatori, Japan (Jan. 25-26, 2018) 50. (in Japanese)

Chinese Hamster 卵巣細胞由来 HSPB1 の機能と構造 /

Functional and structural characterization of HSPB1 from Chinese hamster ovary cell
Masafumi Yohda, Eiryo Sha, Yohei Y. Yamamoto, Toshihiko Oka
“Proceedings of the 52th KURRI Scientific Meeting” Kumatori, Japan (Jan. 25-26, 2018) 51. (in Japanese)

溶液散乱を利用した時計タンパク質複合体の構造解析 /

Structural analysis of protein complexes by small-angle scattering
Hirokau Yagi
“Proceedings of the 52th KURRI Scientific Meeting” Kumatori, Japan (Jan. 25-26, 2018) 53. (in Japanese)

混雑環境下における α -crystallin の構造およびダイナミクス /

Structure and dynamics of α -crystallin under crowding environment
Yusuke Sakamaki, Rintaro Inoue, Ken Morishima, Nobuhiro Sato, Noriko Fujii, Masaaki Sugiyama
“Proceedings of the 52th KURRI Scientific Meeting” Kumatori, Japan (Jan. 25-26, 2018) 55. (in Japanese)

Books

がん・放射線療法 2017

増永慎一郎

学研メディカル秀潤社 2017. (in Japanese)

Reviews

生命科学におけるパラキラリティーの重要性

藤井紀子, 高田匠

眼薬理 **31** (2017) 20-27. (in Japanese)

D-アミノ酸含有タンパク質と老化—健康—病態

藤井紀子

食品加工技術 **37** (2017) 80-84. (in Japanese)

症候性放射線脳壊死診療ガイドライン

症候性放射線脳壊死ガイドライン作成委員会

(青山英史, 岩井謙育, 志賀, 中洲庸子, 成田善孝, 野々口直助, 古瀬元雅, 前林勝也, 松尾孝之, 宮武伸一, 山田恵)

脳神経外科ジャーナル **26(4)** (2017) 2-11. (in Japanese)

白内障と酸化ストレス

高田匠, 金仁求, 藤井紀子

OCULISTA **51** (2017) 28-34. (in Japanese)

紫外線による白内障と皮膚老化はアミノ酸の形でわかる

藤井紀子

環境と健康 特集: 紫外線の影響健康—その功罪を考える **30** (2017) 103-110. (in Japanese)

白内障原因蛋白質の変化をとらえる化学的アプローチ; 白内障におけるホモキラリティーの喪失

藤井紀子, 高田匠

日本白内障学会誌 **29** (2017) 13-20. (in Japanese)

D-アミノ酸と老化; 新規老化マーカーとしての D-アミノ酸の有用性

藤井紀子, 高田匠

アンチ・エイジング医学—日本抗加齢医学会雑誌 **13(3)** (2017) 383-391. (in Japanese)

The age-related increase of D-amino acids and advanced glycation end-products in protein

Noriko Fujii and Takumi Takata.

Glycative Stress Research **4(3)** (2017) 203-211.

細胞の運命を左右する「クラスターDNA 損傷」の探求

赤松憲

放射線と産業 **143** (2017) 21-25. (in Japanese)

D-Amino acids in protein: The mirror of life as a molecular index of aging

Noriko Fujii, Takumi Takata, Norihiko Fujii, Kenzo Aki, Hiroaki Sakaue

BBA - Proteins and Proteomics 2018.

7. Neutron Capture Therapy

Papers

BNCT for head and neck cancer-history at our institution Aihara, T., Hiratsuka, J., Morita, N., Kamitani, N., Harada, T., Suzuki, M., Ono, K., Kumada, H. Practica Otologica, Supplement **149** (2017) 227-240.

DNA Double-strand Breaks Induced by Fractionated Neutron Beam Irradiation for Boron Neutron Capture Therapy

Y. Kinashi, N. Yokomizo, S. Takahashi

Anticancer Research **37(4)** (2017) 1681-1685.

Evaluation of radioactivity in the bodies of mice induced by neutron exposure from an epi-thermal neutron source of an accelerator-based boron neutron capture therapy system

NAKAMURA Satoshi, IMAMICHI Shoji, MASUMOTO Kazuyoshi, ITO Masashi, WAKITA Akihisa, OKAMOTO Hiroyuki, NISHIOKA Shie, IJIMA Kotaro, KOBAYASHI Kazuma, ABE Yoshihisa, IGAKI Hiroshi, KURITA Kazuyoshi, NISHIO Teiji, MASUTANI Mitsuko, ITAMI Jun

Proceedings of the Japan Academy, Series B **93(10)** (2017) 821-831.

Block copolymer-boron cluster conjugate for effective boron neutron capture therapy of solid tumors

Mi Peng, Yanagie Hironobu, Dewi Novriana, Yen Hung-Chi, Liu Xueying, Suzuki Minoru, Sakurai Yoshinori, Ono Koji, Takahashi Hiroyuki, Cabral Horacio, Kataoka Kazunori, Nishiyama Nobuhiro

Journal of Controlled Release **254** (2017) 1-9.

Cerebrospinal fluid dissemination of high-grade gliomas following boron neutron capture therapy occurs more frequently in the small cell subtype of IDH1R132H mutation-negative glioblastoma

Kondo Natsuko, Barth Rolf F., Miyatake Shin-Ichi, Kawabata Shinji, Suzuki Minoru, Ono Koji, Lehman Norman L. Journal of Neuro-Oncology **133(1)** (2017) 107-118.

Note: Development of real-time epithermal neutron detector for boron neutron capture therapy
Tanaka H., Sakurai Y., Takata T., Watanabe T., Kawabata S., Suzuki M., Masunaga S.-I., Taki K., Akabori K., Watanabe K., Ono K.
Review of Scientific Instruments **88(5)** (2017) 056101.

Selective boron delivery by intra-arterial injection of BSH-WOW emulsion in hepatic cancer model for neutron capture therapy
Yanagie Hironobu, Dewi Novriana, Higashi Syushi, Ikushima Ichiro, Seguchi Koji, Mizumachi Ryoji, Murata Yuji, Morishita Yasuyuki, Shinohara Atsuko, Mikado Shoji, Yasuda Nakahiro, Fujihara Mitsuteru, Sakurai Yuriko, Mouri Kikue, Yanagawa Masashi, Iizuka Tomoya, Suzuki Minoru, Sakurai Yoshinori, Masunaga Shin-ichiro, Tanaka Hiroki, Matsukawa Takehisa, Yokoyama Kazuhito, Fujino Takashi, Ogura Koichi, Nonaka Yasumasa, Sugiyama Hirotaka, Kajiyama Tetsuya, Yui Sho, Nishimura Ryohei, Ono Koji, Takamoto Sinichi, Nakajima Jun, Ono Minoru, Eriguchi Masazumi, Hasumi Kenichiro, Takahashi Hiroyuki
The British Journal of Radiology **1074(90)** (2017) 20170004.

Understanding the potentiality of accelerator based-boron neutron capture therapy for osteosarcoma: dosimetry assessment based on the reported clinical experience
Bortolussi Silva, Postuma Ian, Protti Nicoletta, Provenzano Lucas, Ferrari Cinzia, Cansolino Laura, Dionigi Paolo, Galasso Olimpio, Gasparini Giorgio, Altieri Saverio, Miyatake Shin-Ichi, González Sara
J. Radiation Oncology **12(1)** (2017) 130.

Computational investigation of suitable polymer gel composition for the QA of the beam components of a BNCT irradiation field
Tanaka Kenichi, Sakurai Yoshinori, Hayashi Shin-ichiro, Kajimoto Tsuyoshi, Uchida Ryohei, Tanaka Hiroki, Takata Takushi, Bengua Gerard, Endo Satoru
Applied Radiation and Isotopes **127** (2017) 253-259.

Development and Elucidation of a Novel Fluorescent Boron-Sensor for the Analysis of Boronic Acid-Containing Compounds
Hattori Yoshihide, Ogaki Takuya, Ishimura Miki, Ohta Yoichiro, Kirihata Mitsunori
Sensors **17(12)** (2017) 2436.

DEVELOPMENT OF A MULTIMODAL MONTE CARLO BASED TREATMENT PLANNING SYSTEM
Kumada Hiroaki, Takada Kenta, Sakurai Yoshinori, Suzuki Minoru, Takata Takushi, Sakurai Hideyuki, Matsumura Akira, Sakae Takeji
Radiation Protection Dosimetry (2017) 1-5.

Boron neutron capture therapy using reactor epithermal neutron beams could effectively control in-transit and lymph node metastases originating from a cutaneous malignant melanoma
Omori Mamiko, Fujiwara Susumu, Shimizu Hideki, Ikeda Tetsuya, Bito Toshinori, Suzuki Minoru, Masunaga Shin-ichiro, Ono Koji, Nishigori Chikako
The Journal of Dermatology 2017.

Predicted performance of a PG-SPECT system using CZT primary detectors and secondary Compton-suppression anti-coincidence detectors under near-clinical settings for boron neutron capture therapy
Hales, B., Katabuchi, T., Igashira, M., Terada, K., Hayashizaki, N., Kobayashi, T.
Nuclear Instruments and Methods in Physics Research, Section A **875** (2017) 51-56.

Impact of oxygen status on ¹⁰B-BPA uptake into human glioblastoma cells, referring to significance in boron neutron capture therapy
Wada Yuki, Hirose Katsumi, Harada Takaomi, Sato Mariko, Watanabe Tsubasa, Anbai Akira, Hashimoto Manabu, Takai Yoshihiro
Journal of Radiation Research 2018.

Microdosimetric Modeling of Biological Effectiveness for Boron Neutron Capture Therapy Considering Intra- and Intercellular Heterogeneity in ¹⁰B Distribution
Sato Tatsuhiko, Masunaga Shin-ichiro, Kumada Hiroaki, Hamada Nobuyuki
Scientific Reports **8(1)** (2018) 18871.

Proceedings

ホウ素中性子捕捉療法における抹消血リンパ球解析による生物学的被ばく線量測定

Yuko Kinashi

The 14th Congress on Neutron Capture Therapy Koriyama, Japan (Sept. 29-30, 2017). (in Japanese)

Development of prompt gamma rays imaging detector using LaBr₃(Ce) scintillator for boron neutron capture therapy
H. Tanaka, T. Takata, K. Akabori, K. Okazaki, Y. Sakurai, T. Watanabe, M. Suzuki, S. Masunaga, K. Ono
2017IEEE Nuclear Science Symposium and Medical Imaging Conference Atlanta, USA (Oct. 21-28, 2017).

Application of stochastic microdosimetric kinetic model to boron neutron capture therapy

Sato T, Masunaga S, Kumada H and Hamada N.

The 17th International Symposium on Microdosimetry (Micros 2017) Venice (Venezia), Italy (Nov. 13-17, 2017).

Synthesis and Biological Evaluation of Medium-Chain Alkyl Sulfoniododecaborate Containing p-Boronophenylalanine

Yoshihide Hattori, Miki Ishimura, Youichirou Ohta, Hiroshi Takenaka, Kouki Uehara, Tomoyuki Asano and Mitsunori Kirihata

第54回ペプチド討論会 / The 54th Japanese Peptide Symposium Osaka, Japan (Nov.20-22, 2017).

中性子捕捉反応を利用した植物におけるホウ素動態の分析法の開発とその生理機能の解明 /

Visualization of boron in plant tissues using neutron capture radiography

Tadatoshi Kinouchi, Masaru Kobayashi and Sakihito Kitajima

“Proceedings of the 52th KURRI Scientific Meeting” Kumatori, Japan (Jan.25-26, 2018) 65. (in Japanese)

Books

医療・診断をささえるペプチド科学

服部能英、切畑光統

シーエムシー出版 2017.

Reviews

メーキングプレートを用いた中性子捕捉療法ビーム成分分布の品質保証

田中憲一, 梶本 剛, 遠藤 暁, 櫻井良憲, 田中浩基, 高田卓志, 村田 勲, 玉置真悟

放射線 **43** (2017) 3-7. (in Japanese)

Boron Neutron Capture Therapy for Malignant Brain Tumors

Shin-Ichi Miyatake, Shinji Kawabata, Ryo Hiramatsu, Toshihiko Kuroiwa, Minoru Suzuki, Natsuko Kondo, Hiroki Tanaka, Koji Ono

WFNOS Magazine **2(1)** (2017) 2-11.

血清アルブミンを利用したホウ素デリバリーシステム

中村浩之

BIO Clinica **32** (2017) 669-703. (in Japanese)

「展望」中性子捕捉療法のための新しいホウ素薬剤の開発 —血清アルブミンホウ素キャリアー—

中村浩之

Isotope News **753** (2017) 2-7. (in Japanese)

ホウ素中性子捕捉療法(BNCT)用 10B-ホウ素化合物の研究開発

服部能英, 切畑光統

ペプチドニュースレター **106** (2017) 2-4. (in Japanese)

ホウ素中性子捕捉療法におけるゲル線量計の利用

櫻井良憲, 内田良平

放射線医学物理 **37(3)** (2017) 190-194. (in Japanese)

Boron Neutron Capture Therapy of Malignant Gliomas

Shin-Ichi Miyatake, Shinji Kawabata, Ryo Hiramatsu, Toshihiko Kuroiwa, Minoru Suzuki, Koji Ono

Progress in Neurological Surgery **32** (2018) 48-56. (in Japanese)

Others

ホウ素中性子捕捉療法に用いる新規ホウ素化合物の開発の現状

中井 啓

茨城県立医療大学紀要 **22** (2017) 1-9. (in Japanese)

ガドリニウム中性子捕捉反応の生物効果
高垣雅緒, 宇野賀津子, 東丸貴信
Pasken Journal **26-29** (2017) 35-39. (in Japanese)

8. Neutron Radiography and Radiation Application

Papers

Visualization of solidification process in lead-bismuth eutectic
Daisuke Ito, Yasushi Saito, Hirotaka Sato and Takenao Shinohara
Physics Procedia **88** (2017) 58-63.

Optimization of Moderator Size of Thermal and Epithermal Neutron Source Based on a Compact Accelerator for Neutron Imaging
Hasemi Hiroyuki, Kamiyama Takashi, Sato Hirotaka, Kino Koichi, Kiyonagi Yoshiaki, Nakajima Ken
Physics Procedia **88** (2017) 369-375.

Pulsed Neutron Imaging for Non-destructive Testing using Simulated Nuclear Fuel Samples
D. Ito, T. Sano, J. Hori, Y. Takahashi, H. Hasemi, T. Kamiyama, K. Nakajima
Physics Procedia **88** (2017) 89-94.

Proceedings

京大炉における中性子イメージングの概要と J-PARC を用いたイメージング研究
齊藤泰司, 伊藤大介
Proceedings of the Project Meeting on “Construction of the basis for the advanced materials science and analytical study by the innovative use of quantum beam and nuclear sciences” Kumatori, Japan (Dec. 15, 2017) 14-17.
(in Japanese)

Books

Boiling 1st Edition Research and Advances
Y. Saito
Elsevier 2017.

Reviews

中性子ラジオグラフィを用いたフィンチューブ熱交換器への着霜の可視化
—放射線ラジオグラフィを用いた霜研究の新展開—
松本亮介
日本冷凍空調学会学会誌 **92** (2017) 40-44. (in Japanese)

9. TRU and Nuclear Chemistry

Papers

Solubility of $Zr(OH)_4(am)$ and the Formation of Zr(IV) Carbonate Complexes in Carbonate Solutions Containing $0.1-5.0 \text{ mol}\cdot\text{dm}^{-3} \text{ NaNO}_3$
Kobayashi Taishi and Sasaki Takayuki
Journal of Solution Chemistry **9-10** (2017) 1741-1759.

10. Health Physics and Waste Management

Papers

表面線量率及び表面汚染密度の測定による放射性セシウムの表面残存状況の評価
/Evaluation of Residual Radioactive Cs at Surfaces by Monitoring Surface Dose Rate and Surface Contamination Concentration
森芳友, 米田稔, 島田洋子, 福谷哲, 池上麻衣子
環境放射能除染学会誌 **5** (2017) 3-15. (in Japanese)

Long-term predictions of ambient dose equivalent rates after the Fukushima Daiichi nuclear power plant accident
Kinase Sakae, Takahashi Tomoyuki, Saito Kimiaki
Journal of Nuclear Science and Technology **54(12)** (2017)1345-1354.

Transfer Factors of Tellurium and Cesium from Soil to Radish (*Raphanus sativus* var. *sativus*) and
Komatsuna (*Brassica rapa* var. *perviridis*)
FUJIWARA Keiko, TAKAHASHI Tomoyuki, KINOUCHI Tadatoshi, FUKUTANI Satoshi, TAKAHASHI
Sentaro, WATANABE Tetsuhiro, FUNAKAWA Shinya
Japanese Journal of Health Physics **52(3)** (2017) 192-199.

Methodology for Simultaneous Relative-calibration of Multiple Personal Dosimeters in a ²²⁶Ra Irradiation Field
NAKAMURA Hidehito, MAKI Daisuke, YAMADA Tatsuya, KANAYAMA Masaya, MIYAKE
Tomohiro, TAKASHIMA Naoki, TAKAHASHI Tomoyuki, TAKAHASHI Sentaro
Japanese Journal of Health Physics **52(4)** (2018) 307-310.

Proceedings

Reduction and Resource Recycling of High-Level Radioactive Wastes through Nuclear Transmutation: Investigation
on the Lifecycle and Environmental Behaviour of Zirconium and Palladium
K.Iwata, T.Takahashi, N.Takashima, S.Tanaka, S.Takahashi
Global2017 Seoul, Korea (sept.24-28, 2017).

Reviews

廃棄物抽出液中の放射性セシウム除去のための高分子凝集剤の選定
藤川陽子, 竹田 健, 森下かなた, 尾崎博明
環境浄化技術 **17** (2018) 67-77. (in Japanese)

11. Accelerator Physics

Papers

Intense Muon Source with Energy Recovery Internal Target (ERIT) Ring Using Deuterium Gas Target
Y. Mori, H. Okita, Y. Ishi, Y. Yonemura, H. Arima
Memories of the Faculty of Engineering, Kyushu University **77** (2017) 1-9.

Design of an Acceleration Gap for Brightness Enhancement in a Reactor-Based Slow Positron Beamline
Kuzuya Y., Oshima N., Kinomura A., Yabuuchi A.
Acta Physica Polonica A **132(5)** (2017) 1620-1624.

First demonstration of coherent Cherenkov radiation matched to circular plane wave
Sei Norihiro and Takahashi Toshiharu
Scientific Reports **7(1)** (2017) 17440.

逆コンプトン散乱を用いた相対論的電子線分光法の開発
清 紀弘, 高橋 俊晴
日本赤外線学会誌 **27** (2018) 42-49. (in Japanese)

Proceedings

MEASUREMENT OF THIN FILM COATING ON SUPERCONDUCTORS
Y. Iwashita, Y. Fuwa, H. Tongu, H. hayano, T. Kubo, T. Saeki, M. Hino, H. Oikawa
8th International Particle Accelerator Conference (IPAC 2017) Copenhagen (May 14-19, 2017) 1043-1045.

Future Plans of ADS Proton Drivers at Kyoto University Research Reacture Institute
Y. Ishi, Y. Kuriyama, Y. Mori, T. Uesugi
Proceedings of 8th International Particle Accelerator Conference Copenhagen, Denmark (May14-19, 2017).

Emittance Growth at Charge-Exchange Multi-Turn Injection in KURRI FFAG
Y. Ishi, Y. Kuriyama, Y. Mori, T. Uesugi
Proceedings of 8th International Particle Accelerator Conference Copenhagen, Denmark (May 14-19, 2017).

DeeMe Experiment to Search for Muon to Electron Conversion at J-PARC MLF
N. Teshima on behalf of the DeeMe Collaboration
Proceedings of the 19th International Workshop on Neutrinos from Accelerators NUFACT2017 Uppsala, Sweden (Sept. 25-30, 2017) 109.

電子線形加速器をツールとしたマルチ量子ビーム利用拠点の構築
高橋俊晴

Proceedings of the Project Meeting on "Construction of the basis for the advanced materials science and analytical study by the innovative use of quantum beam and nuclear sciences" Kumatori, Japan (Dec. 15, 2017) 95.
(in Japanese)

電子ライナックによる高強度コヒーレントテラヘルツ光源の特性と先端科学への応用
奥田修一, 田中良晴, 高橋俊晴

Proceedings of the Project Meeting on "Construction of the basis for the advanced materials science and analytical study by the innovative use of quantum beam and nuclear sciences" Kumatori, Japan (Dec. 15, 2017) 104.
(in Japanese)

電子線型加速器を用いた医療用放射性核種の製造技術についての基礎検討 /

Examination of Medical Radionuclides Production using an Electron Linear Accelerator
Shun Sekimoto, Satoshi Itostu, Takahiro Tadokoro, Yuko Kani, Yuichiro Ueno, Tsutomu Otsuki
"Proceedings of the 52th KURRI Scientific Meeting" Kumatori, Japan (Jan. 25-26, 2018) 18. (in Japanese)

複合原子力科学のための次世代高繰り返しシンクロトロン設計 /

Design of Next Generation Rapid Cycle Synchrotron for Integrated Radiation and Nuclear Science Yasuhiro Fuwa, Yasutoshi Kuriyama, Tomonori Uesugi, Yoshihiro Ishi
"Proceedings of the 52th KURRI Scientific Meeting" Kumatori, Japan (Jan. 25-26, 2018) 37. (in Japanese)

12. Others

Papers

Educational outcomes of a medical physicist program over the past 10 years in Japan
Kadoya Noriyuki, Karasawa Kumiko, Sumida Iori, Arimura Hidetaka, Kakinohana Yasumasa, Kabuki Shigeto, Monzen Hajime, Nishio Teiji, Shirato Hiroki, Yamada Syogo
Journal of Radiation Research **5(1)** (2017) 669-674.

Immunotherapy of Nivolumab with Dendritic Cell Vaccination Is Effective against Intractable Recurrent Primary Central Nervous System Lymphoma: A Case Report
FURUSE Motomasa, NONOGUCHI Naosuke, OMURA Naoki, SHIRAHATA Mitsuaki, IWASAKI Koichi, INUI Toshio, KUROIWA Toshihiko, KUWABARA Hiroko, MIYATAKE Shin-Ichi
Neurologia medico-chirurgica **57(4)** (2017) 191-197.

Correlation between crystallization temperature and Ge concentration in Ge-TiO₂ nanocomposite thin films
Seishi Abe
Thin Solid Films **636** (2017) 183-187.

Formation of metallic cation-oxygen network for anomalous thermal expansion coefficients in binary phosphate glass
Onodera Yohei, Kohara Shinji, Masai Hirokazu, Koreeda Akitoshi, Okamura Shun, Ohkubo Takahiro
Nature Communications **8** (2017) 15449-1 - 15449-8.

In situ XAFS Study of Palladium Electrodeposition at the Liquid/Liquid Interface
Booth Samuel G., Chang Sin-Yuen, Uehara Akihiro, La Fontaine Camille, Cibirn Giannantonio, Schroeder Sven L.M., Dryfe Robert A.W.
Electrochimica Acta **235** (2017) 251-261.

Concise and Versatile Synthesis of Sulfoquinovosyl Acyl Glycerol Derivatives for Biological Applications

Tanaka Tomohiro, Sawamoto Yasuhiro, Aoki Shin

Chemical and Pharmaceutical Bulletin **65(6)** (2017) 566-572.

Spatial variation and its stochastic modeling of seismic ground motions in hard soil based on three-dimensional-dense- array strong-motion observation records

O. Uchida, H. Uebayashi, K. Kamae,

Journal of Japan Association for Earthquake Engineering **17(3)** (2017) 26-49.

Phase-transformation in iron oxide and formation of Cu/ γ -Fe₂O₃ nanocomposite using radio-frequency sputtering with metal chips on an α -Fe₂O₃ target

Abe Seishi and Watanabe Masato

AIP Advances **7** (2017) 075317.

The significance of bromide in the Brust–Schiffrin synthesis of thiol protected gold nanoparticles

Booth S. G., Uehara A., Chang S.-Y., La Fontaine C., Fujii T., Okamoto Y., Imai T., Schroeder S. L. M., Dryfe R. A. W.

Chemical Science **8(12)** (2017) 7954-7962.

Design, Synthesis, and Anticancer Activities of Cyclometalated Tris(2-phenylpyridine)iridium(III) Complexes with Cationic Peptides at the 4 -Position of the 2-Phenylpyridine Ligand

Yokoi Kenta, Hisamatsu Yosuke, Naito Kana, Aoki Shin

European Journal of Inorganic Chemistry **44** (2017) 5295-5309.

Synthesis of Disaccharide Nucleosides Utilizing the Temporary Protection of the 2,3 -cis-Diol of Ribonucleosides by a Boronic Ester

Someya Hidehisa, Itoh Taiki, Aoki Shin

Molecules **22(10)** (2017) 1650-1670.

Usefulness of a new online patient-specific quality assurance system for respiratory-gated radiotherapy

Kurosawa Tomoyuki, Tachibana Hidenobu, Moriya Shunsuke, Miyakawa Shin, Nishio Teiji, Sato Masanori
Physica Medica **43** (2017) 63-72.

国内に建つ超高層集合住宅の大地震時における最大平均層間変形角の推定と簡易評価/

Estimation and Simplified Evaluation of Peak Inter-story Drift Angle during Massive Earthquake for RC Super High-rise Residential Buildings in Japan

成島慶, 永野正行, 鈴木賢人, 上林宏敏, 田沼毅彦, 小田聡

日本地震工学会論文集 **17(5)** (2017) 96-108. (in Japanese)

中央構造線断層帯(金剛山地東縁-和泉山脈南縁)周辺域の地下構造モデルの高度化と強震動予測

上林宏敏, 大堀道広, 川辺秀憲, 釜江克宏, 山田浩二, 岩田知孝, 関口春子, 浅野公之

日本建築学会地盤震動シンポジウム

「2016年熊本地震に学び、将来の強震動予測を考える」(2017) 63-74. (in Japanese)

Quantitative analysis on the impact of nuclear energy supply disruption on electricity supply security

Kosai Shoki, Unesaki Hironobu

Applied Energy **208** (2017) 1198-1207.

Size-based Differentiation of Cancer and Normal Cells by a Particle Size Analyzer Assisted by a Cell-recognition PC Software

Shashni Babita, Ariyasu Shinya, Takeda Reisa, Suzuki Toshihiro, Shiina Shota, Akimoto Kazunori, Maeda Takuto, Aikawa Naoyuki, Abe Ryo, Osaki Tomohiro, Itoh Norihiko, Aoki Shin

Biological & Pharmaceutical Bulletin **41** (2018).

A Chemical Modulator of p53 Transactivation that Acts as a Radioprotective Agonist

Morita Akinori, Takahashi Ippei, Sasatani Megumi, Aoki Shin, Wang Bing, Ariyasu Shinya, Tanaka Kaoru, Yamaguchi Tetsuji, Sawa Akiko, Nishi Yurie, Teraoka Tatsuro, Ujita Shohei, Kawate Yosuke, Yanagawa Chihiro, Tanimoto Keiji, Enomoto Atsushi, Neno Mitsuru, Kamiya Kenji, Nagata Yasushi, Hosoi Yoshio, Inaba Toshiya
Molecular Cancer Therapeutics **17(2)** (2018) 432-442.

Improved proton CT imaging using a bismuth germanium oxide scintillator
Tanaka Sodai, Nishio Teiji, Tsuneda Masato, Matsushita Keiichiro, Kabuki Shigeto, Uesaka Mitsuru
Physics in Medicine & Biology **63(3)** (2018) 035030.

Visualization of Individual Images in Patterned Organic–Inorganic Multilayers Using GISAXS-CT
Ogawa Hiroki, Nishikawa Yukihiko, Takenaka Mikihiro, Fujiwara Akihiko, Nakanishi Yohei, Tsujii Yoshinobu,
Takata Masaki, Kanaya Toshiji
Langmuir **33(19)** (2017) 4675-4681.

The Formation of OTDD Network Structure in PS-b
Wang Yi-Chin, Inoue Ayano, Hasegawa Hirokazu, Takenaka Mikihiro
Macromolecular Chemistry and Physics **218(12)** (2017) 1700008.

Proceedings

Performance evaluation of TLD sheet toward the dosimetry in the build-up region
T. Suzuki, T. Nishio, H. Masuda, Y. Nagata
Proceedings of the 113th JSMP in a Supplement Issue of the Japanese Journal of Medical Physics (JJMP)
Yokohama, Japan (Apr. 13-16, 2017) 95.

Dose error prediction based on the dose uncertainty accumulation of intensity modulated radiation therapy
E. Shiba, A. Saito, M. Tsuneda, M. Furumi, K. Yahara, T. Ohguri, Y. Murakami, T. Nishio, Y. Korogi, Y. Nagata
Proceedings of the 113th JSMP in a Supplement Issue of the Japanese Journal of Medical Physics
Yokohama, Japan (Apr. 13-16, 2017) 19.

Commissioning of the small-field and large-field proton beams in line scanning therapy for the Eclipse
Proton treatment planning system
Y. Sugama, M. Araya, I. Maeshima, H. Fujimoto, Y. Ito, Y. Seki, D. Amano, G. Shibagaki, T. Nishio, H. Onishi
Proceedings of the 113th JSMP in a Supplement Issue of the Japanese Journal of Medical Physics
Yokohama, Japan (Apr. 13-16, 2017) 51.

Design and Implementation of Single Event Latch-up Measurement and Self-Recovery System for BIRDS CubeSat
Abdulla H. Kafi, BIRDS Project Members, BIRDS Partners, George Maeda, Sangkyun Kim, Hirokazu Masui,
Mengu Cho
Proceedings of 31st International Symposium on Space Technology and Science Matsuyama, Japan (June 3-9, 2017).

Two-phase flow behavior and heat transfer characteristics in kettle reboiler
T. Miyazaki, M. Baba, H. Murakawa, H. Asano, K. Sugimoto, D. Ito
Proceedings of the ASME 2017 Power Conference Joint with ICOPE-17 Charlotte, USA (June26-30, 2017).

Structural modification and biological evaluation of quinomycin class cyclic depsipeptides to develop
antitumor agents targeting the tumor microenvironment
H. Nagasawa, K. Koike, K. Hattori, H. Okuda, T. Hirayama
26th French-Japanese Symposium on Medicinal & Fine Chemistry Strasbourg, France (Sept. 17-20, 2017).

B-3 小型多目的中性子回折計建設の進捗状況 2017 /
The current state for constructing the compact multipurpose neutron diffractometer on the 8-3 beam port, 2017
Kazuhiro Mori, Ryo Okumura, Hirofumi Yoshino, Setsuo Sato, Haruhiro Hiraka, Kenji Iwase, and Akihiro
Okumura “Proceedings of the 52th KURRI Scientific Meeting” Kumatori, Japan (Jan.25-26, 2018) 41.
(in Japanese)

ON THE REASSESSMENT OF SAFETY ASSESSMENT REPORTS AND THE RESTART OF
UNIVERSITY RESEARCH REACTORS IN JAPAN
Hironobu Unesaki, Tsuyoshi Misawa, Ken Nakajima, Hiroto Uebayashi, Jun-Ichi Hori,
Toshihiro Yamamoto, Hiroshi Shiga and Katsuhiko Kamae
European Research Reactor Conference RRFM 2018 Munich, Germany (Mar.11-15, 2018).

Books

原子力安全基盤科学1 原子力発電所事故と原子力の安全

山名 元 (1・2・3・7章), 中島 健 (5章)

京都大学学術出版会 (2017). (in Japanese)

原子力安全基盤科学2 原子力バックエンドと放射性廃棄物

山名元 (第1~5.7章、コラム2、3執筆), 窪田卓見 (第2章執筆), 上原章寛 (第3章、コラム1執筆),

卞哲浩 (6章、コラム5執筆), 石楨浩 (6勝、コラム4執筆), 釜江克宏 (付録執筆)

京都大学学術出版会 (2017). (in Japanese)

原子力年鑑 2018

中島健

日刊工業新聞社 (2017). (in Japanese)

Reviews

2016年ノーベル化学賞紹介【分子機械の設計と合成】

青木 伸

理大科学フォーラム **394** (2017) 42-43. (in Japanese)

生命に学ぶ生物有機化学・超分子化学—有機・錯体化学から生命科学・創薬科学へ—

青木 伸

理大科学フォーラム **397** (2017) 4-5. (in Japanese)

2016年のノーベル化学賞「分子機械」について

青木 伸

化学と教育 **65** (2017) 86-89. (in Japanese)

亜鉛リン酸塩ガラスにおける熱膨張係数異常に資するカチオン—酸素ネットワーク

小野寺陽平, 小原 真司, 正井博和, 是枝聡肇, 大窪貴洋

NEW GLASS **32** (2017) 25-29. (in Japanese)

Others

福島県南相馬・相馬地域仮設住宅の健康に関する仮設懇談会と検診の取り組み:

IFN- α 産生能検査から見えて来たもの

宇野賀津子, 嶋田裕記, 坪倉正治, 尾崎章彦, 橋野洸平, 山本佳奈, 越智小枝, 森田知宏, 高垣雅緒, 八木克巳, 金澤幸夫, 及川友好

Pasken Journal **26-29** (2017) 62-67. (in Japanese)

第24回 WPATH 国際シンポジウム参加報告「希望の性で生きることは基本的人権」

高垣雅緒, 宇野賀津子

藍野学院紀要/ Bulletin of Aino Gakuin 2017, 71-74. (in Japanese)

KURRI Progress Report 2017

Issued in August 2018

Issued by the Institute for Integrated Radiation and Nuclear Science,
Kyoto University
Kumatori-cho, Sennan-gun, Osaka 590-0494 Japan

Tel. +81-72-451-2300
Fax. +81-72-451-2600

In case that corrections are made, an errata will be provided
in the following webpage:
<https://www.rii.kyoto-u.ac.jp/PUB/report/PR/ProgRep2017/ProgRep2017.html>

Publication Team

HASEGAWA, Kei
INO, Yuta
INOUE, Rintaro (Subchief)
ITO, Kei
IWASE, Tomohiro
MORI, Kazuhiro (Chief)
NAKAYAMA, Chiyoko
SAITO, Takeshi
SAKURAI, Yoshinori (Subchief)
SEKIMOTO, Shun
SANO, Hiroaki
TSURUTA, Yachiyo
YOKOTA, Kaori